Charles University in Prague
Faculty of Mathematics and Physics

HABILITATION THESIS

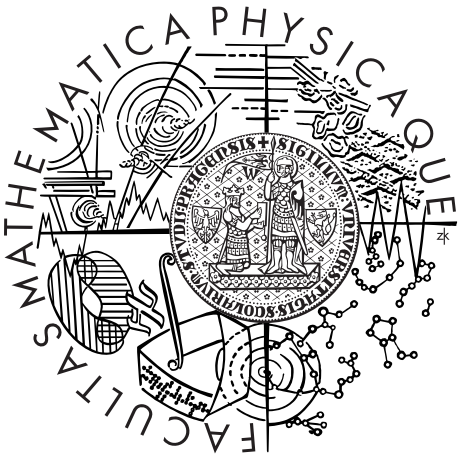

Tomáš Ostatnický

Exciton–photon interaction in two-dimensional systems

Praha 2014

Contents

1 Introduction

In this habilitation thesis, I propose a collection of eighteen journal publications and two chapters in books of which I am a co-author. My part of the work has been done in the Department of chemical physics and optics at the Faculty of Mathematics and Physics, Charles University in Prague and during my post-doc fellowship at the University of Southampton, UK. Also collaborations with the Department of thin films and nanostructures of Academy of Sciences of Czech Republic, Institute de Physique et Chimie des Matériaux de Strasbourg in France, University od California at San Diego, USA, and École Polytechnique Fédérale de Lausanne, Switzerland, were essential for the publications.

The aforementioned papers would not be written without an intense collaboration with experimentalists or without following particular experimental results on low-dimensional semiconductor structures. Most of the published works focus on the optical spectroscopy of semiconductor nanostructures, with picosecond time resolution and also often with high spatial resolution. The sophisticated spectroscopic methods used in the experiments require high preciseness and experience in the experimental part and are also challenging for theoretical work because the experimental data display only a result of indirect observation which is a fractional information about the state of electron excitations in the investigated system. Any need of a proposal of an innovative experimental setup to detect a particular phenomenon, need of an interpretation of the raw experimental data, simulation or identification of a process responsible for the behavior of the optical field, were mostly my motivation for the collaboration with experimentalists. In all publications, I contributed to theoretical parts which were essential in order to detect or interpret the observations.

The collection of publications in this thesis may be divided according to the three main subjects: optical waveguides, semiconductor quantum wells and semiconductor microcavities. Although the mentioned three physical systems may seem to be very different in their composition and physical properties, they reveal one common characteristics: they are effectively two-dimensional nanostructures in which the dynamics of electronic excitations, namely excitons, is observed by the methods of optical spectroscopy with spin (polarization) and ultrafast temporal resolution. The density of excitations in the system is imprinted into the optical field as a result of the exciton–photon interaction, which is a core theme of all the collected papers.

The work published in papers proposed in this thesis had been done in a close collaboration with many researchers who took an essential part in the process of the data acquisition, interpretation and publication. I would like to thank my colleagues at this place for willingness, support and many useful advices, in particular I thank prof. Petr Malý, prof. Bernd Hönerlage, prof. Ivan Pelant, prof. Jan Valenta, prof. Alexey Kavokin and prof. Pavlos Lagoudakis. I would like also to thank my friends who were always disposed to discuss physical problems and who had a large impact on the publications: dr. Kateřina Herynková, dr. Mathieu Gallart, dr. Jean–Pierre Likforman, prof. Leonid Butov, prof. Wolfgang Langbein, dr. Maria Maragkou, dr. Alastair Grundy and dr. Konstantinos Lagoudakis.

2 Two-dimensional semiconductor nanostructures and optical spectroscopy

The scope of the publications collected in this habilitation thesis, namely two–dimensional systems of excitons and photons, fully reflects the recent extensive development of both basic and applied research of nanotechnologies. Moreover, nanotechnologies are not just a subject of scientific research but they can be already found as a part of everyday electronics. The word *nanotechnology* can be understood in several different ways: the prefix *nano-* may represent a technique of fabrication of submicron structures including new methods with the aim at achieving the highest possible integration of electronic components in order to make smaller, more efficient devices. From the point of view of general physics, on the other hand, *nano-* is connected predominantly with the *quantum confinement* [1, 2] — the energetical spectrum of particles is significantly changed due to the breaking of the translation symmetry and thus spatial localization or modification of effective mass in the material by the structures with characteristic size in the nanometer domain. Usually localized states with discrete energetical spectrum (bound states) or delocalized states with notably modified energy dispersion in isolated bands are formed in nanostructures. As a direct consequence, the physical properties of the nanomaterials may significantly differ from those of bulk material: depending on the fabrication process and through precise control of growth conditions, it is possible to tune basic parameters of particles in nanostructures, for example their effective mass, lifetime or interaction energy with other (quasi-) particles.

Two-dimensional nanostructures are favorable for research of their basic physical characteristics in particular thanks to relatively easy way of their fabrication by deposition of uniform layers and also thanks to the in-plane translational symmetry what is a key point in simplifications in effective theories. Boundary conditions are therefore defined in parallel planes and it is thus possible to separate in-plane coordinates (denoted as x and y) from the coordinate with broken translational symmetry, usually denoted as z. The problem then effectively splits into a one-dimensional problem whose boundary conditions define the quantum confinement and a two-dimensional problem with translational symmetry. Systems in two dimensions moreover reveal a large advantage for the methods of optical spectroscopy: while both the surface effects plus the phenomena related to the propagation of excitations inside a bulk sample must be taken into account in experiments, light propagation in the z direction usually does not significantly distort the optical response of two-dimensional systems or a correction can be easily made. The optical image of two-dimensional nanostructures then contains a real imprint of particle density in the plane of a sample.

In the collected publications, we consider and investigate excitons in semiconductor crystals because they are a good model system of a well defined electronic excitation with a well defined energy, effective mass and symmetry. Wannier exciton — bound electron–hole pair [3] — has a nonzero dipole momentum and therefore it is possible to create excitons by pump optical beam which is absorbed in the material. It it also possible to detect the presence and the state of excitons by means of optical spectroscopy.

2.1 Waveguiding structures with semiconductor nanocrystals

Waveguiding samples and experiment

The samples which are researched in the publications [P1–P8] were prepared by ion implantation of silicon into fused silica slabs and subsequently annealed [4]. Under

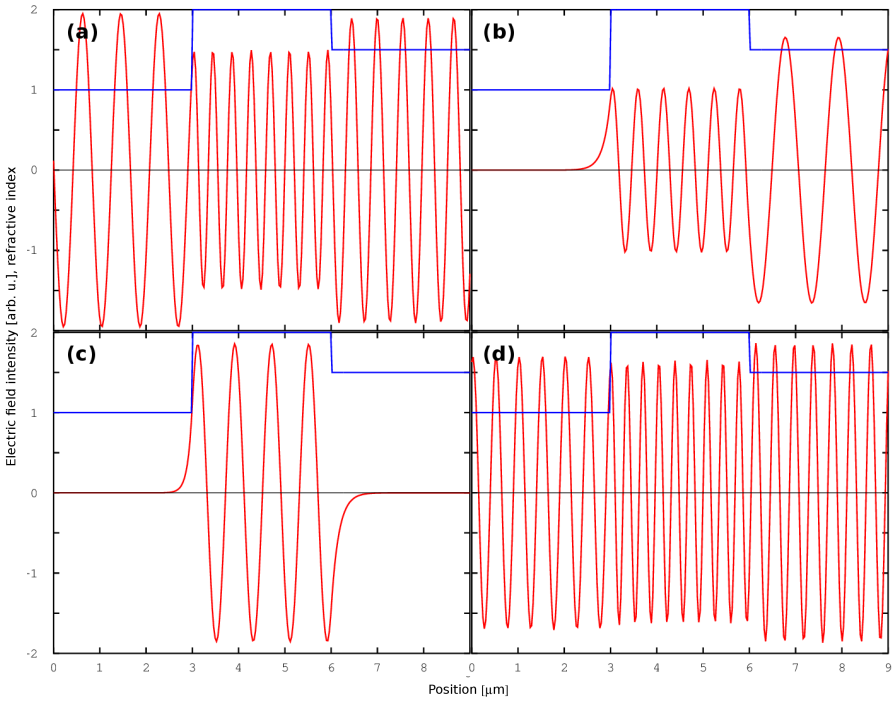

Figure 1: Electric field intensity distribution in direction z for waveguide modes (red color) and respective refractive index. (a) Radiation mode, (b) substrate mode, (c) guided mode, (d) evanescent mode.

the sample surface, a layer of silicon nanocrystals embedded in glass with thickness of several hundreds of microns is created. Quantum confinement of electrons inside the nanocrystals causes a relatively high efficiency of light luminescence after photoexcitation in the UV region. Furthermodre, a nonzero density of the nanocrystals in the sample modifies its refractive index slightly below the surface, creating a planar optical waveguide. We used a series of samples with different concentrations of embedded silicon nanocrystals.

The waveguiding structure in the samples reveals a continuous refractive index profile in the direction normal to the surface due to the kinetics of Si ions in the implantation process [5] and thus due to the variation of Si ion concentration before annealing. In an experiment designed for measurement of optical gain in materials, nanocrystals are excited by a laser beam and they then become a source of electromagnetic field *inside* the waveguide. That is a substantial deviation from conventional experimental setups for measurement of waveguide properties in which the light is coupled into the guiding layer from outside. The experimental setup, used in the research of waveguiding structures with silicon nanocrystals, therefore turns out to reveal particular optical artifacts when using standard spectroscopy methods like *variable stripe length method* [6] and it is therefore necessary to introduce corrections [7].

Theoretical description of electromagnetic field

Dielectric optical planar waveguides are formed by layers of materials which differ in optical density (refractive index) in the optical frequency domain. The variation of

the optical density in z direction can be step-like or continuous. Mathematically, it is possible do decompose any electromagnetic field which satisfies boundary conditions as a linear combination of the proper modes of the structure [8]: proper modes are characterized by frequency ω and wave vector components β_x and β_y in directions x and y while the size of the in-plane wave vector (propagation constant) is denoted $\beta = \sqrt{\beta_x^2 + \beta_y^2}$. We assume an asymmetric waveguide, i.e. the substrate refractive index n_s differs from that of the waveguide cladding n_c and usually the core refractive index n_f fullfils condition $n_\mathrm{c} < n_\mathrm{s} < n_\mathrm{f}$. The wave vector in the j-th layer can be defined as $k_j = \omega n_j / c$ where c is the vacuum light speed. In general, four types of proper modes are distinguished [9] (Fig. 1) and these modes form a complete basis of all states of electromagnetic field in the system:

- **Radiation modes** are delocalized in the whole space. They propagate in all layers including the substrate and the cladding. The optical spectrum is continuous, see Fig. 2. If such mode is coupled to a waveguide, it leaks out rapidly: partly into the substrate and partly to the cladding. Inequality $\beta < k_\mathrm{c}$ holds.

- **Substrate modes** do not propagate in the cladding but rather form an evanescent wave due to $k_\mathrm{s} > \beta > k_\mathrm{c}$. The field is delocalized in the core and the substrate only. When coupled to a waveguide, optical field is radiated into the substrate and propagates far from the core. The spectrum is continuous.

- **Guided modes** can propagate inside the core (if $\beta < k_\mathrm{f}$) and at the same time there exists no wave which can propagate in either cladding or the substrate with the same frequency and propagation constant: $\beta > k_\mathrm{s}, k_\mathrm{c}$. The mode is then localized in the core and its close surrounding with the energy density decreasing exponentially with increasing distance from the core.

- **Evanescent modes** are states of electromagnetic field with imaginary in-plane wave vector: $\beta^2 < 0$. Evanescent modes are principially radiative, i.e. they radiate their energy into the cladding and the substrate. In addition, they do not propagate as a harmonic wave in any direction in the plane of symmetry. These modes serve no information of practical use for light propagation inside the waveguides, however, they are mathematical solution of the wave equation with proper boundary conditions and therefore it is necessary to include them into the basis of physical solutions. Evanescent modes play a role only in the vicinity of the light sources located in the core.

Electric field intensity for the modes listed above can be written in the form:

$$\boldsymbol{E}_{\omega,\boldsymbol{\beta}}(\boldsymbol{r}, t) = \boldsymbol{E}_{\omega,\boldsymbol{\beta}}(z) \exp[\mathrm{i}(\beta_x x + \beta_y y - \omega t)] \,.$$

The symbol $\boldsymbol{r} = (x, y, z)$ denotes here the spatial coordinate. As follows from the discussion above, not all modes are necessarily two-dimensional: only the guided modes are localized in the z direction while the other groups are spatially delocalized. Furthermore for $\beta < k_\mathrm{c}$ there are neither guided nor substrate modes what makes a large difference between this photonic structure and a potential well for particles with a nonzero efective mass. Our research, nevertheless, aimed at light propagation in a close vicinity to the core and therefore we can consider only the guided and the substrate modes which decouple at small angles relative to the plane of symmetry and which then do not reveal fast leakage of energy from the optically active region.

It will be convenient to define several more variables in terms of geometrical optics. Let us, for illustration, consider a structure composed of three layers again depicted in Fig. 2b. The propagation angle ϑ is an angle of incidence of the rays

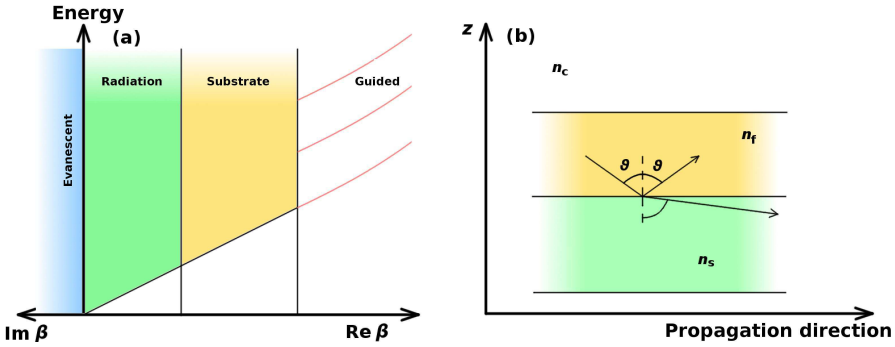

Figure 2: (a) Scheme of the mode dispersion of the dielectric waveguide. (b) Cross–section of the considered structure.

onto core/cladding and core/substrate boundaries from the side of the waveguide core and obviously $\beta = k_\mathrm{f} \sin\vartheta$. We can then define a reflection coefficient r_fc for the core/cladding boundary and r_fs for the core/substrate boundary, according to the Fresnel's formulae.[1] There are, in general, two critical values for the propagation angle denoted as $\vartheta_\mathrm{c} = \arcsin(n_\mathrm{c}/n_\mathrm{f})$ and $\vartheta_\mathrm{s} = \arcsin(n_\mathrm{s}/n_\mathrm{f})$. They refer to the crossover between normal reflection and total internal reflection at the respective core/cladding and the core/substrate boundary. According to the separation to the mode groups above, it is clear that $\vartheta < \vartheta_\mathrm{c}$ for the radiation modes which refract into the cladding, $\vartheta_\mathrm{c} < \vartheta < \vartheta_\mathrm{s}$ for the substrate modes and $\vartheta > \vartheta_\mathrm{s}$ for the guided modes, implying that the rays cannot be refracted into any of the cladding or the substrate. While there exists a radiation or a substrate mode for nonzero frequency when considering fixed $\vartheta < \vartheta_\mathrm{s}$ (modes are in continuum), the guided modes, on the other hand, must satisfy the condition of constructive interference for a defined $\vartheta > \vartheta_\mathrm{s}$:

$$r_\mathrm{fs} r_\mathrm{fc} \exp\left[\mathrm{i}d\sqrt{k_\mathrm{f}^2 - \beta^2}\right] > 0\,.$$

The expression on the left hand side must be real and d is the thickness of the core. With fixed ϑ, we can accomplish the condition only for discrete values of frequency and, consequently, at a fixed frequency, there exist only discrete values of the propagation angle ϑ. If we select an appropriate narrow spectral range, it is possible to observe a critical frequency ω_crit in this range such that there are N guided modes for $\omega \lesssim \omega_\mathrm{crit}$ and $N+1$ guided modes for $\omega \gtrsim \omega_\mathrm{crit}$.

2.2 Quantum wells

Basic definitions, interaction with electromagnetic field

Publications [P9–P13] report on results of research focused on optical spectroscopy of quantum wells of several types and compositions. There was, however, a property common to all structures: they were intrinsic, i.e. with no doping and thus revealing *excitonic resonance* [3] which then dominates optical response at photon energies close to the width of fundamental band gap. The exciton is formed after creation of an

[1] These coefficients differ in general for the two perpendicular linear polarizations TE and TM due to the symmetry of the problem. As the polarization effects are not discussed here, we drop the resolution of TE and TM and the variables here should be understood to stand for any of the polarizations.

electron–hole pair which is stable due to the attractive electrostatic force and reveals optical nonlinearities whose investigation was the subject of the research.

It is possible to fabricate a layered structure, similarly to waveguides, whose layers are made of materials with different band gap widths and thus effective potential energy for particles. Such structure may reveal quantum confinement in the z direction and the wave function of electrons (excitons) can be written:

$$\Psi(\boldsymbol{r}) = \psi_n(z)\psi_{\boldsymbol{k}_\parallel}(x,y)\,,$$

where n is a quantum number of a particle in one-dimensional potential well and $\boldsymbol{k}_\parallel$ is an in-plane wave vector, defined according to periodic boundary condition and Bloch theorem [3,10]. There are principially two different types of electron states in quantum wells: *bound states* and *scattering states*. The *bound states* are localized in the potential well and its close proximity in the z direction while they are delocalized in the remaining two dimensions. The *scattering states* are, on the contrary, fully delocalized in the whole structure. Electron gas in the localized states is then effectively two-dimensional in the xy plane. There is, however, a significant difference from optical waveguides: bound states exist for arbitrary in-plane wave vector $\boldsymbol{k}_\parallel$ and therefore there can exist a bound state even with zero wave vector $\boldsymbol{k}_\parallel = 0$.[2]

The heavy- and light-hole bands split in quantum wells with zinc-blende crystalic structure due to symmetry arguments, resulting in removal of fourfold degeneracy at the Γ point as compared to bulk crystals. This property is favorable for optical applications because it is then possible to optically inject electrons and holes with 100% net spin polarization [11]. It is possible to make many different types of structures with embedded quantum wells having various physical properties. We focused on main three types in the publications:

- In **type I quantum wells**, both an electron and a hole are localized in the same layer (see Fig. 3a) and they form a two-dimensional exciton with large overlap of the respective wave functions. Such exciton has a large dipole momentum [3,10] and consequently relatively large linear and nonlinear optical response.

- **Multiple type I quantum wells** are type I quantum wells separated by a barrier which eliminates particle tunneling. Without electromagnetic field, there is no coupling between the particular wells and the energetical spectrum is equivalent to that of a single well. The level degeneracy reflects the number of wells in the structure. Multiple wells are used in order to increase the optical response.

- **Type I double quantum wells** are composed of two type I wells, separated by a thin tunneling barrier for electrons or holes. As a result of tunneling, the double degeneracy is removed. By applying a DC electric field in the z direction, it is possible to spatially separate electrons and holes (see Fig. 3b): different particles are trapped in different wells what results in smaller spatial overlap and thus also the dipole momentum. Finally, their lifetime increases from tens to hundreds of picosecond [12] because the radiative recombination determines the exciton lifetime in high quality samples.

Exciton spin and its relaxation

The symmetry of crystal lattice of semiconductors can be rotational besides the translational symmetry. This symmetry is partly conserved in quantum wells with

[2]The bound state may not exist in shallow potential wells which reveal only the scattering states.

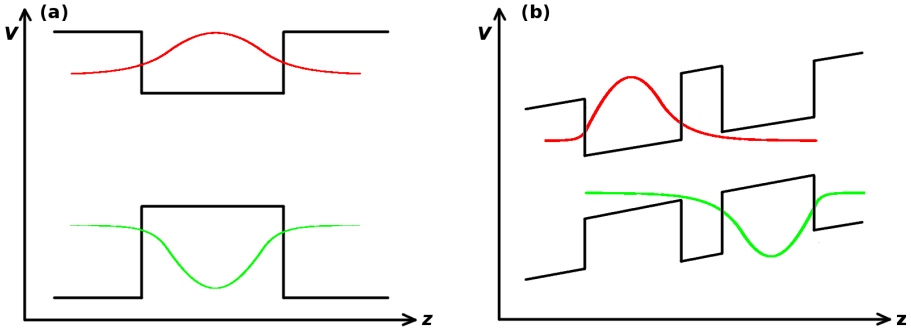

Figure 3: Spatial profile of ground state wave function of electron (red) and hole (green) in exciton in the z direction in type I quantum well (a) and type I double quantum well with applied electric field (b). Potential energy is depicted in black.

the main axis z. As a mathematical consequence of the crystal symmetry (and also rotational symmetry of the electron effective potential in a quantum well), the operator J_z of projection of angular momentum to the z axis commutes with Hamiltonian. The z component of angular momentum is then physically a constant of motion, i.e. magnetic quantum number is a good quantum number for an electron. This is true, however, only for electron at rest because:

$$\left[J_z, p_{x,y}\right] \neq 0$$

due to the absence of translationally-rotational symmetry. On the contrary, $[J_z, p_z]$=0 and therefore quantum confinement has no influence on conservation of angular momentum.

Electron spin is a good quantum number (it is a constant of motion) at the Γ point ($\boldsymbol{k}_{\|} = 0$) and outside it, electron's eigenstates are, in the first approximation, linear combinations of states with differents spins and with a fixed in-plane momentum. Electron spin with nonzero wave vector is not thus conserved but oscillates due to the *spin-orbit interaction* [13] which provides nonzero interaction energy of orbital motion and the spin. We usually apply k·p theory [14] and Kohn–Luttinger Hamiltonian [15] for calculation of the spin-orbit interaction. Beyond these theories, one must count in Dresselhaus term in non-centrosymmetric crystals, Rashba term in quantum wells and other terms according to the actual symmetry breaking of the system [13].

In combination of spin-orbit interaction and random electron scatterings on disorder or phonons, electron's spatial coherence is lost and spin effectively relaxes according to the *Dyakonovo-Perel's spin relaxation mechanism* [16]. Other major mechanisms are *Elliot-Yafet's mechanism* [17], describing spin loss through electron scattering on phonons and disorder with simultaneous electron spin-flip and *Bir-Aronov-Pikus' mechanism* [18] of spin relaxation by its exchange with a sea of holes.

Likewise the electron spin, the spin of an exciton is well defined at the Γ point [19]. Only those states with the symmery equal to that of electromagentic field are dipole active while the other states do not interact with optical field in the first order of perturbation theory. Due to the spin-orbit interaction, the exction spin is not conserved outside the Γ point what can be effectively expressed in terms of power series in size of the wave vector [20]. Direct absorption of a photon can, in principle, create only excitons with small wave vectors compared to the size of the first Brillouin zone and therefore we may neglect the quadratic and higher terms in the power series

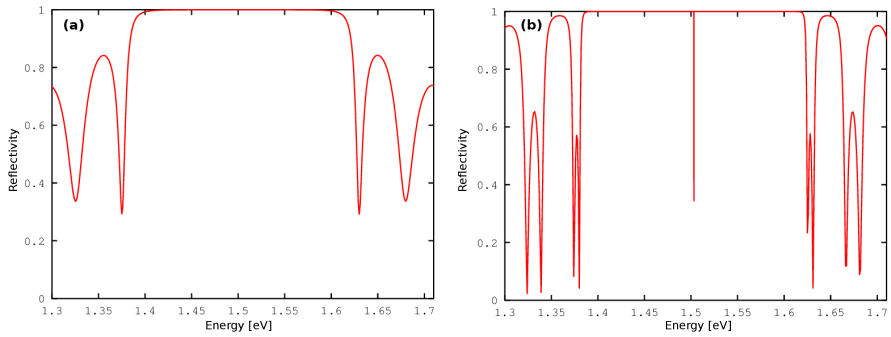

Figure 4: (a) Reflectivity spectrum of a Brag mirror, (b) reflectivity of an empty cavity with the same mirrors as (a).

and we may assume that optical injection creates only excitons with well defined spin. The spin sbsequently relaxes in picosecond time scale what can be measured with help of the ultrafast optical spectroscopy [21, 22].

Besides the exciton-specific features of spin-orbit interaction which come from a complex spin structure, as compared to electrons, also exciton–exciton electrostatic interaction shows up some particularity due to exciton's internal composite structure [23]. Spin of fermions (electrons and holes) can be exchanged during interaction of two excitons and therefore the two interacting excitons can exchange some spin. The effect is observable in four-wave mixing experiments in optical spectroscopy [22] and may be theoretically described in terms of nonlinear model of optical excitations in semiconductors [3, 24–34].

2.3 Microcavities

Empty cavity

As outlined on the Introduction, the last part of the collection of publications [P14–P20] refers about microcavities. These nanostructures mix two-dimensional quantum states of excitons and photons and also the eigenstates of the structure reveal properties partially of an electromagnetic wave and partially of a material wave. I propose rather a wide introduction to microcavities due to the amount of physical phenomena mentioned in the publications: it starts by introducing quantum confinement in optical cavities with dielectric mirrors and ends with topological defects in polariton condensates.

It was shown in the previous parts that photons in dielectric waveguides can be localized in the z direction only if their in-plane wave vector is nonzero while electrons and excitons are effectively two-dimensional in quantum wells irrespectively of their wave vector. Light localization is possible in circuits made of 1D waveguides, in microdisks or microspheres but we never simulate the properties of a 2D photon gas using 0D structures in particular because of their discrete energetical spectrum while the 2D gas has continuous spectrum and the density of states approaches a constant. The use of metallic mirrors, which would fully enclose the photons inside the cavity even for zero wave vector, are not suitable due to their absorption: the photon lifetime would be too short and it would not be possible to make it longer.

Photonic structures with Bragg dielectric mirrors solve the problem. There are altering layers with the optical thickness of $\lambda_{\mathrm{M}}/4$ in the mirrors where $\lambda_{\mathrm{M}}/4$ denotes

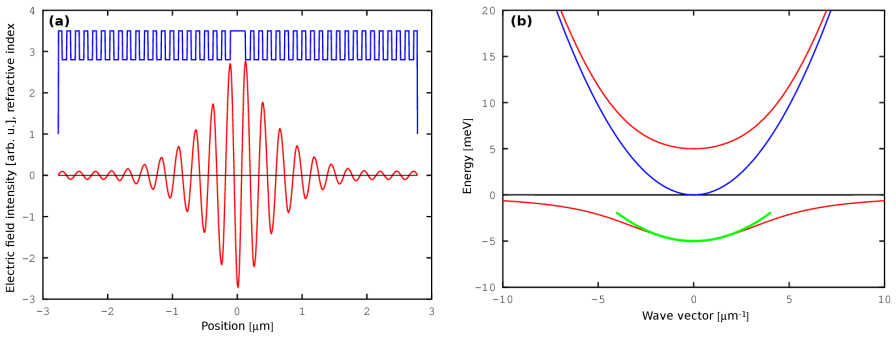

Figure 5: (a) Spatial profile of electric field intensity of an optical mode in a cavity in the z direction (red) and refractive index profile of a cavity and Bragg mirrors (blue). (b) Exciton dispersion, effective mass 0.5 m_e (black) where m_e is free electron mass; cavity photon dispersion with effective mass $5 \cdot 10^{-5} m_\mathrm{e}$ (blue) and that of polariton modes (red color). The green line depicts parabolic dispersion of the lower branch with effective mass $2 \cdot 10^{-4} m_\mathrm{e}$.

the central wavelength of the high-reflection band of the mirror (see Fig. 4a). Periodic structure made of materials with different refractive indices implies a modification of photon dispersion and formation of bands of allowed and forbidden energies. One of the gaps (band of forbidden energy) has its center at the wavelength λ_M. Real mirror consits of a finite number of layers and therefore evanescent modes (those lying in the band gap) can tunnel throught the mirror. Consequently, the mirror reflectivity is smaller than 100% but we can approach this limit arbitrarily by setting up properly the number of layers and refractive indices of layers. The only limitation is the accuracy of the technology during growth.

Optical resonator with Bragg mirrors is similar to the Fabry–Pérot resonator and differs only in the composition of the reflecting elements. The sharp maxima of the transmission satisfy condition:

$$\varphi_\mathrm{M}(\omega) + k_z(\omega) L_\mathrm{C} = m\pi\,, \qquad\qquad m \in \mathbb{N}\,,$$

where $\varphi_\mathrm{M}(\omega)$ is the phase shift of a photon with frequency ω during its reflection at the Bragg mirror (we consider both the mirrors the same), $k_z(\omega)$ denotes the wave vector in the cavity in the direction z at the frequency ω and L_C is the cavity length. If the resonation frequency of the cavity is close to that of the mirrors:

$$j\lambda_\mathrm{M}/2 \approx n_\mathrm{C} L_\mathrm{C}\,,$$

where j is an integer and n_C is the cavity refractive index, we observe a maximum of reflectivity of the whole structure as well as the reflectivity maximum of a single mirror but there is a sharp minimum at the wavelength $\lambda_\mathrm{C} \approx n_\mathrm{C} L_\mathrm{C}$ which represents a cavity optical mode (see Fig. 4b). The reflectivity minimum reveals a resonance which has a small spectral width usually at the order of 0.1 meV thanks to high quality of the resonator (high reflectivity of mirrors). The electric intensity profile at the frequency of the resonance depicted in Fig. 5a clearly shows an increase of the energy density of the field inside the cavity as compared to the space outside. Such increase is responsible for large nonlinearities of cavities into whose an optically nonlinear material is placed.

If we set the resonance frequency of the cavity much different from that of the mirrors, the frequency of the eigenmode is somwhere in between: its particular value

depends on many factors [35, pp. 63]. The important property in this case is, however, removal of the polarization degeneracy of the eigenstates — they split into TE and TM mode at nonzero wave vector.

One should note what is the largest difference between macroscopic cavities (e.g. laser cavity) and microcavities. There are two main points: firstly, there are limited diffraction losses of microcavities due to large ratio of the characteristic lateral size and the cavity length. Secondly, the eigenstates reveal an effectively continuous dispersion in microcavitites while we consider the laser cavity spectrum to be discrete. Furthermore, the microcavity dispersion is close to the parabolic one [35, pp. 62] inside the light cone what is a large deviation from the 3D photons with linear dispersion. We may then define an effective mass of the 2D photons. This effective mass can be tuned by the sample geometry and it varies in the order $10^{-4} - 10^{-5}$ of the free electron mass. We therefore usually apply a model of particles with nonzero mass and finite lifetime to the cavity photons. The annihilation process stands for the photon tunneling through mirrors and coupling to the 3D modes outside the cavity.

Strong interaction, polariton concept

As mentioned above, large optical nonlinearities emerge when an optically nonlinear material is placed into the cavity. Bulk material or low-dimensional objects can be used, usually quantum wells play the role of nonlinear medium due to their relatively simple and known band structure. The exciton absorption is the dominant effect among all contributions to optical absorption near the band edge in intrinsic semiconductors. The exciton–photon interaction energy is proportional to the overlap of their wave functions which is larger by orders of magnitude in a microcavity as compared to free space due to the high density of electromagnetic energy. The interaction energy then may exceed the value $2\hbar/T_2^*$, where T_2^* is an effective dephasing time of exciton. In that case, the photon coherence is conserved during its absorption and re-emission by excitons and therefore it does not undercome scattering but rather coherent oscillation in a common mode with excitons. Mathematically, we may describe the problem of exciton–photon oscillation by the equation for eigen-frequency ω of coupled linear harmonic oscillators with interaction energy V [35, pp. 151]:

$$\begin{aligned}(\omega_0 - \omega - \mathrm{i}\gamma)(\omega_\mathrm{C} - \omega - \mathrm{i}\gamma_\mathrm{c}) &= \frac{V^2}{\hbar^2}\,, \\ V &= \hbar\sqrt{\frac{2\omega_0\omega_\mathrm{LT}L_\mathrm{C}}{L_\mathrm{DBR}+L_\mathrm{C}}}\,,\end{aligned}$$

where ω_0 and γ are the frequency and dephasing rate of the bare exciton resonance and ω_C and γ_C are frequency and dephasing rate of the bare photon resonance. Longitudinal–transverse splitting of exciton is denoted as $\hbar\omega_\mathrm{LT}$ and finally L_DBR is an effective thickness of the Bragg mirror [35, pp. 63]. The eigen-frequencies of the modes of a nonlinear medium inside the cavity are then expressed as:

$$\begin{aligned}\omega_{1,2} &= \frac{\omega_0+\omega_\mathrm{C}}{2} - \frac{\mathrm{i}}{2}\big(\gamma+\gamma_\mathrm{C}\big) \pm \\ &\pm \sqrt{\left(\frac{\omega_0-\omega_\mathrm{C}}{2}\right)^2 - \left(\frac{\gamma-\gamma_\mathrm{C}}{2}\right)^2 + \frac{V^2}{\hbar^2} + \frac{i}{2}\big(\omega_0-\omega_\mathrm{C}\big)\big(\gamma-\gamma_\mathrm{C}\big)}\end{aligned}$$

The imaginary part of the frequency describes homogeneous linewidth of the appropriate spectral line. Let us put $\omega_0 = \omega_\mathrm{C}$ for illustration:

$$\omega_{1,2} = \omega_0 - \frac{\mathrm{i}}{2}\big(\gamma+\gamma_\mathrm{C}\big) \pm \sqrt{\frac{V^2}{\hbar^2} - \left(\frac{\gamma-\gamma_\mathrm{C}}{2}\right)^2}$$

If the term under square root is negative, then the square root is imaginary and the resulting modes are degenerate like in the problem of interaction of a quantum well with light. One of the modes is then a fully material wave while the second is fully photonic. If the term under the square root is positive, on the contrary, degeneracy is clearly removed and the modes split into two. The interaction energy must be sufficiently large for that purpose:

$$V > \hbar \frac{|\gamma - \gamma_C|}{2} .$$

The above condition is necessary but not sufficient: the modes must be physically distinguishable, e.g. two distinct peaks must arise in transmission spectra. We may require that the splitting energy must at least the sum of homogeneous linewidths:

$$\sqrt{\frac{V^2}{\hbar^2} - \left(\frac{\gamma - \gamma_C}{2}\right)^2} > \frac{\gamma + \gamma_C}{2} .$$

If the above conditions are met i.e. if the modes of the cavity split, it is a consequence of the *strong interaction* between the photon and the exciton which comes as a result of their increased wave function overlap due to the photon resonance in the microcavity. The photon and the material waves mix in the new eigenmodes and give rise to quasiparticles — polaritons — with partial material and partial electromagnetic character whose magnitude can be mathematically expressed through Hopfield coefficients [35, pp. 209]. Polaritons are widely known as optical excitations of bulk crystals however the microcavity polaritons differ in particular in dispersion depicted in Fig. 5b. It is important to observe the dispersion minimum at nonzero energy, it is non-parabolic and it contains inflection points. If we consider the dispersion as parabolic around its minimum and we also consider polariton's mixed character of partly material and partly photon wave, we conclude that these are extremely light and interacting particles with non-trivial dispersion — properties which are responsible for an interesting physics in the area of the optical spectroscopy of solid state.

Stimulated scattering and condensation

Polariton's total angular momentum (denoted here also as "spin") is 1 as well as photon's spin and therefore they obey Bose statistics.[3] Therefore, as for other bosons, stimulated scattering processes should be observable, for example stimulated scattering: if two polaritons with equal spins and with in-plane wave vectors $\boldsymbol{k}_1$ and $\boldsymbol{k}_2$ interact and scatter into final states with wave vectors $\boldsymbol{k}_3$ and $\boldsymbol{k}_4$ whose populations are N_3 and N_4 and if $\boldsymbol{k}_1 + \boldsymbol{k}_2 = \boldsymbol{k}_3 + \boldsymbol{k}_4$, the scattering rate is proportional to $N_3 + N_4 + 1$. Such effect can be observed in other bosonic systems in solid state, e.g. in exciton–exciton scattering [36], indeed in polaritonic systems the phenomenon is more pronounced due to weaker band filling.

The total momentum and energy of the particle pair must be conserved in an efficient scattering process. One possible geometry in two-dimensional systems is the scattering on an elastic circle in which two particles with opposite wave vectors (and equal energies) scatter to states with equal energies and opposite wave vectors again, which lie on a circle in reciprocal space due to conservation laws (see Fig. 6). This geometry for parametric interactions allows one to investigate the spin properties of the polariton–polariton interaction which reflects the complex spin structure of the

[3]This is true only in the low density limit as well as for excitons, i.e. band filling effects are negligible. Partial photonic character allows to reach much higher particle density as compared to excitons, until the band filling effects start to take place.

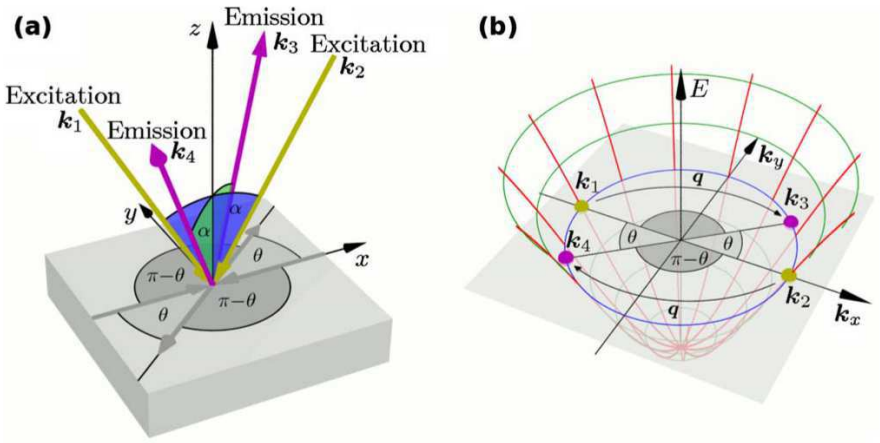

Figure 6: Scattering on elastic circle (a) in real and (b) in reciprocal space. Elastic circle is depicted in (b) by blue line while the red and green lines show the polariton dispersion in a microcavity. The incoming beams with wave vectors $\boldsymbol{k}_{1,2}$ are displayed by yellow line, scattered beams by the magenta line. From [P14].

exciton–exciton scattering due to particular fermion–fermion interaction. The spin of scattered polariton thus may depend on the angle of scattering.

Stimulated scattering is an important feature of the cavity polariton physics. It allows for creation of high density of particles in the minimum of their dispersion and reaching the quantum degeneracy limit. Condensate creation, its properties and dynamics are the large area of the research of microcavities which aims at spontaneous symmetry breaking, macroscopic coherence etc. This area is connected to condensates in other quantum systems but microcavities are very cheap "laboratory" as compared to other physical ssytems because phase transition is possible at room temperature and optical emission directly displays the particle density. The disadvantage is, on the other hand, short lifetime of polaritons due to tunneling through mirrors and is about 10–100 ps and it is sometimes hard to determine whether the system is in thermodynamics equilibrium or not.

Besides the resonant scattering, the condensate can be formed spontaneously. Incoherent electron–hole pairs are injected into the semiconductor optically, electrically or in other way. Then they quickly form bound free excitons and these subsequently relax their energy via optical phonon emission and finally by accoustic phonon emission. After few tens of picoseconds, they reach the polariton band [37]. Energy relaxation continues at sufficiently large polariton density due to stimulated processes (polariton–polariton or phonon–polariton) and finally a macroscopic population of particles in the energetical minimum — the condensate — is formed [38].

Condensates and topological defects

Researchers in the field of cavity polaritons are interested in also other subjects but the condensation kinetics: the major domains are research of spatial propagation and coherence [39], superfluidity [40, 41], topological defects of condensates, their kinetics and mutual interaction [42, 43], etc. The research areas mentioned here are connected with the spatial coherence and phase transition to condensed state which is described as the Kosterlitz–Thouless transition [44] to the superfluid phase.

The polariton system may be assumed to be a two-dimensional, weakly interacting gas with spin (polarization) degree of freedom, the total spin is 1. The lowest-energy state is ordered with long-range coherence of both phase and spin. In two dimensions, however, the ordering is broken by interaction with phonons and therefore the long-range correlations vanish at nonzero temperature. Even though there does not exist correlations at arbitrary distances, there is a local ordering as shown in [44]. The cited model is based on an analysis of thermodynamic variables assigned to topological defects, namely vortices in fluids. Isolated, freely propagating vortices may exist in a system if the Helmholtz free energy of an isolated vortex $F = U - TS$ is negative with U being the internal energy, T is temperature and S is entropy. The condition of negative free energy holds above the critical temperature:

$$T_{\mathrm{KT}} = \frac{\pi\hbar^2 n}{2mk_{\mathrm{B}}}\,,$$

where n is the particle density, m is their effective mass and k_{B} is the Boltzmann constant. The advantage of polaritons is seen from the formula: as compared to the atom nuclei in two dimensions, their mass is smaller by 8 orders of magnitude implying the critical temperature being by 8 orders of magnitude higher. Spontaneous ordering is disturbed by thermal fluctuations in a form of random creation of topological defects. Initially, a vortex pair of type particle–antiparticle (with opposite angular momenta) is virtually excited in the fluid. Above the critical temperature, the vortices dissociate and the particular quasiparticles move freely in the system, destroying the spatial phase coherence which then decreases exponentially with distance. The fluid is then in the normal (non-condensed) phase which is viscous due to the free vortices. At the temperature below T_{KT}, thermal fluctuations appear also as spontaneous creation of vortex–antivortex pairs but they cannot dissociate so they disturb the spatial phase correlations only locally and the phase correlation function decreases as a power law. The superfluid does not exist in terms of the global order in the system nevertheless local correlations provide persistent current loops and thus the superfluidity.

As proposed by the model, vortices are the elementary excitations of the system of spins. The rotation of the wave function phase is denoted by the number k which determine the number of 2π phase rotations due to the periodic boundary condition along a closed loop around the vortex core. We can define spin vortices as well: they are the linear polarization rotation along a closed loop around the core by an integer multiple $2\pi m$. As shown theoretically [45], mixed phase and polarization vortices are the lowes-energy excitations. In such type of vortices, the linear polarization rotates at a closed loop by only $\pm\pi$ and also the wave function's phase change must be $\pm\pi$ along the same loop in order to satisfy the periodic boundary condition. Both the quantum numbers are then half-integer and there exist four distinct basic vortices: $(k, m) = (\pm\frac{1}{2}, \pm\frac{1}{2})$.

The spatial correlation length of polariton condensates can be as large as tens of micrometers [39] and the vortex core diameter is of the order of micrometers. We can therefore directly observe condensates and their topological defects using spatially and spin-resolved optical spectroscopy. Optical spectroscopy may be successfuly used also in order to observe the behavior of the flow of polariton fluid in normal and superfluid phase. In experiments, a phenomenon similar to the spin Hall effect has been observed in the polariton system [46]. This phenomenon is caused by effective spin-orbit interaction which takes place due to the TE and TM polarization splitting of polariton eigenmodes in specially designed cavities. Also flow of the polariton fluid in normal and superfluid phase around defects has been detected [40, 41] and proofs of the existence of superfluid behavior have been proposed.

3 Overview of the results

All the publications collected in this habilitation thesis refer to the optical spectroscopy of two-dimensional semiconductor systems (nanostructures) and it is possible to divide them into three distinct groups as suggested in the Introduction:

1. optical waveguides,
2. semiconductor quantum wells,
3. semiconductor microcavities.

I give a comment to all of the groups in this part of the thesis in which the original results and context of the publications are introduced. The most of the papers contain an extensive experimental part, for example, they present observations of new phenomena whose interpretation was, however, possible only with a theoretical background. Finally, detailed theoretical modelling in order to confirm or refuse hypotheses about the origin of the effects was necessary. I consider such collaboration of the theoretical and experimenal physics as the advantage of the publications due to the wide characterization of the physical system.

3.1 Optical waveguides

Submicron size of a material may notably change its physical properties as compared to bulk. Silicon nanocrystals are one example: they reveal strong photoluminescence in the visible spectral range with quantum efficiency by orders of magnitude higher than the 3D crystal whose band structure contains indirect optical band-to-band transitions and thus phonon scattering is necessary for photoluminescence. Quantum confinement (charge localization) causes delocalization of the wave function in the reciprocal space, leading to a partial overlap of wave functions of electron and hole what makes the optical transitions to be direct.

Silicon nanocrystals revealed themselves as a promising material for construction of an efficient light source based on silicon technology, in particular for construction of a laser which could be integrable to the existing platform of silicon opto-electronics. The *variable stripe length method* (VSL) [6] is widely used for determination of the size of optical gain, which is essential for the laser operation. The method is based on measurement of the photoluminescence intensity when varying the lenght of an optically excited stripe. The method has been applied among others to waveguiding samples with optical waveguides [7]. The measurements reveal, however, optical artifacts whose origin was not clear. Futhermore, the photoluminescence spectra contain distinct unexpected maxima, see Fig. 7 whose position is a characteristics of particular samples. Such mode structure was observed also in other waveguiding samples prepared using a different method [47].

We performed a detailed experimental characterization of the above mentioned modes in [P1–P3] and we proposed the hypothesis about their origin. Waveguiding samples behave similarly to the common (passive) planar waveguides, however they show up one additional property: the light source is *inside* the waveguide core while the light coupling to the passive waveguides is from outside. Nanocrystals in the core of the *active waveguide* therefore emit light to the whole wide spectrum of eigenmodes introduced in the part 2.1 i.e. not only to the guided modes (with continuous spectrum) but also into the substrate modes. When using the particular detection optics, light is collected from a small spatial angle and thus we select only those substrate modes which propagate along the core from their continuum of states. The propagation direction of substrate mode is connected with the angle of mode propagation

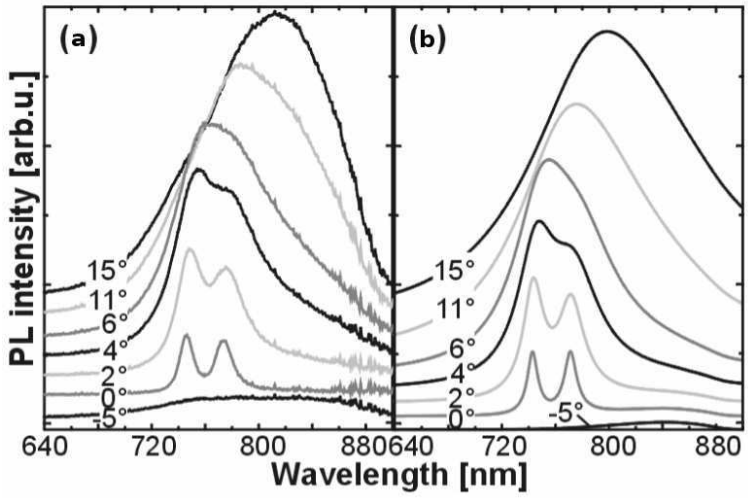

Figure 7: Comparison of experimental (a) and theoretical (b) photoluminescence spectra collected along the waveguiding layer of an active waveguide with silicon nanocrystals. Spectra were detected and simulated at distinct deviations of the detection direction from the direction of guiding, denoted as an angle close to the curves. From [P7].

direction in the core ϑ through the Snell's law while the substrate modes of interest satisfy $\vartheta \lesssim \vartheta_s$. Using Fresnel's formulae, we found that the reflectivity of the wave with $\vartheta \lesssim \vartheta_s$ on the core/substrate boundary is close to one. Light in such type of substrate modes is therefore guided inside the core for several tens of roundtrips before it decouples into the substrate and it must therefore satisfy the condition of constructive interference as well as the guided modes. It is possible only for discrete energies and therefore we observe pronounced maxima in photoluminiscence spectra at particular wavelengths, characteristic for each of the samples. We compare the hypothesis in [P1–P3] with experimental data and we performed additional measurements in order to check the validity of the theory. The additional experiments clearly identified the substrate modes and not the guided modes to be responsible for the phenomenon. We compare the luminiscence and transmission spectra in [P4] and we show that spectral positions of peaks are equal what is a clear confirmation of the theory.

The existence of observable substrate modes in the active planar waveguides with silicon nanocrystals clearly implies the strong influence of mode leakage into the substrate on measurements of the optical gain using the VSL and other methods. The major question is, whether it is possible to reach positive net gain of these modes. Our theoretical model is presented in detail in [P5] where also relevant formulae for an estimate of luminescense response of a bulk or a waveguiding sample in various experimental geometries are derived. With the help of numerics, we have marked distinctions in the response of 3D and 2D samples which comes from the presence of the substrate modes. The calculations show that corrections are essential in order to properly determine the net gain value in VSL experiments. The theory of the active waveguides and theoretical calculations of the optical field distribution across the waveguide, of the optical gain etc. are summarized in the in-book chapter [P7]. The overview of the experimental results with a basic theoretical description is presented in another chapter [P8].

The last publication [P6] dedicated to optical waveguides reports a phenomenon which had not been yet described in the literature. Using the laser-induced transient grating method, we measured the diffusion coefficient of excitons created by the laser beam in a layer of silicon nanocrystals embedded in a waveguide. In this method, the efficiency of diffraction on the transient grating is measured as a function of time and grating period. Then it is possible to determine the diffusion coefficient from the dependency of the time decay constant of the signal on the grating period. The standard analysis of data results in the diffusion coefficient $D = 420$ cm^{2}s^{-1} in our experiment what is a value larger by one order of magnitude than the coefficient for bulk silicon $D_{\mathrm{Si}} \approx 10$ cm^{2}s^{-1}. There must therefore exist another important physical effect besides diffusion which causes significant decay of the grating contrast at the time scale of picoseconds. We proposed a hypothesis based on an optical grating-induced feedback for photons which propagate in the waveguide. The feedback amplifies spontaneously emitted light in the layer with crystals what leads at the end to fast stimulated recombination of the excited states. As we show in the numerical calculations, the rate of stimulated recombnation is affected by the period of grating and therefore significantly influences the measurement of the diffusion coefficient.

3.2 Semiconductor quantum wells

The publications in the area of quantum wells may be separated into two subgropus according to their particular subject: spin-related papers aiming at nonlinear spin interactions in single quantum wells [P9–P11] and the other subgroup with works aiming at spin transport in double quantum wells [P12–P13].

The paper [P9] deals with the basic characterization of the exciton and biexciton wave functions. Based on the group theory, we deduce the spin structure of the symmetrized wave functions of exciton and biexciton states as a combination of the electron and the hole spin for quantum wells made from materials with wurtzite and zinc-blende crystallographics structure and grown in main crystallographic directions. We then apply the method of invariants to these wave functions and we derive appropriate Hamiltonians which describe mixing of the symmetrized states what results e.g. in the mixing of the states with equal spin and wave vector and different band index in quantum wells. The size of this particular effect is also shown numerically.

We deal with nonlinear interactions of excitons in the article [P10], focusing on the spin in optical four-wave mixing. There is a variety of models describing the same thing which are based on semiconductor Bloch equations [24] or microscopic theories with higher electron–hole correlation terms [25–28] and finally there are models which consider level schemes with exciton states [30–34]. From the cited sources, only those microscopic theories with higher-order correlation terms give the correct predictions of both the dynamics and spin of the output signal: in semiconductor Bloch equations, a reduced density matrix is used whose elements are two-point correlation functions while the higher correlations are factorized in the kinetic equations in order to obtain a closed set of equations. Higher order terms, consisting of informations about spin-spin correlations, are absent. This disadvantage is corrected in the models which contain full higher-order terms. Although the microscopic theories are successful, they require time-consuming numerical evaluation. It is then much easier to resolve an empiric model in a form of an exciton level scheme where the polarization of the response can be found analytically. The polarization predictions of the existing models nevertheless fail in some cases, presumably due to an inaccurate symmetry of the starting Hamiltonian. Our model, published in [P10], has been found in order to take into account the full symmetry of the relevant states which take place during the nonlinear interaction and to give appropriate analytic predictions of the physical

properties of the nonlinear optical response. We choose the basic optical excitations in intrinsic semiconductors, namely the exciton and biexciton states as the starting point, taking into account their correct internal structure, according to the composition of the host material (bulk semiconductor, quantum well). The Hamiltonian contains the interaction term for the exciton–exciton scattering which respects the spin structure of particles and which is the key element for the nonlinear interactions. We then derive kinetic equations for the reduced density matrix with four-point correlators whose analytic solution is possible and the calculation of the outgoing polarization reduces to an algebraic problem. Predictions of the model in [P10] agree with the microscopic theories. The complexity of the calculations is, on the other hand, much smaller and the model is applicable to systems with any arbitrary symmetry with only minor modifications.

Time evolution of the exciton spin in GaAs quantum wells is analyzed in the paper [P11]. Using the time- and spin-resolved optical spectroscopy, we measure the dynamics of nonlinear response of excitons in multiple quantum wells. The study is unique due to the use of pump and probe technique whose time-integrated response after excitation by a picosecond pulse is detected in a wide spectral range which covers the most of excitonic resonances of the system. We were able to accurately determine the density of bright and also dark excitons from the differential transmission spectra by spectral shape fitting. We proposed a simple level scheme which describes the system's dynamics, including the spin relaxation. We consider the proper particle (exciton and biexciton) symmetry in the model according to [P9] and we perform numerical fit of the measured dynamics in order to extract the appropriate spin relexation times for particular processes, including spin relaxation of electrons, holes and whole excitons. Even though the resulting data just confirmed the previously published results measured by different techniques, our publication still has some impact due to the complex analysis of the spectra of the response and also thanks to the consistency of the kinetic model. These facts refute doubts about the correctness of interpretation of e.g. degenerate pump and probe experiments on which most of previous publications were based.

In semiconductor double quantum wells, we investigated spin transport of excitons at macroscopic distances. In the paper [P12], the transport is diffusive while it is ballistic in [P13]. In both works, DC voltage is applied across the layered structure what results in spatial separation of electrons and holes to individual quantum wells. The Coulomb interaction across the tunnelling barier is still strong enough in order to allow creation of the bound electron–hole pairs — indirect excitons. Such excitons have long lifetime due to slow radiative recombination and they can therefore travel over large distances (up to tens of micrometers) during diffusive transport, even though their effective mass is large (comparable to the free electron mass). Besides the particle transport, we are interested mainly in the spin transport in our study: as the exciton spin relaxes, according to the part 2.2, it is not clear whether the diffusive spin transport could be efficient. Based on an experiment and subsequent theoretical analysis, we show in [P12] that the spin transport is possible at the distance of several micrometers and we discuss critical parameters which influence the spin transport efficiency.

It is possible to observe ballistic exciton transport at higher exciton densities which are accessible through increase of the energy density in the optical excitation. Hot excitons in double quantum wells quickly relax their energy after optical excitation and access low-energy states whose temperature can drop below the quantum degeneracy limit due to the exciton long lifetime. Exciton–exciton interaction then effectively screen exciton interactions with static defects and low temperature reduces the strength of interactions with phonons. Exciton transport is then ballistic with

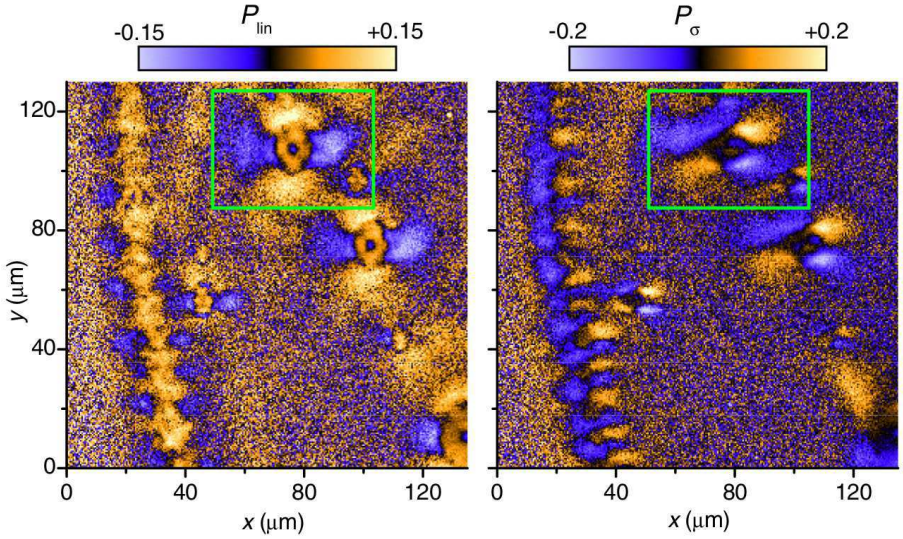

Figure 8: Degree of linear polarization P_{lin} and degree of circular polarization P_σ of indirect excitons in double quantum wells. The green box encloses the same object under the same experimental conditions with the exception of the detection optics which is set to different polarization components. The exciton source is in the centre of the green box. From [P13].

the coherence lenght of the order of few micrometers [48]. We observed spin structures which form spin vortices in linear polarization [P13] in systems of excitons, propagating from a point source (see Fig. 8). We propose a theoretical model for the interpretation of the phenomenon in which we consider coherent exciton propagation and we include spin precession due to spin–orbit interaction. The model outputs are in agreement with the experimental data. The model contributes to understanding of the dynamics of the charge carriers in the researched structure and in general it contributes to the knowledge of the dynamics of quantum degenerate systems of bosons and fermions.

3.3 Semiconductor microcavities

In the publications in the microcavity area included in this habilitation thesis, the research subject are the parametric interactions of polaritons with the special attention to the polariton spin and manifestation of the spin coherence. In the primary works [P14–P15], we develop a theory of spin–spin interactions on the elastic circle: two polaritons with opposite momenta scatter into states on the elastic circle in the opposite positions in reciprocal space due to momentum conservation. We analyze the scattering amplitudes in the paper [P14] using microscopic calculation, taking into account the spatial and spin structure of polaritons. The calculations show that the degree of optical polarization of the scattered particles is not isotropic and it is strongly influenced by the composition and spatial separation of the electron and hole wave function as a result of e.g. applied DC electric field perpendicular to the sample plane. We further analyze the same geometry of the experiment in [P15] considering additionally stimulated processes. There is a clear crossover between spontaneous scattering with low polarization degree and the stimulated scattering regime with almost 100% polarization degree of the final states. Furthermore, we show theoretically the existence of breaking of the spatial symmetry by the presence of the excitation beams. The scattered polaritons in the stimulated regime do not occupy the whole

elastic circle but rather discrete points so that the scattered beams propagate perpendicular to the incoming beams in the real space. Finally we point out that the particular experimental geometry may be used in order to construct logical X–NOR gate whose logical information is stored in the polarization of optical field.

Theory of logical circuits is further discussed in the paper [P16] on a model system made of a microcavity covered by a line of thin metal rectangles. Eigenstates of the microcavity–metal structure are a combination of the Tamm plasmon and exciton–polariton [49] and they have lower energy compared to the cavity without the metal stripe on its surface. The metal areas are then the potential wells for optically excited states what is a promising feature for construction of circuits for optical excitations. The dependency of the particle density in the nanostructure on the external illumination density is nontrivial and reveals a hysteresis loop and therefore bistable behavior. One bit of the logical information may be then represented by the particle density depending in which of the two bistable states the system is. We show, using numerical calculations based on the solution of the Gross–Pitaevskii equation, that a logical information propagates in the chain of the areas with the metallic rectangles on the top in a form of switching the polariton density from one branch of the hysteresis loop to the other one. The gap between the rectangles plays a role of a barrier through which polaritons tunnel from the neighboring well and move the hysteresis loop in the actual well such that the density of polaritons skips to the second hysteresis branch. In this way it is possible to "transport" the information to the logical gate where it is evaluated and the result may be carried in the same manner towards the next gate. We also demonstrate theoretically that the hysteresis loops may be shifted by applying electric field across the structure. It is then possible to construct field effect transistor for polaritons or we may utilize the effect in setting up the logical information in the circuit using electric field and connect integrated electronics and optics.

A possibility of an efficient condensation kinetics in a microcavity is experimentally investigatedin the paper [P17]. Cavity polaritons are promising for construction of efficient coherent light sources in particular due to theoretically higher quantum efficiency as compared to usual lassers and due to the absence of a threshold for coherent emission. Kinetics of the polariton condensation from a thermal state to the bottom of the polariton band is rather complex because the condensation requires several interactions with accoustic phonons in the area where the polariton lifetime is in the picosecond scale. Polaritons cumulate in the zone with negative effective mass (*polariton bottleneck*) and they annihilate due to their short lifetime. Condensation is possible only above some critical density [38] at which the phonon–assisted scateerings are stimulated and the energy relaxation is fast enough. Clearly there is a nonzero threshold on the contrary to the early theoretical estimate. We take an advantage of the relaxation mechanism by optical phonon emission in the study [P17]: the phonon energy is well defined in semiconductor crystals and the interaction energy is by an order of magnitude larger as compared to the accoustic phonon emission. The whole microcavity struture was designed such that the ligh hole (LH) exciton band was above the polariton band minimum approximately by the energy of an optical phonon. The relaxation then was a one–step process of the optical phonon emission from the LH band directly to the bottom of the polariton band. The system was optically pumped at the LH exciton energy and we measured the threshold for coherent emission as a function of the energy diffrence between the LH exciton band and the bottom of the polariton band. We found that this dependency is nontrivial so we conclude that the energy relaxation by optical phonon emission may be efficient and we may use the effect in electronic components where the system is electrically pumped across a proper tunneling barrier.

The study of topological structures and perturbations is an indispensable part of

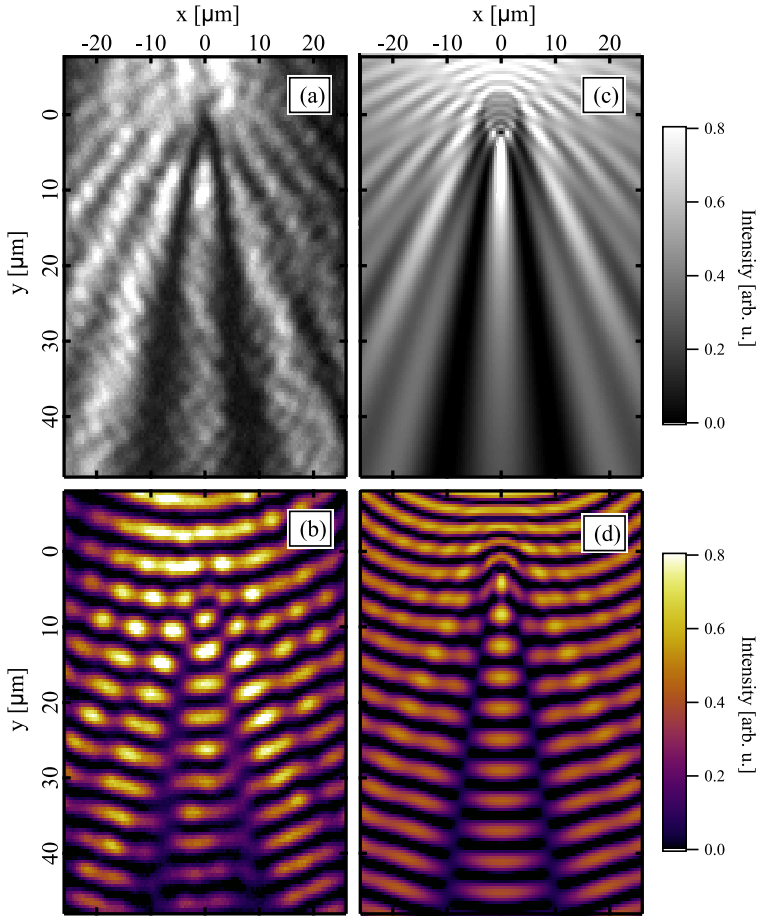

Figure 9: Results of an experiment (a),(b) and theoretical simulation (c),(d) of intensity of 2D optical field in a microcavity in real space when an optical wave approaches a defect. The light is incident on a defect at the position (0,0) with the size of 3 μm and propagates along the y axis. The plots (b) and (d) show an interference patterns after interference with a reference beam. From [P20].

the condensed matter physics. There was a successful observation of phase vortices in polariton condensates [50] but theory [45] predicates the existence of half-phase and half-polarization vortices as being the elementary excitations in the cavity polariton systems. We focus in the paper [P18] on experimental evidence of this type of vortices, using spin-resolved optical spectroscopy. With the help of several different experiments, we unambiguously showed the existence of the mentioned vortices, confirming theoretical models of polariton fluids and quantum systems with the spin degree of freedom in general and we opened the way for both theoretical and experimental research of the dynamics of new topological defects in condensates.

In the last two publications listed in this thesis, we consider linear effects in microcavities without nonlinear medium (with no exciton–photon interactions). The studied system is therefore an effectively two-dimensional non-interacting photon gas. On the contrary to waveguides, cavity photons reveal parabolic dispersion and the state with zero in-plane wave vector is a well defined eigenstate of the system. Study of the photon dynamics in the linear regime is essential in order to understand the influence of the interactions with material on the photon behavior or to study the effect of optical nonlinearities on the characteristics of the photon gas. In the first study [P19], we investigate polariton spin-orbit interaction and its consequences for the so-called

optical spin Hall effect [46]. While the authors of Ref. [46] claim that exciton–photon interaction is necessary for the phenomenon, both theoretical calculations and experimental data in [P19] unambiguously show the opposite. We interpret the phenomenon in terms of photon ballistic transport and effetive spin–orbit interaction. The conclusions refer to and support the paper [P13] where we discuss ballistic transport and spin–orbit interaction in the system of indirect excitons in double quantum wells.

The theory of phase transition to the superfluid state by Kosterlitz and Thouless [44] defines the critical temperature under which there is a nonzero density of particles in locally correlated state in the system. The theory is, however, formulated for spinless particles with an infinite lifetime while cavity polaritons have nonzero spin and the lifetime comparable to the thermalization time. Despite of these facts, theoretical works indicate that cavity polaritons should be able to reach the macroscopically ordered state. Nonetheless it is the experiment which plays the key role and confirms theory. There were several publications claiming on the polariton superfluidity [40,41] in which the fluid was tested with several criteria for superfluidity. In the experiments, the fluid mostly flows around an artificial defect and the fluid density is investigated under different excitation conditions. Since it is possible to create the cavity polaritons in a condensed state at an arbitrary point in the k-space by resonant optical excitation, the influence of the fluid density and velocity on their scattering by the defect and formation of dark solitons is widely studied. We perform a very similar study in the publication [P20] in fully linear regime both experimentally and theoretically — we study the linear scattering of the 2D photon gas on a defect and we also investigate the role of the scattering in formation of structures similar to dark solitons and vortices. Our results show that the criteria widely used up to now in order to indentify the superfluid state are not sufficient for unambiguous confirmation of its existence. The same structures with similar dimensions like in the proposed polariton superfluids were identified in the optical response of the linear system both in the experiment and theory under similar experimental conditions (see Fig. 9). It does not mean, however, that the polariton superfluid does not exist. The clear message is, that we should apply additional criteria for confirmation of the superfluidity and perform supplementary experiments which give an answer to the question what is the critical temperature for superfluid and whether it is possible to reach it.

4 The role of theory in optical spectroscopy

Optical spectroscopy consists of various experimental methods for indirect observation of phenomena which occur in the investigated physical systems. One of the systems of interest are semiconductors which are the subject of the collection of publications in theis thesis. Despite of the experimental character of the methods used in optical spectroscopy, it is not a purely experimental discipline: the data from indirect observations need to be analyzed and interpreted, often with the help of theoretical models and computer simulations. Furthermore, in the era of the extensive development of nanostructures and hybrid structures of various materials, the standard experimental methods are not suitable for research of some particular properties of samples and therefore it is necessary to develop new methods or to improve the older ones. One then needs in some cases theoretical modeling and computer analysis of the design of the setup. Most of the publications in this thesis reflect intensive collaboration of the experiment and theory to which I contributed considerably. This type of collaboration should continue at Faculty of Mathematics and Physics at Charles University in Prague, for example recent publication [51] deals with measurement and theoretical description of Kerr effect in magnetic semiconductors based on GaAs.

References

[1] U. Woggon, *Optical properties of semiconductor quantum dots*, Springer tracts in modern physics vol. 136, Springer, Berlin, 1997.

[2] S. V. Gaponenko, *Optical properties of semiconductor nanocrystals*, Cambridge studies in modern optics, Cambridge University Press, Cambridge, 1998.

[3] H. Haug and S. W. Koch, *Quantum theory of the optical and electronic properties of semiconductors*, World Scientific, Singapore, 2004.

[4] J. Valenta, I. Pelant, K. Luterová, R. Tomasiunas, S. Cheylan, R. G. Elliman, J. Linnros, and B. Hönerlage, Appl. Phys. Lett. **82**, 955 (2003).

[5] R. G. Elliman, M. J. Lederer, and B. Luther-Davies, Appl. Phys. Lett. **80**, 1325 (2002).

[6] K. L. Shaklee and R. F. Leheny, Appl. Phys. Lett. **18**, 475 (1971).

[7] J. Valenta, I. Pelant, and J. Linnros, Appl. Phys. Lett. **81**, 1396 (2002).

[8] A. W. Snyder and J. D. Love, *Optical waveguide theory*, Chapman & Hall, London, 1983.

[9] R. E. Smith and S. N. Houde-Walter, J. Opt. Soc. Am. A **12**, 715 (1995).

[10] U. Rössler, *Solid state theory*, Springer, Berlin, 2009.

[11] M. I. Dyakonov and V. I. Perel, in *Optical Orientation*, edited by F. Meier and B. Zakharchenya, Modern problems in condensed matter sciences vol. 8, chapter Theory of optical spin orientation of electrons and nuclei in semiconductors, North–Holland, Amsterdam, 1984.

[12] T. Fukuzawa, S. S. Kano, T. K. Gustafson, and T. Ogawa, Surf. Sci. **228**, 482 (1990).

[13] M. E. Flatté, J. M. Byers, and W. H. Lau, in *Semiconductor spintronics and quantum computation*, edited by D. D. Awschalom, D. Loss, and N. Samarth, chapter Spin dynamics in semiconductors, Springer, Berlin, 2002.

[14] F. T. Vasko and A. V. Kuznetsov, *Electronic states and optical transitions in semiconductor heterostructures*, Springer, Berlin, 1998.

[15] J. M. Luttinger and W. Kohn, Phys. Rev. **97**, 869 (1955).

[16] M. I. Dyakonov and V. I. Perel, Sov. Phys. JETP **33**, 1053 (1971).

[17] R. J. Elliot, Phys. Rev. **96**, 266 (1954).

[18] G. L. Bir, A. G. Aronov, and G. E. Pikus, Sov. Phys. JETP **42**, 705 (1975).

[19] K. Cho, Phys. Rev. B **14**, 4463 (1976).

[20] B. Hönerlage, R. Lévy, J. B. Grun, C. Klingshirn, and K. Bohnert, Phys. Rep. **124**, 161 (1985).

[21] C. F. Klingshirn, *Semiconductor optics*, Springer, Berlin, 1995.

[22] J.-C. Diels and W. Rudolph, *Ultrafast laser pulse phenomena*, Academic Press, Amsterdam, 2006.

[23] S. Okumura and T. Ogawa, Phys. Rev. B **65**, 035105 (2001).

[24] M. Lindberg and S. W. Koch, Phys. Rev. B **38**, 3342 (1988).

[25] K. Victor, V. M. Axt, and A. Stahl, Phys. Rev. B **51**, 14164 (1995).

[26] M. Lindberg, Y. Z. Hu, R. Binder, and S. W. Koch, Phys. Rev. B **50**, 18060 (1994).

[27] V. M. Axt and A. Stahl, Z. Phys. B **93**, 195 (1997).

[28] T. Östreich, K. Schönhammer, and L. J. Sham, Phys. Rev. B **58**, 12920 (1998).

[29] T. Aoki, M. Kuwata-Gonokami, and A. A. Yamaguchi, Phys. Rev. Lett. **82**, 3108 (1999).

[30] K. Bott, O. Heller, D. Bennhardt, S. T. Cundiff, P. Thomas, E. J. Mayer, G. O. Smith, R. Eccleston, J. Kuhl, and K. Ploog, Phys. Rev. B **48**, 17418 (1993).

[31] E. J. Mayer, G. O. Smith, V. Heuckeroth, J. Kuhl, K. Bott, A. Schulze, T. Meier, D. Bennhardt, S. W. Koch, P. Thomas, R. Hey, and K. Ploog, Phys. Rev. B **50**, 14730 (1994).

[32] G. Finkelstein, S. Bar-Ad, O. Carmel, I. Bar-Joseph, and Y. Levinson, Phys. Rev. B **47**, 12964 (93).

[33] K. Victor, V. M. Axt, G. Bartels, A. Stahl, K. Bott, and P. Thomas, Z. Phys. B **99**, 197 (1996).

[34] T. Häupl, H. Nickolaus, F. Henneberger, and A. Schülzgen, phys. stat. sol. (b) **194**, 219 (1996).

[35] A. V. Kavokin, J. J. Baumberg, G. Malpuech, and F. P. Laussy, *Microcavities*, Oxford University Press, Oxford, 2007.

[36] D. Hägele, S. Pfalz, and M. Östreich, Solid State Commun. **134**, 171 (2005).

[37] F. Tassone, C. Piermarocchi, V. Savona, A. Quattropani, and P. Schwendimann, Phys. Rev. B **56**, 7554 (1997).

[38] J. Kasprzak, M. Richard, S. Kundermann, A. Baas, P. Jeambrun, J. M. J. Keeling, F. M. Marchetti, M. H. Szymańska, R. André, J. L. Staehli, V. Savona, P. B. Littlewood, B. Deveaud, and L. S. Dang, Nature **443**, 409 (2006).

[39] E. Wertz, L. Ferrier, D. Solnyshkov, R. Johne, D. Sanvitto, A. Lemaître, I. Sagnes, R. Grousson, A. V. Kavokin, P. Senellart, G. Malpuech, and J. Bloch, Nat. Phys. **6**, 860 (2010).

[40] A. Amo, J. Lefrère, S. Pigeon, C. Adrados, C. Ciuti, I. Carusotto, R. Houdré, E. Giacobino, and A. Bramati, Nat. Phys. **5**, 805 (2009).

[41] A. Amo, D. Sanvitto, F. P. Laussy, D. Ballarini, E. del Valle, M. D. Martin, A. Lemaître, J. Bloch, D. N. Krizanovskii, M. S. Skolnick, C. Tejedor, and L. Viña, Nature **457**, 291 (2009).

[42] S. Pigeon, I. Carusotto, and C. Ciuti, Phys. Rev. B **83**, 144513 (2011).

[43] A. Amo, S. Pigeon, D. Sanvitto, V. G. Salla, R. Hivet, I. Carusotto, F. Pisanello, G. Leménager, R. Houdré, E. Giacobino, C. Ciuti, and A. Bramati, Science **332**, 1167 (2011).

[44] J. M. Kosterlitz and D. J. Thouless, J. Phys. C:Sol. State Phys. **6**, 1181 (1973).

[45] Y. G. Rubo, Phys. Rev. Lett. **99**, 106401 (2007).

[46] A. V. Kavokin, G. Malpuech, and M. Glazov, Phys. Rev. Lett. **95**, 136601 (2005).

[47] L. Khriachtchev, M. Rsnen, S. Novikov, and J. Sinkkonen, Appl. Phys. Lett. **79**, 1249 (2001).

[48] A. A. High, J. R. Leonard, A. T. Hammack, M. M. Fogler, L. V. Butov, A. V. Kavokin, K. L. Campman, and A. C. Gossard, Nature **483**, 584 (2012).

[49] C. Symonds, A. Lemaître, E. Homeyer, J. C. Plenet, and J. Bellessa, Appl. Phys. Lett. **96**, 151114 (2009).

[50] K. G. Lagoudakis, M. Wouters, M. Richard, A. Baas, I. Carusotto, R. André, L. S. Dang, and B. Deveaud-Plédran, Nat. Phys. **4**, 706 (2008).

[51] N. Tesařová, T. Ostatnický, V. Novák, K. Olejník, J. Šubrt, H. Reichlová, C. T. Ellis, A. Mukherjee, J. Lee, G. M. Sipahi, J. Sinova, J. Hamrle, T. Jungwirth, P. Němec, J. Černe, and K. Výborný, Phys. Rev. B **89**, 085203 (2014).

Statement of the author's contribution to the publications

All twenty publications in the collection in this habilitation thesis present data to which I significantly contributed in the theoretical part. I fitted the properties of a series of samples from characterization measurements in mostly experimental works [P1–P4] with waveguides with silicon nanocrystals and I formulated the model which explains the mode structure, observed in the luminescence spectra. With the help of the model, I contributed to the proposals of experiments which confirm the theory. Theoretical model and calculations which are the main subjects of the paper [P5] is my sole work as well as the most of the publication [P7]. Theory is also my contribution to the chapter [P8] and I contributed to the article [P6] by discussions of experimental results and by performing calculations which support the hypothesis which explains the observations. The models which were published in the theoretical papers considering the spin structure and spin–spin interactions in single quantum wells [P9–P10] are in their majority my work. The co-authors contributed in a form of discussion of some particular details. I participated in the experimental part of [P11] by consulting few points. The data analysis, theoretical model of kinetics, numerical fitting of the dynamics and evaluation of relevant relaxation times was my work. Concerning the papers on spin propagation in double quantum wells [P12–P13], I contributed to the discussion of the experimental data and theoretical interpretation and to subsequent numerical calculations. In the field of microcavities, the papers focused on spin–spin interactions [P14–P15] are in their major part my work: I formulated the theoretical models with some help of co–authors and I also performed all calculations. I contributed to [P16] by performing a part of calculations. My impact on experimental works [P17–P20] consists in the proposal of the experimental setup in [P18] which allowed observation of the effect. In [P17,P19–P20], I contributed in discussions of the optimal experimental setup and by performing supporting calculations during the run of experiment. I took part in data analysis and their interpretation in all papers [P17–P20] and I proposed a theoretical model for every system investigated in the particular publications. Then I used the models to make simulations which confirm our interpretations. Besides my role in the scientific part of the works, I always took part in the manuscript preparation and making the graphical outputs. In general, I consider my contribution to all the publications in the collection to reflect proportionally the number of authors. Theoretical papers [P7,P9–P10,P14–P15] are an exception where I am the author of the most of published work.

Appendix: Collection of publications [P1–P20]

Optical waveguides

[P1] J. Valenta, T. Ostatnický, I. Pelant, R. G. Elliman, J. Linnros, and B. Hönerlage: Microcavity–like leaky mode emission from a planar optical waveguide made of luminescent silicon naocrystals, *J. Appl. Phys.* **96**, 5222 (2004).

[P2] I. Pelant, T. Ostatnický, J. Valenta, K. Luterov, E. Skopalová, T. Mates, and R. G. Elliman: Waveguide cores containing silicon nanocrystals as active spectral filters for silicon–based photonics, *Appl. Phys. B* **83**, 87 (2006).

[P3] K. Luterová, E. Skopalová, I. Pelant, M. Rejman, T. Ostatnický, and J. Valenta: Active planar optical waveguides with silicon nanocrystals: Leaky modes under different ambient conditions, *J. Appl. Phys.* **100**, 074307 (2006).

[P4] P. Janda, J. Valenta, T. Ostatnický, E. Skopalová, I. Pelant, R. G. Elliman, and R. Tomasiunas: Silicon nanocrystals in silica — Novel active waveguides for nanophotonics, *J. Lumin.* **121**, 267 (2006).

[P5] T. Ostatnický, P. Janda, J. Valenta, and I. Pelant: Optical gain in planar waveguides, *Proc. SPIE* **6609**, 66090F (2007).

[P6] I. Pelant, R. Tomasiunas, V. Sirutkaitis, J. Valenta, T. Ostatnický, K. Kůsová, and R. G. Elliman: Ultrafast decay of femtosecond laser–induced grating in silicon–quantum–dot–based optical waveguides, *J. Phys. D: Appl. Phys.* **41**, 015103 (2008).

[P7] T. Ostatnický, M. Rejman, J. Valenta, K. Herynková, and I. Pelant: Guiding and amplification due to silicon nanocrystals embedded in waveguides, in L. Khriachtchev (Ed.): *Silicon Nanophotonics: Basic Principles, Present Status and Perspectives*, World Scientific, Singapore, 2008.

[P8] J. Valenta, T. Ostatnický, and I. Pelant: Waveguides for nanophotonics, in K. D. Sattler (Ed.): *Handbook of nanophysics: Nanoelectronics and nanophotonics*, CRC Press, Boca Raton, 2011.

Semiconductor quantum wells

[P9] T. Ostatnický, P. Gilliot, and B. Hönerlage: The spin structure of excitons and biexcitons in semiconductor quantum wells, *J. Appl. Phys.* **98**, 113516 (2005).

[P10] T. Ostatnický, P. Gilliot, and B. Hönerlage: Determination of the signal polarization state in four–wave mixing experiments on semiconductors, *J. Lumin.* **126**, 94 (2007).

[P11] T. Ostatnický, O. Crégut, M. Gallart, P. Gilliot, B. Hönerlage, and J.–P. Likforman: Electron- and hole-spin relaxation within excitons in GaAs quantum wells by non–degenerate pump–and–probe measurements, *Phys. Rev. B* **75**, 165311 (2007).

[P12] J. R. Leonard, Y. Y. Kuznetsova, Sen Yang, L. V. Butov, T. Ostatnický, A. V. Kavokin, and A. C. Gossard: Spin transport of excitons, *Nano Lett.* **9**, 4204 (2009).

[P13] A. A. High, A. T. Hammack, J. R. Leonard, Sen Yang, L. V. Butov, T. Ostatnický, M. Vladimirova, A. V. Kavokin, T. C. H. Liew, K. L. Campman, and A. C. Gossard: Spin currents in a coherent exciton gas, *Phys. Rev. Lett.* **110**, 246403 (2013).

Semiconductor microcavities

[P14] T. Ostatnický, D. Read, and A. V. Kavokin: Polarization and depolarization in scattering of cavity polaritons, *Phys. Rev. B* **80**, 115328 (2009).

[P15] T. Ostatnický, I. A. Shelykh, and A. V. Kavokin: Theory of polarization–controlled polariton logic gates, *Phys. Rev. B* **81**, 125319 (2010).

[P16] T. C. H. Liew, A. V. Kavokin, T. Ostatnický, M. Kaliteevski, I. A. Shelykh, and R. A. Abram: Exciton–polariton integrated circuits, *Phys. Rev. B* **82**, 033302 (2010).

[P17] M. Maragkou, A. J. D. Grundy, T. Ostatnický, and P. G. Lagoudakis: Longitudinal optical phonon assisted polariton laser, *Appl. Phys. Lett.* **97**, 111110 (2010).

[P18] K. G. Lagoudakis, T. Ostatnický, A. V. Kavokin, Y. G. Rubo, R. André, and B. Deveaud–Plédran: Observation of Half–quantum vortices in an exciton–polariton condensate, *Science* **326**, 974 (2009).

[P19] M. Maragkou, C. E. Richards, T. Ostatnický, A. J. D. Grundy, J. Zajac, M. Hugues, W. Langbein, and P. G. Lagoudakis: Optical analogue of the spin Hall effect in a photonic cavity, *Opt. Lett.* **36**, 1095 (2011).

[P20] P. Cilibrizzi, H. Ohadi, T. Ostatnický, A. Askitopolous, W. Langbein, and P. G. Lagoudakis: Linear wave dynamics explains observations attributed to dark–solitons in a polariton quantum fluids, *Phys. Rev. Lett.*, in press (2014).

JOURNAL OF APPLIED PHYSICS VOLUME 96, NUMBER 9 1 NOVEMBER 2004

Microcavity-like leaky mode emission from a planar optical waveguide made of luminescent silicon nanocrystals

J. Valenta[a] and T. Ostatnický
Department of Chemical Physics & Optics, Faculty of Mathematics & Physics, Charles University, Ke Karlovu 3, CZ-121 16 Prague 2, Czech Republic

I. Pelant
Institute of Physics, Academy of Sciences of the Czech Republic, Cukrovarnicka 10, CZ-162 53 Prague 6, Czech Republic

R. G. Elliman
Electronic Materials Engineering Department, Research School of Physical Sciences and Engineering, Australian National University, Canberra ACT 0200, Australia

J. Linnros
Department of Microelectronics & Information Technology, Royal Institute of Technology, Electrum 229, S-164 40 Kista-Stockholm, Sweden

B. Hönerlage
IPCMS, Groupe d'Optique Nonlinéaire et d'Optoéléctronique, UMR 7504 CNRS-ULP, 23, rue du Loess, 67037 Strasbourg Cedex, France

(Received 3 May 2004; accepted 2 August 2004)

The propagation of light emitted from silicon nanocrystals forming planar waveguides buried in SiO_2 is studied both experimentally and theoretically. Experiments reveal that photoluminescence spectra detected from the sample facet mainly contains narrow (10–20 nm full-with-at-half-maximum) polarization-resolved transverse electric and transverse magnetic modes instead of the usual broad nanocrystal emission band peaked at 700–800 nm. A theoretical model developed in the framework of wave optics identifies these modes as substrate modes propagating along the waveguide boundary (*not* the usual modes guided inside the nanocrystal plane due to its graded index profile). This peculiar observation is the consequence of the high losses in the nanocrystalline waveguide and may occur in other dissipative waveguide structures under conditions that are discussed. © *2004 American Institute of Physics*. [DOI: 10.1063/1.1795984]

I. INTRODUCTION

Light-emitting silicon nanostructures have attracted considerable interest since the discovery of bright visible photoluminescence (PL) in porous silicon by Canham.[1] This interest has been further stimulated by recent reports of optical gain in an ensemble of silicon nanocrystals (Si-NCs).[2–7] Most of the investigators looking for optical gain use samples in the form of a thin Si-NC layer (prepared either by the Si-ion implantation or by the plasma-enhanced chemical vapour deposition method) embedded in a transparent silica matrix, or Si/SiO_2 superlattices. Such structures work as asymmetric *active* planar optical waveguides, where the light is not coupled to the core from outside but originates from an ensemble of emitting Si-NCs inside the waveguide.

Here we report on experimental observations of unusual PL from planar waveguides made of luminescent Si-NCs in SiO_2 matrix. In particular, a significant narrowing of PL lineshape and splitting of the emission into spectrally separated transverse electric (TE) and transverse magnetic (TM) modes. Such behavior is very similar to III-V semiconductor-based microcavity PL TE-TM splitting observed in directions different from surface normal.[8,9] We show that the narrow TE and TM modes, which the waveguide self-selects from a wide spontaneous emission spectrum, are not the usual guided modes, as assumed in our earlier report, but leaky substrate modes. They arise from constructive Fabry-Perot interference of luminescence rays leaving the active Si-NC layer to the substrate near the angle of total internal reflection. The existence of such modes is a general property of thin luminescent layers, irrespective of whether they are in the form of semiconductor microcavities.[9,10] or simple organic/inorganic thin films.[11,12] Hereafter, we deal with a general case of an asymmetric planar waveguide with a graded index profile where these modes are extremely well developed. We show, both experimentally and theoretically, that such experimental dominance of the leaky modes depends strongly upon a coincidence of several parameters, including the waveguide losses experienced by guided modes, the refractive index contrast of the core and cladding and the depth of core layer within the substrate.

II. SAMPLE PREPARATION AND EXPERIMENTAL SET-UPS

The samples used in this study were prepared by implanting 400 keV Si^+ ions into 1 nm thick silica slab (Infrasil) with optically polished surface and edges. Implantation

[a]Author to whom correspondence should be addressed; electronic mail: jan.valenta@mff.cuni.cz

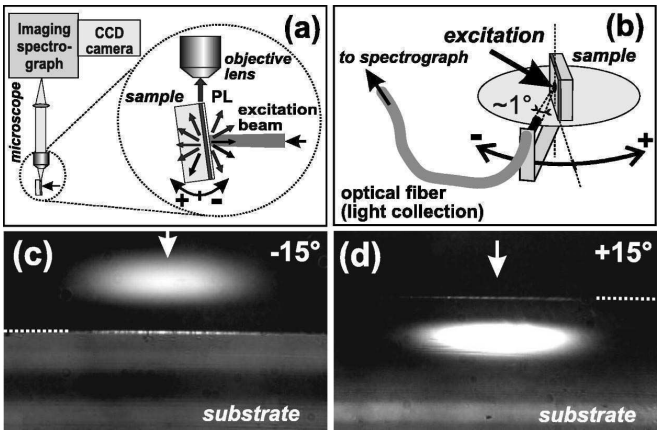

FIG. 1. Sketch of the experimental geometry for the microPL setup (a) and for the goniometer setup (b). Lower panels show PL intensity images (area 2 $\times 1.2$ mm^2) of the excited waveguide (using micro-PL setup) for sample inclination of $\alpha=-15°$ (c) and $\alpha=+15°$ (d). The elliptical spot is the excited region on the surface of the sample, and the narrow line is the PL emanating from the sample facet. The substrate is slightly illuminated with a white lamp giving rise to the lighter gray color in the bottom part of the images. The white arrows indicate the direction of excited beam.

doses of 3, 4, 5, and 6×10^{17} Si cm^{-2} (in four different regions of the slab) were chosen to produce different levels of refractive index contrast between the core and cladding/substrate layers. Peak excess Si concentrations were up to 26 at. % Si. Implanted samples were subsequently annealed for 1 h in N_2 ambient at 1100 °C and 1 h in forming-gas (5% H_2 in N_2) at 500 °C. The presence of Si-NCs in the annealed layers, with diameter between 4–5 nm, was confirmed by Raman scattering (not shown here).

The PL properties of samples were investigated using a continuous wave He-Cd laser (325 nm) as the excitation source (excitation intensity $\sim$0.3 W/cm^2) and a microscope connected to an imaging spectrograph with a CCD camera for detection [Fig. 1(a)]. The detection numerical aperture (NA) was 0.075 (i.e., an angular resolution of about 8.6°). All measurements were performed at room temperature and all PL spectra were corrected for the system response. To achieve better angular resolution a second experimental arrangement was also employed in which the sample was fixed to the centre of a goniometer [Fig. 1(b)]. The PL emission was then collected by a silica optical fiber (core diameter 1 mm) rotated around the sample at a distance of 50 mm, giving an angular resolution slightly less than 1° (NA $\sim$0.01). The output of the fibre was measured using the same detection system described above.

Typical images observed with the microscopic setup [Fig. 1(a)] are illustrated in Figs. 1(c) and 1(d). Here the diameter of the excitation spot, located at about 1 mm from the sample edge, is roughly 1 mm. One can easily recognize PL emission from the excited spot as a bright ellipsoid. However, there is also a second contribution emanating from the facet of the sample. This light is obviously guided in the implanted layer or close to it. The images in Figs. 1(c) and 1(d) were collected for sample inclination angles of −15° and +15°, respectively, i.e., in a geometry for which the excited spot was observed either directly [Fig. 1(c)] or through the substrate [Fig. 1(d)]. The experimental arrangement shown in Fig. 1(a) enables the detection of the PL either from the excited spot or from the edge of sample by positioning the entrance slit of the spectrograph to different locations of the PL image.

III. EXPERIMENTAL RESULTS AND DISCUSSION

Figure 2 (left column) presents PL spectra of four layers produced by implanting to different doses. The broad dotted curves correspond to PL emanating from the sample surface (perpendicularly to the Si-NC layer, i.e., conventional geometry) while the other curves represent PL collected from the facet of the sample (sample inclination was +2.5°). It can be seen that these two types of spectra differ considerably. The facet PL spectra are much narrower and contain (except the 3×10^{17} cm^{-2} sample) narrow TE and TM modes clearly re-

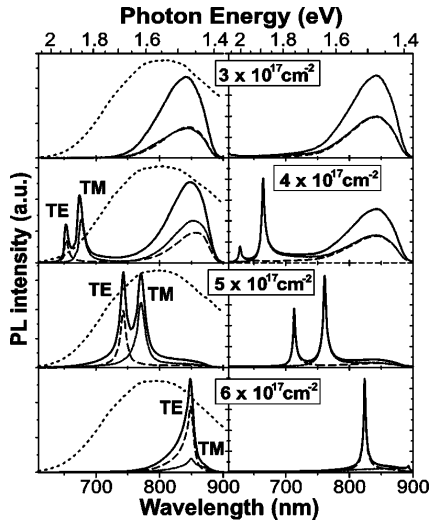

FIG. 2. Left column: Experimental PL spectra for layers implanted with doses 3, 4, 5, and 6×10^{17} Si cm^{-2} (from top down) detected in two different directions: The conventional normal incidence PL spectra (broad dotted line) and PL spectra emanating from the facet of the sample [black line—PL without polarizer, dashed line—with polarizer parallel to the layer (TE mode), short-dashed lines—polarizer perpendicular to the layer (TM mode)]. Right column: Calculated PL spectra from the sample facet ($\alpha=0°$), taking into account the detection NA=0.075. The broad emission bands appearing in the samples 3×10^{17} Si cm^{-2} and 4×10^{17} Si cm^{-2} represent guided modes scattered into the detector collection angle.

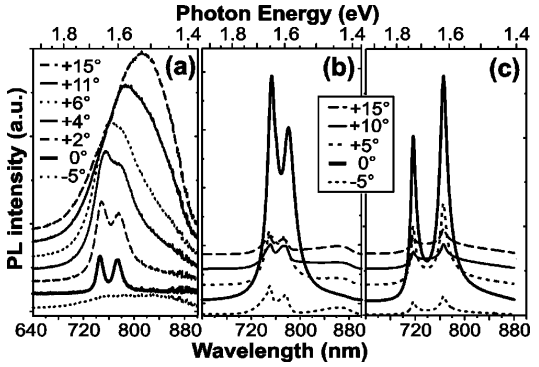

FIG. 3. Angular dependencies (sample 5×10^{17} Si cm^{-2}): Unpolarized PL spectra measured at various angles α with respect to the normal to the output facet in the sample 5×10^{17} Si cm^{-2} using either the goniometer setup (a) or the micro-PL setup (b). The angular resolution is about 8.6° and 1°, respectively. Panel (c) represents model calculations of the angular dependence for aperture collection angle of 8.6°.

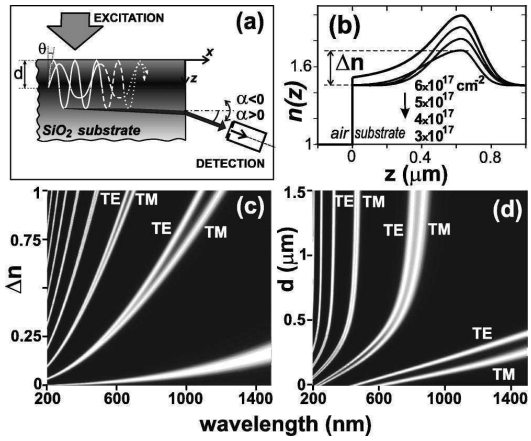

FIG. 4. (a) Cross section of the Si-NC planar waveguide with a graded index profile $n(z)$. Rays of both guided and substrate modes are indicated. (b) Refractive index profiles $n(z)$ in the investigated samples. Lower two panels show calculated spectral positions of the substrate modes: As a function of the refractive index contrast Δn (c) and as a function of the maximum index contrast depth d in the sample 5×10^{17} Si cm^{-2} (d).

solved with a linear polarization filter parallel (TE) or perpendicular (TM) to the layer edge. Such surprising PL spectra from a simple layer of Si-NCs have been reported for the first time only recently.[13,14] Typical PL spectra from Si-NCs consist of a broad band centered at 700–800 nm with FWHM of 150–200 nm, consistent with the dotted curves in Fig. 2.

We stress that the TE/TM mode structure is only resolved in PL spectra collected in a direction close to $\alpha=0°$ (i.e., detection axis lying in the implanted plane). This is clearly illustrated in Fig. 3(a) where PL spectra for several collection angles α are plotted. These results were obtained using the goniometer setup [Fig. 1(b)] with an angular resolution of about 1°. In this case, however, all emission propagating towards the collecting optical fibre is detected. Only in the micro-PL setup we can separate the contribution of light guided along the implanted layer from normal incidence light emission [Fig. 1(a)]. The angular dependence of the separated edge emission is shown in Fig. 3(b) where one can see clear mode structure emitted preferentially to the $\alpha=0°$ direction.

The crucial question to be addressed is how do these narrow lines originate? The waveguide formed by the Si-NC plane "buried" in the SiO_2 matrix is shown schematically in Fig. 4(a). The refractive index profile $n(z)$ across the layer is determined by the Si-NC distribution beneath the surface. Such profiles were obtained by fitting interference fringes in visible-infrared transmission spectra of Si-NC layers (not shown here). These $n(z)$ profiles are displayed in Fig. 4(b) for each of the samples investigated. Their differences from the substrate refracted index $n_{sub}=1.455$ are approximated either by nonsymmetric Gaussian or by Gaussian-Lorentzian curves. The depth of the maximum refractive index contrast Δn below the surface was found to be $d=0.63$ μm in all samples and the profiles are asymmetric, tailing towards the surface, consistent with the implanted Si distribution (not shown).

Figure 4(a) summarizes the following reasoning in the framework of a ray scheme. PL rays, emerging (at depth d) at high enough angles θ, undergo total internal reflection at the core-cladding interface and propagate within the Si-NC core region as normal guided modes (representing continuous spectrum). However, rays emerging at angles θ that are close but slightly below the critical angle $\theta_c=\arcsin[n_{sub}/(n_{sub}+\Delta n)]$ for total reflection at the core-substrate interface can reach the sample surface $z=0$ and be totally reflected at this boundary.[15] This reflection introduces an extra steplike phase shift that causes the splitting of the TE and TM modes.[16,17] The reflected beam then propagates through the core region and undergoes partial reflection from the core-substrate interface. At each such reflection a small part of energy of modes can leak out from the Si-NC layer into the SiO_2 matrix as a substrate mode[18] that finally leaves the sample facet at the detection angle α close to zero [Fig. 4(a)].

It is now demonstrated that this model can simulate the experimental emission spectra with high fidelity when taking into consideration these substrate modes. We assume isotropic radiation of randomly oriented dipoles (Si-NC) that are randomly scattered inside the waveguide (i.e., we neglect their positions with respect to the z axis which would become important when studying microcavity effects). The interest here is on the mode energy, i.e., the output PL intensity, as a function of the angle θ and wavelength λ.[19] With the aid of equations for deriving the cavity enhancement factor[20] we get for the mode amplitude inside the waveguide

$$A(\theta,\lambda)=A_0/(1-tr_1r_2),$$

where A_0 is an effective source strength and $t<1$ is a transmission coefficient [in general $t=t(\theta,\lambda)$] during one roundtrip of the wave in the waveguide. r_1 and r_2 are the reflectivities of the waveguide boundaries that can be calculated (see, e.g., 16) by using a transfer-matrix method. The transfer matrix M is calculated as $M=M_1M_2M_3\cdots M_n$, where

M_k, $0<k\leqslant n$, are transfer matrices for very thin layers into which the structure was "cut," in parallel with the sample surface, for the purpose of numerical calculation. The intensity of a mode is proportional to AA^*. In the present study we used $t=0.995$ [in agreement with experimentally established damping of about 10 cm^{-1} (Ref. 21)] and $n=5000$.

The results of calculations are presented in Fig. 2 (right column). The overall agreement with the experimental data (left column) is excellent, providing strong support for the proposed model that the observed PL spectral narrowing and TE/TM splitting are due to the substrate modes propagating nearly in parallel with the boundary of the waveguide. (We should note that the intensity of the calculated modes here has been modulated by the spontaneous broad PL emission band to allow direct comparison with experiment.) One can easily recognize in Fig. 2 a TE/TM "doublet" whose spectral position is red shifting and the separation between components is increasing with increasing implantation dose. This behavior is displayed more generally in Fig. 4(c) (calculated mode position as a function of the maximum index contrast Δn, which is linked to the implantation energy) and Fig. 4(d) (calculated mode position as a function of the depth d). Similar calculations were performed for the angular dependence of PL for the layer 5×10^{17} Si cm^{-2} and the results are displayed in Fig. 3(c). One can clearly see the narrow modes at angles close to $\alpha=0$ in good agreement with the experimental results [Fig. 3(b)].

The question that remains is why the substrate modes are so significant here. A likely answer to this question is that the regular guided modes experience greater loss during their propagation in the plane of the waveguide. Indeed, the beams responsible for generating the substrate modes travel reduced distances through the core region and once launched, the substrate mode undergoes virtually no loss in traveling to the substrate facet. On the other hand, the standard guided modes are strongly damped on their trip over a macroscopic distance from the place of creation towards the sample edge due to absorption and scattering. The model employed here does not depend on the nature of the core losses but simply on the fact that the loss is significant. The most likely source of loss in the present case is absorption and scattering from nanocrystals, as well as scattering from the "interface" between the core and cladding layers. The latter likely arises from the implantation process where the penetration depth of the Si^+ ions directly reflects the surface roughness of the polished silica substrate, which is of the order of ±10 nm. It is known that microphotonic etched waveguide structures suffer from optical scattering loss due to sidewall roughness and that this loss increases with increasing refractive index contrast Δn.[22] The contribution of this later process is supported by the fact that these substrate modes do not reveal themselves in the edge emission of waveguides with atomically flat sidewalls.

IV. CONCLUSIONS

It has been demonstrated, both experimentally and theoretically, that continuous wave PL can propagate in specific narrow band, highly directional, substrate modes instead of normal guided modes in an active planar optical waveguide. We have analyzed a waveguide made of Si-NCs but the effect is a general property of asymmetric thin films. The waveguide self-selects these modes from the broadband PL emission of the core. The spectral distribution and experimental manifestation of such modes is critically dependent upon several waveguide parameters, predominantly the refractive index difference between the core and cladding/substrate (determined by the implantation dose in the present study), the waveguide loss, the depth d of Si-NCs distribution beneath the surface and also upon the shape of $n(z)$. The role of these modes in facilitating/hampering optical gain requires further analysis.[11]

ACKNOWLEDGMENTS

This work was sponsored by Grant No. 202/03/0789 of GACR, Project No. IAA1010316 of GAAVCR, Ministry of Education of CR project ME 486, Royal Swedish Academy of Sciences and by the Australian Research Council. The authors thank F. Trojanek for help with calculations and A. Poruba, A. Fejfar, and K. Kusova for experimental assistance.

[1] L. T. Canham, Appl. Phys. Lett. **57**, 1046 (1990).
[2] L. Pavesi, L. Dal Negro, C. Mazzoleni, G. Franzo, and F. Priolo, Nature (London) **408**, 440 (2000).
[3] L. Khriachtchev, M. Räsänen, S. Novikov, and J. Sinkkonen, Appl. Phys. Lett. **79**, 1249 (2001).
[4] M. H. Nayfeh, N. Barry, J. Therrien, O. Akcakir, E. Gratton, and G. Belomoin, Appl. Phys. Lett. **78**, 1131 (2001).
[5] M. Ivanda, U. V. Desnica, C. W. White, and W. Kiefer, in *Towards the First Silicon Laser*, NATO Science Series II. Mathematics, Physics and Chemistry, Vol. 93, edited by L. Pavesi, S. Gaponenko, and L. Dal Negro (Kluwer Academic, Dordrecht, 2003), p. 191.
[6] P. M. Fauchet and J. Ruan, in *Towards the First Silicon Laser*, NATO Science Series II. Mathematics, Physics and Chemistry, Vol. 93, edited by L. Pavesi, S. Gaponenko, and L. Dal Negro (Kluwer Academic, Dordrecht, 2003), p. 197.
[7] L. Dal Negro, M. Cazzanelli, L. Pavesi, S. Ossicini, D. Pacifici, G. Franzo, F. Priolo, and F. Iacona, Appl. Phys. Lett. **82**, 4636 (2003).
[8] C. Y. Hu, H. Z. Zheng, J. D. Zhang, H. Zhang, F. H. Yang, and Y. P. Zeng, Appl. Phys. Lett. **82**, 665 (2003).
[9] J. L. Shen, J. Y. Chang, H. C. Liu, W. C. Chou, Y. F. Chen, T. Jung, and M. C. Wu, Solid State Commun. **116**, 431 (2000).
[10] D. T. Shaafsma and D. H. Christensen, Phys. Rev. B **54**, 14618 (1996).
[11] A. Penzkofer, W. Holzer, H. Tillmann, and H.-H. Hőrhold, Opt. Commun. **229**, 279 (2004).
[12] V. Kiisk, I. Sildos, A. Suisalu, and J. Aarik, Thin Solid Films **400**, 130 (2001).
[13] J. Valenta, I. Pelant, K. Luterová, R. Tomasiunas, S. Cheylan, R. G. Elliman, J. Linnros, and B. Hőnerlage, Appl. Phys. Lett. **82**, 955 (2003).
[14] L. Khriachtchev, M. Räsänen, S. Novikov, Appl. Phys. Lett. **83**, 3080 (2003).
[15] The angle of incidence on the (sample/air) boundary is, due to the graded index profile, greater than the critical angle $\theta_c'=\arcsin[1/(n(z=0))]$ for all index profiles displayed in Fig. 4(b).
[16] P. Yeh, *Optical Waves in Layered Media* (Wiley, New York, 1988).
[17] M. Born and E. Wolf, *Principles of Optics* (Pergamon, Oxford, 1968).
[18] We stress that this is not an *evanescent* wave connected with the guided modes. Such waves cannot contribute to the far-field radiation. See E. Wolf and J. T. Foley, Opt. Lett. **23**, 16 (1998).
[19] Note that the detection angle α is linked to the angle θ through $\sin\alpha=n_{\text{substrate}}\sin\{\pi/2-\arcsin[(n_{\text{substrate}}+\Delta n)\sin\theta/n_{\text{substrate}}]\}$.
[20] R. Baets, P. Bienstman, and R. Bockstaele, in *Confined Photon Systems*, edited by H. Benisty, J.-M. Gérard, R. Houdré, J. Rarity, and C. Weisbuch (Springer, Berlin, 1999), Vol. 531.
[21] J. Valenta, I. Pelant, and J. Linnros, Appl. Phys. Lett. **81**, 1396 (2002).
[22] J. H. Jang *et al.*, Appl. Phys. Lett. **83**, 4116 (2003).

Appl. Phys. B (2006)
DOI: 10.1007/s00340-005-2118-5

Applied Physics B
Lasers and Optics

I. PELANT[1]
T. OSTATNICKÝ[2,*]
J. VALENTA[2,✉]
K. LUTEROVÁ[1]
E. SKOPALOVÁ[1]
T. MATES[1]
R.G. ELLIMAN[3]

Waveguide cores containing silicon nanocrystals as active spectral filters for silicon-based photonics

[1] Institute of Physics, Academy of Sciences of the Czech Republic, 16253 Prague 6, Czech Republic
[2] Department of Chemical Physics & Optics, Faculty of Mathematics & Physics, Charles University, 121 16 Prague 2, Czech Republic
[3] Electronic Materials Engineering Department, Research School of Physical Sciences and Engineering, Australian National University, Canberra ACT 0200, Australia

Received: 20 October 2005

ABSTRACT Layers of densely packed luminescent Si nanocrystals embedded in fused silica act as wavelength-specific planar waveguides that filter the wide-band spontaneous emission. The waveguides' light output consists of two spectrally narrow (~ 10 nm), orthogonally polarized, and spatially directed bands. This effect is shown to result from leaky modes of the lossy waveguides. The results have general applicability to lossy, asymmetric waveguides and show the way to produce spectrally narrow emission without the use of optical cavities.

PACS 78.67.Bf; 42.79.Gn; 81.07.Bc

1 Introduction

Silicon-based photonics is an exciting new area of research that aims to produce integrated electronic and photonic functionality in a single silicon chip. Silicon quantum dots or nanocrystals (Si-NCs) are efficient light emitters [1–3], unlike bulk silicon, and have been used to demonstrate silicon-based light-emitting diodes [4, 5]. The Si-NCs can also be employed to fabricate active optical waveguides [6–12]. Some of these Si-NC waveguides, with properly designed refractive-index profile, exhibit spectral filtering of the Si-NC photoluminescence emission. The filtered emission consists of narrow (~ 10 nm), polarization-dependent emission lines [7, 8, 12]. This unexpected effect, which holds promise for potential applications in silicon photonics, was reported by Khriachtchev et al. [7] for Si/SiO_2 waveguides and by our group [12–14] (probably also by Ivanda et al. [15]) for samples containing Si-NC prepared by Si^+ implantation into silica slabs. Full understanding of the phenomenon is, however, still missing. Here we study this filtering effect in more detail and demonstrate, both experimentally and using theoretical modeling, that the origin of the filtering is based, contrary to intuition, on leaky modes of the lossy planar waveguides.

✉ Fax: +420-2-21911249, E-mail: jan.valenta@mff.cuni.cz
Also at: IPCMS, Groupe d'Optique Nonlineaire et d'Optoelectronique, UMR 7504 CNRS-ULP, 67037 Strasbourg Cedex, France

2 Methods

The Si-NC thin-film waveguides were prepared by 400-keV Si^+-ion implantation into optically polished Infrasil slabs. Samples were subsequently annealed for 1 h at 1100 °C in a N_2 ambient to form Si-NCs and further annealed for 1 h at 500 °C in forming gas (N_2/H_2) to enhance the luminescence emission. The presence of Si-NCs and an estimate of their size was determined by Raman scattering, as shown in Fig. 1c. A simple approach, exploiting the shift and half-width of the Raman peak [16], provided an estimation of the Si-NC sizes from 4.4 nm to 5.9 nm.

Photoluminescence was measured at room temperature using a cw He-Cd laser (325 or 442 nm) and detected with a spectrograph coupled to a CCD camera. All spectra were corrected for the system response. Emitted light was coupled to the detection system either using a quartz optical fiber (collection angle $\sim 1°$) or by a microscope objective lens (magnification $\times 2.5$, NA $= 0.075$, collection angle $\sim 8.6°$). To measure a polar radiation diagram, the input of the optical fiber was rotated around the sample by a goniometer.

Phase-shift interferometry and atomic force microscopy (AFM) were used to characterize the surface morphology of the samples.

Neither spectral profiles nor spectral positions of substrate radiation modes can be calculated analytically. Numerical calculations were therefore performed using the formula for the cavity enhancement factor [17]. The relevant reflectivity coefficients on the boundaries were calculated using the transfer matrix method, taking into account the continuous profile of the refractive index. We also considered both the numerical aperture of the given experimental set-up and the loss coefficient in the Si-NC films. Details of this procedure will be published elsewhere.

3 Results and discussion

The visual appearance of our samples is shown in Fig. 1a. The refractive-index change for different implant fluences leads to variations in the color of the implanted regions under ambient (white) light. The resulting Si-NCs are embedded in the silica slabs as a thin ($\sim 1\,\mu$m) buried layer that

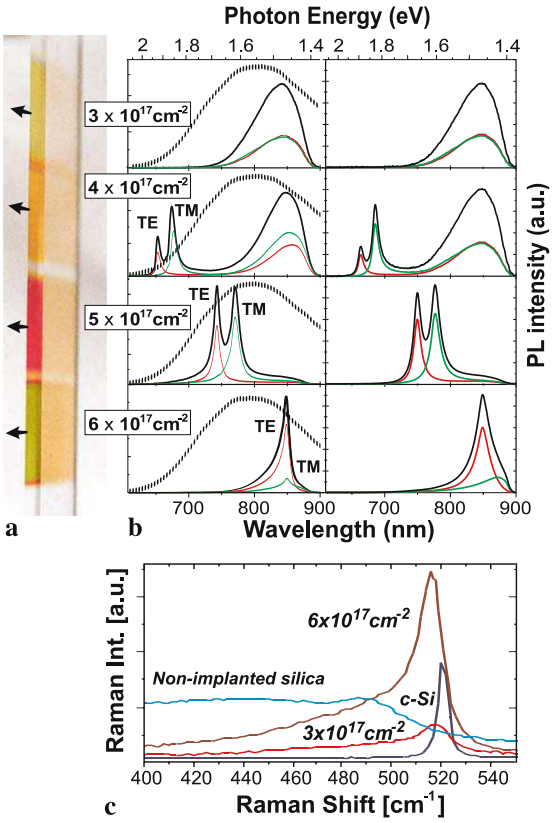

FIGURE 1 Planar optical waveguides formed by Si-NC thin layers embedded in silica slabs. (**a**) Edge view of a silica sheet (Infrasil) $\sim 5.0 \times 1.0 \times 0.1\ \mathrm{cm}^3$ under diffused white light, with colored regions formed by Si-NC films. Corresponding implant fluences, ranging from 3 to $6 \times 10^{17}\ \mathrm{cm}^{-2}$, are indicated. (**b**) *Dotted curves*: conventional broad photoluminescence spectra from Si-NCs measured at normal incidence. *Full lines*: room-temperature photoluminescence spectra taken from the sample facet, in the direction indicated by *arrows* in (**a**). *Left-hand plots* – experimental, *right-hand plots* – calculated. (**c**) Examples of Raman spectra evidencing the presence of Si-NCs (*red* and *brown curves*). *Blue curve* – Raman spectrum of unimplanted Infrasil, *black curve* – reference spectrum of crystalline Si wafer

forms the high- refractive-index core of the waveguide structure. Because the refractive index of the Si-NC film is higher than that of the SiO_2 substrate and extends to the surface, the film acts as a planar asymmetric optical waveguide.

The effect of photoluminescence spectral filtering is highlighted in Fig. 1b. The left-hand column in this figure shows measured room-temperature photoluminescence spectra for four different Si-NC waveguides under UV excitation. The dotted curves represent emission from Si-NCs embedded within the waveguide core, measured from the sample surface, i.e. perpendicular to the Si-NC layer. Such broadband spectra are typical of the inhomogeneously broadened emission from Si-NCs but are undesirable for many optical applications. The solid curves represent spectra taken parallel to the surface, i.e. from the edge (facet) of the waveguide (arrows in Fig. 1a). The two sets of spectra are clearly quite different, the latter being composed of two distinct peaks separated by about 30 nm. Moreover, each of these peaks has a distinct linear polarization: the electric vector $\boldsymbol{E}$ of the short-wavelength peak lies in the Si-NC film (red curves, TE polarization) while the long-wavelength peak is characterized by $\boldsymbol{E}$ perpendicular to the film (green curves, TM polarization). The right-hand column in Fig. 1b represents theoretically calculated spectra, the basis of which will be discussed later.

The strong directionality of the TE/TM peak emission is highlighted in Fig. 2, which shows a polar radiation diagram of the spectrally integrated emission for the sample implanted to a fluence of $5 \times 10^{17}\ \mathrm{cm}^{-2}$. The emission contains surface Lambertian photoluminescence emission peaked at $\sim 90°$ (brownish areas in Fig. 2a), as well as two distinct lobes due to emission emanating from the sample edge (the left-hand lobe) and the internal reflection (the right-hand lobe). The well-developed TE/TM peaks occur within the left-hand lobe, close to the angle $\sim 0°$ only (yellow region in Fig. 2a). This is more clearly seen in Fig. 2b, where the photoluminescence emission was collected using a microscope objec-

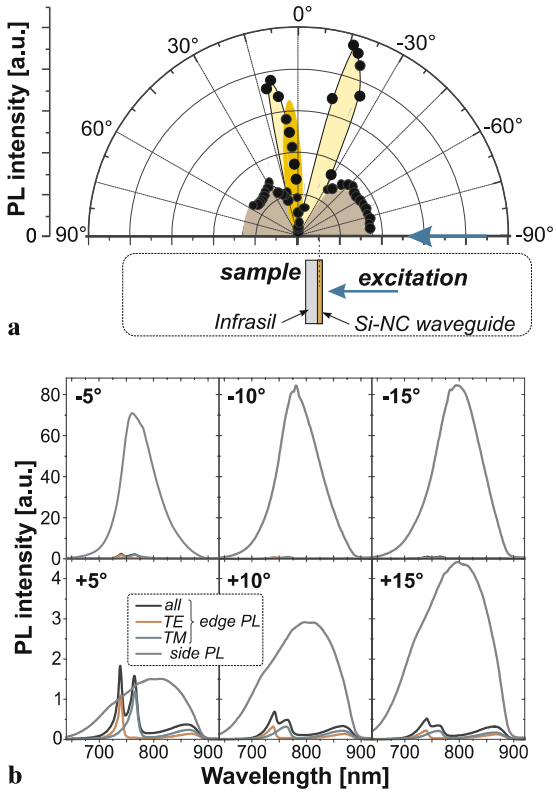

FIGURE 2 Directionality of edge emission (the sample was implanted to a fluence of $5 \times 10^{17}\ \mathrm{cm}^{-2}$). (**a**) Spectrally integrated photoluminescence emission as a function of the polar angle, measured with the sample fixed at the center of a goniometer. (**b**) Micro-photoluminescence spectra for six directions ($\pm 5°$, $\pm 10°$, $\pm 15°$): the direct emission from the excited spot is plotted by *blue lines*, the edge emission by *black lines*, and the polarization-resolved TE and TM modes by *red* and *green lines*, respectively. (The collection angle of the objective lens is $\sim 8.6°$.) Note different intensity scales for *upper* and *lower* plots

tive (with numerical aperture of 0.075, i.e. collection angle of $\sim 8.6°$). The micro-imaging-spectroscopic set-up enabled us to detect separately photoluminescence leaving the excited spot directly (blue lines) and that coming from the edge of the implanted layer (black lines).

With regard to the physical processes that give rise to this novel spectral structure, we consider two distinct mechanisms (summarized in Fig. 3a and b):

(i) The two linearly polarized peaks could simply result from standard guided modes of the planar Si-NC waveguide (Fig. 3a). However, an ideal transparent planar waveguide should transmit a continuous spectrum of guided modes up to a cut-off wavelength [18]. The cut-off wavelength for the first-order modes of our waveguides can be estimated to lie above ~ 1500 nm. Consequently, the Si-NC films should transmit the entire 600–900 nm band emitted by the nanocrystals, which obviously is not the case. Nevertheless, some structure might arise from wavelength-dependent losses, with those modes (wavelengths) that undergo the smallest loss being guided to the edge of the sample. These are likely those modes that are 'weakly guided', i.e. the modes whose electric field is strongly delocalized, and the modes propagate basically as a planar wave in the substrate [18]. Their effective guide thickness tends to infinity [19]. Ray optics describes these modes by an angle of incidence θ that is greater than but very close to the critical angle θ_c for total internal reflection[1]. The situation is depicted in Fig. 3c, which displays schematically the reflectance R and phase shift Φ of TE and TM waves on the boundary between two dielectric media as a function of θ. In our case the boundaries are either the core/air (upper boundary) or the core/SiO_2 substrate (lower boundary). The arrow G labels the angle θ for the strongly delocalized guided modes, which were invoked [20, 21] to be responsible for the filtration effect. The salient feature of the filtering, namely, the separation between TE and TM modes, is then a direct consequence of the asymmetric guide. It is due to different phase shifts Φ for the TE and TM modes under total reflection at both boundaries. In order to fulfill the phase condition that after two successive reflections the phase difference can only be equal to an integral multiple of 2π, suitable wavelengths from the (continuous) emission band are combined with available (continuous) values of Φ. The latter is slightly different for TE and TM polarizations at a given angle of incidence (Fig. 3c) and results in mode wavelengths that are also slightly different.

(ii) The second possible mechanism involves substrate leaky or radiation modes of the Si-NC waveguide (Fig. 3b). These propagate at an angle θ situated close to but below θ_c (arrow S in Fig. 3c). These modes undergo total reflection at the upper boundary (larger index difference) but are only partially reflected on the lower boundary (smaller index difference). Consequently, a small fraction of their power is radiated into the substrate at each bottom reflection. These leaky modes are usually considered undesirable parasitic radiation [18] and thus do not normally receive much attention. If, however, the angle θ is only slightly less than θ_c, the leaky modes propagate near-parallel to the Si-NC plane. Moreover, the number of reflections is very high (R is close to unity), resulting in a narrow spectral width for the modes. The mechanism of spectral filtering in this case remains basically the same as discussed above, the only difference being that a phase shift Φ at the upper boundary only comes to play during the initial stages of propagation.

After a finite number of internal reflections all the radiant power escapes into leaky modes and emerges from the sample facet in a well-defined direction, basically parallel with the Si-NC film (see [14] and Fig. 2). This makes such leaky substrate modes virtually indistinguishable from the guided modes.

The fact that the two mechanisms have a different dependence on the refractive-index difference at the surface provides the basis for testing their validity. The principle is to change locally the cladding layer refractive index between a photoexcitation spot and the sample facet – which can be achieved by putting drops of various liquids on the sample surface close to the sample edge (Fig. 3a and b). If the effect of spectral filtering is due to weakly guided modes, then the edge-emission spectrum should be strongly distorted by such changes in index, since reflections on the upper boundary (now with modified refractive index) control the phase condition for mode creation all along the ray trajectory. If, on the other hand, the filtering is due to the substrate leaky modes, no change in the spectrum is expected since, after propagating ≤ 1 mm from the excitation source, all energy flux in the modes has leaked into the substrate and is no longer influenced by the upper boundary (Fig. 3b).

Results of this experiment are displayed in Fig. 4a and show no change in emission spectrum for liquid refractive indices in the range from 1.359 to 1.657 – clear evidence that the effect is due to leaky substrate modes. (This ob-

[1] Here the lower boundary is of importance only since the refractive-index contrast at the upper boundary is high enough to assure total internal reflection at angles θ safely higher than θ_c

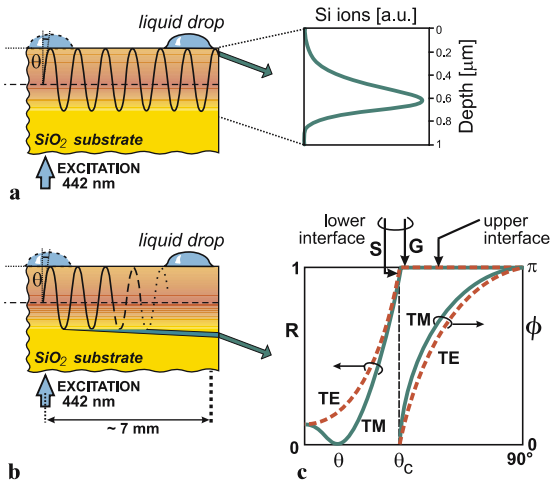

FIGURE 3 Schematics of spectral filtering processes. (**a**) Guided modes of an asymmetric waveguide (*inset* shows implanted Si^+-ion distribution across the Si-NC film as calculated by SRIM (the Stopping and Range of Ions in Matter), which determines the refractive-index profile). (**b**) Substrate radiation (leaky) modes from the Si-NC core. (**c**) Reflectance and phase shifts on the planar boundary between two dielectric media plotted for TE and TM modes versus incident angle θ

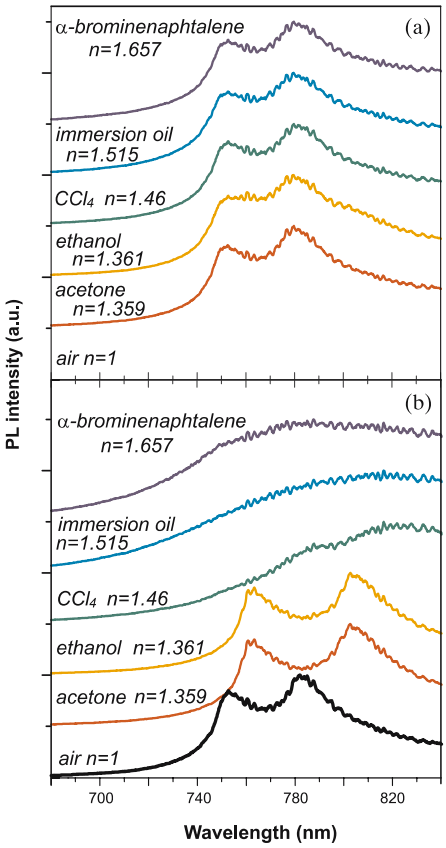

FIGURE 4 Orthogonal polarization emission 'doublet' in the sample implanted to a fluence of 5×10^{17} cm^{-2}. (**a**) Drops of various liquids located on the upper boundary between excitation spot and sample facet, as sketched by the *liquid drops* on the *right* in Fig. 3a and b. *Black curve* – blank upper boundary. (**b**) The same liquids as in (**a**) but located above the excitation spot (the *dotted drops* on the *left* in Fig. 3a and b)

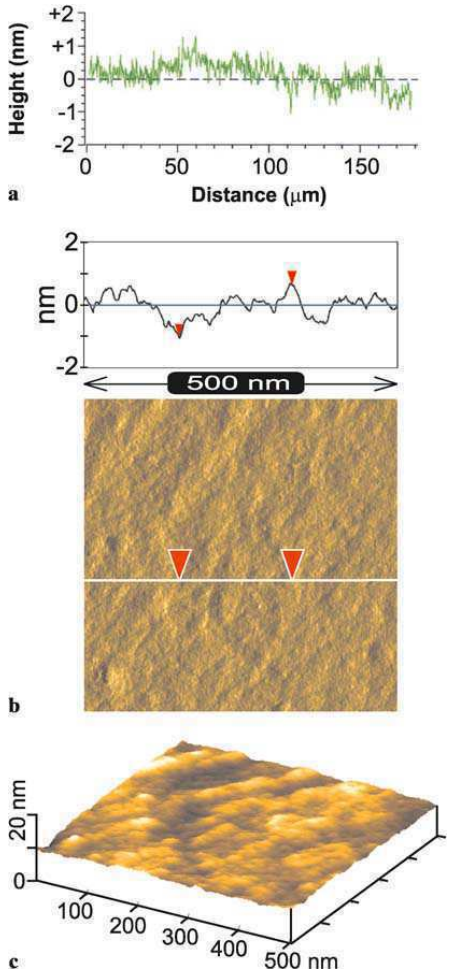

FIGURE 5 Morphology of the sample surface (upper waveguide boundary). (**a**) Line profile measured with a ZYGO phase-shifting interferometer over a range of 180 μm. (**b**) AFM normal force image over an area of 500×500 nm^2. A selected line profile of the local height is also shown, giving the vertical distance between the points marked by *arrows* of about 1.7 nm, in good agreement with the interferometric data. (**c**) Three-dimensional image of the local height in a 500×500 nm^2 area. The z-range of the surface (minimum to maximum) is 3.9 nm, yielding a RMS roughness of 0.5 nm

servation contrasts with a similar experiment performed by shifting the same liquid drops just above the excitation spot – dotted drops in Fig. 3a and b – where reflections of the leaky modes on the upper boundary still occur. The results are shown in Fig. 4b: drastic spectral modifications, scaling with liquid refractive index [22].) As further confirmation of this model, the right-hand column in Fig. 1b shows theoretically calculated edge-emission spectra of the substrate radiation modes for all samples. In calculating these curves the graded index profile of each sample [14] was employed as extracted from interference-modulated optical transmission curves, measured in normal incidence[2]. It is evident that the calculated curves reproduce the measured spectra very well.

Importantly, the dominance of the leaky substrate mode emission implies the suppression of the broadband emission from the Si-NCs. (This latter emission is partly observed in samples implanted to fluences of 3×10^{17} cm^{-2} and 4×10^{17} cm^{-2} – Fig. 1b.) The attenuation of these guided modes is attributed to waveguide losses. Surface and side-wall roughness is often invoked to explain waveguide losses; however, this is not a likely cause in the present case. Indeed, in the present case the waveguide surface morphology (Fig. 5) is very flat with a RMS roughness of ~ 0.5 nm only. This value is substantially lower than typical side-wall roughness in e.g. etched semiconductor waveguides [23] or in typical silica waveguides [24]. The loss is therefore likely due to self-absorption and/or Mie scattering in the waveguide core. (Diffraction of the guided modes at the output facet may also play a role.) The exact nature of the observed waveguide attenuation remains unsolved at present.

[2] We take this opportunity to correct the original version of the calculated curves quoted in [14], where a numerical error made worse the agreement with experiment

4 Conclusions

To summarize, using a combination of experimental and theoretical results we have elucidated the principal role of substrate radiation modes in the spectral filtration effect of thin-film Si-NC waveguides. It is noteworthy that the narrow spectral width of both orthogonal polarization modes is comparable with the emission of Si-NCs in an optical microcavity [25, 26], without fabricating any Bragg reflectors. In a certain sense the investigated waveguides act as a microscopic Lummer–Gehrcke plate. The possibility of selecting the output wavelength via modification of waveguide parameters can be applicable in silicon photonics for Si-laser wavelength tuning, optical signal multiplexing, and optical sensing.

ACKNOWLEDGEMENTS Financial support through Research Grants Nos. 202/03/0789 and 202/01/D030 of GACR, Project No. IAA1010316 of GAAVCR, LC510 Centrum, and the Australian Research Council is greatly acknowledged. The research work at the Institute of Physics is supported by Institutional Research Plan No. AV0Z 10100521. The authors thank F. Trojánek for help with calculations and A. Poruba, A. Fejfar, and K. Kusova for experimental assistance.

REFERENCES

1 G. Amato, C. Delerue, H.-J. von Bardeleben (eds.), *Structural and Optical Properties of Porous Silicon Nanostructures* (Gordon and Breach, Amsterdam 1997)
2 D.J. Lockwood (ed.), *Light Emission in Silicon. From Physics to Devices* (Semicond. Semimet. **49**) (Academic, San Diego, CA 1998)
3 S. Ossicini, L. Pavesi, F. Priolo (eds.), *Light Emitting Silicon for Microelectronics* (Springer Tracts Mod. Phys. **194**) (Springer, Berlin 2003)
4 A. Irrera, D. Pacifici, M. Miritello, G. Franzo, F. Priolo, F. Iacona, D. Sanfilippo, G. Di Stefano, P.G. Fallica, Appl. Phys. Lett. **81**, 1866 (2002)
5 R.J. Walters, G.I. Bourianoff, H.A. Atwater, Nat. Mater. **4**, 143 (2005)
6 L. Dal Negro, M. Cazzanelli, N. Daldosso, Z. Gaburro, L. Pavesi, F. Priolo, D. Pacifici, G. Franzo, F. Iacona, Physica E **16**, 297 (2003)
7 L. Khriachtchev, M. Räsänen, S. Novikov, J. Sinkkonen, Appl. Phys. Lett. **79**, 1249 (2001)
8 L. Khriachtchev, M. Räsänen, S. Novikov, J. Lahtinen, J. Appl. Phys. **95**, 7592 (2004)
9 J. Ruan, P.M. Fauchet, L. Dal Negro, M. Cazzanelli, L. Pavesi, Appl. Phys. Lett. **83**, 5479 (2003)
10 M. Cazzanelli, D. Navarro-Urrios, F. Riboli, N. Daldosso, L. Pavesi, J. Heitmann, L.X. Yi, R. Scholz, M. Zacharias, U. Gösele, J. Appl. Phys. **96**, 3164 (2004)
11 L. Pavesi, L. Dal Negro, C. Mazzoleni, G. Franzo, F. Priolo, Nature **408**, 440 (2000)
12 J. Valenta, I. Pelant, K. Luterová, R. Tomasiunas, S. Cheylan, R.G. Elliman, J. Linnros, B. Hönerlage, Appl. Phys. Lett. **82**, 955 (2003)
13 J. Valenta, I. Pelant, J. Linnros, Appl. Phys. Lett. **81**, 1396 (2002)
14 J. Valenta, T. Ostatnický, I. Pelant, R.G. Elliman, J. Linnros, B. Hönerlage, J. Appl. Phys. **96**, 5222 (2004)
15 M. Ivanda, U.V. Desnica, C.W. White, W. Kiefer, in *Towards the First Silicon Laser*, ed. by L. Pavesi, S. Gaponenko, L. Dal Negro (NATO Sci. Ser. II **93**) (Kluwer, Dordrecht 2003) pp. 191–196
16 G. Viera, S. Huet, L. Boufendi, J. Appl. Phys. **90**, 4175 (2001)
17 R. Baets, P. Bienstman, R. Bockstaele, in *Confined Photon Systems. Fundamentals and Applications*, ed. by H. Benisty, J.-M. Gerard, R. Houdre, J. Rarity, C. Weisbuch (Springer, Berlin 1999) pp. 39–79
18 H.G. Unger, *Planar Optical Waveguides and Fibres* (Clarendon, Oxford 1977)
19 H. Kogelnik, V. Ramaswamy, Appl. Opt. **13**, 1867 (1974)
20 L. Khriachtchev, M. Räsänen, S. Novikov, Appl. Phys. Lett. **83**, 3018 (2003)
21 L. Khriachtchev, S. Novikov, J. Lahtinen, M. Räsänen, J. Phys.: Condens. Matter **16**, 3219 (2004)
22 K. Luterova, E. Skopalova, I. Pelant, M. Rejman, T. Ostatnicky, J. Valenta, in preparation
23 J.H. Jang, W. Zhao, J.W. Bae, D. Selvanathan, S.L. Rommel, I. Adesida, A. Lepore, M. Kwakernaak, J.H. Abeles, Appl. Phys. Lett. **83**, 4116 (2003)
24 S. Janz, in *Silicon Photonics*, ed. by L. Pavesi, D.J. Lockwood (Springer, Berlin, 2004), pp. 323–360
25 S. Chan, P.M. Fauchet, Appl. Phys. Lett. **75**, 274 (1999)
26 F. Iacona, G. Franzo, E.C. Moreira, F. Priolo, J. Appl. Phys. **89**, 8354 (2001)

JOURNAL OF APPLIED PHYSICS **100**, 074307 (2006)

Active planar optical waveguides with silicon nanocrystals: Leaky modes under different ambient conditions

K. Luterová, E. Skopalová, and I. Pelant[a)]
Institute of Physics, Academy of Sciences of the Czech Republic, Cukrovarnická 10, CZ-162 53 Prague 6, Czech Republic

M. Rejman, T. Ostatnický, and J. Valenta
Department of Chemical Physics and Optics, Faculty of Mathematics and Physics, Charles University, Ke Karlovu 3, CZ-121 16 Prague 2, Czech Republic

(Received 9 February 2006; accepted 8 June 2006; published online 6 October 2006)

We study both experimentally and theoretically the propagation of light emitted from silicon nanocrystals forming planar waveguides buried in SiO_2. Photoluminescence spectra detected from the sample facet show significant spectral narrowing—leaky modes—with respect to the spectra measured in standard photoluminescence configuration. The spectral position of the leaky modes responds strongly to a local change of refractive index (liquid drop) on the sample surface. Higher refractive index of the liquid induces higher redshift of the mode position. Experimental data agree with the previously proposed leaky mode model. © *2006 American Institute of Physics*.
[DOI: 10.1063/1.2356781]

INTRODUCTION

Luminescent layers containing silicon nanocrystals are very promising materials for potential all-silicon optoelectronics. Strong effort is aimed nowadays towards successful demonstration of silicon-based laser. Several laboratories reported positive optical gain in systems with silicon nanocrystals.[1–8] Most of these samples are designed in a form of active planar waveguides. A significant narrowing of the photoluminescence (PL) emission spectrum measured in the direction of the waveguide plane (from the sample facet) is, among others, often used as an indication of the presence of stimulated emission in such waveguide structures. However, some recent works showed that in appropriate cases the significant PL spectrum narrowing does not result from stimulated emission, but from the development of a waveguide mode structure in the close vicinity of the waveguide cutoff frequency.[9–11] Such mode structure in PL spectra has so far been interpreted either as substrate leaky modes[12–14] or as a kind of delocalized guided modes near the cutoff frequency.[15–17] The question of which of the two models is valid deserves more detailed discussion.

In the present work, we study behavior of the nanocystalline-waveguide PL spectra at different ambient conditions and give further evidence in favor of the leaky mode model, developed previously by our group.[12,13] We change locally the refractive index (by dropping various liquids) on the sample surface above the excited luminescing spot and monitor subsequently spectral change of the PL. We compare the results with the theoretical spectra calculated using the leaky mode model. Excellent agreement of the experimental and theoretical data affirms the validity of the model.

a)Electronic mail: pelant@fzu.cz

EXPERIMENT

The samples used in this study were prepared by implanting 400 keV Si^+ ions into 1 mm thick silica slab (Infrasil, refractive index $n_s=1.455$) with optically polished surface and edges. Implant fluences of 3, 4, 5, and 6 $\times 10^{17}$ cm^{-2} were applied in four different regions of the slab. They produced different levels of refractive index contrast (with asymmetric graded index profiles[12]) between the core and cladding/substrate layers. Peak excess Si concentrations were up to 26 at. % Si. Implanted samples were subsequently annealed for 1 h in N_2 ambient at 1100 °C and for 1 h in forming gas (5% H_2 in N_2) at 500 °C. Raman scattering confirmed the presence of Si nanocrystals in the annealed layers, with diameter between 3 and 6 nm.[18]

The PL properties of the samples were investigated using a continuous wave He–Cd laser (442 nm) as an excitation source. A silica optical cable collected the PL radiation. The output of the cable was connected to an $f=20$ cm spectrograph equipped with a cooled charge-coupled device (CCD) camera. All measurements were performed at room temperature and all PL spectra were corrected for the system spectral response.

RESULTS AND DISCUSSION

Figure 1 recalls the peculiar waveguiding properties in our Si^+-ion implanted samples. The spectrum recorded in the standard 45° PL geometry [see thin solid line in Fig. 1(c) for the sample implanted to a fluence of 5×10^{17} cm^{-2}] consists of one broad peak (full width at half maximum of ~150 nm) centered at ~860 nm. However, the PL spectra detected from the cleaved facet of the sample—in the waveguide geometry—show, besides the broad peak due to ordinary guided modes, a fundamentally different feature: doublet of two narrow [full width at half maximum (FWHM) of ~20 nm] peaks. Here, the short-wavelength peak is TE po-

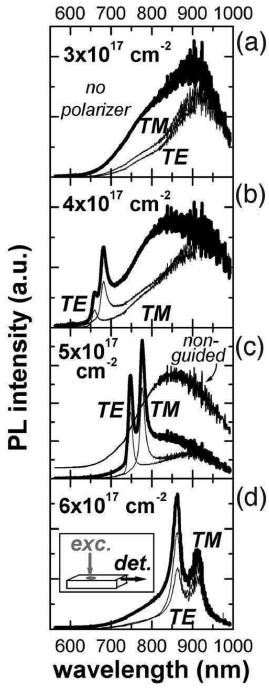

FIG. 1. Room-temperature PL spectra from the sample facet (in the waveguiding geometry schematically depicted in the inset) for layers implanted to a fluence of (a) 3×10^{17} cm^{-2}, (b) 4×10^{17} cm^{-2}, (c) 5×10^{17} cm^{-2}, and (d) 6×10^{17} cm^{-2}, compared to the conventional 45° PL geometry spectrum [curve "nonguided" in panel (c)]. Thick lines—PL without polarizer and thin lines—measurement with a polarizer: TE polarization (vector ***E*** parallel to the waveguiding layer) and TM polarization (***E*** perpendicular to the layer).

larized (vector ***E*** parallel to the sample plane) while the peak on the long-wavelength side is TM polarized (vector ***E*** perpendicular to the sample plane). The position of this doublet shifts with increasing implant fluence (increasing refractive index contrast between substrate and the waveguiding layer) towards longer wavelengths.

We interpret the narrow modes in the edge PL spectra using the leaky mode model[12,13] schematically depicted in Fig. 2. The waveguide refractive index profile can be approximated by nonsymmetrical Gaussian or Gaussian-Lorentzian curves (similar to the implanted Si-ions distribution) with FWHM of about 0.3 μm.[12] The trajectory of relevant optical waves emitted by a chosen Si nanocrystal is shown. In case of ordinary guided modes, the optical wave undergoes total reflections both on the sample surface and at the interface waveguide core/substrate and the wave propagates inside the waveguide core. The leaky modes, on the contrary, are developing in a different way: optical wave, emitted by a silicon nanocrystal to the suitable direction (close to the boundary for the total reflection on the sample surface), undergoes the total reflection on the sample surface only. On the interface between the waveguide core and the substrate, where the refractive index contrast is lower than on the sample surface, the condition for the total reflection is not fulfilled. The light partially reflects and partially refracts at the angle very close to 90°; the refracted part then propagates outside the waveguide core (leaky or radiation mode) but almost parallel to it. The reflected part of light reflects again on the sample surface and interferes with the original refracted wave. The constructive interference arises only for a narrow range of wavelengths. Therefore, only narrow spectral range fulfilling the condition for the constructive interference is selected from the broad PL spectrum and these leaky modes manifest themselves in the PL spectra as very narrow peaks. Different spectral positions of the TE and TM polarized peaks can be then explained by different phase shifts for both polarizations, which are induced during the optical wave total reflection at the sample surface.

The question arises as whether ordinary waveguided light mode propagation within the implanted layer core can also occur in our samples. The answer is yes; this kind of emission can be noticed in samples implanted to fluences of 3×10^{17} and 4×10^{17} cm^{-2} as a wide band peaked at ~850–900 nm [Figs. 1(a) and 1(b)]. However, these guided modes are strongly attenuated in samples implanted to higher total fluences due to waveguide losses. The exact nature of this attenuation is not known at present.[14]

From the point of view of the waveguide optics, we expect the leaky modes to be spectrally situated at slightly lower frequencies than the cutoff frequencies of the waveguide. This is the main observable difference between our leaky mode theory and the approach based on delocalized ordinary waveguide modes as proposed by Khriachtchev *et al.*,[15–17] where these modes approach the cutoff frequency from the higher frequency side. Because values of theoretical cutoff frequencies are not easy to calculate, in particular, for graded index profile, neither is easy to distinguish between the two above models on the basis of spectral PL measuremens themselves. However, we have recently proposed and realized a simple experimental approach of how to do it, which takes advantage of local change of refractive index on the sample surface.[14] In what follows we apply this method in a modified form to investigate further the properties of the TE/TM doublets.

Figure 2(a) depicts the principle of our experiment, based on dropping various liquids onto the excited spot on the sample. By dropping a selected liquid, we change locally the refractive index of the surrounding media on the sample surface (air, formerly). The optical conditions for developing leaky modes will thus be changed on the sample surface. The optical wave travels different distances and undergoes different phase shifts during total reflection. Therefore, also the conditions for constructive interference forming the leaky modes change, which should manifest directly in the PL spectra as a shift of the observed modes. Indeed, the left column in Fig. 2(b) shows the change of the PL spectra in our quartet of the samples upon dropping ethanol onto the sample surface. In all cases, the observed narrow modes undergo a significant redshift.

The right column of Fig. 2(b) demonstrates clearly that the above-mentioned leaky mode model is able to describe the observed redshift of the modes with high fidelity. This column presents the results of theoretical calculations of the

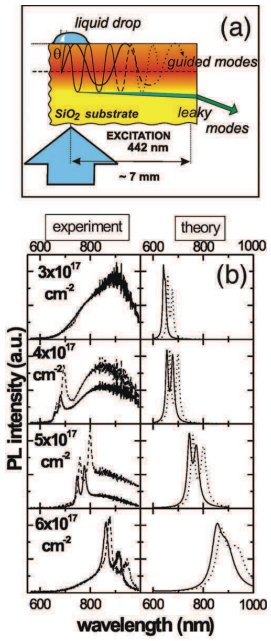

FIG. 2. (Color) (a) Schematic cross section of the asymmetric planar waveguide showing propagation of the guided modes as well as formation of the substrate leaky modes. Surface refractive index change (induced by a liquid drop placed directly above the excited region) influences the development of the leaky modes. (b) Comparison of the PL spectra in the waveguiding geometry for the samples in ambient atmosphere (full lines) and upon dropping ethanol (refractive index $n=1.361$, dotted lines) on the sample surface. Implant fluences are indicated for each sample. Left column: experimental data and right column: theory of leaky modes.

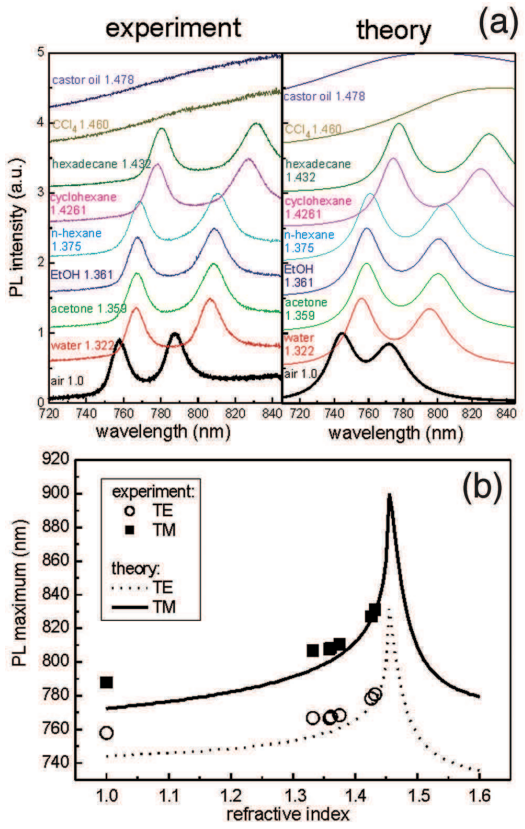

FIG. 3. (Color) (a) PL spectra in the waveguiding geometry showing leaky modes in the layer implanted to a fluence of 5×10^{17} cm^{-2}. Drops of various liquids above the excited spot lead to a redshift of both TE and TM modes. Spectra corresponding to various liquids have been vertically shifted. (b) PL peak position as a function of the refractive index of the liquid. Symbols: experimental data and lines: theory. For liquid refractive index higher than refractive index of the silica substrate ($n_s=1.455$) the theory predicts both disappearance of the distinct doublet structure and a back shift of the broad emission band to shorter wavelengths [see also the right panel in (a)].

leaky mode model developed in the framework of wave optics. In calculating these curves the above mentioned graded index profile of each sample, as determined by fitting interference-modulated optical transmission spectra of the implanted layers, was taken into account, together with refractive index values of applied liquids. Neither spectral profiles nor spectral positions of the substrate leaky modes can be calculated analytically. Numerical calculations were performed using the formula for cavity enhancement factor[19] (for more details, see Refs. 12 and 13) for the whole set of the samples. Taking in account that the theoretical model calculates only the leaky mode part of the PL spectra but not the ordinary, spectrally broad guided modes, both experimental data and the model correspond very well, which provides strong support for the validity of the model.

In order to further support the model, we investigate both experimentally and theoretically the effect of different liquids (different refractive indices) dropped onto the sample implanted to a fluence of 5×10^{17} cm^{-2}. The results are drawn in Fig. 3(a) and again, the measured and the simulated data agree very well. With increasing refractive index of the liquid, we initially observe increasing redshift of the modes. At some point, however, the "doublet" mode structure disappears and a broad PL spectrum can be seen. Actually, this happens when the refractive index of the liquid reaches the refractive index of the sample substrate ($n_s=1.455$), i.e., the point where the waveguide loses its asymmetry, total reflection on the upper boundary is canceled, and the condition for developing narrow TE/TM resolved leaky modes is not fulfilled anymore.

Figure 3(b) plots the PL peak position versus the refractive index of the applied liquids. Further refractive index increase above n_s still keeps the broad spectrum. Theoretically calculated shift goes, somewhat surprisingly, back to shorter wavelengths. However, this can be intuitively understood, since with further increasing refractive index of the liquid above the refractive index of the sample substrate, the role of the substrate and of the capping medium will interchange and (another type of) leaky modes should appear again. Such a back shift is, however, difficult to trace experimentally because of the large spectral bandwidth and possible admixture of normal incidence PL emission.

In calculating the theoretical curves in Figs. 3(a) and

3(b) we considered the liquid droplet thickness infinite, since its real thickness ($\sim$1 mm) is much larger than the waveguide core thickness as determined by the refractive index profile (FWHM of $\sim$0.3 μm).

CONCLUSIONS

In conclusion, by comparing the experimental and theoretical PL spectra under different ambient conditions, we further verified the validity of the leaky mode PL model in the samples containing silicon nanocrystals embedded in a SiO_2 matrix. This phenomenon can find practical applications, for example, as an optical sensor of the refractive index of the media surrounding the sample.

ACKNOWLEDGMENTS

Financial support through Project No. IAA1010316 of GAAV CR and LC510 Research Centrum is greatly acknowledged. Institutional Research Plan No. AV0Z 10100521 supports the research work at the Institute of Physics. The authors thank R. G. Elliman from the Australian National University, Canberra, for providing the samples and V. Kohlová and J. Pšenčík for experimental assistance.

[1]L. Pavesi, L. Dal Negro, C. Mazzoleni, G. Franzo, and F. Priolo, Nature (London) **408**, 440 (2000).
[2]L. Dal Negro *et al.*, Physica E (Amsterdam) **16**, 297 (2003).
[3]L. Dal Negro, M. Cazzanelli, L. Pavesi, D. Pacifici, G. Franzo, F. Priolo, and F. Iacona, Appl. Phys. Lett. **82**, 4636 (2003).
[4]L. Khriachtchev, M. Räsänen, S. Novikov, and J. Sinkkonen, Appl. Phys. Lett. **79**, 1249 (2001).
[5]J. Ruan, P. M. Fauchet, L. Dal Negro, M. Cazzanelli, and L. Pavesi, Appl. Phys. Lett. **83**, 5479 (2003).
[6]K. Luterová, K. Dohnalová, V. Švrček, I. Pelant, J.-P. Likforman, O. Crégut, P. Gilliot, and B. Hönerlage, Appl. Phys. Lett. **84**, 3280 (2004).
[7]M. H. Nayfeh, N. Barry, J. Therrien, O. Aksakir, E. Gratton, and G. Belomoin, Appl. Phys. Lett. **78**, 1131 (2001).
[8]K. Luterová, I. Pelant, I. Mikulskas, R. Tomasiunas, G. Muller, J.-J. Grob, J.-L. Rehspringer, and B. Hönerlage, J. Appl. Phys. **91**, 2896 (2002).
[9]J. Valenta, I. Pelant, and J. Linnros, Appl. Phys. Lett. **81**, 1396 (2002).
[10]K. Luterová, D. Navarro, M. Cazzanelli, T. Ostatnický, J. Valenta, S. Cheylan, I. Pelant, and L. Pavesi, Phys. Status Solidi C **2**, 3429 (2005).
[11]K. Luterová *et al.*, Opt. Mater. (Amsterdam, Neth.) **27**, 750 (2005).
[12]J. Valenta, T. Ostatnický, I. Pelant, R. G. Elliman, J. Linnros, and B. Hönerlage, J. Appl. Phys. **96**, 5222 (2004).
[13]T. Ostatnický, J. Valenta, I. Pelant, K. Luterová, R. G. Elliman, S. Cheylan, and B. Hönerlage, Opt. Mater. (Amsterdam, Neth.) **27**, 781 (2005).
[14]I. Pelant, T. Ostatnický, J. Valenta, K. Luterová, E. Skopalová, T. Mates, and R. G. Elliman, Appl. Phys. B: Lasers Opt. **83**, 87 (2006).
[15]L. Khriachtchev, M. Räsänen, and S. Novikov, Appl. Phys. Lett. **83**, 3018 (2003).
[16]L. Khriachtchev, M. Räsänen, S. Novikov, and J. Lahtinen, J. Appl. Phys. **95**, 7592 (2004).
[17]L. Khriachtchev, M. Räsänen, and S. Novikov, Appl. Phys. Lett. **86**, 141911 (2005).
[18]G. Viera, S. Huet, and L. Boufendi, J. Appl. Phys. **90**, 4175 (2001).
[19]R. Baets, P. Bienstman, and R. Bockstaele, in *Confined Photon Systems*, Lecture Notes in Physics Vol. 531, edited by H. Benisty, J.-M. Gérard, R. Houdré, J. Rarity, and C. Weisbuch (Springer, Berlin, 1999), p. 38.

Available online at www.sciencedirect.com
ScienceDirect
Journal of Luminescence 121 (2006) 267–273
JOURNAL OF LUMINESCENCE
www.elsevier.com/locate/jlumin

Silicon nanocrystals in silica—Novel active waveguides for nanophotonics

P. Janda[a], J. Valenta[a,*], T. Ostatnický[a], E. Skopalová[b], I. Pelant[b], R.G. Elliman[c], R. Tomasiunas[d]

[a]*Department of Chemical Physics & Optics, Faculty of Mathematics and Physics, Charles University, Prague, Czech Republic*
[b]*Institute of Physics, Academy of Sciences of the Czech Republic, Prague, Czech Republic*
[c]*Electronic Materials Engineering Department, Research School of Physical Sciences and Engineering, Australian National University, Canberra, Australia*
[d]*Institute of Materials Science and Applied Physics, Vilnius University, Vilnius, Lithuania*

Available online 7 September 2006

Abstract

Nanophotonic structures combining electronic confinement in nanocrystals with photon confinement in photonic structures are potential building blocks of future Si-based photonic devices. Here, we present a detailed optical investigation of active planar waveguides fabricated by Si^+-ion implantation (400 keV, fluences from 3 to $6\times10^{17}\,cm^{-2}$) of fused silica and thermally oxidized Si wafers. Si nanocrystals formed after annealing emit red-IR photoluminescence (PL) (under UV-blue excitation) and define a layer of high refractive index that guides part of the PL emission. Light from external sources can also be coupled into the waveguides (directly to the polished edge facet or from the surface by applying a quartz prism coupler). In both cases the optical emission from the sample facet exhibits narrow polarization-resolved transverse electric and transverse magnetic modes instead of the usual broad spectra characteristic of Si nanocrystals. This effect is explained by a theoretical model which identifies the microcavity-like peaks as leaking modes propagating below the waveguide/substrate boundary. We present also permanent changes induced by intense femtosecond laser exposure, which can be applied to write structures like gratings into the Si-nanocrystalline waveguides. Finally, we discuss the potential for application of these unconventional and relatively simple all-silicon nanostructures in future photonic devices.

PACS: 78.67.Bf; 42.79.gn; 81.07.Bc

Keywords: Nanocrystals; Waveguide; Silicon; Photonics

1. Introduction

Research on silicon-based photonics is motivated by the aim to combine integrated electronic and photonic structures on a single silicon chip. Silicon quantum dots or nanocrystals (Si-NCs) have attracted much attention due to their strong photoluminescence (PL) [1] and have been used to demonstrate silicon-based light-emitting diodes [2,3]. Ensembles of Si-NCs can also be employed to fabricate active optical waveguides [4–8] that exhibit spectral filtering of the Si-NC PL emission, if the refractive index profile is properly designed. The occurrence of narrow (~10 nm), polarization-dependent emission lines was reported by Khriachtchev et al. [4] for Si/SiO_2 waveguides and by our group [5,9] for samples containing Si-NC prepared by Si^+-implantation into silica slabs. In our previous papers we explained the unexpected waveguiding properties using a model based on substrate leaking modes of a lossy waveguide [10,11].

In this work we compare the propagation of the intrinsic luminescence from Si-NCs with that of external light coupled into the waveguides. This knowledge is crucial for pump-and-probe measurements (e.g. optical gain) and potential application as photonic devices (modulators, amplifiers etc.). In addition we show permanent changes

*Corresponding author. Tel.: +420 221911272; fax: +420 221911249.
E-mail address: jan.valenta@mff.cuni.cz (J. Valenta).

0022-2313/$ - see front matter © 2006 Elsevier B.V. All rights reserved.
doi:10.1016/j.jlumin.2006.08.004

induced by femtosecond laser exposure which can be applied to write 2D structures (gratings etc.) into the Si-nanocrystalline waveguides with sub-micron resolution.

2. Experimental methods

Samples used in this study were prepared by Si^+-ion implantation into 1 mm thick Infrasil (refractive index $n_s = 1.455$) slabs with polished surfaces and edges, and into SiO_2 layers (about 5 μm thick) prepared by thermal oxidation of Si wafers. An implantation energy of 400 keV and ion fluences ranging between 3.0 and $6.0 \times 10^{17}\,cm^{-2}$ were used to fabricate the slab waveguides. In order to form Si nanocrystals the samples were annealed for 1 h at 1100 °C in an N_2 ambient and then passivated for 1 h at 500 °C in forming gas (5% H_2 in N_2).

The implanted layer acts as an asymmetric planar waveguide. The profile of the refraction index depends not only on the implantation energy and fluence but also on the annealing conditions. Although the annealing temperatures, ambients and durations were nominally the same, various sets of samples were annealed in different laboratories and furnaces. Possible variations in the thermal history and levels of oxidation lead to apparent differences in refraction index for nominally identical samples (here, Figs. 2–4 present results from one set of samples and another set with lower refraction index is shown in Figs. 5–7). In order to numerically model the optical properties of particular samples the refraction index profiles were measured separately for each implanted sample. This was done by measuring infrared transmission spectra (see Fig. 2B) and fitting the interference fringes assuming an asymmetric double-Gaussian refraction index profile. The maximum of the profile is typically about 600 nm below surface with a half width of about 300 nm. The peak refraction index has a value as high as 2 for the highest implantation fluence [11]. The diameter of nanocrystals in the samples is estimated to be between 4 and 6 nm using Raman scattering (not shown here) [11].

PL was excited by a continuous wave He–Cd laser (325 nm, excitation intensity ~0.3 W/cm^2). The sample was placed on a rotatable x–y–z stage. A microscope with numerical aperture (NA) of 0.075 (i.e. an angular resolution of about 8.6°) was used to collect light and send it to a detection system consisting of an imaging spectrograph (Jobin Yvon Triax 190) with a CCD camera (Hamamatsu C4880) [9]. All measurements were performed at room temperature and all PL spectra were corrected for the system response.

The coupling of external light into the waveguides was achieved in two ways (Fig. 1):

(a) Prism coupling of light from the upper surface of the sample. Light from the Xe or halogen lamp was collimated into a quartz prism. For better optical contact between the prism and sample an immerse liquid (index of refraction $n = 1.515$) was dropped between the contact surfaces.

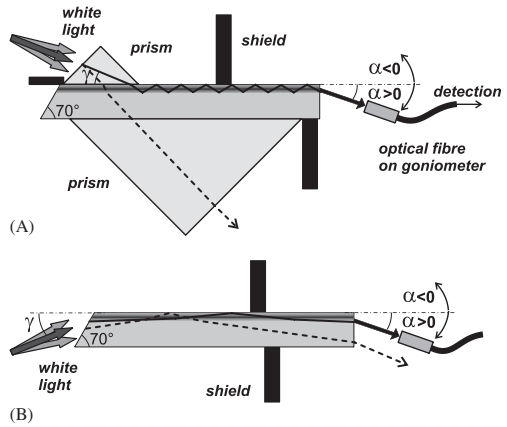

Fig. 1. Two experimental arrangements for coupling of external light into a waveguide sample: (A) coupling through a quartz prism on the upper sample surface. The second prism below sample is used to inhibit the back reflection of light not coupled into the waveguide; (B) focused light directed on the truncated edge of a sample. In both cases light leaving the opposite edge of sample is collected with an optical fiber and sent to a spectrometer. Sketches not to scale.

(b) Direct coupling into the truncated facet (Fig. 1B). The edge of the sample was polished at angle of about 70° in order to separate light refracted to the higher-index waveguide from light entering lower-index substrate. Here a warm-white LED was used as a convenient light source. The angle of incidence γ was between 15° and 30° with respect to the plane of implanted layer. The divergence of incident light was about 10°.

In both external-light-coupling set-ups the signal is collected by an optical fiber (detection NA ~0.008) and guided to the entrance slit of the imaging spectrometer Jobin Yvon Triax 320 (with the low-dispersion grating of 100 grooves/mm). Spectra are detected with the PI-Max intensified CCD (Princeton Instruments).

3. Results and discussion

3.1. Transmission spectra of Si-NC layers

The color of the Si-NC waveguide layers is yellow-brown with the optical density increasing with implantation fluence. The corresponding absorbance spectra are plotted in Fig. 2A (they are measured in a direction perpendicular to the nanocrystal plane using a UV-VIS double beam spectrometer (Hitachi U-3300), the non-implanted area of a silica slab being employed as a reference). The absorption edge has approximately exponential shape. In infrared spectral region several interference fringes are observed (Fig. 2B) which are used to model refraction index profile (see above).

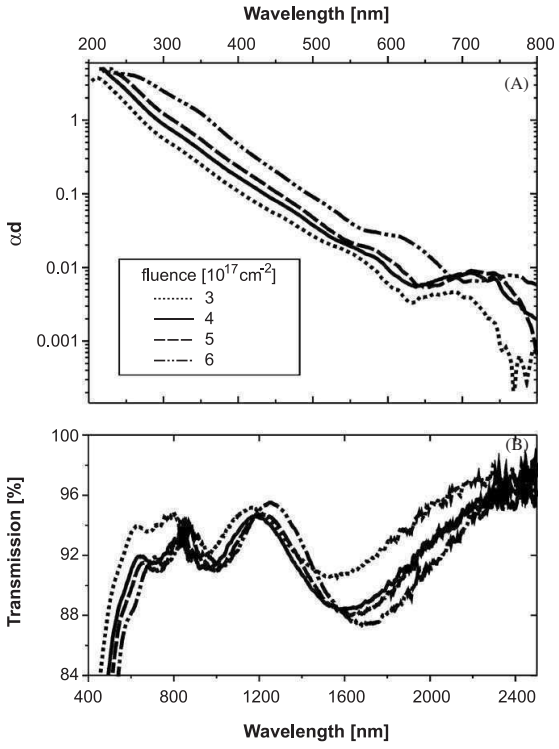

Fig. 2. (A) Absorption spectra of the samples implanted with fluences from 3 to $6 \times 10^{17}\,cm^{-2}$. A non-implanted area of the fused silica slab was used as a reference. (B) Infrared transmission spectra of the same samples. Interference fringes are used to calculate refraction index profiles.

3.2. PL of active planar waveguides

The PL spectra of the active planar waveguides have very different shape depending on the experiment geometry. Two arrangements are used: (i) the light is collected in a direction roughly perpendicular to the sample plane (this is a conventional PL arrangement) or (ii) in the direction close to parallel to the waveguide plane (i.e. from the sample facet–waveguide arrangement)—see inset in Fig. 3. In the former geometry the PL spectra are always broad with a peak around 830 nm, typical of oxide-passivated Si NCs with mean diameter ~5 nm. On the other hand, the waveguide geometry reveals narrow (down to 10 nm) spectral features with a high degree of linear polarization.

Figs. 3A and B show PL spectra of implanted oxide layers (on Si substrates) measured in directions perpendicular and parallel to the layer, respectively. The conventional PL (Fig. 3A) is modulated by deep interference fringes due to high reflectivity of the Si substrate. The facet-PL (Fig. 3B) is not affected by interference; instead a relatively narrow band is observed, the position of which depends on implantation fluence (i.e. refraction index profile). This peak shows partial linear polarization

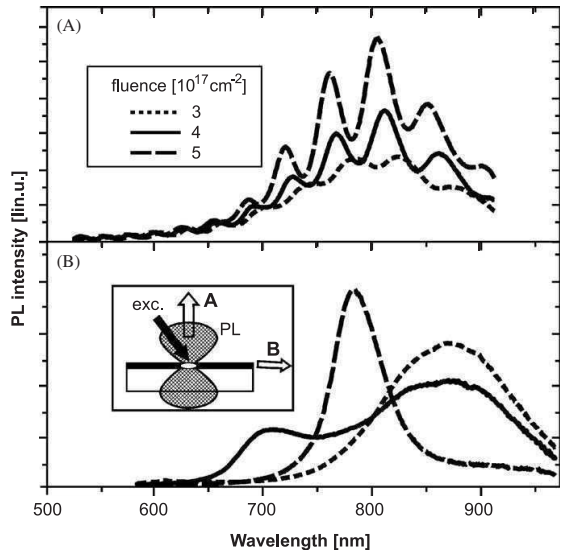

Fig. 3. PL spectra of SiO_2 layers on Si substrates implanted with fluences of 3, 4, and $5 \times 10^{17}\,cm^{-2}$. (A) PL detected in direction perpendicular to the layer. (B) PL detected in direction parallel to the layer (from the facet). The inset illustrates the experimental arrangement.

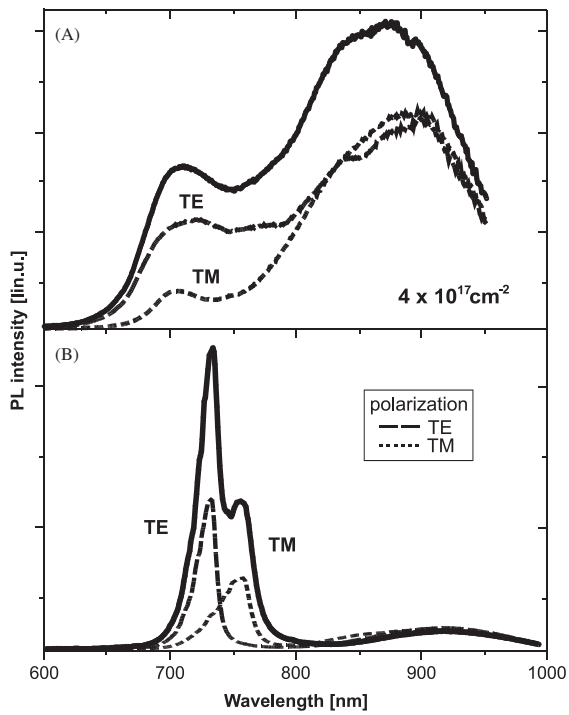

Fig. 4. PL spectra of $4 \times 10^{17}\,cm^{-2}$ layers measured in edge geometry without polarizer (solid line) or with a linear polarizer parallel (TE, dashed line) or perpendicular to the waveguide plane (TM, dotted line). The upper panel (A) concerns SiO_2 layers on Si substrate, while the lower panel (B) is for implanted fused silica slab.

(Fig. 4A). Under identical conditions (of both fabrication and PL-experiment) the facet-PL features are much better resolved in implanted silica slabs (Fig. 4B). Here a clear splitting of the narrow PL peak into two peaks with polarization parallel (transverse electric TE or *s* mode) and perpendicular (transverse magnetic TM or *p* mode) to the Si-NC waveguide plane is observed. The following discussion is restricted to implanted fused silica slabs where the TE/TM splitted modes are nicely resolved.

PL spectra of other set of five samples prepared by implantation to fluences of 4.0, 4.5, 5.0, 5.5, and $6.0 \times 10^{17}\,cm^{-2}$ are plotted in Fig. 5. The upper spectra in Fig. 5A represent PL collected from the plane of implanted layers, while the lower PL spectra with TE/TM double-peaks are collected from the facet at angle $+5^{\circ}$ ($NA_{det} = 0.075$). An angle-resolved facet PL spectra from the layer implanted with dose of $6 \times 10^{17}\,cm^{-2}$ are plotted in Fig. 5B and the polar representation of their integrated intensity is shown in Fig. 5C. The TE/TM split doublets shift to longer wavelength with increasing implantation dose. The facet PL has a very narrow emission cone with the maximum slightly shifted closer to substrate ($\alpha \geqslant 0^{\circ}$) (Figs. 1B and C).

3.3. Theoretical model of the mode structure—radiative substrate modes

The surprising PL observations reported above do not correspond to simple waveguiding in ideal transparent waveguide which should transmit a continuous spectrum of guided modes up to a cut-off wavelength [12]. The cut-off for the first order modes of our waveguides can be estimated to lie above ~1500 nm. Consequently, the waveguides should transmit the entire 600–900 nm band emitted by Si-NCs, which is clearly not the case. There are two possible explanations:

(i) *Delocalized guided modes*: Let us assume wavelength-dependent losses in the waveguide, then those modes

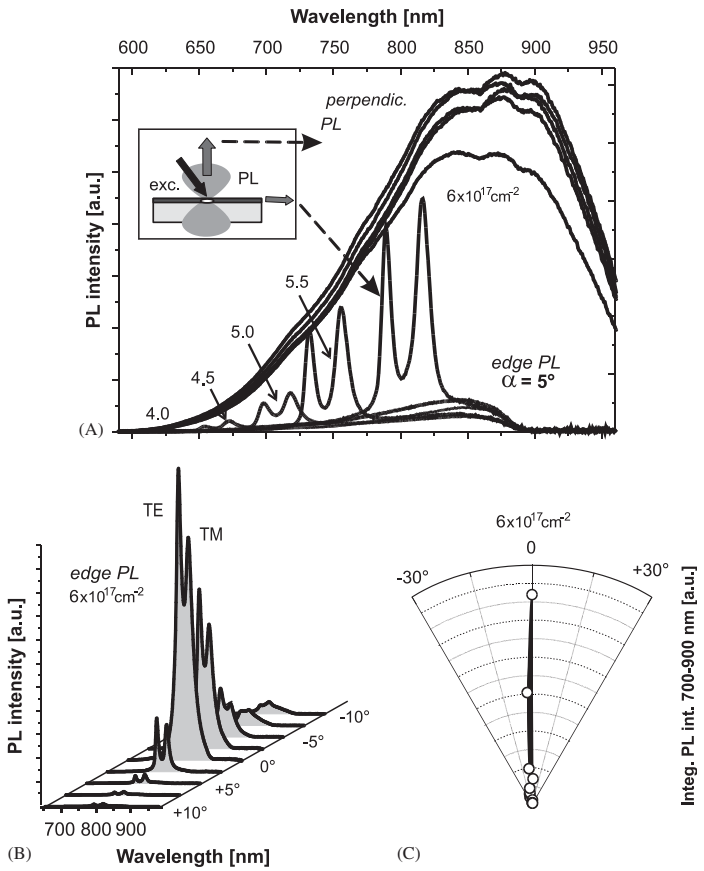

Fig. 5. PL spectra of five fused silica slabs implanted to fluences of $4–6 \times 10^{17}\,cm^{-2}$. (A) Upper curves (a single wide band) correspond to PL emitted in a direction perpendicular to the waveguide, while lower spectra with doublet peaks are facet-PL detected in a direction $\alpha = 5^{\circ}$ (a sketch of the experimental arrangement is shown in the inset). (B) Angle resolved facet PL spectra of the sample $6 \times 10^{17}\,cm^{-2}$. (C) Polar representation of integrated PL intensity of angle resolved facet spectra from the panel B. Most of the PL intensity is emitted in a direction close to 0°.

(wavelengths) that undergo the smallest losses will be advantaged. These are likely those modes that are "weakly guided" with a strongly delocalized electric field. Such modes propagate basically as planar waves in the substrate [13]. Ray optics describes these modes by an angle of incidence θ that is *greater than* but very close to the critical angle θ_c for total internal refection (here the lower core/SiO_2-substrate boundary is of importance only since the refractive index contrast at the upper core/air boundary is high enough to ensure total internal reflection at angles θ safely higher than θ_c). This model was proposed by Khriachtchev et al. [14,15] to explain TE/TM mode structure in Si-NC planar waveguides similar to ours. The spectral separation between TE and TM modes, is then a direct consequence of the asymmetric index profile with different phase shifts expected for the TE and TM modes under total reflection at both boundaries.

(ii) *Radiative substrate modes*: We have previously proposed an alternative mechanism involving substrate leaking or radiation modes of the Si-NC waveguide [10,11]. These modes propagate at angle θ situated close to but *below* θ_c and undergo total reflection at the upper boundary (larger index difference) but are only partially reflected on the lower boundary (smaller index difference). Consequently, a small fraction of their power is radiated into the substrate at each bottom reflection. If the angle θ is only slightly less than θ_c, the leaking modes propagate near-parallel to the Si-NC plane. Moreover, the number of reflections is very high (R is close to unity), resulting in a narrow spectral width for the modes. The mechanism of spectral filtering in this case remains the same as discussed above, the only difference being that a phase shift at the upper boundary only comes to play during the initial stages of propagation. After a finite number of internal reflections all the radiant power escapes into leaking modes and emerges from the sample facet in a well defined direction, basically parallel to the Si-NC film. This makes such substrate modes virtually indistinguishable from the guided modes. The substrate modes are usually considered undesirable parasitic radiation and thus do not normally receive much attention. Indeed, only in cases where guided modes undergo significant losses (absorption and scattering in the waveguide core and diffraction on the narrow output aperture) do the substrate leaking modes play a dominant role.

The fact that the two above proposed mechanisms have a different dependence on the refractive index difference at the surface provides the basis for testing their validity experimentally. The principle is to change locally the cladding layer refractive index. This was done by placing liquid drops on the waveguide/air surface [11,16]. If a drop is above the excited PL spot, the TE/TM modes gradually red-shift and broaden with increasing refraction index of applied liquid and eventually disappear if the index contrast approaches zero. However, when the drop is placed some millimeters away from the spot (between the photo-excited spot and the output facet), no changes in modes is observed, consistent with all the radiant power escaping into radiative substrate modes. These experiments are supported by numerical modeling of the PL spectra which show excellent agreement with experiments and provide unambiguous validation of the leaking modes model [11].

3.4. Coupling and propagation of external light in Si-Nc waveguides

The transmission spectra of the five samples (implantation fluence $4–6 \times 10^{17}\,cm^{-2}$) obtained by white-light coupling through a prism (Fig. 1A) are shown in Fig. 6. In the measured spectral region two broad transmission bands (blue and red) are observed for each sample. The positions of both bands red-shifts with increasing fluence and the position of long-wavelength bands coincides with that of the PL leaking modes (Fig. 5A). Our calculation show that the red and blue bands correspond to second and third order leaking modes (the first one being in infrared). Broadening of the mode structure may be a consequence of the very low number of reflections undertaken by coupled light before escaping to the substrate [17].

Coupling of external light (the warm-white LED) through a truncated facet (Fig. 1B) gives the best result for a coupling angle $\gamma \sim 20^\circ$, as expected (Fig. 7). In this configuration we detect narrow and polarization-split peaks at an output angle $\alpha \sim 2^\circ$. The peaks are, however, not transmission but absorption peaks. This can be understood if it is assumed that the detected light is not from radiative substrate modes (which represent a small portion of transmitted light) but from filtered transmitted light propagating almost parallel to the Si-NC waveguide

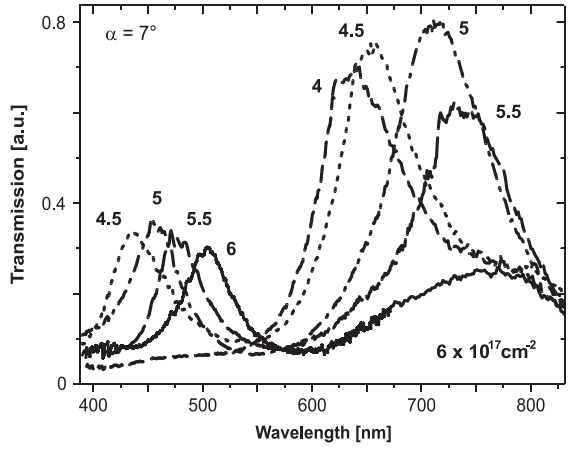

Fig. 6. The transmission spectra of prism-coupled light detected at angle $\alpha = 7^\circ$ from samples presented in Fig. 5.

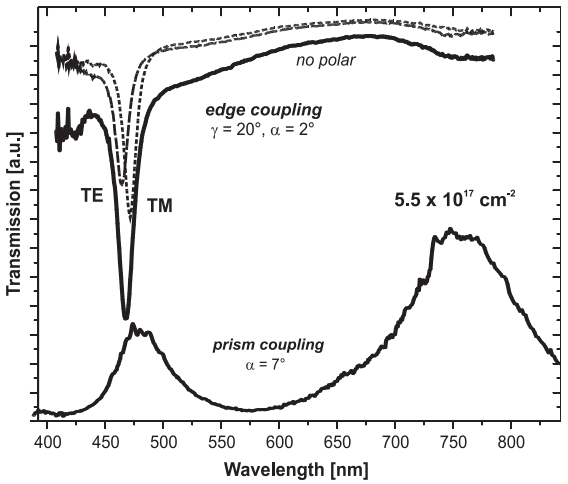

Fig. 7. Comparison of transmission spectra of sample $5.5 \times 10^{17}\,cm^{-2}$ obtained by the direct facet-coupling (upper curves, solid line—no-polarization, dashed and dotted lines correspond to TE and TM polarization, respectively) and by the prism-coupling (lower spectrum).

from which a part of power escaped to the substrate modes. The blue third order modes are much stronger compared to second order because of higher absorption in blue spectral region.

3.5. Leaking modes vs. optical gain

One of the most interesting questions concerning nanocrystal waveguides is the interplay between radiative substrate modes and optical amplification by stimulated emission. Since the first report on optical gain in Si-ion implanted Si-NC layers by Pavesi et al. [18] similar samples have been investigated by other groups with both positive [4] and negative [19] results. Two aspects of this problem are addressed here.

First, experimental artefacts have been shown to play an important role when measuring optical gain close to leaking modes maxima by the commonly used variable-stripe-length (VSL) technique [20]. These artefacts are mainly due to unconventional propagation and coupling of these modes in the detection system, and their interplay with the NA of detection. In order to correct most of these artefacts it has previously been proposed that VSL measurements be combined with a shifting-excitation-spot (SES) technique [20]. Indeed, it should be stressed that the interpretation of VSL results without associated SES measurements can lead to erroneous results.

Secondly, the potential advantages of leaking modes for achieving optical gain are spectral narrowing, low losses, and directionality of propagation. On the other hand the propagation path of radiative modes through a pumped active medium (Si-NCs forming the waveguide) is limited by leakage into the substrate. Attempts to achieve optical gain on leaking modes was successful only under strong nanosecond pulsed pumping (6 ns, 355 nm from THG-Nd:YAG laser) with the gain threshold around $50\,mJ/cm^2$ and maximum gain at TM mode of about $12\,cm^{-1}$ for $100\,mJ/cm^2$ excitation [21].

Further theoretical investigation of the radiative modes in the loss/gain medium is in progress.

3.6. Permanent changes of Si-NC waveguides induced by laser pulses

The Si-NC waveguides in silica may be damaged by high-intensity laser excitation and apparent differences in damage are evident for nanosecond and femtosecond pulses. When irradiated with the 420-nm, 5 ns output of an optical parametric oscillator (OPO) pumped by THG-Nd:YAG (NL 303 + PG122, Ekspla) the damage threshold is very sharp at around $800\,mJ/cm^2$. The damage appears as micrometer-size granular aggregates in the Si-NC followed immediately by complete ablation of the implanted layer. The mechanism is most probably related to heating and even melting of Si-NCs [22] which leads to failure of the silica matrix. This is evidenced by the appearance of cracks and surface ruptures which can lead to complete removal of the SiNC layer.

In contrast, femtosecond laser excitation (400 fs, 400 nm from SHG-Ti:sapphire laser) starts to modify sample at much lower pulse energies $\geqslant 20\,mJ/cm^2$. There are two distinct phases of layer damage. The initial stage appears as darkening (brown coloration) of the excited area. Micro-Raman measurements (not presented here) show that it corresponds to amorphization of the Si-NC layer

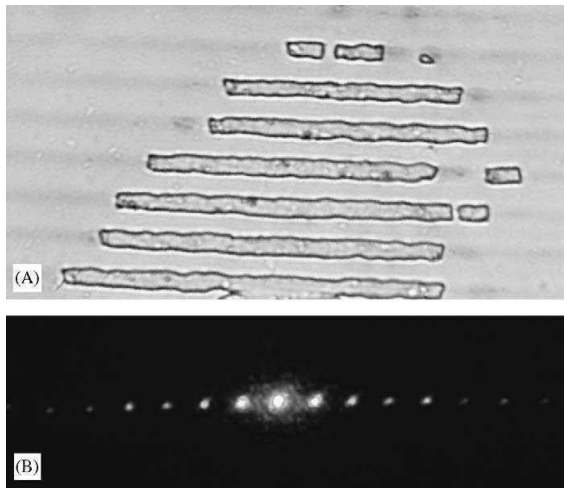

Fig. 8. (A) The diffraction grating (period of about 12 μm) ablated in the Si-NC waveguide (implanted fluence $4 \times 10^{17}\,cm^{-2}$) by an interfering laser pulses from femtosecond laser (SHG-Ti:sapphire laser, 400 fs, 400 nm). (B) A photograph of the pattern produced by diffraction of 633 nm He–Ne laser beam on the ablated grating.

(it appears similar to the implanted layer before annealing). In the second step at higher excitation the layer is ablated. Clearly, the damage mechanism for ultrashort laser pulses (400 fs) is different to that of the longer (5 ns) pulses. The advantage of fs-ablation is that the boundary between the ablated and unchanged area can be very sharp, enabling fs-laser-ablation to be used for lithography to create microstructures in the planar waveguides. In Fig. 8 we demonstrate a diffraction grating with 12 μm period written into $4 \times 10^{17}\,cm^{-2}$ implanted layer by 400 fs, 400 nm fs-pulses.

4. Conclusions

Si-ion implantation into silica slabs or oxide layers on Si wafer followed by annealing is a relatively easy way to fabricate active nanocrystalline planar waveguides. In spite of their simplicity these waveguides show rich optical phenomena which are mainly connected to peculiar radiative substrate modes—so-called leaking modes. This study has investigated the influence of these complex propagation modes on PL, transmission, and gain spectra both experimentally and theoretically. Similar anomalous phenomena connected to the interplay between radiative and guided modes are expected to take place in other types of active waveguides. The possibility of spectral, polarization, and spatial filtering reported for active Si-NC waveguides offer interesting possibilities for application in silicon-based photonic devices or sensors.

Acknowledgement

Financial support through the projects of Research plan MSM0021620835 and Research centre LC510 of MSMT CR, Project no. IAA1010316 of GAAV CR, 202/01/D030 of GACR, the Australian Research Council, and a grant of the Lithuanian State Foundation for Science and Studies (R.T.) is greatly acknowledged. The research work at the Institute of Physics is supported by Institutional Research Plan no. AV0Z 10100521. One of the authors (I.P.) thanks the Laserlab-Europe Integrated Initiative for financial support (vulrc001168).

References

[1] S. Ossicini, L. Pavesi, F. Priolo (Eds.), Light Emitting Silicon for Microelectronics, vol. 194, Springer, Berlin, 2003 Springer Tracts in Modern Physics.
[2] A. Irrera, D. Pacifici, M. Miritello, G. Franzo, F. Priolo, F. Iacona, D. Sanfilippo, G. Di Stefano, P.G. Fallica, Appl. Phys. Lett. 81 (2002) 1866.
[3] R.J. Walters, G.I. Bourianoff, H.A. Atwater, Nature Mater. 4 (2005) 143.
[4] L. Khriachtchev, M. Räsänen, S. Novikov, J. Sinkkonen, Appl. Phys. Lett. 79 (2001) 1249.
[5] J. Valenta, I. Pelant, K. Luterová, R. Tomasiunas, S. Cheylan, R.G. Elliman, J. Linnros, B. Hőnerlage, Appl. Phys. Lett. 82 (2003) 955.
[6] L. Dal Negro, M. Cazzanelli, N. Daldosso, Z. Gaburro, L. Pavesi, F. Priolo, D. Pacifici, G. Franzo, F. Iacona, Physica E 16 (2003) 297.
[7] M. Cazzanelli, D. Navarro-Urrios, F. Riboli, N. Daldosso, L. Pavesi, J. Heitmann, L.X. Yi, R. Scholz, M. Zacharias, U. Gösele, J. Appl. Phys. 96 (2004) 3164.
[8] L. Khriachtchev, M. Räsänen, S. Novikov, J. Lahtinen, J. Appl. Phys. 95 (2004) 7592.
[9] J. Valenta, T. Ostatnický, I. Pelant, R.G. Elliman, J. Linnros, B. Hönerlage, J. Appl. Phys. 96 (2004) 5222.
[10] T. Ostatnicky, J. Valenta, I. Pelant, K. Luterová, R.G. Elliman, S. Cheylan, B. Hönerlage, Opt. Mater. 27 (2005) 781.
[11] I. Pelant, T. Ostatnicky, J. Valenta, K. Luterova, E. Skopalova, T. Mates, R.G. Elliman, Appl. Phys. B 83 (2006) 87.
[12] H.G. Unger, Planar Optical Waveguides and Fibres, Clarendon Press, Oxford, 1977.
[13] H. Kogelnik, V. Ramaswamy, Appl. Opt. 13 (1974) 1867.
[14] L. Khriachtchev, M. Räsänen, S. Novikov, Appl. Phys. Lett. 83 (2003) 3018.
[15] L. Khriachtchev, S. Novikov, J. Lahtinen, M. Räsänen, J. Phys. Condens. Matter 16 (2004) 3219.
[16] K. Luterová, E. Skopalová, I. Pelant, M. Rejman, T. Ostatnický, J. Valenta, J. Appl. Phys., accepted for publication.
[17] P. Janda, J. Valenta, T. Ostatnicky I. Pelant, R.G. Elliman, Thin Sol. Films (in press).
[18] L. Pavesi, L. Dal Negro, C. Mazzoleni, G. Franzo, F. Priolo, Nature 408 (2000) 440.
[19] R.G. Elliman, M.J. Lederer, N. Smith, B. Luther-Davies, Nucl. Instrum. Meth. Phys. Res. B 206 (2003) 427.
[20] J. Valenta, I. Pelant, J. Linnros, Appl. Phys. Lett. 81 (2002) 1396.
[21] K. Luterová, D. Navarro, M. Cazzanelli, T. Ostatnický, J. Valenta, S. Cheylan, I. Pelant, L. Pavesi, Phys. Status Solidi (c) 2 (2005) 3429.
[22] B.V. Kamenev, H. Grebel, L. Tsybeskov, Appl. Phys. Lett. 88 (2006) 143117.

[P5]

Optical gain in planar waveguides

T. Ostatnický[*a], P. Janda[a], J. Valenta[a], I. Pelant[b]
[a]Faculty of Mathematics and Physics, Charles University in Prague, Czech Republic
[b]Institute of Physics, Academy of Sciences of the Czech Republic, Czech Republic

ABSTRACT

Description of optical waveguides is commonly restricted to propagation at distances much larger than the width of the waveguide core and therefore only guided modes are taken into account in theory. Effects connected with leaking of the waves into the substrate may be, however, very important for possible applications in microelectronics. In this paper, we overview our model of photoluminescence of an active planar waveguide and we extend it in order to describe mode formation during propagation in the waveguide. We also include optical amplification into our model and derive formula for description of the Variable Stripe Length (VSL) method widely used for measurement of the net gain coefficient. We demonstrate necessity for corrections of VSL results since their straightforward interpretation may be misleading.

Keywords: planar waveguide, optical gain, silicon nanocrystals, radiative modes

1. INTRODUCTION

High-density integration of current integrated circuits has physical limits due to heat dissipation and other effects. Some of these problems may be solved by incorporation of new types of devices, for example optoelectronic or spintronic.

Electronic chips are mostly fabricated on silicon substrates using planar technologies that enable to create Si/SiO_2 islands, metallic interconnections, *p* and *n*-doped areas etc., but cannot directly integrate devices based on other types of semiconductor materials (GaAs optoelectronic devices etc.). Unlike bulk silicon, which emits light inefficiently, nanostructured silicon could be used to build integrated light sources, which are under recent research.

Luminescence was achieved using porous silicon or silicon nanocrystals[1] and also electroluminescence was demonstrated.[2,3] A source of coherent light based on silicon is, nevertheless, under development because of a small optical gain of Si nanocrystals[4,5] (of the order ~10 cm^{-1}).

Light sources integrated in optoelectronic devices will be probably in a form of active planar or rib waveguides – waveguiding structures with embedded Si nanocrystals or other luminescent bodies. As shown previously,[6,7] these waveguides reveal inavoidable mode leaking of radiation from the waveguide core to the substrate. The radiated field then propagates along the waveguide core and it is detected in spectroscopic experiments together with the guided modes. Although we can take the advantage of this effect for e.g. luminescence spectral filtering in active nanophotonic devices[8] leaking of energy to the substrate is also potentially unwanted effect in integrated devices because it may be responsible for cross talks or other errors.

In this work, we present results of our theoretical investigation of the effects connected with guiding and leaking of light in planar structures on a transparent substrate. The paper may be divided to two main parts: stationary properties (sections 3 and 4) and mode propagation (sections 5 to 7). In the first part, we outline our model which explains our experimental observations in photoluminescence (PL) experiments under low excitation and we show how the parameters of samples may influence measured PL spectra. In the second part, we extend the model in order to describe mode propagation in the direction of the waveguide and we focus on mode formation with and without presence of optical gain. At the end, we show important consequences which follow from our theory for optical spectroscopy but also for future applications in optoelectronics.

[*] Corresponding author e-mail: osty@matfyz.cz; Address: Ke Karlovu 3, 12116 Prague 2, Czech Republic

15th Czech-Polish-Slovak Conference on Wave and Quantum Aspects of Contemporary Optics,
edited by Miroslav Miler, Dagmar Senderáková, Miroslav Hrabovský, Proc. of SPIE Vol. 6609, 66090F, (2007)
0277-786X/07/$18 · doi: 10.1117/12.739493

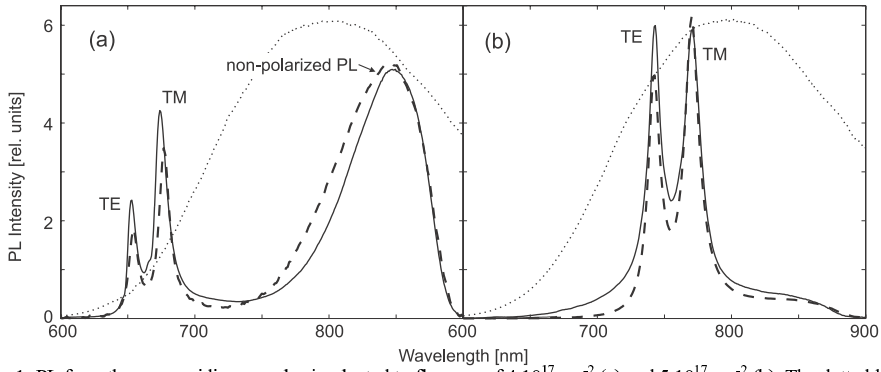

Fig. 1: PL from the waveguiding samples implanted to fluences of $4 \cdot 10^{17}$ cm^{-2} (a) and $5 \cdot 10^{17}$ cm^{-2} (b). The dotted line depicts PL collected in the normal geometry and the solid line the PL measured in the waveguiding geometry. The dashed line is the result of numerical modeling. The TE and TM-polarized peaks are well resolved.

2. EXPERIMENTAL

Our samples are formed by a thin layer (~1 μm thick) of silicon nanocrystals (Si-NCs) with average diameter of about 5 nm (determined by Raman scattering) in 1 mm thick silica slabs . The Si-NC layer was prepared by Si^+-ion implantation to a polished substrate at the energy of 400 keV. The samples were subsequently annealed in order to form Si-NCs in the implanted layer. As a result, active layers of luminescent Si nanocrystals with density controlled by the fluence of Si^+ ions were formed on transparent substrates. The distribution of the Si-NCs density (and thus the refractive index) below the sample surface was non-uniform with a peak at the depth ~0.6 μm[9] (Fig. 4b).

We measured photoluminescence (cw excitation by a He-Cd laser at 325 or 442 nm) of the waveguiding layer in two geometries (cf. Fig. 2): in a standard normal incidence geometry (both excitation and detection nearly perpendicular to the implanted layer) and in the waveguiding geometry (excitation perpendicular to the layer, detected light was collected from the sample edge in the direction parallel with the waveguide).[7] The signal was collected by a microscope objective lens with collection angle about 9°. At the normal incidence, the PL spectra reveal the usual shape (see Fig. 1) of Si nanocrystals – the PL spectrum covers a broad spectral region with the peak around 800 nm and obviously its shape is not affected by the spatial confinement in the waveguiding layer. In the waveguinding geometry, on the contrary, the PL spectrum contains narrow peaks besides a broad spectrum as seen in Fig. 1, the doublet contains the TE and TM polarized modes as verified experimentally. Similar spectral filtering feature of the waveguiding samples was reported also by other groups.[10]

The samples reveal also unique features when the core/substrate is irradiated at angles near $\pi/2$: spectra of absorbance reveal TE and TM-polarized peaks, see Fig. 3. Unlike the PL peaks, resonances are observable in a broader spectral region which is not limited by the spectrum of radiation of the Si-NCs and therefore we observe more TE/TM doublets in absorbance. Spectral positions of the PL maxima coincide with the peaks in the absorbance spectra.

Optical gain is usually measured by the Variable Stripe Length (VSL) method. The principle of the method is, that a spatially wide laser beam is focused by a cylindrical lens to excite a stripe in the sample. Depending on the stripe length ℓ, the intensity of the amplified spontaneous emission (ASE) signal detected in the waveguiding geometry is expected to increase with extending length ℓ due to amplification of the spontaneous emission[11] (the gain coefficient is denoted g):

$$I(\ell) \propto \frac{\exp[g\ell]-1}{g}. \qquad (1)$$

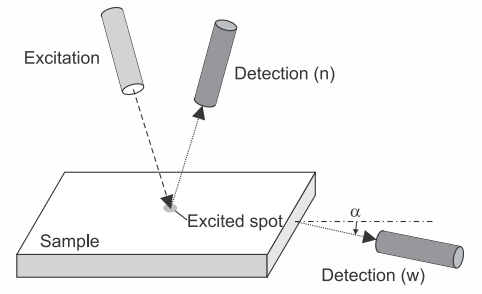

Fig. 2: Sketch of the experimental setup with the normal (n) and the waveguiding (w) geometry.

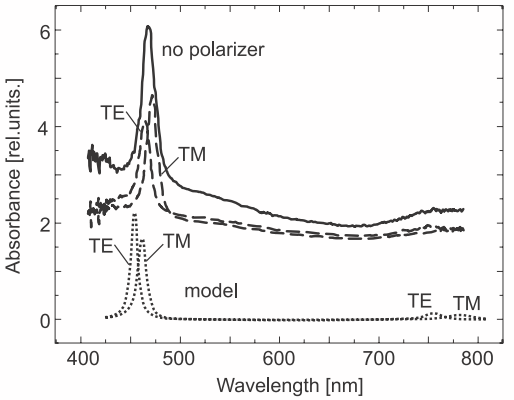

Fig 3: Absorbance of the waveguiding sample implanted to a fluence of $5.5 \cdot 10^{17}$ cm^{-2} in the reflection geometry when the implanted layer was illuminated by white light at an angle near 90°. The solid line is the overall measured signal, dashed lines depict measured TE and TM-polarized spectra and the dotted line is a numerical calculation.

The formula (1) is, however, valid only in the limit of high net gain since it doesn't take into account leaking of waves out of the excited stripe. This fact was pointed out and it was verified experimentally that interpretation of the results of the VSL experiments may be misleading if the results were not corrected for the leaking. For this reason, we proposed a simple experimental method – called Shifting Excitation Spot (SES)[5] – which is suitable for such corrections. Using the VSL and SES methods, it was shown,[5,12] that the measured net gain in the waveguiding samples strongly depends on the spectral position. We explain this fact by a model which follows.

3. MODEL

In this section, we consider a sample with a step-like profile of the refractive index (see Fig. 4a) for clarity. (Numerical calculations in the next section are performed with a real profile of the refractive index.) The waveguide with refractive index n and thickness d is deposited on a substrate with refractive index n_s and it is covered by a cladding with refractive index n_a. We consider that the substrate is transparent and the guiding layer absorbs light (the refractive indexes n_a and $n(\lambda)=n_R(\lambda)+i\lambda\gamma(\lambda)/4\pi$ are generally complex). Nanocrystals randomly distributed in the guiding layer are the source of PL.

Our explanation of occurrence of the narrow peaks in PL spectra (under cw excitation) is based on the existence of the substrate radiative modes besides the guided modes of a waveguide.[13] The guided modes propagate mostly inside the waveguide core and leave a sample through its edge, see Fig. 4a. The radiative modes, on the contrary, leave the waveguide core after several reflections at the core/substrate boundary and then they freely propagate in the lossless substrate until they reach the edge. The crucial point is, that both types of the modes may propagate in the same directions and therefore we cannot separate them when using a detection system with a small numerical aperture.[14]

The total spectral density of the detected radiation may be expressed as $I(\lambda)=I_G(\lambda)+I_R(\lambda)$, where $I_G(\lambda)$ stands for the part of the guided modes and $I_R(\lambda)$ is the part of the radiative modes. The spectrum of the guided modes is broad without any narrow maxima since there exists a guided mode for every wavelength far below the cutoff (the cutoff is expected to be above 2 μm in our samples). Although Khriachtchev *et al.* proposed[10] that the narrow peaks in the PL spectra are formed by the selective absorption due to the mode delocalization, our calculations and experiments have shown[7] that this model is insufficient. We therefore express the spectral profile of the guided modes by an approximate formula:

$$I_G(\lambda, z) = I_0(\lambda)\exp[-\gamma(\lambda)z], \tag{2}$$

where $I_0(\lambda)$ stands for the spectral density of the PL of the nanocrystals (i.e. experimentally measured spectrum in the normal geometry) and a variable z is the distance of an excited spot from the sample edge. We consider that the spectrum of the guided modes does not depend on the observation angle α due to diffraction on the sample edge.[14] On the contrary, there exists an unambiguous relation between the angle of detection of the radiative modes α and their direction of propagation in the waveguide core ϑ (see Fig. 4a). Considering this fact, one may derive[6] the formula for spectral density of the radiative modes:

$$I_R(\lambda, \alpha) = \frac{I_0(\lambda)T(\vartheta)}{\left|1 - r_1(\vartheta)r_2(\vartheta)\exp[2i\kappa(\lambda,\vartheta)d]\right|^2}\frac{d\vartheta}{d\alpha}. \tag{3}$$

Functions r_1 and r_2 are the reflection coefficients for reflection on the two respective core boundaries, T is the transmittance of the core/substrate boundary, $\kappa = \sqrt{\left(\frac{2\pi}{\lambda}n\right)^2 - \beta^2} = \frac{2\pi}{\lambda}n\cos\vartheta$ is the wave vector of the mode in the direction perpendicular to the propagation direction and the term $\frac{d\vartheta}{d\alpha}$ is the correction factor for the spatial density of the PL radiated by a nanocrystal which is isotropic in the core. Assuming an aperture of the detection system with a nonzero size, the detected signal may be calculated using the equation:

$$I_{TOTAL}(\lambda) = \int_{\alpha_0}^{\alpha_1}[I_G(\lambda) + I_R(\lambda, \alpha)]d\alpha, \tag{4}$$

where $\alpha_{0,1}$ denote the limits of the integration over the aperture of the detection system. Formula (3) clearly shows that the shape of PL spectrum of the radiative modes strongly depends on the angle of detection α and therefore we may do the following conclusion.

The PL spectrum contains two components: narrow peaks and a broad spectrum shifted to longer wavelengths compared to the original PL of the intrinsic nanocrystals due to wavelength-dependent absorption. The ratio of the magnitudes of these two parts depends on the absorption coefficient of the core layer and the geometry of the detection system. We may generally state that the higher absorption induces stronger appereance of the radiative modes. This fact directly follows from Eqs. (2) and (3): since $z \gg d$, the guided modes are suppressed when losses in the core are too high, while radiative modes propagate mostly in the transparent substrate. This fact was clearly illustrated in our previous publications[7] where the absorption coefficient increases with the fluence of implantation. At the lowest fluence, a wide PL band is resolved above 700 nm and no radiative modes are seen while the spectra for higher fluences contain both types of PL. The above statements are further supported experimentally[12] – we were able to separate the PL of the guided modes by spatial filtering.

4. NUMERICAL CALCULATIONS

We considered an asymmetric continuous profile of the refractive index below the sample surface. The particular profiles of the refractive indexes were determined on the basis of numerical fitting of infra-red transmission spectra[9] and are schematically plotted in Fig. 4b. We slightly modified the above formulae and we numerically calculated the PL spectra using the standard transfer matrix formalism. The results are plotted in Fig. 1 for the parameters used in the experiments.

The shape of the PL spectrum depends on the conditions of observation (position of a detector and its numerical aperture) and it also strongly depends on the sample parameters and thus the preparation conditions. These facts are summarized in Fig. 5 where we plotted the calculated dependences of PL characteristics (widths of the respective TE and TM peaks and their spectral positions) on the following parameters: the angle of observation α, peak value of the core refractive index Δn (controlled by the fluence of implantation), width of the distribution of nanocrystals σ below

the sample surface and the refractive index of the cladding n_a. We took parameters of the sample implanted with fluence of $5 \cdot 10^{17}$ cm^{-2} as a reference.

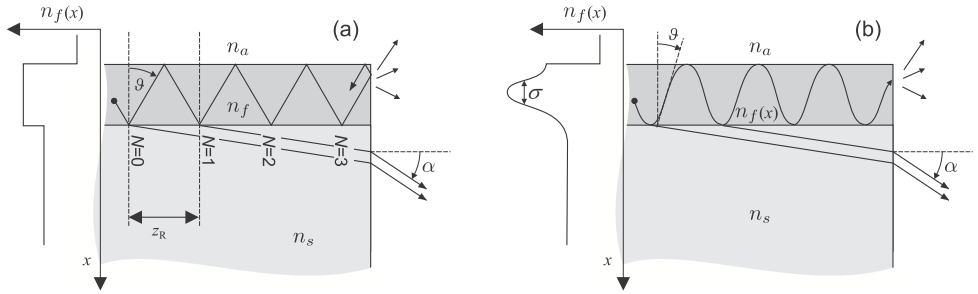

Fig. 4: Ray propagation in a sample with step-like (a) and continuous (b) profile of refractive index of the core.

In our particular case, the planar waveguide is considered to be asymmetric, i.e. $n_a < n_s$. Radiative modes are therefore expected to leak only to the substrate and to be observed only for angles $\alpha > 0$ as seen in Fig. 5a. Change of the observation angle causes change of both the exponential factor in Eq. (3) and reflectivity on the core/substrate boundary and therefore the spectral positions and widths of the PL maxima change. The greater detection angle α is, the smaller is the reflectivity of the core/substrate boundary and the wider PL peaks are.

Figs.5b-d illustrate the possibility of tuning the sample properties by variation of the preparation conditions. We may prepare for example structures for real-time sensing of the refractive index of liquids which is represented by the refractive index of the cladding in Fig. 5d, Ref. 7.

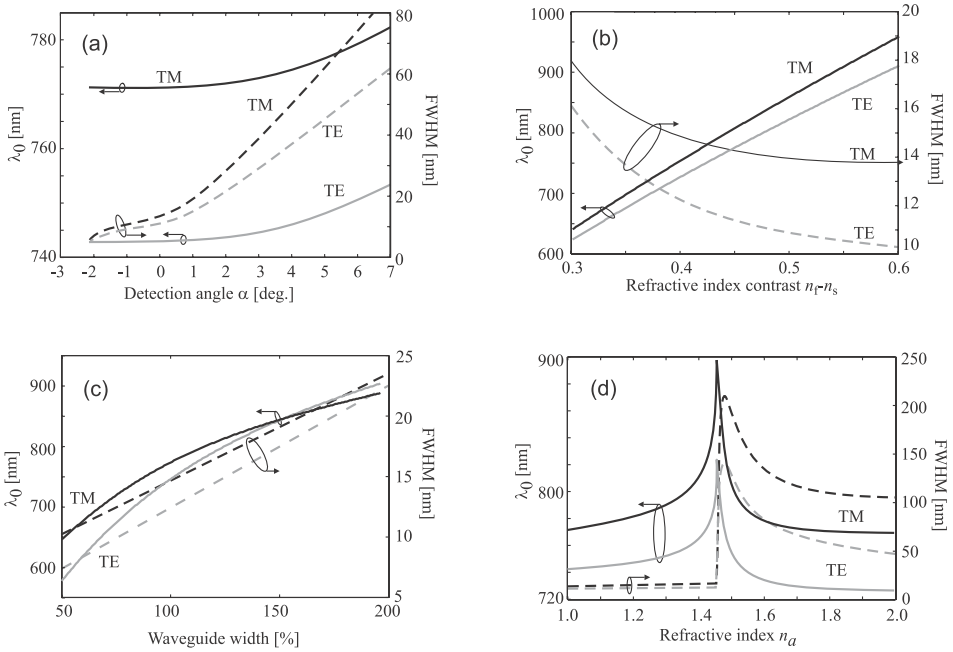

Fig 5: Calculated dependence of the spectral width and spectral position of the modes detected in PL on: (a) detection angle in the waveguiding geometry, (b) contrast of the maximum of the refractive index of the core relative to the refractive index of the substrate, (c) width of distribution of the refractive index of the core (100% means FWHM of the refractive index distribution 6.5 μm) and (d) refractive index of the cladding. We took the parameters of the sample implanted with fluence of $5\cdot10^{17}$ cm^{-2} as a reference.

The grazing incidence absorbance spectra depicted in Fig. 3 are also fully consistent with the model. Although light should be totally reflected by the waveguiding structure, some part is absorbed in the core. The maximum of absorption arises when the phase matching condition is met – this is the same condition as the condition for the peak of PL. Calculated theoretical curve of the absorbance is depicted in Fig. 3 by a dotted line.

5. FORMATION OF MODES

The model formulated in section 3 describes a situation when the waves undergo an infinite number of reflections inside the waveguide core. This situation corresponds to an experiment in which the excitation spot is far from the edge ($z \gg d$). However, as poited out in our previous publication[15] and later by Khriachtchev *et al.*,[10] the shape of the modes in PL undergoes evolution when the distance of the excitation spot from the edge is increased. Interpretation, based on our model, is simple: the smaller is the distance z, the less round-trips between the core boundaries are performed by the wave. Constructive/destructive interference is best met at an infinite number of reflections and therefore we expect the best mode formation at high number of reflections N and therefore at long distances z whereas no modes in the PL spectra are expected at small distances. The effect may be enhanced due to the dominance of radiative modes at long distances and the dominance of the flat spectrum of the guided modes at small distances.

Spectrum of the guided modes is not influenced by the number of internal reflections and therefore we can keep formula (2) for determination of their spectral profile. Formula (3), however, needs a correction for a finite number of reflections:

$$I_{\mathrm{R}}(\lambda,\alpha,z)=\left|\frac{1-[P(\lambda,\alpha)]^{N(\vartheta,z)+1}}{1-P(\lambda,\alpha)}\right|^2 I_0(\lambda)T(\vartheta)\frac{\mathrm{d}\vartheta}{\mathrm{d}\alpha}, \tag{5}$$

$$P(\lambda,\alpha)=r_1(\vartheta)r_2(\vartheta)\exp[2\mathrm{i}\kappa(\lambda,\vartheta)d]\exp[-\gamma(\lambda,\vartheta)z_{\mathrm{R}}/2], \tag{6}$$

where $N(\vartheta,z)$ is the number of reflections of the wave inside the core and z_{R} is the distance between two points of reflection on the core/substrate boundary. The intensity of radiation which remains in the core after N reflections of a ray on the core/substrate boundary (see Fig. 4a) may be expressed as:

$$I(N)=I_0|r_1r_2|^{2N}=I_0\exp[-2\gamma_{\mathrm{eff}}z], \tag{7}$$

and therefore the number of reflections may be evaluated in the following way:

$$N=-\frac{\gamma_{\mathrm{eff}}z}{\log|r_1r_2|}, \tag{8}$$

and $z_{\mathrm{R}}=-\frac{\log|r_1r_2|}{\gamma_{\mathrm{eff}}}$, where γ_{eff} is an effective attenuation coefficient which reflects the leaking to the substrate. It may be calculated from the Poynting vector. In the case of an asymmetric waveguide with the step-like profile of the refractive index, the coefficient may be expressed for TE waves as:[13]

$$\gamma_{\mathrm{eff}}=\frac{\kappa^2}{\beta d}\frac{\rho}{(\kappa+\rho)^2}, \tag{9}$$

$$\rho^2=\left(\frac{2\pi n_{\mathrm{s}}}{\lambda}\right)^2-\beta^2. \tag{10}$$

In structures with more complicated profile of the refractive index, the attenuation coefficient must be evaluated numerically, however Eqs. (7) and (8) remain valid. Results of the calculation of the narrowing of the modes in a sample with step-like profile of the refractive index are plotted in Fig. 6. Presence of the guided modes may cause apparent shift of the PL maxima due to wavelength-dependent absorption. Calculated widths of the maxima and the distance on which they are formed strongly depend on the profile of refractive index: if it changes continuously, modes would be wider and they would form on longer distances z.

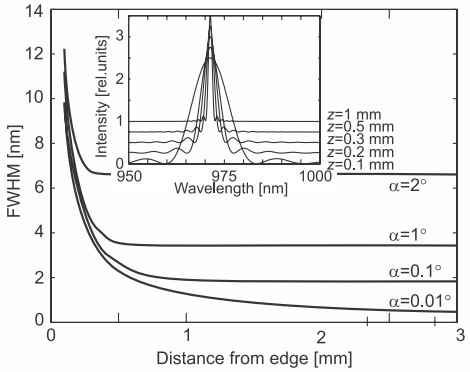

Fig. 6: Width of the radiative modes as a function of the distance of the excitation spot from the sample edge. Default parameters are n_s=1.46, n_f=1.8, γ=10 cm^{-1}, d=1.5 μm. Inset shows spectral profile of the modes.

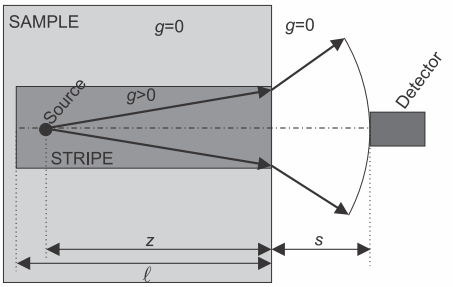

Fig. 7: Sketch for derivation of the ASE signal.

6. OPTICAL GAIN

Considering a homogeneously excited stripe with length ℓ which reveals an optical gain and considering that only the plane waves which propagate in the direction of the excited stripe are detected, one derives formula (1) for dependence of the detected light intensity on ℓ. The formula is widely used in spectroscopy in the VSL method, however it is valid (for real detectors with a nonzero numerical aperture) only in the limit of large optical gain. For the limit of small or zero optical gain and a large numerical aperture of the detector, a rigorous theoretical and experimental review was published,[16] however we use a simplified approach in order to show the main characteristics of the waveguiding samples. First we derive a formula for determination of the ASE signal as a function of the stripe length in a bulk sample. We must take into account that the amount of energy radiated by a nanocrystal and detected by a detector scales with the distance r between the nanocrystal and the detector as $1/r^2$. Let's denote the distance between the edge of the sample and the detector s considering that s is much larger that the width of the excited stripe, let's denote the gain coefficient g and the real part of the refractive index of the sample n_f (see Fig. 7). One may directly derive that the total intensity detected by the detector is:

$$I_G(\ell) \propto \int_0^{\ell} \frac{\exp[(g-\gamma)z]}{(z+n_f s)^2} dz \,. \qquad (11)$$

Note that the above formula describes the situation depicted in Fig. 7 – if the signal is collected using some optical elements in front of the detector, the calculation must be adapted according to the particular situation. The function in Eq. (11) is not integrable analytically, however for large g it clearly reduces to Eq. (1). We plotted the function (11) for various parameters in graph in Fig. 8. Obviously it qualitatively fits the measured ASE curves.[12] The exponential growth of the experimental data slightly above the zero length of the excited stripe is due to diffraction or other optical artifacts which are not taken into account in the present model.

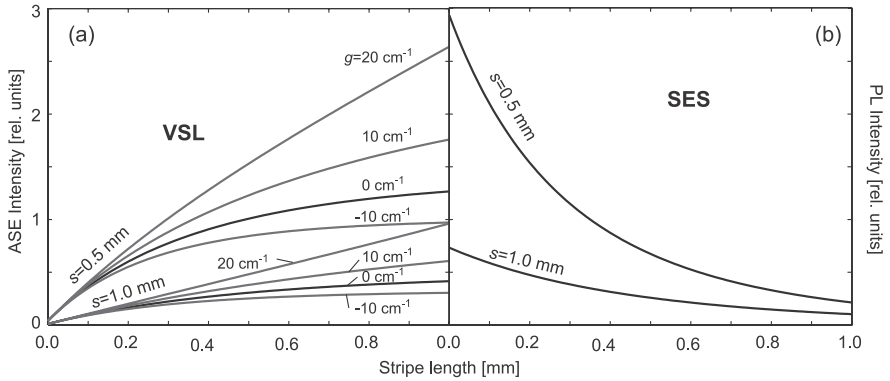

Fig. 8: Calculated intensity detected in a VSL (a) and SES (b) experiments from a bulk sample with refractive index 1.6 and with the detector in the distance 0.5 and 1 mm from the sample edge. Curves of ASE are calculated for zero, positive and negative gain coefficients considering the loss coefficient γ=10 cm^{-1}.

The ASE curves reveal interesting behavior on for larger lengths of the excitation stripe as shown in Fig. 9 where we plot dependence of ASE on the stripe length for the same parameters as in Fig. 8, however on a different scale for ℓ. ASE curves in Fig. 8, when compared with Eq. (1), seem to reveal no net gain or a small net gain and strong saturation. Our calculations show that the apparent saturation is due to the beam divergence and the behavior of superlinear ASE growth arise for larger lengths of the stripe of the order of several mm. In Fig. 9a we show the ASE curves for gain coefficients g=0 cm^{-1} and g=20 cm^{-1} in linear scale with graphs of Eq. (1) for g=20 cm^{-1} and g=4.7 cm^{-1} (best fit). Fig. 9b shows the same curves on an even large scale for ℓ in order to show that fitting by (1) may give incorrect results if performed for small stripe lengths – the net gain may be underestimated.

Discussion of optical amplification in waveguides is more complicated because of the existence of the waves which leak into the substrate. Guided modes propagate in the waveguiding layer and thus they are amplified on the whole path. The formula analogous to Eq. (9) for the guided modes thus differs only in the denominator which is in the first power:

$$I_{\mathrm{RC}}(\ell) \propto \int_0^{\ell} \frac{\exp[(g-\gamma)z]}{z+n_{\mathrm{f}}s}\mathrm{d}z\,. \qquad (12)$$

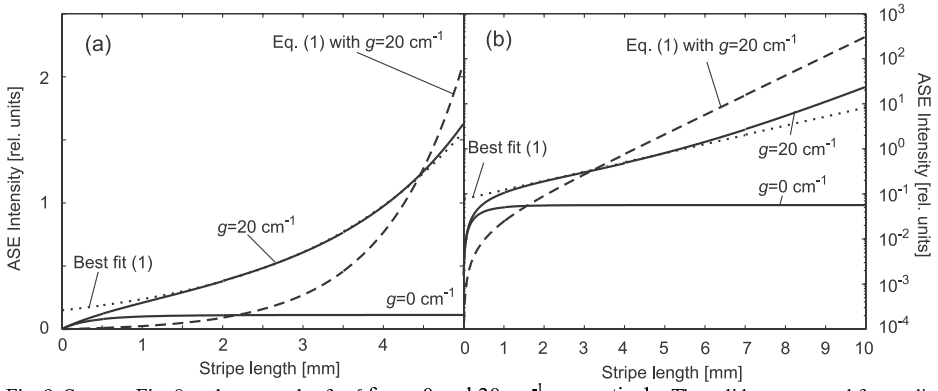

Fig. 9: Same as Fig. 8 on longer scales for ℓ for g=0 and 20 cm^{-1}, respectively. The solid curves stand for predictions of our model based on Eq. (12), the dashed curve is the result of Eq. (1) with g=20 cm^{-1} and the dotted line is the best fit of Eq. (12) by Eq. (1) with g=4.6 cm^{-1}..

The radiative modes, on the contrary, may be amplified only on a part of their path because of their leakage to the substrate. Some of the radiative modes are effectively amplified if the gain coefficient is high enough to compensate the losses by leaking. We divide derivation of the intensity of the detected waves into two parts: (i) a contribution from the wave which remains in the core until it reaches a sample edge and (ii) from the wave refracted to the substrate. For the waves in the core, the same formula as Eq. (12) holds when γ is substituted by γ_{eff} according to Eq. (9) ($\gamma_{\mathrm{eff}}=\gamma$ for the guided modes). Considering the refracted waves, we must take into account that they are amplified only during propagation in the core and that once the wave leaves the core, its intensity decreases with the second power of the distance:

$$I_{\mathrm{RS}}(z)=\frac{I_0}{(z+n_{\mathrm{f}}s)^2}\left|\frac{1-P^{N+1}}{1-P}\right|^2 T\frac{\mathrm{d}\vartheta}{\mathrm{d}\alpha}, \tag{13}$$

$$P=r_1r_2\exp[2i\kappa d]\exp\left[\frac{g\kappa^2 d}{2\pi^2}\right]\exp[(g-\gamma)z_{\mathrm{R}}/2]\,. \tag{14}$$

The total ASE signal in the VSL experiment is expressed as the sum:

$$I(\ell)=\int_0^{\ell} I_{\mathrm{RS}}(z)\mathrm{d}z+C_{\mathrm{C}}I_0\int_0^{\ell}\frac{\exp[(g-\gamma_{eff})z]}{z+n_{\mathrm{f}}s}\mathrm{d}z\,. \tag{15}$$

Here the symbol C_{C} expresses an efficiency of coupling of the guided modes to the detector – generally it is less than 1 due to nonzero numerical aperture of the waveguide. The above function is plotted for various parameters in Fig. 10a-d. The panels a-b in Fig. 10 show for comparison predicted ASE and SES curves for parameters similar to Fig. 8 (bulk sample). The initial rise of the ASE measured at wavelengths of the radiative modes is not an effect of optical gain but a specific (linear optical) characteristics of the waveguiding samples as proven by our calculations. The influence of mode leaking is clearly seen in Figs. 9c-d: the leaking is most efficient for large detection angles α and near the mode maximum at 971.5 nm while the modes are mostly guided far from the resonance or at low detection angles. Leaking causes very complex dependence of the mode coupling to the detector on the distance of the excitation spot from a sample edge. This effect was also observed experimentally.[5] Due to the limited path in the core, leaking waves are amplified with low efficiency compared to the guided modes, as seen in Fig. 10a. Their net gain may be, nevertheless, positive but always lower than the net gain of the guided modes.

7. DISCUSSION

Spectrally narrow modes which leak into the substrate are formed, as demonstrated in the results in the previous two sections, on distances much larger than the waveguide width. This phenomenon was observed experimentally by our group[15] and by Khriachtchev *et al.*[10] Our results do not fit the experimental data exactly because we did not take into account the exact profile of the refractive index of the sample and we did not consider that the excitation spot has a nonzero size. The qualitative agreement between the experiment and calculations is, however, excellent and we may conclude that our model describes the PL experiments with high precision.

In our calculations of SES and ASE curves, we considered a specific experimental setup depicted in Fig. 7 which models an experiment in which the PL signal is collected by an optical fiber without any optics between the sample and the fiber. Additional optical elements, however, make the calculations more complex. Optics usually display the sample edge on an input of a detector (e.g. an optical fiber, an entrance slit of a spectrometer) and its influence is therefore that only the numerical aperture is changed and the effective distance between the sample and the detector is $s\rightarrow 0$. The values $s\approx 1$ mm used above are not therefore underestimated and the results of calculations may be qualitatively compared with experimental data.

The curves in Fig. 8 qualitatively reproduce the measured data[12] except for the initial rise for $\ell\rightarrow 0$ which is due to diffraction, as noted above. Although the ASE signal in the VSL experiments increase sublinearly, simulations show

that it is not due to the saturation of optical gain but it is caused by the decrease of the coupling efficiency between the source and the detector. The effect of varying coupling may be eliminated by putting the detector far from the sample.

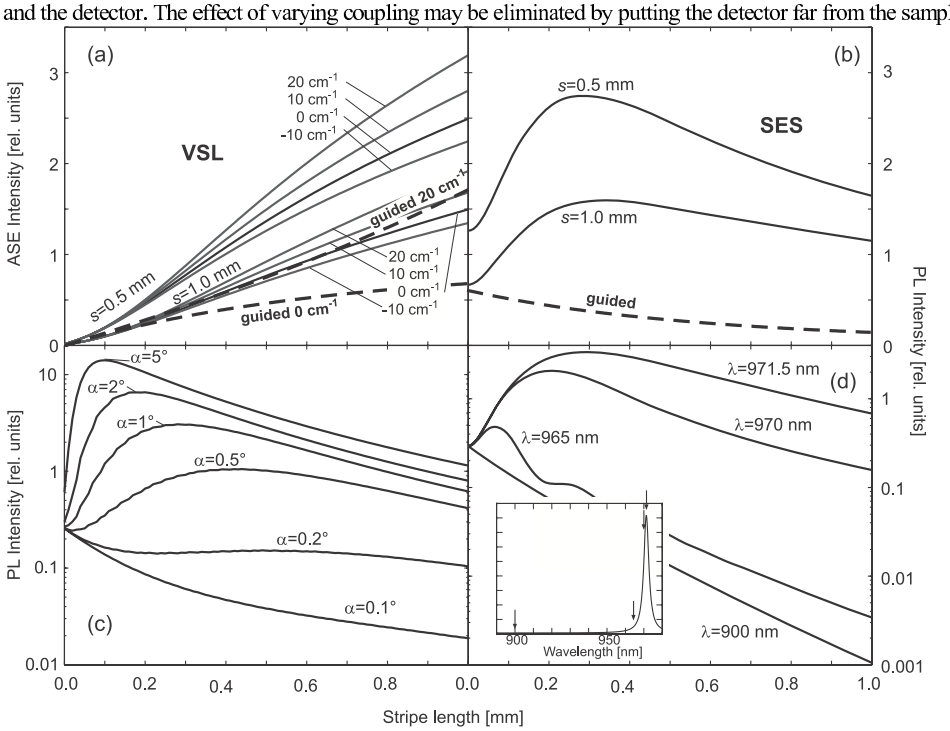

Fig. 10: Calculated ASE (a) and SES (b-d) curves from a waveguiding sample according to Eq. (15) for leaking waves (solid) and guided modes (dashed). Parameters of the sample were: refractive index n_s=1.46, n_f=1.8,γ=10 cm^{-1}, d=1.5 μm. Default detection angle was considered α=1º, distance of the detector from the sample edge s=0.5 mm, detection wavelength 971.5 nm (in the maximum of a mode). Figs. (c) and (d) show how the shape of the SES curves change with detection angle an wavelength.

This setup corresponds to the Fraunhofer limit of diffraction, i.e. we detect only a plane wave with well defined direction and the formula (11) reduces to Eq. (1).

Simulations on the waveguiding samples in Fig. 10 are in a good agreement with our experimental data.[5] Guided modes reveal the usual behavior: they are amplified on the whole path through the sample until they reach the edge. The effective losses are only due to the divergence, i.e. due to the varying coupling to the detector. When compared to the bulk samples, the coupling coefficient decrease only with the first power of the distance between the excited spot and the detector and therefore the superlinear growth of the ASE signal may be more likely observed than in the bulk samples.

Leaking waves, on the other hand, reveal themselves very unusually. In the SES experimental setup, the PL intensity grows with the distance z and after reaching some limit, it starts to decrease. The limiting distance z is determined by the angle of the mode propagation in the waveguide core and therefore by the angle of observation. The SES experiments may be interpreted as follows. The wave is radiated in the core and it subsequently propagates in the core and partly leaks to the substrate. The longer is the distance of propagation, the more energy is transferred to the substrate. We detect the sum of the wave which remains in the core and the wave refracted to the substrate from the edge, however the refracted wave is usually stronger because of absorption in the core and diffraction at the edge. With increasing distance z, the intensity of PL is increasing until the growth is overridden by the decay due to decreasing coupling to the detector.

Presence of the positive optical gain is responsible for the growth of ASE in the VSL configuration and therefore the optical amplification may be detected by the direct comparison of the integrated SES and VSL measurements. Determination of the gain coefficient is, however, difficult and the changes in PL are not pronounced as nicely as if the measurement is performed on the guided modes.

The gain measurement should give better results if measured on the guided modes only. We show in Fig. 10d that the guided modes may be experimentally separated by spectral filtering – if the detected signal is selected from the broad PL spectrum outside the TE and TM-polarized peaks, only guided modes are coupled to the detector. Analysis of the net optical gain is then based on Eq. (12) or on a more complex theory in Ref. 16.

8. CONCLUSIONS

We develop a model which describes formation and optical amplification of the modes in optical waveguides (both leaking and guided). The behavior of the guided modes is affected only by the effective reduction of the dimensionality of the sample to 2D (compared to bulk samples) and therefore the effective losses due to divergence of the radiated field are lower than in bulk samples. This fact may result in observation of superlinear increase of the ASE signal on waveguides containing Si nanocrystals, however we stress out that one must still compare ASE and SES curves in order to identify whether the net gain is positive or negative. A special attention must be, nevertheless, paid to the leaking waves since they cause a variety of unwanted effects.

Leaking waves may cause problems not only in spectroscopic experiments but they may play an important role in micro-optoelectronics on integrated devices. The source of signal (guided modes) then may be also the source of the noise guided by the substrate. It may therefore appear desirable to cut off the noise by addition of an absorbing layer to the substrate or in another way, if necessary.

9. ACKNOWLEDGEMENTS

The authors thank to Prof. R.G. Elliman from Australian National University Canberra for ion-implantation of waveguiding samples. This work was supported by the Grant Agency of the Academy of Sciences of the Czech Republic (grant IAA 1010316), by the Ministry of Education of the Czech Republic in the framework of the research centre LC510 and the research plans MSM 0021620834 and AV0Z 10100521.

REFERENCES

1. L.T. Canham, "Silicon quantum wire array fabrication by electrochemical and chemical dissolution of wafers", *Appl. Phys. Lett.* **57**, 1046-1048, 1990.
2. L. Tsybeskov, S.P. Duttagupta, K.D. Hirschman, and P.M. Fauchet, "Stable and efficient electroluminescence from a porous silicon-based bipolar device", *Appl. Phys. Lett.* **68**, 2058-2060, 1996.
3. K. Luterová, I. Pelant, J. Valenta, J.-L. Rehspringer, D. Muller, J.J. Grob, J. Dian, and B. Hönerlage, "Red electroluminescence in Si^+-implanted sol–gel-derived SiO_2 films", *Appl. Phys. Lett.* **77**, 2952-2954, 2000.
4. L. Khriachtchev, M. Räsänen, S. Novikov, and J. Sinkkonen, "Optical gain in Si/SiO_2 lattice: Experimental evidence with nanosecond pulses", *Appl. Phys. Lett.* **79**, 1249-1251, 2001.
5. J. Valenta, I. Pelant, and J. Linnros, "Waveguiding effects in the measurement of optical gain in a layer of Si nanocrystals", *Appl. Phys. Lett.* **81**, 1396-1398, 2002.
6. J. Valenta, T. Ostatnický, I. Pelant, R.G. Elliman, J. Linnros, and B. Hönerlage, "Microcavity-like leaky mode emission from a planar optical waveguide made of luminescent silicon nanocrystals", *J. Appl. Phys.* **96**, 5222-5225, 2004.
7. I. Pelant, T. Ostatnický, J. Valenta, K. Luterová, E. Skopalová, T. Mates, and R.G. Elliman, "Waveguide cores containing silicon nanocrystals as active spectral filters for silicon-based photonics", *Appl. Phys. B* **83**, 87-91, 2006.
8. P. Janda *et al.*, *J. Lumin.*, in print, 2006.
9. R.G. Elliman, M.J. Lederer, and B. Luther-Davis, "Optical absorption measurements of silica containing Si nanocrystals produced by ion implantation and thermal annealing", *Appl. Phys. Lett.* **80**, 1325-1327, 2002.

10. L. Khriachtchev, M. Räsänen, and S. Novikov, "Efficient wavelength-selective optical waveguiding in a silica layer containing Si nanocrystals", *Appl. Phys. Lett.* **83**, 3018-3020, 2003.
11. K.L. Shaklee, R.F. Leheny, and R.E. Nahory, "Stimulated Emission from the Excitonic Molecules in CuCl", *Phys. Rev. Lett.* **26**, 888-891, 1971.
12. K. Luterová, M. Cazzaneli, J.-P. Likforman, D. Navarro, J. Valenta, T. Ostatnický, K. Dohnalová, S. Cheylan, P. Gilliot, B. Hönerlage, L. Pavesi, and I. Pelant, "Optical gain in nanocrystalline silicon: comparison of planar waveguide geometry with a non-waveguiding ensemble of nanocrystals", *Opt. Mater.* **27**, 750-755, 2005.
13. M. Dietrich: *Theory of dielectric optical waveguides*, Academic Press, Boston, 1991.
14. T. Ostatnický, J. Valenta, I. Pelant, K. Luterová, R.G. Elliman, S. Cheylan, and B. Hönerlage, "Photoluminescence from an active planar waveguide made of silicon nanocrystals: dominance of leaky substrate modes in dissipative structures", *Opt. Mater.* **27**, 781-786, 2005.
15. J. Valenta, I. Pelant, K. Luterová, R. Tomasiunas, S. Cheylan, R.G. Elliman, J. Linnros, and B. Hönerlage, "Active planar optical waveguide made from luminescent silicon nanocrystals", *Appl. Phys. Lett.* **82**, 955-958, 2003.
16. L. Dal-Negro, P. Bettotti, M. Cazzanelli, D. Pacifici, and L. Pavesi, "Applicability conditions and experimental analysis of the variable stripe length method for gain measurements", *Opt. Commun.* **229**, 337-348, 2004.

J. Phys. D: Appl. Phys. **41** (2008) 015103 (5pp) doi:10.1088/0022-3727/41/1/015103

Ultrafast decay of femtosecond laser-induced grating in silicon-quantum-dot-based optical waveguides

I Pelant[1,6], R Tomašiūnas[2], V Sirutkaitis[3], J Valenta[4], T Ostatnický[4], K Kůsová[1] and R G Elliman[5]

[1] Institute of Physics, Academy of Sciences of the Czech Republic, Cukrovarnická 10, CZ-162 53, Prague 6, Czech Republic
[2] Institute of Materials Science and Applied Research, Vilnius University, Sauletekio 10, 10223 Vilnius, Lithuania
[3] Laser Research Centre, Vilnius University, Sauletekio 10, 10223 Vilnius, Lithuania
[4] Charles University, Faculty of Mathematics and Physics, Ke Karlovu 3, 121 16 Praha 2, Czech Republic
[5] Electronic Materials Engineering Department, Research School of Physical Sciences and Engineering, Australian National University, Canberra ACT 0200, Australia

E-mail: pelant@fzu.cz

Received 17 September 2007, in final form 25 October 2007
Published 12 December 2007
Online at stacks.iop.org/JPhysD/41/015103

Abstract
Femtosecond transient laser-induced grating (LIG) experiments were performed in planar optical waveguides made of luminescent silicon quantum dots. The LIG was created by interference of two pulses from the frequency-doubled output of a Ti–sapphire laser (400 nm, 400 fs, 1 kHz). The LIG exhibits an extremely fast decay in time (several picoseconds) that was found to decrease with decreasing grating period. The standard models based on lateral carrier diffusion cannot explain this observation (this procedure yields an unrealistically high diffusion constant of 420 $cm^2\ s^{-1}$). Instead, the results are explained by exciton diffusion and/or enhanced exciton radiative decay rate in a cavity represented by the periodically modulated planar waveguide (Purcell effect).

1. Introduction

Silicon quantum dots (silicon nanocrystals, Si-ncs) are efficient light emitters and have been employed to fabricate silicon-based light-emitting devices, such as light-emitting diodes. They have also been employed to fabricate active optical waveguide structures [1–3], in which complex spectral filtering of the self-guided photoluminescence (PL) has been observed [2, 3]. Many properties of such waveguides, which hold promise for exploitation in silicon photonics, remain to be explored and interpreted.

Transient laser-induced-grating (LIG) experiments are known to provide insight into fast non-equilibrium carrier recombination and diffusion in semiconductors. The LIG can decay in time due to both carrier recombination and lateral diffusion. When applied with picosecond laser pulses, a clear discrimination between both contributions can usually be obtained and the carrier ambipolar diffusion constant extracted [4,5]. Here we report on the application of ultrashort (femtosecond) laser pulses to investigate LIG decay in planar waveguides made of Si-ncs. We show that the observed grating efficiency decay is extremely fast, of the order of picoseconds, and we discuss possible reasons for such an unusual decay in a system composed of Si nanocrystals, which commonly exhibit much slower photocarrier recombination—in the microsecond range or even longer [6].

2. Experimental

Samples investigated in this study were prepared by implanting Si^+ ions into slabs of synthetic silica substrates (Infrasil)

[6] Author to whom any correspondence should be addressed.

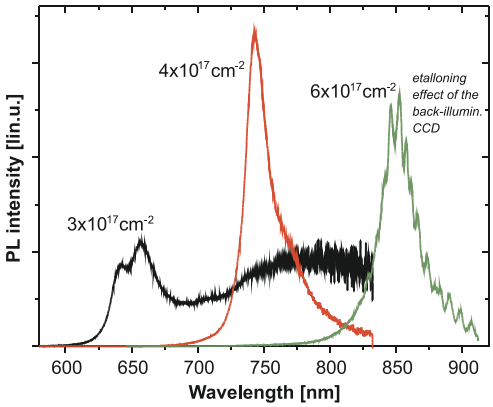

Figure 1. PL spectra taken from the edge of investigated samples ('waveguiding geometry'). Excitation with the 442 nm line of a cw HeCd laser, $T = 295$ K. Owing to insufficient resolving power the doublet structure of the peaks can be discerned in the sample 3×10^{17} cm^{-2} only.

with dimensions of about $8 \times 5 \times 1$ mm^3. The implantation energy was 400 keV and several implant fluences from 1 up to 6×10^{17} cm^{-2} were applied to different samples. A post-implant anneal at 1100 °C in N_2 ambient for 1 h caused precipitation of dispersed excess Si^+-ions into luminescent Si-ncs with a typical diameter of 4–5 nm. A further anneal for 1 h at 500 °C in forming gas (N_2/H_2) was employed to passivate non-radiative defects and enhance the Si-nc PL intensity [7]. Peak excess Si concentrations were up to 26 at% Si. To give an idea of how densely the Si-nc are packed, we suppose (i) the nanocrystal diameter to be 5 nm and (ii) only 50% of the implanted Si atoms have been accumulated to form the nanocrystals. For the excess Si concentration of 20 at% we get in this way the mean distance between nanocrystals of about 16 nm. The ensembles of Si-ncs with the nanocrystal concentration peaking at a mean depth of ∼630 nm (the total thickness of the Si-nc layers being about 800 nm) represent planar waveguides buried in fused silica [3]. Room-temperature PL spectra of the three samples implanted to the highest fluences, as taken in the waveguiding geometry (i.e. from the edge of the samples), are shown in figure 1. The spectra consist of relatively narrow peaks whose position is systematically red shifted with increasing implant fluence. These peaks represent radiative modes of the waveguides [3] and are in fact TE/TM doublets; here, their doublet structure is clearly resolved in the 3×10^{17} cm^{-2} sample only.

In the LIG technique, two coherent laser pulses interfere in the sample, creating a periodic, spatially modulated pattern. Diffraction of a third, time-delayed pulse is used to monitor the decay of the grating with time. Frequency-doubled pulses ($\lambda_p = 400$ nm, $h\nu = 3.1$ eV) of ∼400 fs duration, provided by a cw doubled Nd^{3+}–YAG laser-pumped Ti–sapphire laser, were split into two pump pulses of equal intensity. These were used to define an LIG in the waveguides parallel to the sample surface. The grating period Λ was varied by varying the angle θ between the writing pulses ($\Lambda = \lambda_p/2\sin(\theta/2)$). The pump spot diameter was about 300 μm and the pump

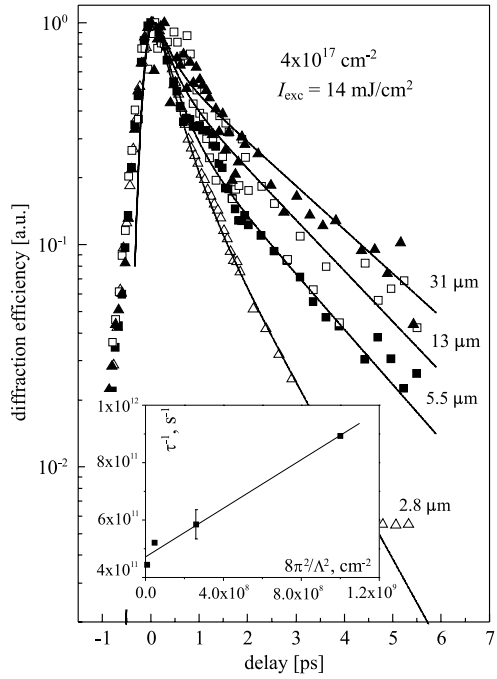

Figure 2. Normalized LIG decay curves for different grating periods Λ (next to the curves) in a waveguide implanted to a fluence of 4×10^{17} cm^{-2}. Pump energy density ∼14 mJ cm^{-2}. The lines are guides to the eye. Inset represents 'standard' evaluation of the data (see text).

energy density ranged from ∼2.8 mJ cm^{-2} to ∼14 mJ cm^{-2} (peak power density $I_{exc} \sim 30$ GW cm^{-2}). A weaker, time-delayed test pulse of the fundamental frequency (800 nm) in the optically transparent region of the samples, with a diameter of ∼100 μm, was aligned with the LIG and its diffracted intensity monitored using a conventional Si photodiode. All experiments were performed at room temperature.

3. Results and discussion

In what follows we focus our attention on the sample implanted to a fluence of 4×10^{17} cm^{-2}, in which the observed phenomena are most evident. The LIG dynamics in this sample are shown in figure 2. It can be seen that the grating decay time τ_g decreases with decreasing grating period Λ—an effect that is both distinct and interesting. In particular, our primary interest has been focused on the potential photocarrier lateral diffusion between nanocrystals because of the fundamental importance of this effect for electrical pumping of potential light-emitting devices based on Si-ncs. Such a lateral carrier diffusion, even if the Si-ncs are localized in an insulating matrix such as SiO_2, cannot be *a priori* excluded. It is true that in our samples the *mean* internanocrystal spacing (∼16 nm) is quite large for an efficient charge transport. However, taking into account the non-uniform distribution of the nanocrystals and their tendency to form larger clumps with higher volume density, at many a

place the separation between *surfaces* of neighbouring Si-ncs may be considerably smaller, several tenths of nanometer only. Then, carrier tunnelling can occur (an observation of picosecond carrier tunnelling between Si-ncs has already been reported [8]). Moreover, the remaining excess Si atoms as well as the defects in the SiO_2 matrix could increase conductivity between the individual Si-ncs. As a result, a percolation conducting path in the Si-ncs/SiO_2 system can be established. To extract information about such carrier diffusion, however, is not easy.

It is almost certain that within the duration of the excitation pulse, *nonlinear* recombination processes (both radiative and non-radiative) occur in the excited Si-ncs, since, estimating the absorption cross section of Si-ncs at 400 nm for the samples with 20% excess Si concentration to be $\sigma \approx 2 \times 10^{-16}\,\mathrm{cm}^2$ [9, 10] and considering the pump energy density of $\sim$10 mJ cm^{-2}, we get the initial mean number of electron–hole pairs per nanocrystal as high as 3–5 (nevertheless, we were checking carefully that the pump power density was always below the threshold for irreversible sample changes, i.e. below the threshold for writing down a 'permanent grating' [11]). These nonlinear recombination processes in principle can be described by nonlinear terms in the relevant kinetic equations dealing with the time evolution of the LIG carrier population [4, 12] and could manifest themselves through a non-exponential decay of the LIG diffraction efficiency in time. However, the very formulation of such kinetic equations would be very difficult if not impossible, in view of the fact that the physics of highly excited Si-ncs has not been well understood till now. Instead, we apply here a simplified treatment of the experimental data, which is based on the following approach.

In order to estimate the involvement of carrier diffusion we have used the linear parts (in log scale) of the LIG decay curves at long delays only where the number of e–h pairs per Si-ncs can be supposed to be already low and the LIG decay should be driven mainly by relatively slow carrier lateral diffusion and recombination. The decay is then expected to be a single-exponential with a decay time τ_g; this is indeed the case (see figure 2). In this way we obtain $\tau_g(\Lambda = 2.8\,\mu\mathrm{m}) \approx 1.12$ ps, $\tau_g(\Lambda = 5.5\,\mu\mathrm{m}) \approx 1.71$ ps, $\tau_g(\Lambda = 13\,\mu\mathrm{m}) \approx 1.92$ ps and $\tau_g(\Lambda = 31\,\mu\mathrm{m}) \approx 2.25$ ps. Standard evaluation then consists of plotting $(\tau_g)^{-1}$ against $8\pi^2/\Lambda^2$, the slope of which yields the diffusion constant of carriers D [4]. Such a plot is shown in the inset of figure 2 and yields a value of D about 420 cm^2 s^{-1}, which is unrealistically high, bearing in mind that D in bulk Si is of the order of 10 cm^2 s^{-1} [13]. Carrier diffusion thus seems not to be involved in our ultrafast LIG decay. One has therefore to suggest another interpretation of the experimental data, in particular, of the peculiar variation of τ_g with Λ.

To assist in this regard, additional pump–probe experiments were undertaken. These used basically the same experimental set-up as above, only one of the writing beams was blocked and the energy density of the remaining one increased. The results, displayed in figure 3, revealed that the 'slow components' (delay $\geqslant$1.5 ps) of pump/probe and of LIG dynamics with large grating period Λ coincide. The decay

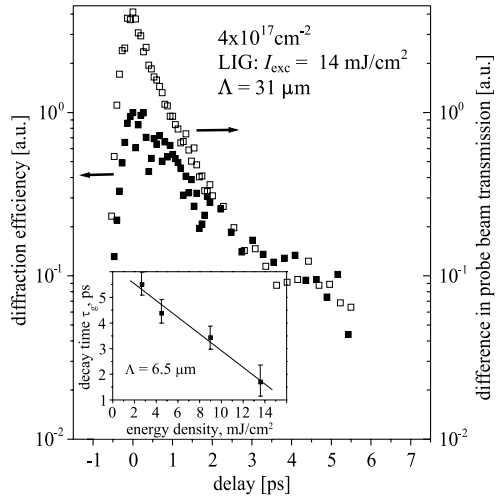

Figure 3. Comparison of the LIG dynamics ($\Lambda = 31\,\mu$m, full squares) with a pump-and-probe decay curve (open squares), measured on one and the same place of the sample. The 'slow' parts of both curves coincide for delays $\geqslant$1.5 ps. Inset shows decrease in τ_g with increasing pump energy density. At the initial stage of decay both the curves are not directly comparable because the energy density of the pump beam in the pump-and-probe experiment was chosen slightly higher ($\sim$21 mJ cm^{-2}) than that of the total pump in the case of LIG ($\sim$14 mJ cm^{-2}).

time τ_g was also studied as a function of pump intensity and it was found that increasing the pump intensity led to a reduction of τ_g (inset of figure 3).

The most obvious interpretation of these observations—fast non-radiative Auger recombination of carriers in Si-ncs—cannot readily account for the fact that the decay time depends on the grating period Λ. We therefore speculate about the following effects.

(i) Exciton (not free carrier) migration and tunnelling between neighbouring nanocrystals was proposed to be responsible for fast LIG decay in CdTe/ZnSe quantum dots under femtosecond pumping [14]. Both optical and acoustic phonons can participate in this exciton tunnelling at room temperature in order to compensate for the energy difference between different nanocrystals [15]. Due to the concentration gradient, the exciton diffusion tends to smooth the LIG and such a migration process should manifest itself predominantly at small Λ, in good agreement with our observation, see figure 2. Quite recent theoretical calculations confirm even the possibility of resonant (no-phonon) energy transfer between Si quantum dots [16] following the Förster mechanism. The energy transfer rate varies as $\sim 1/R^6$ where R is the interdot distance; for a very small R (of the order of nanocrystal radius) the transfer rate has been shown to increase even much faster. In this case submicrosecond transfer time can be possibly achieved.

(ii) Radiative recombination of excitons in the LIG is very probably involved in the LIG decay because intense PL is observed in our experiments under 400 nm femtosecond

pumping and the occurrence of a very fast (subpicosecond) component of Si-ncs luminescence has been evidenced recently by our group using an independent experimental set-up [17]. It is very interesting to note in this context that superradiance of an inhomogeneously broadened ensemble of semiconductor quantum dots has been experimentally demonstrated under 1.5 ps quasi-resonant excitation (i.e. excitation below the barrier bandgap energy and above the exciton ground state energy of the quantum dot) quite recently [18]. This effect of cooperative radiation leads to the enhancement of the exciton radiative recombination rate and thus to PL decay shortening. The basic requirement for the onset of the collective superradiant coupling, namely, a closely spaced ensemble of nanocrystals, has been met in our samples: we recall that the mean distance between (5 nm sized) Si-ncs in our samples with the excess Si concentration of 20 at% can be estimated to amount to ∼16 nm while Scheibner *et al* [18] observed the effect of superradiance in CdSe/ZnSe quantum dots up to the average interdot spacing of 150 nm. Nonetheless, even if we admit that a kind of superradiance occurs in our ensembles of Si-ncs, this effect alone can hardly explain the striking observation, namely, the LIG decay shortening with decreasing Λ. To this end we invoke the effect of the periodic modulation of the refractive index by the LIG, which defines a resonant optical structure that enhances the overlap between the Si-ncs emission frequencies and the available spectral density of photon modes. As a result, the spontaneous radiative lifetime of the nanocrystals can be modified (Purcell effect [19]). A variation of Λ can therefore affect the enhancement of the dipole-field coupling and cause changes in the radiative lifetime of the LIG as a function of Λ.

To assess the magnitude of the Purcell effect the following simplified model was employed: periodic modulation of the refractive index with a Gaussian envelope across the plane of the waveguide (see inset to figure 4)

$$n(x) = n_{\mathrm{F}} + \frac{\Delta n}{2}\left[1 + \cos\left(\frac{2\pi x}{\Lambda}\right)\exp\left(-\frac{x^2}{\sigma^2}\right)\right], \quad (1)$$

where Δn stands for the maximum of the induced change in the refractive index and σ is the (Gaussian) beam width. The propagation of light waves in this structure was then calculated using an effective refractive index [20] for the guided modes in the waveguide. Since the increase in the dipole moment implies a decrease in τ_{g}, figures 2 and 4 display qualitatively the same behaviour. For large values of Λ ($\geqslant 35\,\mu$m) the effect in figure 4 shows a tendency to disappear. This agrees with the observation in figure 3, namely, that decay curves for an LIG with $\Lambda = 31\,\mu$m and for a probe beam passing through a non-periodic excited spot ($\Lambda \to \infty$) are basically identical. Estimating the nonlinear susceptibility of Si-ncs (with the mean diameter of 5 nm) embedded in an SiO_2 matrix under femtosecond pumping to be [21] $\chi^{(3)} \approx 0.2 \times 10^{-9}$ (esu) $\approx 3 \times 10^{-18}$ ($\mathrm{m^2\,V^{-1}}$) we get a nonlinear refractive index $\gamma = 3\chi^{(3)}/4c\varepsilon_0 n_{\mathrm{F}}^2 \approx 3 \times 10^{-12}\,\mathrm{cm^2\,W^{-1}}$. The maximum induced refractive index change $\Delta n = \gamma I_{\mathrm{exc}}$ thus amounts (for $I_{\mathrm{exc}} \sim 30\,\mathrm{GW\,cm^{-2}}$) to the orders of 0.01–0.1. This, referring to figure 4, can result in a substantial increase in the dipole moment magnitude. Since the first-order signal dynamics in a four-wave mixing process (as observed in our experiment) is driven by the speed of deformation of the cosine-like interference profile, i.e. predominantly by the maximum dipole enhancement (figure 4), the increase in the radiative recombination rate due to the Purcell effect could be quite significant.

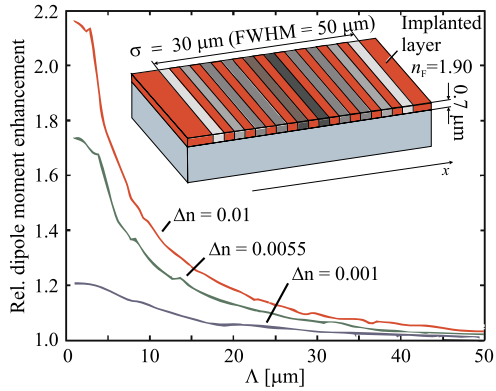

Figure 4. Calculated effective dipole moment enhancement for Si-ncs located at the maximum of the modulation profile as a function of Λ. The inset shows a scheme of the structure under consideration. For computational reasons, the Gaussian pump spot width was considered $\sigma = 30\,\mu$m only. The parameters Δn next to the curves are the amplitudes of the nonlinear refractive index modulation.

(iii) An increase in the (linear) dipole coupling between the nanocrystals and the optical field can also lead to an increase in the nonlinear dipole interaction, i.e. an increase in the stimulated emission rate and the appearance of optical amplification. Here it is worth stressing the following facts. The ultrashort blue pump pulses (∼100 fs, ∼400 nm) from a frequency-doubled Ti–sapphire system have proved recently to be very efficient in producing room-temperature positive optical gain in ensembles of densely arranged Si-ncs. Experiments using the variable-stripe-length method [22, 23] yielded values of the gain coefficient as high as $25\,\mathrm{cm^{-1}}$.

4. Conclusions

In conclusion, we have performed transient LIG experiments with picosecond resolution in planar waveguides composed of luminescent Si-ncs. We explain the observed very fast LIG decay time and its variations with grating period by a model invoking exciton diffusion and/or enhancement of the radiative recombination rate in the periodic distribution of the electromagnetic field amplitude. An additional contribution to the LIG decay shortening can originate from possible involvement of stimulated emission in the waveguide.

Acknowledgments

One of the authors (IP) thanks the Laserlab-Europe Integrated Initiative for financial support (vulrc001168). This research has been partially supported by the Institutional Research Plan AV0Z 10100521, MŠMT Research Centre LC510, GAAVCR projects Nos A1010316 and A1010413, GACR No 202/07/0818, the Australian Research Council and by a grant of the Lithuanian State Foundation for Science and Studies. The authors thank Professor P Malý for helpful discussions. This work is also a part of the research plan MSM 0021620834 that is financed by the Ministry of Education of the Czech Republic.

References

[1] Dal Negro L, Cazzanelli M, Daldosso N, Gaburro Z, Pavesi L, Priolo F, Pacifici D, Franzo G and Iacona F 2003 *Physica* E **16** 297
[2] Khriachtchtev L, Räsänen M and Novikov S 2003 *Appl. Phys. Lett.* **83** 3018
[3] Valenta J, Ostatnický T, Pelant I, Elliman R G, Linnros J and Hönerlage B 2004 *J. Appl. Phys.* **96** 5222
[4] Eichler H J, Günter P and Pohl D W 1986 *Laser-Induced Dynamic Gratings* (Berlin: Springer)
[5] Tomašiūnas R, Pelant I, Kočka J, Knápek P, Lévy R, Gilliot P, Grun J B and Hönerlage B 1996 *J. Appl. Phys.* **79** 2481
[6] Linnros J, Lalic N, Galeckas A and Grivickas V 1999 *J. Appl. Phys.* **86** 6128
[7] Cheylan S and Elliman R G 2001 *Appl. Phys. Lett.* **78** 1912
[8] Lockwood R, Hryciw A and Meldrum A 2006 *Appl. Phys. Lett.* **89** 263112
[9] Ossicini S, Pavesi L and Priolo F 2006 *Light Emitting Silicon for Microphotonics* (*Tracts in Modern Phys.* vol 194) (Berlin: Springer)
[10] Daldosso N, Melchiorri M, Pavesi L, Pucker G, Gourbilleau F, Chausserie S, Belarouci A, Portier X and Dufou C 2006 *J. Lumin.* **121** 344
[11] Janda P, Valenta J, Ostatnický T, Skopalová E, Pelant I, Elliman R G and Tomašiūnas R 2006 *J. Lumin.* **121** 267
[12] Kudrna J, Trojánek F, Malý P and Pelant I 2001 *Appl. Phys. Lett.* **79** 626
[13] Linnros J and Grivickas V 1994 *Phys. Rev.* B **50** 16943
[14] Van Dao L, Lowe M, Hannaford P, Makino H, Takai T and Yao T 2002 *Appl. Phys. Lett.* **81** 1806
[15] Takagahara K 1999 *Phys. Rev.* B **60** 2638
[16] Allan G and Delerue C 2007 *Phys. Rev.* B **75** 195311
[17] Trojánek F, Neudert K, Malý P, Dohnalová K and Pelant I 2006 *J. Appl. Phys.* **99** 116108
[18] Scheibner M, Schmidt T, Worschech L, Forchel A, Bacher G, Passow T and Hommel D 2007 *Nature Phys.* **3** 106
[19] Baets R, Bienstman P and Bockstaele R 1999 *Confined Photon Systems Fundamentals and Applications* (Berlin: Springer)
[20] Kapany N S and Burke J J 1972 *Optical Waveguides* (London: Academic)
[21] Vijaya Prakash G, Cazzanelli M, Gaburro Z, Pavesi L, Iaconna F, Franzo G and Priolo F 2002 *J. Appl. Phys.* **91** 4607
[22] Ruan J, Fauchet P M, Dal Negro L, Cazzanelli M and Pavesi L 2003 *Appl. Phys. Lett.* **83** 5479
[23] Luterová K, Dohnalová K, Švrček V, Pelant I, Likforman J-P, Crégut O, Gilliot P and Hönerlage B 2004 *Appl. Phys. Lett.* **84** 3280

[P7]

CHAPTER 10

GUIDING AND AMPLIFICATION OF LIGHT DUE TO SILICON NANOCRYSTALS EMBEDDED IN WAVEGUIDES

Tomáš Ostatnický, Martin Rejman, and Jan Valenta

Department of Chemical Physics and Optics, Faculty of Mathematics and Physics, Charles University, Ke Karlovu 3, CZ-121 16 Prague 2, Czech Republic

Kateřina Herynková, Ivan Pelant

Institute of Physics, Academy of Sciences of the Czech Republic, v.v.i., Cukrovarnická 10, CZ-162 53 Prague 6, Czech Republic

In this chapter, we summarize our progress in both experimental and theoretical investigations of spontaneous emission of silicon nanocrystals embedded in planar waveguides. We give an overview of our photoluminescence measurements which reveal peculiar phenomena like spectral filtering of the signal or polarization splitting of the spectra. We discuss possible interpretations of the observed events and we present a model which is capable of explanation of all the peculiarities. Finally we apply the model in order to investigate the consequences of the waveguiding effects for the light amplification, propagation and spectroscopy measurements.

1. Introduction

Nanocrystalline silicon attracts attention in many research groups because of its prospective applicability in optoelectronic devices as an amplifier or a source of light. High concentrations of Si nanocrystals and high optical quality of the active media are desired to get a positive net optical gain. To accomplish the requirements, samples prepared by using various methods have been checked in experiments addressing optical

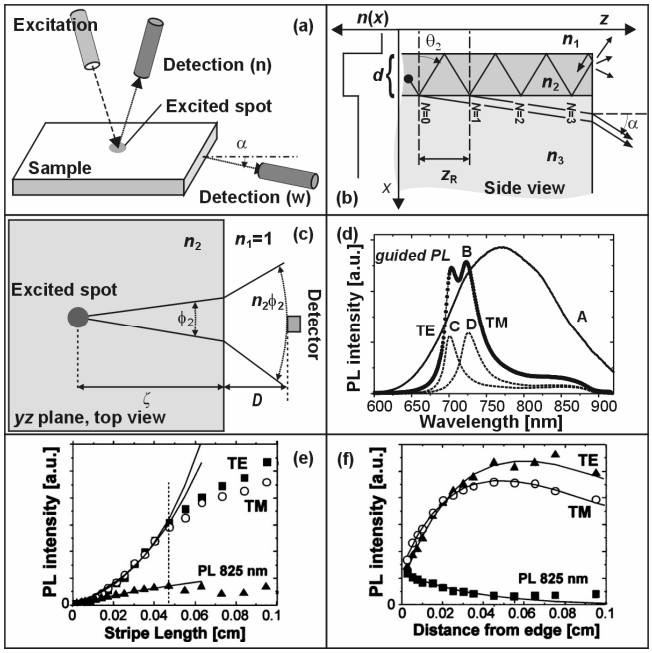

Fig. 1. (a) Experimental setup with two possible detection positions: standard (n) and waveguiding (w). (b) Propagation and decoupling of substrate modes; (c) sketch for derivation of coupling coefficients; (d) measured PL in standard (A) and waveguiding geometry (B) and in the waveguiding geometry with a linear polarizer (C,D); (e) measured ASE intensity at various spectral positions: at maxima of TE and TM modes and at 825 nm; (f) measured SES signal at the same spectral positions.[2]

gain: Si^+ ion implantation,[1,2] plasma–enhanced chemical vapour deposition,[3] reactive Si deposition,[4] magnetron sputtering[5] or others.[6] The samples prepared by these methods have a form of a thin SiO_2 layer (few micrometers thick) doped with Si nanocrystals, located on an optically thick Si or silica substrate. The thin "sheet" which contains nanocrystals then may reveal waveguiding properties because of the refractive index mismatch between the sheet and the SiO_2 matrix.

The waveguiding property and the "planar" method of fabrication are advantageous for integration of components in optoelectronics, however, it was found that the characteristics of a photoluminescence (PL) emission of the samples are strongly affected by the presence of the waveguide[2,7-12] and depend upon many parameters of the sample preparation.[9,13,14] We have investigated the PL emission of the Si nanocrystals embedded in waveguides both theoretically and experimentally and we summarize our findings in this chapter.

Effects connected with waveguiding in the implanted samples were firstly discussed in detail by our group[2] and confirmed by an independent observation of the same phenomenon on samples prepared by reactive deposition[7] — in the experiments, photoluminescence from the active layer was collected in the "waveguiding" configuration along the layer with Si nanocrystals (see Fig. 1a for the experimental setup). Compared to a PL spectrum collected in the standard configuration (perpendicular to the sample plane), the spectra reveal a disturbance of the wide PL band and a narrowing to one or more pairs of modes resolved in linear polarization (Fig. 1d). The unusual behaviour of the PL spectra was observed in measurements of amplified spontaneous emission (ASE) using the variable stripe length (VSL) method[2,15] where the shape of the ASE curves strongly depended on the wavelength of detected radiation (see Figures 1e-1f).

Numerical analysis of the problem shows that the spectrally narrow modes are formed very close to the cut-off frequency of the waveguide. This fact has led us to the interpretation[8,16,17] of our observations, namely, that the modes are formed by the waves leaking from the waveguide core slightly below the critical angle for the total reflection on the core/substrate boundary. Another interpretation was given by Khriachtchev *et al.*[7,9,10] in terms of particular guided modes which are spatially delocalized near the cut-off frequency and therefore their losses due to absorption in the core are lower than losses of the ordinary guided modes.

In this chapter, we develop a consistent model which predicts the observed behaviour and we discuss both hypotheses (delocalization and wave leaking) in order to find which of them plays a major role in formation of the PL spectra. We then show the consequences of the

waveguiding and related effects for spectroscopic measurements, applications in optics and optoelectronics, gain measurements and construction of a lasing device. After a short introduction to waveguide theory in section 2, our model is discussed in more details in section 3. Since the original model does not take into account propagation of the modes along the waveguiding layer, we present its phenomenological extension in section 4, and in section 5 we present numerical calculations of the wave propagation in active waveguides.

2. Characterization of Waves in Waveguides

Discussion of propagation of the optical field through *passive* waveguides is usually limited to the discussion of the guided waves, *i.e.* waves (modes) which are spatially confined in the waveguide core. In the *active* devices, however, the sources of photons are located inside the guiding layer and therefore the amount of energy coupled to the guided modes may be comparable or smaller than the energy coupled to other modes. On that account, all waves must be considered when dealing with active devices.

In this section, we review the general theory of planar (slab) waveguides.[18–20] We consider a structure with three layers[a] of a dielectric described by a (generally complex) refractive indices n_1 (cladding), n_2 (core) and n_3 (substrate), see Fig. 1b; we assume for the sake of clarity for the real parts of the refractive indices $n_2 > n_3 > n_1$. The thickness of the core d is comparable with or larger than the vacuum wavelength of the optical radiation λ. The cladding and the substrate are optically thick and therefore considered to be infinite. The z axis is the propagation axis and the x axis is perpendicular to the waveguide layer.

Electromagnetic field from a source within a waveguide is coupled only to the states of a field which are allowed by boundary conditions — to the modes of the waveguide. According to the symmetry of the

[a] The structure with a step-like profile of the refractive index is taken into account for the sake of clarity. The theory may be, however, generalized to an arbitrary profile of refractive index including a continuous graded profile. Comparison of calculated PL spectra with our experimental data has been done considering the real parameters of our samples, *i.e.* graded profile of refractive index across the waveguide.

waveguide, the intensity of electric field of a TE mode may be written as $\vec{E}(x,z,t) = \hat{y}E(x,z)\mathrm{e}^{-\mathrm{i}\omega t}$, where $\hat{y}$ is a unit vector in the y direction, $\omega = 2\pi c/\lambda$ is the frequency of the mode, c is the light velocity and

$$E(x,z) = \{A_{m\beta}\exp[\alpha_{m\beta}(x-x_m)] + B_{m\beta}\exp[-\alpha_{m\beta}(x-x_m)]\}\mathrm{e}^{\mathrm{i}\beta z} \quad (1)$$

in every layer denoted by the index m (m=1,2,3). The modes are fully characterized by the propagation constant β, which may be interpreted in terms of the angle of propagation θ_2 (see Fig. 1b) of a ray: $\beta = (2\pi n_2 \sin\theta_2)/\lambda$. A variable $\alpha_{m\beta} = [\beta^2 - (2\pi n_m/\lambda)^2]^{1/2}$ determines the profile of the mode in the x direction, x_m is a coordinate of the boundary between the m-th and (m+1)-st layer and the variables A and B are constants for every layer and mode, fully determined by the boundary conditions and normalization.[20] The axial system has been adapted by rotation in order to ensure $\vec{E} \parallel \hat{y}$. In our case of a three-layer structure, the modes may be resolved into three groups depending on their spatial profile in the direction of the x axis, hence depending on the values of the coefficients $\alpha_{m\beta}$. Let us consider for instance a lossless structure, *i.e.* n_m real. The maximum value of β for propagating waves is clearly $2\pi n_2/\lambda$, therefore $\alpha_{2\beta}$ is always imaginary and the field intensity in the core is nonzero. Other α's, on the contrary, may be real or imaginary.

For both $\alpha_{1\beta}$ and $\alpha_{3\beta}$ imaginary, the mode takes the form of a propagating wave in all three layers and it is called the *radiation mode*. In terms of the ray optics, a ray emitted by a source inside the waveguide is refracted either to the substrate or to the cladding and only a small portion of its energy is reflected back to the core. The energy of the mode is therefore radiated from the waveguide core on short distances compared to the waveguide thickness d.

If the coefficients $\alpha_{1\beta}$ and $\alpha_{3\beta}$ are, on the contrary, both real, the profile of the mode in the cladding and the substrate given by Eq. (1) takes the form of evanescent waves and the mode energy is localized predominantly in the core. The mode is bound to the layer with the highest refractive index and propagates along the z axis, and it is called the *guided mode*. In terms of the ray optics, a ray is incident on both boundaries core/cladding and core/substrate at an angle larger than the critical angle for total internal reflection, therefore it is totally reflected and its energy cannot leave the core. Near the critical propagation

constant $\beta_C = 2\pi n_3 / \lambda \leq \beta$, the coefficient $\alpha_{3\beta}$ is close to zero and thus the attenuation of the evanescent wave in the substrate is very weak and the wave penetrates into the substrate to depths comparable or even larger than the core thickness.[21]

Substrate radiation modes[b] *(substrate modes)* are the last kind of the waveguide modes. They are characterized by a real coefficient $\alpha_{1\beta}$ and an imaginary coefficient $\alpha_{3\beta}$. The wave may propagate in the substrate but it is totally reflected at the core/cladding boundary. The substrate modes are very similar to the radiation modes since the energy radiated by an emitting nanocrystal to that mode may leave the core on short distances in the z direction, however the energy of the modes with the propagation constant near the critical propagation constant, *i.e.* $\beta \leq \beta_C$, may reside inside the core layer at large distances from the source, by orders of magnitude larger than the core thickness. The propagation angle θ_2 of such mode is near the critical angle for total reflection on the core/substrate boundary, thus the reflectivity is slightly below 1 and only a small portion of energy is lost during one round-trip of the ray across the core layer (*cf.* Fig. 1b). The angle of propagation of the mode in the substrate is near $\pi/2$ implying that the mode propagates along the core/substrate boundary and in many experiments these modes cannot be distinguished from regular guided modes. Since the substrate modes propagate mostly outside the core, their characteristics are determined by the optical constants of the substrate. Nevertheless, the aforementioned substrate modes with $\beta \approx \beta_C$ are affected by the core properties near the source. Therefore they behave like guided modes at the distances smaller than a characteristic distance[18] of their leakage to the substrate but at the larger distances they behave more like free plane waves in the substrate.

[b] In our previous publications, substrate radiation modes have been inaccurately denoted as "leaky" waves or leaky modes. The label *leaky modes* should be rather reserved for a special sort of unphysical solutions of the wave equation with boundary conditions determined by the symmetry of a waveguide.[20]

3. Spectral Filtering of the Modes

In this section, we present a simple model which explains how the TE and TM modes are formed and which types of the waveguide modes take part in the spectral filtering process. We consider a large planar waveguide with the radiating nanocrystals uniformly distributed in the *yz* plane and therefore the system is assumed to have a full translational symmetry in both *y* and *z* directions. This model is therefore not able to simulate phenomena which arise from the wave propagation (for appropriate models, see sections 4 and 5) since the symmetry-breaking due to the sample edge is not included in the description, however the principle of the peak formation in the PL spectra is best illustrated.

The main idea of the model follows from the aforementioned fact that the substrate modes with the propagation constant slightly below the critical value undergo several round-trips in the core before their energy leaves the core. Due to the interference effects (similarly to the Fabry–Perot interferometer),[22] the nanocrystals couple effectively only to the resonant modes, *i.e.* to the modes whose phase is reconstructed after one round-trip. These modes, in addition, refract to the substrate under an angle near $\pi/2$, therefore they are hardly distinguishable from the guided modes in experiments and we observe a superposition of the guided and the substrate modes in the PL spectra. Using the detection system with a small numerical aperture,[2] substrate modes with a fixed propagation angle are selected (*cf.* Fig. 1b) and the resonances arise for certain wavelengths only. These resonances are then observed as sharp peaks in the PL spectra.

To give a more quantitative description, let us consider nanocrystals randomly oriented and randomly located in the waveguide core which radiate the optical field with intensity of electric field $E_0(\lambda)$ under an angle θ_2. The total field at the position of the nanocrystal is evaluated as a sum of the field E_0, the field after one round-trip in the core, the field after two round-trips *etc.* Mathematically, we express the field as an infinite series:

$$E_{\text{internal}}(\lambda,\theta_2) = E_0(\lambda)\{1 + r_{21}r_{23}\exp[\mathrm{i}4\pi n_2 d\cos\theta_2/\lambda] + \\ + (r_{21}r_{23}\exp[\mathrm{i}4\pi n_2 d\cos\theta_2/\lambda])^2 + \ldots\} = \frac{E_0(\lambda)}{1 - r_{21}r_{23}\exp[\mathrm{i}4\pi n_2 d\cos\theta_2/\lambda]}, \quad (2)$$

where r_{21} and r_{23} represent the reflection coefficients at the core/cladding and the core/substrate boundaries, respectively, which depend upon the propagation angle θ_2. Note that the summation is possible in lossless structures only if $|r_{21}r_{23}|<1$, therefore Eq. (2) is valid only for the radiation and the substrate modes, the guided modes (with $|r_{21}|=|r_{23}|=1$) will be discussed hereafter. Function $|E_{\text{internal}}(\lambda,\theta_2)|^2$ defined by Eq. (2) stands for light intensity in the core of the waveguide and has maxima at the resonances for the wavelengths λ for which the condition $\mathrm{Im}(r_{21}r_{23}\exp[\mathrm{i}4\pi n_2 d\cos\theta_2/\lambda]) = 0$ is fulfilled.

3.1. *Substrate and radiation modes*

Considering only the substrate modes, $|r_{21}|=1$ and $|r_{23}|<1$. The more is the value $|r_{23}|$ close to unity, the narrower are the peaks in the intensity $|E_{\text{internal}}(\lambda)|^2$. Additionally, the peak value increases with increasing $|r_{23}|$ and thus the substrate modes are most visible for angles θ_2 approaching the critical angle for total internal reflection on the core/substrate boundary. For radiation modes, the value $|r_{23}|$ is usually much less than unity and thus the spectra of the radiation modes reveal only broad peaks with a small peak-valley contrast.

In experiments, the detector has a nonzero numerical aperture and therefore radiation from a nonzero spatial angle is collected. The total intensity recorded by the detector is then

$$I_S(\lambda,\alpha) = \int_{\alpha-\Delta\alpha/2}^{\alpha+\Delta\alpha/2} |E_{\text{internal}}(\lambda,\theta_2)|^2 T_{23}(\theta_2) T_S(\alpha') \frac{\mathrm{d}\theta_2}{\mathrm{d}\alpha'} \mathrm{d}\alpha', \quad (3)$$

where the detection angle is given by its mean value α (*cf.* Figs. 1a-b) and $\Delta\alpha/2$ denotes the numerical aperture of the detector. The symbols T_{23} and T_S stand for the respective transmittances at the core/substrate boundary and at the sample edge, which are given by the Fresnel formulae. The detection angle α' and the propagation angle θ_2 are connected by the Snell's law

$$n_2^2 \sin^2 \theta_2 = n_3^2 - \sin^2 \alpha' . \quad (4)$$

The expression $\mathrm{d}\theta_2 / \mathrm{d}\alpha'$ in Eq. (3) stands for the angular mode density and reflects the fact that the nanocrystals radiate isotropically in the core.

3.2. *Guided modes*

For the guided modes, the field intensity $|E_0(\lambda)|^2$ in the core is enhanced similarly to Eq. (2), however losses due to radiation at the sample edge should be included in order to get a physically correct formula. Such derivation is beyond this simple model and therefore we consider that the intensity of the electric field is given by the formula

$$E_{\text{guided}}(\lambda, \theta_2) = F(\lambda, \theta_2) E_0(\lambda), \quad (5)$$

with $F(\lambda,\theta_2)$ being the enhancement factor similar to the factor in Eq. (2). The detected intensity is

$$I_{\mathrm{G}}(\lambda, \alpha) = \int_{\alpha-\Delta\alpha/2}^{\alpha+\Delta\alpha/2} \mathrm{d}\alpha' \int_0^{\pi} \mathrm{d}\theta_2 \left| E_0(\lambda) F(\lambda, \theta_2) \right|^2 T_{\mathrm{G}}(\lambda, \theta_2) D_{\mathrm{G}}(\lambda, \theta_2, \alpha'), \quad (6)$$

where $T_{\mathrm{G}}(\lambda,\theta_2)$ stands for the transmittance of the mode denoted by its wavelength λ and propagation angle θ_2 through the sample edge and $D_G(\lambda,\theta_2,\alpha')$ is the diffraction efficiency from the mode to the diffraction angle α'. The enhancement factor $F(\lambda,\theta_2)$ has sharp maxima, *i.e.* only the guided modes with well resolved propagation angle are allowed by the waveguide, therefore we may simplify[c] Eq. (6):

$$I_{\mathrm{G}}(\lambda, \alpha) = \int_{\alpha-\Delta\alpha/2}^{\alpha+\Delta\alpha/2} \left| E_0(\lambda) F(\lambda) \right|^2 T_{\mathrm{G}}(\lambda) D_{\mathrm{G}}(\lambda, \alpha') \mathrm{d}\alpha' . \quad (7)$$

Decoupling of electromagnetic waves from a dielectric waveguide to free space (evaluation of the functions $T_{\mathrm{G}}(\lambda)$ and $D_{\mathrm{G}}(\lambda,\alpha')$) cannot be described simply by the Snell's law but we must take into account diffraction and full boundary conditions. Such approach is, however, beyond the scope of this paper, therefore we assess the situation only qualitatively. It is well known that diffraction on a slit with aperture

[c] We consider here for the sake of simplicity one guided mode for all wavelengths, however Eq. (7) may be extended to a general case of multimode guiding.

width comparable to the light wavelength produces a wide diffraction maximum in the Fraunhoffer limit, thus we may conclude that the function $D_G(\lambda,\alpha')$ has a broad peak[16] in the second variable. The guided modes, unlike the substrate modes, cannot be distinguished one from the other by selecting the angle of detection.

The magnitude of the transmittance T_G may be estimated from the Fresnel formulae; we assume that for the angle of incidence at the waveguide edge well above the critical value for the total internal reflection at the boundary the transmittance is low while for smaller angles, the modes are decoupled more effectively. Simple derivation gives that the guided modes near the cut-off wavelength are only weakly decoupled for $n_2^2 - n_3^2 > 1$. In waveguides where $n_2^2 - n_3^2 < 1$, all guided modes may be radiated from the waveguide core with high transmittance.

3.3. *All modes together, comparison with experiment*

The total intensity at the detector is

$$I(\lambda) = I_S(\lambda) + I_G(\lambda) + I_R(\lambda). \tag{8}$$

The symbol $I_R(\lambda)$ denotes the spectrum of the radiation modes which is almost flat and always less intense when compared to the spectrum of the substrate modes as seen from Eq. (2). Therefore it plays a minor role and hence it is not discussed from now on. The detected PL spectrum then consists of the two major components which compete with each other: the broad spectrum of the guided modes and the spectrum of the substrate modes with narrow peaks. Visibility of the respective components is determined by the numerical aperture of the detection system and mainly by the geometrical properties of the sample since these determine the strength of decoupling of the guided modes.

The spectra of the substrate modes reveal one more property which has not been discussed yet. The phase of the reflection coefficient r_{23} in Eq. (2) does not vary with the incident angle θ_2 when considering substrate and radiation modes, however the phase of the coefficient r_{21} does change from 0 to π in the region of substrate modes (see Fig. 3 in Ref. 17). The phase is, in addition, dependent upon the mode polarization and therefore the peaks of the TE and TM modes split in the PL spectra.

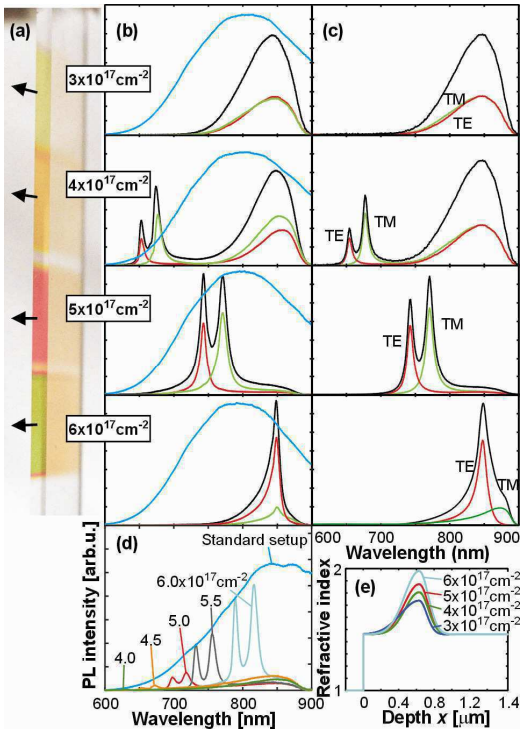

Fig. 2. (a) Photograph of the edge of a set of implanted layers with direction of PL indicated by arrows, the edge is on the left; (b) measured PL from samples implanted to different Si-ion fluences (indicated on the left) in standard (blue line) and waveguiding geometry (black line, red and green lines stand for TE and TM resolved polarizations); (c) theoretically calculated PL spectra; (d) comparison of PL measured in the waveguiding geometry for different series of implant fluences with the PL measured in the standard geometry (broad band); (e) profiles of refractive index of the samples with indicated implant fluences.[17]

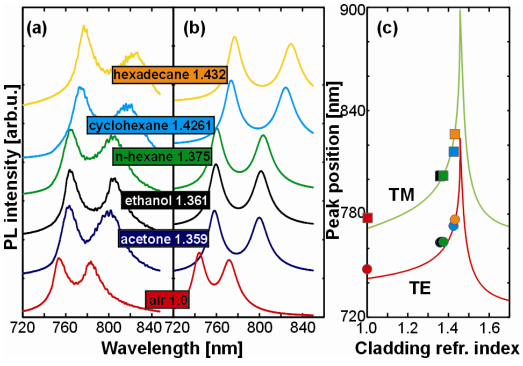

Fig. 3. (a) Measured PL spectra with a drop of various liquids above the excitation spot; (b) theoretical PL spectra; (c) comparison of experimental (points) and theoretically calculated positions of PL maxima for different refractive indices of the liquids. The sample with an implant fluence of $5 \cdot 10^{17}$ cm^{-2}.[24]

In the three-layer waveguides as discussed in this chapter, the TE mode peak is red-shifted with respect to the TM mode peak. The spectral positions of the peaks may merge or interchange in the waveguides with other profile of the refractive index.

We compared the predictions of our model with the PL spectra measured on samples prepared by Si^+ ion implantation (for details of the experimental set-up and sample preparation, see Refs. 2, 8 and 17). With the help of near-IR transmission measurement and the SRIM software,[23] we obtained the refractive index profiles of our waveguides (see Fig. 2e) which were then used in numerical simulations. The samples with higher implant fluences reveal higher peak values of the refractive index. The experimental spectra are shown in Fig. 2b and our theoretical simulations in Fig. 2c. Fig. 2d shows the PL spectra from another series of samples implanted to different fluences where the scaling of the narrow peak intensities can be clearly seen — the peak magnitudes follow well the spectral course of PL of free nanocrystals (PL measured in the standard setup).

The experimental data in Fig. 2b reveal significant modulation of the PL spectra when detecting in the waveguiding geometry. In the standard geometry (blue line), only the broad PL spectrum characteristic of Si nanocrystals is displayed and its shape is almost independent of the density of nanocrystals. Measurements in the waveguiding geometry, on the contrary, reveal the two abovementioned distinct linearly polarized peaks (black line without resolution of polarization, red and green lines represent TE and TM polarization, respectively) which move to longer wavelengths with increasing density of nanocrystals, and a broader peak centred around 850 nm which is unpolarized and its spectral position remains the same in all samples. The broad peak is interpreted as the spectrum of the guided modes: for the lowest concentration of nanocrystals (implant fluence of 3×10^{17} cm^{-1}), our calculations show that the cut-off wavelengths are below 600 nm and above 1.5 μm and thus the substrate modes are missing in the selected spectral region. The interpretation is supported by the fact that the broad peak is not polarized, its shape and magnitude are only weakly dependent on nanocrystal density (Fig. 2d) and its spectrum is similar to the spectrum measured in the standard geometry (absorption cuts the spectrum of the

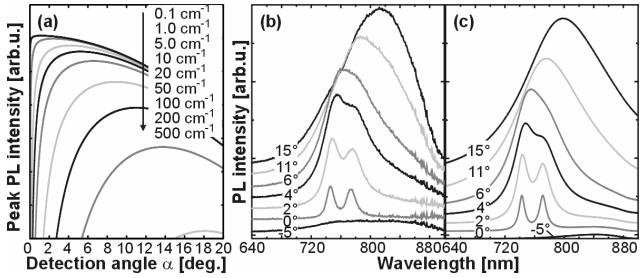

Fig. 4. (a) Theoretical dependence of peak PL intensity on the angle of detection α for various absorption coefficients of the core; (b) measured PL spectra at different detection angles; (c) numerical simulations of the measurements. The sample with an implant fluence of 5×10^{17} cm^{-2}.

guided modes below 750 nm). The substrate modes are not influenced by the absorption since they propagate mostly in the transparent substrate.

According to Eq. (8) and the subsequent discussion, the theoretical spectra represent the sum of the contributions from the two types of the modes. We are not able to determine the spectrum of the guided modes analytically within this model and thus we treat the experimental PL spectrum from the sample with the lowest nanocrystal density as the spectrum of the guided modes in all samples. The spectra of the substrate modes are then calculated according to Eq. (3) and added to the spectrum of the guided modes. Comparison of the resulting theoretical spectra in Fig. 2c to the experimental data in Fig. 2b gives an excellent agreement indicating a good precision of our model.

In experiments, we are able to set the detection angle α or the numerical aperture of the detector, therefore the angular properties of the PL should be discussed. The angle of detection may influence the detected spectra in two distinct ways: (1) magnitude of the photoluminescence and (2) shape of the spectra. The spectrum of the guided modes changes with the angle of detection only slightly,[16] therefore we discuss here only the substrate modes which reveal the most significant changes. The variance of the peak magnitude of the spectra may be evaluated directly from Eq. (3) considering $|E_0(\lambda)| = \text{const.}$ and considering exact resonance, *i.e.* $\mathrm{Im}\{r_{21}r_{23}\exp[\mathrm{i}4\pi n_2 d\cos\theta_2/\lambda]\} = 0$ — it is plotted in Fig. 4a for several absorption coefficients of the core

material taken at the wavelength of 500 nm. The peak position of the PL magnitude is not constant and shifts towards the larger values of the detection angle with increasing absorption coefficient. Besides the overall intensity, the PL spectra change also in shape when the angle α is varied as seen in our experimental results depicted in Fig. 4b. With increasing angle α, the peaks broaden and shift towards longer wavelengths. The interpretation is straightforward within our model: increase of the angle α implies decrease of the angle θ_2 and therefore decrease of the reflection coefficient r_{23} and, in addition, change of the phase of the reflection coefficient r_{21}. The former is responsible for the peak broadening while the latter causes a change of the phase matching condition and thus the spectral shift of the peaks. Our theoretical simulations in Fig. 4c agree with the experimental results in Fig. 4b which indicates correct interpretation and modelling. We feel that these experiments with detection at different angles can be hardly interpreted in terms of delocalized guided modes since there is no reason for the guided modes to reveal markedly different spectra in different diffraction directions.

3.4. *Differentiation of the substrate modes from the guided modes*

In order to support experimentally our model, we performed a novel experiment published in Refs. 17 and 24. The refractive index of the cladding layer may be easily modulated for example by dropping a small volume of liquid onto the sample. If the refractive index of the whole layer is changed, the PL spectra should change due to the obvious change of the phase of the reflection coefficient r_{21}. The measured spectra for the sample implanted to the fluence of 5×10^{17} cm^{-2} are depicted in Fig. 3a and our numerical simulations in Fig. 3b. The theoretically estimated dependence of the peak positions and their comparison to the experiments are the plotted in Fig. 3c. The guided and the substrate modes may be then unambiguously resolved if a small drop of the liquid is placed only between the excitation spot and the sample edge. The modes with their characteristic spectra form within a short distance from the excitation spot where the waveguide is not modified by the liquid. The guided modes then pass through a modified waveguide where the

cut-off frequency and thus the resonance condition for the delocalized modes are shifted. If the model based on delocalized guided modes were valid, we would thus expect a shift of the spectral positions of the peaks. The substrate modes, on the contrary, are already decoupled from the core at the position of the liquid and propagate freely in the substrate and therefore the core/cladding boundary cannot influence them. The PL spectra are then, in the case of validity of our model of substrate modes, expected to remain unchanged when compared to the original spectra without any liquid above the sample. The experimental data[17] prove the correctness of the concept of the substrate modes since the spectra do not modify when dropping a liquid between the excitation spot and the edge.

Obviously the active waveguides may be used as sensitive detectors of refractive index changes (we estimate their sensitivity up to 10^{-5}) which may be tuned for particular applications via tailoring the preparation parameters as shown in Ref. 25. The spectral region in which the detector may work is not limited only to the PL band of nanocrystalline silicon as shown experimentally in Ref. 14. The data presented therein show that light with a broad spectrum may be coupled to the substrate modes from outside. The modes which fulfil the resonance condition are then absorbed in the core and the reflection reveal dips at the theoretical spectral positions of the PL peaks, which is in agreement with our model.

4. Wave Propagation in Waveguides

In this section, we introduce an advanced model capable of describing the wave propagation in the direction along the waveguide layer. Within this theory, we are able to interpret the mechanism of the mode formation and we may evaluate the influence of the net optical gain or losses on the PL intensity. Although the model is formulated in terms of the ray optics (and an approximative description of the wave propagation), it gives good qualitative predictions and it is helpful when interpreting the experiments. A more subtle but with difficulty interpretable model usable for quantitative predictions is introduced in section 5.

Since we are interested here in wave propagation, we must take into consideration the fact that nanocrystals emit generally spherical waves and thus the signal recorded by a spatially limited detector decreases with the distance from the source as already discussed in Ref. 26 for a special case. The real detector collects the signal from a nonzero spatial angle as well as the input aperture has a nonzero spatial area and therefore there are two limiting cases for which we develop our theory: (1) A small detector with a large numerical aperture (NA), typically an optical fibre capable of high spatial resolution and small angular resolution, and (2) A detector with a small NA thus with a high angular resolution. Since the energy density of a spherical wave decreases as $1/r^2$, where r denotes a distance from a source, the intensity detected in the case 1 by a spatially small detector also decreases as $1/r^2$. In the latter case, on the contrary, when the characteristic size of the input lens of the detector is much larger than r, the signal would be independent of the distance from the source. We therefore denote the coupling coefficient as $\rho(\zeta)$ in the following text for spherical waves, *i.e.* for the case 1. The positive variable $\zeta = -z_N$ denotes the distance between the excited spot and the sample edge, z_N being the position of the excited spot at the axis z. For detectors with a small NA and high angular resolution, we put $\rho(\zeta)=1$.

We divide the initial discussion into the guided and the substrate modes while the radiation modes are omitted for the sake of simplification (as discussed above, they play only a minor role).

4.1. *Guided modes*

It was stated above in section 3 that the PL from Si nanocrystals couples to the guided modes in the whole spectral region and that the spectrum of the guided modes is nearly equal to the spectrum of the PL of the unperturbed nanocrystals.[d] A wave emitted by a nanocrystal at a distance ζ from the sample edge is amplified or attenuated depending on the gain

[d] The spectral intensity of the modes is proportional to the number of the guided modes. Therefore the spectral intensity of the light carried out by the modes may reveal jumps at distinct wavelengths which correspond to the cut-off wavelengths.

and the loss coefficients, and the intensity transmitted through the edge takes the form (according to Eq. (6))

$$I_{\mathrm{G},2}(\lambda,\alpha,\zeta)=I_0(\lambda)\left|F(\lambda)\right|^2\rho_{\mathrm{G}}(\zeta)\exp\left[\left(g(\lambda)-\gamma(\lambda)\right)\zeta\right]\times \\ \times\int_{\alpha-\Delta\alpha/2}^{\alpha+\Delta\alpha/2}T_{\mathrm{G}}(\lambda,\theta_2)D_{\mathrm{G}}(\lambda,\theta_2,\alpha')\mathrm{d}\alpha', \tag{9}$$

where $g(\lambda)$ and $\gamma(\lambda)$ stand for the gain and the loss coefficient, respectively, $I_0(\lambda)=|E_0(\lambda)|^2$ is the spectral intensity of the PL and $\rho_{\mathrm{G}}(\zeta)$ is the coupling coefficient. The dependence of the gain and the loss coefficients on wavelength reflects only properties of the material (the role of mode delocalization is neglected since our calculations show it is small) and we consider in the following that the major portion of the energy of guided modes is localized inside the core.

The coupling coefficient cannot be expressed simply as $1/\zeta$ since the detector is outside the waveguide core and the wave refraction at the sample edge, illustrated in Fig. 1c, is responsible for a slight modification. Considering only rays near the normal incidence in Fig. 1c, the intensity radiated to the angle ϕ_2 is $I_0\phi_2/2\pi$. After refraction, this energy further propagates in the *yz* plane with divergence given by an angle $\phi_0=n_2\phi_2$ and at the position of the detector (its distance from the sample edge being *D*), the energy is spread over the arc with length $\phi_2(n_2D+\zeta)$. In the *xz* plane, the wave decoupled from the waveguide is also divergent, however the distance *D* is fixed and the divergence contributes to the coupling coefficient by a constant term $1/D$. It is then easy to express the coupling coefficient for the guided modes as

$$\rho_{\mathrm{G}}(\zeta)=\frac{1}{n_2D+\zeta}. \tag{10}$$

Note that this formula is valid only for the spatially small detector, for a large detector with small NA we should write $\rho_{\mathrm{G}}(\zeta)=1$.

4.2. *Substrate modes*

Unlike the guided modes, where we usually cannot resolve the particular guided modes by the angle of detection and the PL spectrum is similar to

the PL spectrum of unperturbed nanocrystals, the substrate modes reveal maxima and minima in the spectra according to the constructive or destructive interference, respectively. The shape of the spectra depends on the number of internal reflections in the core and thus on the distance which the mode propagates. To express the shape of the spectrum mathematically, we then modify Eq. (3) in order to account for the coupling and Eq. (2) must be adapted to the finite number of reflections. The intensity emitted from the substrate then reads

$$I_{\mathrm{S},3}(\lambda,\alpha,\zeta)=\rho_{\mathrm{S}}(\theta_2,\zeta)\int_{\alpha-\Delta\alpha/2}^{\alpha+\Delta\alpha/2}\left|E_{\mathrm{internal}}(\lambda,\theta_2,\zeta)\right|^2 T_{23}(\theta_2)T_{\mathrm{S}}(\alpha')\frac{\mathrm{d}\theta_2}{\mathrm{d}\alpha'}\mathrm{d}\alpha', \quad (11)$$

where

$$\left|E_{\mathrm{internal}}(\lambda,\theta_2,\zeta)\right|^2=\left|\frac{1-\left[P(\lambda,\theta_2)\right]^{N(\theta_2,\zeta)+1}}{1-P(\lambda,\theta_2)}\right|^2 I_0(\lambda), \quad (12)$$

$$P(\lambda,\theta_2)=r_{21}(\theta_2)r_{23}(\theta_2)\exp\left[\left(g(\lambda)-\gamma(\lambda)\right)z_{\mathrm{R}}/2\right]\exp\left[\mathrm{i}4\pi n_2 d\cos\theta_2/\lambda\right]. \quad (13)$$

Here $N(\theta_2,\zeta)$ is the number of reflections of the wave inside the core and z_{R} is the distance between two points of reflection on the core/substrate boundary (see Fig. 1b). The intensity of radiation which remains in the core may be expressed by a formula similar to Eq. (9), however we account for the wave leaking by the effective attenuation coefficient γ_{eff}:[18]

$$I_{\mathrm{S},2}(\lambda,\alpha,\zeta)=I_0(\lambda)\rho_{\mathrm{G}}(\zeta)\exp[(g(\lambda)-\gamma(\lambda)-2\gamma_{\mathrm{eff}}(\lambda,\theta_2))\zeta]\times \int_{\alpha-\Delta\alpha/2}^{\alpha+\Delta\alpha/2}T_{\mathrm{G}}(\lambda,\theta_2)D_{\mathrm{G}}(\lambda,\theta_2,\alpha')\mathrm{d}\alpha'. \quad (14)$$

In order to evaluate N, we consider that after N reflections of a ray on the core/substrate boundary (see Fig. 1b) the intensity in the core with $g=\gamma=0$ may be expressed as $I_{\mathrm{S},2}(N,\zeta)=I_0\left|r_{21}r_{23}\right|^{2N}=I_0\exp\left[-2\gamma_{\mathrm{eff}}\zeta\right]$. The number of reflections may be then evaluated in the following way:

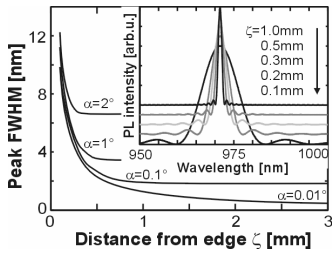

Fig. 5. Calculated dependence of the PL peak width on the length of propagation of the substrate mode for several angles of detection; inset: spectral profiles of PL for α=1°.[25]

$$N = -\gamma_{\text{eff}}\,\zeta / \ln\left|r_{21}r_{23}\right|, \tag{15}$$

$$z_{\text{R}} = -\ln\left|r_{21}r_{23}\right| / \gamma_{\text{eff}}\,. \tag{16}$$

The effective attenuation coefficient may be calculated from the Poynting vector.[18] In the case of an asymmetric waveguide with the step-like profile of the refractive index, the coefficient may be expressed for TE waves as

$$\gamma_{\text{eff}} = -\mathrm{i}\frac{{\alpha_{2\beta}}^2}{\beta d}\frac{\alpha_{3\beta}}{\left(\alpha_{2\beta}+\alpha_{3\beta}\right)^2}, \tag{17}$$

with $\alpha_{2,3\beta}$ defined in section 2 and $\beta=2\pi n_2 \sin\theta_2/\lambda$. In structures with more complicated profile of the refractive index, the attenuation coefficient and the reflection coefficients must be evaluated numerically, however Eqs. (13) to (16) remain valid. The coupling coefficient may be, after simplifications and considering θ_2 near the critical angle θ_{C}, evaluated from the geometry of the system as

$$\rho_S\left(\theta_2,\zeta\right) = \left[\sqrt{2\frac{\theta_C-\theta_2}{n_3}\sqrt{n_2^2-n_3^2}}\left(\zeta+n_2 D\right)\left(\zeta+n_3 D\right)\right]^{-1}. \tag{18}$$

The PL spectrum of the modes radiated to the substrate obviously reveals narrow peaks for sufficiently large number of reflections, *i.e.* after a sufficiently long propagation of the mode. The modes which are excited near the sample edge undergo only several reflections and their spectrum is almost flat. With the increasing propagation length, the resonances become better resolved and the spectrum gets narrower as shown in

Fig. 5 where we plot the results of the numerical evaluation of Eqs. (11)-(13) for the special case of a step-like profile of the refractive index. For different profiles, the modes may form at distances differing by orders of magnitude as seen when comparing *e.g.* Refs. 10 and 27.

4.3. *Optical gain*

Our aim in this paragraph is to discover the role of the optical gain in waveguiding samples. Let us consider the VSL measurement of the net optical gain: a stripe of the length ℓ is optically excited and we detect the total light intensity radiated from the sample in the waveguiding setup. The PL comes from all excited nanocrystals in the stripe and thus the total ASE intensity may be expressed as an integral of Eqs. (9), (11) and (14):

$$I_{\mathrm{ASE}}(\lambda,\alpha)=\int_0^{\ell}\left[I_{\mathrm{G},2}(\lambda,\alpha,\zeta)+I_{\mathrm{S},2}(\lambda,\alpha,\zeta)+I_{\mathrm{S},3}(\lambda,\alpha,\zeta)\right]\mathrm{d}\zeta\ . \quad (19)$$

The above formula is composed of the respective contributions from the guided modes, the substrate modes diffracted from the core and the substrate modes refracted from the substrate. The three contributions have generally different magnitudes because of different mechanisms of decoupling of the associated waves at the sample edge. Since the efficiencies of the wave decoupling and the enhancement factor of the guided modes (see Eq. (7)) are unknown and depend on the particular sample geometry, we separate phenomenologically our discussion into two general cases: 1. majority of the guided modes (substrate modes cannot be distinguished in PL spectra) and 2. majority of the substrate modes.

1. If the *guided modes are dominant*, the energy of the radiating dipole in a silicon nanocrystal is coupled mainly to the guided modes. We may therefore neglect the contributions from the substrate modes and evaluate only the integral of Eq. (9). For the detector with a very small numerical aperture (*i.e.* when detecting plane waves, $\rho=1$), the integration yields the well known formula[15]

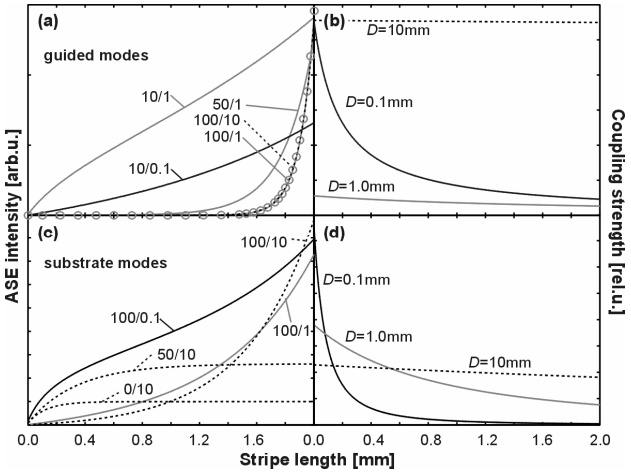

Fig. 6. Calculated ASE intensity from Eq. (19) as a function of the excited stripe length for the guided (a) and the substrate (c) modes; a small detector with a large NA is supposed. Coupling coefficients are plotted for comparison for the guided (b) and the substrate (d) modes. Scales of the curves are set for better comparison of their behavior. Numbers in (a) and (c) mean (gain coefficient in cm^{-1})/(distance D between the sample and the detector in mm). Circles in (a) denote ASE intensity according to Eq. (20) with $(g-\gamma)$=100 cm^{-1}.

$$I_{\mathrm{ASE}}(\ell) \propto \frac{\exp[(g-\gamma)\ell]-1}{g-\gamma}, \tag{20}$$

where $(g-\gamma)$ denotes the net gain. The result for a spatially small detector with a large NA obviously differs, however the result is not analytically integrable. We thus give only the numerical results in Fig. 6a — we compare evaluated Eq. (20) with Eq. (19) for the guided modes and the small detector for several values of the gain coefficient and the position of the detector. In order to give a clear interpretation of the graph, we plot in Fig. 6b the strength of coupling $\rho(\zeta)$ of the excited elements to the detector (the strength of coupling may be directly measured in the Shifting Excitation Spot[2] experiment (SES)). It is obvious from Figures 6a and 6b that Eq. (20) is valid only in special cases of the detection of plane waves by a spatially large detector or by a small detector at the

distance from the sample edge much larger than the length of the excited stripe. In the latter case, however, we may expect experimental complications because of the low PL intensity.

2. If the *substrate modes are dominant*, we consider that we detect ASE emission at the wavelength of one of the modes because at other wavelengths the contribution due to the substrate modes is negligible as discussed above and then the ASE intensity is modelled according to the discussion in the previous paragraph. The dominance of the substrate modes is caused by inefficient decoupling of the waves from the core at the sample edge and thus the major contribution comes only from the third term in Eq. (19). We plot in Figs. 6c-d the ASE intensity and the magnitudes of the coupling coefficient for several values of the gain coefficient and of the distance of the detector from the sample edge. The curves obviously show that Eq. (20) cannot be used for evaluation of the net gain in this case. For clear resolution of the net gain, one should use the SES method.

The theory developed in this section fits very well our experimental observations in VSL experiments. By choosing proper wavelength, we are able to select whether we detect guided or substrate modes and then we can directly compare their characteristics in one sample. An instructive result published in Ref. 28 means that the guided modes are more effectively amplified in the presence of a positive net optical gain than the substrate modes, as follows from the theory. We are also able to explain the unusual behaviour of the ASE and SES curves presented in Figs. 1e-f. The SES curve in Fig. 1f for the guided mode at 825 nm decreases monotoneously as the coupling coefficient decreases. The curves for the substrate TE and TM modes, however, initially increase and for longer distance of the excited spot from the edge they start to decrease due to the decrease of the coupling coefficient. The initial increase follows from the initial refraction of the waves into the substrate — since energy is radiated to the core and we detect the waves from the substrate, there is a nonzero propagation length necessary for leakage of the energy from the core. The position at which the SES curve reaches its peak depends on the detection angle (numerical aperture of the detector) as shown experimentally in Ref. 8 and as may be shown using our model.

5. Numerical Analysis of the Modes

Both models presented above are based on assumptions which simplify either the real geometry of the problem (consideration of the infinite waveguide in section 3) or the level of physical description (simple use of rays in section 4). In this section, we present a rigorous model which correctly describes propagation of the optical waves along the waveguide. The calculations in this section are performed numerically because it is impossible to derive the final expressions analytically.

The structure under description has three layers, two of them being infinite (the cladding and the substrate). According to the discussion in Ref. 20, the mode spectrum is then composed of discrete guided modes and the continuum of the substrate and the radiation modes. Presence of the continuum represents an unwanted feature in the numerical evaluation and therefore we overcome this problem by considering that all the layers are finite and the top and the bottom of the whole guiding structure is covered by a medium with reflectivity r=1. The waves propagate in the z direction and we consider the edge at the coordinate z=0. We assume the infinite structure in the y direction and we consider detection of the signal in the limit of Fraunhoffer diffraction (propagation of "plane" waves). The thickness of the cladding and the substrate is set to 0.6 mm, thus the angular resolution of the pattern diffracted from the edge is resolved with precision better than 0.15°.

The spatial profile of the intensity of electric field is given by Eq. (1) for TE modes, *i.e.* for the waves whose vector of electric intensity lies in the y direction — the numerical analysis is performed only for the TE waves since the mode splitting is well explained by the simplified models and TM modes reveal similar behaviour to TE ones in other characteristics. Using the theory of Ref. 20, the calculations have been performed in the way briefly summarized in the following. First, the allowed propagation modes (*i.e.* modes with $\mathrm{Re}\,\beta > 0$) were found numerically — let us assume that the 2×2 transfer matrix for the whole structure without mirrors is T_β and the relation between the field coefficients at the two opposite boundaries of the structure is[e]

[e] The medium with index 0 is an infinitesimally thin layer at the top of the cladding with refractive index n_0=n_1,

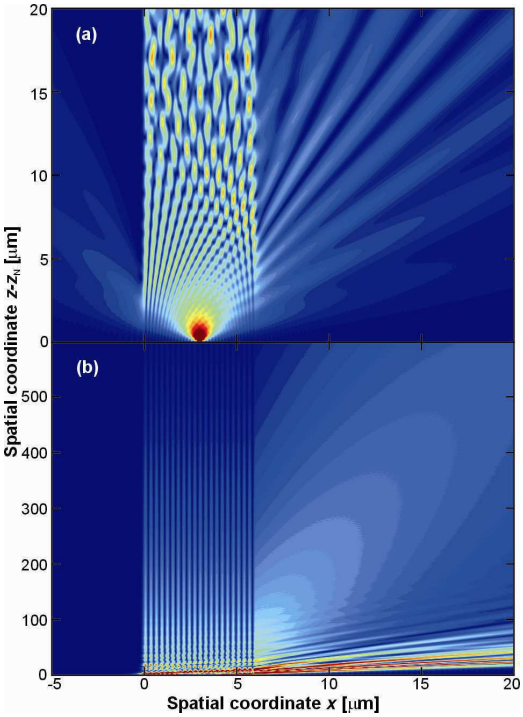

Fig. 7. (a) Distribution of the light intensity at wavelength 624.4 nm in the sample with 6 μm thick core; all modes are plotted. The coordinate x means depth below the sample surface. (b) Detailed view of decoupling of the lowest–order substrate mode at long propagation distances; only substrate modes are plotted for clarity. Dark blue colour denotes minimum intensity, maximum intensity is dark red.

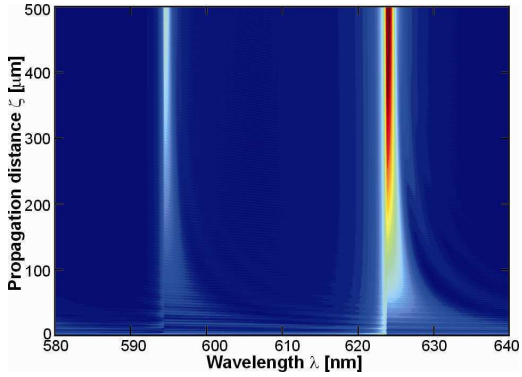

Fig. 8. Dependence of the light intensity on wavelength (horizontal axis) and propagation distance of the substrate modes (vertical axis). The waveguide has a core 6 μm thick.

$$\begin{pmatrix} A_{3\beta} \\ B_{3\beta} \end{pmatrix} = T_\beta \begin{pmatrix} A_{0\beta} \\ B_{0\beta} \end{pmatrix}. \tag{21}$$

Boundary conditions imply $A_{0\beta}=B_{0\beta}$ and $A_{3\beta}=B_{3\beta}$ and the (generally complex) coefficients β which fulfil the above constraints were found iteratively. The second step consisted in calculation of the field distribution at the sample edge. We consider a nanocrystal at the coordinates $(x_N, z_N = -\zeta)$ which is coupled to the waveguide modes. The field $E_{rad}(x,z_N)$ radiated by the nanocrystal may be decomposed to the modes as follows:

$$E_{\mathrm{rad}}(x, z_{\mathrm{N}}) = \sum_m \frac{[E_{\beta_m}(x', z_{\mathrm{N}}), \delta(x' - x_{\mathrm{N}})]}{\sqrt{[E_{\beta_m}(x', z_{\mathrm{N}}), E_{\beta_m}(x', z_{\mathrm{N}})]}} E_{\beta_m}(x, z_{\mathrm{N}}), \tag{22}$$

where $[\cdot,\cdot]$ stands for a scalar product (integral over the x coordinate) and the summation goes over all allowed propagating modes. The field distribution at the sample edge is then, according to the propagating factor in Eq. (1), expressed as

$$E_{\mathrm{rad}}(x, z = 0) = \sum_m \frac{[E_{\beta_m}(x', z_{\mathrm{N}}), \delta(x' - x_{\mathrm{N}})]}{\sqrt{[E_{\beta_m}(x', z_{\mathrm{N}}), E_{\beta_m}(x', z_{\mathrm{N}})]}} E_{\beta_m}(x, z_{\mathrm{N}}) \exp[-i\beta_m z_{\mathrm{N}}]. \tag{23}$$

In the third step, we calculated the field diffracted from the sample edge in the Fraunhoffer limit by performing the Fourier transform on the function $E_{rad}(x,z=0)$ and considering field refraction according to Snell's law and Fresnel formulae for simplification.

In the numerical results presented below, we consider a model system with the cladding with refractive index n_1=1 and width w_1 = 600 μm, the substrate with refractive index n_3 = 1.46 and width w_3 = 600 μm and the core has refractive index n_2 = 1.8 and its width is d = 6 μm. Formation and propagation of the modes is illustrated in Figures 7a and 7b where we plotted the distribution of the light intensity in the structure (the coordinate x = 0 refers to the core/cladding boundary). The beams which leave the core to the right are the substrate modes — we may assign an angle of propagation to each of them. It is interesting that obviously they are not radiated from the core at one distinct point but they decouple over long distances. This property is better visualized in the detailed view in Fig. 7b where we may identify the substrate modes which are rapidly

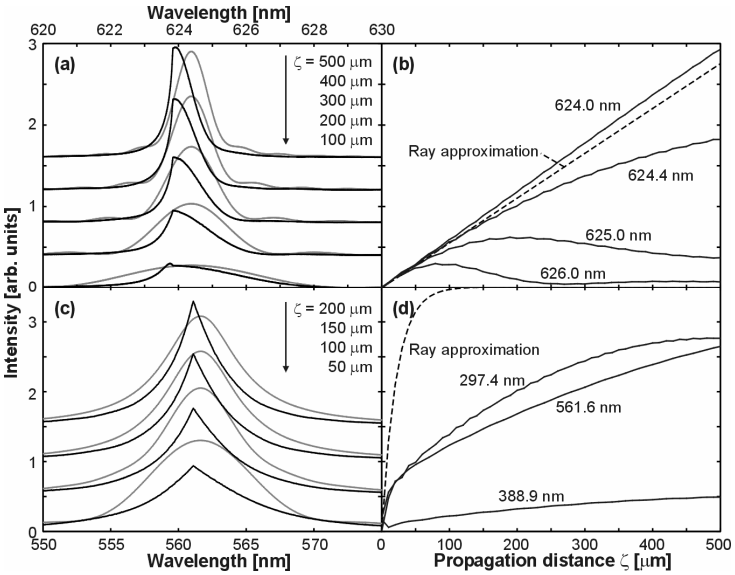

Fig. 9. (a), (c) Narrowing of the substrate mode during propagation along the waveguide. Spectral profiles of the modes at several distances from the excited spot calculated by the numerical model (black lines) and results of the ray model for comparison (gray lines). (b), (d) Calculated energy decoupled from the core as a function of the propagation distance from the excited spot (solid) and results of the ray model for comparison (dashed line). Parameters of the curves denote wavelengths in the vicinity of the resonance of the mode (b) and wavelengths of several resonant modes (d). The core thicknes is 6 μm (a), (c) and 0.6 μm (b), (d), respectively.

decoupled from the core and one mode which decouples at much longer distances comparable to 0.5 mm.

The results depicted in Fig. 7 directly support the model from section 4 based on the assumption of the gradual decoupling of the waves from the core to the substrate. As we have shown, this fact is responsible for gradual narrowing of the PL spectra when increasing $|z_N|=\zeta$, *i.e.* when the excited spot is moved further from the sample edge. We performed calculations in order to confirm this hypothesis and the results are plotted in Fig. 8 — the dependence of the PL intensity measured at the angle α=2.5º on wavelength λ and distance $|z_N|=\zeta$ between the nanocrystal and

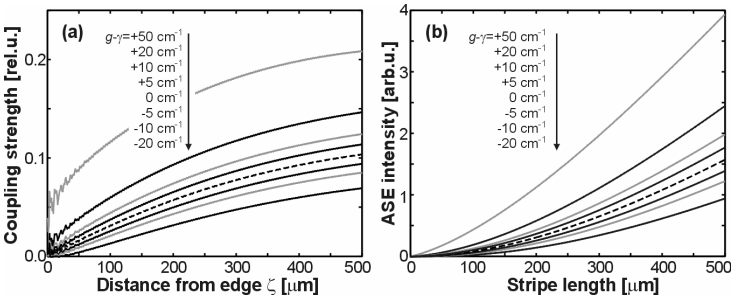

Fig. 10. (a) Calculated coupling strength of the excited spot at the distance ζ from the sample edge considering a sample with the core thickness of 6 μm for several values of gain coefficient at the resonant wavelength 624.4 nm of the substrate mode (*cf.* Figs. 7, 8); (b) calculated ASE intensity recorded from the sample with same parameters as in (a).

the sample edge. The cuts of this graph in the directions of both axes ζ, λ are plotted in Figures 9a and 9b. In Fig. 9a, the mode narrowing is obvious and we compare these numerical results with the results of the model from section 4 (plotted as grey lines). We may conclude that the approximate model gives accurate results and is therefore usable as an estimate for practical use in evaluation of experiments. The rate of energy decoupling from the core is depicted in Fig. 9b for several wavelengths around the resonance together with the estimate performed according to Ref. 18. Decoupling rate is obviously well estimated by the theoretical curve for the resonant mode and thus the ray model is usable also in this case. Graphs similar to those in Figures 9a and 9b are plotted in Figures 9c and 9d for the waveguide core with thickness of 0.6 μm together with comparison with the simplified model. The energy flow from the core to the substrate is more pronounced when compared to the waveguide with the wider core. We may interpret this feature in terms of ray propagation: as seen from Eqs. (16) and (17), the distance z_R between the two points of reflection of the ray is proportional to the waveguide thickness and therefore the energy loss due to transmission to the substrate is faster in thin waveguides. Although qualitative discussion well reflects the situation, quantitative comparison in Fig. 9d fails. The limitations of the ray model from section 4 are thus clearly seen — it gives good numerical predictions only when $d>>\lambda$, *i.e.* when wave

propagation is well described by ray optics. The narrowing of the modes, nevertheless, may be roughly estimated by using the ray model also for structures with $d \sim \lambda$ as seen in Fig. 9c.

We may include small optical losses or optical gain (up to tens cm^{-1}) into the numerical model in the form of a complex refractive index. We present in Fig. 10a the dependence of the intensity of light emitted by a nanocrystal and transmitted through the structure with gain or losses on the distance of propagation. The detection angle is $\alpha = 2.5°$, wavelength 624.4 nm and other parameters equal to those in Fig. 7. By integration of the curves in Fig. 10a, we get the ASE intensity depicted in Fig. 10b. According to section 4, all the ASE curves seem to have exponential behaviour near the origin $\zeta = |z_N| = 0$, however this is not a consequence of the optical gain but the result of the mode leaking.

We may conclude this section by stating that the approximate models are capable of a qualitative description of the mode propagation and leaking in the waveguiding structures. They give good quantitative results if the waveguide core is wide enough ($d>>\lambda$) but one should use them only as rough estimates in other cases where numerical calculation should be applied in order to get quantitatively correct results.

6. Conclusions and Acknowledgements

The results presented in this chapter show that the substrate modes, usually considered as an unwanted artificial feature, have properties very different from the guided modes of the waveguide. Because of their limited lifetime inside the core, they cannot be effectively absorbed or amplified and therefore they are hardly controllable. In spectroscopic measurements, it appears almost impossible to evaluate the magnitude of the net optical gain from the VSL measurements on the substrate modes and therefore it is desirable to avoid (by properly designing the core parameters) the presence of the substrate modes in most applications including optical spectroscopy. The spatial separation of the substrate and the guided modes can be exploited in order to filter out the substrate modes, *e.g.* by using a detection with high spatial resolution or using techniques for decoupling of the guided waves from the core (by placing a prism on the top plane of the sample *etc.*).

The substrate modes may be, however, of importance in nano-silicon active optoelectronic devices where light is emitted, guided or amplified. Because of usual small optical gain in Si nanocrystals, the intensity of the substrate modes may be comparable to or even larger than the intensity of the guided modes and they may be then a source of noise. Devices must be then constructed in order to avoid wave propagation in the substrate — one may use for example absorbing substrate or a special geometry of the device in order to physically block the waves.

Although the substrate modes represent in most cases a parasitic feature in waveguiding devices, it appears, however, possible to use them in a wide range of applications in nano–optics. They may be used for optical sensing profiting from their sensitivity to the refractive index of the cladding. Another promising application may be the use of active waveguides as simple tunable sources of narrow–line directional optical emission and as tunable optical filters. However, further research in this direction is needed.

Financial support through research projects GAAVCR IAA1010316, GACR 202/01/D030, GACR 202/07/0818, Centrum LC510 and the institutional research plan AV0Z 10100521 (Institute of Physics) is greatly appreciated. This work is also a part of the research plan MSM 0021620834 that is financed by the Ministry of Education of the Czech Republic. Thanks are also due to Prof. R.G. Elliman (ANU Canberra) for kindly supplying samples used throughout this study.

References

1. L. Pavesi, L. Dal Negro, C. Mazzoleni, G. Franzo and F. Priolo, *Nature* **408**, 440 (2000).
2. J. Valenta, I. Pelant and J. Linnros, *Appl. Phys. Lett.* **81**, 1396 (2002).
3. L. Dal Negro, M. Cazzanelli, L. Pavesi, D. Pacifici, G. Franzo, F. Priolo and F. Iacona, *Appl. Phys. Lett.* **82**, 4636 (2003).
4. L. Khriachtchev, M. Räsänen, S. Novikov and J. Sinkkonen, *Appl. Phys. Lett.* **79**, 1249 (2001).
5. J. Ruan, P.M. Fauchet, L. Dal Negro, M. Cazzanelli and L. Pavesi, *Appl. Phys. Lett.* **83**, 5479 (2003).
6. M. Cazzanelli, D. Navarro-Urrios, F. Riboli, N. Daldosso, L. Pavesi, J. Heitmann, L.X. Yi, R. Scholz, M. Zacharias and U. Gösele, *J. Appl. Phys.* **96**, 3164 (2004).

7. L. Khriachtchev, M. Räsänen and S. Novikov, *Appl. Phys. Lett.* **83**, 3018 (2003).
8. J. Valenta, T. Ostatnický, I. Pelant, R.G. Elliman, J. Linnros and B. Hönerlage, *J. Appl. Phys.* **96**, 5222 (2004).
9. L. Khriachtchev, M. Räsänen, S. Novikov and J. Lahtinen, *J. Appl. Phys.* **95**, 7592 (2004).
10. L. Khriachtchev, S. Novikov, J. Lahtinen and M. Räsänen, *J. Phys.: Condens. Matter* **16**, 3219 (2004).
11. D. Navarro-Urrios, F. Riboli, Massimo Cazzanelli, A. Chiasera, N. Daldosso, L. Pavesi, C.J. Oton, J. Heitmann, L.X. Yi, R. Scholz and M. Zacharias, *Opt. Mater.* **27**, 763 (2005).
12. R. Ferre, B. Garrido, P. Pellegrino, M. Perálvarez, C. García, J. A. Moreno, J. Carreras and J. R. Morante, *J. Appl. Phys.* **98**, 084319 (2005).
13. J. Valenta, I. Pelant, K. Luterová, R. Tomasiunas, S. Cheylan, R.G. Elliman, J. Linnros and B. Hönerlage, *Appl. Phys. Lett.* **82**, 955 (2003).
14. P. Janda, J. Valenta, T. Ostatnický, E. Skopalová, I. Pelant, R.G. Elliman and R. Tomasiunas, *J. Lumin.* **121**, 267 (2006).
15. K. L. Shaklee, R. F. Leheny and R. E. Nahory, *Phys. Rev. Lett.* **26**, 888 (1971).
16. T. Ostatnický, J. Valenta, I. Pelant, K. Luterová, R.G. Elliman, S. Cheylan and B. Hönerlage, *Opt. Mater.* **27**, 782 (2005).
17. I. Pelant, T. Ostatnický, J. Valenta, K. Luterová, E. Skopalová, T. Mates and R.G. Elliman, *Appl. Phys. B* **83**, 87 (2006).
18. D. Marcuse, *Theory of Dielectric Optical Waveguides* (Academic Press, Boston, 1991).
19. A.W. Snyder and J.D. Love, *Optical Waveguide Theory* (Chapman&Hall, London, 1991).
20. R. E. Smith and S. N. Houde-Walter, *J. Opt. Soc. A* **12**, 715 (1995).
21. H. Kogelnik and V. Ramaswamy, *Appl. Opt.* **13**, 1867 (1974).
22. M. Born and E. Wolf, *Principles of Optics: Electromagnetic Theory of Propagation, Interference and Diffraction of Light* (Pergamon Press, Oxford, 1993).
23. The software package SRIM developed by J.F. Ziegler *et al*., http://www.srim.org.
24. K. Luterová, E. Skopalová, I. Pelant, M. Rejman, T. Ostatnický and J. Valenta, *J. Appl. Phys.* **100**, 074307 (2006).
25. T. Ostatnický, P. Janda, J. Valenta and I. Pelant, *Proc. SPIE* **6609**, 66090F (2007).
26. L. Dal-Negro, P. Bettotti, M. Cazzanelli, D. Pacifici and L. Pavesi, *Opt. Commun.* **229**, 337 (2004).
27. K. Luterová, D. Navarro, M. Cazzanelli, T. Ostatnický, J. Valenta, S. Cheylan, I. Pelant and L. Pavesi, *phys. stat. sol. (c)* **9**, 3429 (2005).
28. K. Luterová, M. Cazzanelli, J.-P. Likforman, D. Navarro, J. Valenta, T. Ostatnický, K. Dohnalová, S. Cheylan, P. Gilliot, B. Hönerlage, L. Pavesi and I. Pelant, *Opt. Mater.* **27**, 750 (2005).

[P8]

37

Waveguides for Nanophotonics

Jan Valenta
Charles University

Tomáš Ostatnický
Charles University

Ivan Pelant
Institute of Physics of the Academy of Sciences of the Czech Republic

37.1 Introduction

The term *nanophotonics* may be understood as abbreviation from "photonics of nanostructures." This rapidly evolving research area deals with light interaction in nanostructured materials and their applications in photonic devices like light sources, modulators, detectors, etc.

37.1.1 Basic Types of Waveguides for Nanophotonics

Optical waveguides are structures that are able to confine and guide optical electromagnetic field. *Classical waveguides* (optical fibers, Figure 37.1a) use refractive index difference between the core and the cladding layer to guide light by total internal reflection. When the size of waveguide approaches the wavelength of light, the confinement decreases and losses increase. Therefore, the size of practical classical waveguides is limited to several hundreds of nanometers. Somewhat better confinement can be achieved in more complex waveguides with guiding properties determined by the formation of photonic bands due to their regular spatial structure (Figure 37.1b and c): (1) *photonic crystal waveguides* using "defects" in periodic structures of photonic crystals to confine light and (2) *plasmonic waveguides* based on metallic nanostructures with plasmon resonance (see, e.g., Pavesi and Guillot 2006). Due to limited space, we are going to describe only a special type of the "classical" waveguides formed by luminescing silicon nanocrystals (Si-nc).

37.1.2 Silicon Nanophotonics

The recent years can be characterized by the association of microelectronics with optoelectronics or photonics. While the microelectronics is based almost exclusively on silicon (indirect band-gap semiconductor), photonic light sources are currently made out of direct band-gap III–V compounds (family of GaAs materials). In order to reduce the material diversity, an effort to develop an efficient, electrically pumped silicon-compatible light-emitting device is becoming very strong (Pavesi and Lockwood 2004). This tendency to "siliconize photonics" is driven also by the need to reduce the overheating of silicon integrated circuits due to the ohmic resistance of excessively long multilevel metal interconnects (Pavesi and Guillot 2006). Supplementary advantages like the reduction in charging (RC) time constant (speeding up the circuit performance) and prevention from crosstalks can be obtained as a bonus.

Since bulk silicon, as an indirect band-gap semiconductor, is a very bad light emitter, nanometer-sized silicon nanocrystals, brightly luminescent at room temperature, represent one of the possible solutions (Pavesi and Lockwood 2004). It is then expected that the light signal originating in Si-nc and carrying the required information propagates in a low-loss medium which assures, at the same time, a good directionality of the radiation. It has been discovered recently that slabs of fused quartz SiO_2 "doped" with Si-nc are able to accomplish both the role of a light emitter and that of a waveguide (Khriachtchev et al. 2001, Valenta et al. 2003a, Khriachtchev et al. 2004). We shall call this type of nanophotonic waveguides (which generate the luminous signal themselves and therefore there is no need to

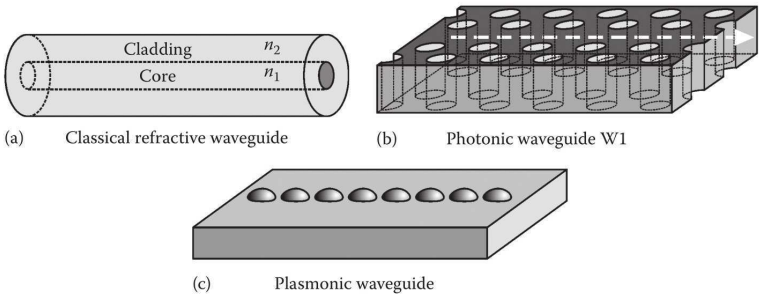

FIGURE 37.1 Nanophotonic waveguides: (a) "Classical" waveguide based on total internal reflection using the core with higher refractive index than the cladding. (b) Photonic crystal waveguide formed by a "defect" in the regular structure—here is the W1 waveguide formed by a row of missing holes. (c) Plasmonic waveguide formed by a row of metallic nanocrystals.

couple the light to them from an external source) "active waveguides." In this chapter, we shall describe the preparation methods of active nanocrystalline waveguides, their experimentally observed properties, and relevant theoretical description. We shall also briefly mention their various application possibilities.

37.2 Fabrication of Planar and Rib Waveguides

There have been many various methods of how to grow thin sheets of luminescent Si-nc embedded in an optically transparent matrix: (1) *Implantation of fused quartz* (SiO_2) slabs with Si^+ ions (Figure 37.2) (Cheylan et al. 2000), (2) *reactive Si deposition onto fused quartz* (Khriachtchev et al. 2002), (3) *plasma-enhanced chemical vapor deposition* (PECVD) of substoichiometric silicon oxide SiO_x thin films on a Si substrate (Iacona et al. 2000), (4) *co-sputtering of a Si wafer and a piece of glass* using fused quartz plates or Si wafers as a substrate (Imakita et al. 2005), (5) *crystallization of Si/SiO_2 superlattices* with nm-thick amorphous Si or SiO layers (Riboli et al. 2004), and (6) *embedding of porous silicon grains into sol-gel derived SiO_2 layers* (Luterová et al. 2004), to list at least the most frequently used. Most of these techniques comprise high-temperature (1100°C–1200°C) annealing of deposited SiO_x films in order to achieve the phase separation between Si-nc and the SiO_2 matrix. The thickness of the resulting sheets containing Si-nc can vary from hundreds of nanometers to tens of micrometers. Due to the difference in refractive index between the matrix ($n_{silica} \approx 1.45$) and silicon ($n_{Si} \approx 3$) such sheets act as planar or rib waveguides. Interestingly, the attractive waveguiding features that we are going to discuss, namely, the wavelength selective guiding of light (which can be also called "spectral filtering") and microcavity-like behavior, are critically dependent upon the preparation method: Till now, they have been discovered only in samples fabricated using the first two methods. We describe them in detail.

Implantation of accelerated Si^+ ions can be applied either to fused quartz (silica) slabs or to a thin SiO_2 layer thermally

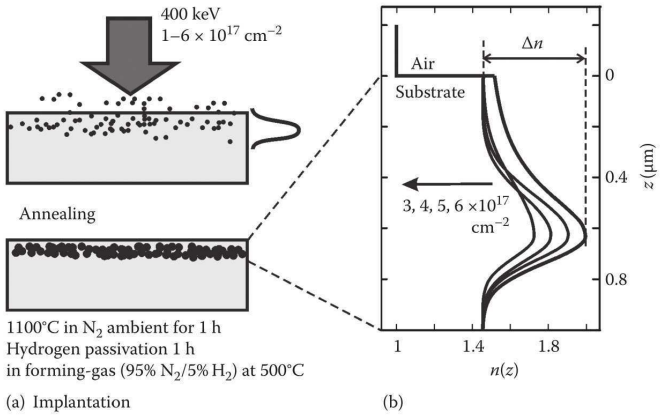

FIGURE 37.2 (a) The schematics of a Si-nc planar waveguide preparation. (b) Refractive index profiles (n as a function of the depth z beneath the surface) of silicon nanocrystalline waveguides (implanted with 400 keV Si^+ ions and different implant fluences), extracted from optical transmission measurements. (After Valenta, J. et al., *J. Appl. Phys.*, 96, 5222, 2004.)

grown on a silicon wafer. Implantation energy varies usually between 30 and 600 keV and implant fluences (ion doses) are of the order of 10^{16}–10^{17} cm^{-2}. The attractive waveguide properties of fabricated planar waveguides, i.e., pronounced emission line narrowing and high output beam directionality in the visible region, have been found in waveguides prepared from 1 mm thick silica (Infrasil) slabs with optically polished surface and edges, using the implantation energy of 400 keV and the implant fluences 1×10^{17} cm^{-2} to 6×10^{17} cm^{-2}. Because the Si^+ ions are almost monoenergetic, their stopping distance beneath the silica slab surface has only a small dispersion, which results in narrow and slightly skewed implant distribution, as reflected in the resulting refractive index profiles shown in Figure 37.2 (Valenta et al. 2004). Peak excess Si concentration was up to 26 atomic%. Spherical silicon nanocrystals with diameter distribution roughly from 4 to 6 nm were formed by annealing the implanted samples at 1100°C in a nitrogen ambient for 1 h. To enhance several times the luminescence intensity of Si-nc, an additional anneal at 500°C in forming gas ($N_2 + H_2$) for 1 h was applied (Cheylan and Elliman 2001). The last operation promotes enhanced hydrogen passivation of non-radiative defects.

The reactive silicon deposition has yielded substoichiometric SiO_x films on circular 1 mm-thick substrate silica plates (Khriachtchev et al. 2001, 2004). Electron beam evaporation and radio frequency cells were used as silicon and oxygen sources. The SiO_x layer thickness was ~2 μm and the value of the x parameter varied around $x = 1.70$. The as-grown material contained amorphous Si inclusions. Annealing of these "suboxide" films at 1100°C in nitrogen atmosphere resulted in the formation of well-defined Si-nc with diameters of 3–4 nm, as evidenced by Raman spectroscopy. Extensive investigations of this type of silica waveguides containing Si-nc discovered a small effective optical birefringence inside the layers, however, without radically influencing the properties of the waveguides (Khriachtchev et al. 2007). Refractive index profile across the thickness of these waveguides is flat, unlike the preceding case of the implanted layers.

The reason why Si-nc waveguides fabricated using other techniques do not show the spectral filtering effect are not fully clear at present. Of course, the condition *sine non qua* is asymmetry of the waveguide, i.e., the waveguiding layer must not be sandwiched between two materials (cladding layers) having the same effective refractive index, as we shall see in the next section. One can speculate about several further critical parameters: suitable composition and optical quality of the matrix, suitable density of Si-nc (in the order of 10^{18} cm^{-3}), favorable layer thickness (around 1 μm), excellent flatness and parallelism of both interfaces and, last but not least, certain optimum value of propagation losses (several dB/cm). The dominant losses in the waveguides under discussion are probably due to self-absorption and Mie light scattering on Si-nc clusters, not due to surface roughness (Pelant et al. 2006).

The above discussion has dealt implicitly with planar waveguides. Rib-loaded waveguides containing nanocrystals seem, in principle, even more desirable for nanophotonic applications. They can be also prepared using the ion implantation technique in either thin SiO_2 films thermally grown on Si or in polished fused quartz slabs, as described above. The rib structure can be formed (using standard photolithography and etching) by two possible means: either before or after the implantation procedure. Figure 37.3a represents schematics of such a rib waveguide structure.

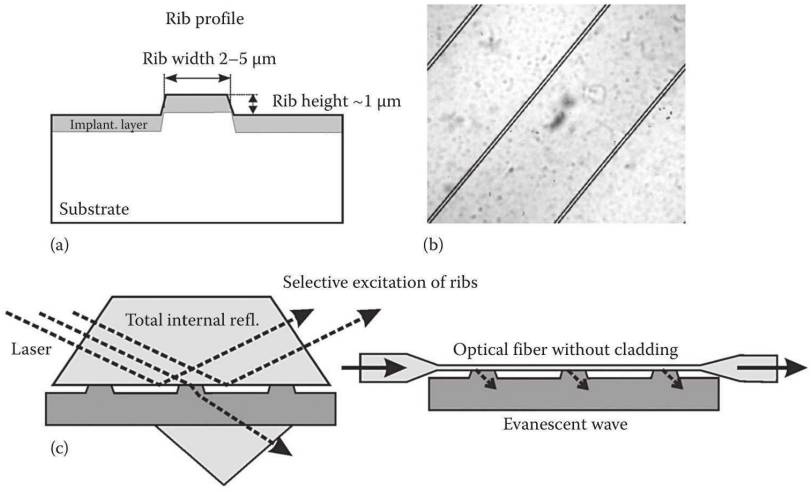

FIGURE 37.3 (a) Sketch of a rib waveguide structure with silicon nanocrystals, prepared on a polished silica slab. The ribs were fabricated by optical lithography before Si^+ implantation. (b) Microscopic (reflection) image of a part of the structure. The spacing between the ribs is 100 μm. (After Skopalová, E., Mode structure in the light emission from planar waveguides with silicon nanocrystals, Diploma thesis, Charles University, Prague, Czech Republic, 2007.) (c) Methods to selectively excite the rib waveguides through the TIR prism or the evanescent field of a fiber.

Lateral confinement of the light in a narrow rib is expected, in comparison with the planar waveguides, to have some advantages: saving considerable space in photonics circuits and offering much wider variability in their design. On the other hand, the transition from the two-dimensional to the one-dimensional case can degrade the optical quality of the waveguide and introduce additional losses, such as those due to sidewall roughness or even due to considerably deformed rib cross section. Indeed, measurements of propagation losses in similar waveguides has given values above 10 dB/cm and this loss coefficient even increases for rib widths below 4 μm (Pellegrino et al. 2005). Therefore, in what follows, we discuss predominantly the two-dimensional nanocrystalline waveguides and limited space only will be given to the rib structures.

37.3 Experimental Techniques

37.3.1 Techniques to Study Internal Photoluminescence Propagation in Waveguides

One of the most important advantages of active waveguides is that light sources are embedded in the waveguide. In our material, Si nanocrystals forming the waveguide core can efficiently emit luminescence in the orange-red-infrared spectral range when excited with the UV-blue light (usually focused laser beam). Such internally produced light is automatically coupled to all possible modes of the waveguide: radiation, substrate, and guided modes (see Section 37.5). The emission modes may be distinguished by measuring their propagation direction, spectra, and polarization, which imposes requirements to experimental setup.

Two types of setups can be conveniently applied to study luminescence from active waveguides: (1) The micro-imaging-spectroscopy setup is based on a microscope connected to an imaging spectrograph with a CCD camera (Figure 37.4a). For good angular resolution low numerical aperture (NA) objective lenses should be used (in our experiments, we used mostly the lens with 2.5 × magnification and NA = 0.075, i.e., an angular resolution of about 8.6°). The sample is fixed to an x–y–z table with a rotating holder and excited by a laser beam (325 nm from the cw He–Cd laser), approximately perpendicular to the objective axis. (2) In order to achieve better angular resolution, an experimental arrangement based on a goniometer is employed (Figure 37.4b). Here, the sample is fixed to the center of the goniometer, and the photoluminescence emission is collected by a silica optical fiber (core diameter 1 mm) rotated around the sample at a distance of 50 mm, giving an angular resolution slightly less than 1° (NA ~ 0.01). The output of the fiber can be coupled to the same detection system (a spectrograph with a CCD camera), as described above.

Typical images observed with the microscopic setup (Figure 37.4a) are illustrated in Figure 37.4c and d. Here, the diameter of the excitation spot, located about 1 mm from the sample edge, is roughly 1 mm. One can easily recognize PL emission from the excited spot as a bright ellipsoid. However, there is

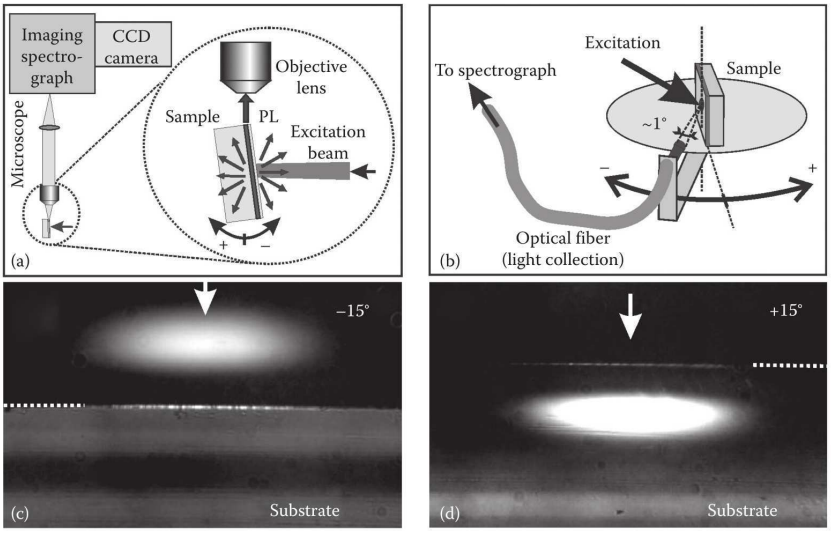

FIGURE 37.4 (a) Micro-spectroscopy setup for studying spatially resolved emission from waveguides, (b) collection of signals from a waveguide using optical fiber mounted on a goniometer. (c,d) Luminescence microimages of the active planar waveguide (obtained with the setup illustrated in panel a) where the elliptical spot is the spot excited by the laser beam and the light line is emission emanating from the sample facet. The inclination of the sample with regard to optical axis is −15° and +15°, respectively. (Adapted from Valenta, J. et al., *J. Appl. Phys.*, 96, 5222, 2004.)

also a second contribution emanating from the facet of the sample. This light is obviously guided in the implanted layer or close to it. The images in Figure 37.4c and d were collected for sample inclination angles of −15° and +15°, respectively, i.e., in a geometry for which the excited spot was observed either directly (Figure 37.4c) or through the substrate (Figure 37.4d). The experimental arrangement shown in Figure 37.4a enables the detection of the PL either from the excited spot or from the edge of sample by positioning the entrance slit of the spectrograph to different locations of the PL image. All experiments described in this chapter were performed at room temperature.

37.3.2 Techniques to Study Propagation of Light from External Sources

The coupling of external light to narrow submicrometer waveguides is a difficult task. The most used approaches are as follows: (1) *Prism coupling of light* from the surface of the sample (Figure 37.5a). Light from Xe lamp, halogen lamp, or LED is collimated into a prism in contact with waveguide. For better optical contact, an immerse liquid should be dropped between the prism and the sample (the best optical contact—i.e., minimizing reflections on interface—is achieved when refractive index of the immersion liquid is between the values for the materials to be connected). A second prism may be placed on the opposite surface of waveguide to couple out the passing beam to avoid total internal reflection. (2) *Direct coupling into the facet* (Figure 37.5b, sometimes called *end-fire coupling*). The edge of the sample can be polished at some angle (here 70°) in order to separate light refracted to the higher index waveguide from light entering lower index substrate. For both the external light coupling setups the signal can be collected by an optical fiber and guided to the entrance slit of the imaging spectrometer with a CCD detector. The other coupling methods described in literature are *grating coupling* and *evanescent wave coupling* (sometimes called waveguide-to-waveguide coupling) (see Figure 37.5c and d).

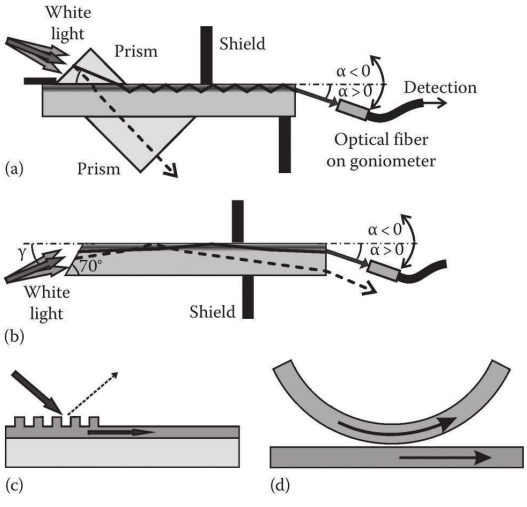

FIGURE 37.5 External light coupling into a narrow waveguide: (a) prism coupling, (b) end-fire coupling, (c) grating coupling, and (d) evanescent-wave coupling. (Adapted from Janda, P. et al., *J. Lumin.*, 121, 267, 2006; Pavesi and Guillot, 2005.)

37.3.3 Techniques to Study Losses and Optical Amplification in Waveguides

The losses in waveguide are divided into *insertion* (*coupling*) *losses* and *propagation losses*, which contain *scattering*, *radiation*, and *absorption* (Figure 37.6a). If the waveguide material can be pumped to reach population inversion, the guided light may be amplified by stimulated emission. In this case, the absorption coefficient α becomes negative and it is called the gain coefficient $g(g = -\alpha)$.

The most used methods to measure losses in waveguides are (Figure 37.6b through e) (1) *"cutback" method* detecting light output from waveguide with different length, (2) *scattering detection* from different points of waveguide surface, (3) *Fabry–Perot resonance* method, which can be applied to waveguides with good facets, and (4) *shifting excitation spot* (SES) method which can be applied to active waveguides.

Optical gain is measured by the *variable stripe-length* (VSL) method or by the *pump-and-probe* (PP) method. The principle of the VSL method consists in excitation of a narrow stripe-like region at the edge of a sample (Figure 37.7a) (Shaklee and Leheny 1971, Valenta et al. 2003b, Dal Negro et al. 2004). If the pumping is able to induce population inversion in studied material, photons passing through the excited region can be amplified by stimulated emission. It corresponds to a single-pass optical amplifier. If the emission from the sample edge $I^{VSL}(l,\lambda)$ is detected as a function of the stripe length l, the net optical gain $G(\lambda)$ is calculated from a simple equation

$$I^{VSL}(l,\lambda) = \frac{I_{sp}(\lambda)}{G(\lambda)}\left[\exp(G(\lambda)\cdot l) - 1\right], \tag{37.1}$$

where

I_{sp} is the intensity of spontaneous emission

$G(\lambda) = [g(\lambda) - K]$ is net optical gain (K stands for losses and $g(\lambda)$ is material gain coefficient, i.e., negative absorption coefficient) (Valenta et al. 2002)

Equation 37.1 is valid only when $I_{sp}(\lambda)$ and $g(\lambda)$ are constant over the whole excited stripe. It means that the exciting power density and properties of sample must be uniform. Also, the coupling of the output emission to a detector must be constant, independent of x, for any part of the stripe. In reality, the geometry and emission properties of the sample are never perfectly constant and the coupling of light is influenced by directionality of emitted light, limited collection angle (numerical aperture), the confocal effect of imaging optics, etc. (Valenta et al. 2003b) Therefore, the SES method has been proposed to correct the VSL method

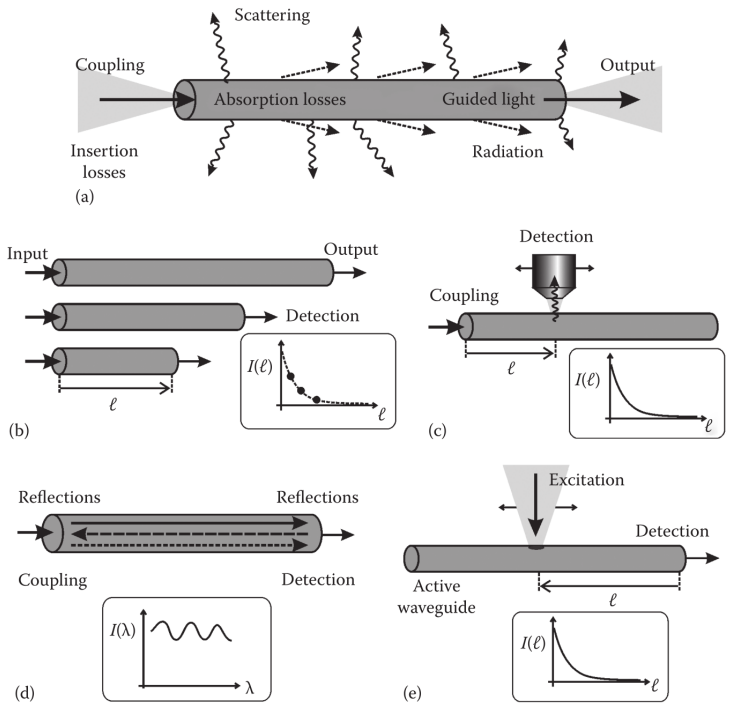

FIGURE 37.6 (a) Schematic illustration of losses in a waveguide. Methods to measure losses: (b) cutback, (c) scattering light detection, (d) Fabry–Perot resonance, and (e) shifting excitation spot methods.

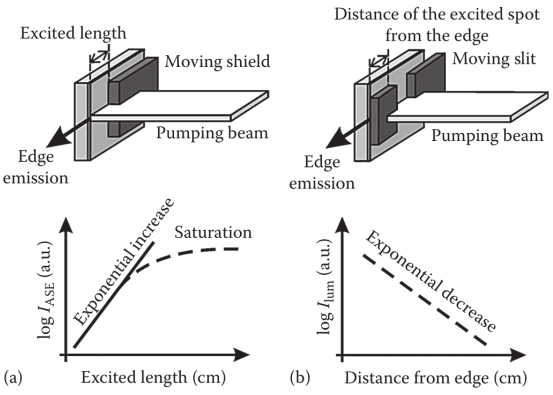

FIGURE 37.7 The principle of the (a) VSL and (b) SES methods and typical dependence of the detected signal as function of the excited length and the distance from edge, respectively (lower panel). (Adapted from Park, J.H. and Steckl, A.J., *Appl. Phys. Lett.*, 85, 4588, 2004.)

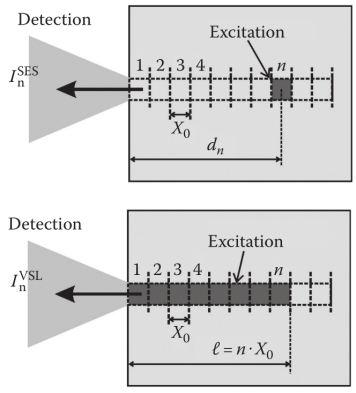

FIGURE 37.8 Schematic illustration of the principle of combining the SES and VSL experiments.

(Valenta et al. 2002). The principle of the SES method takes advantage of the fact that instead of the whole stripe only small segments are excited and measured separately (Figure 37.7b).

Figure 37.8 illustrates the procedure to compare the VSL and SES results. The most transparent approach consists of SES measurement with the spot width equal to the shift step. Let us assume that the VSL measurement is done using the same elemental steps x_0 as the SES experiment (obviously, also the stripe width and excitation density must be the same for both SES and VSL). Then we can compare the VSL signal I_n^{VSL} for a stripe consisting of n elemental steps ($l = n{\cdot}x_0$) with integrated SES signal I_n^{iSES}, i.e., sum of SES signals from n steps

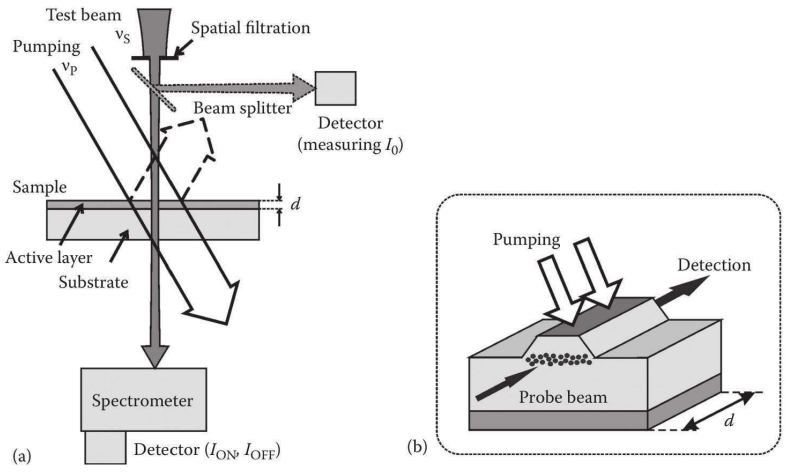

FIGURE 37.9 The basic arrangement of the pump-and-probe experiment for a (a) planar and (b) rib waveguide.

$$I_n^{\mathrm{iSES}} = \sum_{k=1}^{n} I_k^{\mathrm{SES}}.$$

Integrated SES signal should contain the same amount of spontaneous emission as the VSL measurement (including losses and effects of imperfect experimental conditions), the only difference being that in VSL experiment some photons go through the excited area and might be amplified by stimulated emission or affected by induced absorption. Which effect takes place is clear from plotting both I_n^{VSL} and I_n^{iSES} in one figure.

Similarly, we can calculate the differential VSL intensity I_n^{dVSL}, i.e., the difference of signals obtained for stripe lengths $l = n \cdot x_0$ and $l = (n-1) \cdot x_0$

$$I_n^{\mathrm{dVSL}} = I_n^{\mathrm{VSL}} - I_{n-1}^{\mathrm{VSL}}$$

and compare it with I_n^{SES}. Again, the detected signal comes from spontaneous emission in the nth excited spot that is passing through the excited or unexcited area for the dVSL and SES, respectively. In the ideal case, we can use equations $I_n^{\mathrm{dVSL}} = \mathrm{const}\exp[(g-K)d_n]$ and $I_n^{\mathrm{SES}} = \mathrm{const}\exp(-Kd_n)$ to derive the net optical gain $g(\lambda)$

$$g(\lambda) = \frac{\ln\left(I_n^{\mathrm{dVSL}}(\lambda) / I_n^{\mathrm{SES}}(\lambda)\right)}{d_n},$$

where d_n is the distance of the center of the nth spot from the edge.

The PP technique is based on the application of two beams: the first one is pumping the active sample and the second one is testing the state created by the pumping beam. In case of studying stimulated emission, the test beam may be amplified by stimulated emission. In general, the test beam spot must be situated inside the pumping spot in order to test area pumped as homogeneously as possible. In case of pulsed beams, the temporal coincidence of both pumping and testing pulses must be controlled (the test beam may be delayed after pumping pulses to study decay of the effect). If the thickness of the active layer is small, the induced effect on the test beam may be difficult to detect. Therefore, for waveguide samples, the test beam is often coupled to the waveguide, which is excited from the surface (Figure 37.9b). Then, changes of the outcoupled light with and without pumping are detected.

37.4 Main Experimental Observations in Active Si-nc Waveguides

The most important observations for active planar waveguides are (1) spectral filtering, (2) TE (transverse electric) and TM (transverse magnetic) mode splitting, and (3) high directionality of TE, TM mode emission. These effects are illustrated in Figure 37.10; the panel (a) shows that the PL leaving the edge of waveguide layer is substantially different from the PL perpendicular to the layer. The perpendicular PL is formed by a single band that corresponds to the well-known emission of Si nanocrystals, but the edge PL contains two narrow PL bands. Both narrow lines are linearly polarized, one in the direction of the waveguide layer (TE mode) and the second one perpendicular to the layer (TM mode). The spectral position of the TE and TM modes depends on the exact profile of the refractive index, it means on the implantation fluence (see also Figure 37.16, which shows spectra of another set of samples). The panels (b) and (c) illustrate that the TE and TM modes are emitted only in an extremely narrow angle (a few degrees), basically in the direction of the waveguide plane (only slightly inclined to the substrate, i.e., under positive angles in our notation).

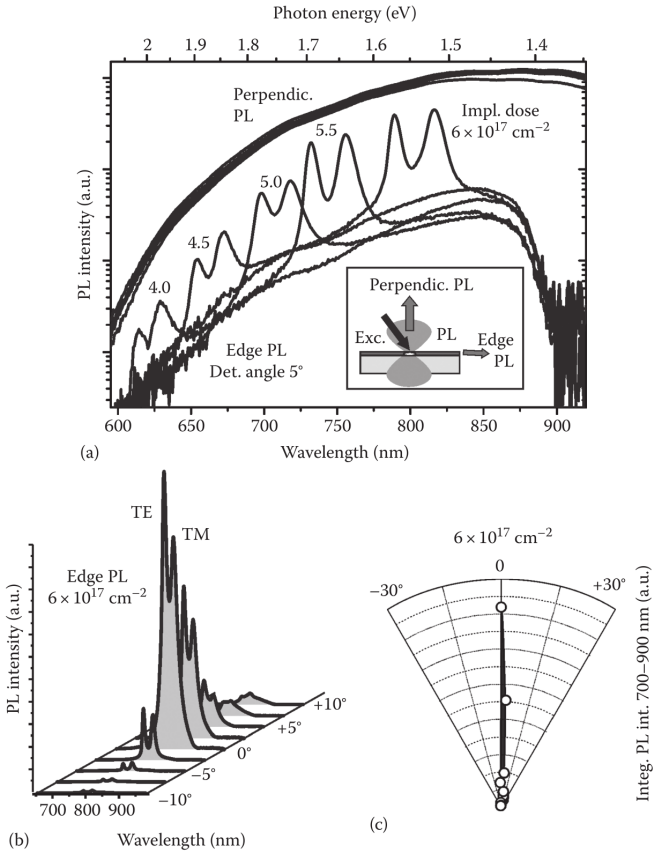

FIGURE 37.10 PL spectra of five fused silica slabs implanted to the fluences of 4×10^{17} cm^{-2} to 6×10^{17} cm^{-2}. (a) Upper curves (a single wide band) correspond to PL emitted in a direction perpendicular to the waveguide, while lower spectra with doublet peaks are facet-PL detected in a direction $\alpha = 5°$ (a sketch of the experimental arrangement is shown in the inset). (b) Angle-resolved facet PL spectra of the sample 6×10^{17} cm^{-2}. (c) Polar representation of integrated PL intensity of the angle-resolved facet spectra from the panel b. Most of the PL intensity is emitted in a direction close to 0°. (Adapted from Janda, P. et al., *J. Lumin.*, 121, 267, 2006.)

The coupling and propagation of *external* light in active Si-nc waveguides were studied by the direct (end-fire) and the prism coupling (Figure 37.5a and b). The results for one sample are illustrated in Figure 37.11. For prism coupling, two broad transmission bands (in the blue and red spectral region) are observed in the measured spectral range. The positions of both bands coincide with those of the PL modes (Figure 37.10a). Our calculations show that the red and blue bands corresponds to the second and third order of substrate modes (the first order being in the infrared region), see Section 37.5 and Figure 37.14. Broadening of the mode structure may be a consequence of the very low number of reflections undertaken by coupled light before escaping to the substrate. Coupling of external light through a truncated facet (Figure 37.5b) gives the best result for a coupling angle $\gamma \sim 20°$, as expected (Figure 37.11, upper curves). In this configuration, the narrow and polarization-split peaks at an output angle $\alpha \sim 2°$ are detected. The peaks are, however, not transmission but absorption peaks. This can be understood if it is assumed that the detected light comes not from substrate modes (which represent a small portion of transmitted light) but from filtered transmitted light propagating almost parallel to the Si-nc waveguide from which a part of power escaped to the substrate modes which were subsequently absorbed in the waveguide core. The blue third order modes are much stronger compared to second order because of higher absorption in the blue spectral region.

Experimental observation of rib waveguides indicates (Figure 37.12) that normal guiding of light is improved—see increased intensity of the long-wave edge of PL spectra in Figure 37.12a and b. This is due to the introduction of confinement in the second lateral direction of waveguide (in this case the confining refractive index profile is symmetrical and the contrast higher (compared to the implanted layer profile) as the surrounding medium is air). On the other hand, roughness of

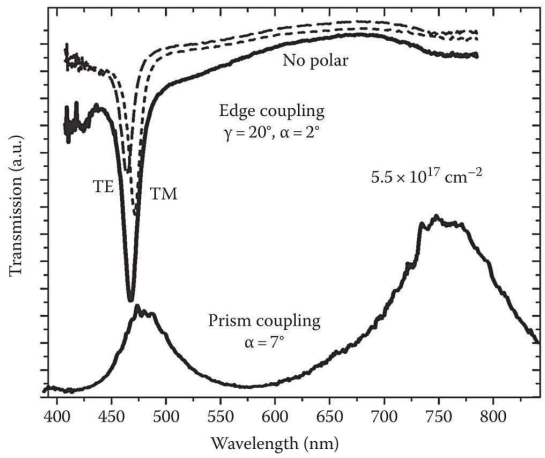

FIGURE 37.11 Comparison of transmission spectra of a sample 5.5×10^{17} cm^{-2} obtained by the direct facet-coupling (upper curves, solid line—no polarization, dashed and dotted lines correspond to TE and TM polarization, respectively) and by the prism coupling (lower spectrum). (Adapted from Janda, P. et al., *J. Lumin.*, 121, 267, 2006.)

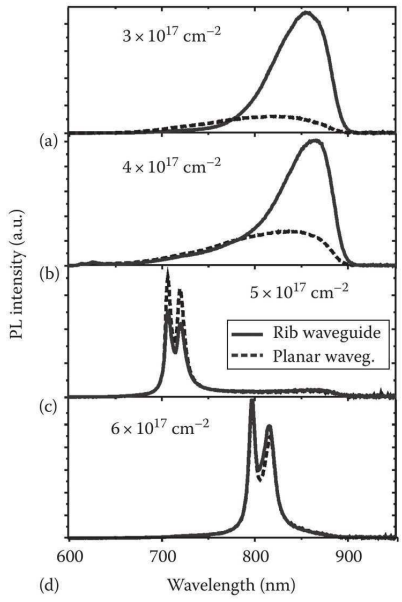

FIGURE 37.12 Comparison of the edge PL spectra from planar and rib waveguides (dashed and continuous line, respectively) in samples implanted to a fluence of (a) 3×10^{17} cm^{-2}, (b) 4×10^{17} cm^{-2}, (c) 5×10^{17} cm^{-2}, and (d) 6×10^{17} cm^{-2}.

the rib edges can introduce significant losses due to scattering. The influence of rib structure on the substrate (leaky) modes is less significant (see Figure 37.12c and d). This is because these modes propagate mostly in substrate, where the effect of side walls is negligible.

37.5 Theoretical Description of Active Lossy Waveguides

Light coupling to a waveguide and its further propagation may be understood in terms of coupling between the waveguide modes and nanocrystals emitting photons. Light field inside the waveguide may be expressed as a coherent superposition of excited waveguide modes, which arise as a solution of a homogeneous wave equation with proper boundary conditions [the waveguide modes are an orthonormal basis of the waveguide optical field (Snyder and Love 1983)]. It is therefore necessary to distinguish between various types of the waveguide modes in order to explain different types of energy transport in the waveguides.

Let us consider a common model structure with three transparent layers (see Figure 37.13): the top *cladding* layer with the refractive index n_1, the bottom *substrate* with the refractive index n_3 and the *core* with the refractive index $n_2 > n_3 > n_1$ and thickness d. We may imagine the modes as rays emerging from inside the waveguide core propagating toward one of the core boundaries. At the boundary, the ray may be either totally reflected back to the core or it may be partially reflected and partially refracted. The ray then travels toward the other boundary where it totally or partially reflects again. Only these modes which are totally reflected twice during one round-trip may propagate in the core without losses: these are the common *guided modes*. There are, in addition, lossy modes which are called the *substrate radiation modes* (they are refracted only into the substrate) and the *radiation modes* refracted both to the substrate and the cladding.

In many applications, considering traveling of light at large distances compared to its wavelength (and thus working in the far-field limit), we may consider only the guided modes as efficient carriers of energy between a source and a detector. In silicon-based nanophotonics devices, however, the situation may be even more complicated. The typical distances between components on a chip may be comparable to the light wavelength and the far-field approach fails. It is therefore important to analyze an influence of the substrate radiation modes on the response. We may rule out the radiation modes at this stage: compared to the substrate modes, they play only a negligible role in the overall system behavior.

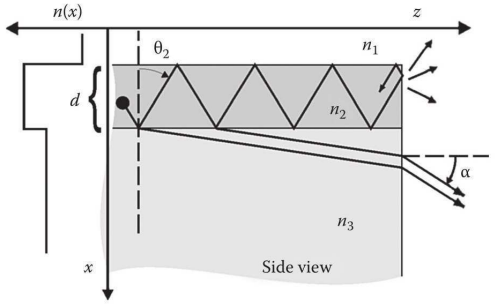

FIGURE 37.13 Schematic representation of propagation and decoupling of substrate modes.

Once light is emitted by a nanocrystal inside the waveguide mode, it undergoes internal reflections at the core/cladding and the core/substrate boundaries. The overall intensity of electric field of an excited mode inside the waveguide core may be written as superposition of the partial waves:

$$E_{\text{mode}}(\lambda,\theta_2) = E_0(\lambda)\left(1 + r_{21}r_{23}\exp\left[\frac{4\pi i n_2 d\cos(\theta_2)}{\lambda}\right] + \cdots\right)$$
$$= \frac{E_0(\lambda)}{1 - r_{21}r_{23}\exp[4\pi i n_2 d\cos(\theta_2)/\lambda]}. \quad (37.2)$$

Here, r_{21} and r_{23} are the reflection coefficients at the respective boundaries which depend upon the propagation angle θ_2. The wavelength is λ and $E_0(\lambda)$ is an effective emission amplitude of a nanocrystal to the waveguide mode. Considering the guided modes and thus $|r_{21}| = |r_{23}| = 1$, the electric field intensity reveals sharp resonances implying there are well-defined discrete guided modes. The energy carried by each mode is finite, indeed. Unlike the guided modes, the electric field intensity is finite for the substrate modes and there are no sharp resonances in the spectra. We may, however, resolve some weak resonances, depending on the phase factor of the term $r_{21}r_{23}\exp[4\pi i n_2 d\cos(\theta_2)/\lambda]$: the electric field is maximum if this term is positive and real.

It is clear from the ray optics that there are substrate modes which refract to the substrate at the angles near $\pi/2$ which means that they propagate nearly parallel to the core/substrate boundary; these modes may be understood as a crossover between the guided modes and the substrate radiation modes which decouple rapidly from the core, possessing mixed characteristics of the both types of modes. As the modes may be assigned to a distinct guided mode of the nth order (energy of the substrate mode is slightly below the cutoff energy of the nth guided mode), we denote each series of the substrate modes to be of the nth order (see Figure 37.14). The Fresnel formulae give us $|r_{21}| = 1$ and $|r_{23}| \approx 1$ in such a case (Figure 37.15) and it is then clear from Equation 37.2 that these substrate modes reveal sharp resonances in the spectra (for a fixed angle $\theta_2 < \arcsin(n_2/n_3)$). Energy carried by the substrate modes may be therefore comparable to the energy carried by guided modes. The most important point here is that this type of substrate modes cannot be experimentally distinguished from the guided modes at short distances from the source as they propagate near the core/substrate boundary. The substrate modes therefore significantly contribute to the system response and they may play an important role in many experiments as well as in real on-a-chip devices.

Although the guided and the substrate modes propagate in a similar direction, they may behave in very different ways because they propagate in two different environments. In our particular case, the guided modes are mostly localized inside the waveguide core doped by Si-nc providing a possibility of reabsorption or optical amplification. The substrate modes, on the contrary, propagate in a transparent substrate and they are therefore neither amplified nor attenuated. Rigorous derivation of PL spectra in real waveguides accounting for losses or

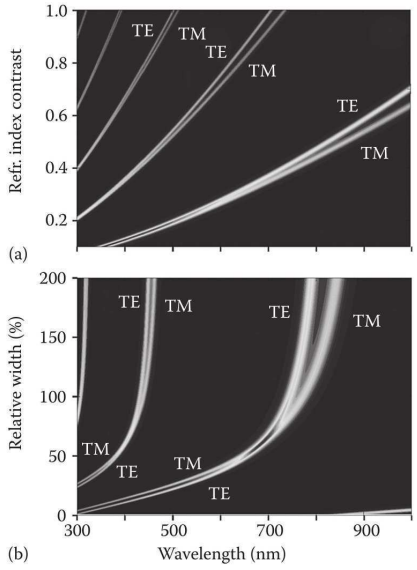

FIGURE 37.14 Calculated spectral positions of the substrate modes as a function of (a) the refractive index contrast $\Delta n = n_2 - n_3$ and (b) the relative thickness of the waveguide core compared to the sample 5×10^{17} Si cm^{-2}. Color scale indicates intensity increasing from deep blue up to red for the highest intensity. Several orders of modes are seen starting from the first one in infrared region.

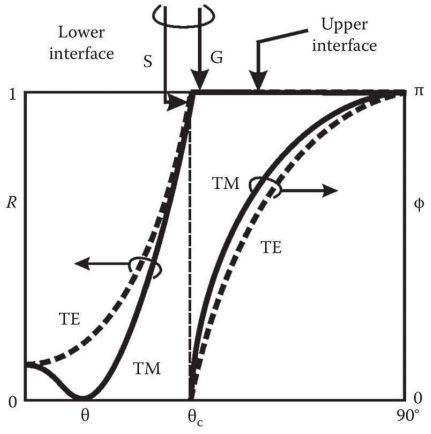

FIGURE 37.15 Reflectance $R = |r_{ij}|^2$ and phase shifts ϕ on the planar boundary between two dielectric media plotted for TE and TM modes versus incident angle θ. S and G stand for substrate and guided modes, respectively. (Adapted from Pelant, I. et al., *Appl. Phys. B*, 83, 87, 2006.)

amplification, decoupling of the light from the waveguide and real detection geometry is presented elsewhere (Ostatnický et al. 2008); here we summarize only the main results.

Considering lossy waveguide core, the substrate modes become dominant in the optical response of a waveguide when detected in the direction parallel to the core/substrate boundary

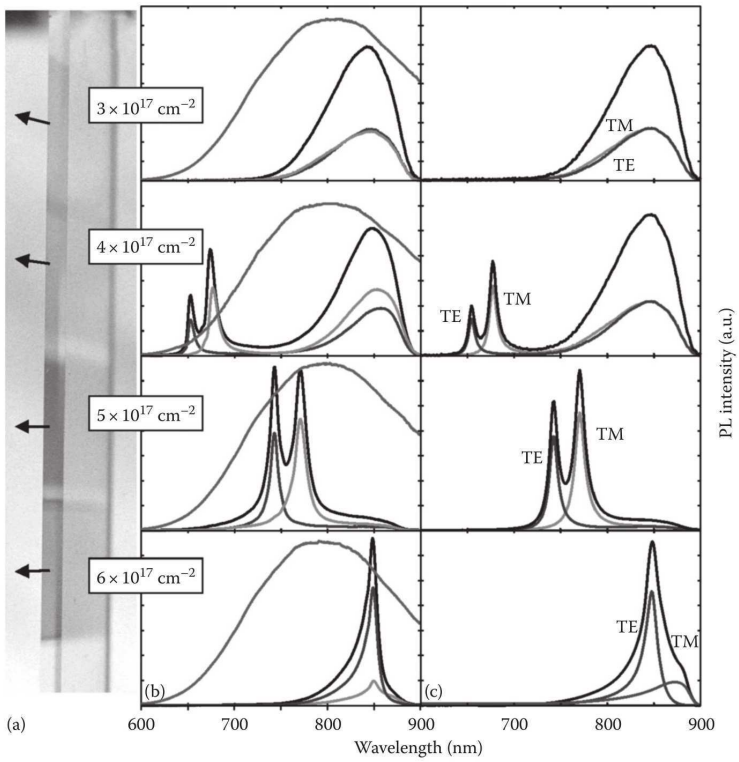

FIGURE 37.16 (a) Photograph of the edge of a set of Si^+ ion implanted layers with direction of PL indicated by arrows, the edge is on the left. (b) Measured PL from samples implanted to different Si ion fluences in standard (blue lines) and waveguiding geometry (black lines, the red and green lines stand for TE and TM resolved polarizations). (c) Theoretically calculated PL spectra. We note that these results were obtained on different set of samples than in Figure 37.10. The mode positions are not exactly the same for samples with identical implantation dose because the annealing conditions were slightly different. Therefore the refractive index profiles are not identical. (Adapted from Pelant, I. et al., *Appl. Phys. B*, 83, 87, 2006.)

using a detector with a small numerical aperture. This situation is clearly illustrated through the comparison of our experimental data with the theoretical estimates in Figure 37.16 (we considered a continuous refractive index profile in our calculations). The broad part of the emission spectra originates from the (attenuated) guided modes and the narrow peaks are due to the substrate modes. The double-peak structure is further resolved as two single peaks with the respective TE and TM polarizations. In order to explain this point, we should remark that the coefficient r_{23} is real for the substrate modes while the coefficient r_{21} is in general complex. Considering a fixed angle of incidence θ_2, r_{21} gives different values of the phase shift for the respective TE and TM polarizations (see Figures 37.14 and 37.15). Therefore, the resonance condition is met at different wavelengths for different polarizations. From these considerations, the necessity of waveguide asymmetry for the appearance of the TE–TM polarization–resolved modes follows.

The TE–TM splitting was also reported in Khriachtchev et al. (2004) but the respective peaks have an opposite order in the spectra compared to our experiments. Our numerical calculations have shown that the TE–TM splitting depends strongly on the refractive index profile of the waveguide core. For the three-layer structures, the TE mode is positioned always at the high-energy side of the PL spectra. It is, nevertheless, possible to fabricate a structure with multiple layers or with a graded refractive index profile, which provides an arbitrary TE–TM splitting (including both negative and positive values and also their degeneracy); this feature is well illustrated in Figure 37.14b where the respective TE and TM modes interchange depending on the thickness of the guiding layer.

The appearance of the substrate modes is well controllable by the parameters of the particular layers of the waveguide. Clearly, the optical thickness of the core d determines the resonance condition through the exponent in the denominator in Equation 37.2 and the ratio n_2/n_1 has influence on the phase of the r_{21} term. The latter may be used in detectors integrated on a chip—the cladding can be made of a material which changes its refractive index due to the changes of the surrounding environment conditions and the position of the emission peak then may

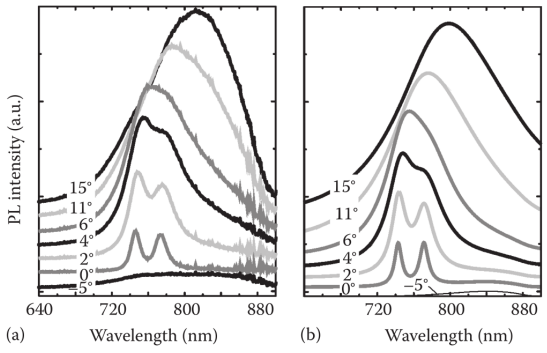

FIGURE 37.17 (a) Measured PL spectra at different detection angles α relative to the waveguide axis. (b) Numerical simulation of the measurements from the panel a. The sample with an implantation fluence of 5×10^{17} cm^{-2}. (Adapted from Ostatnický, T. et al., Guiding and amplification of light due to silicon nanocrystals embedded in waveguides, in Khriachtchev, L. (ed), *Silicon Nanophotonics*, World Scientific, Singapore, 2008, 267–296.)

be correlated with some external variable (temperature, pH, etc., see Figure 37.20) (Luterová et al. 2006).

As the sharp resonance in the spectra of the substrate modes is restricted only to the region where $r_{23} \approx 1$, we may expect disappearance of the substrate modes at large detection angles, i.e., when the substrate modes do not propagate parallel to the core/substrate boundary. This feature is illustrated in Figure 37.17 in comparison to the experimental and the theoretical data. We see a very good agreement justifying the correctness of our model.

An important aspect of nanodevices is the magnitude of the decoupling length for the substrate modes, i.e., the distance at which the substrate modes completely leak out from the waveguide core. Our calculations (Ostatnický et al. 2008) show that this distance may be few micrometers but also it may be as large as several hundreds of micrometers. As a consequence, the appearance of the substrate modes and their decoupling from the waveguide core may be of a big importance in nanodevices on the contrary to the fiber optics where the optical response to any excitation is provided solely by the guided modes at the typical distances of the order from meters to kilometers.

37.6 Application of Active Nanocrystalline Waveguides

37.6.1 Amplification of Light

The significant narrowing of substrate leaky mode emission suggests immediately that optical amplification could be responsible for this observation. The VSL method (described in Section 37.3.3) has been applied to the planar asymmetric Si-nc waveguides in several laboratories (Khriachtchev et al. 2001, Ivanda et al. 2003, Luterová et al. 2005). It is tempting to interpret the frequently observed initial weak exponential growth of the VSL curve (Figure 37.18a) as a manifestation of

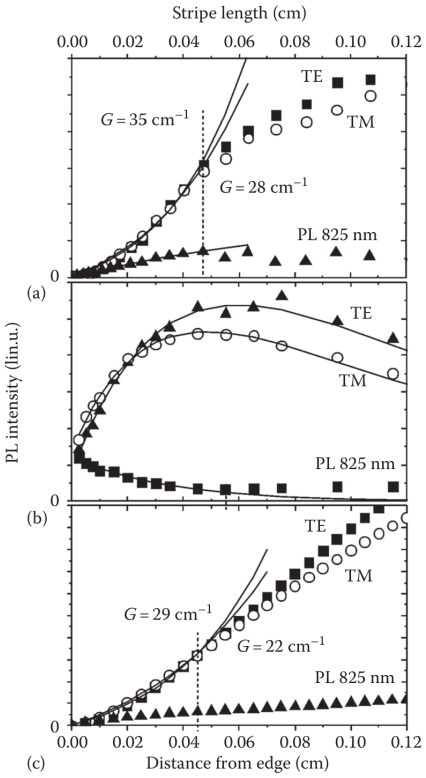

FIGURE 37.18 VSL and SES measurements on a sample implanted to the dose of 4×10^{17} cm^{-2} under continuous wave excitation 325 nm, 0.26 W/cm^2: (a) VSL measurement at the peak of TE and TM modes and for non-guided PL around 825 nm. The fits (lines) give values of $G = 35$ and 28 cm^{-1} for TE and TM modes, respectively, and losses of 11 cm^{-1} for non-guided PL. (b) Results of the SES measurement performed under identical conditions as the VSL. (c) Integration of data from panel (b). The gain fits (lines) give values of $G = 29$ and 22 cm^{-1} for TE and TM modes, respectively. (Adapted from Valenta, J. et al., *Appl. Phys. Lett.*, 81, 1396, 2002.)

the occurrence of optical gain. High output directionality of the substrate mode emission apparently supports such interpretation. However, it has turned out that, as shown above, it is very difficult if not impossible to evaluate correctly the optical gain magnitude of the substrate modes, because the nonlinear growth can originate in the mode leaking itself. Figure 37.18 demonstrates that the evaluation of the VSL experiments can yield a false optical gain if proper comparison between the VSL and SES results is not taken into account. On the other hand, VSL measurements employing a high pulsed laser excitation, performed on a similar sample, revealed a characteristic switch from the light attenuation ($G < 0$) to amplification ($G > 0$) with increasing excitation energy density (Figure 37.19). It may be also of interest here to call the reader's attention to recent articles reporting firmly positive optical gain on leaky

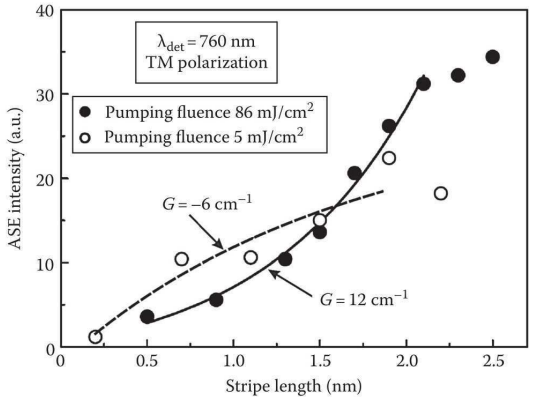

FIGURE 37.19 Time-resolved VSL measurement of optical amplification at position of the TM mode (760 nm) under pumping by 6 ns pulses, 355 nm. The fit with Equation 37.1 gives the net gain coefficient of (–6 ± 6) and (12 ± 2) cm^{-1}, for pumping fluence of 5 and 86 mJ/cm^2, respectively. The threshold for positive gain is about 50 mJ/cm^2. Sample was implanted to a dose of 4×10^{17} cm^{-2}. (After Luterova, K. et al., *Phys. Status Solidi (c)*, 2, 3429, 2005.)

substrate modes in asymmetric thin-film organic waveguides (Nakanotani et al. 2007, Yokoyama et al. 2008).

At present, checking the reliability of the VSL method in the case of active asymmetric thin waveguides represents an issue requiring further investigation.

37.6.2 Other Applications

Although the benefit of the waveguide spectral filtering for nanocrystalline thin-film laser design is still controversial, the substrate modes may be attractive for other nanophotonic applications. Firstly, they provide a way how to *generate easily the spectrally narrow, polarization resolved and directional emission* in the wavelength range 650–950 nm without the necessity of building optical (micro)cavities. Moreover, this emission can be spectrally tuned simply by engineering the silicon excess content, as shown in Figures 37.10 and 37.16. Potential feasibility of these properties for *demultiplexing optical signal in photonic circuits* is evident, but improvement in quality of the rib waveguides is anticipated.

Secondly, spectral sensitivity of the radiative substrate modes to surrounding (organic) compounds can be utilized in *photonic sensing* (Figure 37.20): Magnitude of the refractive index

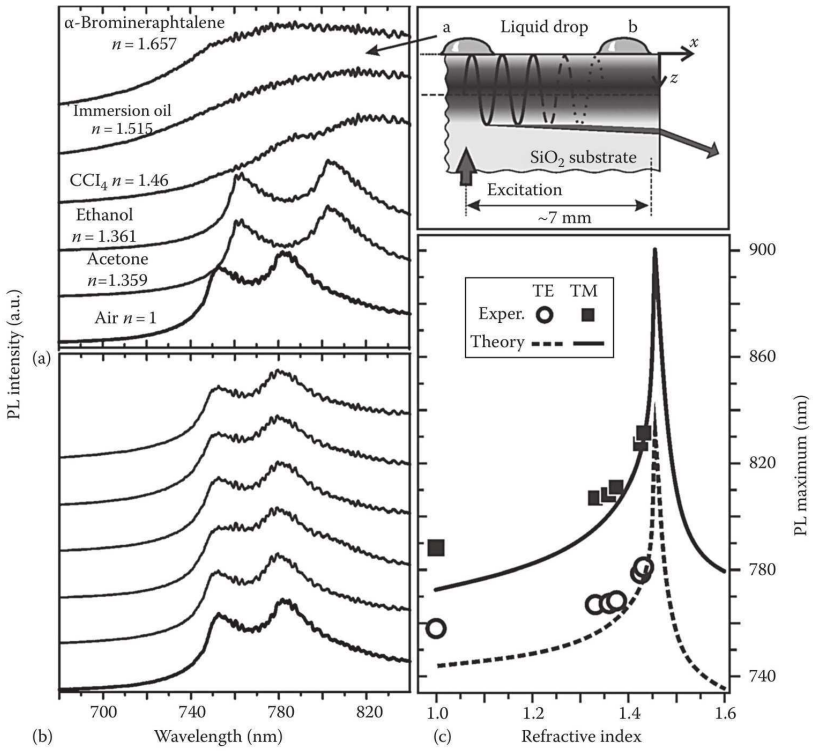

FIGURE 37.20 The influence of a drop of liquid on the PL spectra: (a) the drop is on the excited spot and (b) the drop is out of excited spot (between the spot and the sample edge). (c) Comparison of experimental (points) and calculated (line) positions of PL maxima for different refractive indices of liquid drops. Sample is implanted to a dose of 5×10^{17} cm^{-2}. (Adapted from Pelant, I. et al., *Appl. Phys. B*, 83, 87, 2006; Luterová et al., 2007.)

n_1 of the compound (playing role of the cladding layer) affects markedly the spectral position of the TE–TM doublet. When n_1 exceeds the magnitude of the core refractive index ($n_2 \approx 1.45$), the condition of total reflection $|r_{21}| = 1$ is canceled and the TE–TM doublet completely disappears. A more systematic research in this direction is, however, missing.

Finally, the *active waveguides* give the chance to circumvent the *coupling problem* connected with discrete photonic elements, i.e., the problem of how to inject efficiently light from an external source in a waveguide (Orobtchouk 2006). The *active waveguides eliminate the need of any optical couplers* and enable it to design integrated photonic circuits. Theoretical analysis of active Si-nc devices integrating optical emission and waveguiding, compatible with silicon VLSI processing technology, have been submitted quite recently (Milgram et al. 2007, Redding et al. 2008).

37.7 Conclusions

Active waveguides formed by densely packed silicon nanocrystals represent a promising type of nanophotonic waveguides. In contrast to other types of nanowaveguides (based on photonic waveguides, plasmonic structures, etc.), it can be prepared by various technological approaches available and well mastered in many research and industrial laboratories. Its potential applications range from optical amplifiers and filters to optical sensors. The descriptions of characterization techniques and theory of waveguide modes in this chapter are applicable to many other waveguide structures.

Acknowledgments

This work was supported by the Czech Ministry of Education, Youth and Sports through the research center LC510 and research plans MSM0021620835 and 60840770022, the project 202/07/0818 of the Grant Agency of the Czech Republic, and the projects IAA101120804 and KAN401220801 of the Grant Agency of the Academy of Sciences. Research carried out in the Institute of Physics was supported by the Institutional Research Plan AV0Z10100521. The authors thank Prof. R.G. Elliman (Australian National University, Canberra) and Ing. V. Jurka for the fabrication of waveguides.

References

Cheylan, S. and Elliman, R. G. 2001. Effect of hydrogen on the photoluminescence of Si nanocrystals embedded in a SiO_2 matrix. *Applied Physics Letters* 78: 1225–1227.

Cheylan, S., Langford, N., and Elliman, R. G. 2000. The effect of ion-irradiation and annealing on the luminescence of Si nanocrystals in SiO_2. *Nuclear Instruments and Methods in Physical Research: Section B* 166–167: 851–856.

Dal Negro, L., Bettotti, P., Cazzanelli, M., Pacifici, D., and Pavesi, L. 2004. Applicability conditions and experimental analysis of the variable stripe length method for gain measurements. *Optics Communications* 229: 337–348.

Iacona, F., Franzò, G., and Spinella, C. 2000. Correlation between luminescence and structural properties of Si nanocrystals. *Journal of Applied Physics* 87: 1295–1303.

Imakita, K., Fujii, M., Yamaguchi, Y., and Hayashi, S. 2005. Interaction between Er ions and shallow impurities in Si nanocrystals. *Physical Review B* 71: 115440-1–115440-7.

Ivanda, M., Desnica, U. V., White, C. W., and Kiefer, W. 2003. Experimental observation of optical amplification in silicon nanocrystals. In L. Pavesi, S. Gaponenko, and L. Dal Negro (Eds.), *Towards the First Silicon Laser*, NATO Science Series, II: Mathematics, Physics and Chemistry, Vol. 93, pp. 191–96. Dordrecht, the Netherlands: Kluwer Academic Publishers.

Janda, P., Valenta, J., Ostatnický, T., Skopalová, E., Pelant, I., Elliman, R. G., and Tomasiunas, R. 2006. Nanocrystalline silicon waveguides for nanophotonics. *Journal of Luminescence* 121: 267–273.

Khriachtchev, L., Räsänen, M., Novikov, S., and Sinkkonen, J. 2001. Optical gain in Si/SiO_2 lattice: Experimental evidence with nanosecond pulses. *Applied Physics Letters* 79: 1249–1251.

Khriachtchev, L., Novikov, S., and Lahtinen, J. 2002. Thermal annealing of Si/SiO_2 materials: Modification of structural and photoluminescence emission properties. *Journal of Applied Physics* 92: 5856–5862.

Khriachtchev, L., Räsänen, M., Novikov, S., and Lahtinen, J. 2004. Tunable wavelength-selective waveguiding of photoluminescence in Si-rich silica wedges. *Journal of Applied Physics* 95: 7592–7601.

Khriachtchev, L., Navarro-Urios, D., Pavesi, L., Oton, C. J., Capuj, N. E., and Novikov, S. 2007. Spectroscopy of silica layers containing Si nanocrystals: Experimental evidence of optical birefringence. *Journal of Applied Physics* 101: 044310-1–044310-6.

Luterová, K., Dohnalová, K., Švrček, V., Pelant, I., Likforman, J.-P., Crégut, O., Gilliot, P., and Hönerlage, B. 2004. Optical gain in porous silicon grains embedded in sol-gel derived SiO_2 matrix under femtosecond excitation. *Applied Physics Letter* 84: 3280–3282.

Luterová, K., Navarro, D., Cazzanelli, M., Ostatnicky, T., Valenta, J., Cheylan, S., Pelant, I., and Pavesi, L. 2005. Stimulated emission in the active planar optical waveguide made of silicon nanocrystals. *Physica Status Solidi (c)* 2: 3429–3434.

Luterová, K., Skopalová, E., Pelant, I., Rejman, M., Ostatnický, T., and Valenta, J. 2006. Active planar optical waveguides with silicon nanocrystals: Leaky modes under different ambient conditions. *Journal of Applied Physics* 100: 074307.

Milgram, J. N., Wojcik, P., Mascher, P., and Knights, A. P. 2007. Optically pumped Si nanocrystal emitter integrated with low loss silicon nitride waveguides. *Optics Express* 15: 14679–14788.

Nakanotani, H., Adachi, C., Watanabe, S., and Katoh, R. 2007. Spectrally narrow emission from organic films under continuous-wave excitation. *Applied Physics Letters* 90: 231109-1–231109-3.

Orobtchouk, R. 2006. In L. Pavesi and G. Guillot (Eds.), *Optical Interconnects. The Silicon Approach*, pp. 263–290. Berlin, Germany: Springer-Verlag.

Ostatnický, T., Rejman, M., Valenta, J., Herynková, K., and Pelant, I. 2008. Guiding and amplification of light due to silicon nanocrystals embedded in waveguides. In L. Khriachtchev (Ed.), *Silicon Nanophotonics*, pp. 267–296. Singapore: World Scientific.

Park, J. H. and Steckl, A. J. 2004. Laser action in Eu-doped GaN thin-film cavity at room temperature. *Applied Physics Letters* 85: 4588–4590.

Pavesi, L. and Guillot, G. (Eds.). 2006. *Optical Interconnects. The Silicon Approach*. Berlin, Germany: Springer-Verlag.

Pavesi, L. and Lockwood, D. J. (Eds.). 2004. *Silicon Photonics*. Berlin, Germany: Springer-Verlag.

Pelant, I., Ostatnický, T., Valenta, J., Luterova, K., Skopalova, E., Mates, T., and Elliman, R. G. 2006. Waveguides cores containing silicon nanocrystals as active spectral filters for silicon-based photonics. *Applied Physics B* 83: 87–91.

Pellegrino, P., Garrido, B., Garcia, C., Arbiol, J., Morante, J. R., Melchiorri, M., Daldosso, N., Pavesi, L., Schedi, E., and Sarrabayrouse, G. 2005. Low-loss rib waveguides containing Si nanocrystals embedded in SiO2. *Journal of Applied Physics* 97: 074312-1–074312-8.

Redding, B., Shi, S., Creazzo, T., and Prather, D. W. 2008. Electromagnetic modeling of active silicon nanocrystal waveguides. *Optics Express* 16: 8792–8799.

Riboli, F., Navarro-Urios, D., Chiasera A., Daldosso, N., Pavesi, L., Oton, C. J., Heitmann, J., Yi, L. X., Scholz, R., and Zacharias, M. 2004. Birefringence in optical waveguides made by silicon nanocrystal superlattices. *Applied Physics Letter* 85: 1268–1270.

Shaklee, K. L. and Leheny, R. F. 1971. Direct determination of optical gain in semiconductor crystals. *Applied Physics Letters* 18: 475–477.

Skopalová, E. 2007. Mode structure in the light emission from planar waveguides with silicon nanocrystals. Diploma thesis. Prague, Czech Republic: Charles University.

Snyder, A. W. and Love, J. D. 1983. *Optical Waveguide Theory*. London, U.K.: Chapman & Hall.

Valenta, J., Pelant, I., and Linnros, J. 2002. Waveguiding effects in the measurement of optical gain in a layer of Si nanocrystals. *Applied Physics Letters* 81: 1396–1398.

Valenta, J., Pelant, I., Luterová, K., Tomasiunas, R., Cheylan, S., Elliman, R., Linnros, J., and Honerlage, B. 2003a. Active planar optical waveguide made from luminescent silicon nanocrystals. *Applied Physics Letters* 82: 955–957.

Valenta, J., Luterová, K., Tomašiunas, R., Dohnalová, K., Hőnerlage, B., and Pelant, I. 2003b. Optical gain measurements with variable stripe length technique. In L. Pavesi, S. Gaponenko, and L. Dal Negro (Eds.), *Towards the First Silicon Laser*, NATO Science Series, II: Mathematics, Physics and Chemistry, Vol. 93, pp. 223–242. Dordrecht, the Netherlands: Kluwer Academic Publishers.

Valenta, J., Ostatnický, T., Pelant, I., Elliman, R. G., Linnros, J., and Hőnerlage, B. 2004. Microcavity-like leaky mode emission from a planar optical waveguide made of luminescent silicon nanocrystals. *Journal of Applied Physics* 96: 5222–5225.

Yokoyama, D., Moriwake, M., and Adachi, C. 2008. Spectrally narrow emissions from edges of optically and electrically pumped anisotropic organic films. *Journal of Applied Physics* 103: 123104-1–123104-13.

JOURNAL OF APPLIED PHYSICS **98**, 113516 (2005)

The spin structure of excitons and biexcitons in semiconductor quantum wells

T. Ostatnický[a)]
Groupe d'Optique Nonlinéaire et d'Optoéléctronique, Institut de Physique et Chimie des Matériaux de Strasbourg (IPCMS), Unité Mixte de Recherche (UMR) 7504, Centre National de la Recherche Scientifique-Université Louis Pasteur (CNRS-ULP), 23 rue du Loess, B.P. 43, 67034 Strasbourg Cedex 2, France and Faculty of Mathematics and Physics, Charles University in Prague, Ke Karlovu 3, 12116 Prague 2, Czech Republic

P. Gilliot and B. Hönerlage
Groupe d'Optique Nonlinéaire et d'Optoéléctronique, Institut de Physique et Chimie des Matériaux de Strasbourg (IPCMS), Unité Mixte de Recherche (UMR) 7504, Centre National de la Recherche Scientifique-Université Louis Pasteur (CNRS-ULP), 23 rue du Loess, B.P. 43, 67034 Strasbourg Cedex 2, France

(Received 9 March 2005; accepted 12 October 2005; published online 9 December 2005)

We report on symmetry-based calculations of the spin structure of excitons and biexcitons in quantum wells. Depending on the point-group symmetry of the material and the growth directions of the quantum wells, we derive Hamiltonians appropriate for the description of excitons and biexcitons. We show possible paths of coherent spin-flip processes of a particle and their consequences for experimental observations. © *2005 American Institute of Physics*.
[DOI: 10.1063/1.2133901]

I. INTRODUCTION

The spin in semiconductors has been studied extensively in the last few years. In experiments, one usually employs optical excitation and detection because of the strong coupling of the optical field to electron-hole pairs. There are many experimental techniques for the observation of the spin evolution. We focus here on four-wave mixing (FWM) because of its sensitivity to the coherent evolution of the system.

We consider that the system is composed of excitons and biexcitons in their ground states. Spin-orbit coupling and electron-hole exchange cause coherent evolution of the exciton and biexciton spins after their creation by a polarized optical field (symmetry of the electron-hole exchange interaction is determined by the symmetry of the crystal lattice). These changes of spin may occur as rotations of the mean spin analogous to the behavior in a magnetic field. Processes, which do not affect the particle's spin but destroy its coherence (e.g., various scattering processes), then may cause spin relaxation. Crystal symmetry also determines the symmetry of the biexciton states which can be observed experimentally.[1,2] It is clear that the knowledge of the exciton and biexciton symmetries is essential when dealing with phenomena of optical orientation connected with excitons and biexcitons.

Symmetry of excitons and their molecules was extensively studied both theoretically and experimentally[3–7] in bulk semiconductors but only rarely in quantum wells (QWs).[8,9] A systematic study for quantum wells is, however, missing. We report on the theoretical derivation of coupling of exciton subbands in a QW with zinc-blende and wurtzite structure of the lattice, grown in various crystallographic directions.

Based on symmetry considerations, we calculate the symmetrized wave functions of excitons and biexcitons in semiconductor quantum wells. Then we derive the Hamiltonian for the symmetrized excitons and biexcitons using the method of invariants[7,10] for particles at the Γ point. At the end of the paper, we show possible consequences of the derived results.

One can find similar calculations in Ref. 11 for static stress which reduces the symmetry of a bulk crystal in the same manner as the one-dimensional quantum confinement. Since the stress can be understood as a perturbation, the exchange interactions are not strong enough to significantly influence, e.g., biexciton wave functions. Quantum confinement causes much stronger interactions such that perturbational approach fails and exact calculations of symmetrized wave functions are needed.

II. ZINC-BLENDE IN THE [001] DIRECTION

In the following situations, we consider the materials which have the zinc-blende crystal structure (point-group symmetry T_d). The twofold degenerate conduction band has Γ_6 symmetry and the fourfold degenerate valence band has Γ_8 symmetry. The split-off band with Γ_7 symmetry is neglected since the spin-orbit interaction is usually strong with respect to the interactions considered here and therefore the valence bands do not mix. The growth axis (axis perpendicular to the plane of the QW) is considered in this section to be parallel to the z crystallographic axis. The point-group symmetry of such well is D_{2d}.[9] Using Ref. 12, we find that the

[a)]Author to whom correspondence should be addressed; electronic mail: osty@matfyz.cz

symmetry of the heavy-hole (hh) band is Γ_6 and the symmetry of the light-hole (lh) band is Γ_7. The symmetrized wave functions are then

$$\left.\begin{aligned}\Gamma_6:\quad \Phi_1 &= |-1\rangle\beta = \left|\tfrac{3}{2}-\tfrac{3}{2}\right\rangle,\\ \Phi_2 &= |1\rangle\alpha = \left|\tfrac{3}{2}+\tfrac{3}{2}\right\rangle,\end{aligned}\right\}\text{hh}$$

$$\left.\begin{aligned}\Gamma_7:\quad \Phi_3 &= \tfrac{1}{\sqrt{3}}[|-1\rangle\alpha+\sqrt{2}|0\rangle\beta] = \left|\tfrac{3}{2}-\tfrac{1}{2}\right\rangle,\\ \Phi_4 &= \tfrac{1}{\sqrt{3}}[|1\rangle\beta+\sqrt{2}|0\rangle\alpha] = \left|\tfrac{3}{2}+\tfrac{1}{2}\right\rangle.\end{aligned}\right\}\text{lh} \qquad (1)$$

These wave functions are equal to those given in Ref. 5 for bulk material except for a different numbering of the states. The conduction band has Γ_6 symmetry and one finds that the symmetries of excitons are $\Gamma_6\otimes(\Gamma_6\oplus\Gamma_7)=\Gamma_1\oplus\Gamma_2\oplus\Gamma_3\oplus\Gamma_4\oplus2\Gamma_5$. The symmetrized exciton wave functions Ψ are listed below:

$$\begin{aligned}
&\Gamma_1{:}\Psi_1 = \tfrac{1}{\sqrt{2}}[\Phi_2\alpha-\Phi_1\beta],\\
&\Gamma_2{:}\Psi_2^{(z)} = -(i/\sqrt{2})[\Phi_2\alpha+\Phi_1\beta],\\
&\Gamma_3{:}\Psi_3 = \tfrac{1}{\sqrt{2}}[\Phi_3\alpha-\Phi_4\beta],\\
&\Gamma_4{:}\Psi_4^{(z)} = -(i/\sqrt{2})[\Phi_3\alpha+\Phi_4\beta],\\
&\Gamma_5{:}\Psi_5^{(x)} = \tfrac{1}{\sqrt{2}}[\Phi_1\alpha+\Phi_2\beta],\\
&\qquad\Psi_6^{(y)} = (i/\sqrt{2})[\Phi_1\alpha-\Phi_2\beta],\\
&\qquad\Psi_7^{(x)} = \tfrac{1}{\sqrt{2}}[\Phi_4\alpha+\Phi_3\beta],\\
&\qquad\Psi_8^{(y)} = -(i\sqrt{2})[\Phi_4\alpha-\Phi_3\beta].
\end{aligned} \qquad (2)$$

The symbols in parentheses in superscripts of Ψ denote the spin projection to the coordinate system of the quantum well. The hh excitons have indices 1, 2, 5 and 6, the others are lh excitons. Symmetries of biexcitons are given by the formula[7]

$$\begin{aligned}&\Gamma_1^{++}\otimes[\Gamma_6\otimes\Gamma_6]_-\otimes[(\Gamma_6\oplus\Gamma_7)\otimes(\Gamma_6\oplus\Gamma_7)]_-\\ &\quad=2\Gamma_1\oplus\Gamma_3\oplus\Gamma_4\oplus\Gamma_5,\end{aligned} \qquad (3)$$

where $[A_1\otimes A_2]_-$ denotes the antisymmetric part of a direct product of representations A_1 and A_2. Using the same method as presented in Ref. 7, we construct two-hole wave functions with appropriate symmetry properties (antisymmetric with respect to exchange of the two holes and symmetric with respect to the crystallographic axes). We multiply these wave functions by the electron part of the wave function which has the form $\alpha^{(1)}\beta^{(3)}-\beta^{(1)}\alpha^{(3)}$ and then we project the result on a basis of two-exciton states. The numbers in superscript distinguish here between two different electrons. The calculated biexciton wave functions are

$$\begin{aligned}
\Gamma_1{:}\Psi_1^{\mathrm{BX}} &= -\tfrac{1}{2\sqrt{2}}[\Psi_1^A\Psi_1^B+\Psi_2^A\Psi_2^B+\Psi_5^A\Psi_5^B+\Psi_6^A\Psi_6^B+P_{AB}],\\
\Psi_2^{\mathrm{BX}} &= -\tfrac{1}{2\sqrt{2}}[\Psi_3^A\Psi_3^B+\Psi_4^A\Psi_4^B+\Psi_7^A\Psi_7^B+\Psi_8^A\Psi_8^B+P_{AB}],\\
\Gamma_3{:}\Psi_3^{\mathrm{BX}} &= \tfrac{1}{2\sqrt{2}}[\Psi_1^A\Psi_3^B+\Psi_2^A\Psi_4^B+\Psi_5^A\Psi_7^B-\Psi_6^A\Psi_8^B+P_{AB}],\\
\Gamma_4{:}\Psi_4^{\mathrm{BX}} &= -(i/2\sqrt{2})[\Psi_1^A\Psi_4^B-\Psi_2^A\Psi_3^B-\Psi_5^A\Psi_8^B-\Psi_6^A\Psi_7^B+P_{AB}],\\
\Gamma_5{:}\Psi_5^{\mathrm{BX}} &= \tfrac{1}{2\sqrt{2}}[\Psi_1^A\Psi_7^B+\Psi_2^A\Psi_8^B-\Psi_3^A\Psi_5^B+\Psi_4^A\Psi_6^B+P_{AB}],\\
\Psi_6^{\mathrm{BX}} &= -(i/2\sqrt{2})[\Psi_1^A\Psi_8^B-\Psi_2^A\Psi_7^B+\Psi_3^A\Psi_6^B+\Psi_4^A\Psi_5^B+P_{AB}].
\end{aligned} \qquad (4)$$

The letters A and B distinguish between the two contributing excitons, P_{AB} means permutation of the excitons. In these wave functions, we identify pure lh or hh biexcitons with symmetry Γ_1 which can be excited by optical fields with polarizations $\sigma^+\sigma^-$. All other biexcitons are mixed—they are composed of one lh and one hh exciton. The Γ_3 biexciton transforms like two dipole-active states $xx-yy=\sigma^+\sigma^+-\sigma^-\sigma^-$ and the Γ_4 biexciton as $xy=\sigma^+\sigma^+-\sigma^-\sigma^-$. We can conclude that one expects a signature of two mixed biexcitons when using two σ^+-polarized pulses for excitation. The Γ_5 biexcitons are not accessible by two-photon absorption (if the incident beam is perpendicular to the QW plane).

Without going into details, we present an effective exciton Hamiltonian which has the structure

$$\hat{H} = \hat{H}_e + \hat{H}_h + \hat{H}_{e\text{-}h} + \hat{H}_Q, \qquad (5)$$

where the first term stands for electron Hamiltonian, the second for the hole Hamiltonian, the third term represents the electron-hole exchange Hamiltonian, and the last term is a k-linear term. The particular terms are then expressed using the method of invariants.[7,10] The k-linear term has contributions only from the in-plane momentum, therefore we do not take it into account since we consider excitation perpendicular to the QW plane. The electron Hamiltonian is a constant, the hole Hamiltonian introduces lh-hh splitting and we thus express it as follows:

$$\hat{H}_h = \frac{\Delta_{\mathrm{lh}}}{2}\left(\hat{J}_z^2-\frac{1}{4}\right). \qquad (6)$$

The symbol $\hat{\mathbf{J}}=(\hat{J}_x,\hat{J}_y,\hat{J}_z)$ is the operator of the hole's angular momentum and we define the electron spin operator $\hat{\boldsymbol{\sigma}}=(\hat{\sigma}_x,\hat{\sigma}_y,\hat{\sigma}_z)$. The electron-hole exchange term has the form[9]

$$\hat{H}_{e\text{-}h} = \Delta_0\mathbb{I}_e\otimes\mathbb{I}_h + \Delta_{11}(\hat{\sigma}_x\hat{J}_x+\hat{\sigma}_y\hat{J}_y) + \Delta_{12}\hat{\sigma}_z\hat{J}_z + \Delta_{21}(\hat{\sigma}_x\hat{J}_x^3+\hat{\sigma}_y\hat{J}_y^3) + \Delta_{22}\hat{\sigma}_z\hat{J}_z^3 + \Delta_3[\hat{\sigma}_x\{\hat{J}_x,(\hat{J}_y^2-\hat{J}_z^2)\}+\hat{\sigma}_y\{\hat{J}_y,(\hat{J}_x^2-\hat{J}_z^2)\}], \qquad (7)$$

where $\mathbb{I}_{e,h}$ stand for identity operators on a subspace of electrons and holes, respectively. The curly braces {} stand for an anticommutator: $\{\hat{A},\hat{B}\}=\frac{1}{2}(\hat{A}\hat{B}+\hat{B}\hat{A})$. The Hamiltonian is not diagonal and therefore there exist some couplings between the states even for zero wave vector. We do not discuss these couplings here (see the discussion) and we only give the energies of the states which diagonalize the Hamiltonian:

$$
\begin{aligned}
E_{5,7(6,8)} &= \Delta_0 + \tfrac{1}{2}\Delta_{\mathrm{lh}} - \tfrac{1}{2}\Delta_{12} - \tfrac{13}{8}\Delta_{22} \pm \Big[\Big(-\tfrac{1}{2}\Delta_{\mathrm{lh}} + \Delta_{12} \\
&\quad + \tfrac{7}{4}\Delta_{22}\Big)^2 + 3\Big(\Delta_{11} + \tfrac{7}{4}\Delta_{21} - \tfrac{1}{2}\Delta_3\Big)^2\Big]^{1/2}, \\
E_{3,4} &= \Delta_0 - \tfrac{1}{2}\Delta_{12} - \tfrac{1}{8}\Delta_{22} \mp \Big(2\Delta_{11} + 5\Delta_{21} + \tfrac{3}{2}\Delta_3\Big), \qquad (8) \\
E_{1,2} &= \Delta_0 + \Delta_{\mathrm{lh}} + \tfrac{3}{2}\Delta_{12} + \tfrac{27}{8}\Delta_{22} \mp \tfrac{3}{2}(\Delta_{21} - \Delta_3).
\end{aligned}
$$

The biexciton Hamiltonian generally contains electron-electron exchange, hole-hole exchange, electron-hole exchange, and one-particle energies. In the basis of the functions defined above, all interactions of electrons cancel and thus the electron-electron and electron-hole exchanges are identically zero matrices. The hole-hole exchange Hamiltonian contains 16 terms (see Appendix). They couple both Γ_1 states (pure lh and hh biexcitons). Other than Γ_1 states are eigenstates of this Hamiltonian.

As we will discuss later, terms which have a high order in $\hat{J}_j^n$ correspond to a high order if the exchange interaction is treated in a perturbational approach. Therefore, it seems to be sufficient to consider only terms Δ_0, Δ_{lh}, Δ_{11}, and Δ_{12}. This is similar to bulk material where usually only the isotropic electron-hole exchange interaction is considered and the cubic term is neglected. The energies of the states then reduce to

$$
\begin{aligned}
E_{5,7(6,8)} &= \Delta_0 + \tfrac{1}{2}\Delta_{\mathrm{lh}} - \tfrac{1}{2}\Delta_{12} \pm \Big[\Big(-\tfrac{1}{2}\Delta_{\mathrm{lh}} + \Delta_{12}\Big)^2 + 3\Delta_{11}^2\Big]^{1/2}, \\
E_{3,4} &= \Delta_0 - \tfrac{1}{2}\Delta_{12} \mp 2\Delta_{11}, \qquad (9) \\
E_{1,2} &= \Delta_0 + \Delta_{\mathrm{lh}} + \tfrac{3}{2}\Delta_{12}.
\end{aligned}
$$

III. ZINC-BLENDE IN THE [011] DIRECTION

The point-group symmetry of such QW is C_{2v}. The conduction band has Γ_5 symmetry as well as both hole subbands. The symmetrized hole wave functions are Φ_{1-4} given in (1), the only difference is that all have Γ_5 symmetry. Excitons have symmetries $2\Gamma_5 \otimes \Gamma_5 = 2(\Gamma_1 \oplus \Gamma_2 \oplus \Gamma_3 \oplus \Gamma_4)$ and taking into account both hole subbands, symmetrized exciton wave functions are

$$
\begin{aligned}
&\Gamma_1: \Psi_1^{(z)} = -\tfrac{1}{\sqrt{2}}[\Phi_2\alpha - \Phi_1\beta], \\
&\qquad \Psi_2^{(z)} = -\tfrac{1}{\sqrt{2}}[\Phi_3\alpha - \Phi_4\beta], \\
&\Gamma_2: \Psi_3^{(x)} = \tfrac{1}{\sqrt{2}}[\Phi_1\alpha + \Phi_2\beta], \\
&\qquad \Psi_4^{(x)} = \tfrac{1}{\sqrt{2}}[\Phi_4\alpha + \Phi_3\beta], \\
&\Gamma_3: \Psi_5 = -(i/\sqrt{2})[\Phi_2\alpha + \Phi_1\beta], \\
&\qquad \Psi_6 = -(i/\sqrt{2})[\Phi_3\alpha + \Phi_4\beta], \\
&\Gamma_4: \Psi_7^{(y)} = (i/\sqrt{2})[\Phi_1\alpha - \Phi_2\beta], \\
&\qquad \Psi_8^{(y)} = (i/\sqrt{2})[\Phi_4\alpha - \Phi_3\beta].
\end{aligned} \qquad (10)
$$

Exciton states with odd indices are hh and those with even indexes are lh excitons. The wave functions are equal to the wave functions presented for the case of the [001] orientation, they differ only in symmetry and index. Biexcitons have symmetries $3\Gamma_1 \oplus \Gamma_2 \oplus \Gamma_3 \oplus \Gamma_4$:

$$
\begin{aligned}
&\Gamma_1: \Psi_1^{\mathrm{BX}} = \tfrac{1}{2\sqrt{2}}[\Psi_1^A\Psi_1^B + \Psi_3^A\Psi_3^B + \Psi_5^A\Psi_5^B + \Psi_7^A\Psi_7^B + P_{AB}], \\
&\qquad \Psi_2^{\mathrm{BX}} = \tfrac{1}{2\sqrt{2}}[\Psi_2^A\Psi_2^B + \Psi_4^A\Psi_4^B + \Psi_6^A\Psi_6^B + \Psi_8^A\Psi_8^B + P_{AB}], \\
&\qquad \Psi_3^{\mathrm{BX}} = \tfrac{1}{2\sqrt{2}}[\Psi_1^A\Psi_2^B + \Psi_3^A\Psi_4^B + \Psi_5^A\Psi_6^B + \Psi_7^A\Psi_8^B + P_{AB}], \\
&\Gamma_2: \Psi_4^{\mathrm{BX}} = -\tfrac{1}{2\sqrt{2}}[\Psi_1^A\Psi_4^B - \Psi_2^A\Psi_3^B + \Psi_5^A\Psi_8^B - \Psi_6^A\Psi_7^B + P_{AB}], \\
&\Gamma_3: \Psi_5^{\mathrm{BX}} = -\tfrac{1}{2\sqrt{2}}[\Psi_1^A\Psi_6^B - \Psi_2^A\Psi_5^B - \Psi_3^A\Psi_8^B + \Psi_4^A\Psi_7^B + P_{AB}], \\
&\Gamma_4: \Psi_6^{\mathrm{BX}} = -\tfrac{1}{2\sqrt{2}}[\Psi_1^A\Psi_8^B - \Psi_2^A\Psi_7^B + \Psi_3^A\Psi_6^B - \Psi_4^A\Psi_5^B + P_{AB}].
\end{aligned} \qquad (11)
$$

Again, the first two biexcitons with Γ_1 symmetry are pure hh and lh, respectively. All other biexcitons are mixed. The Γ_1 states have the usual structure $\sigma^+\sigma^-$. The Γ_3 biexciton is accessible by two-photon absorption too, but by photons having polarizations $xy = \sigma^+\sigma^+ - \sigma^-\sigma^-$. Other biexciton states are not accessible by two-photon absorption.

When compared to (6), the hole part of the exciton Hamiltonian has one more term:

$$
\hat{H}_h = c_0\mathbb{I}_h + c_1\hat{J}_x^2 + c_2\hat{J}_z^2. \qquad (12)
$$

This Hamiltonian differs from (6) because it couples hole subbands via the term proportional to $\hat{J}_x^2$. This coupling also causes interaction between exciton subbands what we show below. The electron-hole exchange Hamiltonian can be expanded into the form

$$
\hat{H}_{e\text{-}h} = \Delta_0\mathbb{I}_e \otimes \mathbb{I}_h + \Delta_{11}\hat{\sigma}_x\hat{J}_x + \Delta_{12}\hat{\sigma}_x\{\hat{J}_x,\hat{J}_y^2\} + \Delta_{13}\hat{\sigma}_x\hat{J}_x^3 + \Delta_{21}\hat{\sigma}_y\hat{J}_y + \Delta_{22}\hat{\sigma}_y\{\hat{J}_y,\hat{J}_x^2\} + \Delta_{23}\hat{\sigma}_y\hat{J}_y^3 + \Delta_{31}\hat{\sigma}_z\hat{J}_z + \Delta_{32}\hat{\sigma}_z\{\hat{J}_z,\hat{J}_x^2\} + \Delta_{33}\hat{\sigma}_z\hat{J}_z^3. \qquad (13)
$$

This Hamiltonian is block diagonal and couples pairs of the states with the same spin from the two principal exciton bands (light and heavy holes). Because of the simple structure of the Hamiltonian, its diagonalization is very simple but the result has many terms which are not given here explicitly.

Besides the one-exciton contributions, the biexciton Hamiltonian contains only hole-hole exchange terms because electron-hole and electron-electron exchange terms are zero matrices. This Hamiltonian has 25 terms and we give them in the Appendix. The biexciton Hamiltonian couples all three states with symmetry Γ_1 while the other states are eigenstates of the Hamiltonian.

IV. ZINC-BLENDE IN THE [111] DIRECTION

The point-group symmetry of such quantum wells is C_{3v}. Electrons in the lowest conduction subband have wave functions with symmetry Γ_4 and the hole subbands have symmetries

$$\left.\begin{aligned}&\Gamma_5:\quad \chi_1=\tfrac{1}{\sqrt{2}}\left[\left|\tfrac{3}{2}-\tfrac{3}{2}\right\rangle-i\left|\tfrac{3}{2}+\tfrac{3}{2}\right\rangle\right],\\&\Gamma_6:\quad \chi_2=(i/\sqrt{2})\left[\left|\tfrac{3}{2}-\tfrac{3}{2}\right\rangle+i\left|\tfrac{3}{2}+\tfrac{3}{2}\right\rangle\right],\end{aligned}\right\}\ \text{heavy holes}$$
$$\left.\begin{aligned}&\Gamma_4:\quad \chi_3=\left|\tfrac{3}{2}-\tfrac{1}{2}\right\rangle,\\&\qquad\ \chi_4=\left|\tfrac{3}{2}+\tfrac{1}{2}\right\rangle.\end{aligned}\right\}\ \text{light holes}\tag{14}$$

The exciton wave functions then have symmetries $\Gamma_4\otimes(2\Gamma_4\oplus\Gamma_5\oplus\Gamma_6)=\Gamma_1\oplus\Gamma_2\oplus3\Gamma_3$. The symmetrized exciton wave functions are

$$\begin{aligned}&\Gamma_1:\Psi_1^{(z)}=\tfrac{1}{\sqrt{2}}[\chi_3\alpha-\chi_4\beta],\\&\Gamma_2:\Psi_2=-(i/\sqrt{2})[\chi_3\alpha+\chi_4\beta],\\&\Gamma_3:\Psi_3^{(-)}=\chi_3\beta,\\&\qquad\Psi_4^{(+)}=\chi_4\alpha,\end{aligned}\tag{15}$$

$$\begin{aligned}&\Psi_5=\tfrac{1}{\sqrt{2}}[i\chi_1-\chi_2]\alpha,\\&\Psi_6=\tfrac{1}{\sqrt{2}}[\chi_1-i\chi_2]\beta,\\&\Psi_7^{(-)}=\tfrac{1}{\sqrt{2}}[\chi_1-i\chi_2]\alpha,\\&\Psi_8^{(+)}=\tfrac{1}{\sqrt{2}}[i\chi_1-\chi_2]\beta,\end{aligned}$$

with χ_{1-4} defined by Eq. (14). Wave functions with indices 1–4 refer to lh excitons and indices 5–8 to hh excitons. The biexciton wave functions have symmetries $2\Gamma_1\oplus2\Gamma_3$:

$$\begin{aligned}&\Gamma_1:\Psi_1^{\mathrm{BX}}=\tfrac{1}{2}[\Psi_5^A\Psi_6^B-\Psi_7^A\Psi_8^B+P_{AB}],\\&\qquad\Psi_2^{\mathrm{BX}}=-\tfrac{1}{2\sqrt{3}}[\Psi_1^A\Psi_1^B+\Psi_2^A\Psi_2^B+2\Psi_3^A\Psi_4^B+P_{AB}],\\&\Gamma_3:\Psi_3^{\mathrm{BX}}=-\tfrac{1}{2\sqrt{2}}[\Psi_1^A\Psi_5^B+i\Psi_2^A\Psi_5^B+\sqrt{2}\Psi_4^A\Psi_8^B\\&\qquad\qquad+P_{AB}],\\&\qquad\Psi_4^{\mathrm{BX}}=\tfrac{1}{2\sqrt{2}}[-\Psi_1^A\Psi_6^B+i\Psi_2^A\Psi_6^B+\sqrt{2}\Psi_3^A\Psi_7^B+P_{AB}],\\&\qquad\Psi_5^{\mathrm{BX}}=\tfrac{1}{2\sqrt{2}}[\Psi_1^A\Psi_7^B+i\Psi_2^A\Psi_7^B+\sqrt{2}\Psi_4^A\Psi_6^B+P_{AB}],\\&\qquad\Psi_6^{\mathrm{BX}}=-\tfrac{1}{2\sqrt{2}}[\Psi_1^A\Psi_8^B-i\Psi_2^A\Psi_8^B-\sqrt{2}\Psi_3^A\Psi_5^B+P_{AB}].\end{aligned}\tag{16}$$

The Γ_1 biexcitons are again pure lh and hh states, respectively. The others are mixed having holes from both subbands. The Γ_1 biexcitons can be reached by the usual two-photon transition with photons which have opposite circular polarizations or by two photons with parallel linear polarizations. The biexcitons with indices 3 and 4 can be excited by $\sigma^+\sigma^+$ and $\sigma^-\sigma^-$ photons, respectively. The last two biexcitons (5 and 6) do not couple to light field via two-photon transitions.

The exciton Hamiltonian has only a constant contribution from an electron and the contribution from a hole can be expressed by Eq. (6). The electron-hole exchange term reads, for this point-group symmetry,

$$\begin{aligned}\hat{H}_{e\text{-}h}=\Delta_0\mathbb{I}_e\otimes\mathbb{I}_h+\Delta_{11}(\hat{\sigma}_+\hat{J}_-+\hat{\sigma}_-\hat{J}_+)+\Delta_{12}\hat{\sigma}_z\hat{J}_z+\Delta_{21}(\hat{\sigma}_+\{\hat{J}_+,\hat{J}_-^2\}+\hat{\sigma}_-\{\hat{J}_-,\hat{J}_+^2\})+\Delta_{22}\hat{\sigma}_z\hat{J}_z^3+\Delta_3(\hat{\sigma}_-\{\hat{J}_+,\{\hat{J}_+,\hat{J}_-\}\}\\+\hat{\sigma}_+\{\hat{J}_-,\{\hat{J}_+,\hat{J}_-\}\}).\end{aligned}\tag{17}$$

We have introduced new operators $\hat{J}_+=\hat{J}_x+i\hat{J}_y$, $\hat{J}_-=\hat{J}_x-i\hat{J}_y$, $\hat{\sigma}_+=\hat{\sigma}_x+i\hat{\sigma}_y$, and $\hat{\sigma}_-=\hat{\sigma}_x-i\hat{\sigma}_y$. Although it is possible to analytically diagonalize the above Hamiltonian, we think it has no sense since the results would have too complex and inconvenient structure.

The biexciton Hamiltonian, on the contrary to the [001]- and [011]-oriented QWs, has nonzero contributions from the electron-electron and electron-hole exchange terms so one finds them together with all hole-hole exchange terms in the Appendix (22 terms in total). This Hamiltonian is diagonal in the basis of symmetrized biexciton wave functions except for the coupling of states 1 and 2 (Γ_1 symmetry, pure lh and hh).

V. WURTZITE IN THE [001] DIRECTION

This quantum well has the same point-group symmetry C_{6v} as a bulk material. This point group is very similar to that C_{3v} of the zinc-blende QWs grown in the [111] direction. We then expect similar results, in particular, for the

structure of the Hamiltonian. Electron wave functions have Γ_7 symmetry and the hole wave functions have Γ_7 (lh) and Γ_9 (hh). The exciton wave functions have symmetries $\Gamma_7 \otimes (\Gamma_7 \oplus \Gamma_9) = \Gamma_1 \oplus \Gamma_2 \oplus 2\Gamma_5 \oplus \Gamma_6$:

$$\begin{aligned}
&\Gamma_1: \Psi_1^{(z)} = \tfrac{1}{\sqrt{2}}[\Phi_3\alpha - \Phi_4\beta],\\
&\Gamma_2: \Psi_2 = (i/\sqrt{2})[\Phi_3\alpha + \Phi_4\beta],\\
&\Gamma_5: \Psi_3^{(-)} = \Phi_3\beta,\\
&\quad \Psi_4^{(+)} = \Phi_4\alpha,\\
&\quad \Psi_5^{(-)} = \Phi_1\alpha,\\
&\quad \Psi_6^{(+)} = \Phi_2\beta,\\
&\Gamma_6: \Psi_7 = \Phi_2\alpha,\\
&\quad \Psi_8 = \Phi_1\beta.
\end{aligned} \tag{18}$$

Similar to the C_{3v} point group, wave functions with indices 1–4 are appropriate for the lh excitons and wave functions with indices 5–8 for the hh excitons. Only the excitons with Γ_5 symmetry are dipole active and they are coupled to circularly polarized light. The symmetrized biexciton wave functions have the symmetries $2\Gamma_1 \oplus \Gamma_5 \oplus \Gamma_6$:

$$\begin{aligned}
&\Gamma_1: \Psi_1^{\mathrm{BX}} = \tfrac{1}{2}[\Psi_5^A\Psi_6^B + \Psi_7^A\Psi_8^B + P_{AB}],\\
&\quad \Psi_2^{\mathrm{BX}} = -\tfrac{1}{2\sqrt{3}}[\Psi_1^A\Psi_1^B + \Psi_2^A\Psi_2^B + 2\Psi_3^A\Psi_4^B + P_{AB}],\\
&\Gamma_5: \Psi_3^{\mathrm{BX}} = \tfrac{1}{2\sqrt{2}}[\Psi_1^A\Psi_5^B - i\Psi_2^A\Psi_5^B + \sqrt{2}\Psi_4^A\Psi_8^B + P_{AB}],\\
&\quad \Psi_4^{\mathrm{BX}} = -\tfrac{1}{2\sqrt{2}}[\Psi_1^A\Psi_6^B + i\Psi_2^A\Psi_6^B - \sqrt{2}\Psi_3^A\Psi_7^B + P_{AB}],\\
&\Gamma_6: \Psi_5^{\mathrm{BX}} = -\tfrac{1}{2\sqrt{2}}[\Psi_1^A\Psi_8^B + i\Psi_2^A\Psi_8^B - \sqrt{2}\Psi_3^A\Psi_5^B + P_{AB}],\\
&\quad \Psi_6^{\mathrm{BX}} = \tfrac{1}{2\sqrt{2}}[\Psi_1^A\Psi_7^B - i\Psi_2^A\Psi_7^B + \sqrt{2}\Psi_4^A\Psi_6^B + P_{AB}].
\end{aligned} \tag{19}$$

The first two biexcitons are pure lh and hh with Γ_1 symmetry. The Γ_5 biexcitons are not directly accessible by two-photon absorption and the Γ_6 biexcitons have $\sigma^-\sigma^-$ and $\sigma^+\sigma^+$ orientations of dipoles, respectively (cf. the first two Γ_3 biexcitons in C_{3v}).

Similar to C_{3v}, the electron Hamiltonian is a constant and the hole Hamiltonian is expressed by (6). The electron-hole exchange term reads

$$\hat{H}_{e\text{-}h} = \Delta_0 \mathbb{I}_e \otimes \mathbb{I}_h + \Delta_{11}(\hat{\sigma}_+\hat{J}_- + \hat{\sigma}_-\hat{J}_+) + \Delta_{12}\hat{\sigma}_z\hat{J}_z + \Delta_{21}(\hat{\sigma}_+\{\hat{J}_+,\hat{J}_-^2\} + \hat{\sigma}_-\{\hat{J}_-,\hat{J}_+^2\}) + \Delta_{22}\hat{\sigma}_z\hat{J}_z^3 + i\Delta_3(\hat{\sigma}_+\{\hat{J}_z,\hat{J}_-\} - \hat{\sigma}_-\{\hat{J}_z,\hat{J}_+\}). \tag{20}$$

The imaginary unit preceding Δ_3 on the last line follows directly from tables of coupling coefficients.[12] It arises due to the usage of the unusual anticommutators $\{\hat{J}_z,\hat{J}_\pm\}$. One can easily verify that the last term in the above formula is Hermitian and has the K^+ symmetry with respect to the time reversal.

The biexciton Hamiltonian for the C_{6v} point group has nonzero contributions from all exchange terms. We give them in the Appendix (22 terms in total). The biexciton Hamiltonian has two blocks, one is appropriate for the Γ_1 biexcitons and the other for the Γ_5 and Γ_6 biexciton states.

VI. WURTZITE IN THE [011] AND [111] DIRECTIONS

The point group appropriate for such quantum wells is C_S. This point group has low symmetry and our results would have too many terms. Additionally, it is not usual to fabricate quantum wells from a material having the wurtzite structure with other than the [001] growth direction of the QW.

VII. DISCUSSION

In the preceding sections, we used the terms "symmetrized wave functions," "coherent spin flip," and "coupling of states" without their precise definition. These terms are explained here and we show what consequences follow from the above calculations.

The choice of an orthonormal basis of exciton wave functions for calculations is arbitrary. The exciton and biexciton wave functions were, however, expressed considering their symmetry with respect to the crystal lattice. The reason is that the resulting Hamiltonian of the electron-hole exchange has a simple form. Since photons with wave vector perpendicular to the QW plane have a well-defined symmetry, the Hamiltonian of dipole interaction is also very simple allowing exciton-photon coupling only to four states. This fact may reasonably simplify discussions of the system's dynamics after optical excitation.

One finds nondiagonal terms in the exciton Hamiltonians derived above. These *coupling* terms are responsible for transitions from one spin state to another—they cause *coherent spin flip* or spin beating. Note that this process is coherent and does not mean any spin relaxation, the spin relaxes if the phase of an exciton is perturbed by another process, e.g., scattering. The dynamics of an exciton after excitation by polarized light can be viewed as periodical coherent changes of its spin (spin flips) defined within the basis of symmetrized wave functions.

Let us calculate the consequence of the coupling of two states. Our aim here is to determine what is the mean popu-

lation of some state coupled to a resonantly excited dipole-active state. Let us assume the states $|1\rangle$ and $|2\rangle$ differ in the energy by an amount Δ and their coupling strength is ξ. The Hamiltonian is then

$$\hat{H} = \begin{pmatrix} 0 & \xi \\ \xi^* & \Delta \end{pmatrix}, \tag{21}$$

where the asterisk denotes complex conjugate. Let us assume that the state $|1\rangle$ is coupled to light while the second state is dipole inactive. The eigenenergies are then

$$E_{1,2} = \frac{\Delta}{2}\left[1 \pm \sqrt{1 + \frac{4|\xi|^2}{\Delta^2}}\right] \approx \begin{cases} \frac{\Delta}{2}\left[1 \pm \left(1 + \frac{2|\xi|^2}{\Delta^2}\right)\right] & \text{for } |\xi| \ll \Delta \\ \frac{\Delta}{2} \pm \left(|\xi|^2 + \frac{\Delta^2}{8|\xi|}\right) & \text{for } |\xi| \gg \Delta. \end{cases} \tag{22}$$

The first line on the right-hand side refers to the case of coupling of two nondegenerate states (e.g., light- and heavy-hole excitons in a narrow QW) and the eigenenergies can be further estimated to be approximately Δ and $-|\xi|^2/\Delta$, respectively. The second line in the above formula then describes coupling of nearly degenerate states ($\Delta \to 0$) and the eigenenergies can be estimated to be $\pm|\xi|$. It is a simple algebraic exercise to derive that the mean populations of the states are

$$\bar{n}_{1,2} = \frac{|\xi|^2}{|\xi|^2 + E_{2,1}^2}. \tag{23}$$

Assuming nondegenerate states and weak coupling, one gets the mean population of the dipole-inactive level $\approx(\xi/\Delta)^2$, for nearly degenerate states this population is $\approx\frac{1}{2}$. The latter result is obvious: When the coupling strength exceeds the energy difference between the states, we get the well-known Rabi oscillations in a two-level system and therefore the mean populations of the levels must be equal. The former result can be explained using virtual transitions. A weak interaction causes transition between the states. Due to energy mismatch, this transition is only virtual and the system must return to the initial state after a time given by the uncertainty relation between energy and time. The time, for which the exciton is allowed to be in the dipole-inactive state, is inversely proportional to the energy splitting of the states. Probability of the virtual transition is directly proportional to the coupling strengths and thus the result $\bar{n}_2 \approx (|\xi|/\Delta)^2$ is what we expected.

In order to estimate which terms in the Hamiltonians are the most important, one believes that the strongest contributions are due to the particle-particle exchange interactions of the lowest order in the momentum operators. The strongest contribution then comes from the crystal field, i.e., from the splitting of the hole subbands. The second strongest contributions come from electron-hole (electron-electron, hole-hole) exchange interactions of the type $\hat{\sigma}_k \hat{J}_\ell$, etc. The method of invariants which was used above is well capable for the derivation of the structure of the Hamiltonian, however, other theories are needed for the evaluation of the coupling strengths.

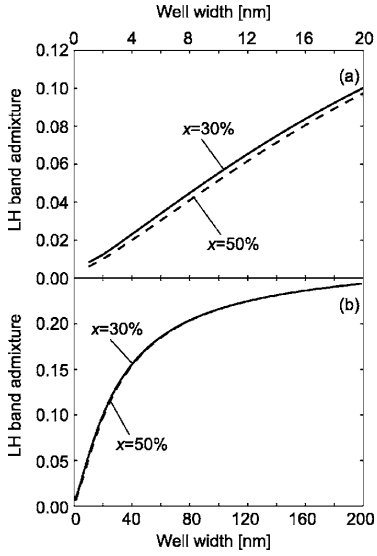

FIG. 1. Calculation of the admixture of excited lh excitons when a $Ga_{1-x}Al_xAs$ is optically excited resonantly with hh exciton, according to (23). We show the results for various QW widths on a short scale (a) and a long scale (b).

We performed numerical calculations in order to evaluate the admixture of excited lh excitons when hh excitons are resonantly excited. Based on the procedure described in Ref. 13, we varied the QW width and we calculated the variable n_1 defined in (23). The results are shown in Fig. 1 for $Ga_{1-x}Al_xAs$ QWs considering $x=30\%$ and $x=50\%$. The lh exciton admixture is negligible for narrow wells, however, it increases with increasing QW width and it asymptotically reaches the value of 25% for bulk materials. It is then clear that variation of the QW width may significantly modify the behavior of the sample in magnetic fields because of different g factors of lh and hh excitons. Phenomena connected with the band mixing then may be observable in the Faraday rotation experiments.

In all types of quantum wells under investigation, the Hamiltonians are not diagonal in the basis of the symmetrized wave functions. We have found using the bases of symmetrized wave functions that coupling caused by electron-hole exchange interaction always mixes heavy-hole and light-hole excitons with the same spin. For example, in the zinc-blende [001] QW, states with x polarizations are coupled and they are not coupled to any other state. It is then obvious that coupling preserves polarization. The strongest interaction is always the electron-hole exchange of the lowest order in the hole operators.

The zinc-blende [011] QW is the only exception from the above statements. The lowest-order mixing comes from the hole band structure [it is proportional to the constant c_2 in (12)]. QW has the lowest symmetry of the examined structures and thus one does not expect, for example, conserva-

tion of circular polarization because the eigenstates are nondegenerate and linearly polarized. Symmetry considerations show that there is a significant mixing between the two circularly polarized states: although it does not come from mixing of the hole subbands, electron-hole interaction causes mixing of the light-hole positively polarized exciton with heavy-hole negatively polarized exciton and vice versa.

Based on the above derivation, we can estimate that when exciting at the heavy-hole exciton resonance by polarized light, the ratio of populations of the light- and heavy-hole excitons with the same spin will be $3\Delta_{11}^2/\Delta_{\mathrm{lh}}^2$. The coupling between states does not reveal as a strong effect. Electron-hole exchange interaction in GaAs is of the order of meV (Refs. 9 and 14) and light-hole/heavy-hole splitting of 10 meV, therefore the admixture of the light-hole excitons is expected to be of the order of 1%. This amount may, however, influence measurements such as the Faraday rotation since the g factors of holes from the two bands may differ. In the [011]-oriented QW, selection rules for the polarization of the FWM signal may be relaxed: In four-wave-mixing experiments, response to two-beam excitation with opposite circular polarizations is mostly forbidden. Due to the lack of symmetry in the discussed particular case, excitons can change their spin and thus we expect that the response under the aforementioned conditions is no more forbidden.

Let us discuss now the biexciton levels. In FWM experiments, one is interested in four-particle correlations since they are responsible for polarization selection rules. These correlations are induced mainly by exciton-exciton scattering and biexciton formation. Using the symmetrized exciton wave functions given above, full discussion of the scattering-induced correlations is possible including biexciton formation which is strongly dependent on the QW symmetry as we have shown above. It is, however, beyond the scope of this paper.

According to Ref. 8, we have shown that for all QW symmetries, biexcitons formed from two electrons and two holes from the same band have Γ_1 symmetry. However, since we took into account also mixed biexcitons, we have found wave functions which are generally dependent on the symmetry of the QW. We confirm that at least one of the mixed biexcitons can be excited by two cocircularly polarized photons. In addition, our results show that there should be *two* biexcitons with $\sigma^+\sigma^+$ two-photon selection rule and two more which are not directly accessible by two-photon absorption. Knowledge of dipole selection rules for two-photon excitation of biexcitons is, however, needed for correct discussion of the results of both pump-probe and FWM experiments.

VIII. CONCLUSIONS

On the basis of the symmetry of a quantum well, we calculate symmetry-adapted wave functions of excitons and biexcitons. By the method of invariants, we also express the Hamiltonians of the excitons and biexcitons and we are able to extract energies of the eigenstates. The Hamiltonians contain nondiagonal terms which are responsible for coherent spin flip of excitons and biexcitons (mixing of wave functions) leading to spin beating. These spin-flip processes are induced by electron-hole exchange within an exciton and mainly hole-hole exchange within a biexciton.

We compare the results for four different structures: QW grown in the [001], [011], and [111] directions made from material with zinc-blende structure and QW grown in the [001] direction made from material with wurtzite structure. We show that there are different spin-flip channels in those QW. It was found that the spin is mostly conserved but there is always coupling between the light-hole and heavy-hole exciton band. Only in [011] quantum wells which have low symmetry, one finds that circular polarization is not conserved what may reveal as a strong effect in four-wave mixing experiments. Based on the obtained results, one can design a proper setup of an experiment to detect, e.g., mixed biexcitons using various methods like pump-probe or FWM experiment.

We calculate numerically the amount of the admixture of lh excitons when a $Ga_{1-x}Al_xAs$ QW is excited resonantly with the hh exciton. The results show a strong dependence of the mixing on the QW width and therefore a strong dependence of the spin dynamics in magnetic fields (due to the difference of g factors of hh and lh excitons).

ACKNOWLEDGMENTS

The authors would like to thank S. Cronenberger, H. Rahimpour Soleimani, and M. Gallart for fruitful discussions. The authors also thankfully acknowledge financial support from French Foreign Ministry in form of a PhD grant in the framework of a thesis in "cotutelle."

APPENDIX: BIEXCITON HAMILTONIAN

The lists below contain invariant expansion of the biexciton Hamiltonian. The number in parentheses in superscript of an operator denotes a number of a particle which it acts on.

(1) T_d [001]

h-h exchange: $\hat{J}_x^{(2)}\hat{J}_x^{(4)}+\hat{J}_y^{(2)}\hat{J}_y^{(4)}$,

$\hat{J}_z^{(2)}\hat{J}_z^{(4)}$,

$\hat{J}_x^{(2)}\{\hat{J}_x^{(4)},\hat{J}_y^{(4)^2}-\hat{J}_z^{(4)^2}\}+\hat{J}_y^{(2)}\{\hat{J}_y^{(4)},\hat{J}_x^{(4)^2}-\hat{J}_z^{(4)^2}\}+P_{24}$,

$\hat{J}_x^{(2)}\hat{J}_x^{(4)^3}+\hat{J}_y^{(2)}\hat{J}_y^{(4)^3}+P_{24}$,

$\{\hat{J}_x^{(2)},\hat{J}_z^{(2)}\}\cdot\{\hat{J}_x^{(4)},\hat{J}_z^{(4)}\}+\{\hat{J}_y^{(2)},\hat{J}_z^{(2)}\}\cdot\{\hat{J}_y^{(4)},\hat{J}_z^{(4)}\}$,

$\hat{J}_z^{(2)}\hat{J}_z^{(4)^3}+P_{24}$,

$\hat{J}_z^{(2)^2}\hat{J}_z^{(4)^2}$,

$(\hat{J}_x^{(2)^2}-\hat{J}_y^{(2)^2})(\hat{J}_x^{(4)^2}-\hat{J}_y^{(4)^2})$,

$\{\hat{J}_x^{(2)},\hat{J}_y^{(2)}\}\{\hat{J}_x^{(4)},\hat{J}_y^{(4)}\}$,

$\hat{J}_z^{(2)^3}\hat{J}_z^{(4)^3}$,

$\hat{J}_z^{(2)}\{\hat{J}_x^{(2)},\hat{J}_y^{(2)}\}\cdot\hat{J}_z^{(4)}\{\hat{J}_x^{(4)},\hat{J}_y^{(4)}\}$,

$\hat{J}_z^{(2)^2}\{\hat{J}_x^{(2)},\hat{J}_y^{(2)}\}\cdot\hat{J}_z^{(4)^2}\{\hat{J}_x^{(4)},\hat{J}_y^{(4)}\}$,

$\hat{J}_z^{(2)^2}\{\hat{J}_x^{(2)},\hat{J}_y^{(2)}\}\cdot\{\hat{J}_x^{(4)},\hat{J}_y^{(4)}\}+P_{24}$,

$\{\hat{J}_x^{(2)},\hat{J}_y^{(2)^2}-\hat{J}_z^{(2)^2}\}\cdot\{\hat{J}_x^{(4)^2},\hat{J}_y^{(4)^2}-\hat{J}_z^{(4)^2}\}+\{\hat{J}_y^{(2)},\hat{J}_x^{(2)^2}-\hat{J}_z^{(2)^2}\}\cdot\{\hat{J}_y^{(4)},\hat{J}_x^{(4)^2}-\hat{J}_z^{(4)^2}\}$,

$\hat{J}_x^{(2)^3}\hat{J}_x^{(4)^3}+\hat{J}_y^{(2)^3}\hat{J}_y^{(4)^3}$,

$\hat{J}_x^{(2)^3}\{\hat{J}_x^{(4)},\hat{J}_y^{(4)^2}-\hat{J}_z^{(4)^2}\}+\hat{J}_y^{(2)^3}\{\hat{J}_y^{(4)},\hat{J}_x^{(4)^2}-\hat{J}_z^{(4)^2}\}+P_{24}$.

(2) T_d [011]

h-h exchange: $\hat{J}_x^{(2)}\hat{J}_x^{(4)}$,

$\hat{J}_y^{(2)}\hat{J}_y^{(4)}$,

$\hat{J}_z^{(2)}\hat{J}_z^{(4)}$,

$\{\hat{J}_x^{(2)}\{\hat{J}_x^{(4)},\hat{J}_y^{(4)^2}\}\}+P_{24}$,

$\{\hat{J}_y^{(2)}\{\hat{J}_y^{(4)},\hat{J}_x^{(4)^2}\}\}+P_{24}$,

$\{\hat{J}_z^{(2)}\{\hat{J}_z^{(4)},\hat{J}_x^{(4)^2}\}\}+P_{24}$,

$\hat{J}_x^{(2)}\hat{J}_x^{(4)^3}+P_{24}$,

$\hat{J}_y^{(2)}\hat{J}_y^{(4)^3}+P_{24}$,

$\hat{J}_z^{(2)}\hat{J}_z^{(4)^3}+P_{24}$,

$\{\hat{J}_y^{(2)},\hat{J}_z^{(2)}\}\cdot\{\hat{J}_y^{(4)},\hat{J}_z^{(4)}\}$,

$\{\hat{J}_x^{(2)},\hat{J}_z^{(2)}\}\cdot\{\hat{J}_x^{(4)},\hat{J}_z^{(4)}\}$,

$\{\hat{J}_x^{(2)},\hat{J}_y^{(2)}\}\cdot\{\hat{J}_x^{(4)},\hat{J}_y^{(4)}\}$,

$\hat{J}_x^{(2)^3}\hat{J}_x^{(4)^3}$,

$\hat{J}_y^{(2)^3}\hat{J}_y^{(4)^3}$,

$\hat{J}_z^{(2)^3}\hat{J}_z^{(4)^3}$,

$\{\hat{J}_x^{(2)},\hat{J}_y^{(2)^2}\}\cdot\{\hat{J}_x^{(4)},\hat{J}_y^{(4)^2}\}$,

$\{\hat{J}_y^{(2)},\hat{J}_x^{(2)^2}\}\cdot\{\hat{J}_y^{(4)},\hat{J}_x^{(4)^2}\}$,

$\{\hat{J}_z^{(2)},\hat{J}_x^{(2)^2}\}\cdot\{\hat{J}_z^{(4)},\hat{J}_x^{(4)^2}\}$,

$\{\hat{J}_x^{(2)^3}\{\hat{J}_x^{(4)},\hat{J}_y^{(4)^2}\}\}+P_{24}$,

$\{\hat{J}_y^{(2)^3}\{\hat{J}_y^{(4)},\hat{J}_x^{(4)^2}\}\}+P_{24}$,

$\{\hat{J}_z^{(2)^3}\{\hat{J}_z^{(4)},\hat{J}_x^{(4)^2}\}\}+P_{24}$,

$\hat{J}_x^{(2)^2}\hat{J}_x^{(4)^2}$,

$\hat{J}_z^{(2)^2}\hat{J}_z^{(4)^2}$,

$\hat{J}_x^{(2)^2}\hat{J}_z^{(4)^2}+P_{24}$,

$\{\hat{J}_x^{(2)},\{\hat{J}_y^{(2)},\hat{J}_z^{(2)}\}\}\{\hat{J}_x^{(4)},\{\hat{J}_y^{(4)},\hat{J}_z^{(4)}\}\}$.

(3) T_d [111]

e-e exchange: $\hat{\sigma}_+^{(1)}\hat{\sigma}_-^{(3)}+P_{13}$,

$\hat{\sigma}_z^{(1)}\hat{\sigma}_z^{(3)}$.

h-h exchange: $\hat{J}_z^{(2)}\hat{J}_z^{(4)}$,

$\hat{J}_z^{(2)}\hat{J}_z^{(4)^3}+P_{24}$,

$\hat{J}_z^{(2)^3}\hat{J}_z^{(4)^3}+P_{24}$,

$\hat{J}_+^{(2)}\hat{J}_-^{(4)}+P_{24}$,

$\{\hat{J}_+^{(2)},\{\hat{J}_+^{(4)},\hat{J}_-^{(4)^2}\}\}+\{\hat{J}_-^{(2)},\{\hat{J}_-^{(4)},\hat{J}_+^{(4)^2}\}\}+P_{24}$,

$\{\hat{J}_+^{(2)},\hat{J}_-^{(2)^2}\}\cdot\{\hat{J}_-^{(4)},\hat{J}_+^{(4)^2}\}+P_{24}$,

$\hat{J}_+^{(2)^2}\hat{J}_-^{(4)^2}+P_{24}$,

$\{\hat{J}_z^{(2)},\hat{J}_+^{(2)^2}\}\cdot\{\hat{J}_z^{(4)},\hat{J}_-^{(4)^2}\}+P_{24}$,

$i\{\hat{J}_+^{(2)^2},\{\hat{J}_z^{(4)},\hat{J}_-^{(4)^2}\}\}-i\{\hat{J}_-^{(2)^2},\{\hat{J}_z^{(4)},\hat{J}_+^{(4)^2}\}\}+P_{24}$,

$(\hat{J}_-^{(2)^3}-\hat{J}_+^{(2)^3})\cdot(\hat{J}_-^{(4)^3}-\hat{J}_+^{(4)^3})$,

$\{\hat{J}_+^{(2)},\hat{J}_-^{(2)}\}\cdot\{\hat{J}_+^{(4)},\hat{J}_-^{(4)}\}$,

$(\hat{J}_+^{(2)^3}+\hat{J}_-^{(2)^3})\cdot(\hat{J}_+^{(4)^3}+\hat{J}_-^{(4)^3})$,

$\hat{J}_+^{(2)}\{\hat{J}_-^{(4)},\{\hat{J}_+^{(4)},\hat{J}_-^{(4)}\}\}+\hat{J}_-^{(2)}\{\hat{J}_+^{(4)},\{\hat{J}_+^{(4)},\hat{J}_-^{(4)}\}\}+P_{24}$,

$\{\hat{J}_+^{(2)},\hat{J}_-^{(2)^2}\}\cdot\{\hat{J}_-^{(4)},\{\hat{J}_+^{(4)},\hat{J}_-^{(4)}\}\}+\{\hat{J}_-^{(2)},\hat{J}_+^{(2)^2}\}\cdot\{\hat{J}_+^{(4)},\{\hat{J}_+^{(4)},\hat{J}_-^{(4)}\}\}+P_{24}$,

$\{\hat{J}_+^{(2)},\{\hat{J}_+^{(2)},\hat{J}_-^{(2)}\}\}\cdot\{\hat{J}_-^{(4)},\{\hat{J}_+^{(4)},\hat{J}_-^{(4)}\}\}+P_{24}$.

e-h exchange: $[\hat{\sigma}_z^{(1)}\hat{J}_z^{(2)}+P_{13}]+P_{24}$,

$[\hat{\sigma}_z^{(1)}\hat{J}_z^{(2)^3}+P_{13}]+P_{24}$,

$[\hat{\sigma}_-^{(1)}\hat{J}_+^{(2)}+\hat{\sigma}_+^{(1)}\hat{J}_-^{(2)}+P_{13}]+P_{24}$,

$[\hat{\sigma}_-^{(1)}\{\hat{J}_-^{(2)},\hat{J}_+^{(2)^2}\}+\hat{\sigma}_+^{(1)}\{\hat{J}_+^{(2)},\hat{J}_-^{(2)^2}\}+P_{13}]+P_{24}$,

$[\hat{\sigma}_+^{(1)}\{\hat{J}_-^{(2)},\{\hat{J}_+^{(2)},\hat{J}_-^{(2)}\}\}+\hat{\sigma}_-^{(1)}\{\hat{J}_+^{(2)},\{\hat{J}_+^{(2)},\hat{J}_-^{(2)}\}\}+P_{13}]+P_{24}$.

(4) $C_{6v}[111]$

e-e exchange: $\hat{\sigma}_+^{(1)}\hat{\sigma}_-^{(3)}+P_{13}$,

$\hat{\sigma}_z^{(1)}\hat{\sigma}_z^{(3)}$.

h-h exchange: $\hat{J}_z^{(2)}\hat{J}_z^{(4)}$,

$\hat{J}_z^{(2)^2}\hat{J}_z^{(4)^2}$,

$\hat{J}_z^{(2)^3}\hat{J}_z^{(4)^3}$,

$\hat{J}_z^{(2)}\hat{J}_z^{(4)^3}+P_{24}$,

$(\hat{J}_+^{(2)^3}+\hat{J}_-^{(2)^3})\cdot(\hat{J}_+^{(4)^3}+\hat{J}_-^{(4)^3})$,

$(\hat{J}_+^{(2)^3}-\hat{J}_-^{(2)^3})\cdot(\hat{J}_+^{(4)^3}-\hat{J}_-^{(4)^3})$,

$\hat{J}_+^{(2)}\hat{J}_-^{(4)}+P_{24}$,

$\{\hat{J}_+^{(2)},\{\hat{J}_+^{(4)},\hat{J}_-^{(4)^2}\}\}+\{\hat{J}_-^{(2)},\{\hat{J}_-^{(4)},\hat{J}_+^{(4)^2}\}\}+P_{24}$,

$i(\{\hat{J}_+^{(2)},\{\hat{J}_z^{(4)},\hat{J}_-^{(4)}\}\}-\{\hat{J}_-^{(2)},\{\hat{J}_z^{(4)},\hat{J}_+^{(4)}\}\})+P_{24}$,

$\{\hat{J}_+^{(2)},\hat{J}_-^{(2)^2}\}\cdot\{\hat{J}_-^{(4)},\hat{J}_+^{(4)^2}\}+P_{24}$,

$i(\{\{\hat{J}_+^{(2)},\hat{J}_-^{(2)^2}\},\{\hat{J}_z^{(4)},\hat{J}_+^{(4)}\}\}-\{\{\hat{J}_-^{(2)},\hat{J}_+^{(2)^2}\},\{\hat{J}_z^{(4)},\hat{J}_-^{(4)}\}\})+P_{24}$,

$\{\hat{J}_z^{(2)},\hat{J}_-^{(2)}\}\cdot\{\hat{J}_z^{(4)},\hat{J}_+^{(4)}\}+P_{24}$,

$\hat{J}_+^{(2)^2}\hat{J}_-^{(4)^2}+P_{24}$,

$\{\hat{J}_z^{(2)},\hat{J}_+^{(2)^2}\}\cdot\{\hat{J}_z^{(4)},\hat{J}_-^{(4)^2}\}+P_{24}$,

$i(\{\hat{J}_+^{(2)^2},\{\hat{J}_z^{(4)},\hat{J}_-^{(4)^2}\}\}-\{\hat{J}_-^{(2)^2},\{\hat{J}_z^{(4)},\hat{J}_+^{(4)^2}\}\})+P_{24}$.

e-h exchange: $[\hat{\sigma}_z^{(1)}\hat{J}_z^{(2)}+P_{13}]+P_{24}$,

$[\hat{\sigma}_z^{(1)}\hat{J}_z^{(2)^3}+P_{13}]+P_{24}$,

$[\hat{\sigma}_+^{(1)}\hat{J}_-^{(2)}+\hat{\sigma}_-^{(1)}\hat{J}_+^{(2)}+P_{13}]+P_{24}$,

$[\hat{\sigma}_+^{(1)}\{\hat{J}_+^{(2)},\hat{J}_-^{(2)^2}\}+\hat{\sigma}_-^{(1)}\{\hat{J}_-^{(2)},\hat{J}_+^{(2)^2}\}+P_{13}]+P_{24}$,

$i[\hat{\sigma}_+^{(1)}\{\hat{J}_z^{(2)},\hat{J}_-^{(2)}\}-\hat{\sigma}_-^{(1)}\{\hat{J}_z^{(2)},\hat{J}_+^{(2)}\}+P_{13}]+P_{24}$.

[1] H. P. Wagner, W. Langbein, and J. M. Hvam, Phys. Rev. B **59**, 4584 (1999).
[2] S. Adachi, S. Muto, K. Hazu, T. Sota, K. Suzuki, S. F. Chichibu, and T. Mukai, Phys. Rev. B **67**, 205212 (2003).
[3] E. Hanamura, J. Phys. Soc. Jpn. **39**, 1506 (1975).
[4] C. Comte, Opt. Commun. **14**, 79 (1975).
[5] K. Cho, Phys. Rev. B **14**, 4463 (1976).
[6] S. Suga and K. Cho, Phys. Rev. B **13**, 943 (1976).
[7] B. Hönerlage, R. Lévy, J. B. Grun, C. Klingshirn, and K. Bohnert, Phys. Rep. **124**, 161 (1985).
[8] S. B.-T. de Leon and B. Laikhtman, Europhys. Lett. **59**, 728 (2002).
[9] U. Rössler, S. Jorda, and D. Brodio, Solid State Commun. **73**, 209 (1990).
[10] G. L. Bir and G. L. Pikus, *Symmetry and Strain-Induced Effects in Semiconductors* (Wiley, New York, 1974).
[11] T. Koda, T. Murahashi, T. Mitani, S. Sakoda, and Y. Onodera, Phys. Rev. B **5**, 705 (1972).
[12] G. F. Koster, *Properties of the Thirty-Two Point Groups* (Massachusetts Institute of Technology, Cambridge, 1963).
[13] Y. Chen, B. Gil, P. Lefebvre, and H. Mathieu, Phys. Rev. B **37**, 6429 (1988).
[14] S. Jorda, U. Rössler, and D. Brodio, Phys. Rev. B **48**, 1669 (1993).

Available online at www.sciencedirect.com
ScienceDirect
Journal of Luminescence 126 (2007) 94–102
JOURNAL OF LUMINESCENCE
www.elsevier.com/locate/jlumin

Determination of the signal polarization state in four-wave mixing experiments on semiconductors

T. Ostatnický[a,b,*], P. Gilliot[b], B. Hönerlage[b]

[a]*Faculty of Mathematics and Physics, Charles University, Ke Karlovu 3, 12116 Prague 2, Czech Republic*
[b]*IPCMS, Groupe d'Optique Nonlinéaire et d'Optoélectronique, UMR 7504 CNRS–ULP, 23, rue du Læss-B.P. 43, 67034 Strasbourg Cedex 2, France*

Received 29 November 2005; received in revised form 5 April 2006; accepted 30 May 2006
Available online 17 August 2006

Abstract

Based on symmetry considerations, we develop a simple model for the determination of the polarization state of the four-wave mixing (FWM) response on semiconductors depending on the polarization of incoming photons. The model describes interactions within the system of polaritons taking into account their composite character and thus the correct symmetry. We separate the FWM response into three main contributions which may differ in symmetry. They are: polariton–polariton scattering, bipolariton-mediated scattering and scattering due to phase space filling. We then derive algebraic equations for each of the channels for calculation of the respective FWM response polarizations. Compared to microscopic theories, solution of these equations is much faster and therefore the theory becomes very useful if one wants to determine the polarization state of the response in a particular experiment. Thanks to the correct description of symmetries of various types of interactions, our model is more accurate in predictions than the optical Bloch equations.

PACS: 42.62.Fi; 71.35.Gg; 78.47.+p

Keywords: Four-wave mixing; Bipolariton; Crystal symmetry; Bulk semiconductors

1. Introduction

Four-wave mixing (FWM) is a very well-known experimental technique. It provides many informations about the temporal evolution of populations as well as coherences in an investigated system. This experimental method is proper for exploration of properties of semiconductors using pico- and femtosecond optical pulses. In this paper, we present a new theoretical approach to the description of the polarization state of the FWM signal.

Although optical bloch equations (OBEs) are well capable for description of the response of atomic systems, they fail if they are applied to description of semiconductors; for example, the slow initial rise of the FWM signal [1–5] cannot be sufficiently explained. It is possible to modify these equations by adding the biexciton level [6,7], exciton–exciton interactions (excitation-induced dephasing (EID)) [8], etc. (Refs. [9–12]). The predictions of these modified OBE still significantly differ from the experimental observations. We can also emphasize the fact that the exciton–exciton interaction (which is essential for the creation of the FWM response [13–15]) is assumed to be not spin-sensitive in the OBE models (expect for energy renormalization of the biexciton state). The importance of the spin dependence of the exciton–exciton interaction, has, however, been shown both experimentally and theoretically [16].

A rigorous and systematic description of the system of interacting electrons and holes was developed in the framework of semiconductor bloch equations (SBE) [17–19] as well as in theories which take into account four-particle correlations [20–23]. These models well describe the response of semiconductors—both the polarizations and the dynamics. They involve, however, important numerical calculations. In addition, it is hard

*Corresponding author. Faculty of Mathematics and Physics, Charles University, Ke Karlovu 3, 12116 Prague 2, Czech Republic.
Tel.: +42 0221911273; fax: +42 0221911249.
E-mail address: osty@matfyz.cz (T. Ostatnický).

0022-2313/$ - see front matter © 2006 Elsevier B.V. All rights reserved.
doi:10.1016/j.jlumin.2006.05.011

to include the correct symmetry of the crystal and symmetry-breaking effects. A Weakly Interacting Boson Model (WIBM) [24–26] is one of these microscopic theories and it significantly simplifies the situation by an assumption that excitons are bosons with only fractional fermion character which leads to Pauli blocking (PB).

In this paper, we propose a simple model for calculation of the polarization state of the FWM response from a semiconductor. Similarly, a model calculation of the FWM response can be found in Ref. [21] and that of a six-wave mixing evidencing the six-particle Coulomb correlation in Ref. [27]. These theoretical considerations are based on a microscopic description of quantum wells (QWs) in the frame of a two-band model and demonstrate the importance of high-order Coulomb correlations. Our model, which is based mainly on symmetry considerations, takes into account more complicated band structure effects in a general way. The model is able to state whether the polarization of the response is stationary or not if we know the polarization states of three incoming pulses. If the polarization of the FWM signal is stationary, the model is able to predict its state. Although we present dependence of the polarization of the FWM response on the polarizations of the excitation beams for a particular case of a bulk hexagonal crystal in Tables 3–6, the general result is represented by Eqs. (19)–(21). The model is then adapted for the systems of various symmetries, where e.g. dipole-forbidden excitonic states contribute to the FWM response.

The model takes into account the strong exciton–photon coupling, therefore we assume polaritons as the elementary excitations of a crystal. This allows us to describe the system without using a perturbation theoretical approach and to determine the optical response to the excitating optical fields at any arbitrary photon energy: this means one can equally well work close to resonance or off resonance.

2. Model

The requirements on our model are the following: it should give correct predictions of the polarization state of the FWM signal in any arbitrary FWM direction if we assume a weak excitation of an intrinsic crystal by three optical pulses. The polarization states of the excitation pulses are arbitrary as well as their respective time delays. We do not require prediction of the dynamics of the polarization of the FWM signal. The model therefore states if the polarization of the FWM signal is either non-stationary or stationary (and gives then the stationary polarization prediction). The model should be as simple as possible but must take into account symmetry properties of the system under investigation (crystal symmetry plus stationary external fields).

In this work we follow the concept of the WIBM [24,26] which uses a simplified approach to the interacting electron–hole system when compared to a rigorous formulation. According to the WIBM model and Refs. [28–30], we describe electron–hole pairs as bosons (excitons) with a fractional Fermi character. Every boson denoted by its spin number and wave vector interacts weakly with other bosons. The state of a crystal is then either a vacuum state or an m-boson state. The vacuum state means that no bosons are excited, the m-boson state corresponds to m excited bosons. Following Bott et al. [8] we assign an energetical level to every m-boson state and the wave function of this state is given by a direct product of the wave functions of the excited bosons. It has been shown that the third-order FWM response is due to m-particle states of m up to two. Therefore, in the following text, we truncate the system of levels above the two-particle states.

Excitons are created by absorption of a photon. The fermionic nature of excitons reveals in PB and exciton–exciton scattering. It is possible to create two excitons with identical quantum numbers but they interact repulsively and thus the oscillator strength for the creation of the second exciton is decreased (in particular, in QWs). The exciton–exciton scattering is described as an interaction of two electron–hole pairs and we keep the possibility of exchange of either electrons or holes between the interacting excitons [21], what is beyond the bosonic approximation of excitons. Exchange of fermions leads to a change of the exciton momenta and also of the spin state. Since dipole active excitons interact strongly with the optical field, one should rather consider polaritons than excitons as elementary excitations of the crystal. Then, consistently, molecules of excitons will be described in terms of Ivanov's model of bipolaritons [31,32]. We denote the "two-polariton states" as to be states from a continuum composed of two polaritons with well-defined particular wave vectors in the following. The "bipolariton states" are then the discrete bound states of two polaritons.

The interactions involved in the model are following:

- Creation of a polariton on the crystal boundary by absorption of one photon coming from the outside of the crystal.
- Annihilation of a polariton at the crystal boundary; the energy is transferred to an outgoing photon.
- PB due to the fractional Fermi character of polaritons.
- Polariton–polariton scattering involving the excitonic part of the polariton wave function.

We assume here that the interaction with all external fields is already included in the basis of polariton wave functions—we assume that this basis diagonalizes the Hamiltonian in the absence of non-stationary fields. We furthermore assume that the interaction with impurities, phonons, etc. causes loss of coherence and does not affect the polarization state of the FWM signal. In the following, we develop a mathematical description of the polariton spin state in the framework of the assumptions listed above.

2.1. Polariton spin and creation

In order to minimize the complexity of discussion of the spin of excitons, we neglect wave vector-dependent exchange interactions [33]. This is possible if one assumes a semiconductor with a direct gap at the Γ point and that the wave vectors of the excitons are sufficiently small. Then, the excitonic spin state is determined by the spin of an electron from a conduction band (we assume it is M times degenerate at the Γ point) and the spin of a hole from a valence band (N times degenerate at the Γ point). Excitons can thus be in $M \times N$ different spin states.

Following Refs. [33,34], we calculate symmetrized wave functions of excitons at the Γ point. We express the excitonic Hamiltonian in this basis including external stationary fields. We then diagonalize the Hamiltonian and find a new set of basis functions $|\alpha_j\rangle, j = 1, \ldots, M \times N$.

Because of the strong dipole interaction, some of the excitons interact with photons giving rise to polaritons which conserve the spin of the exciton contained by the polariton wave function. We will use a short notation for these polariton wave functions $|\alpha_j \boldsymbol{k}\rangle$, $j = 1, \ldots, M \times N$, characterized by the wave vector $\boldsymbol{k}$.

Concerning an infinite crystal, polaritons are the eigenstates of the Hamiltonian describing an excited electron–hole system. Real crystals are, however, limited in space and thus polaritons couple to an external electromagnetic field—an "external" photon can be annihilated while a polariton is created and vice versa. Strength of coupling between the electromagnetic field and a final state can be expressed as

$$f(\boldsymbol{k}', \boldsymbol{k}) = \mu_S \mathscr{E}_{\boldsymbol{k}'} \langle S|\boldsymbol{e}\rangle \delta[\boldsymbol{k} - \boldsymbol{q}_{\mathrm{LPB}}(n\boldsymbol{k}')], \tag{1}$$

where $\boldsymbol{k}'$ and $\boldsymbol{k}$ are the wave vectors of the external electromagnetic field and a polariton, respectively, $\mathscr{E}_{\boldsymbol{k}'}$ is the amplitude of an external electromagnetic field, $\boldsymbol{e}$ and $|S\rangle$ are the spin vectors of the electromagnetic field and the polariton, respectively, δ is a delta function, μ_S is the dipole matrix element for the polariton with the spin S, $\boldsymbol{q}_{\mathrm{LPB}}(n\boldsymbol{k}')$ is the wave vector of a polariton associated with the appropriate photon wave vector [35] and n is the refractive index connected with the background dielectric constant of the crystal. We assume for clarity that the system is not excited above the fundamental excitonic resonance allowing excitation of the lower polariton branch only.

2.2. Pauli blocking

PB due to the fractional Fermi character of polaritons and Coulomb scattering [13–15,36] are the main interactions giving rise to FWM, and we describe them separately. All other interactions are assumed to be too weak in order to change the polarization state of the FWM signal. They may be described by spin-independent relaxation times in a dynamical model. In this subsection, we describe our approach to the description of PB.

According to the WIBM model, we describe PB by assuming changes of the strength of coupling between the electromagnetic field and a two-polariton state compared to the strength of coupling between the field and a one-polariton state (1). In order to estimate its strength, we approximate the dipole matrix elements for transitions from a one-polariton state with spin S and wave vector $\boldsymbol{K}$ to a two-polariton state with a new polariton having the spin S' and the wave vector $\boldsymbol{k}$ by a photon with the wave vector $\boldsymbol{k}'$ and the spin $\boldsymbol{e}$ by the formula:

$$f^{(2)}(\boldsymbol{k}', \boldsymbol{k}) \approx \mu_{S'} \mathscr{E}_{\boldsymbol{k}} \delta[\boldsymbol{k} - \boldsymbol{q}_{\mathrm{LPB}}(n\boldsymbol{k}')] \times \left[\langle S'|\boldsymbol{e}\rangle - v \sum_j |\langle S|\boldsymbol{e}_j\rangle|^2 \langle S'|\boldsymbol{e}_j\rangle \right], \tag{2}$$

where $v > 0$ is a coefficient of the blocking, summation in the last term goes over all orthonormal elements of the polariton spin basis. The last term $[\langle S'|\boldsymbol{e}\rangle - v\sum_j |\langle S|\boldsymbol{e}_j\rangle|^2 \langle S'|\boldsymbol{e}_j\rangle]$ can be directly calculated from the Hamiltonian given in Ref. [25] (volume normalization is included in v).

2.3. Polariton–polariton Coulomb scattering

Scattering of two polaritons is determined by the Coulomb interaction (both direct and exchange) of their excitonic parts. At this point, the excitons must be decomposed into fermions—to the electron–hole pairs. Coulomb interaction of two excitons then must be understood as the interaction of four fermions. There are two possibilities of the elastic scattering process:

$$(e_1, h_1)_{\boldsymbol{k}_1} + (e_2, h_2)_{\boldsymbol{k}_2} \to (e_1, h_1)_{\boldsymbol{k}_1 + \boldsymbol{q}} + (e_2, h_2)_{\boldsymbol{k}_2 - \boldsymbol{q}}, \tag{3}$$

$$(e_1, h_1)_{\boldsymbol{k}_1} + (e_2, h_2)_{\boldsymbol{k}_2} \to (e_1, h_2)_{\boldsymbol{k}_1 + \boldsymbol{q}} + (e_2, h_1)_{\boldsymbol{k}_2 - \boldsymbol{q}}, \tag{4}$$

where the parentheses denote excitons with appropriate wave vectors in the subscripts and letters e_i and h_j denote an electron from the ith exciton and a hole from the jth exciton, respectively. The vector $\boldsymbol{q}$ is the exchanged momentum. Interaction (3) is the interaction of two bosons which change their momenta but their spins are conserved. Interaction (4) takes explicitly the composite character of the interacting bosons into account: two incoming excitons exchange either electrons or holes. Simultaneously with the exchange of fermions, they exchange momentum and spin. The exchange of fermions is therefore able to change the spin state of the contributing bosons.

There are three types of exciton–exciton interactions: [37]: boson–boson direct scattering, boson–boson exchange and exchange of fermions. It was shown in Ref. [30] that the exchange of fermions is the dominant interaction in the limit of the small wave vectors $\boldsymbol{k}_j$ and small exchanged momentum $\boldsymbol{q}$. We therefore assume in the following that only the exchange of fermions is an effective polariton–polariton scattering process unless it is forbidden—in such case, boson–boson direct scattering must be taken into account.

The Hamiltonian for fermion exchange has the form [37]

$$H_{SS'}^{S_f S_f'} = \mathscr{S}_{\mathrm{exch}}^{\mathrm{e}}(S_f, S_f', S, S') H_{\mathrm{exch}}^{\mathrm{e}}(\boldsymbol{Q}, \boldsymbol{Q}', \boldsymbol{q}) + \mathscr{S}_{\mathrm{exch}}^{\mathrm{h}}(S_f, S_f', S, S') H_{\mathrm{exch}}^{\mathrm{h}}(\boldsymbol{Q}, \boldsymbol{Q}', \boldsymbol{q}), \quad (5)$$

$$\mathscr{S}_{\mathrm{exch}}^{\mathrm{e}}(S_f, S_f', S, S') = \sum_{s_e s_e'} \sum_{j_h j_h'} \langle s_e, j_h | S \rangle \langle s_e', j_h' | S' \rangle \times \langle S_f | s_e' j_h \rangle \langle S_f' | s_e, j_h' \rangle, \quad (6)$$

$$\mathscr{S}_{\mathrm{exch}}^{\mathrm{h}}(S_f, S_f', S, S') = \mathscr{S}_{\mathrm{exch}}^{\mathrm{e}}(S_f, S_f', S', S). \quad (7)$$

The sums are performed over the spin states of electrons (s_e, s_e') and holes (j_h, j_h'). The variables S, S' and S_f, S_f' denote the initial and the final spin states of the incoming and the outgoing excitons, respectively. Functions $\mathscr{S}_{\mathrm{exch}}^{\mathrm{e,h}}$ stand for the spin-dependent part of the Hamiltonian while the operators $H_{\mathrm{exch}}^{\mathrm{e,h}}$ describe the wave vector-dependent part of the Hamiltonian: $\boldsymbol{Q}$ and $\boldsymbol{Q}'$ are the wave vectors of the incoming excitons and $\boldsymbol{q}$ is the exchanged momentum. We show results of calculations of the spin part of the exchange of electrons in Tables 1 and 2 for crystals with wurtzite structure (the spin basis is defined in Ref. [34]). We show for clarity only results for dipole active excitons even though dipole inactive states must be, in addition, considered throughout all calculations in the model. We consider linear polarization for the incoming and the outgoing polaritons with combinations of spins "X" and "Y" (Table 1) or circular polarization with combinations of spins "+" $= (X + \mathrm{i}Y)/\sqrt{2}$ and "−" $= (X - \mathrm{i}Y)/\sqrt{2}$ (Table 2).

In order to describe correctly Coulomb scattering from an initial to a final state, one has to clearly distinguish different scattering channels. Depending on the number of scattering events, one should discriminate between direct scattering from the initial to the final state and multiple-step processes which include one or more intermediate (two-polariton) states. Outside the bipolariton resonance, direct scattering is the most important since we assumed only a weak exciton–exciton interaction. The situation differs when assuming both the initial and final states resonant with the bipolariton where the Coulomb interaction causes strong coupling and leads to bipolariton-mediated scattering. Such processes will be described using the bipolariton model [31,32, Hamiltonian (3.4) therein].

Table 1
The spin part of the electron exchange between two polaritons, from Eq. (6) for spins in the direction of the principal axes

$\langle S_f S_f' \lvert \mathscr{S}_{\mathrm{exch}}^{\mathrm{e}} \rvert SS' \rangle$	$\lvert XX \rangle$	$\lvert XY \rangle$	$\lvert YX \rangle$	$\lvert YY \rangle$
$\langle XX \rvert$	$\frac{1}{2}$	0	0	$-\frac{1}{2}$
$\langle XY \rvert$	0	$\frac{1}{2}$	$\frac{1}{2}$	0
$\langle YX \rvert$	0	$\frac{1}{2}$	$\frac{1}{2}$	0
$\langle YY \rvert$	$-\frac{1}{2}$	0	0	$\frac{1}{2}$

The rows stand for the initial states and the columns for the final states.

Table 2
Same as Table 1 for circular spins of the polaritons

$\langle S_f S_f' \lvert \mathscr{S}_{\mathrm{exch}}^{\mathrm{e}} \rvert SS' \rangle$	$\lvert ++ \rangle$	$\lvert +- \rangle$	$\lvert -+ \rangle$	$\lvert -- \rangle$
$\langle ++ \rvert$	1	0	0	0
$\langle +- \rvert$	0	0	0	0
$\langle -+ \rvert$	0	0	0	0
$\langle -- \rvert$	0	0	0	1

2.4. FWM signal creation

In order to discuss the FWM signal creation in the framework of our model, we assume highly directional excitation pulses with wave vectors $\boldsymbol{k}_1'$, $\boldsymbol{k}_2'$, $\boldsymbol{k}_3'$ and polarizations ϕ_1, ϕ_2 and ϕ_3, respectively, arriving at the crystal's surface at times $t_1 < t_2 < t_3$. Although we are going to build up only an algebraic formalism to study the polarization of the FWM signal (but not its dynamics), we need the density matrix formalism in order to explain the mechanism of the generation of the signal. Then we can determine which coherences are non-zero after the excitation. Coherences are given as usual by the non-diagonal elements of the density matrix and populations as the diagonal elements. We use the notation $\varrho(|a\rangle, |b\rangle)$ for a slowly varying envelope of the coherence between the states $|a\rangle$ and $|b\rangle$.

We have defined above the system of levels which is capable for description of any arbitrary state of the polaritons inside a crystal. This definition is in full agreement with the usual procedure [8]. In order to describe the bipolariton-mediated scattering, it is necessary to include the bipolariton state which is a superposition of the two-polariton states. It has, on the contrary to general two-polariton states, a well-defined symmetry.

Now we discuss the evolution of the coherences connected with the excitation pulses. Before any of the pulses arive, the crystal is in the ground state and all coherences are zero. After the impact of the first pulse, correlations between the ground state and the states with the wave vectors around $\boldsymbol{k}_1 = \boldsymbol{q}_{\mathrm{LPB}}(n\boldsymbol{k}_1')$ are excited. We have to consider selection rules for spin:

$$\varrho(|\alpha_j \boldsymbol{k}_1\rangle, |0\rangle) \propto \frac{\mathrm{i}}{\hbar} \mu_{\alpha_j} \mathscr{E}_{\boldsymbol{k}_1'} \langle \alpha_j | \phi_1 \rangle. \quad (8)$$

The action of the second pulse is more complicated—it creates two types of coherences: one between the ground state and the two-polariton states and the second (called the "spin coherence") between two one-polariton states. The PB affects only the first mentioned coherence and we can write

$$\varrho(|\alpha_j \boldsymbol{k}_1\rangle |\alpha_\ell \boldsymbol{k}_2\rangle, |0\rangle) \propto -\frac{\mu_{\alpha_j} \mu_{\alpha_\ell}}{\hbar^2} \mathscr{E}_{\boldsymbol{k}_1'} \mathscr{E}_{\boldsymbol{k}_2'} \langle \alpha_j | \phi_1 \rangle \langle \alpha_\ell | \phi_2 \rangle \times (1 - v \langle \alpha_\ell | \alpha_j \rangle), \quad (9)$$

$$\varrho(|\alpha_j \boldsymbol{k}_1\rangle, |\alpha_\ell \boldsymbol{k}_2\rangle) \propto \frac{\mu_{\alpha_j}\mu^*_{\alpha_\ell}}{\hbar^2}\, \mathscr{E}_{\boldsymbol{k}'_1}\mathscr{E}^*_{\boldsymbol{k}'_2}\langle\alpha_j|\phi_1\rangle\langle\phi_2|\alpha_\ell\rangle. \tag{10}$$

On the level of two-polariton states, polaritons can interact via Coulomb interaction and can scatter to other two-polariton states. The spin coherences correlate only one-polariton states which do not undergo any changes except dephasing. The polariton–polariton interaction causes (as a first-order perturbation) creation of coherences:

$$\varrho(|\alpha_j \boldsymbol{k}_1 + \boldsymbol{q}\rangle|\alpha_\ell \boldsymbol{k}_2 - \boldsymbol{q}\rangle, |0\rangle) \propto \mathscr{S}(\alpha_j, \alpha_\ell, \alpha_m, \alpha_n)\varrho(|\alpha_m \boldsymbol{k}_1\rangle|\alpha_n \boldsymbol{k}_2\rangle, |0\rangle), \tag{11}$$

$$\varrho(|\alpha_j \boldsymbol{k}_1 + \boldsymbol{q}\rangle|\alpha_\ell \boldsymbol{k}_2 - \boldsymbol{q}\rangle, |\alpha_o \boldsymbol{k}_3\rangle) \propto \mathscr{S}(\alpha_j, \alpha_\ell, \alpha_m, \alpha_n)\varrho(|\alpha_m \boldsymbol{k}_1\rangle|\alpha_n \boldsymbol{k}_2\rangle, |\alpha_o \boldsymbol{k}_3\rangle), \tag{12}$$

i.e. the initial two-polariton state with appropriate wave vectors and spins scatters to a different two-polariton state by fermion exchange. The polaritons exchange some momentum and in general, they can change their spins. The polariton–polariton interaction should be evaluated up to an infinite order but according to the above discussion of polariton–polariton scattering, we use the first-order perturbation theory (where interaction of the bosonized polaritons is the perturbation) for metastable scattering states (which are not resonant with bipolaritons) because we assume only weak polariton–polariton interactions. For the two-polariton states resonant with a bipolariton state, we consider the bipolariton-mediated scattering in addition to the first-order process:

$$\varrho(|\Gamma_s \boldsymbol{k}_1 + \boldsymbol{k}_2\rangle, |0\rangle) \propto \mathscr{M}(\alpha_j, \alpha_\ell, \Gamma_s)\varrho(|\alpha_j \boldsymbol{k}_1\rangle|\alpha_\ell \boldsymbol{k}_2\rangle, |0\rangle), \tag{13}$$

$$\varrho(|\alpha_m \boldsymbol{k}_1 + \boldsymbol{q}\rangle|\alpha_n \boldsymbol{k}_2 - \boldsymbol{q}\rangle, |0\rangle) \propto \mathscr{M}^*(\alpha_m, \alpha_n, \Gamma_s)\varrho(|\Gamma_s \boldsymbol{k}_1 + \boldsymbol{k}_2\rangle, |0\rangle), \tag{14}$$

where $|\Gamma_s \boldsymbol{K}\rangle$ denotes the bipolariton state with a symmetry Γ_s and a wave vector $\boldsymbol{K}$ and $\mathscr{M}(\alpha_j, \alpha_\ell, \Gamma_s)$ stands for the coupling coefficient between the bipolariton with the symmetry Γ_s and the two-polariton state where the polaritons have spins $\alpha_{j,\ell}$. The coupling coefficient reflects the spin structure of the bipolariton [33]. We note that the usage of the bipolariton model does not make any difference in the selection rules for the bipolariton creation when compared to the more traditional giant oscillator strength model.

Coulomb scattering causes creation of two-polariton states with a very big spread of the individual wave vectors. These states decay radiatively and contribute to a luminescence signal. The highly directional third pulse can cause induced decay of one polariton from the two-polariton state and because of wave vector conservation, a one-polariton state with the wave vector $\boldsymbol{k}_D = \boldsymbol{k}_1 + \boldsymbol{k}_2 - \boldsymbol{k}_3$ is left in the crystal. Finally, this polariton is radiated as the FWM signal. The third pulse can also form a two-polariton state with a polariton with the wave vector $\boldsymbol{k}_1$ and because of the previous correlation to the state with the wave vector $\boldsymbol{k}_2$, a scattered two-polariton state $|\beta_1 \boldsymbol{k}_2\rangle|\beta_2 \boldsymbol{k}_1 - \boldsymbol{k}_2 + \boldsymbol{k}_3\rangle$ is forced to decay to the one-polariton state $|\beta_2 \boldsymbol{k}_1 - \boldsymbol{k}_2 + \boldsymbol{k}_3\rangle$ and the FWM signal in the direction $\boldsymbol{k}_1 - \boldsymbol{k}_2 + \boldsymbol{k}_3$ is emitted from the crystal. The initial coherence $\varrho(|\alpha_j \boldsymbol{k}_1\rangle, |\alpha_\ell \boldsymbol{k}_2\rangle)$ also allows creation of the signal in the direction $-\boldsymbol{k}_1 + \boldsymbol{k}_2 + \boldsymbol{k}_3$. The coherences responsible for the FWM signal are thus $\varrho(|\alpha_j \boldsymbol{k}_1\rangle|\alpha_\ell \boldsymbol{k}_2\rangle, |\alpha_m \boldsymbol{k}_3\rangle)$ with cyclic permutation of the indices j, ℓ, m and $1, 2, 3$. We can express

$$\varrho(|\alpha_j \boldsymbol{k}_D\rangle|\alpha_\ell \boldsymbol{k}_3\rangle, |\alpha_m \boldsymbol{k}_3\rangle) \propto \mu^*_{\alpha_m}\mathscr{E}^*_{\boldsymbol{k}'_3}\langle\phi_3|\alpha_m\rangle\varrho(|\alpha_j \boldsymbol{k}_D\rangle|\alpha_\ell \boldsymbol{k}_3\rangle, |0\rangle) + \mathscr{S}(\alpha_j, \alpha_\ell, \alpha_n, \alpha_o)\varrho(|\alpha_n \boldsymbol{k}_1\rangle|\alpha_o \boldsymbol{k}_2\rangle, |\alpha_m \boldsymbol{k}_3\rangle). \tag{15}$$

The coupling of the radiated FWM signal with the spin ϕ to the above coherence is then

$$\mu^*_{\alpha_j}\langle\phi|\alpha_j\rangle\langle\alpha_m|\alpha_\ell\rangle\varrho(|\alpha_j \boldsymbol{k}_D\rangle|\alpha_\ell \boldsymbol{k}_3\rangle, |\alpha_m \boldsymbol{k}_3\rangle). \tag{16}$$

Because of possibility of permutation of indices in the above formulas, the polarization of the FWM signal induced by Coulomb scattering is independent of the order of the pulses in time but leads to different directions of diffraction.

The signal induced by the PB is now calculated separately. The origin of the signal is in a diffraction of one of the pulses by a population grating created by the two other pulses. On the contrary to atomic systems and OBE, the probability of transition to two-polariton states is non-zero but its strength is reduced (2) compared to transitions to one-polariton states.

Let us discuss, as an example, the mechanism of this contribution to wave mixing in the direction $\boldsymbol{k}_1 - \boldsymbol{k}_2 + \boldsymbol{k}_3$. The first pulse creates polarization with spin ϕ_1. The second pulse creates population grating (of one-polariton states) if $\langle\phi_1|\phi_2\rangle \neq 0$ with the spin

$$|\phi_G\rangle = \sum_j |\alpha_j\rangle\langle\alpha_j|\phi_1\rangle\langle\phi_2|\alpha_j\rangle. \tag{17}$$

The last pulse then correlates the one-polariton states with the ground and the two-polariton states. In the case of $\langle\phi_G|\phi_3\rangle \neq 0$, some of the induced coherences have the wave vector in the FWM direction $\boldsymbol{k}_1 - \boldsymbol{k}_2 + \boldsymbol{k}_3$ and the amplitude of the FWM signal is then proportional to the sum of the appropriate coherences. Due to the fractional Fermi character of polaritons, the sum is non-zero and it can be shown that the third-order response spin state of the diffracted polariton is given by

$$|\psi\rangle = \sum_j |\alpha_j\rangle\langle\alpha_j|\phi_1\rangle\langle\phi_2|\alpha_j\rangle\langle\alpha_j|\phi_3\rangle \tag{18}$$

and for the other directions by the cyclic permutation of indices. Independent of the value of the parameter v, for $t_1 < t_2 < t_3$ and no temporal overlap of the excitation pulses, the response is zero in the direction $\boldsymbol{k}_D = \boldsymbol{k}_1 + \boldsymbol{k}_2 - \boldsymbol{k}_3$ since two contributions of the same magnitude cancel each other.

2.5. Calculation of the spin

We separate the problem into four subproblems: the Coulomb scattering channel (direct and exchange part), the bipolariton channel and the PB channel. We calculate the polarization state of all four contributions to the FWM response and finally compare them. If the signals are non-zero and are not in the same spin state, the conclusion is that the spin state of the FWM response is not stationary and labelled "determined by dynamics" (*dbd.*) similar to Ref. [18].

As we have seen in the previous discussion, we use a closed set of wave vectors in order to describe all coherences which contribute in creation of the third-order FWM signal. We then restrict ourselves only to the wave vectors given by the wave vectors of the excitation beams and the diffracted beams in the FWM direction. Every beam is then assumed to be represented by a plane wave—this simplification does not change predictions of the spin of the FWM signal.

Let us consider the exciton spin basis $|\alpha_j\rangle$ which diagonalizes the exciton Hamiltonian including external fields and various types of exchange interactions and also let us consider the polarization of the ℓth optical field to be ϕ_ℓ. At the Γ point of the reciprocal lattice, there are (in the absence of external fields) well-resolved dipole-active and dipole-inactive states, respectively. Including wave vector-dependent exchange interaction and external fields, the eigenstates of the Hamiltonian are the admixtures of the states at the Γ point and therefore all exciton states can become dipole-active and therefore their contribution is included in the model. Then we define $|\phi_\ell \boldsymbol{k}_\ell\rangle$ to be the superposition of the spin eigenstates which is excited by the ℓth optical field. We can then draw a level scheme depicted in Fig. 1 which represents the interactions leading to the FWM signal creation via the scattering process. With the help of Fig. 1 and Eq. (18), we can derive equations for

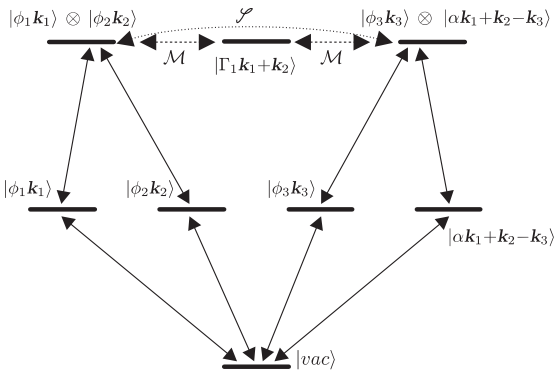

Fig. 1. Level scheme appropriate for the scattering and bipolariton channels if the incoming pulses are coupled to polaritons with spins ϕ_j. The full lines represent dipole interactions, dashed lines bipolariton formation and annihilation and dotted line stands for polariton–polariton off-resonant scattering path.

determination of the FWM polarization in a compact form (it can be shown that these equations are equivalent to Eqs. (13)–(16) and (18)):

$$|\psi^{\mathrm{D}}\boldsymbol{k}_{\mathrm{D}}\rangle = \boldsymbol{P}_{\boldsymbol{k}_{\mathrm{D}}} \sum_j \mathscr{S}(\alpha_j, \phi_3, \phi_1, \phi_2)|\alpha_j \boldsymbol{k}_{\mathrm{D}}\rangle$$

for the first-order polariton−polariton scattering, (19)

$$|\psi^{\mathrm{B}}\boldsymbol{k}_{\mathrm{D}}\rangle = \boldsymbol{P}_{\boldsymbol{k}_{\mathrm{D}}} \sum_j \mathscr{M}(\phi_1, \phi_2, \Gamma_{\mathrm{s}})\mathscr{M}^*(\alpha_j, \phi_3, \Gamma_{\mathrm{s}})|\alpha_j \boldsymbol{k}_{\mathrm{D}}\rangle$$

for the bipolariton-mediated scattering (resonant with the bipolariton Γ_{s}), (20)

$$|\psi^{\mathrm{F}}\boldsymbol{k}_{\mathrm{D}}\rangle = \boldsymbol{P}_{\boldsymbol{k}_{\mathrm{D}}} \sum_j \langle\alpha_j|\phi_1\rangle\langle\alpha_j|\phi_2\rangle\langle\phi_3|\alpha_j\rangle|\alpha_j \boldsymbol{k}_{\mathrm{D}}\rangle$$

for the PB, (21)

$\boldsymbol{P}_{\boldsymbol{q}}$ is the projection operator of the (polariton) spin to the spin states of a photon propagating in the direction $\boldsymbol{q}$. We get the stationary response only when the allowed states $|\alpha \boldsymbol{k}_{\mathrm{D}}\rangle$ and states in the superpositions $|\phi_\ell \boldsymbol{k}_\ell\rangle$ have equal energies and when all three spins given by the formulas (19)–(21) are equal. For other than $\boldsymbol{k}_{\mathrm{D}}$ diffraction direction, we find the appropriate formulas by permutation of indices.

3. Discussion

As we have shown in the previous section, the polarization state of the FWM response is given by contributions from three different processes: polariton–polariton scattering, bipolariton-mediated scattering and phase space filling. As an example, we calculate polarizations of all contributions to the FWM signal for an isotropic crystal with a bipolariton having Γ_1 symmetry. We assume that all excitation optical fields propagate almost in the same direction. This example corresponds to a bulk hexagonal crystal with wurtzite structure (ZnO, CdS, CdSe, GaN) when the optical beams are parallel to the main axis and we spectrally resolve only the FWM response from one of three excitonic series.

The results are summarized in Tables 3–6. We list results for all combinations of circular and linear polarizations of the incoming beams and for all three diffraction directions. We give spins of particular channels in the tables and also the spin of the overall response. The meaning of the symbol "*dbd.*" is that the state and dynamics of the resulting spin of the FWM response depends on material constants and cannot be determined from symmetry considerations alone.

Table 3 presents calculated polarizations of the FWM response for three linearly polarized excitation pulses. Spins of FWM responses for one circularly and two linearly polarized incoming pulses are listed in Table 4, two circularly and one linearly polarized pulse give the response summarized in Table 5 and Table 6 stands for three circularly polarized excitation pulses. Every cell in the tables is appropriate for some combination of polarizations

Table 3
Polarization of the FWM signal for three linearly polarized excitation pulses

$\boldsymbol{k}_1$	$\boldsymbol{k}_2$	$\boldsymbol{k}_3$	$-\boldsymbol{k}_1+\boldsymbol{k}_2+\boldsymbol{k}_3$		$\boldsymbol{k}_1-\boldsymbol{k}_2+\boldsymbol{k}_3$		$\boldsymbol{k}_1+\boldsymbol{k}_2-\boldsymbol{k}_3$	
X'	X'	X'	X'	X'	X'	X'	X'	X'
			X'	$\boldsymbol{X'}$	X'	$\boldsymbol{X'}$	X'	$\boldsymbol{X'}$
X'	X'	Y'	Y'	0	Y'	0	Y'	Y'
			0	$\boldsymbol{Y'}$	0	$\boldsymbol{Y'}$	0	$\boldsymbol{Y'}$
X'	Y'	Y'	X'	X'	X'	0	X'	0
			0	$\boldsymbol{X'}$	0	$\boldsymbol{X'}$	0	$\boldsymbol{X'}$
Y'	Y'	Y'	Y'	Y'	Y'	Y'	Y'	Y'
			Y'	$\boldsymbol{Y'}$	Y'	$\boldsymbol{Y'}$	Y'	$\boldsymbol{Y'}$

The meaning of the letters in each box is following: the upper left corner is the response of the scattering channel, the upper right corner is the response from the bipolariton channel, the lower left corner is the response from the Pauli blocking and the lower right corner gives the overall polarization.

Table 4
Polarization of the FWM signal for two linearly polarized and one circularly polarized excitation pulses

$\boldsymbol{k}_1$	$\boldsymbol{k}_2$	$\boldsymbol{k}_3$	$-\boldsymbol{k}_1+\boldsymbol{k}_2+\boldsymbol{k}_3$		$\boldsymbol{k}_1-\boldsymbol{k}_2+\boldsymbol{k}_3$		$\boldsymbol{k}_1+\boldsymbol{k}_2-\boldsymbol{k}_3$	
X'	X'	σ^+	*dbd.*	X'	*dbd.*	X'	*dbd.*	σ^-
			X'	***dbd.***	X'	***dbd.***	X'	***dbd.***
X'	Y'	σ^+	*dbd.*	X'	*dbd.*	Y'	σ^+	0
			0	***dbd.***	0	***dbd.***	0	σ^+
Y'	X'	σ^+	*dbd.*	Y'	*dbd.*	X'	σ^+	0
			0	***dbd.***	0	***dbd.***	0	σ^+
Y'	Y'	σ^+	*dbd.*	Y'	*dbd.*	Y'	*dbd.*	σ^-
			Y'	***dbd.***	Y'	***dbd.***	Y'	***dbd.***

of the excitation pulses (rows) and diffraction direction (columns). The symbols in boxes stand for (from left and top) the polarization coming from the polariton–polariton scattering channel, Γ_1 bipolariton, PB and the overall response. Symbols $\sigma^{\pm}$ denote circular polarizations, X' some arbitrary linear polarization and Y' linear polarization perpendicular to X'. The present model is capable to predict polarizations of the particular channels but gives no information about the relative strengths of the responses. We can, however, state that the response is determined mainly by the exciton–exciton scatterings (without bipolaritons) and PB when working in resonance with excitons or by the bipolariton channel when bipolaritons are resonantly excited.

Tables 3 and 6 (linear and circular polarizations of the excitation beams, respectively) do not contain any *dbd.* terms due to the symmetry of the considered crystal.

Table 5
Polarization of the FWM response for two circularly and one linearly polarized excitation pulse

$\boldsymbol{k}_1$	$\boldsymbol{k}_2$	$\boldsymbol{k}_3$	$-\boldsymbol{k}_1+\boldsymbol{k}_2+\boldsymbol{k}_3$		$\boldsymbol{k}_1-\boldsymbol{k}_2+\boldsymbol{k}_3$		$\boldsymbol{k}_1+\boldsymbol{k}_2-\boldsymbol{k}_3$	
σ^+	σ^+	X'	*dbd.*	σ^-	*dbd.*	σ^-	σ^+	0
			σ^+	***dbd.***	σ^+	***dbd.***	σ^+	$\boldsymbol{\sigma^+}$
σ^+	σ^-	X'	σ^-	σ^-	σ^+	σ^+	*dbd.*	X'
			0	$\boldsymbol{\sigma^-}$	0	$\boldsymbol{\sigma^+}$	0	***dbd.***
σ^-	σ^+	X'	σ^+	σ^+	σ^-	σ^-	*dbd.*	X'
			0	$\boldsymbol{\sigma^+}$	0	$\boldsymbol{\sigma^-}$	0	***dbd.***
σ^-	σ^-	X'	*dbd.*	σ^+	*dbd.*	σ^+	σ^-	0
			σ^-	***dbd.***	σ^-	***dbd.***	σ^-	$\boldsymbol{\sigma^-}$

Table 6
Polarization of the FWM response for three circularly polarized pulses

$\boldsymbol{k}_1$	$\boldsymbol{k}_2$	$\boldsymbol{k}_3$	$-\boldsymbol{k}_1+\boldsymbol{k}_2+\boldsymbol{k}_3$		$\boldsymbol{k}_1-\boldsymbol{k}_2+\boldsymbol{k}_3$		$\boldsymbol{k}_1+\boldsymbol{k}_2-\boldsymbol{k}_3$	
σ^+	σ^+	σ^+	σ^+	0	σ^+	0	σ^+	0
			σ^+	$\boldsymbol{\sigma^+}$	σ^+	$\boldsymbol{\sigma^+}$	σ^+	$\boldsymbol{\sigma^+}$
σ^+	σ^+	σ^-	σ^-	σ^-	σ^-	σ^-	0	0
			0	$\boldsymbol{\sigma^-}$	0	$\boldsymbol{\sigma^-}$	0	**0**
σ^+	σ^-	σ^-	0	0	0	σ^+	0	σ^+
			0	**0**	0	$\boldsymbol{\sigma^+}$	σ^+	$\boldsymbol{\sigma^+}$
σ^-	σ^-	σ^-	σ^-	0	σ^-	0	σ^-	0
			σ^-	$\boldsymbol{\sigma^-}$	σ^-	$\boldsymbol{\sigma^-}$	σ^-	$\boldsymbol{\sigma^-}$

However, in an experimental situation in which one uses linear polarizations which are not perpendicular one to the other, responses of the particular channels may have different polarizations resulting in a non-stationary polarization of the overall response as shown experimentally in Refs. [1,11].

Looking at the other tables appropriate for mixed circular and linear polarizations, Tables 4 and 5, we may observe many *dbd.* terms caused mainly by polariton–polariton scattering. The reason is that the response of the direct and exchange scattering have different polarizations and the overall polarization cannot be evaluated using only symmetry considerations since the ratio of the strengths of the direct and exchange scatterings are crystal-dependent.

The tables of results reveal one very interesting fact: concerning the combination of polarizations XXY and the diffraction direction $\boldsymbol{k}_1+\boldsymbol{k}_2-\boldsymbol{k}_3$, one expects Y-polarized stationary signal. Contrary, for the $\sigma^+\sigma^+\sigma^-$ excitation, we expect no response in the selected direction. These expectations are in full agreement with the experimental results [12] but they were not sufficiently discussed using OBE. Our model, on the other hand, explains them in a

straightforward way. Let us assume a two-polariton state composed of polaritons with spins XX or $\sigma^+\sigma^+$. Using Tables 1 and 2 we find that the former can scatter to a two-polariton pair with spins YY while the latter cannot scatter to any two-polariton state where both spins are dipole-allowed (except $\sigma^+\sigma^+$). Thus, the former can be annihilated by a Y-polarized photon giving the Y response while the latter cannot be annihilated by a σ^--polarized photon and gives no response in the presented configuration. As the crucial point of the wave mixing lies in the polariton–polariton scattering, the spin mixing is due to exchange of fermions during this process. The composite character of the polaritons cannot be thus omitted in any model which deals with the spins of particles.

Our theory may be applied also to crystals with zinc-blende structure (GaAs, CuBr). FWM polarizations, summarized in Tables 3–6, are valid also for these crystals except for the bipolariton response. Besides the Γ_1 bipolariton, there are five more bipolariton states with symmetries $\Gamma_{3,5}$ [33] which significantly modify the evaluated polarizations. Bipolaritons with symmetries $\Gamma_{3,5}$ cause, for example, scattering from the two-polariton state $\sigma^+\sigma^+$ to $\sigma^-\sigma^-$ and thus the combination $\sigma^+\sigma^+\sigma^-$ gives the σ^- response in the forbidden direction $\boldsymbol{k}_1+\boldsymbol{k}_2-\boldsymbol{k}_3$. The resonant energy of the response then would coincide with the energy of the $\Gamma_{3,5}$ bipolaritons.

Since we did not verify our results experimentally and we did not find any relevant experimental study, we use the existing theory of Lindberg et al. [18] (calculation based on SBE) in order to demonstrate the accuracy of our model. We take our data for the FWM direction $\boldsymbol{k}_1+\boldsymbol{k}_2-\boldsymbol{k}_3$ and the contribution from the polariton–polariton scattering from Tables 3–6. The predicted polarizations agree in all cases with only one exception: combination of incoming fields $X'Y'\sigma^+$. Our model predicts a definite and stationary polarization whereas the microscopic model predicts *dbd*. in this case. We may explain this discrepancy by the fact that we consider $\boldsymbol{k}_1\approx\boldsymbol{k}_2\approx\boldsymbol{k}_3$ in our tables and therefore the exchanged momentum in the scattering process is $\boldsymbol{q}\approx 0$. In a general case, exchanged momentum would play some role in Tables 1 and 2 and would modify FWM polarizations. In particular, the response to the $X'Y'\sigma^+$ excitation would be *dbd*. but the other elements remain unchanged.

We did not discuss so far to which structures the theory is applicable. The major question is the dimensionality of the crystal since the recent research is focused mainly on low-dimensional structures. Besides the PB effect which is dimension-independent, the wave mixing is due to polariton–polariton scattering during which the sum of the wave vectors of interacting particles is conserved. This wave vector conservation is valid for all components of wave vectors in bulk crystals but only for in-plane wave vectors in QWs. In addition to the wave vector conservation, scattering conserves energy. We can therefore approximately assume that all components of wave vector are conserved during scattering involving also QWs but not quantum wires and quantum dots. The theory may thus be applied to bulk crystals and QWs.

4. Conclusions

We show in this paper that the polarization state of the FWM response is determined by the symmetries of exciton eigenstates and by the symmetry of the exciton–exciton interactions. We then present a model which takes all these symmetries into account and based on it, we derive simple algebraic equations by which the polarization of the FWM response can be determined.

For exciton–exciton interactions, we consider the three most important effects which take place in FWM experiments. We show that they may differ in the symmetry and thus they may give different polarizations in the response. The three respective contributions then interfere in the overall signal giving either stationary or non-stationary polarization. The present model is then capable to describe the stationary polarizations.

Compared to other theories, Eqs. (19)–(21) make the calculations of the FWM polarization simple and accurate. The accuracy of the model is supported in Section 3 by the comparison to a microscopic model [18]. Microscopic theories require, however, more complex calculations. Modified OBE, on the other hand, are as simple as the present model but they do not give the correct predictions for the signal polarization since dark states are omitted (we take them explicitly into account) and exciton–exciton interactions are not described including their symmetry properties.

As an example, we show the calculations for a wurtzite crystal without presence of any external fields in Tables 3–6. Besides these sample calculations, the model can be used for a system of an arbitrary symmetry where the symmetry of the crystal lattice, external fields and various types of exchange interactions may be taken into account.

The model is also useful for the reverse problem: how to set the polarizations of the incoming optical fields to observe a desired process. Based on the level scheme, the theory can be extended to a dynamical model which is able to describe also the dynamics of the polarization of the response.

We have shown that we can apply the theory to bulk crystals and QWs. Because of missing wave vector conservation rule in the structures with lower dimensionality, we cannot use the same model for quantum wires and quantum dots.

Acknowledgments

The authors are grateful to P. Malý and M. Gallart for helpful discussions. We thankfully acknowledge financial support in form of a Ph.D. grant for T. Ostatnický by the French Government. This work is a part of the research plan MSM 0021620834 that is financed by the Ministry of Education of the Czech Republic.

References

[1] O. Buccafusca, X. Chen, W.J. Walecki, A.L. Smirl, J. Opt. Soc. Am. B 15 (1998) 1218.
[2] D.-S. Kim, J. Shah, T.C. Damen, W. Schäfer, F. Janke, S. Schmitt-Rink, K. Köhler, Phys. Rev. Lett. 69 (1992) 2725.
[3] W. Schäfer, D.S. Kim, J. Shah, T.C. Damen, J.E. Cunningham, K.W. Goossen, L.N. Pfeiffer, K. Köhler, Phys. Rev. B 53 (1996) 16429.
[4] J. Shah, Ultrafast Spectroscopy of Semiconductors and Semiconductor Nanostructures, second ed., Springer, Berlin, 1999.
[5] S. Weiss, M.-A. Mycek, J.-Y. Bigot, S. Schmitt-Rink, D.S. Chemla, Phys. Rev. Lett. 69 (1992) 2685.
[6] G. Finkelstein, S. Bar-Ad, O. Carmel, I. Bar-Joseph, Y. Levinson, Phys. Rev. B 47 (1993) 12964.
[7] E.J. Mayer, G.O. Smith, V. Heuckeroth, J. Kuhl, K. Bott, A. Schulze, T. Meier, D. Bennhardt, S.W. Koch, P. Thomas, R. Hey, K. Ploog, Phys. Rev. B 50 (1994) 14730.
[8] K. Bott, O. Heller, D. Bennhardt, S.T. Cundiff, P. Thomas, E.J. Mayer, G.O. Smith, R. Eccleston, J. Kuhl, K. Ploog, Phys. Rev. B 48 (1993) 17418.
[9] K. Bott, E.J. Mayer, G.O. Smith, V. Heuckeroth, M. Hübner, J. Kuhl, T. Meier, A. Schulze, M. Lindberg, S.W. Koch, P. Thomas, R. Hey, K. Ploog, J. Opt. Soc. Am. B 13 (1996) 1026.
[10] E.J. Mayer, G.O. Smith, V. Heuckeroth, J. Kuhl, K. Bott, A. Schulze, T. Meier, S.W. Koch, P. Thomas, R. Hey, K. Ploog, Phys. Rev. B 51 (1995) 10909.
[11] A.L. Smirl, Semiconductor Quantum Optoelectronics, in: Proceedings of the 50th Scottish Universities Summer School in Physics, SUSSP Publications and Institute of Physics Publishing, Bristol, 1999.
[12] G.O. Smith, E.J. Mayer, V. Heuckeroth, J. Kuhl, K. Bott, T. Meier, A. Schulze, D. Bennhardt, S.W. Koch, P. Thomas, R. Hey, K. Ploog, Solid State Commun. 94 (1995) 373.
[13] P. Kner, W. Schäfer, R. Lövenich, D.S. Chemla, Phys. Rev. Lett. 81 (1998) 5386.
[14] Th. Östreich, K. Schönhammer, L.J. Sham, Phys. Rev. Lett. 74 (1995) 4698.
[15] Th. Östreich, K. Schönhammer, L.J. Sham, Phys. Rev. B 58 (1998) 12920.
[16] L.J. Sham, Th. Östreich, J. Lumin. 87–89 (2000) 179 and references therein.
[17] Y.Z. Hu, R. Binder, S.W. Koch, S.T. Cundiff, H. Wang, D.G. Steel, Phys. Rev. B 49 (1994) 14382.
[18] M. Lindberg, R. Binder, Y.Z. Hu, S.W. Koch, Phys. Rev. B 49 (1994) 16942.
[19] M. Lindberg, S.W. Koch, Phys. Rev. B 38 (1988) 3342.
[20] M. Lindberg, Y.Z. Hu, R. Binder, S.W. Koch, Phys. Rev. B 50 (1994) 18060.
[21] M.Z. Maialle, L.J. Sham, Phys. Rev. Lett. 73 (1994) 3310.
[22] S. Schmitt-Rink, S. Mukamel, K. Leo, J. Shah, D.S. Chemla, Phys. Rev. A 44 (1991) 2124.
[23] K. Victor, V.M. Axt, A. Stahl, Phys. Rev. B 51 (1995) 14164.
[24] T. Aoki, G. Mohs, M. Kuwata-Gonokami, A.A. Yamaguchi, Phys. Rev. Lett. 82 (1999) 3108.
[25] M. Kuwata-Gonokami, T. Aoki, C. Ramkumar, R. Shimano, Yu.P. Svirko, J. Lumin. 87–89 (2000) 162.
[26] Yu.P. Svirko, M. Shirane, H. Suzuura, M. Kuwata-Gonokami, J. Phys. Soc. Japan 68 (1999) 674.
[27] V.M. Axt, S.R. Bolton, U. Neukirch, L.J. Sham, D.S. Chemla, Phys. Rev. B 63 (2001) 115303 and references therein.
[28] V. Chernyak, S. Mukamel, J. Opt. Soc. Am. 13 (1996) 1302.
[29] J. Inoue, T. Brandes, A. Shimizu, Phys. Rev. B 61 (2000) 2863.
[30] S. Okumura, T. Ogawa, Phys. Rev. B 65 (2001) 035105.
[31] A.L. Ivanov, M. Hasuo, N. Nagasawa, H. Haug, Phys. Rev. B 52 (1995) 11017.
[32] A.L. Ivanov, H. Haug, L.V. Keldysh, Phys. Rep. 296 (1998) 237.
[33] B. Hönerlage, R. Lévy, J.B. Grun, C. Klingshirn, K. Bohnert, Phys. Rep. 124 (1985) 161.
[34] K. Cho, Phys. Rev. B 14 (1976) 4463.
[35] K. Henneberger, Phys. Rev. Lett. 80 (1998) 2889.
[36] H.P. Wagner, A. Schätz, W. Langbein, J.M. Hvam, A.L. Smirl, Phys. Rev. B 60 (1999) 4454.
[37] C. Ciuti, V. Savona, C. Piermarocchi, A. Quattropani, P. Schwendimann, Phys. Rev. B 58 (1998) 1998.

PHYSICAL REVIEW B **75**, 165311 (2007)

Electron- and hole-spin relaxation within excitons in GaAs quantum wells by non-degenerate pump-and-probe measurements

T. Ostatnický,[1,2] O. Crégut,[1] M. Gallart,[1] P. Gilliot,[1] B. Hönerlage,[1] and J.-P. Likforman[1,3,*]

[1]*IPCMS-GONLO, Université Louis Pasteur, CNRS UMR 7504, 23 Rue du Lœss, Boîte Postale 43, 67034 Strasbourg Cedex, France*

[2]*Faculty of Mathematics and Physics, Charles University, Ke Karlovu 3, 12116 Praha 2, Czech Republic*

[3]*Matériaux et Phénomènes Quantiques, CNRS UMR 7162, Université Paris VII, 10 Rue Alice Domont et Léonie Duquet, 75205 Paris Cedex 13 Paris, France*

(Received 4 April 2006; revised manuscript received 2 November 2006; published 12 April 2007)

We report on an experimental investigation of electron-, hole-, and exciton-spin relaxation times in intrinsic GaAs quantum wells. We present non-degenerate pump-and-probe measurements followed by a detailed analysis of the differential transmission spectra in order to identify different spin relaxation channels. Dynamics of spin relaxation is generally considered to be multiexponential and therefore a dynamical model taking into account four exciton states is used in order to determine the various relaxation times. In contrast to other experimental work, we also consider transitions to different biexciton states. This allows us to identify spin relaxation processes of electrons, holes, and excitons and to assign them fitted time constants.

DOI: 10.1103/PhysRevB.75.165311 PACS number(s): 72.25.Rb, 78.47.+p

INTRODUCTION

Spin dynamics has been one of the most intensively explored fields in semiconductor physics. Changes in spin orientations are observed experimentally using various methods of ultrafast laser spectroscopy including luminescence,[1] pump-and-probe spectroscopy,[2–5] four-wave mixing,[6,7] as well as other types of spectroscopies.[8,9] In this paper, we report on the observation of spin orientation changes of excitons, electrons, and holes in intrinsic GaAs quantum wells through non-degenerate pump-and-probe experiment at low temperature (4 K).

Differential transmittance (DT) in pump-and-probe experiments is usually considered to be caused by phase space filling and Coulomb interactions between optically excited electrons and holes. Spins of electrons and holes may relax on different time scales and therefore one expects at least two relaxation times in the observed spin-resolved differential transmittance.[2,7] Since electrons and holes bind to form excitons, there is an additional relaxation channel caused by long-range exchange interaction.[10] It corresponds to a simultaneous spin-flip of electron and hole. This relaxation channel will be denoted as exciton-spin relaxation (exciton spin-flip) in the following.

Bar-Ad and Bar-Joseph[2] identified two relaxation times in the dynamics of GaAs quantum wells (QWs) (measured in a degenerate pump-probe experiment) and they assigned, similarly as one does for bulk material, the longer time constant to the electrons and the shorter one to the holes. However, for GaAs, there is no experimental evidence that this attribution still holds in quantum wells. In later publications, many authors aimed to clearly identify which particle is at the origin of which spin-flip process using four-wave mixing,[6,7] photoluminescence,[1] or spin-resolved pump-and-probe experiments[7] but, to the best of our knowledge, hardly any experimental proof was given that supports the original assignment by Bar-Ad and Bar-Joseph. An exception is Ref. 3 on CdTe/CdMnTe, where the authors perform non-degenerate pump-and-probe experiments and, from the study of the dynamics of differential transmittance at light-hole and heavy-hole exciton resonances, they clearly obtain two relaxation times which they assign to electron- and hole-spin relaxation. Since exciton spin relaxation is not taken into account, this assignment may not be correct. Furthermore, transitions to biexcitons, which influence the dynamics of DT spectra, are not taken into account either. In the following, we will focus on these two points.

In this work, we take advantage of the possibility to excite biexcitons, which are bound states of two excitons. These states have a well-defined symmetry and energy and the optical transitions between excitons and biexcitons are governed by selection rules. We demonstrate that non-degenerate, spectrally, and spin-resolved differential transmission experiments, coupled to a numerical fitting procedure, which takes into account not only phase-space filling but also induced absorption to biexciton states,[11] renormalization of the band-edge, and other effects due to Coulomb interaction between carriers, allow the determination of spin-relaxation times. It is then possible to assign them to the three spin relaxation channels: involving electrons, holes, or excitons. Indeed, since optical transitions from the light-hole (lh) and heavy-hole (hh) bands (see Fig. 1) share one and the same electronic band we are able to attribute each extracted time constants to the spin relaxation of one of the three types of quasiparticles. With respect to earlier papers, our analysis gives more insight into the spin dynamics in quantum wells.

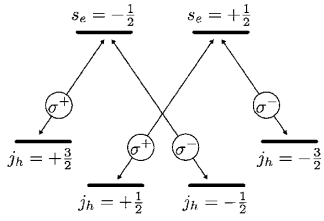

FIG. 1. Level scheme and selection rules of optical excitations in our semiconductor quantum well structure.

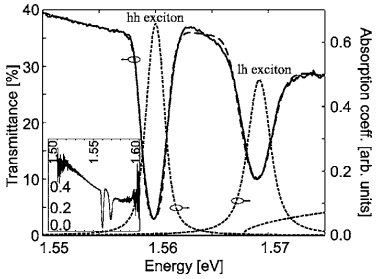

FIG. 2. Transmission spectrum of our sample around the excitonic resonances and over the whole measured spectrum (inset). The fitted transmission spectrum is depicted by a dashed line and corresponding absorption spectra of the two excitonic resonances and the electron-hole continuum by dotted lines.

First it involves a more precise quantitative evaluation of the experimental data as it describes the different nonlinear processes that are involved in the excitonic absorption changes in detail. In particular, the biexcitonic induced absorption is explicitly evaluated here, while its neglect, in previous publications, lead to an underestimated exciton absorption change. Second, using the selection rules for transitions between different exciton and biexciton states, we confirm points which were only assumption in the analysis of the data previously published. For example, the electron and hole spin relaxation times, which were roughly assigned to long and short decay times, are identified here without ambiguity and are clearly distinguished from the spin relaxation of the whole exciton.

The paper is structured as follows: after this Introduction, we describe the experimental setup and present typical measured pump and probe spectra. Then we present a numerical analysis of the recorded spectra and a dynamical model that is appropriate to describe the evolution of spins in quantum wells. In the subsequent sections, we discuss the obtained relaxation times with respect to the literature and then summarize our results.

EXPERIMENTS

Our sample consists of 30 periods of 10-nm-thick GaAs QWs, with 200 nm $Ga_{0.4}Al_{0.6}As$ barriers, grown by molecular beam epitaxy on a GaAs substrate. The sample was chemically etched over an area of about 3×3 mm^2. The etched part is not supported by any substrate and no strain is expected, nor is any observed, in the excitonic absorption lines, for example. Antireflection coatings were deposited on both sides of the sample. The sample is held at 4 K using a cold-finger helium-flow cryostat. The transmittance of the sample is shown in Fig. 2 (solid line) and presents two resonances: the heavy-hole (hh) and light-hole (lh) excitonic optical transitions.

The laser source is a homemade femtosecond titanium: sapphire oscillator that includes a multipass cavity in order to reduce the repetition rate and to increase the energy per pulse.[12] The total length of our cavity is about 11.6 m and it produces 30 fs pulses of 15 nJ at a repetition rate of 13 MHz.

The pump pulses are spectrally filtered through a Fabry-Perot cavity to a spectral width of 2 meV full width at half maximum (FWHM), bringing their duration to 1 ps. Their temporal profile was characterized by cross-correlation with unfiltered pulses from the laser (duration 30 fs) and shows a single-sided exponential decrease. The rising time of the pump pulse is 150 fs and the falling time is 500 fs. The zero time delay is chosen as the delay for which the cross-correlation signal is maximum. Pump pulses are circularly polarized and resonantly excite only the hh excitonic transition with total angular momentum +1, that is, excitons formed with +3/2 heavy holes and −1/2 electrons ($|+3/2,-1/2\rangle$). Taking into account the pump pulse intensity, the spot size on the sample, the measured transmission, and the number of QWs, we estimate that the population density of photocreated $|+1\rangle$ excitons is about 10^{10} cm^{-2} per well.

The broadband linearly polarized probe pulses, 100 times weaker than the pump, extend over both hh and lh excitonic transitions. A quarter-wave plate transforms the two circularly polarized components of the transmitted probe beam into two linearly polarized, mutually perpendicular components, which are separated by a linear polarizer cube. The two beams are then directed at different heights onto the entrance slit of a spectrometer, and are detected as two different spectra on our two-dimensional charge coupled device (CCD) camera. In this way, the two circular components of the transmitted probe are registered simultaneously as a function of the pump-probe time delay. We estimate that the intensity of one circular component propagating in the direction of detection of the other circular component is less than 1% of the intensity of the beam. For each time delay, the two transmitted probe spectra are recorded in the presence and then in the absence of the pump pulses and two DT spectra are calculated, one for each probe polarization ($\sigma+$ and $\sigma-$).

The analysis of our results takes into account the fact that the wave function of an exciton needs to be developed over the electronic states of two valence and conduction bands. As a consequence, even if an excitonic transition is selectively excited by tuning both photon energy and polarization of the excitation, band filling effects can be seen on a different excitonic transition if it shares a common electronic band although such exciton states are not populated.[13] For example, a hh exciton population with spin −1 can induce an absorption variation at the +1 lh exciton transition because they are equally built from electrons in +1/2 valence band states. Similarly, a dark exciton population with spin +2, although not optically active, can induce a bleaching of the hh exciton transition with spin spin +1, as the heavy-hole +3/2 valence band is shared by the two excitons. Such effects are specific to pump-and-probe transmission experiments and cannot be observed in luminescence measurements where only optically active exciton populations can give rise to emission. In our experiments, the spectrally narrow, circularly polarized ($\sigma+$), pump pulses are in resonance only with the hh excitonic transition (Fig. 1). Thus, immediately after propagation of the pump pulses through the sample, only two electronic bands are populated: the hh band with angular momentum +3/2 and the electron band with

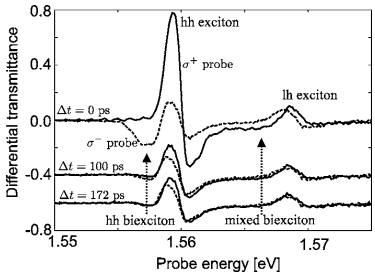

FIG. 3. Measured differential transmittance (DT) spectra. We present data for three delays Δt between pump and probe pulses. Pump pulses are $\sigma+$ polarized, probe pulses are either $\sigma+$ or $\sigma-$. The dotted arrows show the positions of the induced absorption due to exciton-biexciton transitions.

spin $-1/2$. The broadband probe pulses ($\sim$70 meV) cover the hh as well as the lh excitonic optical transitions. Since the probe pulses are linearly polarized, all the indicated excitonic transitions (see Fig. 1) are probed simultaneously as a function of the time-delay Δt between the pump and the probe pulses.

Let us first consider that, after optical pumping, absorption changes are originating from saturation of the optical transitions due to populations of electron and hole states. Then, the transmission change of the probe pulse with polarization $\sigma-$ at the lh optical transition is not sensitive to the population of hh states with angular momentum $+3/2$ but it is sensitive to the population of electrons with spin $-1/2$ (see Fig. 1). In the same way, the $\sigma-$ probe transmission change at the hh excitonic transition is only sensitive to the population of spin $+1/2$ electrons and $-3/2$ holes. Note that the last two bands are not initially populated by the pump pulse and, therefore, the population of these states results from electron or hole spin-flip processes.

However, saturation of the excitonic absorption due to a population of holes in the valence or electrons in the conduction band, respectively, is not the only source of probe transmission changes. A blueshift of the excitonic lines is also expected because of Coulomb interactions between excitons.[14,15] Spectral broadening of the absorption lines also occurs due to exciton interactions. In addition, absorption to the biexciton ground state is induced for a probe pulse of $\sigma-$ polarization after optical pumping of hh excitons with a pump pulse of $\sigma+$ polarization. All these processes are clearly visible in DT spectra, as described below, and will be considered in our interpretation.

In Fig. 3, we show DT spectra for three different time delays between the pump and probe pulses. At zero time delay, DT spectra for $\sigma+$ (solid line) and $\sigma-$ (dotted line) differ considerably. At the hh exciton line (1.56 eV), the DT signal for the $\sigma+$ probe presents two contributions: absorption saturation and a blueshift. Absorption saturation due to state filling is expected after the pump pulse has led to a population of hh exciton states. The DT signal for the $\sigma-$ probe is much lower in amplitude and mainly shows a blueshift and an important induced absorption just below the hh exciton resonance (marked by a dotted arrow). The latter is attributed to the presence of biexciton states: Since the pump pulse produced hh excitons with total angular momentum $+1$, the probe pulse with $\sigma-$ polarization can be absorbed to excite hh biexcitons,[13] i.e., biexcitons formed by two hh excitons of opposite angular momenta. This transition, neglected in Ref. 2, is allowed and has to be considered if the carrier spin dynamics is determined through non-degenerate pump-and-probe measurements.

At the lh exciton resonance (1.569 eV), mainly a blueshift of the exciton resonance and an absorption saturation are the main features that are observed for the $\sigma-$ probe pulse (dotted line). As we will discuss in the following, the latter can be explained by the fact that the electron band with spin $s_e = -1/2$ is populated by the pump pulses. The $\sigma+$ probe reveals an induced absorption between the lh and hh resonances and absorption saturation at the lh exciton resonance. The origin of these effects will be discussed later and will be attributed to electron spin-flip and biexcitons creation.[16,17] In our experiments, this small induced absorption becomes observable since we can compare the DT spectra for $\sigma+$ and $\sigma-$ probe-pulse polarizations which are measured simultaneously.

At longer time delays, DT spectra for $\sigma+$ and $\sigma-$ probes become more and more similar, first at the lh, later also at the hh exciton resonance. This is the signature of different spin relaxation processes: If the population of electrons with spin $-1/2$ equals the population of electrons with spin $+1/2$, one expects the same signal amplitude for the $\sigma-$ and $\sigma+$ probe polarizations at the lh exciton resonance (see Fig. 3). Indeed, it depends only on the electron population: no light holes have been excited by the pump pulse nor created by further relaxation because the energy needed cannot be provided at low temperature. In addition, the heavy hole spin populations equilibrate with time and, at the hh resonance, DT signals for the $\sigma+$ and $\sigma-$ probe again become similar (as shown in Fig. 3). Thus comparing the DT dynamics at different photon energies allows us to discriminate exciton- from electron- and hole-spin relaxation processes.

NUMERICAL ANALYSIS OF THE MEASURED DATA

In this section we describe our fitting procedure for the DT spectra. We consider four basic changes of both the hh and the lh absorption lines after optical pumping:[3,15,18,19] blueshift, bleaching, broadening, and induced absorption to biexciton states (DT originating from absorption changes of the electron-hole continuum or from electron-hole correlations are neglected). Typical changes in DT spectra resulting from the particular modifications of the absorption lines enumerated above are depicted in Fig. 4. Let us consider that the absorption coefficient of an unperturbed exciton transition is described by the function $\alpha_0(E)=f(E-E_0)$, where E_0 is the resonance energy. Blueshift of the transition means that, after optical excitation, the absorption coefficient changes to $\alpha(E)=f(E-E_0-S)$. Bleaching changes the absorption coefficient to $\alpha(E)=Lf(E-E_0)$, $0<L<1$ and broadening is accounted for by $\alpha(E)=f[(E-E_0)R]$. Biexciton induced absorption is then described by a different function. Here, we suppose that it has a Gaussian shape and that it adds to the

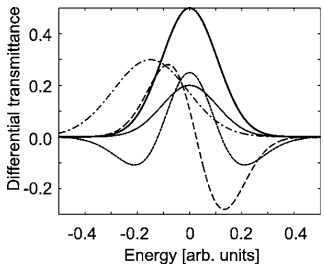

FIG. 4. Spectral shape of DT spectra of an inhomogeneously broadened absorption line (thick line) that undergoes bleaching (thick line), blueshift (dashed line), broadening (dotted line), and biexciton induced absorption (dash-dotted line).

linear absorption $\alpha_0(E)$ while remaining centered at the exciton-biexciton transition energy E_B: $\alpha(E)=I\exp[(E-E_B)^2/\sigma_B^2]+\alpha_0$.

This choice is supported by the fact that the exciton-biexciton transition is inhomogeneously broadened (because of wave vector distribution of the hh excitons). In addition, the use of a symmetric function reduces the number of free parameters. For every time delay Δt between pump and probe pulses, we fit the DT spectra for both the σ+ and $\sigma-$ polarizations of the probe pulse. The spectrum of the probe pulse covers both the hh and the lh exciton resonances and therefore we fit all four aforementioned features for each exciton resonance. For each time delay, the fitting procedure yields 16 values, namely: $S^{\pm}_{\mathrm{lh,hh}}(\Delta t)$ for blueshifts, $L^{\pm}_{\mathrm{lh,hh}}(\Delta t)$ for bleaching, $R^{\pm}_{\mathrm{lh,hh}}(\Delta t)$ for broadening, and $I^{\pm}_{\mathrm{lh,hh}}(\Delta t)$ for biexciton induced absorption (its role is important as discussed in Refs. 19–21), where the subscripts lh and hh stand for the light-hole and heavy-hole resonances, respectively, and the superscripts + and − stand for the polarizations σ + and $\sigma-$ of the probe pulses. The behavior of these functions will be studied in the next section using a dynamical model.

Biexcitons require further comments since their spin structure is very important but was rarely discussed in detail. Based on symmetry considerations, we have calculated the spin structure of biexcitons and their selection rules in quantum wells made of cubic materials.[22] Like for bulk material with the same band structure, we find that the biexciton ground state consists of six different states: one pure hh state composed of two hh excitons with spins +1 and −1, one pure lh state formed by two lh excitons with spins +1 and −1, and four mixed states, which consist of one hh and one lh exciton. (Some of these biexcitons have indeed already been observed experimentally[16,17]). Two of the mixed biexcitons states are not accessible by two-photon absorption. The other two, however, may be excited by absorption of two cocircularly polarized photons. When a hh exciton $|+1\rangle$ is present in the sample after optical pumping, absorption of a $\sigma-$ photon slightly below the hh resonance leads to excitation of the hh biexciton. It is also possible to absorb a σ+ photon below the lh exciton resonance giving rise to a mixed biexciton. Immediately after optical pumping, we expect therefore to observe induced absorption at energies below the hh exciton for $\sigma-$ probe pulses and below the lh exciton for σ+ probe pulses as seen in Fig. 3 (dotted arrows). The selection rules for transitions between hh excitons and the different biexciton states are summarized in Fig. 7.

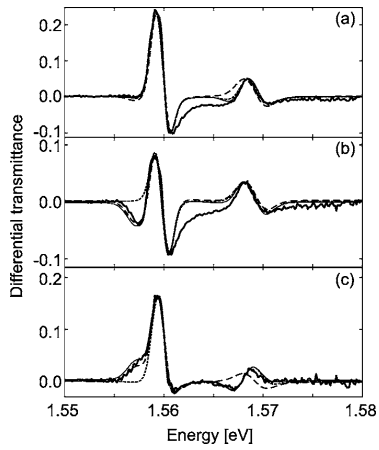

FIG. 5. Fit (thin line) of DT spectra (thick solid lines) with σ+ probe (a), $\sigma-$ probe (b), and their difference (c) at Δt=60 ps. Dotted and dashed lines show the fits without taking hh biexciton and mixed biexciton states, respectively, into account.

Exciton and biexciton parameters (resonance energy and width, binding energy) were obtained from the numerical adjustment of the linear transmission spectra (dashed line in Fig. 2). The measured and fitted transmission curves slightly differ in the region between the exciton resonances. This difference, however insignificant, is caused by correlations between lh and hh excitons, which change the DT spectra[20] but will not be taken into consideration here.

The biexciton absorption lines are treated as follows: Concerning the hh biexciton, we fit the DT spectrum at the hh exciton only up to 1.561 eV for zero time delay between pump and $\sigma-$ probe pulses. We thus determine the biexciton parameters [binding energy, spectral width, and absorption strength $I^{-}_{\mathrm{hh}}(0)$] as well as the hh exciton bleaching and blueshift parameter (spectral broadening is negligible). We keep the resonance energy and spectral width of the biexciton absorption fixed for all nonzero time delays of the probe. $I^{-}_{\mathrm{hh}}(t)$ varies in time since it depends on the $|+1\rangle$ exciton density. It is more complicated to extract the parameters of the mixed biexciton since the exciton-exciton correlations modify the absorption spectra in the same spectral region. As shown in Fig. 5(c), these correlation effects can be almost eliminated when studying the difference of the DT probe spectra of σ + and $\sigma-$ polarizations. Figure 5(c) also shows the influence of biexcitons on the DT spectra. The induced absorption appearing around 1.567 eV is attributed to the mixed biexciton states. We will now determine the mixed biexciton parameters from these curves in a similar way to those of the hh biexciton.

Because of the absorption of the pump pulses during their propagation across the large number of quantum wells in our sample, pump-induced changes are not equal in all quantum

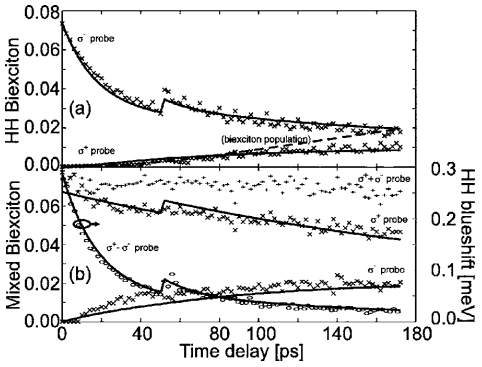

FIG. 6. Dynamics of induced absorption to the hh biexciton state (a), induced absorption to mixed biexciton states (crosses) and hh exciton blueshift (circles) (b) extracted from DT spectra. Fits are plotted by solid lines, the dashed line in (a) shows the total population of hh biexciton states. lh exciton blueshift is not shown since it is rather stationary and the extracted data do not play a role in the dynamical model.

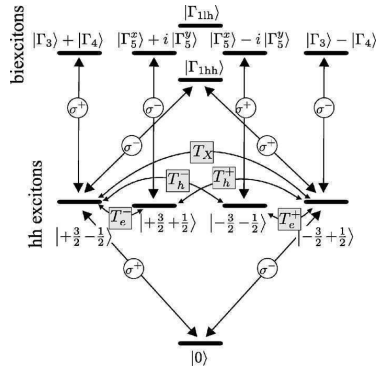

FIG. 7. Level scheme, selection rules of optical transitions, and relaxation channels used in our model for the simulation of the experimental data. The relaxation channels indicated are $|\pm\frac{3}{2},+\frac{1}{2}\rangle\leftrightarrow|\pm\frac{3}{2},-\frac{1}{2}\rangle$: spin relaxation of electrons (time constant T_e), $|+\frac{3}{2},\pm\frac{1}{2}\rangle\leftrightarrow|-\frac{3}{2},\pm\frac{1}{2}\rangle$: spin relaxation of holes (time constant T_h), and $|-\frac{3}{2},+\frac{1}{2}\rangle\leftrightarrow|+\frac{3}{2},-\frac{1}{2}\rangle$: spin relaxation of excitons (time constant T_x).

wells. This propagation effect, which may cause distortions in DT spectra, is included in our model: the energy distribution of the excitation field and the absorption spectrum of each single quantum well are calculated in order to evaluate the resulting DT spectra of the sample.

Since the spectral broadening of the absorption lines due to the excitation is negligible $[R^{\pm}_{\mathrm{lh,hh}}(\Delta t)\approx 0]$, we keep only 12 free parameters $S^{\pm}_{\mathrm{lh,hh}}(\Delta t)$, $L^{\pm}_{\mathrm{lh,hh}}(\Delta t)$, and $I^{\pm}_{\mathrm{lh,hh}}(\Delta t)$ among the 16 defined above for each time delay and polarization of the probe. Although this number remains large we are not able to fit the spectra with the required accuracy when one of the effects is not included. Note that the dips below each exciton resonance reflect induced absorption to a biexciton state. Dips above exciton resonances are a signature of a blueshift of the resonances and the combination of such a dip with a peak in the DT signal identifies a bleaching of the resonance. Numerical fitting over the whole spectrum of DT allows us to get results of greater precision. In Fig. 5, we show the results if hh or mixed biexcitons are not considered, respectively, by dotted and dashed lines.

The temporal evolution of some parameters extracted in this way are shown in Fig. 6. The curves are modeled in the next section. The magnitude of the noise obviously determines the accuracy of the numerical fit. The small abrupt signal increase appearing at 45 ps is due to some secondary pump pulse which arrives delayed at the sample and which could not be eliminated. The effect of this pulse is included in our model where it causes no major problem.

DYNAMICAL MODEL

Our goal, here, is to develop a dynamical model suitable for the description of the spin dynamics of electrons and holes bound in excitons created by optical pumping. The system is excited by a spectrally narrow pulse, which populates only the lowest-lying states, i.e., hh excitons, and temperature is so low that higher energy states cannot be populated. Therefore populations of lh exciton states will be neglected in the following. The scheme, which represents the dynamical model, is depicted in Fig. 7. We use the notation $|j_h+s_e\rangle=|j_h,s_e\rangle$ in order to indicate the z-component of the angular momentum of excitons and of the individual fermions within the exciton wave function. According to calculations of the spin structure of excitons and biexcitons,[22] we denote hh excitons by the projection of their angular momentum onto the quantization axis as ±1 (dipole-active states) and ±2 (dipole-inactive states). States carrying a dipole moment are shifted to higher energies with respect to the dipole-inactive states due to electron-hole exchange interaction, which is of the order of fractions of meV and which we will determine below. In Fig. 7, arrows which point from the ground state $|0\rangle$ to hh excitons denote dipole-active transitions. Arrows which interconnect hh excitons represent spin relaxation of electrons $|\pm\frac{3}{2},+\frac{1}{2}\rangle\leftrightarrow|\pm\frac{3}{2},-\frac{1}{2}\rangle$ (T_e being the time constant), spin relaxation of holes $|+\frac{3}{2},\pm\frac{1}{2}\rangle\leftrightarrow|-\frac{3}{2},\pm\frac{1}{2}\rangle$ (T_h), and spin relaxation of excitons $|-\frac{3}{2},+\frac{1}{2}\rangle\leftrightarrow|+\frac{3}{2},-\frac{1}{2}\rangle$($T_x$). Note that there is no exciton spin-flip between the dipole-inactive states.[10] The rate equations for heavy-hole exciton populations $n_j(t)$ where j denotes the total angular momentum of the exciton are[10]

$$\frac{dn_{+2}}{dt}=-\left(\frac{1}{T_e^+}+\frac{1}{T_h^+}\right)n_{+2}+\frac{n_{+1}}{T_e^-}+\frac{n_{-1}}{T_h^-}. \tag{1a}$$

$$\frac{dn_{+1}}{dt}=\frac{n_{+2}}{T_e^+}-\left(\frac{1}{T_e^-}+\frac{1}{T_h^-}+\frac{1}{T_X}\right)n_{+1}+\frac{n_{-1}}{T_X}+\frac{n_{-2}}{T_h^+}. \tag{1b}$$

$$\frac{dn_{-1}}{dt}=\frac{n_{+2}}{T_h^+}+\frac{n_{+1}}{T_X}-\left(\frac{1}{T_e^-}+\frac{1}{T_h^-}+\frac{1}{T_X}\right)n_{-1}+\frac{n_{-2}}{T_e^+}. \tag{1c}$$

$$\frac{dn_{-2}}{dt} = \frac{n_{+1}}{T_h^-} + \frac{n_{-1}}{T_e^-} - \left(\frac{1}{T_e^+} + \frac{1}{T_h^+}\right) n_{-2}. \tag{1d}$$

The relaxation times $T_e^{\pm}$ stand for electron spin-relaxation time. The superscript "−" indicates relaxation from the dipole-active states to the dipole-inactive states and "+" for the reverse transition. (The rates differ as a consequence of energy splitting between the two types of states.[10]) Similarly, $T_h^{\pm}$ denote hole spin relaxation times and T_X stands for the exciton spin relaxation time. In contrast to Refs. 6 and 10, we do not consider recombination of excitons. If the characteristic time of radiative recombination even depends on the localization of excitons, it is slow when compared to the spin relaxation that we observe here and thus recombination occurs on a longer time scale than that of our experiment. According to Fig. 7, both types of hh excitons may be promoted to mixed biexcitons by either $\sigma+$ or $\sigma-$ probe pulses. The sum of induced absorption strengths denoted as $(\sigma^+ + \sigma^-)$ is proportional to the total number of excitons in the sample, which is constant as shown in Fig. 6. The simultaneous presence of $|+1\rangle$ and $|-1\rangle$ excitons (and also of $|\pm 2\rangle$ excitons) leads to continuous hh biexciton formation (as has been shown experimentally in[23]). The rate equation that describes the formation of biexcitons reads

$$\frac{d}{dt} n_{BX}(t) = \frac{1}{T_{BX}} [n_{+1}(t) n_{-1}(t) + n_{+2}(t) n_{-2}(t)]. \tag{2}$$

The above rate equations (1) are thus extended by nonlinear terms, which describe the decrease of the population of free excitons according to Eq. (2). The constant T_{BX} is the inverse of the characteristic biexciton formation rate. The reverse process, leading to the dissociation of a biexciton into two excitons, is not likely at low temperature, as opposed to the situation in bulk crystals where polaritons can be created at any energy.

The spin relaxation of biexcitons has to be included as well and the way they are involved in our measurements needs to be examined. Spin relaxation of a hh and lh biexciton population is quite improbable: such a process is not elastic as it implies a dissociation of the biexciton into two excitons. Transfers between mixed biexcitons are more likely as they are quasidegenerated. They arise from the spin-flip of a hole (hh between $\pm 3/2$ states or lh between $\pm 1/2$ states). Such processes would be different from intraexciton hole spin flip, which is described in our paper by the time constant T_h, because of the difference between the exciton and biexciton envelope wave functions. In our experiments, the biexciton generation by collision between two excitons is taken into account and described by Eq. (2). It involves only hh excitons and biexcitons, and no mixed or lh biexcitons because the pump pulses do not excite the lh transition. As discussed above, the hh biexciton spin is stable and will not relax. Moreover, no dissociation of a biexciton into two excitons occurs at low temperature. Thus the biexciton spin relaxation does not affect the spin dynamics of the whole system. Biexciton states play, however, a major role in our measurements: by looking at the exciton-biexciton induced absorption, biexciton states are used as a probe of the different exciton populations and of their spin. The spin relaxation of the biexcitons which are created in this process may be ignored because it occurs after the absorption of the probe pulse.

lh exciton states are missing in the scheme since they are not directly coupled to hh excitons and they are not excited by the pump pulses. We include, however, the mixed biexciton states in our model in order to describe the induced absorption correctly.

Using the above model, we numerically adjust the data obtained by the procedure described in the previous section. Concerning the bleaching $L^{\pm}_{\mathrm{lh,hh}}(\Delta t)$: the electron and hole band fillings are determined from the exciton population calculated with the dynamical equations, and the bleaching of each excitonic transition is deduced in turn.[13] The fitted parameters are

(1) the spin-flip times of electrons, holes, and excitons, and

(2) the characteristic constant of biexciton formation T_{BX}.

In addition, as a consequence of repulsive exchange interaction, we assume that population of electron and hole states causes a blueshift of the respective exciton resonances, which involve at least one particle of the same spin. We also consider that a simultaneous population of electron and hole states causes a blueshift of the exciton resonances. Thus the influence of electrons on the blueshift generally differs from the influence of holes due to their different effective masses and density of states. Therefore we define a parameter, which is a ratio of the strength of the influence of the two types of particles. In addition, similarly to Ref. 10, we consider that the relaxation from dipole-active states to dipole-inactive states is more probable than the reverse due to the lower energy of dipole-inactive states in quantum wells. We assume that $T_j^+ = \kappa T_j^-(\mathrm{j=e,h})$, where $\kappa = 1/[1+\exp(\Delta/\mathrm{k_B T})]$, Δ is the splitting between the states and T is the temperature of the sample.

We use the five functions from the previous section [Eqs. (1) and (2)] for the numerical analysis of our data: We introduce strengths of biexciton induced absorption for both hh and mixed biexcitons and for both polarizations of the probe pulses. In addition, we consider the difference between blueshifts of the two hh-exciton transitions and follow the evolution of the excitonic spins. To fit the experimental data, we used the simplex method in a six-dimensional space without any constraints applied to the free parameters. We were able to repeatedly get the results within 10% of the values presented below changing randomly the initial values for the fit and therefore we conclude that the published numbers are determined with an accuracy better than 10%. The measured dynamics unambiguously determine the dynamics of the particular hh exciton states and it is not possible to fit the data using two sets of parameters which differ considerably (we are also able to estimate the relaxation times without computations as discussed in the next section). We tried to use less parameters but the fits to the curve did not produce satisfactory results.

The numerical fit to the data in Fig. 6 results in the following time constants: $T_e^- = 250$ ps (spin relaxation time of

electrons), $T_h^-=30$ ps (spin relaxation time of heavy holes), $T_X \gg 100$ ps (spin relaxation time of excitons), and $T_{BX}=120$ ps. In addition to these time constants, we conclude that the influence of electrons on the blueshift is 34% when compared to that of holes and that the reduction of the relaxation rate from dipole-inactive to dipole-active states (when compared to the reverse process) is $\kappa=73\%$. This corresponds to a splitting between the states of the order of 0.1 meV. The fitted curves are shown in Fig. 6 by solid lines.

DISCUSSION

Although the numerical fitting procedure described above is complex, one may draw some qualitative conclusions about the spin dynamics without it, leaving the calculations to be used to extract numerical values for the relaxation times. One can clearly resolve induced absorption to hh biexciton states for the $\sigma-$ probe in Fig. 3 (marked by a dotted arrow) for $\Delta t=0$ ps which shows the presence of a population of $|+1\rangle$ hh excitons. During spin relaxation, the negative dip below the hh exciton resonance [shown in Fig. 6(a)] decreases for the $\sigma-$ probe as the population of hh $|+1\rangle$ excitons relaxes. This negative dip increases for the $\sigma+$ probe showing an increase in the population of $|-1\rangle$ excitons. However, this growth is clearly slower than the relaxation of the $|+1\rangle$ excitons. Comparison of curves in Fig. 6(a) leads to the conclusion that exciton spin relaxation is slow: if single fermion spin relaxation was negligible, the decrease of hh biexciton induced absorption for the $\sigma-$ probe would be as fast as the increase of the induced absorption for the $\sigma+$ probe. Exciton population clearly relaxes to dipole-inactive states via electron or hole spin relaxation since the overall induced absorption to the hh biexciton decreases while the total number of excitons is constant. Therefore the single-fermion spin relaxation from the $|+1\rangle$ excitons to the dark states is much faster than the exciton spin relaxation.

Looking at Fig. 3, we see differences between DT spectra for the $\sigma+$ and the $\sigma-$ probe and therefore the spins of neither electrons nor holes are relaxed after ~200 ps. This fact shows us that the spin of one type of fermions relaxes on a short time scale while the spin of the other type of fermions and the spin of the excitons relaxes slowly, on the time scale of hundreds of picoseconds.

The question now is, which spins (that of electrons or holes) relaxe faster. In order to answer this, one must perform a numerical analysis of the different absorption lines in order to get more quantitative information about the system. We know, according to the spin structure of biexcitons, that a relaxation of hole spin from the initial state $|+1\rangle=|+3/2, -1/2\rangle$ to the $|-2\rangle=|-3/2,-1/2\rangle$ state is connected with the bleaching of the hh biexciton induced absorption but not with a change in the induced absorption to mixed states. Electron relaxation also causes changes in the induced absorption to hh biexciton states but, as opposed to hole relaxation, it changes also the induced absorption to mixed biexciton states for $\sigma+$ and $\sigma-$ probe polarizations (see Fig. 7). Therefore the dynamics of induced absorption to the mixed biexciton states for the $\sigma+$ and $\sigma-$ probe polarizations mainly reflects the electron spin dynamics. Since it is much slower than the dynamics of $\sigma-$ probe hh biexciton absorption, we conclude that the fast relaxation is connected with hole spin. This confirms unambiguously the proposed attribution[2] of the fast and slow relaxation to electron and holes, respectively.

Our results are indeed very similar to data published by Bar-Ad and Bar-Joseph:[2] The hole-spin relaxation time of 50 ps and that of electrons are thus comparable to our results of 30 and 250 ps, respectively. This is no surprise since they studied quantum wells which are very comparable to ours. Nevertheless, spin relaxation times of both the electron and the hole strongly depend on quantum confinement, i.e., well width and barrier height. A comparison with existing experimental data in literature is thus made difficult if we do not use quantities that characterize the effect of the confinement on the spin relaxation rate independently of the quantum well geometry (i.e., width and depth). Concerning the heavy hole, spin relaxation is caused by the mixing with the light-hole band. Lifting the degeneracy at the Γ point due to quantum confinement slows down the spin relaxation. This effect was seen by many authors.[2,3,7,13,24,25] It is therefore possible to compare the spin relaxation rate of the heavy hole in GaAs quantum wells with different well widths and barrier heights by analyzing T_h versus the valence band splitting $\Delta E_{hh\text{-}lh}$ at $k=0$, which is easily extracted from the linear absorption spectrum. Some previous works have shown that $T_h \sim (\Delta E_{hh\text{-}lh})^x$ with $x=3.2$.[25,7] In our sample, $\Delta E_{hh\text{-}lh}=10$ meV and $T_h=30$ ps. The spin relaxation rate is almost one order of magnitude smaller than the value expected from this power law as also reported by other authors.[2,13] The discrepancy between the latter results and the law mentioned above evidences that other parameters have to be considered to understand the hole spin relaxation. For example, exciton localization can play a nontrivial role: On one hand, the wave function of an exciton localized on a characteristic scale $\sim a_0$ develops in k-space up to $k_0 \sim a_0^{-1}$. The hole-relaxation rate is then influenced by the mixing of the heavy-hole and light-hole valence subbands which is no longer zero for sufficiently large k-values. On the other hand, the localization, by hindering the motion of the exciton center of mass, prevents the scattering between different spin states. In order to discuss in detail the consequence of exciton localization on the hole spin dynamics one has to know the exact geometry of the sample and the entire valence band dispersion for the quantum well.

D'yakonov and Kachorovskii have shown that the spin relaxation of the electron in the conduction band behaves as E_1^2 where E_1 is the first electron confined state in the quantum well.[26] We have collected in the literature the spin relaxation decay rate of the electron, T_e^{-1}, in GaAs/AlGaAs quantum wells with different well widths and barrier aluminum contents.[2,7,25,27] These data, as well as ours, are plotted as a function of the electron confinement energy E_1 in Fig. 8. E_1 was calculated using the effective mass theory in the envelope function framework. The experimental data are nicely adjusted using the expression $T_e^{-1}(\mathrm{ps}^{-1})=4.10^{-3}+1.12.10^{-6}(E_1)^{2.06}$. This behavior is an indication that a D'yakonov-Perel-like[28] relaxation process is responsible for the spin relaxation of the electron in most GaAs/AlGaAs quantum wells.

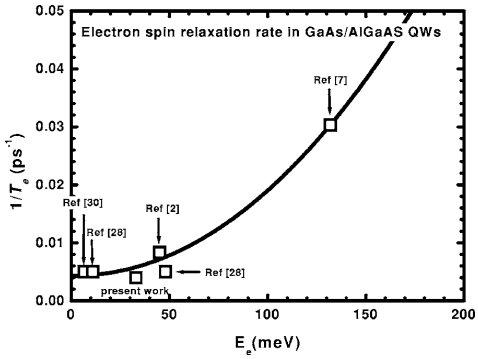

FIG. 8. Electron spin relaxation rate as a function of the first electron confinement energy E_1 in GaAs/AlGaAs quantum wells with different well widths and barrier aluminum contents.

We did not discuss the fitted value of the parameter κ that reveals the lowest probability of spin relaxation from dipole-inactive to dipole-active states yet. Applying Eq. (2.5)[10] to the value determined by our fit, we obtain a splitting between the states of the order of 0.1 meV, which is a reasonable value.

CONCLUSIONS

In this paper, we present results of spin-resolved nondegenerate pump-and-probe experiments on intrinsic GaAs multiple quantum wells. We analyze differential transmittance spectra and numerically extract the dynamics of the various changes related to the heavy-hole and light-hole exciton resonances. In order to fit the experimental data, we propose a model for the relaxation dynamics that takes, in particular, biexciton states into account.

The extracted time constants show that the spin relaxation is driven predominantly by the relaxation of the hole spins (T_h=30 ps). Electrons relax on a much longer time scale (T_e=250 ps) and exciton spin relaxation is negligible. This result is striking as far as the relaxation of the exciton pseudospin and as a whole is expected to be enhanced in quantum wells.[10,29,30] The comparison with similar work, in which spin relaxation rates of both individual types of carriers are measured, reveals that our value of T_h is longer as expected with respect to the valence band splitting $\Delta E_{hh\text{-}lh}$ but stays in the 5–50 ps range given in the literature. On the other hand, our value of T_e is consistent with previous data if it is considered with respect to the confinement energy E_1 of the electron in the quantum well. In particular, our results are very close to those obtained in the work of Bar-Ad and Bar-Joseph[2] who used a sample with characteristics similar to ours. Moreover, a review of the different experimental values from the literature reveals a quadratic dependence of T_e with regard to E_1 which denotes a D'yakonov-Perel-like relaxation mechanism for the electron.

The originality of our work lies in the consideration of three relaxation channels for the spins of electrons and holes forming excitons and in the numerical adjustment of the dynamics of differential transmittance spectra. We take advantage of the presence of different biexciton states to which the transitions are mutually allowed or forbidden in pump-and-probe experiments using circularly polarized laser pulses. We are then able to attribute the extracted time constants to particular processes using a detailed model calculation. In particular, we can confirm the attribution of the spin relaxation times of electrons and holes given by Bar-Ad and Bar-Joseph.[2]

ACKNOWLEDGMENTS

The authors are grateful to P. Maly and H. Rahimpour Soleimani for their assistance and for helpful discussions. T.O. acknowledges financial support from the French Government. We also thank V. Thierry-Mieg for providing us with high-quality GaAs samples.

*Electronic address: jean-pierre.likforman@paris7.jussieu.fr

[1] A. Vinattieri, J. Shah, T. C. Damen, D. S. Kim, L. N. Pfeiffer, M. Z. Maialle, and L. J. Sham, Phys. Rev. B **50**, 10868 (1994).
[2] S. Bar-Ad and I. Bar-Joseph, Phys. Rev. Lett. **68**, 349 (1992).
[3] R. Akimoto, K. Ando, F. Sasaki, S. Kobayashi, and T. Tani, Phys. Rev. B **56**, 9726 (1997).
[4] A. Tackeuchi, T. Kuroda, S. Muto, and O. Wada, Physica B **272**, 318 (1999).
[5] H. Kalt, D. Tröndle, S. Wachter, I. J. Blewett, G. Brown, and I. Galbraith, Phys. Status Solidi B **221**, 477 (2000).
[6] O. Ikeuchi, S. Adachi, H. Sasakura, and S. Muto, J. Appl. Phys. **93**, 9634 (2003).
[7] S. Adachi, T. Miyashita, S. Takeyama, Y. Takagi, and A. Tackeuchi, J. Lumin. **72**, 307 (1997).
[8] K. Morita, H. Sanada, S. Matsuzaka, C. Y. Hu, Y. Ohno, and H. Ohno, Physica E (Amsterdam) **21**, 1007 (2004).
[9] A. V. Kimel, V. V. Pavlov, R. V. Pisarev, V. N. Gridnev, F. Bentivegna, and T. Rasing, Phys. Rev. B **62**, R10610 (2000).
[10] M. Z. Maialle, E. A. de Andrada e Silva, and L. J. Sham, Phys. Rev. B **47**, 15776 (1993).
[11] H. Rahimpour-Soleimani, S. Cronenberger, O. Crégut, J.-P. Likforman, M. Gallart, T. Ostatniký, P. Gilliot, and B. Hönerlage, Appl. Phys. Lett. **85**, 5263 (2004).
[12] S. H. Cho, F. X. Kartner, U. Morgner, E. P. Ippen, J. G. Fujimoto, J. E. Cunningham, and W. H. Knox, Opt. Lett. **26**, 560 (2001).
[13] H. Rahimpour Soleimani, S. Cronenberger, M. Gallart, P. Gilliot, J. Cibert, O. Crégut, B. Hönerlage, and J. P. Likforman, Appl. Phys. Lett. **87**, 192104 (2005).
[14] S. Schmitt-Rink, D. S. Chemla, and D. A. B. Miller, Phys. Rev. B **32**, 6601 (1985).
[15] N. Peyghambarian, H. M. Gibbs, J. L. Jewell, A. Antonetti, A. Migus, D. Hulin, and A. Mysyrowicz, Phys. Rev. Lett. **53**, 2433 (1984).
[16] H. P. Wagner, W. Langbein, and J. M. Hvam, Phys. Rev. B **59**,

4584 (1999).
[17] S. Adachi, S. Muto, K. Hazu, T. Sota, K. Suzuki, S. F. Chichibu, and T. Mukai, Phys. Rev. B **67**, 205212 (2003).
[18] K. Litvinenko, D. Birkedal, V. G. Lyssenko, and J. M. Hvam, Phys. Rev. B **59**, 10255 (1999).
[19] T. Meier, S. W. Koch, M. Phillips, and H. Wang, Phys. Rev. B **62**, 12605 (2000).
[20] T. Meier, S. W. Koch, P. Brick, C. Ell, G. Khitrova, and H. M. Gibbs, Phys. Rev. B **62**, 4218 (2000).
[21] C. Sieh, T. Meier, F. Jahnke, A. Knorr, S. W. Koch, P. Brick, M. Hübner, C. Ell, J. Prineas, G. Khitrova, and H. M. Gibbs, Phys. Rev. Lett. **82**, 3112 (1999).
[22] T. Ostatnický, P. Gilliot, and B. Hönerlage, J. Appl. Phys. **98**, 113516 (2005).
[23] R. Spiegel, G. Bacher, A. Forchel, B. Jobst, D. Hommel, and G. Landwehr, Phys. Rev. B **55**, 9866 (1997).
[24] B. Baylac, X. Marie, T. Amand, M. Brousseau, J. Barrau, and Y. Shekun, Surf. Sci. **326**, 161 (1995).
[25] I. Brener, W. H. Knox, K. W. Goossen, and J. E. Cunningham, Phys. Rev. Lett. **70**, 319 (1993).
[26] M. I. D'yakonov and V. Yu. Kachorovskii, Sov. Phys. Semicond. **20**, 110 (1986).
[27] R. C. Miller, W. T. Tsang, and W. A. Nordland, Jr., Phys. Rev. B **21**, 1569 (1980).
[28] M. I. D'yakonov and V. I. Perel', Zh. Eksp. Teor. Fiz. **65**, 362 (1973).
[29] A. Takeuchi, S. Muto, T. Inata, and T. Fujii, Appl. Phys. Lett. **56**, 2213 (1990).
[30] Ph. Roussignol, P. Rolland, R. Ferreira, C. Delalande, G. Bastard, A. Vinattieri, L. Carraresi, M. Colocci, and B. Etienne, Surf. Sci. **267**, 360 (1992).

NANO LETTERS

2009
Vol. 9, No. 12
4204-4208

Spin Transport of Excitons

J. R. Leonard,*,† Y. Y. Kuznetsova,† Sen Yang,† L. V. Butov,† T. Ostatnický,‡ A. Kavokin,‡,§ and A. C. Gossard‖

Department of Physics, University of California at San Diego, La Jolla, California 92093-0319, School of Physics and Astronomy, University of Southampton, SO17 1BJ, Southampton, United Kingdom, Dipartimento di Fisica, Universita' "Tor Vergata" via della Ricerca Scientifica, 00133 Rome, Italy, and Materials Department, University of California at Santa Barbara, Santa Barbara, California 93106-5050

Received July 27, 2009; Revised Manuscript Received August 26, 2009

ABSTRACT

We report on observation of the spin transport of spatially indirect excitons in GaAs/AlGaAs coupled quantum wells (CQW). Exciton spin transport over substantial distances, up to several micrometers in the present work, is achieved due to orders of magnitude enhancement of the exciton spin relaxation time in CQW with respect to conventional quantum wells.

Spin physics in semiconductors includes a number of interesting phenomena in electron transport, such as current-induced spin orientation (the spin Hall effect),[1−3] spin-induced contribution to the current,[4] spin injection,[5] and spin diffusion and drag.[6−11] Besides the fundamental spin physics, there is also considerable interest in developing semiconductor electronic devices based on the spin transport, which may offer advantages in dissipation, size, and speed over charge-based devices; see ref 12 and references therein.

Optical methods have been used as a tool for precise injection, probe, and control of electron spin via photon polarization in semiconductors. A major role in the optical properties of semiconductors near the fundamental absorption edge is played by excitons. The spin dynamics of excitons in GaAs single quantum wells (QW) was extensively studied in the past; see refs 13−15 and references therein. It was found that the spin relaxation time of excitons in single QW is of the order of a few tens of picoseconds. Because of the short spin relaxation time, no spin transport of excitons was observed until this work.

Here, we report on the observation of the spin transport of spatially indirect excitons in GaAs coupled quantum wells (CQW). The spin relaxation time of indirect excitons is orders of magnitude longer than one of regular direct excitons. In combination with a long lifetime of indirect excitons, this makes possible spin transport of indirect excitons over substantial distances.

The spin dynamics of excitons can be probed by the polarization resolved spectroscopy. In GaAs QW structures, the σ^+ (σ^-) polarized light propagating along the z axis creates a heavy hole exciton with the electron spin state $s_z = -1/2 (s_z = +1/2)$ and hole spin state $m_h = +3/2 (m_h = -3/2)$. In turn, heavy hole excitons with $S_z = +1$ (-1) emit σ^+ (σ^-) polarized light. Excitons with $S_z = \pm 2$ are optically inactive. The polarization of the exciton emission $P = (I_+ - I_-)/(I_+ + I_-)$ is determined by the recombination and spin relaxation processes. For an optically active heavy hole exciton, an electron or hole spin-flip transforms the exciton to an optically inactive state (Figure 1a) causing no decay of emission polarization. The polarization of emission decays only when both the electron and hole flip their spins. This can occur in the two-step process due to the separate electron and hole spin flips and the single-step process due to the exciton spin flip.[13−15] The rate equations describing these processes[14,15] yield for the case when the splitting between $S_z = \pm 1$ and ± 2 states Δ is smaller than $k_B T$ the polarization of the exciton emission $P = \tau_P/(\tau_P + \tau_r)$ and the relaxation time of the emission polarization $\tau_P^{-1} = 2(\tau_e + \tau_h)^{-1} + \tau_{ex}^{-1}$, where τ_{ex} time for exciton flipping between $S_z = \pm 1$ states, τ_e and τ_h electron and hole spin flip times, and τ_r exciton recombination time.[30] The requirement $\Delta \ll k_B T$ is typically fulfilled for indirect excitons. Indeed, for regular direct excitons in single GaAs QW, $\Delta \lesssim 100$ μeV.[16] It is determined by the exchange interaction between the electron and hole in the exciton and scales $\propto \tau_r^{-1}$.[13−16] For indirect excitons in the studied CQW, τ_r is about thousand times larger than for direct excitons[17] and therefore $\Delta \lesssim 100$ neV $\ll k_B T$.

In GaAs single QW, τ_h and τ_{ex} are typically in the range of tens of picoseconds and are much shorter than τ_e so that

* To whom correspondence should be addressed, jleonard@physics.ucsd.edu.
† Department of Physics, University of California at San Diego, La Jolla.
‡ School of Physics and Astronomy, University of Southampton.
§ Dipartimento di Fisica, Universita' "Tor Vergata" via della Ricerca Scientifica.
‖ Materials Department, University of California at Santa Barbara.

10.1021/nl9024227 CCC: $40.75
Published on Web 09/25/2009

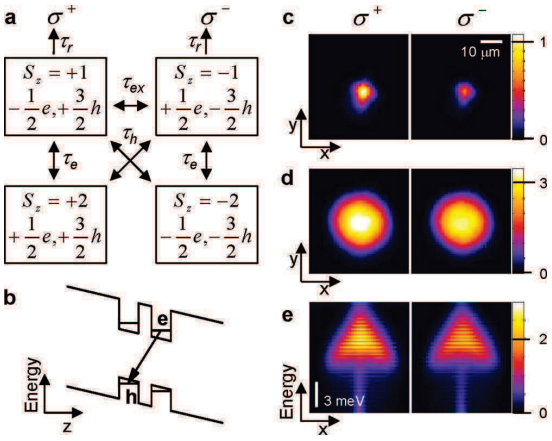

Figure 1. Diagrams and PL images for excitons. (a) Exciton spin diagram. (b) Energy diagram of the CQW structure: e, electron; h, hole. $x-y$ images of the PL intensity of indirect excitons in σ^+ and σ^- polarizations for (c) $P_{ex} = 4.7$ μW and (d) $P_{ex} = 310$ μW; $V_g = -1.1$ V, $E_{ex} = 1.582$ eV. (e) x-energy images of the PL intensity of indirect excitons in σ^+ and σ^- polarizations; $V_g = -1.1$ V, $E_{ex} = 1.572$ eV, $P_{ex} = 140$ μW.

$\tau_P \approx \tau_{ex}$.[14,15,18] The short τ_{ex} results in fast depolarization of the exciton emission within tens of picoseconds in GaAs single QW[14,15] making exciton spin transport over substantial distances problematic. However, τ_{ex} is determined by the strength of the exchange interaction between the electron and hole. This gives an opportunity to control the depolarization rate by changing the electron−hole overlap, e.g., in QW structures with different QW widths or with an applied electric field.[14,15]

The electron−hole overlap is drastically reduced in CQW structures. An indirect exciton in CQW is composed from an electron and a hole confined in different wells (Figure 1b). As a result of the small electron−hole overlap, the recombination time τ_r of indirect excitons is orders of magnitude longer than that of regular direct excitons and is typically in the range between tens of nanoseconds to tens of microseconds.[19] Long lifetimes of indirect excitons make possible their transport over large distances.[20−23] However, the ability to travel is required yet insufficient condition for spin transport. Exciton spin transport over substantial distances also requires a long spin relaxation time. The small electron−hole overlap for indirect excitons should also result to a large $\tau_{ex} \propto \tau_r^2$ and in turn τ_P, thus making possible exciton spin transport over substantial distances.

We probed exciton spin transport in a GaAs/AlGaAs CQW structure with two 8 nm GaAs QWs separated by a 4 nm $Al_{0.33}Ga_{0.67}As$ barrier (see sample details in ref 17 where the same sample was studied). The electric field across the sample was controlled by an applied gate voltage V_g. The excitons were photoexcited by a continuous wave Ti:sapphire laser tuned to the direct exciton energy, $E_{ex} = 1.572$ eV, and focused to a spot of $\sim$5 μm in diameter. The spatial profile of the laser excitation spot was deduced from the profile of the bulk GaAs emission from the excitation spot. The excitation was circularly polarized (σ^+).

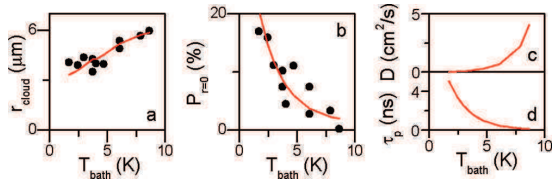

Figure 2. Temperature dependence. Experimental (points) and simulated (curves) (a) exciton cloud radius and (b) degree of circular polarization at the exciton cloud center as a function of temperature. (c, d) Fit parameters, diffusion coefficient D and polarization relaxation time τ_P as a function of temperature.

The emission images in σ^+ and σ^- polarizations were taken by a CCD camera with an interference filter 800 ± 5 nm, which covers the spectral range of the indirect excitons. The spatial resolution was 1.4 μm. The spectra were measured using a spectrometer with a resolution of 0.3 meV. The characteristic x-energy spectra and $x-y$ images are shown in Figure 1c−e. The exciton density n was estimated from the energy shift as in ref 23. For recent discussions of the exciton−exciton interaction strength and the exciton density estimation see refs 24 and 25. We note that the results on exciton spin transport reported here are practically insensitive to the interaction strength.

Phenomenological Model for Exciton Spin Transport. Rate equations combining the exciton spin relaxation equations[14,15] with the drift-diffusion equation[23] yield

$$2\frac{\partial n_{\pm 1}}{\partial t} = 2\nabla[D\nabla n_{\pm 1} + 2\mu n_{\pm 1}\nabla(u_0 n_b)] - \frac{1}{\tau_r}n_{\pm 1} - \frac{1}{2\tau_P}(n_{\pm 1} - n_{\mp 1}) + \Lambda\delta_{+,\pm} \quad (1)$$

where D is the exciton diffusion coefficient, $\mu \approx D/k_BT$ mobility, u_0 interaction energy estimated by $u_0 = 4\pi^2 d/\varepsilon$, $n_b = n_{+1} + n_{-1}$, and Λ generation rate of +1 excitons.[30] Both bright and dark exciton states are accounted for in eq 1; however the fast hole spin flip process allowed the simplification of the set of four coupled equations for four exciton spin species to the form of eq 1, which contain only two bright exciton states $n_{\pm 1}$.[30] $n_{+1}(r)$, $n_{-1}(r)$, and $P(r)$ were calculated using eq 1 and compared to the experimental data.

Temperature Dependence. Increasing the temperature leads to the increase of the exciton cloud radius r_{cloud} and decrease of the circular polarization of exciton emission at the excitation spot center $P_{r=0}$ (Figure 2a,b). The exciton cloud expansion $r_{cloud} \sim (D\tau_r)^{1/2}$ is determined by the exciton diffusion coefficient D. The circular polarization of exciton emission $P = \tau_P/(\tau_P + \tau_r)$ is determined by the depolarization time of the emission τ_P. Therefore, the measurements of r_{cloud}, P, and τ_r allow estimating D and τ_P. D and τ_P were extracted from the measured r_{cloud}, $P_{r=0}$, and τ_r[17] via numerical simulations using eq 1. The obtained temperature dependencies for D and τ_P are plotted in Figure 2c,d. The data show that (i) the depolarization time of the emission of indirect excitons reaches several nanoseconds, orders of magnitude longer than that of direct excitons in single QW,[14,15] (ii) the

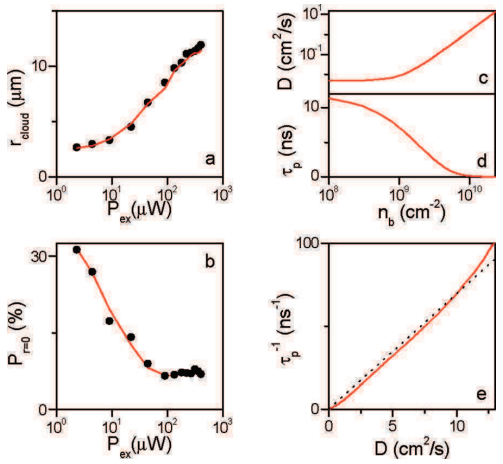

Figure 3. Density dependence. Experimental (points) and simulated (curves) (a) exciton cloud radius and (b) degree of circular polarization at the exciton cloud center as a function of excitation density. (c, d) Fit parameters, diffusion coefficient D and polarization relaxation time τ_P as a function of $n_b = n_{+1} + n_{-1}$. (e) $1/\tau_P$ vs D.

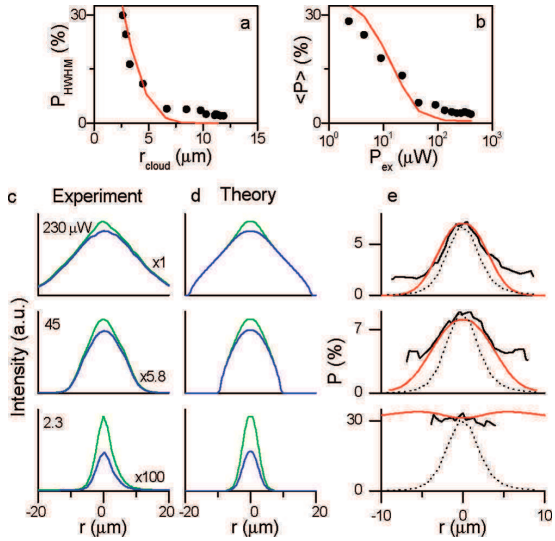

Figure 4. Exciton spin transport. (a) Experimental (points) and simulated (curve) polarization at HWHM of the exciton cloud P_{HWHM} as a function of r_{cloud}. (b) Experimental (points) and simulated (curve) spatially average polarization (P) as a function of excitation density. (c) PL intensity of indirect excitons in σ^+ and σ^- polarizations (green and blue curves) as a function of r for $P_{ex} = 2.3$, 45, and 230 μW with estimated densities at $r = 0$ of 9 $\times$ 10^8, 2 $\times$ 10^{10}, and 4 $\times$ 10^{10} cm $^{-2}$, respectively. (d) Simulated $n_{+1}(r)$ and $n_{-1}(r)$ for the same exciton densities as in (c). (e) Experimental (black curves) and simulated (red curves) PL polarization as a function of r for the same exciton densities as in (c, d). The profile of the bulk emission, which presents the excitation profile, is shown by dotted line. $T_{bath} = 1.7$ K. The simulations in (a, b, d, e) use $D(n)$ and $\tau_P(n)$ in Figure 3c,d.

polarization rapidly decreases with increasing temperature, and (iii) the decrease of polarization is correlated with the increase of the diffusion coefficient.

Density Dependence. Increasing the density leads to the increase of r_{cloud} and decrease of $P_{r=0}$ (Figure 3a,b). At low densities, r_{cloud} is essentially equal to the excitation spot radius. Similar to the case of temperature dependence, these measurements of r_{cloud} and P allow estimating D and τ_P as a function of density. The measured r_{cloud} and $P_{r=0}$ were simulated using eq 1 with D and τ_P as fitting parameters. The obtained density dependencies for D and τ_P are plotted in Figure 3c,d. The polarization degree of the exciton emission and the polarization relaxation time reduce with increasing density (Figure 3b,d). Similar to the case of temperature dependence, the decrease of polarization is correlated with the increase of the diffusion coefficient. Figure 3e shows τ_P^{-1} vs D for the data in Figure 3c,d.

Spatial Dependence: Exciton Spin Transport. The polarization at half-width at half-maximum (HWHM) of the exciton cloud P_{HWHM} is observed up to several micrometers away from the origin (Figure 4a). This gives a rough estimate for the length scale of exciton spin transport. Figure 4a,b also shows P_{HWHM} and the spatially average polarization (P) calculated using eq 1 with D and τ_p in Figure 3c,d obtained from fitting r_{cloud} and $P_{r=0}$ data in Figure 3a,b.

Essential characteristics of the exciton spin transport are presented in Figure 4c−e. Figure 4c shows the measured PL in σ^+ and σ^- polarization as a function of the distance from the excitation spot center r. Figure 4d shows the corresponding $n_{+1}(r)$ and $n_{-1}(r)$ calculated using eq 1 with D and τ_P in Figure 3c,d. The polarization profiles are wider than the excitation spot that directly shows exciton spin transport (Figure 4e). The measured and calculated data on exciton spin transport are in agreement (Figure 4).

The parameters used in the calculations of exciton spin transport D, τ_P, and τ_r were obtained from other experiments, different from exciton spin transport experiments: D, from exciton transport; τ_P, from emission polarization at the excitation spot center, and τ_r, from PL kinetics. The agreement between the calculated and measured data (Figure 4) indicates that the major characteristics of exciton spin transport are determined by D, τ_P, and τ_r. The following assumptions were made in the model: (i) splitting between optically active and dark exciton states is small $\Delta \ll k_BT$, (ii) hole spin flip is fast $\tau_h \ll \tau_e, \tau_{ex}$ and $\nabla[D\nabla\bar{n} + \mu\bar{n}\nabla(u_0 n_{total})] \ll \bar{n}/(2\tau_h)$, and (iii) conversion of the direct excitons into indirect excitons is fast $\tau_c \ll \tau_{P,d}$; see ref 30. The agreement between the experiment and the model (see Figure 4) indicates that these assumptions are justified and the model accurately describes exciton spin transport.

Discussion. Spin transport requires the ability of particles to travel maintaining spin polarization. This, in turn, requires large τ_r, D, and τ_P. Large τ_r and D are required to achieve exciton transport over substantial distances since the exciton diffusion length is determined by $(D\tau_r)^{1/2}$, while large τ_P is required for maintaining spin polarization during the transport. Large τ_r is characteristic for indirect excitons for which it is orders of magnitude larger than that for regular direct excitons. Large D is achieved with increasing exciton density (Figure

3a,c). This behavior is consistent with the localization−delocalization transition: Excitons are localized at low densities due to disorder and delocalized at high densities when the disorder is screened by repulsively interacting indirect excitons.[23,25] Localized excitons do not travel beyond the excitation spot while delocalized excitons spread over the distance $\sim(D\tau_r)^{1/2}$. This accounts for the density dependence of r_{cloud} and D (Figure 3a,c). r_{cloud} and D also increase with temperature (Figure 2a,c), because of thermal activation of indirect excitons over maxima of the disorder potential.

For indirect excitons with a small electron−hole overlap $\tau_{ex} \propto \tau_r^2$ is large, $\tau_{ex} \gg \tau_e$, and $\tau_P \approx \tau_e/2$ so that the polarization relaxation is governed by the electron spin relaxation and, therefore, can be long. Indeed, τ_P for indirect excitons at low temperatures and low densities reaches 10 ns (Figures 2d and 3d), much longer than τ_P for regular excitons, which is in the range of tens of picoseconds.[14,15] This orders of magnitude enhancement of the spin relaxation time for indirect excitons is achieved due to a small electron−hole overlap.

However, P and τ_P for indirect excitons drop with increasing temperature and density (Figures 2 and 3). For qualitative understanding of this behavior, we compare the variations of the polarization relaxation time and diffusion coefficient. Figures 2c,d and 3c,d show that τ_P^{-1} increases with D when the temperature or density is varied. This behavior complies with the D'yakonov-Perel' (DP) spin relaxation mechanism[26] for which the spin relaxation time $\tau_{e,ex}^{-1} = \langle\Omega_{e,ex}^2\tau\rangle$, where $\Omega_{e,ex}$ is the frequency of spin precession caused by the energy splitting between different spin states, $\tau \approx m_{ex}D/(k_BT)$ momentum scattering time, and m_{ex} exciton mass.

Parts a and e of Figure 4 show that the length scale for exciton spin transport reaches several micrometers. It is large enough (i) for studying exciton spin transport by optical experiments, (ii) for studying spin-polarized exciton gases in microscopic patterned devices, e.g., in in-plane lattices,[25] in which the period can be below a micrometer, and (iii) for the development of spin-optoelectronic devices where *spin* fluxes of excitons can be controlled in analogy to the control of fluxes of unpolarized excitons in ref 27 (the distance between source and drain in the excitonic transistor in ref 27 was 3 μm; however, it is expected that the dimensions can be reduced below 1 μm by using e-beam lithography). The length scale for exciton spin transport exceeds the length scale for electron spin transport in metals where it is typically below 1 μm.[28]

Estimation of Spin Splitting. The measured dependence $\tau_P^{-1}(D)$ can be used to estimate the spin splitting. For the splitting of electron states caused by the Dresselhaus mechanism,[29] which is a likely scenario, $\Omega_e = 2\beta k/\hbar$ where k is the electron wave-vector. For the average thermal k of an electron in an exciton $k_T = (2m_{ex}k_BT/\hbar^2)^{1/2}m_e/m_{ex}$, one obtains $\tau_P^{-1} = 2\tau_e^{-1} = 16\beta^2m_e^2D/\hbar^4$ (m_e is electron mass) and the measured $\tau_P^{-1}(D)$ (Figure 3c) leads to the estimate of the spin splitting constant $\beta \approx 25$ meV Å.

The value of β for $\langle 001\rangle$ oriented QW can be also roughly estimated as $\beta = \gamma_c\langle k_z^2\rangle \approx \gamma_c(\pi/a)^2$, where a is the extension of the electron wave function in the QW and $\gamma_c \approx 27.5$ eV Å^3 is the bulk GaAs Dresselhaus constant.[29] For the studied CQW structure with a confining potential of 8 nm width and 260 meV depth, we obtain $\beta \approx 20$ meVÅ, in agreement with the experiment.

In conclusion, the spin transport of indirect excitons has been observed. It originates from a long spin relaxation time and long lifetime of indirect excitons. The phenomenological model for exciton spin transport is in agreement with the experiment.

Acknowledgment. This work is supported by DOE and EPSRC. We thank Misha Fogler, Lu Sham, and Congjun Wu for discussions.

Supporting Information Available: Details of exciton spin dynamics, the phenomenological model for exciton spin transport, and direct to indirect exciton conversion. This material is available free of charge via the Internet at http://pubs.acs.org.

References

(1) D'yakonov, M. I.; Perel', V. I. Current-induced spin orientation of electrons in semiconductors. *Phys. Lett. A* **1971**, *35*, 459.
(2) Hirsch, J. E. Spin Hall Effect. *Phys. Rev. Lett.* **1999**, *83*, 1834.
(3) Sih, V.; Myers, R. C.; Kato, Y. K.; Lau, W. H.; Gossard, A. C.; Awschalom, D. D. Spatial imaging of the spin Hall effect and current-induced polarization in two-dimensional electron gases. *Nat. Phys.* **2005**, *1*, 31.
(4) D'yakonov, M. I.; Perel', V. I. Possibility of orienting electron spins with current. *Zh. Eksp. Teor. Fiz. Pis'ma Red.* **1971**, *13*, 657. *Sov. Phys. JETP Lett.* **1971**, *13*, 467.
(5) Aronov, A. G.; Pikus, G. E. Spin injection into semiconductors. *Fiz. Tekh. Poluprovodn.* **1976**, *10*, 1177. *Sov. Phys. Semicond.* **1976**, *10*, 698.
(6) Dzhioev, R. I.; Zakharchenya, B. P.; Korenev, V. L.; Stepanova, M. N. Spin diffusion of optically oriented electrons and photon entrainment in n-gallium arsenide. *Fiz. Tverd. Tela* **1997**, *39*, 1975. *Phys. Solid State* **1997**, *39*, 1765.
(7) Kikkawa, J. M.; Awschalom, D. D. Lateral drag of spin coherence in gallium arsenide. *Nature* **1999**, *397*, 139.
(8) D'Amico, I.; Vignale, G. Spin diffusion in doped semiconductors: The role of Coulomb interactions. *Europhys. Lett.* **2001**, *55*, 566.
(9) Weber, C. P.; Gedik, N.; Moore, J. E.; Orenstein, J.; Stephens, J.; Awschalom, D. D. Observation of spin Coulomb drag in a two-dimensional electron gas. *Nature* **2005**, *437*, 1330.
(10) Carter, S. G.; Chen, Z.; Cundiff, S. T. Optical Measurement and Control of Spin Diffusion in n-Doped GaAs Quantum Wells. *Phys. Rev. Lett.* **2006**, *97*, 136602.
(11) Appelbaum, I.; Huang, Biqin; Monsma, D. J. Electronic measurement and control of spin transport in silicon. *Nature* **2007**, *447*, 295.
(12) Awschalom, D. D.; Flattté, M. E. Challenges for semiconductor spintronics. *Nat. Phys.* **2007**, *3*, 153.
(13) Andreani, L. C.; Bassani, F. Exchange interaction and polariton effects in quantum-well excitons. *Phys. Rev. B* **1990**, *41*, 7536.
(14) Maialle, M. Z.; de Andrada e Silva, E. A.; Sham, L. J. Exciton spin dynamics in quantum wells. *Phys. Rev. B* **1993**, *47*, 15776.
(15) Vinattieri, A.; Shah, Jagdeep; Damen, T. C.; Kim, D. S.; Pfeiffer, L. N.; Maialle, M. Z.; Sham, L. J. Exciton dynamics in GaAs quantum wells under resonant excitation. *Phys. Rev. B* **1994**, *50*, 10868.
(16) See, e.g.: Ivchenko, E. L. *Optical spectroscopy of semiconductor nanostructures*; Alpha Science International: Harrow, U.K., 2005.
(17) Butov, L. V.; Imamoglu, A.; Mintsev, A. V.; Campman, K. L.; Gossard, A. C. Photoluminescence kinetics of indirect excitons in GaAs/Al$_x$Ga$_{1-x}$As coupled quantum wells. *Phys. Rev. B* **1999**, *59*, 1625.
(18) Uenoyama, T.; Sham, L. J. Carrier relaxation and luminescence polarization in quantum wells. *Phys. Rev. B* **1990**, *42*, 7114.
(19) Alexandrou, A.; Kash, J. A.; Mendez, E. E.; Zachau, M.; Hong, J. M.; Fukuzawa, T.; Hase, Y. Electric-field effects on exciton lifetimes in

symmetric coupled GaAs/$Al_{0.3}Ga_{0.7}As$ double quantum wells. *Phys. Rev. B* **1990**, *42*, 9225.
(20) Hagn, M.; Zrenner, A.; Böhm, G.; Weimann, G. Electric-field-induced exciton transport in coupled quantum well structures. *Appl. Phys. Lett.* **1995**, *67*, 232.
(21) Larionov, A. V.; Timofeev, V. B.; Hvam, J.; Soerensen, K. Interwell excitons in GaAs/AlGaAs double quantum wells and their collective properties. *Sov. Phys. JETP* **2000**, *90*, 1093.
(22) Gärtner, A.; Holleithner, A. W.; Kotthaus, J. P.; Schul, D. Drift mobility of long-living excitons in coupled GaAs quantum wells. *Appl. Phys. Lett.* **2006**, *89*, 052108.
(23) Ivanov, A. L.; Smallwood, L. E.; Hammack, A. T.; Yang, Sen; Butov, L. V.; Gossard, A. C. Origin of the inner ring in photoluminescence patterns of quantum well excitons. *Europhys. Lett.* **2006**, *73*, 920.
(24) Schindler, C.; Zimmermann, R. Analysis of the exciton-exciton interaction in semiconductor quantum wells. *Phys. Rev. B* **2008**, *78*, 045313.
(25) Remeika, M.; Graves, J. C.; Hammack, A. T.; Meyertholen, A. D.; Fogler, M. M.; Butov, L. V.; Hanson, M.; Gossard, A. C. Localization-Delocalization Transition of Indirect Excitons in Lateral Electrostatic Lattices. *Phys. Rev. Lett.* **2009**, *102*, 186803.
(26) D'yakonov, M. I.; Perel', V. I. Spin orientation of electrons associated with the interband absorption of light in semiconductors. *Zh. Eksp. Teor. Fiz.* **1971**, *60*, 1954. *Sov. Phys. JETP* **1971**, *33*, 1053.
(27) High, A. A.; Novitskaya, E. E.; Butov, L. V.; Hanson, M.; Gossard, A. C. Control of Exciton Fluxes in an Excitonic Integrated Circuit. *Science* **2008**, *321*, 229.
(28) Bass, J.; Pratt, W. P., Jr. Spin-diffusion lengths in metals and alloys, and spin-flipping at metal/metal interfaces: an experimentalist's critical review. *J. Phys.: Condens. Matter* **2007**, *19*, 183201.
(29) D'yakonov, M. I.; Kachorovskii, V. Yu. Spin relaxation of two-dimensional electrons in noncentrosymmetric semiconductors. *Fiz. Tekh. Poluprovodn.* **1986**, *20*, 178. *Sov. Phys. Semicond.* **1986**, *20*, 110.
(30) Supplementary online materials.

NL9024227

Spin Currents in a Coherent Exciton Gas

A. A. High,[1] A. T. Hammack,[1] J. R. Leonard,[1,*] Sen Yang,[1] L. V. Butov,[1] T. Ostatnický,[2] M. Vladimirova,[3] A. V. Kavokin,[3,4,5] T. C. H. Liew,[6] K. L. Campman,[7] and A. C. Gossard[7]

[1]*Department of Physics, University of California at San Diego, La Jolla, California 92093-0319, USA*
[2]*Faculty of Mathematics and Physics, Charles University in Prague, Ke Karlovu 3, 121 16 Prague, Czech Republic*
[3]*Laboratoire Charles Coulomb, Université Montpellier 2, CNRS, UMR 5221, F-34095 Montpellier, France*
[4]*School of Physics and Astronomy, University of Southampton, SO17 1BJ Southampton, United Kingdom*
[5]*Spin Optics Laboratory, State University of Saint Petersburg, 1 Ulianovskaya 198504, Russia*
[6]*Mediterranean Institute of Fundamental Physics, 31 via Appia Nuova, Rome 00040, Italy*
[7]*Materials Department, University of California at Santa Barbara, Santa Barbara, California 93106-5050, USA*
(Received 27 March 2013; published 11 June 2013)

We report the observation of spin currents in a coherent gas of indirect excitons. The realized long-range spin currents originate from the formation of a coherent gas of bosonic pairs—a new mechanism to suppress the spin relaxation. The spin currents result in the appearance of a variety of polarization patterns, including helical patterns, four-leaf patterns, spiral patterns, bell patterns, and periodic patterns. We demonstrate control of the spin currents by a magnetic field. We also present a theory of coherent exciton spin transport that describes the observed exciton polarization patterns and indicates the trajectories of the spin currents.

DOI: 10.1103/PhysRevLett.110.246403 PACS numbers: 71.35.−y, 72.25.Dc

Studies of electron spin currents in semiconductors led to the discoveries of the spin Hall effect [1–6], persistent spin helix [7], and spin drift, diffusion and drag [8–10]. An important role in spin current phenomena is played by spin-orbit (SO) coupling. It is the origin of the spin Hall effect and persistent spin helix. It also creates spin structures with the spin vector perpendicular to the momentum of the electrons in metals [11] and topological insulators [12–14]. While phenomena caused by SO coupling are ubiquitous in fermionic systems, they have yet to be explored in bosonic matter. Available experimental data for bosons include the optical spin Hall effect in photonic systems [15–17] and spin patterns in atomic condensates [18,19].

Here, we report the observation of spin currents in a system of matter bosons in semiconductors—indirect excitons. Excitons—bound pairs of electrons and holes—form a model system to study spin currents of bosons [20]. Spin-orbit coupling for an exciton originates from the combined Dresselhaus and Rashba effects for the electron and the hole [21–23]. An indirect exciton can be formed by an electron and a hole confined in separate quantum-well (QW) layers [see Fig. 1(a)]. The spatial separation reduces the overlap of electron and hole wave functions thus producing indirect excitons with lifetimes orders of magnitude longer than those of direct excitons [24,25]. Due to their long lifetimes, indirect excitons can travel over large distances before recombination [26] and can cool down below the temperature of quantum degeneracy and form a condensate [27].

The condensation of indirect excitons was predicted to cause the suppression of exciton scattering [24]. The measured strong enhancement of the exciton coherence length [27] experimentally shows the suppression of exciton scattering. The suppression of scattering results in the suppression of the Dyakonov-Perel and Elliott-Yafet mechanisms of spin relaxation [28]. Furthermore, the spatial separation between an electron and a hole suppresses the Bir-Aronov-Pikus mechanism of spin relaxation for indirect excitons [29,30]. The suppression of these mechanisms of spin relaxation results in a strong enhancement of the spin relaxation time in a condensate of indirect excitons. While the spin relaxation times of free fermions—electrons and holes—can be short [29], the formation of a coherent gas of their bosonic pairs results in a strong enhancement of their spin relaxation times. This mechanism to suppress the spin relaxation and facilitate long-range spin currents can be called coherent pairing.

Previous studies identified the external ring and localized bright spot (LBS) rings in the emission pattern of indirect excitons [see Fig. 1(c)] as sources of cold excitons [27]. These rings form on the boundaries between electron-rich and hole-rich regions; the former is created by current through the structure (specifically, by the current filament at the LBS center in the case of the LBS ring), whereas the latter is created by optical excitation [see Fig. 1(b)]; see Ref. [27] and references therein. In Ref. [27], we presented the studies of spontaneous coherence of indirect excitons in the ring region.

Here, we present the studies of spin currents and associated spin patterns around the sources of cold excitons—the rings. We present the observation of patterns of circular polarization, corresponding to spin perpendicular to the QW plane. We also show that the observed polarization

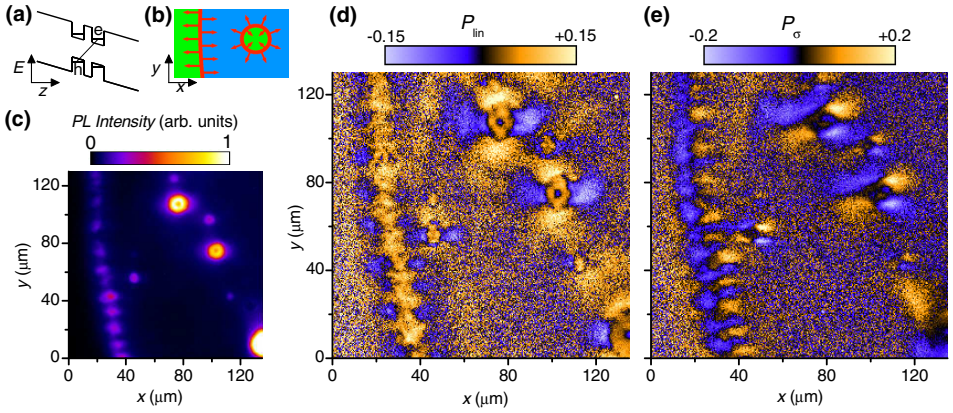

FIG. 1 (color online). Polarization patterns in exciton emission. (a) Diagram of the CQW: e, electron; h, hole. (b) Schematic of exciton formation in the external ring (left) and LBS ring (right); excitons (red) form on the boundary of hole-rich (blue) and electron-rich (green) areas. Exciton transport is indicated by red arrows. (c) A segment of the emission pattern of indirect excitons showing the external ring (left) and multiple LBS. (d),(e) Patterns of linear $P_{\rm lin} = (I_x - I_y)/(I_x + I_y)$ (d) and circular $P_\sigma = (I_{\sigma^+} - I_{\sigma^-})/(I_{\sigma^+} + I_{\sigma^-})$ (e) polarization of the emission of indirect excitons in the region shown in (c). $T_{\rm bath} = 0.1$ K.

patterns are controlled by a magnetic field: these data prove that the pattern of linear polarization corresponds to spin orientation rather than merely to the orientation of an exciton dipole. We also deduce trajectories of electron and hole spin currents from the measured polarization patterns.

The exciton polarization currents and associated spin textures are revealed by the polarization pattern of the emitted light measured by polarization-resolved imaging [see Figs. 1(d) and 1(e)]. Experiments are performed in an optical dilution refrigerator. The photoexcitation is nonresonant and spatially separated so that the exciton polarization is not induced by the pumping light.

The binding energy released at the exciton formation in the rings and the current filament at the LBS center heat the exciton gas. The former heating source depletes the exciton condensate in the rings [27]. The latter is so strong that no condensate forms in the LBS ring center and the exciton gas is classical there [27]. Excitons cool down with increasing distance r away from the heating sources so that they can approach the condensation temperature at $r = r_0$ where the condensation is detected by interferometric measurements [27].

The indirect excitons in a GaAs coupled quantum well structure (CQW) may have four spin projections on the z direction normal to the CQW plane: $J_z = -2, -1, +1, +2$. The states $J_z = -1$ and $+1$ contribute to left- and right-circularly polarized emission and their coherent superposition to linearly polarized emission, whereas the states $J_z = -2$ and $+2$ are dark [29]. The electron and hole spin projections on the z axis are given by J_z, while in-plane projections of electron and hole spins can be deduced from the off-diagonal elements of the exciton spin density matrix, which can be obtained from the measured polarization pattern (see the Supplemental Material [31]). The exciton states linearly polarized along the axes of symmetry are generally split due to in-plane anisotropy induced by the crystallographic axis orientation and strain.

The observed polarization patterns are qualitatively similar for both sources of cold excitons—the external ring and LBS ring. A LBS ring is close to a model radially symmetric source of excitons with a divergent (hedgehog) momentum distribution [see Fig. 1(b)] and we concentrate on the polarization textures around the LBS here. All LBS rings in the emission pattern show similar spin textures [see Figs. 1(d) and 1(e)].

A ring of linear polarization is observed around each LBS center [see Figs. 1(d) and 2(a)]. This ring is observed in the region $r < r_0$ where the exciton gas is classical. The linear polarization originates from the thermal distribution of excitons over the linearly polarized exciton states. Heating of the exciton gas by the current filament reduces the polarization degree in the LBS center and, as a result, leads to the appearance of a ring of linear polarization. No such polarization reduction is observed in the external ring, consistent with the absence of heating by current filaments in the external ring area [see Fig. 1(d)].

A helical exciton polarization texture that winds by 2π around the origin emerges in the LBS area at $r > r_0$ where the condensate forms (the latter is measured by shift interferometry); see Figs. 1(d), 2(a), and 2(c). The LBS exhibits a divergent hedgehog-shaped momentum distribution [see Fig. 3(d)]. The exciton polarization is perpendicular to exciton momentum [see Figs. 2(a) and 3(d)]. This produces vortices of linear polarization which emerge in concert with spontaneous coherence below the critical temperature

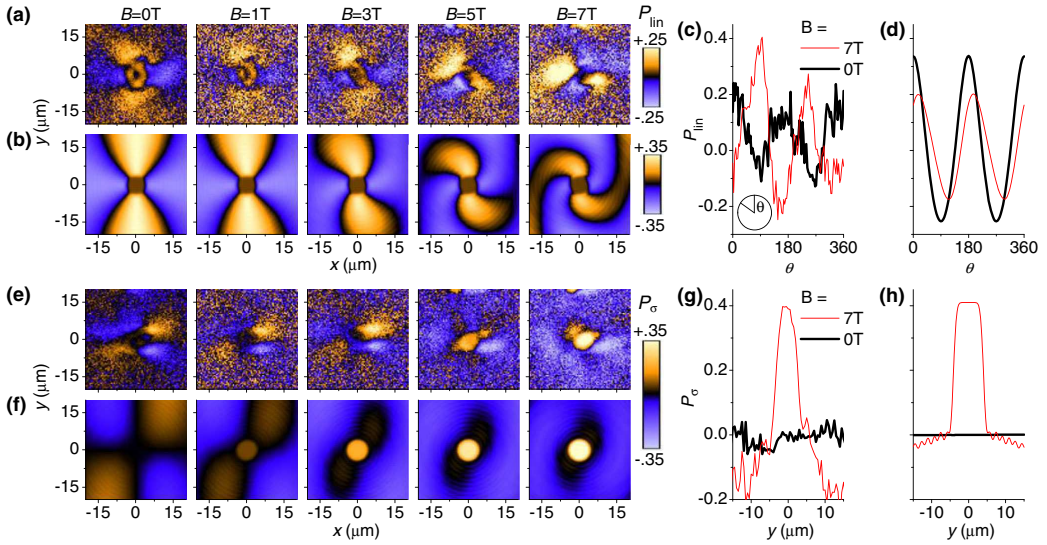

FIG. 2 (color online). Control of polarization patterns. Measured (a) and simulated (b) patterns of linear polarization of the emission of indirect excitons P_{lin} in the region of LBS for different magnetic fields perpendicular to the QW plane B. Measured (c) and simulated (d) azimuthal variation of P_{lin} at a distance from the LBS center $r = 9$ μm for $B = 0$ (black) and 7 T (red). Angles are measured from the y axis. Measured (e) and simulated (f) patterns of circular polarization of the emission of indirect excitons P_σ in the region of LBS for different B. Measured (g) and simulated (h) cross sections of P_σ at $x = 0$ for $B = 0$ (black) and 7 T (red). For all data, $T_{bath} = 0.1$ K; the LBS is at (105,75) in Fig. 1(c). See the Supplemental Material [31].

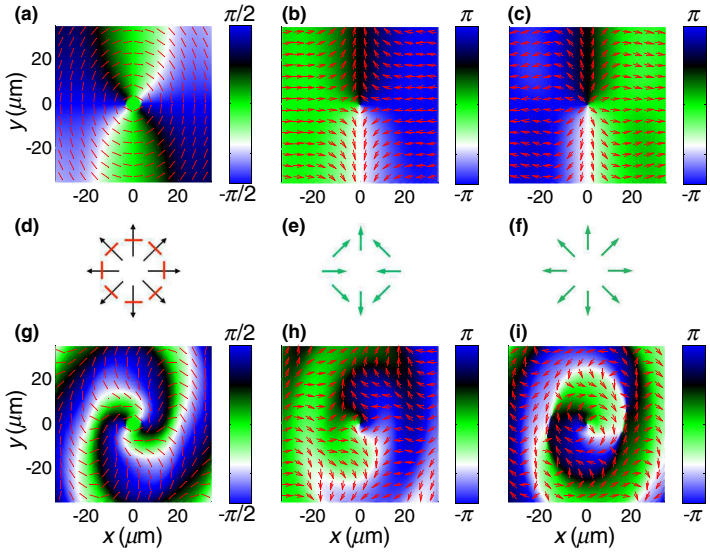

FIG. 3 (color online). Spin textures. Simulated in-plane exciton polarization (a), electron spin (b), and hole spin (c) patterns. (d) Schematic of exciton momentum (black arrows) and linear polarization (red lines) patterns. Schematic of effective magnetic fields given by the Dresselhaus SO interaction for electrons (e) and holes (f). Exciton polarization (g), electron spin (h), and hole spin (i) patterns in applied magnetic field $B = 7$ T. The lines (arrows) and the color visualize the orientation of the linear polarization (spin).

(see the Supplemental Material [31]). The observed radial exciton polarization currents are associated with spin currents carried by electrons and holes bound into excitons as detailed below.

Applied magnetic fields bend the spin current trajectories creating spiral patterns of linear polarization around the origin [see Figs. 2(a) and 2(c)]. The spiral direction of the exciton polarization current clearly deviates from the radial direction of the exciton density current [see Figs. 2(a) and 2(c)]. The control of the polarization patterns by a magnetic field shows that they are associated with spin.

Regular patterns are also observed in circular polarization [see Figs. 1(e) and 2(e)]. A LBS source of excitons generates a four-leaf pattern of circular polarization [see Figs. 1(e) and 2(e)]. This pattern vanishes with increasing temperature (see the Supplemental Material [31]). An applied magnetic field transforms the four-leaf pattern to a bell-like pattern of circular polarization with a strong circular polarization in the center and polarization inversion a few micrometers away from the center [see Figs. 2(e) and 2(g)].

Polarization patterns are also observed in the external ring region [see Figs. 1(d) and 1(e)]. At low temperatures, the macroscopically ordered exciton state (MOES) forms in the external ring. The MOES is characterized by a spatially ordered array of higher-density beads and is a condensate in momentum space [27]. The polarization texture in the external ring region appears as the superposition of the polarization textures produced by the MOES beads with each being similar to the texture produced by a LBS [see Figs. 1(d) and 1(e)]. A periodic array of beads in the MOES [see Fig. 1(c)] creates periodic polarization textures [see Figs. 1(d) and 1(e)]. The periodic polarization textures in the external ring region vanish above the critical temperature of the MOES (see the Supplemental Material [31]).

Below we present a theoretical model which describes the appearance of the exciton polarization textures and links them to spin currents carried by electrons and holes bound into bright and dark exciton states. This model is based on ballistic exciton transport out of the LBS origin and coherent precession of spins of electrons and holes. The former originates from the suppression of scattering and the latter from the suppression of spin relaxation in the condensate of indirect excitons. The states with different spins are split due to the splitting of linearly polarized exciton states and SO interaction, which is described by the Dresselhaus Hamiltonian $H_e = \beta_e(k_x^e\sigma_x - k_y^e\sigma_y)$ for electrons and $H_h = \beta_h(k_x^h\sigma_x + k_y^h\sigma_y)$ for holes [21–23] ($\mathbf{k}_{e,h}$ are electron and hole wave vectors given by $k_e = k_{\rm ex}m_e/(m_e + m_h)$ and $k_h = k_{\rm ex}m_h/(m_e + m_h)$, m_e and m_h are in-plane effective masses of the electron and heavy hole, respectively, $k_{\rm ex}$ is the exciton wave vector, $\beta_{e,h}$ are constants, and $\sigma_{x,y}$ are Pauli matrices). In the basis of four exciton states with spins $J_z = +1, -1, +2, -2$, the coherent spin dynamics in the system is governed by a model matrix Hamiltonian:

$$\hat{H} = \begin{bmatrix} E_b - (g_h - g_e)\mu_B B/2 & -\delta_b & k_e\beta_e e^{-i\phi} & k_h\beta_h e^{-i\phi} \\ -\delta_b & E_b + (g_h - g_e)\mu_B B/2 & k_h\beta_h e^{i\phi} & k_e\beta_e e^{i\phi} \\ k_e\beta_e e^{i\phi} & k_h\beta_h e^{-i\phi} & E_d - (g_h + g_e)\mu_B B/2 & -\delta_d \\ k_h\beta_h e^{i\phi} & k_e\beta_e e^{-i\phi} & -\delta_d & E_d + (g_h + g_e)\mu_B B/2 \end{bmatrix}, \quad (1)$$

where E_b and E_d are energies of bright and dark excitons in an ideal isotropic QW, and δ_b and δ_d describe the effect of in-plane anisotropy resulting in the splitting of exciton states linearly polarized along the axes of symmetry. The angle φ is measured from the x axis. The details of this model are presented in the Supplemental Material [31]. Exciton propagation out of the origin governed by this Hamiltonian results in the appearance of a vortex of linear polarization with the polarization perpendicular to the radial direction and a four-leaf pattern of circular polarization in $B = 0$, as well as spiral patterns of linear polarization and bell-like patterns of circular polarization in finite magnetic fields. This model qualitatively reproduces the main features of the experiment for both linear [see Figs. 2(a)–2(d)] and circular [see Figs. 2(e)–2(h)] polarizations.

This model describes the exciton polarization currents and allows us to deduce the spin currents carried by electrons and holes bound to excitons as detailed in the Supplemental Material [31]. Figures 3(b) and 3(c) show the electron and hole spin textures deduced from the measured exciton polarization texture [see Figs. 2(a) and 3(a)]. One can see that both the electron and hole spin tend to align along the effective magnetic fields given by the Dresselhaus SO interaction $\mathbf{B}_{\rm eff(e)} = (2\beta_e/g_e\mu_B) \times (-k_{e,x}, k_{e,y})$, $\mathbf{B}_{\rm eff(h)} = (2\beta_h/g_h\mu_B)(k_{h,x}, k_{h,y})$ [see Figs. 3(e) and 3(f)], consistent with the model. The patterns of $P_{\rm lin}$ corresponding to the simulations in Fig. 3 are shown in Fig. 2(b).

The model can be improved by including nonlinear effects. In the Supplemental Material [31], we present simulations of exciton spin currents using Gross-Pitaevskii type equations, which treat the excitons as a coherent field outside the LBS center and include dispersion and interaction. In particular, the nonlinear effects change the momenta and effective magnetic fields for

propagating excitons. The simulation results are similar to that within the density matrix approach and are in agreement with the experiment. Nonlinear spin-related phenomena form interesting perspectives for future studies. In conclusion, long-range spin currents governed by spin-orbit interaction and controlled by an applied magnetic field have been observed in a coherent exciton gas.

We thank Misha Fogler, Jorge Hirsch, Leonid Levitov, Yuriy Rubo, Lu Sham, Ben Simons, and Congjun Wu for discussions. This work was supported by DOE. The development of spectroscopy in the dilution refrigerator was also supported by ARO and NSF. A. V. K. acknowledges financial support from the Russian Ministry of Education and Science. T. O. was supported by the Ministry of Education and the Grant Agency of the Czech Republic. A. A. H. was supported by an Intel fellowship. J. R. L. was supported by a Chateaubriand Fellowship. T. C. H. L. was supported by the EU FP7 Marie Curie EPOQUES project. The collaboration was supported by EU ITN INDEX.

*jleonard@physics.ucsd.edu

[1] M. I. Dyakonov and V. I. Perel, Phys. Lett. **35A**, 459 (1971).
[2] J. E. Hirsch, Phys. Rev. Lett. **83**, 1834 (1999).
[3] S. Murakami, N. Nagaosa, and S.-C. Zhang, Science **301**, 1348 (2003).
[4] J. Sinova, D. Culcer, Q. Niu, N. A. Sinitsyn, T. Jungwirth, and A. H. MacDonald, Phys. Rev. Lett. **92**, 126603 (2004).
[5] Y. K. Kato, R. C. Myers, A. C. Gossard, and D. D. Awschalom, Science **306**, 1910 (2004).
[6] J. Wunderlich, B. Kaestner, J. Sinova, and T. Jungwirth, Phys. Rev. Lett. **94**, 047204 (2005).
[7] J. D. Koralek, C. P. Weber, J. Orenstein, B. A. Bernevig, S.-C. Zhang, S. Mack, and D. D. Awschalom, Nature (London) **458**, 610 (2009).
[8] J. M. Kikkawa and D. D. Awschalom, Nature (London) **397**, 139 (1999).
[9] C. P. Weber, N. Gedik, J. E. Moore, J. Orenstein, J. Stephens, and D. D. Awschalom, Nature (London) **437**, 1330 (2005).
[10] S. A. Crooker, M. Furis, X. Lou, C. Adelmann, D. L. Smith, C. J. Palmstrom, and P. A. Crowell, Science **309**, 2191 (2005).
[11] M. Hoesch, M. Muntwiler, V. N. Petrov, M. Hengsberger, L. Patthey, M. Shi, M. Falub, T. Greber, and J. Osterwalder, Phys. Rev. B **69**, 241401(R) (2004).
[12] M. Köning, H. Buhmann, L. W. Molenkamp, T. Hughes, C.-X. Liu, X.-L. Qi, and S.-C. Zhang, J. Phys. Soc. Jpn. **77**, 031007 (2008).
[13] J. E. Moore, Nature (London) **464**, 194 (2010).
[14] M. Z. Hasan and C. L. Kane, Rev. Mod. Phys. **82**, 3045 (2010).
[15] A. Kavokin, G. Malpuech, and M. Glazov, Phys. Rev. Lett. **95**, 136601 (2005).
[16] C. Leyder, M. Romanelli, J. Ph. Karr, E. Giacobino, T. C. H. Liew, M. M. Glazov, A. V. Kavokin, G. Malpuech, and A. Bramati, Nat. Phys. **3**, 628 (2007).
[17] M. Maragkou, C. E. Richards, T. Ostatnický, A. J. D Grundy, J. Zajac, M. Hugues, W. Langbein, and P. G. Lagoudakis, Opt. Lett. **36**, 1095 (2011).
[18] L. E. Sadler, J. M. Higbie, S. R. Leslie, M. Vengalattore, and D. M. Stamper-Kurn, Nature (London) **443**, 312 (2006).
[19] Y.-J. Lin, K. Jiménez-García, and I. B. Spielman, Nature (London) **471**, 83 (2011).
[20] L. V. Keldysh and A. N. Kozlov, Sov. Phys. JETP **27**, 521 (1968).
[21] E. I. Rashba and E. Ya Sherman, Phys. Lett. A **129**, 175 (1988).
[22] C. Wu and I. Mondragon-Shem, arXiv:0809.3532v1.
[23] J.-W. Luo, A. N. Chantis, M. van Schilfgaarde, G. Bester, and A. Zunger, Phys. Rev. Lett. **104**, 066405 (2010).
[24] Yu. E. Lozovik and V. I. Yudson, Sov. Phys. JETP **44**, 389 (1976).
[25] T. Fukuzawa, S. S. Kano, T. K. Gustafson, and T. Ogawa, Surf. Sci. **228**, 482 (1990).
[26] M. Hagn, A. Zrenner, G. Böhm, and G. Weimann, Appl. Phys. Lett. **67**, 232 (1995).
[27] A. A. High, J. R. Leonard, A. T. Hammack, M. M. Fogler, L. V. Butov, A. V. Kavokin, K. L. Campman, and A. C. Gossard, Nature (London) **483**, 584 (2012).
[28] M. I. Dyakonov, *Spin Physics in Semiconductors* (Springer, New York, 2008).
[29] M. Z. Maialle, E. A. de Andrada e Silva, and L. J. Sham, Phys. Rev. B **47**, 15 776 (1993).
[30] J. R. Leonard, Y. Y. Kuznetsova, S. Yang, L. V. Butov, T. Ostatnický, A. Kavokin, and A. C. Gossard, Nano Lett. **9**, 4204 (2009).
[31] See the Supplemental Material at http://link.aps.org/supplemental/10.1103/PhysRevLett.110.246403 for the theory of exciton spin currents, experimental data on the temperature dependence of polarization patterns, and movies showing polarization and spin textures versus magnetic field.

[P13] supplement

Supplementary Materials.
Spin currents in a coherent exciton gas.

A.A. High,[1] A.T. Hammack,[1] J.R. Leonard,[1] Sen Yang,[1] L.V. Butov,[1] T. Ostatnický,[2] M. Vladimirova,[3] A.V. Kavokin,[3,4,5] T.C.H. Liew,[6] K.L. Campman,[7] and A.C. Gossard[7]

[1]*Department of Physics, University of California at San Diego, La Jolla, CA 92093-0319, USA*
[2]*Faculty of Mathematics and Physics, Charles University in Prague, Ke Karlovu 3, 121 16 Prague, Czech Republic*
[3]*Université Montpellier 2, CNRS, Laboratoire Charles Coulomb UMR 5221, F-34095, Montpellier, France*
[4]*School of Physics and Astronomy, University of Southampton, SO17 1BJ, Southampton, United Kingdom*
[5]*Spin Optics Laboratory, State University of Saint Petersburg, 1, Ulianovskaya, 198504, Russia*
[6]*Mediterranean Institute of Fundamental Physics, 31, via Appia Nuova, Rome, 00040, Italy*
[7]*Materials Department, University of California at Santa Barbara, Santa Barbara, CA 93106-5050, USA*

(Dated: May 20, 2013)

THEORY OF EXCITON SPIN CURRENTS: DENSITY MATRIX APPROACH

Ballistic exciton transport with coherent spin precession

In zinc-blend semiconductor quantum wells (e.g. in GaAs/AlGaAs system), the lowest energy exciton states are formed by electrons with spin projections to the structure axis of $+1/2$ and $-1/2$ and heavy holes whose quasi-spin (sum of spin and orbital momentum) projection to the structure axis is $+3/2$ or $-3/2$. Consequently, the exciton spin defined as a sum of electron spin and heavy hole quasi-spin may have one of four projections to the structure axis: $-2, -1, +1, +2$ [1]. These states are usually nearly degenerate, while there may be some splitting between them due to the short and long-range exchange interactions. Here we derive the exciton Hamiltonian in the basis of $+1, -1, +2, -2$ states, accounting for the spin-orbit interaction [2, 3], long- and short-range exchange interactions [4] and Zeeman effect, but neglecting exciton-exciton interactions. We consider excitons propagating ballistically in plane of a quantum well. We shall characterize them by a fixed wave-vector k_{ex}.

In order to build the 4×4 matrix Hamiltonian for excitons, we start with simpler 2×2 Hamiltonians describing the spin-orbit Dresselhaus effect and Zeeman effect for electrons and holes.

The electron Hamiltonian in the basis of $(+1/2, -1/2)$ spin states writes:

$$H_e = \beta_e(k_{e,x}\sigma_x - k_{e,y}\sigma_y) - \frac{1}{2}g_e\mu_B B\sigma_z. \tag{1}$$

Here g_e is the electron g-factor, μ_B is the Bohr magneton, B is a magnetic field normal to the quantum well plane, β_e is the Dresselhaus constant describing spin-orbit interactions of electrons, the Pauli matrices are $\sigma_x = \begin{bmatrix} 0 & 1 \\ 1 & 0 \end{bmatrix}$, $\sigma_y = \begin{bmatrix} 0 & -i \\ i & 0 \end{bmatrix}$, $\sigma_z = \begin{bmatrix} 1 & 0 \\ 0 & -1 \end{bmatrix}$. Hence

$$H_e = \begin{bmatrix} -\frac{1}{2}g_e\mu_B B & \beta_e(k_{e,x} + ik_{e,y}) \\ \beta_e(k_{e,x} - ik_{e,y}) & \frac{1}{2}g_e\mu_B B \end{bmatrix} = \begin{bmatrix} -\frac{1}{2}g_e\mu_B B & \beta_e k_e e^{i\phi} \\ \beta_e k_e e^{-i\phi} & \frac{1}{2}g_e\mu_B B \end{bmatrix}. \tag{2}$$

Here ϕ is the angle between the electron wave-vector $\mathbf{k_e}$ and the chosen x-axis. The exciton Hamiltonian needs to be written in the basis of $(+1, -1, +2, -2)$ exciton states, which correspond to $(-1/2, +1/2, +1/2, -1/2)$ electron states. The electron spin-flip couples $+1$ and $+2$ states and -1 and -2 states. For each of these two couples of states we apply the Hamiltonian (2), which results in the following electronic contribution to the 4×4 exciton Hamiltonian:

$$\widehat{H_e} = \begin{bmatrix} g_e\mu_B B/2 & 0 & k_e\beta_e e^{-i\phi} & 0 \\ 0 & -g_e\mu_B B/2 & 0 & k_e\beta_e e^{i\phi} \\ k_e\beta_e e^{i\phi} & 0 & -g_e\mu_B B/2 & 0 \\ 0 & k_e\beta_e e^{-i\phi} & 0 & g_e\mu_B B/2 \end{bmatrix}. \tag{3}$$

The similar reasoning applies to the heavy hole contribution to the Hamiltonian: The hole Hamiltonian written in the basis of $(+3/2, -3/2)$ states is

$$H_h = \beta_h(k_{h,x}\sigma_x + k_{h,y}\sigma_y) - \frac{1}{2}g_h\mu_B B\sigma_z.$$

Here g_h is the heavy hole g-factor, β_h is the Dresselhaus constant for heavy holes [2, 3]. Hence,

$$H_h = \begin{bmatrix} -\frac{1}{2}g_h\mu_B B & \beta_h(k_{h,x} - ik_{h,y}) \\ \beta_h(k_{h,x} + ik_{h,y}) & \frac{1}{2}g_h\mu_B B \end{bmatrix} = \begin{bmatrix} -\frac{1}{2}g_h\mu_B B & \beta_h k_h e^{-i\phi} \\ \beta_h k_h e^{i\phi} & \frac{1}{2}g_h\mu_B B \end{bmatrix}. \tag{4}$$

Here ϕ is the angle between the hole wave vector k_h and the chosen x-axis. The exciton Hamiltonian is written in the basis of $(+1, -1, +2, -2)$ exciton states, which correspond to $(+3/2, -3/2, +3/2, -3/2)$ hole states. The hole spin-flip couples $+1$ and -2 states and -1 and $+2$ states. For each of these two couples of states we apply the Hamiltonian (4), which results in the following hole contribution to the 4×4 exciton Hamiltonian:

$$\widehat{H_h} = \begin{bmatrix} -g_h\mu_B B/2 & 0 & 0 & k_h\beta_h e^{-i\phi} \\ 0 & g_h\mu_B B/2 & k_h\beta_h e^{i\phi} & 0 \\ 0 & k_h\beta_h e^{-i\phi} & -g_h\mu_B B/2 & 0 \\ k_h\beta_h e^{i\phi} & 0 & 0 & g_h\mu_B B/2 \end{bmatrix}. \tag{5}$$

For the translational motion of an exciton as a whole particle the exciton momentum is given by $\mathbf{P}_{ex} = (m_e + m_{hh})\mathbf{v}_{ex}$, where m_e and m_{hh} are in-plane effective masses of an electron and of a heavy hole, respectively, v_{ex} is the exciton speed. Having in mind that the exciton translational momentum is a sum of electron and hole translational momenta given by $\mathbf{P}_{e,h} = m_{e,hh}\mathbf{v}_{e,h}$, $\mathbf{v}_{e,h}$ being the electron (hole) speed, one can easily see that $\mathbf{v}_h = \mathbf{v}_e = \mathbf{v}_{ex}$. Having in mind that $\mathbf{P}_{ex} = \hbar\mathbf{k}_{ex}$, $\mathbf{P}_{e,h} = \hbar\mathbf{k}_{e,h}$ we have $\mathbf{k}_{ex} = \mathbf{k}_h + \mathbf{k}_e$, $k_e = \frac{m_e}{m_e+m_{hh}}k_{ex}$, $k_h = \frac{m_{hh}}{m_e+m_{hh}}k_{ex}$.

Besides the contributions from electron and hole spin orbit interactions and Zeeman splitting, there may be a purely excitonic contribution to the Hamiltonian, which is composed from the Hamiltonian for bright excitons written in the basis $(+1, -1)$:

$$H_b = E_b I - \delta_b\sigma_x = \begin{bmatrix} E_b & -\delta_b \\ -\delta_b & E_b \end{bmatrix}, \tag{6}$$

and the Hamiltonian for dark excitons written in the basis $(+2, -2)$:

$$H_d = E_d I - \delta_d\sigma_x = \begin{bmatrix} E_d & -\delta_d \\ -\delta_d & E_d \end{bmatrix}, \tag{7}$$

where I is the identity matrix. The terms with δ_b and δ_d describe the splittings of bright and dark states polarized along x and y axes in the plane of the structure due to the long-range exchange interaction. Such splitting may appear due to some in-plane anisotropy in the structure induced by strain or monolayer fluctuations of interfaces. We assume that it induced the splitting of X- and Y-polarized excitons, while it can be easily generalized to the splitting in diagonal or random axes. $E_b - E_d$ is the splitting between bright $+1$ and -1 and dark $+2$ and -2 exciton states which may be also split due to the short range exchange interaction. Note that Eqs. (6,7) can be simply obtained from the exciton Hamiltonians written in the basis of (X, Y) polarizations. E.g. for the bright excitons:

$$H_{XY} = \begin{bmatrix} E_b - \delta_b & 0 \\ 0 & E_b + \delta_b \end{bmatrix}, \tag{8}$$

$$H_b = C^{-1}H_{XY}C,$$

where $C = \frac{1}{\sqrt{2}}\begin{bmatrix} 1 & 1 \\ i & -i \end{bmatrix}$, $C^{-1} = \frac{1}{\sqrt{2}}\begin{bmatrix} 1 & -i \\ 1 & i \end{bmatrix}$ are the transformation matrices from linear to circular basis and vice versa [5]. The same reasoning applies to the dark excitons as well. The sum of Hamiltonians (6,7) in the 4×4 basis writes:

$$H_0 = \begin{bmatrix} E_b & -\delta_b & 0 & 0 \\ -\delta_b & E_b & 0 & 0 \\ 0 & 0 & E_d & -\delta_d \\ 0 & 0 & -\delta_d & E_d \end{bmatrix}. \tag{9}$$

Let us consider the excitons propagating with a wavevector $\mathbf{k}_{ex}$. We shall describe them by a spin density matrix $\hat{p} = |\Psi >< \Psi|$, where $\Psi = (\Psi_{+1}, \Psi_{-1}, \Psi_{+2}, \Psi_{-2})$ is the exciton wave-function projected to four spin states. The elements of this density matrix ρ_{ij} are dependent on the distance from the excitation spot $r = v_{ex}t$ and the polar angle ϕ. The elements of the upper left quarter of the density matrix are linked to the intensity of light emitted by bright exciton states I and to the components of the Stokes vector S_x, S_y and S_z of the emitted light:

$$\rho_{11} = \frac{1}{2} + S_z, \rho_{12} = S_x - iS_y, \rho_{21} = S_x + iS_y, \rho_{22} = \frac{1}{2} - S_z. \tag{10}$$

These expressions can be summarized using the Pauli matrices as $\begin{bmatrix} \rho_{11} & \rho_{12} \\ \rho_{21} & \rho_{22} \end{bmatrix} = \frac{1}{2}\hat{I} + \mathbf{S}\hat{\sigma}$, where $\hat{I}$ is the identity matrix.

The components of the Stokes vector are directly proportional to the polarization degree of light measured in XY axes, diagonal axes and the circular basis. The circular polarization degree of light emitted by propagating excitons can be obtained as

$$\rho_c = 2S_z = (\rho_{11} - \rho_{22})/(\rho_{11} + \rho_{22}), \tag{11}$$

the linear polarization degree can be found from

$$\rho_l = 2S_x = (\rho_{12} + \rho_{21})/(\rho_{11} + \rho_{22}), \tag{12}$$

the linear polarization degree measured in the diagonal axes (also referred to as a diagonal polarization degree) is given by

$$\rho_d = 2S_y = i(\rho_{12} - \rho_{21})/(\rho_{11} + \rho_{22}). \tag{13}$$

The dynamics of this density matrix is given by the quantum Liouville equation:

$$i\hbar\frac{d\hat{\rho}}{dt} = [\widehat{H}, \hat{\rho}], \tag{14}$$

where the Hamiltonian is composed from the electron, hole and exciton contributions given by Eqs. (3,5,9) as follows:

$$\hat{H} = \begin{bmatrix} E_b - (g_h - g_e)\mu_B B/2 & -\delta_b & k_e\beta_e e^{-i\phi} & k_h\beta_h e^{-i\phi} \\ -\delta_b & E_b + (g_h - g_e)\mu_B B/2 & k_h\beta_h e^{i\phi} & k_e\beta_e e^{i\phi} \\ k_e\beta_e e^{i\phi} & k_h\beta_h e^{-i\phi} & E_d - (g_h + g_e)\mu_B B/2 & -\delta_d \\ k_h\beta_h e^{i\phi} & k_e\beta_e e^{-i\phi} & -\delta_d & E_d + (g_h + g_e)\mu_B B/2 \end{bmatrix}. \tag{15}$$

The Hamiltonian (15) includes the electron, hole, and exciton contributions. Magnetic field affects the electron and hole contributions via the Zeeman splitting. Its effect on the exciton contributions, originating from the change of short and long-range exchange interactions, is neglected in the model. A qualitative agreement with the experiment justifies this approximation.

Note, that in a similar way one can describe the Rashba effect for electrons and holes on the exciton spin density matrix. Our estimations show that for the value of bias we use in these experiments the Rashba effect is much weaker than the Dresselhaus effect [6]. Therefore we limit ourself to the consideration of the Dresselhaus effect for electrons and holes. In order to make sure that the observed exciton polarization textures are indeed governed by the Dresselhaus effect, we have performed also the simulations accounting for the Rashba instead of Dresselhaus mechanism of spin-orbit coupling. These simulations produce exciton polarization patterns qualitatively different from the experimental data.

An example of how the Dresselhaus effect affects the polarization of propagating exciton

In order to obtain the spatial distribution of Stokes vector components in the cw regime we assume that all excitons propagate in radial directions from a point-like or a ring-like source. Their polarization state in a point characterized by the polar coordinates (r, ϕ) is readily obtained from the elements of the density matrix $\hat{\rho}(t, \phi)$ with $t = r/v_{ex}$. The exciton speed v_{ex} governs the spatial scale of the polarization textures.

Let us consider the simplest example of how the Dresselhaus effect affects the polarization of propagating excitons. In order to do it, we shall commute both parts in Eq. (14) with the Hamiltonian. As a result we shall have:

$$i\hbar\frac{d[\widehat{H},\hat{\rho}]}{dt}=[\hat{H},[\widehat{H},\hat{\rho}]]. \tag{16}$$

Now we take a time derivative from both parts of Eq. (14) and substitute the expression (16) in its right part:

$$-\hbar^2\frac{d^2\hat{\rho}}{dt^2}=[\hat{H},[\widehat{H},\hat{\rho}]]. \tag{17}$$

Let us suppose that initially we have an exciton state composed by bright excitons linearly polarized along x-axis and dark excitons linearly polarized along y-axis. It is described by the density matrix:

$$\hat{\rho}_0=\begin{bmatrix}1&1&0&0\\1&1&0&0\\0&0&1&-1\\0&0&-1&1\end{bmatrix}.$$

How this matrix would evolve in time due to the Dresselhaus effect on the electron spin? Let us assume $B=0$ for simplicity, and calculate the commutator of the Hamiltonian (3)

$$\widehat{H_e}=\begin{bmatrix}0&0&k_e\beta_e e^{-i\phi}&0\\0&0&0&k_e\beta_e e^{i\phi}\\k_e\beta_e e^{i\phi}&0&0&0\\0&k_e\beta_e e^{-i\phi}&0&0\end{bmatrix}.$$

with the density matrix $\hat{\rho}_0$. One can easily see that

$$[\widehat{H_e},\hat{\rho}_0]=2k_e\beta_e\begin{bmatrix}0&0&0&-\cos\phi\\0&0&-\cos\phi&0\\0&\cos\phi&0&0\\\cos\phi&0&0&0\end{bmatrix}.$$

The double commutator in the right part of Eq. (14) can be now found as:

$$[\widehat{H_e},[\widehat{H_e},\hat{\rho}_0]]=4(k_e\beta_e)^2\begin{bmatrix}0&\cos\phi e^{-i\phi}&0&0\\\cos\phi e^{i\phi}&0&0&0\\0&0&0&-\cos\phi e^{i\phi}\\0&0&-\cos\phi e^{-i\phi}&0\end{bmatrix}.$$

Let us substitute this expression back to Eq. (17) and look at the dynamics of the element $\rho_{12}=S_x-iS_y$ describing the linear and diagonal polarization degrees of bright excitons. One can easily see that $\hbar^2\frac{d^2\rho_{12}}{dt^2}=-\hbar^2\frac{d^2(S_x-iS_y)}{dt^2}=4(k_e\beta_e)^2\cos\phi e^{-i\phi}$. Separating the real and imaginary parts of this equation, we find the dynamics of the Stokes vector components: $\hbar^2\frac{d^2(S_x)}{dt^2}=-4(k_e\beta_e)^2\cos^2\phi$; $\hbar^2\frac{d^2(S_y)}{dt^2}=-2(k_e\beta_e)^2\sin 2\phi$.

Our initial conditions are: at $t=0, S_x=S_{x0}>0, S_y=0$. One can see that for $\phi=-\pi/2,\pi/2$ the polarization does not change: $S_x=S_{x0}, S_y=0$. For $\phi=0,\pi$, we have $S_y=0$, while S_x decreases and, eventually, inverts its sign. The negative S_x corresponds to Y-polarization. For any other value of ϕ both S_x and S_y change with time. Namely, S_x decreases, S_y builds up. The sign of S_y is negative (corresponds to the polarization along $(1,-1)$ axis) if $0<\phi<\pi/2$ and $\pi<\phi<3\pi/2$. The sign of S_y is positive (corresponds to the polarization along $(1,1)$ axis) if $\pi/2<\phi<\pi$ and $3\pi/2<\phi<2\pi$. This describes a polarization vortex.

In the same way one can show that the Hamiltonian (9) describing the exchange induced linear polarization splitting converts any linear polarization different from X and Y polarizations to the circular polarization.

Spin currents carried by electrons and holes bound into excitons

It is important to note that the present formalism addresses the spin part of the exciton wavefunction, which is a product of electron and hole spin functions. E.g. the probability to find the exciton in the spin state +1 is given by

a product of probabilities to find an electron in the spin state $-1/2$ and the heavy hole in the spin state $+3/2$. The four component exciton wave-function

$$\Psi = (\Psi_{+1}, \Psi_{-1}, \Psi_{+2}, \Psi_{-2},) = \left(\Psi_{e,-1/2}\Psi_{h,+3/2}, \Psi_{e,+1/2}\Psi_{h,-3/2}, \Psi_{e,+1/2}\Psi_{h,+3/2}, \Psi_{e,-1/2}\Psi_{h,-3/2}\right), \tag{18}$$

where $\Psi_{e,+1/2}$ and $\Psi_{e,-1/2}$ are the components of the electron spinor wave function, $\Psi_{h,+3/2}$ and $\Psi_{h,-3/2}$ are the components of the heavy hole spinor wave function. We shall normalize exciton, electron and hole wave functions to 1, namely:

$$\Psi_{+1}\Psi^*_{+1} + \Psi_{-1}\Psi^*_{-1} + \Psi_{+2}\Psi^*_{+2} + \Psi_{-2}\Psi^*_{-2} = \Psi_{e,+\frac{1}{2}}\Psi^*_{e,+\frac{1}{2}} + \Psi_{e,-\frac{1}{2}}\Psi^*_{e,-\frac{1}{2}} = \Psi_{h,+\frac{3}{2}}\Psi^*_{h,+\frac{3}{2}} + \Psi_{h,-\frac{3}{2}}\Psi^*_{h,-\frac{3}{2}} = 1. \tag{19}$$

Now, the exciton spin density matrix is given by

$$\hat{\rho} = |\Psi\rangle\langle\Psi| = \begin{bmatrix} \Psi_{+1}\Psi^*_{+1} & \Psi_{+1}\Psi^*_{-1} & \Psi_{+1}\Psi^*_{+2} & \Psi_{+1}\Psi^*_{-2} \\ \Psi_{-1}\Psi^*_{+1} & \Psi_{-1}\Psi^*_{-1} & \Psi_{-1}\Psi^*_{+2} & \Psi_{-1}\Psi^*_{-2} \\ \Psi_{+2}\Psi^*_{+1} & \Psi_{+2}\Psi^*_{-1} & \Psi_{+2}\Psi^*_{+2} & \Psi_{+2}\Psi^*_{-2} \\ \Psi_{-2}\Psi^*_{+1} & \Psi_{-2}\Psi^*_{-1} & \Psi_{-2}\Psi^*_{+2} & \Psi_{-2}\Psi^*_{-2} \end{bmatrix} =$$

$$= \begin{bmatrix} \Psi_{e,-\frac{1}{2}}\Psi^*_{e,-\frac{1}{2}}\Psi_{h,+\frac{3}{2}}\Psi^*_{h,+\frac{3}{2}} & \Psi_{e,-\frac{1}{2}}\Psi^*_{e,+\frac{1}{2}}\Psi_{h,+\frac{3}{2}}\Psi^*_{h,-\frac{3}{2}} & \Psi_{e,-\frac{1}{2}}\Psi^*_{e,+\frac{1}{2}}\Psi_{h,+\frac{3}{2}}\Psi^*_{h,+\frac{3}{2}} & \Psi_{e,-\frac{1}{2}}\Psi^*_{e,-\frac{1}{2}}\Psi_{h,+\frac{3}{2}}\Psi^*_{h,-\frac{3}{2}} \\ \Psi_{e,+\frac{1}{2}}\Psi^*_{e,-\frac{1}{2}}\Psi_{h,-\frac{3}{2}}\Psi^*_{h,+\frac{3}{2}} & \Psi_{e,+\frac{1}{2}}\Psi^*_{e,+\frac{1}{2}}\Psi_{h,-\frac{3}{2}}\Psi^*_{h,-\frac{3}{2}} & \Psi_{e,+\frac{1}{2}}\Psi^*_{e,+\frac{1}{2}}\Psi_{h,-\frac{3}{2}}\Psi^*_{h,+\frac{3}{2}} & \Psi_{e,+\frac{1}{2}}\Psi^*_{e,-\frac{1}{2}}\Psi_{h,-\frac{3}{2}}\Psi^*_{h,-\frac{3}{2}} \\ \Psi_{e,+\frac{1}{2}}\Psi^*_{e,-\frac{1}{2}}\Psi_{h,+\frac{3}{2}}\Psi^*_{h,+\frac{3}{2}} & \Psi_{e,+\frac{1}{2}}\Psi^*_{e,+\frac{1}{2}}\Psi_{h,+\frac{3}{2}}\Psi^*_{h,-\frac{3}{2}} & \Psi_{e,+\frac{1}{2}}\Psi^*_{e,+\frac{1}{2}}\Psi_{h,+\frac{3}{2}}\Psi^*_{h,+\frac{3}{2}} & \Psi_{e,+\frac{1}{2}}\Psi^*_{e,-\frac{1}{2}}\Psi_{h,+\frac{3}{2}}\Psi^*_{h,-\frac{3}{2}} \\ \Psi_{e,-\frac{1}{2}}\Psi^*_{e,-\frac{1}{2}}\Psi_{h,-\frac{3}{2}}\Psi^*_{h,+\frac{3}{2}} & \Psi_{e,-\frac{1}{2}}\Psi^*_{e,+\frac{1}{2}}\Psi_{h,-\frac{3}{2}}\Psi^*_{h,-\frac{3}{2}} & \Psi_{e,-\frac{1}{2}}\Psi^*_{e,+\frac{1}{2}}\Psi_{h,-\frac{3}{2}}\Psi^*_{h,+\frac{3}{2}} & \Psi_{e,-\frac{1}{2}}\Psi^*_{e,-\frac{1}{2}}\Psi_{h,-\frac{3}{2}}\Psi^*_{h,-\frac{3}{2}} \end{bmatrix}. \tag{20}$$

This representation allows us to obtain useful links between the elements of exciton, electron and hole density matrices, in particular:

$$\hat{\rho}_e = |\Psi_e\rangle\langle\Psi_e| = \begin{bmatrix} \Psi_{e,+\frac{1}{2}}\Psi^*_{e,+\frac{1}{2}} & \Psi_{e,+\frac{1}{2}}\Psi^*_{e,-\frac{1}{2}} \\ \Psi_{e,-\frac{1}{2}}\Psi^*_{e,+\frac{1}{2}} & \Psi_{e,-\frac{1}{2}}\Psi^*_{e,-\frac{1}{2}} \end{bmatrix} = \begin{bmatrix} \rho_{22}+\rho_{33} & \rho_{24}+\rho_{31} \\ \rho_{13}+\rho_{42} & \rho_{11}+\rho_{44} \end{bmatrix}, \tag{21}$$

$$\hat{\rho}_h = |\Psi_h\rangle\langle\Psi_h| = \begin{bmatrix} \Psi_{h,+\frac{3}{2}}\Psi^*_{h,+\frac{3}{2}} & \Psi_{h,+\frac{3}{2}}\Psi^*_{h,-\frac{3}{2}} \\ \Psi_{h,-\frac{3}{2}}\Psi^*_{h,+\frac{3}{2}} & \Psi_{h,-\frac{3}{2}}\Psi^*_{h,-\frac{3}{2}} \end{bmatrix} = \begin{bmatrix} \rho_{11}+\rho_{33} & \rho_{14}+\rho_{32} \\ \rho_{23}+\rho_{41} & \rho_{22}+\rho_{44} \end{bmatrix}. \tag{22}$$

We know that the components of electron and hole density matrices are linked with the projections of electron and hole spins as:

$$\hat{\rho}_e = \begin{bmatrix} \frac{1}{2}+S_{e,z} & S_{e,x}-iS_{e,y} \\ S_{e,x}+iS_{e,y} & \frac{1}{2}-S_{e,z} \end{bmatrix}, \hat{\rho}_h = \begin{bmatrix} \frac{1}{2}+S_{h,z} & S_{h,x}-iS_{h,y} \\ S_{h,x}+iS_{h,y} & \frac{1}{2}-S_{h,z} \end{bmatrix}, \tag{23}$$

(here, for the heavy hole we have assigned spin $+1/2$ to the state $+3/2$ and spin $-1/2$ to the state $-3/2$ accounting for the orbital momentum of these states of $+1$ and -1, respectively). Therefore, the z-component of spin polarization carried by electrons can be expressed as

$$S_{e,z} = (\rho_{22}+\rho_{33}-\rho_{11}-\rho_{44})/2, \tag{24}$$

and the z-component of spin polarization carried by holes can be expressed as

$$S_{h,z} = (\rho_{11}+\rho_{33}-\rho_{22}-\rho_{44})/2. \tag{25}$$

The in-plane component of electron and hole spins can be extracted from the off-diagonal elements of the density matrix. Namely, the x-component of electron spin is given by

$$S_{e,x} = (\rho_{13}+\rho_{31}+\rho_{24}+\rho_{42})/2, \tag{26}$$

the x-component of the hole spin is given by

$$S_{h,x} = (\rho_{14}+\rho_{23}+\rho_{32}+\rho_{41})/2, \tag{27}$$

the y-component of electron spin is given by

$$S_{e,y} = i(-\rho_{13}+\rho_{31}+\rho_{24}-\rho_{42})/2, \tag{28}$$

and the y-component of the hole spin is given by

$$S_{h,y} = i(\rho_{14}-\rho_{23}+\rho_{32}-\rho_{41})/2. \tag{29}$$

Effective fields

Spin-orbit effect for electrons and holes can be accounted by introducing an in-plane effective magnetic field:

$$H_{eff(e,h)} = -\frac{1}{2} g_{e,h} \mu_B \left(\mathbf{B}_{eff} \hat{\sigma}\right). \tag{30}$$

In the case of Dresselhaus Hamiltonian for electrons:

$$-\frac{1}{2} g_e \mu_B \mathbf{B}_{eff} = \beta_e \left(k_{e,x}, -k_{e,y}\right). \tag{31}$$

For holes the field is collinear to the wave-vector:

$$-\frac{1}{2} g_h \mu_B \mathbf{B}_{eff} = \beta_h \left(k_{h,x}, k_{h,y}\right). \tag{32}$$

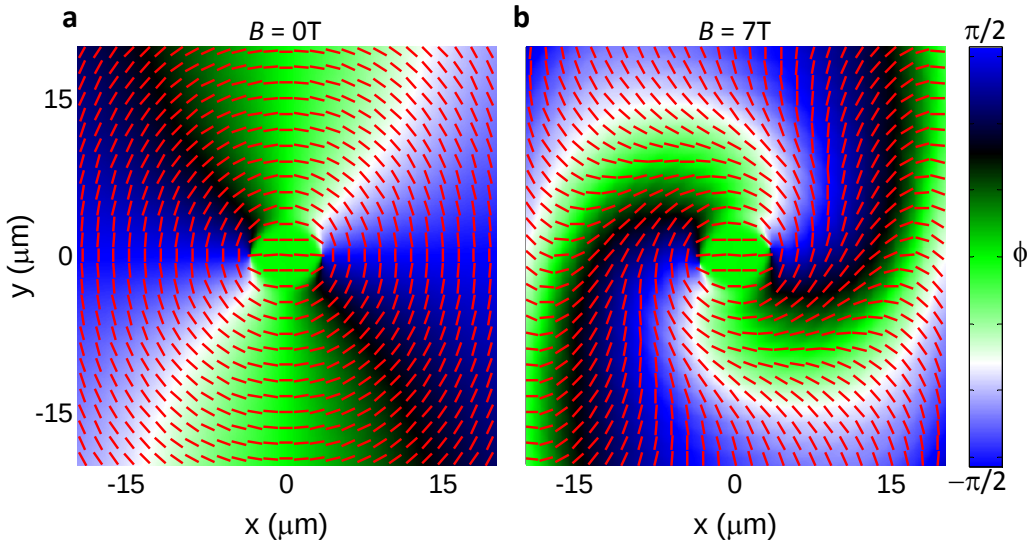

FIG. S1: **Simulated polarization patterns.** Simulated in-plane exciton polarization in magnetic field $B = 0$ (a) and 7 T (b). The lines and the color visualize the orientation of the linear polarization. The polarization plane comes to itself after rotation by π. Therefore, the color bar extending from $-\pi/2$ to $\pi/2$ describes the polarization rotation by 2π. For all data in the paper, magnetic fields are perpendicular to the QW plane.

Simulations

The system is modeled using Eq. (15) and parameters are adjusted to match the experimental data (see Fig. 2 in the main text). The same set of parameters is used for linear and circular polarizations and for all magnetic fields. The parameters are $\beta_e = 2.7$ μeVμm, $\beta_h = 0.92$ μeVμm, $\delta_b = 0.5$ μeV, $\delta_d = -13$ μeV, $E_b - E_d = 5$ μeV, $k_{ex} = 15.4$ μm^{-1}, $T = 0.1$ K, $g_e = -0.01$, and $g_h = +0.0085$. Some of the parameters were obtained in earlier studies and some of them were put as fitting parameters. All fitting parameters were chosen to be consistent with the data published in earlier studies: β_e is consistent with our earlier measurements [6], β_h – with the calculated values [2, 3], T – with the calculated temperature of indirect excitons for the studied structure [7], exciton splittings – with typical exciton splittings in GaAs structures [8], g-factors – with typical g-factors in quantum wells with ~ 8 nm width [9], and k_{ex} was taken within the light cone in the structure (we checked that the model leads to qualitatively similar patterns for various k_{ex}).

The images are presented with spatial averaging over 1.5 μm. The initial exciton state considered by this model is a ring around the LBS center where the exciton gas is classical. The ring radius is taken 4 μm. On this ring, the simulations consider the classical exciton energy distribution with $T = 0.1$ K, $k_{ex} = 0$. No simulations were performed inside this ring, the polarization in the ring is shown there. Beyond this ring, the exciton gas is coherent and the simulations consider ballistic exciton transport with coherent spin precession.

Figure S1 (an enlarged version of Fig. 3a,g in the main text) presents simulated patterns of in-plane projection of the Stokes vector of emitted light which directly maps the pseudospin of bright excitons (see e.g. [10, 11]. The patterns of light polarization corresponding to these simulations are shown in Fig. 2b in the main text. Figure S1 visualizes a vortex (a) and a spiral (b) pattern of linear polarization in zero (a) and a finite (b) magnetic field. The simulations produce the observed exciton polarization textures as described in the main text.

THEORY OF EXCITON SPIN CURRENTS: GROSS-PITAEVSKII EQUATIONS

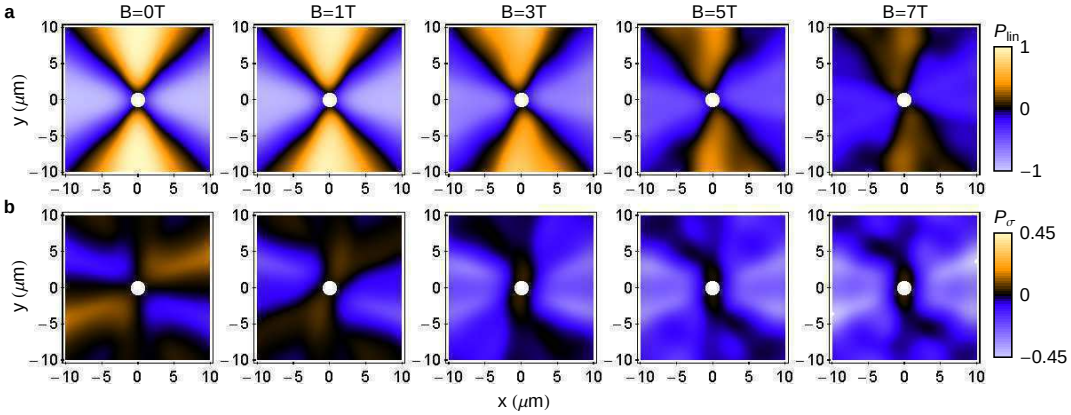

FIG. S2: **Gross-Pitaevskii simulation.** Spatial distribution of the linear (a) and circular (b) polarization degrees vs magnetic field. As in the case of the density matrix calculations, the results are spatially averaged over 1.5μm. Parameters: $m_{ex} = 0.21m_e$, $\beta_e = 10\mu$eVμm; $\beta_h = \beta_e/3$; $\delta_b = 2\mu$eV; $\delta_d = 0.5\mu$eV; $E_b - E_d = 2\mu$eV; $W = 0.2\alpha$, $\alpha n = 1\mu$eV. The source area was taken circular with a radius of 1μm.

The spin density matrix theory is convenient for the description of (partially) coherent and (partially) polarized exciton gases. However, the treatment of non-linear effects in a partially coherent system is a challenging task. An approach, which we consider in this section is to assume a perfectly coherent condensate of excitons. In this case, the excitons can be described by a spatially dependent four-component wavefunction, $(\psi_{+1}(\mathbf{x}), \psi_{-1}(\mathbf{x}), \psi_{+2}(\mathbf{x}), \psi_{-2}(\mathbf{x}))$. The dynamics of the wavefunction can be described by the Gross-Pitaevskii equation:

$$i\hbar\frac{d}{dt}\begin{pmatrix}\psi_{+1}(\mathbf{x})\\ \psi_{-1}(\mathbf{x})\\ \psi_{+2}(\mathbf{x})\\ \psi_{-2}(\mathbf{x})\end{pmatrix} = \left(\hat{H} - \frac{\hbar^2\hat{\nabla}^2}{2m_{ex}}\right)\begin{pmatrix}\psi_{+1}(\mathbf{x})\\ \psi_{-1}(\mathbf{x})\\ \psi_{+2}(\mathbf{x})\\ \psi_{-2}(\mathbf{x})\end{pmatrix} + \alpha n(\mathbf{x})\begin{pmatrix}\psi_{+1}(\mathbf{x})\\ \psi_{-1}(\mathbf{x})\\ \psi_{+2}(\mathbf{x})\\ \psi_{-2}(\mathbf{x})\end{pmatrix} + W\begin{pmatrix}\psi^*_{-1}(\mathbf{x})\psi_{+2}(\mathbf{x})\psi_{-2}(\mathbf{x})\\ \psi^*_{+1}(\mathbf{x})\psi_{+2}(\mathbf{x})\psi_{-2}(\mathbf{x})\\ \psi^*_{-2}(\mathbf{x})\psi_{+1}(\mathbf{x})\psi_{-1}(\mathbf{x})\\ \psi_{+2}(\mathbf{x})\psi_{+1}(\mathbf{x})\psi_{-1}(\mathbf{x})\end{pmatrix}. \quad (33)$$

Here $\hat{H}$ is the same Hamiltonian (15), although to correctly define the operation of the $k-$dependent spin-orbit terms one should replace $k_e = \frac{m_e}{me+m_{hh}}\hat{k}_{ex}$ and $k_h = \frac{m_h}{me+m_{hh}}\hat{k}_{ex}$ where $\hat{k}_{ex} = -i\hat{\nabla}$. Note that the Gross-Pitaevskii equation allows to work with a distribution of wavevectors, and accounts for the dispersion of excitons via the term $-\frac{\hbar^2\hat{\nabla}^2}{2m_{ex}}$, where m_{ex} is the exciton effective mass. The last two terms in Eq. 33 are nonlinear terms. In the initial simplified approach presented here we assume a spin-independent scattering rate, α, where each spin fraction scatters with the total density, $n(\mathbf{x}) = |\psi_{+1}(\mathbf{x})|^2 + \psi_{-1}(\mathbf{x})^2 + |\psi_{+2}(\mathbf{x})|^2 + |\psi_{-2}(\mathbf{x})|^2$. The last term, proportional to W, represents a parametric scattering process unique to indirect exciton systems where two bright excitons convert into

two dark excitons (or vice versa). Note that all non-linear scattering processes conserve the total spin projection of excitons.

To describe the excitation of our system, we introduce a fixed wavefunction boundary condition along a circular boundary representing the edges of the classical region around the LBS center. We choose a linearly polarized dark exciton density at this boundary, assuming that dark excitons have lower energy than bright excitons. We do not aim to use the Gross-Pitaevskii equation in the hot LBS center where the exiton gas is classical, however, we expect it to offer a qualitative description of the propagation of coherent excitons away from the LBS source in the region beyond the LBS center where the exciton gas is coherent. The indirect excitons have a long lifetime and thus we employ an absorbing boundary condition to allow solution of the problem. The absorbing boundary introduces a loss mechanism in the system, such that a steady state is reached where the excitons excited at the LBS balance the flow of excitons away from the studied region (we assume that upon crossing the absorbing boundary excitons never return).

By solving Eq. 33 numerically for the steady state, the linear and circular polarization degrees are calculated for increasing magnetic fields (Fig. S2). The simulated patterns are qualitatively similar to both the experimentally measured patterns and the patterns simulated using the spin density matrix theory. We note that the Gross-Pitaevskii model does not take into account the partial polarization and energy distribution of excitons in the initial state. The used approximation also does not account for the difference in interaction strength for different exciton states. These features contribute to the difference between the presented non-linear simulation and experiment.

EXPERIMENT

Experimental setup

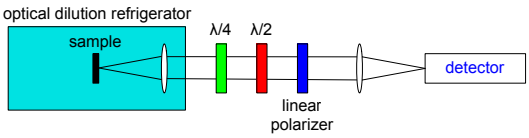

FIG. S3: **Experimental setup.** Schematic of polarization-resolved imaging.

The electric-field-tunable $n^+ - i - n+$ GaAs/$Al_xGa_{1-x}As$ CQW structure was grown by molecular-beam epitaxy. A sketch of the band diagram of the structure is shown in Fig. 1a. The i region consists of two 8-nm GaAs QWs separated by a 4-nm $Al_{0.33}Ga_{0.67}As$ barrier and surrounded by two 200-nm $Al_{0.33}Ga_{0.67}As$ barrier layers. The n^+ layers are Si-doped GaAs with $N_{Si} = 5 \times 10^{17}$ cm^{-3}. The electric field in the z direction is monitored by the external gate voltage V_g applied between the n^+ layers.

The schematic of the polarization-resolved imaging experiment is presented in Fig. S3. The sample is in an optical dilution refrigerator. Light emitted by the sample is collected and made parallel by an objective inside the refrigerator. Polarization selection is done by a combination of quarter-wave plate ($\lambda/4$), half-wave plate ($\lambda/2$), and linear polarizer. The linear polarizer is aligned such that y-axis polarized emission is transmitted to the detector. The detector is a combination of an interference filter of linewidth ± 5 nm adjusted to the emission wavelength of indirect excitons $\lambda = 800$ nm (due to the interference filter, only the emission of indirect excitons is measured: the contribution of the weak emission of direct excitons or any other emission, such as low-energy bulk emission, is cut off by the interference filter), a spectrometer operating in dispersionless zeroth-order mode, and a liquid nitrogen cooled CCD.

Measurements of linear polarization. The quarter-wave plate is aligned so that the fast and slow axis are along the x- and y-axis. Hence, x- and y-polarized emission I_x and I_y are transmitted unchanged. To measure I_y, the half-wave plate fast axis is aligned along the y-axis. Then, I_y is transmitted unchanged, and is then transmitted through the linear polarizer. To measure I_x, the half-wave plate axis is aligned 45° relative to the y-axis. Then, I_x is rotated to the y-axis and is transmitted through the linear polarizer.

Measurements of circular polarizations. The quarter-wave plate is aligned so that the fast and slow axis are rotated by 45° with respect to the y-axis. Then, circularly polarized emission $I_{\sigma+}$ and $I_{\sigma-}$ are converted to x- and y-polarized light. This light is then selected as described above.

In all experiments, the photoexcitation is nonresonant (> 400 meV above the energy of indirect excitons) and spatially separated (the 10 μm-wide excitation spot is > 80 μm away from both the LBS and external ring) so that

neither the exciton polarization nor coherence is induced by the pumping light.

In this paper, we present the measurements of exciton spin currents and demonstration of control of the spin currents by magnetic field. Electronic control of exciton spin currents and development of circuit devices exploring exciton spin currents for information processing form the subject for future studies

Patterns of linear polarization and coherence in the LBS ring region

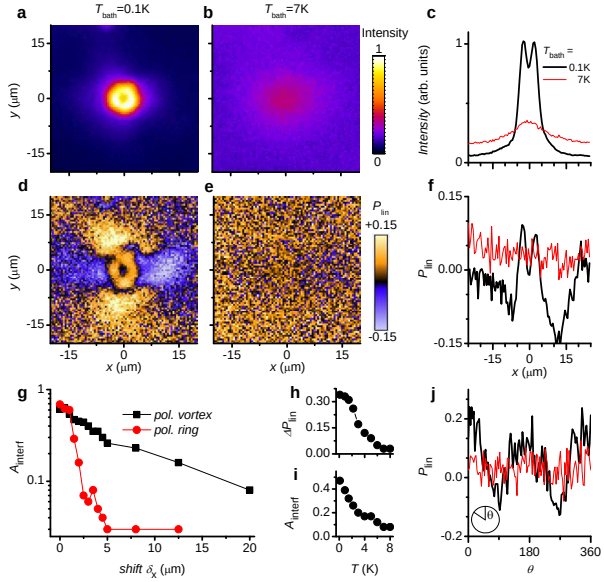

FIG. S4: **Pattern of linear polarization in the LBS region: temperature dependence.** Measured PL intensity in the region of LBS centered at $(105, 75)$ in Fig. 1c at $T_{bath} = 0.1$ (a) and 7 (b) K. (c) PL Intensity profile through the center of the LBS for $T_{bath} = 0.1$ (black) and 7 (red) K. Measured linear polarization of the emission of indirect excitons $P_{lin} = (I_x - I_y)/(I_x + I_y)$ at $T_{bath} = 0.1$ (d) and 7 (e) K. P_{lin} profile (f) vs x through the LBS center and (j) vs azimuthal angle measured from the y-axis at $r = 9$ μm from the LBS center for $T_{bath} = 0.1$ (black) and 7 (red) K. (g) The exciton coherence degree measured by shift-interferometry: Interference visibility A_{interf} vs. shift δ_x for the vortex of linear polarization (squares), 18 μm left of LBS center, and the polarization ring (points), 2 μm left of LBS center for the LBS centered at $(80, 105)$ in Fig. 1c. $T_{bath} = 0.1$ K. Emergence of the vortex of linear polarization and spontaneous coherence at low temperatures: (h) The amplitude of azimuthal variation of P_{lin} at $r = 10$ μm from the LBS center and (i) interference visibility A_{interf} in the polarization vortex for $\delta_x = 2$ μm vs. temperature.

The ring of linear polarization vanishes with increasing temperature (Fig. S4d-f). The vortex of linear polarization vanishes with increasing temperature (Fig. S4d-f,j).

The coherence of an exciton gas is imprinted on the coherence of emission, which is described by the first-order coherence function $g_1(\delta_x)$. In turn, this function is given by the amplitude of the interference fringes $A_{\rm interf}(\delta_x)$ in 'the ideal experiment' with perfect spatial resolution. In real experiments, the measured $A_{\rm interf}(\delta_x)$ is given by the convolution of $g_1(\delta_x)$ with the point-spread function (PSF) of the optical system used in the experiment [12]. Both for a classical gas and quantum gas $g_1(\delta_x)$ is close to 1 at $\delta_x = 0$ and drops with increasing δ_x within the coherence length ξ. The difference between the classical and quantum gas is in the value of ξ. For a classical gas, ξ_{cl} is close to the thermal de Broglie wavelength $\lambda_{dB} = \sqrt{\frac{2\pi\hbar^2}{mT}}$, which is well below the PSF width in the studied temperature range ($\xi_{cl@0.1K} \sim 0.3$ μm, the PSF width is ~ 1.5 μm). Spontaneous exciton coherence with a large coherence length ξ is observed in the region of the polarization vortex (Fig. S4g, black squares). In contrast, ξ is short in the region of the polarization ring (Fig. S4g, red circles), which is close to the hot LBS center. Large $\xi \gg \xi_{cl}$ in the region of the polarization vortex indicates a coherent exciton state with a much narrower than classical exciton distribution in

momentum space, characteristic of a condensate. Small $\xi \sim 1.5$ μm in the region of the polarization ring indicates a classical exciton state with ξ measuring the PSF width. The coherence measurements are discussed in detail in [13]. With reducing temperature, the exciton spin textures emerge in concert with coherence (Fig. S4h and S4i).

Patterns of circular polarization in the LBS ring region

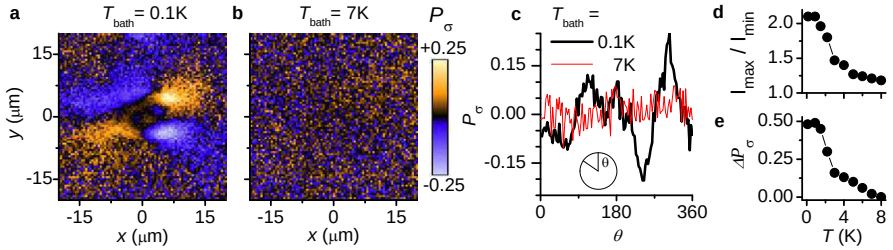

FIG. S5: **Pattern of circular polarization in the LBS region: temperature dependence.** Measured circular polarization of the emission of indirect excitons $P_\sigma = (I_{\sigma^+} - I_{\sigma^-})/(I_{\sigma^+} + I_{\sigma^-})$ in the LBS region at $T_{bath} = 0.1$ (a) and 7 (b) K. (c) The azimuthal variation of P_σ at $r = 9$ μm from the LBS center for $T_{bath} = 0.1$ (black) and 7 (red) K. (d) The ratio of maximum to minimum in the azimuthal variation of the total emission intensity of indirect excitons I_{max}/I_{min} at $r = 8\mu$m from the LBS center vs. temperature. (e) The amplitude of variation of P_σ around the LBS centered at (105, 75) in Fig. 1c, vs. temperature.

The four-leaf pattern of circular polarization vanishes with increasing temperature (Fig. S5a-c,e). At low temperature, the flux of excitons from the LBS center is anisotropic: the emission intensity is enhanced along the polarization direction in the polarization ring (Fig. S6a). To quantify the flux anisotropy, we use the ratio of maximum to minimum in the azimuthal variation of the total emission intensity of indirect excitons I_{max}/I_{min} at distance $r = 8$ μm from the origin. At high temperature, the exciton flux anisotropy vanishes (Fig. S5d). The four-leaf pattern and flux anisotropy emerge in concert (Fig. S5d and S5e). The four-leaf pattern of circular polarization is associated with a skew of the exciton fluxes in orthogonal circular polarizations (Fig. S6).

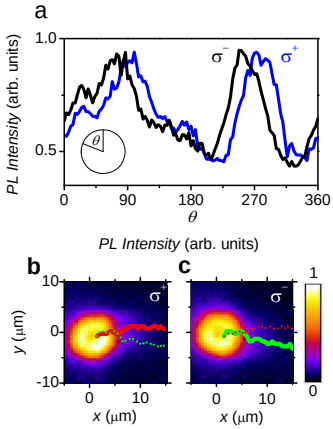

FIG. S6: **Pattern of circular polarization in the LBS region: azimuthal dependence.** (a) Azimuthal variation of the emission intensity of indirect excitons at $r = 8$ μm in σ^+ (blue) and σ^- (black) polarizations. Angles are measured from the y-axis. (b,c) Traces of the σ^+ (red) and σ^- (green) emission peak around $\theta = 270^\circ$ [see (a)]; The emission image in σ^+ (b) and σ^- (c) polarization is also shown.

Polarization patterns in the external ring region

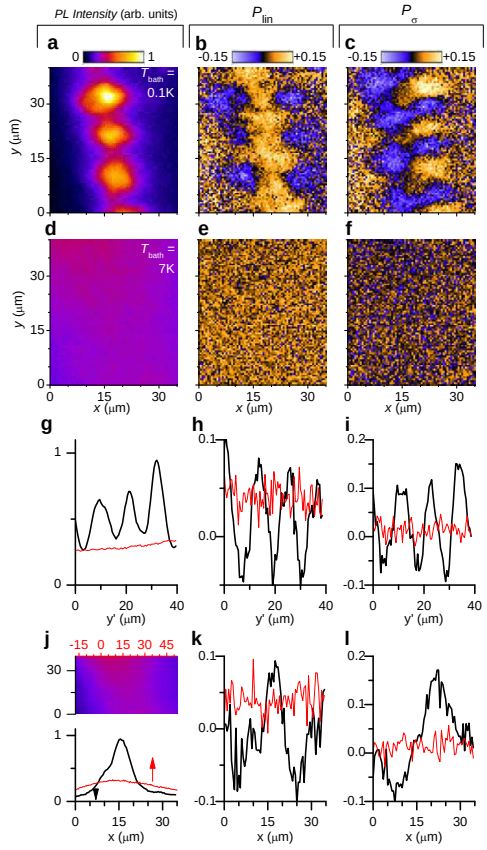

FIG. S7: **Polarization textures in the region of external ring: temperature dependence.** (a,d) Emission of indirect excitons in the external ring region. Pattern of linear (b,e) and circular (c,f) polarization in the region of external ring. $T_{bath} = 0.1$ (a-c) and 7 (d-f) K. PL intensity (g), P_{lin} (h), and P_σ (i) profiles taken along the external ring (along an axis 9 degrees of vertical positioned at maximum variation) for $T_{bath} = 0.1$ (black) and 7 (red) K. PL intensity (j), P_{lin} (k), and P_σ (l) profiles taken across the external ring (along the x-axis positioned at maximum variation) for $T_{bath} = 0.1$ (black) and 7 (red) K. The image in (j) shows the external ring at $T_{bath} = 7$ K.

The fragmentation of the external ring vanishes with increasing temperature (Fig. S7a,d,g), consistent with earlier results [14]. The periodic polarization textures in the region of the external ring vanish with increasing temperature (Fig. S7b,c,e,f,h,i,k,l).

Both the position of the external ring and the wavelength of the exciton density wave formed in the ring are controlled by the laser excitation indicating that the exciton density modulation in the MOES is not governed by defects in the sample. The observation of polarization textures around the MOES beads, which are not associated with defects, shows that the polarization textures do not arise due to defects.

The role of excitonic effects in the formation of spin textures in the exciton system

The excitonic terms describing the spin precession in the Hamiltonian due to splitting of exciton states are present for excitons and absent for free electrons and holes. To verify the role of excitonic effects in the formation of spin

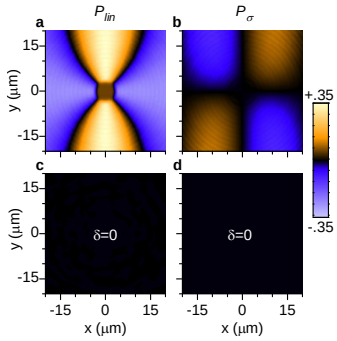

FIG. S8: **Importance of the excitonic effects.** Simulated P_{lin} and P_σ (a,b) with the excitonic effects [nonzero excitonic terms in Hamiltonian (15), the values are presented in Section Simulations] and (c,d) without excitonic effects [zero excitonic terms in Hamiltonian (15), $\delta_b = \delta_d = E_b - E_d = 0$]. No spin texture forms in the absence of excitonic terms.

textures, we performed the simulations with and without the excitonic terms in the Hamiltonian (15). No spin texture forms in the absence of excitonic terms, see Fig. S8. Simulations also indicate that at $B = 0$, a pattern of circular polarization appears when all the excitonic terms in the Hamiltonian are nonzero, while a pattern of linear polarization appears when one excitonic term is nonzero.. This shows that the excitonic effects are important for the formation of spin textures in the exciton system.

SUPPLEMENTAL VIDEOS

The file "movie 1 linear polarization vs magnetic field.gif" contains a movie of the linear polarization data and simulations presented in Figure 2 of the text, along with exciton spin texture presented in Figure 3 of the text.

The file "movie 2 circular polarization vs magnetic field.gif" contains a movie of the circular polarization data and simulations presented in Figure 2 of the text.

The file "movie 3 exciton electron hole textures vs magnetic field.gif" contains a movie of the results presented in Figure 3 of the text.

[1] See e.g. E.L. Ivchenko, G.E. Pikus, *Superlattices and other heterostructures: Symmetry and optical phenomena* (Springer, Berlin, 1997).
[2] E.I. Rashba, E.Ya Sherman, *Physics Letters A* **129** 175 (1988).
[3] Jun-Wei Luo, A.N. Chantis, M. van Schilfgaarde, G. Bester, A. Zunger, *Phys. Rev. Lett.* **104** 066405 (2010).
[4] E.L. Ivchenko, *Optical spectroscopy of semiconductor nanostructures* (Alpha Science, 2005).
[5] See e.g. M. Born, E. Wolf, *Principles of optics* (Pergamon, London, 1970).
[6] J.R. Leonard, Y.Y. Kuznetsova, Sen Yang, L.V. Butov, T. Ostatnický, A. Kavokin, A.C. Gossard, *Nano Lett.* **9** 4204 (2009).
[7] L.V. Butov, A.L. Ivanov, A. Imamoglu, P.B. Littlewood, A.A. Shashkin, V.T Dolgopolov, K.L. Campman, A.C. Gossard, *Phys. Rev. Lett.* **86** 5608 (2001).
[8] C. Leyder, M. Romanelli, J.Ph. Karr, E. Giacobino, T.C.H. Liew, M.M. Glazov, A.V. Kavokin, G. Malpuech, A. Bramati, *Nature Physics* **3** 628 (2007).
[9] M.J. Snelling, E. Blackwood, C.J. McDonagh, R.T. Harley, C.T.B. Foxon, *Phys. Rev. B* **45** 3922 (1992).
[10] A. Kavokin, G. Malpuech, M. Glazov, *Phys. Rev. Lett.* **95** 136601 (2005).
[11] A.V. Kavokin, J.J. Baumberg, G. Malpuech, F.P. Laussy, *Microcavities* (Oxford University Press, Oxford, 2007), Chapt. 3.
[12] M.M. Fogler, Sen Yang, A.T. Hammack, L.V. Butov, A.C. Gossard, *Phys. Rev. B* **78** 035411 (2008).
[13] A.A. High, J.R. Leonard, A.T. Hammack, M.M. Fogler, L.V. Butov, A.V. Kavokin, K.L. Campman, A.C. Gossard, *Nature* **483** 584 (2012).
[14] L.V. Butov, A.C. Gossard, D.S. Chemla, *Nature* **418** 751 (2002).

PHYSICAL REVIEW B **80**, 115328 (2009)

Polarization and depolarization in scattering of cavity polaritons

Tomas Ostatnicky,[1] Dean Read,[1] and Alexey V. Kavokin[1,2]
[1]*School of Physics and Astronomy, University of Southampton, Highfield, Southampton SO17 1BJ, United Kingdom*
[2]*Dipartimento di Fisica, Universita di Roma II, 1 via della Ricerca Scientifica, Roma 00133, Italy*
(Received 28 January 2009; revised manuscript received 15 August 2009; published 29 September 2009)

We consider theoretically the elastic scattering of two exciton polaritons having opposite wave vectors in a planar microcavity. We derive the scattering amplitudes accounting for the vector polarization of polaritons and the interference of different scattering channels. We obtain a nontrivial dependence of the scattering amplitudes and the polarizations on the scattering angle and polarization of initial states. Generation of polariton spin currents as a result of scattering of linearly polarized polaritons is predicted. We also describe depolarization of exciton polaritons due to their scattering and show that it may be complete in certain scattering directions. This analysis provides a basis for engineering of spin- and electric field-sensitive optical logic gates based on exciton polaritons.

DOI: 10.1103/PhysRevB.80.115328 PACS number(s): 71.36.+c, 42.65.−k, 03.67.Mn

I. INTRODUCTION

Exciton polaritons in microcavities are composite bosons, which efficiently scatter each other due to multiple channels of direct and exchange Coulomb interaction of their constituent electrons and holes.[1–3] In the strong coupling regime, the exciton polaritons in microcavities are characterized by two dispersion branches split typically by several meV. Due to a strongly nonparabolic dispersion of the lower-polariton branch, various configurations for the resonant polariton-polariton scattering are possible.[2] The resonant scattering processes are responsible for the operations of the microcavity-based optical parametric oscillators (OPO).[4–6] Among various geometries of the polariton-based OPO studied until now, one of the most attractive implies scattering of two exciton polaritons having equal energies and opposite in-plane wave vectors on a so-called elastic circle [e.g., a circle in a two-dimensional (2D) reciprocal space characterized by some fixed value of the kinetic energy for the exciton polaritons,[7] see Fig. 1]. The advantage of this configuration is in the fully symmetric final quantum states (referred to as the signal and idler states), which is favorable for realization of the parametric oscillations.[8] The signal and idler states are characterized by the same polariton lifetime, which is not the case in the most popular microcavity OPO geometry based on the excitation of polaritons at the so called "magic angle" and their subsequent scattering to the lower and upper energy states.[4,5] On the other hand, the excitation geometry, which involves simultaneous generation of polaritons with opposite in-plane wave vectors, is more complex and harder to model due to the multitude of possible final states, as the scattering to any pair of states belonging to the same diameter of the elastic circle is allowed by the energy and wave vector conservation laws. Surprisingly, recent experimental studies revealed a strong angular dependence of the scattering probability on the polar angle. Moreover, they demonstrated the polarization selection rules in polariton-polariton scattering, which provided grounds for realization of the all-optical XNOR gates9 (i.e., gates which implement logical XNOR operation on polarized light beams).[9]

The experimental data of Ref. 9 has been interpreted using the spin-dependent Gross-Pitaevskii (GP) equations, which assume a single fully coherent polariton state characterized by a spinor wave function analogous to the classical Jones vector. Although a powerful and insightful method of modeling, the GP equations have two important shortcomings. First, they do not account for the possible depolarization of the polaritons during their scattering; second, they imply a contact interaction between the polaritons which is independent of their wave vectors. Here, we present a theoretical model, which relaxes the two above restrictions of the GP equations and allows for the description of a full range of polarization-dependent effects in polariton-polariton scattering, including depolarization. When applied to the specific scattering geometry of the experiment,[9] our formalism allows for the prediction of a nontrivial angular polarization dependence of the amplitude of polariton-polariton scattering and sheds light on the mechanisms of polarization relaxation in the polariton gases.

The spin-dependent Boltzmann equations describing the scattering of exciton polaritons with acoustic phonons and the polariton-polariton scattering have been formulated in Ref. 10, which treats the polariton spin dynamics within the Born-Markov approximation. Here, we extend the model of Ref. 10 accounting for the variations of the polariton-polariton scattering amplitudes with the vector of exchanged

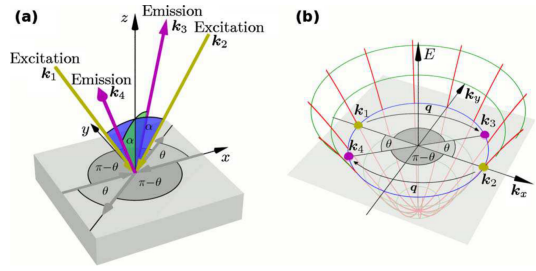

FIG. 1. (Color online) (a) Considered geometry of polariton-polariton scattering in real space with α being the angle of incidence and θ being the scattering angle. (b) In the reciprocal space, the dispersion of the lower-polariton branch is shown and the elastic circle is highlighted by the blue color.

momentum, which appears to be very important in the specific OPO geometry we consider. Moreover, we numerically evaluate the scattering amplitudes using a microscopic model which enables us to analyze the polariton pseudospin distributions on the elastic circle for different pump polarizations.

Introduction of the scattering amplitudes angular dependence in the model leads to appearance of new terms in the Boltzmann equations for the pseudospin components. These terms are responsible for the occurrence of new, interesting spin-related phenomena neglected so far, in particular, appearance of the circular polarization as a result of scattering of two linearly polarized polaritons and vice versa. In order to reveal the impact of these terms, we assume that the final states for polariton-polariton scattering are initially empty. This allows us to neglect stimulation of polariton-polariton scattering and consider only the spontaneous processes. We therefore use the density matrix formalism and a powerful algebraic analysis rather than the full (Boltzmann) rate equations given in Ref. 10. This approach enables us to formulate simple and universal polarization selection rules for polariton-polariton scattering.

The rest of this paper is organized as follows: Section II presents our model and polarization selection rules, Sec. III presents the numerical results for polariton pseudospin distributions, Sec. IV contains the conclusive remarks.

II. THEORETICAL MODEL

A. Scattering Hamiltonian

We consider a planar semiconductor microcavity in the strong exciton-light coupling regime. The cavity is pumped by two cw laser beams, which produce macroscopic populations of two cavity modes with opposite in-plane wave vectors $\boldsymbol{k}_1$ and $\boldsymbol{k}_2=-\boldsymbol{k}_1$. The angle of incidence of the two laser beams is the same (angle α in Fig. 1(a)). The polaritons scatter from the pump states to the final states obeying the momentum and energy conservation rule. In the configuration we consider, the pair interactions may scatter polaritons only to the states on the elastic circle defined by the in-plane momentum $|\boldsymbol{k}|=|\boldsymbol{k}_1|=|\boldsymbol{k}_2|$. These allowed final states are then fully identified by the scattering angle θ [Figs. 1(a) and 1(b)]. We shall consider the spontaneous polariton polariton scattering from the macroscopically populated pump states to the empty final states. We neglect depletion of the pump states due to the scattering and the longitudinal-transverse splitting (TE-TM splitting) of the exciton-polariton eigenstates is taken to be zero.

As pointed out in many publications,[11–14] excitons are not ideal bosons due to the fermionic nature of their constituents (electrons and holes). This is why also the cavity polaritons show some fermionic properties. The fermionic effects are negligible in the low-density limit, but they become important as soon as polariton-polariton interactions start playing a role. Strictly speaking, polariton-polariton scattering needs to be considered as a result of interactions of four fermions.[3,11,13] It is, however, possible and convenient to use an effective scattering Hamiltonian for the polaritons having the total angular momenta $s=\pm 1$ (which are strongly coupled to the optical field of the cavity mode). Using the above assumptions, one can easily see that such an effective Hamiltonian would couple the states on the elastic circle only to the pump states $\boldsymbol{k}_1$ and $\boldsymbol{k}_2$:

$$H_{\mathrm{SC}}=\tfrac{1}{2}\sum_{s,\boldsymbol{q}}\left[V_1(\boldsymbol{k}_1,\boldsymbol{k}_2,\boldsymbol{q})a^{+}_{s,\boldsymbol{k}_1+\boldsymbol{q}}a^{+}_{s,\boldsymbol{k}_2-\boldsymbol{q}}a_{s,\boldsymbol{k}_1}a_{s,\boldsymbol{k}_2}+V_2(\boldsymbol{k}_1,\boldsymbol{k}_2,\boldsymbol{q})a^{+}_{s,\boldsymbol{k}_1+\boldsymbol{q}}a^{+}_{-s,\boldsymbol{k}_2-\boldsymbol{q}}a_{s,\boldsymbol{k}_1}a_{-s,\boldsymbol{k}_2}\right]. \quad (1)$$

Here, $a_{s,\boldsymbol{k}}$ is the annihilation operator for a polariton having a wave vector $\boldsymbol{k}$ and spin s (the band index is omitted here since we consider only polaritons from the lower dispersion branch). The amplitudes V_1 and V_2 describe scattering of the polaritons with parallel and antiparallel spins. In general, $V_1\neq V_2$, as we shall discuss below in detail. The spin dependence of polariton-polariton interactions is at the origin of many peculiar effects in the polarization dynamics of exciton polaritons,[10,15] including the self-induced Larmor precession,[16] the rotation of linear polarization due to polariton-polariton scattering[17] and the buildup of linear polarization of the Bose-Einstein condensates of exciton-polaritons.[18]

Considering the scattering on the elastic circle, we define the wave vectors $\boldsymbol{k}_3(\theta)$ and $\boldsymbol{k}_4(\theta)$ of the scattered polaritons according to Fig. 1 (the argument will not be explicitly mentioned from now on) and present the exchanged momenta $\boldsymbol{q}=\boldsymbol{k}_3-\boldsymbol{k}_1$ and $\boldsymbol{q}'=\boldsymbol{k}_4-\boldsymbol{k}_1$. The Hamiltonian (1) then reads:

$$H_{\mathrm{SC}}=\sum_{s,\theta}\left(\beta_1(\theta)a^{+}_{s,\boldsymbol{k}_3}a^{+}_{s,\boldsymbol{k}_4}a_{s,\boldsymbol{k}_1}a_{s,\boldsymbol{k}_2}+\left[\beta_2(\theta)a^{+}_{s,\boldsymbol{k}_1+\boldsymbol{q}}a^{+}_{-s,\boldsymbol{k}_2-\boldsymbol{q}}+\beta_2'(\theta)a^{+}_{-s,\boldsymbol{k}_1+\boldsymbol{q}}a^{+}_{s,\boldsymbol{k}_2-\boldsymbol{q}}\right]a_{s,\boldsymbol{k}_1}a_{-s,\boldsymbol{k}_2}\right), \quad (2)$$

where the summation over the angle θ goes from 0 to π and we have defined more convenient scattering amplitudes (omitting the initial momenta in the arguments for clarity):

$$\beta_1(\theta)=\tfrac{1}{2}[V_1(\boldsymbol{q})+V_1(\boldsymbol{q}')], \quad (3)$$

$$\beta_2(\theta)=\tfrac{1}{2}V_2(\boldsymbol{q}), \quad (4)$$

$$\beta_2'(\theta)=\tfrac{1}{2}V_2(\boldsymbol{q}')=\beta_2(\pi-\theta). \quad (5)$$

The matrix elements of the Hamiltonian (2) for selected spins of the initial and final states are shown in Table I. They should be interpreted carefully: the nonzero matrix element $\langle XX|H_{\mathrm{SC}}|XX\rangle$ (where the bra and ket vectors denote the final and initial spin states, respectively) expresses only the fact that in the case of excitation by two X-polarized beams, the conditional probability of finding the X-polarized polariton in the direction $\boldsymbol{k}_3$ when we observe another X-polarized polariton in the direction $\boldsymbol{k}_4$ is nonzero (and proportional to the matrix element squared). It does not mean, however, that the final states are X polarized because also the matrix element $\langle YY|H_{\mathrm{SC}}|XX\rangle$ is nonzero and a Y-polarized component in the emission is expected to appear as well. Surprisingly, the emission will not be polarized at all if $\beta_2=\beta_2'=0$ or $\beta_1=0$ because both the aforementioned matrix elements have the same magnitude and the probability of scattering to the states $|XX\rangle$ and $|YY\rangle$ is equal. We then find that the final states are in a non–polarized entangled state $(|XX\rangle+|YY\rangle)/\sqrt{2}$.

TABLE I. Matrix elements of the Hamiltonian (3) for selected spin combinations of the incoming and outgoing polaritons. Polarization state $L(\varphi)$ is defined as the linear polarization rotated by an angle φ with respect to the X-polarized state and we define $\varepsilon=\exp[-i\varphi]$. The notation in the table is as follows: $\sigma^+\sigma^-$ for the initial state denotes the $s=1$ polariton in the state $\boldsymbol{k}_1$ and $s=-1$ polariton in the state $\boldsymbol{k}_2$. Same for the final states. The matrix element for the $\sigma^-\sigma^+$ configuration may be retrieved by permutation of β_2 and β_2'.

	Final state						
Initial state	$\sigma^+\sigma^+$	$\sigma^+\sigma^-$	$\sigma^-\sigma^-$	XX	XY	YY	$XL(\varphi)$
$\sigma^+\sigma^+$	β_1	0	0	$\beta_1/2$	$i\beta_1/2$	$-\beta_1/2$	$\varepsilon^*\beta_1/2$
$\sigma^+\sigma^-$	0	β_2	0	$(\beta_2+\beta_2')/2$	$-i(\beta_2-\beta_2')/2$	$(\beta_2+\beta_2')/2$	$(\varepsilon\beta_2+\varepsilon^*\beta_2')/2$
$\sigma^-\sigma^-$	0	0	β_1	$\beta_1/2$	$-i\beta_1/2$	$-\beta_1/2$	$\varepsilon\beta_1/2$
XX	$\beta_1/2$	$(\beta_2+\beta_2')/2$	$\beta_1/2$	$(\beta_1+\beta_2+\beta_2')/2$	0	$(\beta_2+\beta_2'-\beta_1)/2$	$(\beta_1+\beta_2+\beta_2')\cdot(\cos\varphi)/2$
XY	$-i\beta_1/2$	$i(\beta_2-\beta_2')/2$	$i\beta_1/2$	0	$(\beta_1+\beta_2-\beta_2')/2$	0	$(\beta_1+\beta_2-\beta_2')\cdot(\sin\varphi)/2$
YY	$-\beta_1/2$	$(\beta_2+\beta_2')/2$	$-\beta_1/2$	$(\beta_2+\beta_2'-\beta_1)/2$	0	$(\beta_1+\beta_2+\beta_2')/2$	$(\beta_2+\beta_2'-\beta_1)\cdot(\cos\varphi)/2$

B. Scattering amplitudes

In order to quantitatively characterize the emission from a microcavity in the limit of spontaneous scattering on the elastic circle, we shall evaluate or estimate the amplitudes of the coefficients β_1, β_2, and β_2'. One can expand:

$$V_1(\mathbf{q},\mathbf{k}_1,\mathbf{k}_2)|X_H|^{-4} = V_{\mathrm{dir}}(\mathbf{q},\mathbf{k}_1,\mathbf{k}_2) + V_{\mathrm{exch}}(\mathbf{q},\mathbf{k}_1,\mathbf{k}_2), \quad (6)$$

$$V_2(\mathbf{q},\mathbf{k}_1,\mathbf{k}_2)|X_H|^{-4} = V_{\mathrm{dir}}(\mathbf{q},\mathbf{k}_1,\mathbf{k}_2) + V_{\mathrm{super}}. \quad (7)$$

The beta coefficients are then retrieved following the definitions (3)–(5). X_H denotes the Hopfield coefficient describing the excitonic fraction of polariton states at the elastic circle. In Eqs. (6) and (7), the scattering amplitudes were decomposed[11,14] into the exciton direct-scattering part V_{dir} and the exchange-scattering parts V_{exch}, V_{super}. The part V_{super} is an effective exchange contribution originating in higher-order processes, which involve virtual excitation of the optically forbidden exciton states with spins ± 2 (superexchange). Scattering between the optically active polariton states and the dark excitons has been addressed in detail in Refs. 19–21.

We performed numerical calculations of the direct scattering amplitude for exciton-polaritons on the elastic circle using the microscopic model.[22,23] We found that the scattering amplitudes do not depend on the particular orientation of the contributing wave vectors and thus we use the notation $q=|\boldsymbol{q}|$ and $k_j=|\boldsymbol{k}_j|$ in the following. We also carried out numerical calculations of the exchange term V_{exch}, which displayed a virtually constant behavior for small q. We therefore consider that both the exchange and the superexchange terms are constant around the elastic circle. Clearly, the characteristic scale on which these terms might change is given by the inverse exciton Bohr radius a_B^{-1}, which is orders of magnitude larger than the radius of the elastic circle which we consider.

The direct term, on the contrary, reveals a strong dependence on the exchanged momentum for $q \ll a_B^{-1}$, according to Refs. 22 and 23, and provides zero scattering amplitude for $q=0$ in the 2D exciton gas limit. The scattering amplitude varies as $(qa_B)^3$ and is estimated as $V_{\mathrm{dir}}(0.1a_B^{-1})/V_{\mathrm{exch}} \approx 1.5\cdot 10^{-4}$ giving only a negligible contribution to the overall scattering amplitudes in Eqs. (6) and (7). The small amplitude of the direct term is, nevertheless, caused by compensation of the electron-electron and hole-hole repulsion by electron-hole attraction, and the direct term completely vanishes if the effective masses of the fermions become equal. The different shape of the electron and the hole wave functions in realistic quantum wells (QWs) cause the nonzero amplitude of the direct Coulomb interaction. We show here that this direct term may become orders of magnitude larger in narrow QWs compared to the ideal 2D exciton gas because of the wave function penetration into the barriers (for the discussion of the effect of charge separation see Ref. 14).

We derived an analytical expression for the direct scattering term amplitude considering a real exciton wave function in a narrow QW in the integral form (see Appendix) and then evaluated it numerically. The effect of charge separation on the amplitude of the direct term is obvious from Eq. (A3): the larger difference between the square of the electron and hole wave function is, the larger value of the scattering amplitude. In real, narrow GaAs QWs, coincidentally, the ratio between the electron and the hole mass is about 1/6, which is why electrons deeply penetrate into the QW barriers when the hole are kept localized in the QW layer. The effect of delocalization is even more pronounced in QWs with low-band offsets, e.g., InGaAs/GaAs with low In content. The amplitude of the direct term therefore strongly depends on the QW width and composition.

We plot the direct term amplitude in the units of the exchange interaction amplitude in Fig. 2(a) for the frequently used GaAs/$Al_{0.3}Ga_{0.7}As$ and $In_{0.04}Ga_{0.96}As$/GaAs QWs of the widths 2.5 and 5 nm, respectively. The electron wave function spreading into narrow QW barriers causes the significant increase of the direct scattering amplitude, which now has a nonzero value at zero exchanged momentum [the particular wave functions are plotted in the inset of Fig. 2(b)]. When inspecting the angular dependence of the spin and intensity of the scattered signal on the elastic circle, not only the offset but also the absolute value of the amplitude variations with the exchanged momentum are important. In this case, the variations are larger by over two orders of magnitude in the case of the $In_{0.04}Ga_{0.96}As$/GaAs QW, as compared to the GaAs/$Al_{0.3}Ga_{0.7}As$ QW, in the range of wave vectors up to 2 μm^{-1}.

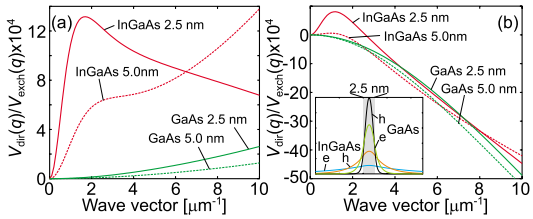

FIG. 2. (Color online) Ratio between the direct and exchange-scattering amplitude considering zero (a) and nonzero (b) applied voltage perpendicular to the QW plane for real QWs. Nonzero voltage is assumed to induce spatial shift of each of the particle wave functions by 1 nm in opposite directions. Different QW compositions and widths are taken into account. The curve offsets were removed for clarity, their values are: (a) InGaAs 2.5 nm: 0.22, InGaAs 5 nm: 0.089, GaAs 2.5 nm: 0.007, GaAs 5 nm: 0.002, (b) InGaAs 2.5 nm: 0.27, InGaAs 5 nm: 0.17, GaAs 2.5 nm: 0.30, GaAs 5 nm: 0.24. Inset: calculated electron (e) and hole (h) wave functions squared in 2.5 nm wide QW for the two GaAs/AlGaAs and InGaAs/GaAs compositions.

A further electron-hole separation may be induced by applying an electric field in normal to the QW plane direction. Although the exciton oscillator strength may be reduced in this case due to the quantum confined Stark effect, the system may be kept in the strong coupling regime if the Q factor of the cavity is high enough. In this case, the direct term and its variation along the elastic circle are further increased as one can see from Fig. 2(b), where we plot the amplitude of the direct term for the InGaAs/GaAs and GaAs/AlGaAs QWs considering the electron and the hole centers of mass spatially separated by 1 nm. The difference between the scattering amplitudes in the two types of III-V QWs we considered almost vanishes at strong applied bias.

To estimate the magnitude of external electric field needed for the efficient charge separation, let us consider a plane capacitor formed by two plates electrically charged with the density ρ. Considering the QW excitons, the charge density may be estimated as $\rho=e(1-S)/\pi a_B^2$, where S is the electron-hole overlap integral, e is the electron charge and a_B is the exciton Bohr radius. The electric field created by one of the planes and acting upon another one is independent on the distance between them, $E_P=\rho/2\varepsilon$ where ε is static dielectric constant. The electron-hole system is in equilibrium if the field E_P is compensated by an external field of the same magnitude. This allows estimating of the external field as $E=\frac{e}{2\pi\varepsilon}\frac{1-S}{a_B^2}$. Substituting $\varepsilon_r=10$ and the Bohr radius $a_B=10$ nm, we obtain $E\approx(1-S)\cdot 30$ kV/cm. The reduction of the electron-hole overlap S due to the spatial separation of electron and hole centers of mass by 1 nm is, approximately, 30% and 50% in 5 and 2.5 nm wide InGaAs/GaAs QWs, respectively, and 55% and 85% in 5 and 2.5 nm wide GaAs/AlGaAs QWs, respectively. These numbers imply the required external electric field intensities in the range 10–25 kV/cm, depending on the QW composition and width. These values are in a good agreement with the results of Ref. 24, which gives an estimate of the same order for CdTe/CdZnTe QWs.

Finally, the magnitude of the superexchange scattering channel may be estimated from the T-matrix calculations published in Refs. 20 and 21. We use the ratio $V_{super}/V_{exch}=T^{+-}/T^{++}=-0.28+0.01i$ for all QWs under consideration.

C. Spin and polarization of the final states

As pointed out above, the Hamiltonian (2) and its matrix elements in Table I do not directly show either the degree of polarization or the polarization of the final states themselves. We therefore develop an algebraic procedure for calculation of both these quantities from the Hamiltonian (2). The system of interacting polaritons is described by the density matrix $\rho(t)$ with an initial condition $\rho(t=0)=\rho_0$. We assume that the dephasing in the system is strong due to interactions between polaritons and phonons what allows one to use the Born-Markov approximation[10] for evaluation of the density matrix dynamics. This procedure yields:

$$\frac{d\rho(t)}{dt}=-\frac{2\pi}{\hbar^2}\delta(E_f-E_i)\{H_{SC},[H_{SC},\rho(t)]\}, \tag{8}$$

where $E_{f,i}$ are the energies of the final and the initial state, respectively, and the Dirac delta function is responsible for energy conservation. As we discussed above, the final states are weakly populated and therefore the system response in an arbitrary scattering direction is governed only by the populations of the initial states and the scattering angle θ (i.e., no stimulated scattering). This assumption allows us to substitute $\rho(t)=\rho_0$ in the right hand side of Eq. (8). It is also obvious that we do not need to know the evolution of the whole density matrix, which is why we fragment it to the submatrices whose evolution is of particular interest.

We define the 2×2 spin-density matrix $\rho_{\boldsymbol{k}}$ for a state with a wave vector $\boldsymbol{k}$ in the basis of spins $\{\sigma^+,\sigma^-\}$. The 4×4 joint density matrix for the final states is therefore defined as a direct product $\rho_{\boldsymbol{k}_3(\theta),\boldsymbol{k}_4(\theta)}=\rho_{\boldsymbol{k}_3(\theta)}\otimes\rho_{\boldsymbol{k}_4(\theta)}$ and it fully describes the spin states of the scattered polaritons. The equation of motion for this density matrix can be straightforwardly derived from Eq. (8) within the assumptions made:

$$\frac{d\rho_{\boldsymbol{k}_3(\theta),\boldsymbol{k}_4(\theta)}(t)}{dt}=-\frac{4\pi}{\hbar^2}\delta(E_f-E_i)H_B^+(\theta)\rho_{\boldsymbol{k}_1,\boldsymbol{k}_2}H_B(\theta), \tag{9}$$

where the joint density matrix for the initial states is $\rho_{\boldsymbol{k}_1,\boldsymbol{k}_2}=\rho_{\boldsymbol{k}_1}\otimes\rho_{\boldsymbol{k}_2}$ and the Hamiltonian sub-block H_B reads:

$$H_B(\theta)=\begin{pmatrix}\beta_1(\theta) & 0 & 0 & 0\\ 0 & \beta_2(\theta) & \beta_2'(\theta) & 0\\ 0 & \beta_2'(\theta) & \beta_2(\theta) & 0\\ 0 & 0 & 0 & \beta_1(\theta)\end{pmatrix}. \tag{10}$$

We are interested in the polarization of the radiation emerging in some definite direction denoted by the wave-vector $\boldsymbol{k}_3$ (see Fig. 1). The polarization properties of the radiation are fully described by the pseudospin vector $\boldsymbol{S}_{\boldsymbol{k}_3}$. We define the spin matrix in the usual way[10] $\rho_{\boldsymbol{k}_3}=\frac{1}{2}N_{\boldsymbol{k}_3}+\boldsymbol{S}_{\boldsymbol{k}_3}\cdot\boldsymbol{\sigma}$, where $N_{\boldsymbol{k}_3}$ is the polariton population in the direction $\boldsymbol{k}_3$ and $\boldsymbol{\sigma}$ is the vector of Pauli matrices. The population and pseudospin components of the final state may be retrieved by evaluation

of appropriate quantum-mechanical mean values:

$$N_{\boldsymbol{k}_3}(t) = \sum_s \langle a^+_{s,\boldsymbol{k}_3} a_{s,\boldsymbol{k}_3}\rangle = \mathrm{Tr}[(\boldsymbol{I}\otimes\boldsymbol{I})\rho_{\boldsymbol{k}_3(\theta),\boldsymbol{k}_4(\theta)}(t)], \quad (11)$$

$$S_{x,\boldsymbol{k}_3}(t) = \frac{1}{2}\sum_s \langle a^+_{s,\boldsymbol{k}_3} a_{-s,\boldsymbol{k}_3}\rangle = \frac{1}{2}\mathrm{Tr}[(\boldsymbol{\sigma}_x\otimes\boldsymbol{I})\rho_{\boldsymbol{k}_3(\theta),\boldsymbol{k}_4(\theta)}(t)], \quad (12)$$

$$S_{y,\boldsymbol{k}_3}(t) = \frac{\mathrm{i}}{2}\sum_s s\langle a^+_{s,\boldsymbol{k}_3} a_{-s,\boldsymbol{k}_3}\rangle = \frac{1}{2}\mathrm{Tr}[(\boldsymbol{\sigma}_y\otimes\boldsymbol{I})\rho_{\boldsymbol{k}_3(\theta),\boldsymbol{k}_4(\theta)}(t)], \quad (13)$$

$$S_{z,\boldsymbol{k}_3}(t) = \frac{1}{2}\sum_s s\langle a^+_{s,\boldsymbol{k}_3} a_{s,\boldsymbol{k}_3}\rangle = \frac{1}{2}\mathrm{Tr}[(\boldsymbol{\sigma}_z\otimes\boldsymbol{I})\rho_{\boldsymbol{k}_3(\theta),\boldsymbol{k}_4(\theta)}(t)]. \quad (14)$$

The symbol $\boldsymbol{I}$ denotes here the 2×2 unit matrix. Considering finite lifetime of polaritons τ and cw excitation, the steady-state pseudospin components may be derived as $S_j^{\mathrm{steady}} = \tau[\mathrm{d}S_j/\mathrm{d}t]_{\mathrm{coh}}$, where the "coh" index denotes the coherent temporal evolution according to Eq. (9). Using Eqs. (9) and (11)–(14), we obtain the steady-state pseudospin components:

$$N_3^{\mathrm{steady}} \propto (\beta_1^2 + |\beta_2|^2 + |\beta_2'|^2)N_1N_2 + 8\,\mathrm{Re}[\beta_2(\beta_2')^*]S_{1x}S_{2x} + 8\,\mathrm{Re}[\beta_2^*\beta_2']S_{1y}S_{2y} + 4(\beta_1^2 - |\beta_2|^2 - |\beta_2'|^2)S_{1z}S_{2z}, \quad (15)$$

$$S_{3x}^{\mathrm{steady}} \propto 2\beta_1\,\mathrm{Re}(\beta_2')S_{1x}N_2 + 2\beta_1\,\mathrm{Re}(\beta_2)N_1S_{2x} + 4\beta_1\,\mathrm{Im}(\beta_2)S_{1z}S_{2y} + 4\beta_1\,\mathrm{Im}(\beta_2')S_{1y}S_{2z}, \quad (16)$$

$$S_{3y}^{\mathrm{steady}} \propto 2\beta_1\,\mathrm{Re}(\beta_2')S_{1y}N_2 + 2\beta_1\,\mathrm{Re}(\beta_2)N_1S_{2y} - 4\beta_1\,\mathrm{Im}(\beta_2)S_{1z}S_{2x} - 4\beta_1\,\mathrm{Im}(\beta_2')S_{1x}S_{2z}, \quad (17)$$

$$S_{3z}^{\mathrm{steady}} \propto (\beta_1^2 - |\beta_2|^2 + |\beta_2'|^2)S_{1z}N_2 + (\beta_1^2 + |\beta_2|^2 - |\beta_2'|^2)N_1S_{2z} + 4\,\mathrm{Im}[\beta_2(\beta_2')^*]S_{1y}S_{2x} + 4\,\mathrm{Im}[\beta_2^*\beta_2']S_{1x}S_{2y}. \quad (18)$$

Compared to Ref. 10, we obtained several new terms in the kinetic equations for the pseudospin components. The origin and the role of these terms are discussed in the next Section.

III. RESULTS AND DISCUSSION

A. Polarization selction rules

Here, we consider the polarization selection rules which govern polariton-polariton scattering on the elastic circle. The final state polarizations are analyzed as a function of the scattering angle. The angle dependence of the scattering amplitudes comes from the direct Coulomb scattering term, while the exchange and superexchange contributions are virtually insensitive to the scattering angle if the radius of the elastic circle is much less than the inverse exciton Bohr radius.

The total polarization degree of a polariton quantum state $\boldsymbol{k}_3$ can be defined as $P = 2|\boldsymbol{S}_3|/N_3$. Obviously, this quantity ranges between 0 (nonpolarized state) and 1 (fully polarized state). We note that Eqs. (16)–(18) account for the possible depolarization of the final states with respect to the initial states. For example, if considering fully colinearly polarized initial states, we obtain for the total polarization degree of the final states:

$$P = \frac{2|\beta_1\,\mathrm{Re}(\beta_2 + \beta_2')|}{\beta_1^2 + |\beta_2|^2 + |\beta_2'|^2 + 2\,\mathrm{Re}(\beta_2^*\beta_2')}. \quad (19)$$

P is zero if $\beta_2 = \beta_2' = 0$ or $\beta_1 = 0$ (cf. Table I and the discussion at the end of Sec. II A) and equals 1 if $\beta_2 = \beta_2' = \pm\beta_1/2$. The ratios β_2/β_1 and β_2'/β_1 determine the degree of polarization and also the orientation of the pseudospin vector. The exchange interaction couples the initial states with colinear polarizations to the final states with the parallel and perpendicular linear polarizations with the same probability (see Table I). This is why, in this configuration, only the superexchange term and the direct interaction term affect the polarization degree of the final states. The coefficients β_2 and β_2' may be negative if the exchanged momentum is small and therefore the inversion of linear polarization is often observed in the polariton-polariton scattering experiments.[16,17]

The effect of depolarization in polariton-polariton scattering has not been addressed theoretically so far, to the best of our knowledge. Here, we show that it is indeed a general feature of polariton-polariton scattering in the spontaneous regime. This effect limits accuracy of the Gross-Pitaevskii equations which assume full coherence and polarization in the system. On the other hand, the depolarization effect is likely to be reduced if the scattering of polaritons is stimulated by final state populations. In this regime, a selected polarization is likely to be amplified, so that the total polarization degree increases.

When compared to Ref. 10, we observe the new terms in Eqs. (16)–(18). These terms emerge from the fact that we consider the complex and angle-dependent scattering amplitude V_2 and therefore $\beta_2 \neq \beta_2'$ and $\mathrm{Im}\,\beta_2 \neq 0$ in general. Except for these differences, the results of Ref. 10 in the limit of spontaneous scattering are fully reproduced. Knowing the angular dependence of V_2 we are able to predict the dependence of the pseudospin components on the scattering angle.

Moreover, we find a new possibility of polarization conversion as a result of polariton-polariton scattering. In order to illustrate this, let us consider Eq. (18). The last two terms in it describe creation of the circular polarization component from two incoming polaritons with linear polarizations rotated by 45° with respect to each other. As the states on the elastic circle with nonzero wave vectors are created, this means creation of the spin currents with well defined propagation directions. We recall that polariton spin currents may be generated in microcavities due to the Optical Spin Hall effect[25,26] caused by the TE-TM splitting of exciton-polaritons and their elastic scattering by a static disorder potential. The effect we propose here does not require either disorder scattering, or TE-TM splitting but exploits the specific selection rules in the polariton-polariton scattering.

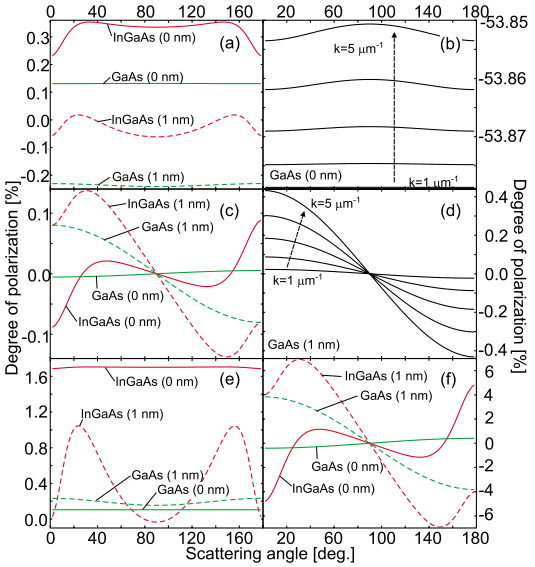

FIG. 3. (Color online) Linear polarization degree P_x in scattering of colinearly (a–b,e) and cross-linearly (c–d,f) polarized pump beams as a function of scattering angle. Spontaneous scattering only is considered in (a–d) while (e–f) display calculations with stimulation of the polariton scattering taken into account. We compare different QW compositions (a,c,e–f) (circle radius 2 μm^{-1}) and elastic circle radii for "GaAs (0 nm)" QW (b) and "GaAs (1 nm)" QW (d). The numbers in parentheses mean spatial shift of the particle wave functions due to the applied electric field. Curves in (a,e) have nonzero offsets which were removed for clarity: (a) GaAs (0 nm): −52%, GaAs (1 nm): +4%, InGaAs (0 nm): −11%, InGaAs (1 nm): −2%, (e) GaAs (0 nm): −100%, GaAs (1 nm): +60%, InGaAs (0 nm): −100%, InGaAs (1 nm): −35%. The QW width is always 2.5 nm.

Note that the total spin is conserved by the process we consider, because the build up of some degree of circular polarization in one direction is compensated by appearance of an opposite circular polarization degree in the opposite scattering direction. Equations (16) and (17) allow for an inverse process: the creation of linear polarization from one linearly and one circularly polarized initial state. This process is reflected by the elements of the rightmost column in Table I.

We note that the process described above is possible due to the existence of a nonzero imaginary part of the scattering amplitude V_2. The argument is that V_2 contains contributions in both first and second order of the perturbation theory (direct and superexchange terms, respectively), which bring different phases, so their sum is a complex number with nonzero real and imaginary parts.

B. Numerical simulations

The numerical solutions of Eqs. (16)–(18) are plotted in Figs. 3 and 4. Here we consider a microcavity with a 2.5 nm wide $In_{0.04}Ga_{0.96}As/GaAs$ or $GaAs/Al_{0.3}Ga_{0.7}As$ QW. We

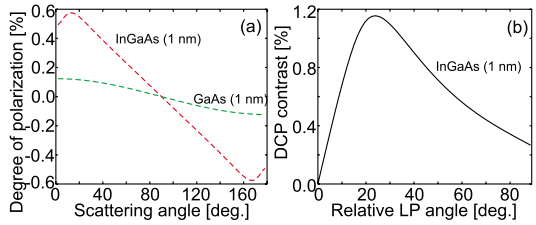

FIG. 4. (Color online) (a) Degree of circular polarization around the elastic circle for two different 2.5 nm wide QW compositions above the stimulated threshold. (b) Dependence of the degree of circular polarization (DCP) contrast on the elastic circle on the angle between vectors of linear polarization of the incident beams.

have fixed $V_{super}/V_{exch}=-0.28+0.01i$ following the results of Schumacher *et al.*[20,27]

The linear polarization degree of the final states defined as $P_x=2S_{3x}/N_3$ is plotted in Figs. 3(a)–3(d) in the case of colinear (X polarized) and cross-linear polarizations of the initial states, respectively, as a function of the scattering angle. The curves in Figs. 3(a) and 3(c) are calculated accounting for the electron and hole spatial separation due to an applied electric field for both types of QWs, Figs. 3(b) and 3(d) illustrates the wave vector dependence of the degree of polarization in the GaAs/AlGaAs QW.

We observe from Fig. 3(a) that the inversion of the linear polarization degree in the case of scattering of collinearly polarized polaritons takes place unless $\mathrm{Re}\,\beta_2>0$. Without the strong direct Coulomb interaction, the linear polarization degree would be $P_x=2(V_{super}/V_{exch})/[1+(V_{super}/V_{exch})^2]\approx 52\%$ in the steady-state regime, however the direct interaction compensates the effect of the linear polarization rotation and the degree of linear polarization is expected to reach the value of only 11% in narrow InGaAs/GaAs QWs. The contrast of the degree of linear polarization around the elastic circle is of only a few tenths of per cent due to the nearly quadratic behavior of the direct term amplitude as a function of the exchanged wave vector [see Fig. 2(a)]. The contrast is increased if the wave vector of incident beams (elastic circle radius) is increased as shown in Fig. 3(b).

Figure 3(c) shows nontrivial variations of the degree of linear polarization as a function of the scattering angle if we consider excitation by cross-polarized beams (note that the X-polarized beam is incident at $\theta=180°$). The degree depends very strongly on the particular shapes of the electron and hole wave functions, and obviously the polarization of the emitted light may be controlled by the applied voltage. The dependence of the polarization degree on the elastic circle radius for a GaAs/AlGaAs QW subjected to the external bias is shown in Fig. 3(d). The elastic circle radius affects the value of the exchanged wave vector, which governs the final state polarizations.

The calculations presented in Figs. 3(a)–3(d) show only a weak variation of the linear polarization degree on the elastic circle (below one per cent). However, so far we have neglected the final state stimulation of the polariton-polariton scattering, which is expected to magnify the polarization variation. In order to reveal this effect, we have solved the

equations of motion for polariton pseudospin taking into account the stimulated processes in polariton–polariton scattering. The results are plotted in Figs. 3(e) and 3(f) for the same parameters as in Figs. 3(a) and 3(c). One can see that the polarization degree as well as its variations strongly increase. The variations may be as large as several per cent in this case. We also observe that depolarization takes place even in the stimulated regime (polarization degree is only 35% in InGaAs QW).

The buildup of the circular polarization and generation of polariton spin currents by linearly polarized optical pumps is demonstrated in Fig. 4. There the pumps have linear polarizations whose planes are rotated by 22° with respect to each other [at this angle the highest circular polarization degree is observed, see Fig. 4(b)]. In this calculation, we considered the stimulated scattering regime, in which case the circular polarization contrast exceeds one per cent. This effect, which may be cautiously referred to as the intrinsic optical spin Hall effect, is relatively weak in the model microcavities we have considered. On the other hand its magnitude depends on the spatial separation of electrons and holes in the QW growth direction so that it can be tuned by applying an external bias.

IV. CONCLUSIONS

We have analyzed the polarization selection rules for the elastic scattering of exciton polaritons in a semiconductor microcavity in the strong coupling regime. We show that the polarization of scattered polaritons may be different from the polarization of pumping light. In particular, linear polarization may be rotated by 90 degrees and circular polarization may be builtup from linearly polarized pumping. We show that when scattered in particular directions the polaritons lose their polarization and become unpolarized.

Using a microscopic model, we have calculated the scattering angle dependence of the polariton-polariton scattering amplitudes on the elastic circle. We have shown that the amplitude of the direct Coulomb scattering process is angle dependent and reveals the pronounced minima and maxima as one goes around the elastic circle. The angular dependence is more pronounced in QWs with spatially separated electron and hole centers of mass. This offers an opportunity to tune the final state polarization by the external electric field. On the other hand, the contributions from the exchange and superexchange polariton coupling mechanisms are virtually independent of the scattering angle. We have found terms previously neglected in the pseudospin kinetic equations arising from the wave vector dependence of the scattering amplitudes and their imaginary components. These terms are shown to be responsible for a variety of effects. We have demonstrated that polariton spin currents (circular polarization currents) may be generated using linearly polarized pump beams. This analysis provides a basis for engineering of spin-sensitive optical logic gates based on exciton polaritons.

The demonstrated sensitivity of the direct scattering term to the QW geometry and to the applied voltage offers the opportunity to control the polariton-polariton interactions and their spin selection rules via the microcavity design (e.g., introducing coupled QWs or superlattices) and external fields. We believe that the effects predicted in this paper may be used in future field-controlled spintronic devices.

ACKNOWLEDGMENTS

We acknowledge enlightening discussions with I. A. Shelykh, H. Ouerdane, and M. M. Glazov. We thank the EPSRC for financial support.

APPENDIX

The direct scattering term is given by the integral:[23]

$$V_{\mathrm{dir}} = \int \varphi_3^*(\boldsymbol{r}_1,\boldsymbol{r}_1')\varphi_4^*(\boldsymbol{r}_2,\boldsymbol{r}_2')V(\boldsymbol{r}_1,\boldsymbol{r}_1',\boldsymbol{r}_2,\boldsymbol{r}_2') \times \varphi_1(\boldsymbol{r}_1,\boldsymbol{r}_1')\varphi_2(\boldsymbol{r}_2,\boldsymbol{r}_2')\mathrm{d}\boldsymbol{r}_1 \ldots \boldsymbol{r}_2', \tag{A1}$$

where the nonprimed $\boldsymbol{r}$'s are the electron coordinates and the primed ones are the hole coordinates. Symbol V stands for the Coulomb potential and φ's are the initial and the final state wave functions with appropriate indices. Note that the vectors are three-dimensional. We factorize the wave functions as products of the in-plane and z-components as $\varphi_{\boldsymbol{k}}(\boldsymbol{r},\boldsymbol{r}')=N\mathrm{e}^{-i\boldsymbol{k}\cdot\boldsymbol{R}}\psi(\boldsymbol{\rho})\chi(z)\chi'(z')$ where N is the normalization constant, $\boldsymbol{k}$ is the in-plane wave vector, $\boldsymbol{R}$ is the center-of-mass coordinate, $\boldsymbol{\rho}$ is the relative electron-hole coordinate and χ and χ' are the respective wave functions of an electron and a hole in a QW. Considering $\psi(\boldsymbol{\rho})=\exp[-\rho/a_{\mathrm{B}}]$ and $|\boldsymbol{k}| \ll a_{\mathrm{B}}^{-1}$, we may do a straightforward evaluation, restricting only to the most important terms:

$$V_{\mathrm{dir}}(q) \approx \frac{e^2}{\varepsilon a_{\mathrm{B}}}\frac{a_{\mathrm{B}}^2}{S}\frac{\pi}{4a_{\mathrm{B}}q}\Bigg\{\int [\chi^2(z_1)\chi^2(z_2)+\chi'^2(z_1)\chi'^2(z_2)-2\chi^2(z_1)\chi'^2(z_2)]f(q,z_1,z_2)\mathrm{d}z_{1,2} - \frac{3(qa_{\mathrm{B}})^2}{4}\int [\chi^2(z_1)\chi^2(z_2)\gamma'^2+\chi'^2(z_1)\chi'^2(z_2)\gamma^2-\chi^2(z_1)\chi'^2(z_2)(\gamma^2+\gamma'^2)]f(q,z_1,z_2)\mathrm{d}z_{1,2} - \frac{3(qa_{\mathrm{B}})^4}{64}\int [\chi^2(z_1)\chi^2(z_2)\gamma'^4+\chi'^2(z_1)\chi'^2(z_2)\gamma^4-2\chi^2(z_1)\chi'^2(z_2)(2(\gamma^4+\gamma'^4)-3\gamma^2\gamma'^2)]f(q,z_1,z_2)\mathrm{d}z_{1,2}\Bigg\} \tag{A2}$$

$$f(q,z_1,z_2) = \int_0^\infty \frac{x}{\sqrt{x^2 + q^2(z_1 - z_2)^2}} J_0(x)\mathrm{d}x. \tag{A3}$$

Here, e stands for the electron charge, ε is the static dielectric constant, S is the normalization surface, J_0 is the Bessel function, γ and γ' are the respective electron and hole reduced masses. The exchanged wave vector is denoted by q.

[1] F. Tassone and Y. Yamamoto, Phys. Rev. B **59**, 10830 (1999).
[2] C. Ciuti, P. Schwendimann, B. Deveaud, and A. Quattropani, Phys. Rev. B **62**, R4825 (2000).
[3] M. Combescot, O. Betbeder-Matibet, and R. Combescot, Phys. Rev. Lett. **99**, 176403 (2007).
[4] R. M. Stevenson, V. N. Astratov, M. S. Skolnick, D. M. Whittaker, M. Emam-Ismail, A. I. Tartakovskii, P. G. Savvidis, J. J. Baumberg, and J. S. Roberts, Phys. Rev. Lett. **85**, 3680 (2000).
[5] M. Saba, C. Ciuti, J. Bloch, V. Thierry-Mieg, R. André, Le Si Dang, S. Kundermann, A. Mura, G. Bongiovanni, J. L. Staehli, and B. Deveaud, Nature (London) **414**, 731 (2001).
[6] C. Diederichs, J. Tignon, G. Dasbach, C. Ciuti, A. Lemaître, J. Bloch, P. Roussignol, C. Delalande, Nature (London) **440**, 904 (2006).
[7] W. Langbein and J. M. Hvam, Phys. Rev. Lett. **88**, 047401 (2002).
[8] M. Romanelli, C. Leyder, J.-P. Karr, E. Giacobino, and A. Bramati, Phys. Rev. Lett. **98**, 106401 (2007).
[9] C. Leyder, T. C. H. Liew, A. V. Kavokin, I. A. Shelykh, M. Romanelli, J. Ph. Karr, E. Giacobino, and A. Bramati, Phys. Rev. Lett. **99**, 196402 (2007).
[10] I. A. Shelykh, A. V. Kavokin, G. Malpuech, Phys. Status Solidi B **242**, 2271 (2005).
[11] C. Ciuti, V. Savona, C. Piermarocchi, A. Quattropani, and P. Schwendimann, Phys. Rev. B **58**, 7926 (1998).
[12] M. Combescot, O. Betheder-Matibet, and F. Dubin, Phys. Rep. **463**, 215 (2008).
[13] S. Okumura and T. Ogawa, Phys. Rev. B **65**, 035105 (2001).
[14] C. Schindler and R. Zimmermann, Phys. Rev. B **78**, 045313 (2008).
[15] I. A. Shelykh, R. Johne, D. D. Solnyshkov, A. V. Kavokin, N. A. Gippius, and G. Malpuech, Phys. Rev. B **76**, 155308 (2007).
[16] D. N. Krizhanovskii, D. Sanvitto, I. A. Shelykh, M. M. Glazov, G. Malpuech, D. D. Solnyshkov, A. Kavokin, S. Ceccarelli, M. S. Skolnick, and J. S. Roberts, Phys. Rev. B **73**, 073303 (2006).
[17] P. Renucci, T. Amand, X. Marie, P. Senellart, J. Bloch, B. Sermage, and K. V. Kavokin, Phys. Rev. B **72**, 075317 (2005).
[18] J. Kasprzak, R. André, Le Si Dang, I. A. Shelykh, A. V. Kavokin, Yuri G. Rubo, K. V. Kavokin, and G. Malpuech, Phys. Rev. B **75**, 045326 (2007).
[19] I. A. Shelykh, L. Vina, A. V. Kavokin, N. G. Galkin, G. Malpuech, and R. Andre, Solid State Commun. **135**, 1 (2005).
[20] S. Schumacher, N. H. Kwong, and R. Binder, Phys. Rev. B **76**, 245324 (2007).
[21] R. Takayama, N. H. Kwong, I. Rumyantsev, M. Kuwata-Gonokami, and R. Binder, Eur. Phys. J. B **25**, 445 (2002).
[22] M. Combescot, O. Betbeder-Matibet, and R. Combescot, Phys. Rev. B **75**, 174305 (2007).
[23] M. M. Glazov, H. Ouerdane, L. Pilozzi, G. Malpuech, A. V. Kavokin, and A. D'Andrea, arXiv:0902.1410 (unpublished).
[24] A. V. Kavokin and A. I. Nesvizhskii, Phys. Rev. B **49**, 17055 (1994).
[25] A. Kavokin, G. Malpuech, and M. Glazov, Phys. Rev. Lett. **95**, 136601 (2005).
[26] C. Leyder, M. Romanelli, J. Ph. Karr, E. Giacobino, T. C. H. Liew, M. M. Glazov, A. V. Kavokin, G. Malpuech, and A. Bramati, Nat. Phys. **3**, 628 (2007).
[27] The T matrix has been calculated considering the 2D exciton gas implying $V_{\mathrm{dir}} \approx 0$. Its amplitude therefore contains only the information about the exchange and superexchange interaction, depending on the spins [cf. Eqs. (3)–(7)].

PHYSICAL REVIEW B **81**, 125319 (2010)

Theory of polarization-controlled polariton logic gates

T. Ostatnický,[1,2] I. A. Shelykh,[3] and A. V. Kavokin[1,4]
[1]*School of Physics and Astronomy, University of Southampton, Highfield, Southampton SO17 1BJ, United Kingdom*
[2]*Faculty of Mathematics and Physics, Charles University, Ke Karlovu 3, 121 16 Praha 2, Czech Republic*
[3]*Science Institute, University of Iceland, Dunhagi 3, IS-107 Reykjavik, Iceland*
[4]*Faculta di Fisica, Universita di Roma II "Tor Vergata," 1 via della Ricerca Scientifica, 00173 Roma, Italy*
(Received 3 September 2009; revised manuscript received 23 February 2010; published 15 March 2010)

Elastic scattering of exciton polaritons in planar semiconductor microcavities has been used to create X-NOR logic gates. Polaritons with identical linear polarization scatter preferentially at the right angle and rotate their polarization by 90°. On the other hand, scattering of polaritons having orthogonal linear polarizations is suppressed. We show that these effects are a consequence of the multiple scattering in microcavities which involve three and more polaritons. The theory quantitatively reproduces the experimental data of C. Leyder *et al.* [Phys. Rev. Lett. **99**, 196402 (2007)].

DOI: 10.1103/PhysRevB.81.125319 PACS number(s): 71.36.+c, 42.65.Yj, 72.25.Rb

I. INTRODUCTION

Exciton polaritons, also referred to as cavity polaritons, are elementary excitations in semiconductor microcavities.[1] Being a combination of bosonic crystal excitations [quantum well (QW) excitons] and photons, cavity polaritons posses a number of peculiar properties, which make them promising candidates for observation of interesting collective phenomena, including high-T_c Bose-Einstein condensation (BEC) (Ref. 2) and superfluidity.[3]

An important peculiarity of a polariton system is the spin structure of a polariton state: being formed usually by heavy-hole excitons, polaritons have two allowed spin projections on the structure growth axis (± 1), corresponding to the right and left circular polarizations of counterpart photons. The exciton states having spin projections ± 2 (dark states) are split-off in energy and affect the polariton dynamics in the second order with respect to perturbation caused by Coulomb interaction between the exciton polaritons.[4] The polarization of light emitted by a microcavity is the same as the polarization of exciton polaritons. From the formal point of view the spin structure of cavity polaritons is analogous to spin structure of the electrons (both are two-level systems), which is why a concept of a pseudospin vector $\mathbf{S}$ is suitable for the description of their polarization.[5] The pseudospin is a quantum analogy of the Stockes vector of a classical light. It is linked with a 2×2 spin-density matrix ρ of a polariton quantum state by a relation,

$$\rho = \frac{N}{2}\mathbf{I} + \mathbf{S}\cdot\sigma, \tag{1}$$

where N is the occupation number of the polariton state, $\mathbf{I}$ is the identity matrix, and σ is the Pauli-matrix vector. The orientation of the pseudospin determines the polarization of emission from a microcavity. The parameter $\rho = 2|\mathbf{S}|/N$ is the total polarization degree of light emitted by the cavity, which may vary between 0 and 1. The z component of the pseudospin is linked with the circular polarization degree of emitted light $\rho_c = 2S_z/N$, while S_x and S_y characterize the linear polarization degree of emitted light measured in (x,y) axes (ρ_l) and in the diagonal axes (ρ_d), respectively: $\rho_l \equiv 2S_x/N$, $\rho_d \equiv 2S_y/N$.

In the absence of an external magnetic field the "spin-up" and "spin-down" states of the exciton polaritons corresponding to their spin projections $+1$ and -1 to z axis and the pseudospin parallel and antiparallel to z axis, respectively, are degenerate. On the other hand, the interaction of polaritons in triplet configuration (identical spin projections on the structure growth axis) is usually much stronger than that of polaritons in singlet configuration[6–8] (spin projections of different signs). This may lead to lifting of degeneracy of the spin-up and spin-down polariton states if their populations are not equal. The spin state which is stronger populated has a higher energy than the spin state which is less populated. This interaction-induced spin splitting may be described as an effective magnetic field applied in z direction which causes the Larmor precession of the polariton pseudospin in the (x,y) plane.[9] This precession, also referred to as the self-induced Larmor precession, is responsible for the mixing of linearly polarized polariton states which manifests itself in remarkable nonlinear effects in polariton spin relaxation.[8] The difference in the polariton-polariton interaction constants in singlet and triplet configurations is also responsible for the predominantly linear polarization of BECs of exciton polaritons, recently observed in microcavities at the conditions close to the thermal equilibirum.[10]

From the point of view of potential applications, it has been recently pointed out that the controllable manipulation of the pseudospin of cavity polaritons can provide a basis for the construction of optoelectronic devices of the new generation, referred to as spin-optronic devices,[11] which can be of importance in various technological implementations including the classical or quantum information transfer. With respect to the conventional spintronics operating with electrically charged spin carriers, the spin optronics has an advantage of strongly reducing the dramatic impact of carrier spin relaxation or decoherence,[12] which severely limits the functionality of spintronic devices. Macroscopically large coherence lengths of exciton polaritons and their bosonic properties led to formulation of several concepts of spin-optronic devices based on microcavities. These include in particular mesoscopic optical interferometers,[13] optical

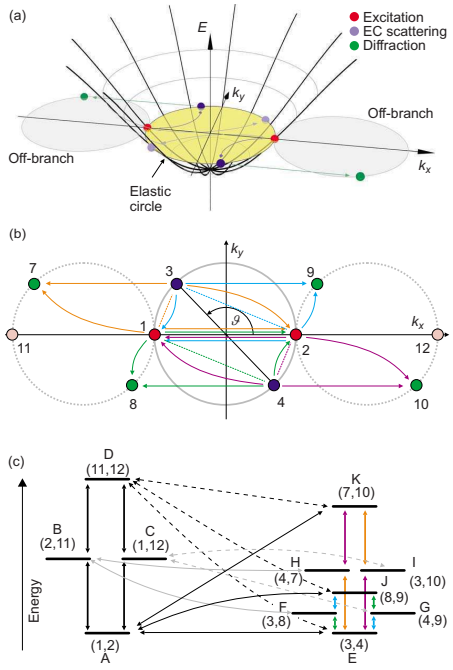

FIG. 1. (Color online) (a) Scheme of the polariton dispersion in the two-dimensional reciprocal space and scattering of counterpropagating polaritons (denoted as "Excitation") forming scattered pairs on the elastic circle ("EC scattering") and their further diffraction to off-branches ("Diffraction"). (b) Diffraction of the EC scattered state to the off-branch states (lying on the dashed circles). Lines denote the pair of interacting polaritons and arrows with the appropriate color denote the possible diffraction processes. (c) Level scheme for visualization of the virtual processes. Numbers refer to the states in (b).

circuits,[14] and highly efficient sources of entangled photon pairs.[15]

The polarization-controlled X-NOR gate is the only spinoptronic device concept which has been realized experimentally already.[16] It consists of a semiconductor microcavity in the strong-coupling regime optically excited by two linearly polarized light beams incident at the opposite oblique angles [see Fig. 1(a)]. The device operates due to elastic polariton-polariton scattering which changes distribution of the exciton polaritons on the so-called elastic circle, i.e., the circle in the reciprocal space corresponding to the constant energy, equal to the energy of the pump beams. It has been demonstrated experimentally that polaritons are scattered preferentially at the right angle in this configuration (i.e., in the directions which are characterized by in-plane wave vector components orthogonal to those of the pump beams[17]). Moreover, the scattering only takes place if two pumping light beams are colinearly polarized. On the other hand, if the polarizations of two incident beams are orthogonal, the scattering vanishes. This surprising experimental observation has been theoretically reproduced in Ref. 16 using the spin dependent Gross-Pitaevskii (GP) equations, which describe the ensemble of exciton polaritons by a single spinor wave function. Being a powerful tool for numerical modeling of the coherent polariton dynamics, GP equations account for polariton-polariton scattering in all orders assuming contact interactions described by two phenomenological constants α_1 and α_2 which characterize the scattering of polaritons with parallel and antiparallel spins, respectively. GP equations do not provide information on the probabilities and polarization selection rules of each individual scattering act and, while the agreement between simulation and experiment is excellent, the physical reasons of the unusual characteristics of the polariton X-NOR gates remained obscure.

The goal of this paper is to describe the most important features of polariton logic gates in terms of the spin- and angle-dependent scattering of exciton polaritons. We show that the peculiar nonuniform distribution of the polaritons on the elastic circle observed in Refs. 16 and 17 is due to the diffraction of scattered polaritons on the grating created by two pump pulses.

II. POLARITON X-NOR GATE IN THE SPONTANEOUS SCATTERING REGIME

Polarization selection rules in the course of polariton-polariton scattering have been analyzed in our recent publication.[18] We have shown that a single spontaneous scattering act of two identically linearly polarized exciton polaritons results in two weakly polarized polariton states having their preferential polarization in the plane orthogonal to the polarization plane of two initial states. This small preferential polarization of the final states may be amplified in the case of stimulated scattering. On the other hand, no significant angular dependence of the scattering amplitudes has been found for the realistic microcavity structures within this model. This result is in apparent contradiction with the experiments[17] and the Gross-Pitaevskii model.[16] Having in mind that the GP equations implicitly account for polariton-polariton scattering in all orders, the only possible explanation of this contradiction is that the experimentally observed strong angular dependence of the scattered polariton population is due to the processes involving two or more polariton scattering events.

To start we note that there is no process which could break the cylindrical symmetry of the microcavity potential acting upon exciton polaritons under weak excitation (i.e., if pump-induced blueshift of the excited states is small compared to the disorder potential in the sample); however, when the pump power is sufficiently large, the pump beams themselves provide the symmetry-breaking effect. This effect can be described as an appearance of a pump-induced transient grating on which the polaritons diffract from the elastic circle (EC) to off-branches[19] shifted in the reciprocal space by the grating vector $\pm(\boldsymbol{k}_1-\boldsymbol{k}_2)$, where $\boldsymbol{k}_{1,2}$ are the in-plane wave vectors of excitation beams [see Fig. 1(a)]. The transitions to the off-branches do not conserve energy so that they must be accompanied by processes which restore the energy conservation within time inversely proportional to the energy mismatch, according to the uncertainty relations. There is a rich variety of processes which may restore the energy con-

servation, including scattering back to elastic circle, phonon scattering, polariton decay by tunneling of a photon through Bragg mirrors (photon would have energy of a polariton on the EC and wave vector of the off-branch state), or return of polaritons to their initial states. The retarded return processes influence the phase of the involved polariton so that the interference of polaritons coming back from the virtual states with other polaritons is not necessarily constructive. In this paper, we show that the diffraction of the virtual states is responsible for modulation of the polariton population on the elastic circle even though this effect is weak compared to the direct scattering from the pump states to the states on the elastic circle.

We distinguish between *EC scattering* and *diffraction* throughout the paper. We define *EC scattering* as a wave vector conserving elastic-scattering process for a pair of polaritons. In particular, the resonant scattering of pump polaritons to the states at the elastic circle is EC scattering. The diffraction is scattering of a single exciton polariton on a diffraction grating formed by two pump beams which leads to the change of the polariton wave vector by $\pm(\boldsymbol{k}_1-\boldsymbol{k}_2)$. When we refer to both processes together, we shall use the term *scattering*.

The system reveals a rich variety of possible pair interactions which populate real or virtual states and contribute to the overall dynamics. There are, nevertheless, several processes in the limit of weak polariton-polariton interactions, which are more probable than others: these are (1) resonant processes (scattering around the EC) and (2) virtual processes, enhanced by the large conjoint population of the involved states. The strongest transitions from one to the other pump beam are stimulated due to their large macroscopic populations. The exchanged wave vector is $\pm(\boldsymbol{k}_1-\boldsymbol{k}_2)$ in this case and therefore this group of processes represents the diffraction.

In order to describe the system dynamics in the spontaneous EC scattering regime (i.e., considering low population of the EC), we consider a polariton pair and investigate its evolution, accounting for the background populations $n_{1,2}$ of the pump beams. Considering only those single-polariton states which may be populated by a single EC scattering or diffraction,[20] single polaritons may occupy only states 1–12 depicted in Fig. 1(b). All the two-polariton states allowed by the dynamics may be denoted as follows: the initial state is $A=(1,2)$, where the numbers in parentheses denote the contributing single-polariton states, the final EC scattered state (for a fixed scattering angle ϑ) is $E=(3,4)$. These states on the EC are coupled to the virtual states $B-D, F-K$ by diffraction, see description of levels in Fig. 1(c). The states D, J and K are virtual off-branch states. Their relative influence on the scattering of polaritons depends on the scattering angle. The state D and, in many cases, one of the states J and K or sometimes even both of them can be neglected as they have a little influence on the population of the elastic circle. On the other hand, for specific scattering angles one of the states J or K may lie close to the EC and play a more important role in its population, consequently. In the numerical calculation we always keep the states D, J, and K in consideration. According to the Fig. 1(c), diffraction of e.g., single-polariton state 3 may be regarded as scattering of the states $1,3\rightarrow 2,7$ or $2,3\rightarrow 1,9$ and therefore it leads to efficient coupling of the state E to G and H. Note, however, that there is no state (1,1) in the level scheme. To clarify this point, we need to consider both the polariton pair and the background population—wave vector conservation requires that the transition $(1,2)\rightarrow(1,1)$ is accompanied by the increase of the population of state 2 by 1 polariton, making the initial and the final-state equivalent. Clearly the states $A-D$ form a group coupled by diffraction and also all states within the second group $E-K$ are coupled by diffraction. These two groups are then coupled by EC scattering as depicted in Fig. 1(c). The relevant effective Hamiltonian for the first group $(A-D)$ accounting only for diffraction reads as

$$H_{A-D}=\begin{pmatrix} 0 & V_{\mathrm{D}} & V_{\mathrm{D}} & 0 \\ V_{\mathrm{D}} & \hbar\omega_{11} & 0 & V_{\mathrm{D}} \\ V_{\mathrm{D}} & 0 & \hbar\omega_{11} & V_{\mathrm{D}} \\ 0 & V_{\mathrm{D}} & V_{\mathrm{D}} & 2\hbar\omega_{11} \end{pmatrix}, \tag{2}$$

where we denote $\hbar\omega_{11}$ the energy mismatch between the single-polariton state 11 and the EC which can be evaluated as $\hbar\omega_{11}=4\hbar^2k_0^2/m^*$ in parabolic approximation, where k_0 is the EC radius and m^* is the polariton effective mass (in the presence of strong excitation field, parabolic approximation may be altered by a more proper dispersion accounting for the Bogoliubov renormalization[19,21]). The effective Hamiltonian for the group $(E-K)$ has the following form:

$$H_{E-K}=\begin{pmatrix} 0 & V_{\mathrm{D}} & V_{\mathrm{D}} & V_{\mathrm{D}} & V_{\mathrm{D}} & 0 & 0 \\ V_{\mathrm{D}} & \hbar\omega_8 & 0 & 0 & 0 & V_{\mathrm{D}} & 0 \\ V_{\mathrm{D}} & 0 & \hbar\omega_8 & 0 & 0 & V_{\mathrm{D}} & 0 \\ V_{\mathrm{D}} & 0 & 0 & \hbar\omega_7 & 0 & 0 & V_{\mathrm{D}} \\ V_{\mathrm{D}} & 0 & 0 & 0 & \hbar\omega_7 & 0 & V_{\mathrm{D}} \\ 0 & V_{\mathrm{D}} & V_{\mathrm{D}} & 0 & 0 & 2\hbar\omega_8 & 0 \\ 0 & 0 & 0 & V_{\mathrm{D}} & V_{\mathrm{D}} & 0 & 2\hbar\omega_7 \end{pmatrix}, \tag{3}$$

where $\hbar\omega_{7,8}=2\hbar^2k_0^2(1\mp\cos\vartheta)/m^*$. We calculate the effective coupling V_{D} as the Hamiltonian matrix element $\langle\Psi_{\mathrm{f}}|H'|\Psi_{\mathrm{i}}\rangle$, where $\Psi_{\mathrm{i,f}}$ are the initial and the final states, respectively, and H' is the microscopic diffraction Hamiltonian relevant for the selected group of states. Let us take for instance the transition $E\rightarrow H$. In this case, the part of microscopic Hamiltonian which applies is $H'=V(a_7^+a_2^+a_3a_1+\mathrm{H.c.})$ and the initial and final states are

$$\Psi_{\mathrm{i}}=a_3^+a_4^+|n_1,n_2\rangle, \tag{4}$$

$$\Psi_{\mathrm{f}}=a_7^+a_4^+|n_1-1,n_2+1\rangle, \tag{5}$$

where $|n_1,n_2\rangle$ is a state created by pump beams with mean numbers of polaritons $n_{1,2}$ in the states 1 and 2, respectively. Considering $n_{1,2}\gg 1$, we finally obtain $V_{\mathrm{D}}=V\sqrt{n_1n_2}$.

Coupling of the states, according to the above Hamiltonians, is depicted in Fig. 1(c) by vertical lines. As we stated before, the two groups of states shown in this figure are coupled by EC scattering (whose amplitude is V). Note that not only the states A and E are coupled, we must take into

account also EC coupling of the virtual states. The coupled states are connected by horizontal lines in Fig. 1(c). The corresponding EC coupling Hamiltonian is

$$H_{\mathrm{EC}} = V[(|A\rangle + |D\rangle)(\langle E| + \langle J| + \langle K|) + |B\rangle(\langle F| + \langle H|) + |C\rangle(\langle G| + \langle I|) + \mathrm{H.c.}]. \quad (6)$$

Population of the polaritons scattered to a fixed angle ϑ is defined by $N_{\mathrm{tot}}(\vartheta)=2\Sigma_{\ell=E}^{K} n_\ell(\vartheta)$, where n_ℓ are the individual populations of the states $E-K$ and the prefactor "2" arises due to the two-particle nature of the states. This definition includes both contributions from the EC states and diffracted polaritons lying on the off-branches. To account only for the states on the EC, the definition should be revised

$$N_{\mathrm{EC}}(\vartheta) = 2n_E + \sum_{\ell=F}^{I} n_\ell. \quad (7)$$

We evaluate the population $N_{\mathrm{EC}}(\vartheta)$ within the second-order perturbation theory for the EC scattering. On the other hand, we account for the diffraction by exact diagonalization of the appropriate Hamiltonians due to the large coupling terms. All states are then divided to the groups, whose kinetics is treated nonperturbatively while the intergroup interactions are expanded to perturbation series. It is then straightforward to diagonalize the particular group Hamiltonians: $H_{a-d}=T^{(0)}H_{A-D}T^{(0)^+}$ and $H_{e-k}=T^{(\vartheta)}H_{E-K}T^{(\vartheta)^+}$, where $T^{(m)}$ are the relevant transformation matrices. By this diagonalization, we define a new set of eigenenergies $\hbar\omega_a,\ldots,\hbar\omega_k$, eigenstates $|a\rangle=\Sigma_{\ell=A}^{D}T_{a,\ell}^{(0)}|\ell\rangle$ etc. as a linear combination of the original states. The EC populations may be then redefined as $N_{\mathrm{EC}}(\vartheta)=\Sigma_{\ell=e}^{k} n_\ell(\vartheta)P_\ell(\vartheta)$, factor $P_\ell(\vartheta)$ being a number of the polaritons from the state $|\ell\rangle$ lying on the EC [cf. Eq. (7)],

$$P_\ell(\vartheta) = 2[T_{\ell,E}^{(\vartheta)}]^2 + \sum_{j=F}^{I}[T_{\ell,j}^{(\vartheta)}]^2. \quad (8)$$

Applying the standard second-order perturbative approach, we obtain the steady-state population of, e.g., a final state f in the form

$$n_f = \frac{2}{\hbar^2}\sum_{\ell=a}^{d}\frac{|(H_{\mathrm{EC}})_{f,\ell}|^2}{\Gamma^2+(\omega_f-\omega_\ell)^2}n_\ell, \quad (9)$$

where Γ is the polariton dephasing rate. Considering further the initial condition $n_A=n_1=n_2$, and $n_{B-D}=0$, we obtain after transformation $n_{a-d}=|T_{a-d,A}^{(0)}|^2 n_A$ and the EC scattering Hamiltonian is transformed as $(H_{\mathrm{ec}})_{\ell,j}=\Sigma_{m,n}T_{\ell,m}^{(\vartheta)}(H_{\mathrm{EC}})_{m,n}T_{j,n}^{(0)}$ (the last term comes from the Hermitian conjugate of a real matrix). Substituting this expression to the above equation and considering explicit form (6) of the EC scattering Hamiltonian, we finally obtain

$$N_{\mathrm{EC}}(\vartheta) = \frac{V^2 n_1}{\hbar^2}\sum_{j=a}^{d}\sum_{\ell=e}^{k}\frac{[T_{j,A}^{(0)}]^2 P_\ell(\vartheta)}{(\omega_j-\omega_\ell)^2+\Gamma^2}\sum_{[m,n]}|T_{j,m}^{(0)}T_{\ell,n}^{(\vartheta)}|^2, \quad (10)$$

$$[m,n] \in \{[A,E];[A,J];[A,K];[B,F];[B,H];[C,G];[C,I];[D,E];[D,J];[D,K]\}. \quad (11)$$

The above equation is the illustrative result considering only one circular polarization and resonant scattering on the EC. In reality, however, one usually deals with both polarizations and the polariton population distributed in the whole reciprocal space. To account for all possible final states, we simply let the state E be anywhere in the reciprocal space and directly apply the equations above. Considering the spin, each polariton may carry an angular momentum ± 1 and therefore we redefine polariton states as, e.g., $|A\pm\pm\rangle=(1\pm,2\pm)$. Each of the two-polariton states A to K is then split to four levels having different spin configurations of the participating polaritons. Coupling strengths between the states are no more equal but depend on the spin configuration of the initial and final states and the spin-dependent populations of the initial states $n_{1\pm}$ and $n_{2\pm}$.

In the numerical calculation we take the polariton effective mass of $m^*=10^{-5}m_e$, where m_e is a free-electron mass, the in-plane momentum of the pump beams $k_0=0.9\ \mu\mathrm{m}^{-1}$ and the dephasing rate $\Gamma=0.2\ \mathrm{ps}^{-1}$. We calculated the distributions of polariton populations in the k-space, using the second-order perturbation theory without stimulation of the EC scattering, keeping scattering amplitudes $V_{1,2}$ (scattering of polaritons with parallel or antiparallel spins, respectively[18]) constant around the EC and considering various combinations of polarizations of the excitation beams. The result for cocircular polarizations is shown in Fig. 2(a). Clearly the polariton population is distributed in the vicinity of the EC with the radius $0.9\ \mu\mathrm{m}^{-1}$ and is further modulated depending on the scattering angle. Note, however, that this modulation is due to the coupling to the virtual states by diffraction on the pump-induced grating. The evaluated polariton population $N(k=k_0,\vartheta)$ on the EC is depicted in Fig. 2(b), and Fig. 2(c) shows its wave-vector dependence for three fixed values of the scattering angle.

It follows from Fig. 2(b) that the polariton population depends on the spins of interacting polaritons and the spin structure of the excitation beams. Scattering of cocircularly or linearly polarized beams demonstrates preferential spontaneous scattering to the angles around 90°, while counter-circularly polarized beams are preferentially backscattered. According to Fig. 2(c), diffraction also causes variations of the radial distribution of the polariton density around the EC.

In the case of the linear copolarized excitation beams the scattering is accompanied by inversion of the linear polarization, as it was noticed in Refs. 8, 16, and 18. The inversion of polarization results from the interplay of first-order

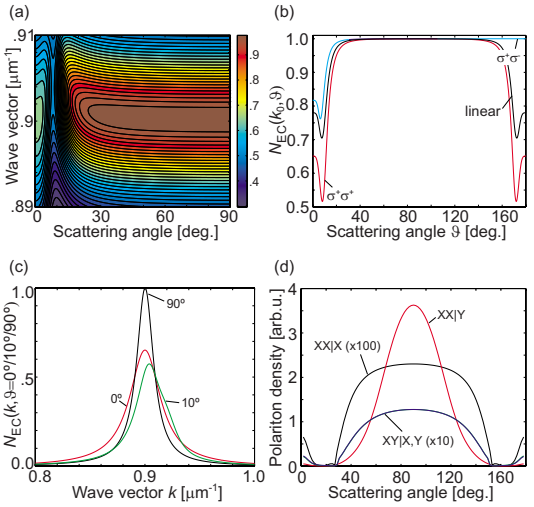

FIG. 2. (Color online) (a) Calculated steady-state populations of the polariton states in the k space for the cocircular polarizations of excitation beams (far below stimulation threshold). (b) Population of the EC for various combinations of the polarizations of the pump beams. (c) Population of the polariton states at scattering angles 0, 10, and 90° for cocircularly polarized excitation. (d) Polarization-resolved steady-state polariton population on the EC under strong cw excitation slightly above threshold ($1.12\ P_{\mathrm{thr}}$) with colinear or crosslinear polarizations. Notation $AB|C$ means that excitation beams have polarizations A and B, and C-polarized component is detected ($A,B,C=X,Y$).

polariton-polariton exchange interaction between the copolarized components in the circular spin basis and the second-order exchange process between countercircularly polarized components via dark states.[22] The second-order exchange process is comparable in magnitude to the first-order exchange process, due to the high density of intermediate dark states characterized by the excitonlike dispersion. The polarization degree of the scattered states may be estimated from the T matrix for polariton-polariton interaction.[23] Note, however, that the calculation of Schumacher *et al.* comprises a two-dimensional approximation of the exciton gas and therefore the use of the T matrix itself may result in an overestimation of the polarization degree because of the neglect of the direct-scattering channel.[18] Using the algebra of Ref. 18 and considering $T_{\mathrm{R}}^{+-}/T_{\mathrm{R}}^{++}=-0.28$ from Ref. 23, we find for the degree of linear polarization

$$\rho_{\ell}=\frac{2T_{\mathrm{R}}^{+-}/T_{\mathrm{R}}^{++}}{1+(T_{\mathrm{R}}^{+-}/T_{\mathrm{R}}^{++})^2}\approx -52\%. \tag{12}$$

The negative sign here means that the polarization plane of the final states is rotated by 90° with respect to the polarization of the pump beams. Compared to the experimental data of Ref. 6, the polarization degree we obtain is 2.5 times higher. In the real experiment, the final linear polarization degree could have been reduced due to the self-induced Larmor precession of polariton pseudospins, neglected in our model. If the pumps are linearly crosspolarized the scattering results in a depolarized signal around the EC as discussed in Ref. 18 while only a small polarization degree resulting from the weak direct-scattering term is expected.

Preferential scattering to the 90° direction shown in Fig. 2(a) may be qualitatively explained in terms of the above simplified model with levels $A-K$ ascribed to one circular polarization. As noted in the beginning of this section, polaritons may remain in the virtual state for a limited time inversely proportional to the virtual state detuning from the EC. Clearly the larger time polaritons are in the virtual state, the larger influence of the diffraction is and the larger (negative) modulation of the coupling strength is. Scattering is therefore the least influenced by diffraction if the virtual states are separated from the EC by the largest amount of energy, what is actually the case of scattering to the angle $\vartheta=90°$. If $\vartheta\approx 0$ or 180°, on the contrary, small energy separation of the levels F,G or H,I from the level E causes relatively high population of the virtual off-branch states and therefore large reduction of the coupling strength between the initial state and the states on the elastic circle.

III. POLARITON X-NOR GATE IN THE STIMULATED REGIME

The above discussion of the regime of spontaneous scattering proves our assumption that the excitation causes the symmetry breaking resulting in the modulation of the polariton-polariton scattering amplitudes. In the spontaneous regime this modulation is rather weak and hardly can be experimentally detected. However, the effect can be drastically amplified in the stimulated regime. Stimulation provides also the dramatic increase of linear polarization degree of the scattered beams which may achieve almost 100%.

For the analysis of the stimulated scattering case we shall operate with the spin-density matrix of the system using the first-order Born-Markov approximation. Consider the particles which can scatter from initial states 1 and 2 to final states 3 and 4 on the EC. The appropriate part of the interaction Hamiltonian can be written as $H_{\mathrm{scatt}}=H^{+}+H^{-}$ where

$$\begin{aligned}H^{+}=&V_1(a_{1+}^{+}a_{2+}^{+}a_{3+}a_{4+}+a_{1-}^{+}a_{2-}^{+}a_{3-}a_{4-})\\&+V_2(a_{1+}^{+}a_{2-}^{+}a_{3+}a_{4-}+a_{1-}^{+}a_{2+}^{+}a_{3-}a_{4+})\\&+V_3(a_{1+}^{+}a_{2-}^{+}a_{3-}a_{4+}+a_{1-}^{+}a_{2+}^{+}a_{3+}a_{4-}),\end{aligned} \tag{13}$$

and $H^{-}=(H^{+})^{+}$. Scattering amplitudes are denoted V_{1-3} here, V_1 describing the spin triplet configuration and $V_{2,3}$ describing the singlet configuration. In order to account for the diffraction on the transient grating, we do not further introduce the virtual states in the Hamiltonian but rather consider V_{1-3} as effective scattering amplitudes defined as

$$V_j(\vartheta)=\frac{N_{\mathrm{EC}}(\vartheta)}{N'_{\mathrm{EC}}(\vartheta)}\tilde{V}_j(\vartheta), \tag{14}$$

where $N(\vartheta)$ and $N'(\vartheta)$ come from Eq. (10) as the populations coupled and uncoupled to the virtual states, respectively. The decoupling of the EC scattering and the diffraction present in the Eq. (14) is valid as long as we may

consider that diffraction on the grating formed by pump beams is the strongest process in the system. We therefore require $n_{1,2} \gg n_{3,4}$ otherwise the large population of the states on EC would introduce a new efficient diffraction channel and the approximation of Eq. (14) would break. The condition is satisfied in the experiment of Ref. 16. The bare scattering amplitude $\tilde{V}_j(\vartheta)$ can be estimated using microscopic calculations,[22,24] considering the amplitude of the direct scattering in real three-dimensional structures.[18] The second-order exchange processes do not contribute to the Hamiltonian in the basis restricted to the bright states only, however the Hamiltonian presented above may be regarded as an effective one with the scattering amplitudes which give a correct form of the scattering T matrix within the chosen Born-Markov approximation. The second-order processes therefore may be accounted for in the scattering amplitudes $V_{2,3}$.

The Liouville–von Neumann equation for the density matrix ϱ of the system reads as ($\hbar=1$)

$$\partial_t \varrho = -\int_{-\infty}^{t} \{H_{\mathrm{scatt}}(t);[H_{\mathrm{scatt}}(t');\varrho(t')]\}. \tag{15}$$

In the Born-Markov approximation one replaces t' by t and retains only energy-conserving terms which yields

$$\delta^{-1}(\Delta E)\partial_t \varrho = 2(H^+\varrho H^- + H^-\varrho H^+) - (H^+H^- + H^-H^+)\varrho - \varrho(H^+H^- + H^-H^+) \tag{16}$$

where the term $\delta^{-1}(\Delta E)$ ensures the conservation of energy. For time evolution of the mean values of any arbitrary operator $\hat{A}, \langle\hat{A}\rangle = \mathrm{Tr}(\varrho\hat{A})$ one has

$$\partial_t\langle\hat{A}\rangle = \mathrm{Tr}(\varrho[H^-;[\hat{A};H^+]]) + \mathrm{Tr}(\varrho[H^+;[\hat{A};H^-]]). \tag{17}$$

This formula can be used for calculation of temporal dynamics of the occupancies and pseudospins defined as

$$N_j = \mathrm{Tr}\{\varrho(a^+_{j,+}a_{j,+} + a^+_{j,-}a_{j,-})\}, \tag{18}$$

$$S_{x,j} = \mathrm{Re}\ \mathrm{Tr}\{\varrho a^+_{j,+}a_{j,-}\}, \tag{19}$$

$$S_{y,j} = \mathrm{Im}\ \mathrm{Tr}\{\varrho a^+_{j,+}a_{j,-}\}, \tag{20}$$

$$S_{z,j} = \frac{1}{2}\mathrm{Tr}\{\varrho(a^+_{j,+}a_{j,+} - a^+_{j,-}a_{j,-})\}. \tag{21}$$

The resulting explicit formulas are listed in the Appendix. Figure 2(d) shows the resulting distributions of polaritons on the EC in the stimulated regime under different excitation conditions (the pump beams are subtracted). One can see that the colinear excitation exceeds 98.5% spin inversion slightly above the threshold (the spin inversion further increases with increasing pump power) and a strong emission in the 90° direction with full width at half maximum of 50°, in accordance with the experimental data of Ref. 16. Crosslinear excitation, on the other hand, for the same excitation intensity yields the scattering signal which is more that one order of magnitude weaker and is almost unpolarized.

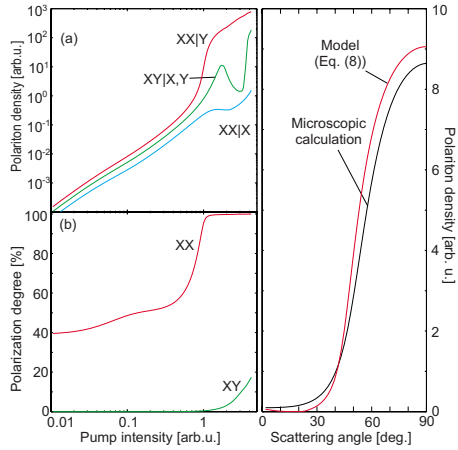

FIG. 3. (Color online) (a) Pump intensity dependence of the polarized polariton population on the EC. The polariton population at the scattering angle 90° under different pump and detection conditions is shown. Pump intensity is plotted relative to the threshold for the colinear excitation. (b) Pump intensity dependence of the maximum of polarization degree for colinearly (red) and crosslinearly (green) polarized pumps. The sign of the polarization degree shown by the red curve is inverted for clarity. (c) Comparison of the full microscopic calculation and the presented model for pump power of 1.12 units, assuming cocircular polarizations of the excitation beams.

In order to explain why the polariton-polariton scattering and polarization inversion under colinear pump is stronger by orders of magnitude than the scattering with crosslinearly polarized beams, we plot the intensity dependence of the polariton population and the maximum polarization degree in Figs. 3(a) and 3(b). The gate performance in Fig. 2(d) is plotted for the pump intensity of 1.12 (in the units corresponding to the horizontal scale in Fig. 3). The stimulation threshold is reached for the colinear but not crosslinear pumps, which is why the scattered signal is so much different in the two cases. The gate may therefore operate only within the interval of pump intensities between the two stimulation thresholds for colinear and crosslinear pump polarizations.

The initial degree of polarization at very low pump power is about −40% in the present calculation, which is far below the experimentally observed value[6] −(15–20)% and also below our theoretical prediction −11% for the narrow InGaAs QWs.[18] There is no contradiction with our previous publication[18] as here we consider an 8-nm-wide QW while the QW of 2.5 nm width has been considered in Ref. 18. As the QW width determines the magnitude of the direct-scattering term, the linear polarization degree of the scattered polaritons in an 8-nm-wide QW is much higher compared to a 2.5-nm-wide QW. Considering further complex polarization dynamics in the case of the excitation geometry of Ref. 6, we find that the theoretical estimation and experimental data are fully compatible.

Figure 3(b) illustrates another interesting feature of the stimulated scattering on the EC. Although the polarization

degree in the spontaneous regime of scattering of crosslinearly polarized polaritons does not exceed 0.1%, stimulation causes the polarization amplification, which is essential for operation of future spin-optronic devices.

The use of approximation (14) simplifies the calculations significantly and also allows one to understand the physical origin of the population modulation on the EC observed in experiments. We verified the accuracy of Eq. (14) by a numerical calculation. For this purpose, we have derived the kinetic equations for the polariton system on the elastic circle in the stimulation regime accounting for the diffraction in the microscopic Hamiltonian and thus without simplifying assumption of Eq. (14). We have used the same approach as in Sec. II; i.e., we have considered the same states involved in the dynamics, the diffraction (restricted to the first diffraction maxima only) has been accounted for nonperturbatively and the EC scattering has been considered within the Born-Markov approximation. Considering cocircular excitation for simplicity, we obtain in this way the results depicted in Fig. 3(c) using the same input parameters for the exact and simplified calculations. One can see that even though there is some small difference between the curves, the approximate model still gives very good predictions.

IV. CONCLUSIONS

We have analyzed the most efficient channels of polariton-polariton scattering on the elastic circle in terms of multiwave mixing. We show that the multiple polariton scattering processes are responsible for changes in the scattering probability of the order of few percents in the linear regime. The increase in the excitation intensity leads to a drastic increase in this modulation due to the final-state bosonic stimulation. The multiple polariton scattering process can be conveniently represented as a combination of the polariton scattering with a subsequent diffraction to the off-branch states by a polarization grating created by two pump pulses. The polaritons from off-branch states then go back to the elastic circle, so that the energy is conserved.

This scenario explains preferential scattering of the polaritons at 90° in the case of colinearly polarized light beams. In this case, none of the intermediate off-branch states is close in energy to the elastic circle polaritons so that destructive interference caused by virtual diffraction processes is suppressed.

We show that the polarization degree of the scattered polaritons strongly depends on the pump intensity and that the final polarization degree may be strongly amplified above the stimulation threshold. This feature opens a possibility of construction of a spin-optronic transistor with a smooth dependence of the output polarization on the polarization of the gate input. The results of this work may be applied for optimization of the design of polariton logic gates by considering various spin configurations or introducing more control beams.

ACKNOWLEDGMENTS

We thank Y. G. Rubo for enlightening discussions. T.O. and A.V.K. acknowledge support from EPSRC-GB and the Chair of Excellence grant POLAROMA.

APPENDIX

We define the scattering probabilities as $W_j=|V_j|^2$ and $W_{j\ell}=V_jV_\ell^*=W_{12}^R+iW_{12}^I$. Following Eq. (17) and definitions (18)–(21), we obtain the following equations of motion for the different pseudospin components. Polariton population

$$\frac{d}{dt}N_3 = N_{11} + N_{12} + N_{22} + N_{13} + N_{23} + N_{33},$$

$$N_{11} = \frac{W_1}{2}[(N_1N_2 + 4S_{1z}S_{2z})(N_3 + N_4 + 2) - (N_3N_4 + 4S_{3z}S_{4z})(N_1 + N_2 + 2)]$$
$$+ 2W_1[(N_1S_{2z} + S_{1z}N_2)(S_{3z} + S_{4z}) - (S_{1z} + S_{2z})(S_{3z}N_4 + N_3S_{4z})],$$

$$N_{12} = 4W_{12}^R[(N_1 - N_3)\boldsymbol{S}_2 \cdot \boldsymbol{S}_4 + (N_2 - N_4)\boldsymbol{S}_1 \cdot \boldsymbol{S}_3] + 8W_{12}^I[(S_{1z} - S_{3z})\boldsymbol{S}_2 \times \boldsymbol{S}_4 + (S_{2z} - S_{4z})\boldsymbol{S}_1 \times \boldsymbol{S}_3],$$

$$N_{22} = \frac{W_2}{2}[(N_1N_2 - 4S_{1z}S_{2z})(N_3 + N_4 + 2) - (N_3N_4 - 4S_{3z}S_{4z})(N_1 + N_2 + 2)]$$
$$- 2W_2[(N_1S_{2z} - S_{1z}N_2)(S_{3z} - S_{4z}) - (S_{1z} - S_{2z})(N_3S_{4z} - S_{3z}N_4)],$$

$$N_{13} = 4W_{13}^R[(N_1 - N_4)\boldsymbol{S}_2 \cdot \boldsymbol{S}_3 + (N_2 - N_3)\boldsymbol{S}_1 \cdot \boldsymbol{S}_4] + 8W_{13}^I[(S_{1z} - S_{4z})\boldsymbol{S}_2 \times \boldsymbol{S}_3 + (S_{2z} - S_{3z})\boldsymbol{S}_1 \times \boldsymbol{S}_4],$$

$$N_{23} = -4W_{23}^R[(N_1 + N_2 + 2)\boldsymbol{S}_3 \cdot \boldsymbol{S}_4 - (N_3 + N_4 + 2)\boldsymbol{S}_1 \cdot \boldsymbol{S}_2] + 8W_{23}^I[(S_{1z} - S_{2z})\boldsymbol{S}_3 \times \boldsymbol{S}_4 + (S_{3z} - S_{4z})\boldsymbol{S}_1 \times \boldsymbol{S}_2],$$

$$N_{33} = \frac{W_3}{2}[(N_1N_2 - 4S_{1z}S_{2z})(N_3 + N_4 + 2) - (N_3N_4 - 4S_{3z}S_{4z})(N_1 + N_2 + 2)]$$

$$- + 2W_3[(N_1S_{2z} - S_{1z}N_2)(S_{3z} - S_{4z}) - (S_{1z} - S_{2z})(N_3S_{4z} - S_{3z}N_4)].$$

Z component of the pseudospin

$$\frac{d}{dt}S_{3z} = Z_{11} + Z_{12} + Z_{22} + Z_{13} + Z_{23} + Z_{33},$$

$$Z_{11} = \frac{W_1}{2}[(N_1S_{2z} + S_{1z}N_2)(N_3 + N_4 + 2) - (N_1 + N_2 + 2)(N_3S_{4z} + S_{3z}N_4)]$$

$$+ \frac{W_1}{2}[(N_1N_2 + 4S_{1z}S_{2z})(S_{3z} + S_{4z}) - (S_{1z} + S_{2z})(N_3N_4 + 4S_{3z}S_{4z})],$$

$$Z_{12} = 4W_{12}^R(S_{1z} - S_{3z})\boldsymbol{S}_2 \cdot \boldsymbol{S}_4 + 2W_{12}^I(N_1 - N_3)\boldsymbol{S}_2 \times \boldsymbol{S}_4,$$

$$Z_{22} = -\frac{W_2}{2}[(N_1S_{2z} - S_{1z}N_2)(N_3 + N_4 + 2) - (N_1 + N_2 + 2)(N_3S_{4z} - S_{3z}N_4)]$$

$$+ \frac{W_2}{2}[(N_1N_2 - 4S_{1z}S_{2z})(S_{3z} - S_{4z}) - (S_{1z} - S_{2z})(N_3N_4 - 4S_{3z}S_{4z})],$$

$$Z_{13} = 4W_{13}^R(S_{2z} - S_{3z})\boldsymbol{S}_1 \cdot \boldsymbol{S}_4 + 2W_{13}^I(N_2 - N_3)\boldsymbol{S}_1 \times \boldsymbol{S}_4,$$

$$Z_{23} = 4W_{23}^R(S_{3z} - S_{4z})\boldsymbol{S}_1 \cdot \boldsymbol{S}_2 + 2W_{23}^I(N_3 + N_4 + 2)\boldsymbol{S}_1 \times \boldsymbol{S}_2,$$

$$Z_{33} = \frac{W_3}{2}[(N_1S_{2z} - S_{1z}N_2)(N_3 + N_4 + 2) + (N_1 + N_2 + 2)(N_3S_{4z} - S_{3z}N_4)]$$

$$+ \frac{W_3}{2}[(N_1N_2 - 4S_{1z}S_{2z})(S_{3z} - S_{4z}) + (S_{1z} - S_{2z})(N_3N_4 - 4S_{3z}S_{4z})].$$

Y component of the pseudospin

$$\frac{d}{dt}S_{3y} = Y_{11} + Y_{12} + Y_{22} + Y_{13} + Y_{23} + Y_{33}$$

$$Y_{11} = -\frac{W_1}{2}[N_4(N_1 + N_2 + 2) - N_1N_2]S_{3y} - 2W_1[S_{4z}(S_{1z} + S_{2z}) - S_{1z}S_{2z}]S_{3y} + 2W_1[S_{2y}\boldsymbol{S}_1 \cdot \boldsymbol{S}_4 - S_{2x}\boldsymbol{S}_1 \times \boldsymbol{S}_4],$$

$$Y_{12} = W_{12}^R[N_2(N_3 + N_4 + 2) - N_3N_4 + 4S_{2z}S_{4z}]S_{1y} - 4W_{12}^RS_{3y}\boldsymbol{S}_2 \cdot \boldsymbol{S}_4 + 2W_{12}^I[S_{2z}(N_3 + N_4 + 2) + S_{4z}(N_2 - N_3)]S_{1x},$$

$$Y_{22} = -\frac{W_2}{2}[N_4(N_1 + N_2 + 2) - N_1N_2]S_{3y} + 2W_2[S_{4z}(S_{1z} - S_{2z}) - S_{1z}S_{2z}]S_{3y} + 2W_2[S_{1y}\boldsymbol{S}_2 \cdot \boldsymbol{S}_4 + S_{1x}\boldsymbol{S}_2 \times \boldsymbol{S}_4],$$

$$Y_{13} = W_{13}^R[N_1(N_3 + N_4 + 2) - N_3N_4 + 4S_{1z}S_{4z}]S_{2y} - 4W_{13}^RS_{3y}\boldsymbol{S}_1 \cdot \boldsymbol{S}_4 + 2W_{13}^I[S_{1z}(N_3 + N_4 + 2) + S_{4z}(N_1 - N_3)]S_{2x},$$

$$Y_{23} = -W_{23}^R[N_3(N_1 + N_2 + 2) - N_1N_2 + 4S_{1z}S_{2z}]S_{4y} + 4W_{23}^RS_{3y}\boldsymbol{S}_1 \cdot \boldsymbol{S}_2 + 2W_{23}^I[S_{1z}(N_2 - N_3) - S_{2z}(N_1 - N_3)]S_{4x},$$

$$Y_{33} = -\frac{W_3}{2}[N_4(N_1 + N_2 + 2) - N_1N_2]S_{3y} - 2W_3[S_{4z}(S_{1z} - S_{2z}) + S_{1z}S_{2z}]S_{3y} + 2W_3[S_{2y}\boldsymbol{S}_1 \cdot \boldsymbol{S}_4 + S_{2x}\boldsymbol{S}_1 \times \boldsymbol{S}_4].$$

X component of the pseudospin

$$\frac{d}{dt}S_{3x} = X_{11} + X_{12} + X_{22} + X_{13} + X_{23} + X_{33}$$

$$X_{11} = -\frac{W_1}{2}[N_4(N_1+N_2+2)-N_1N_2]S_{3x} - 2W_1[S_{4z}(S_{1z}+S_{2z})-S_{1z}S_{2z}]S_{3x} + 2W_1[S_{2x}\boldsymbol{S}_1\cdot\boldsymbol{S}_4 + S_{2y}\boldsymbol{S}_1\times\boldsymbol{S}_4],$$

$$X_{12} = W_{12}^R[N_2(N_3+N_4+2)-N_3N_4+4S_{2z}S_{4z}]S_{1x} - 4W_{12}^R S_{3x}\boldsymbol{S}_2\cdot\boldsymbol{S}_4 - 2W_{12}^I[S_{2z}(N_3+N_4+2)+S_{4z}(N_2-N_3)]S_{1y},$$

$$X_{22} = -\frac{W_2}{2}[N_4(N_1+N_2+2)-N_1N_2]S_{3x} + 2W_2[S_{4z}(S_{1z}-S_{2z})-S_{1z}S_{2z}]S_{3x} + 2W_2[S_{1x}\boldsymbol{S}_2\cdot\boldsymbol{S}_4 - S_{1y}\boldsymbol{S}_2\times\boldsymbol{S}_4],$$

$$X_{13} = W_{13}^R[N_1(N_3+N_4+2)-N_3N_4+4S_{1z}S_{4z}]S_{2x} - 4W_{13}^R S_{3x}\boldsymbol{S}_1\cdot\boldsymbol{S}_4 - 2W_{13}^I[S_{1z}(N_3+N_4+2)+S_{4z}(N_1-N_3)]S_{2y},$$

$$X_{23} = -W_{23}^R[N_3(N_1+N_2+2)-N_1N_2+4S_{1z}S_{2z}]S_{4x} + 4W_{23}^R S_{3x}\boldsymbol{S}_1\cdot\boldsymbol{S}_2 - 2W_{23}^I[S_{1z}(N_2-N_3)-S_{2z}(N_1-N_3)]S_{4y},$$

$$X_{33} = -\frac{W_3}{2}[N_4(N_1+N_2+2)-N_1N_2]S_{3x} - 2W_3[S_{4z}(S_{1z}-S_{2z})+S_{1z}S_{2z}]S_{3x} + 2W_3[S_{2x}\boldsymbol{S}_1\cdot\boldsymbol{S}_4 - S_{2y}\boldsymbol{S}_1\times\boldsymbol{S}_4].$$

[1] See, e.g., G. Khitrova, H. M. Gibbs, F. Jahnke, M. Kira, and S. W. Koch, Rev. Mod. Phys. **71**, 1591 (1999).

[2] J. Kasprzak, M. Richard, S. Kundermann, A. Baas, P. Jeambrun, J. M. J. Keeling, F. M. Marchetti, M. H. Szymańska, R. André, J. L. Staehli, V. Savona, P. B. Littlewood, B. Deveaud, and Le Si Dang, Nature (London) **443**, 409 (2006).

[3] A. Amo, D. Sanvitto, F. P. Laussy, D. Ballarini, E. del Valle, M. D. Martin, A. Lemaître, J. Bloch, D. N. Krizhanovskii, M. S. Skolnick, C. Tejedor, and L. Viña, Nature (London) **457**, 291 (2009).

[4] Scattering between cavity polaritons and dark exciton states has been studied experimentally and theoretically in I. A. Shelykh, L. Vina, A. V. Kavokin, N. G. Galkin, G. Malpuech, and R. Andre, Solid State Commun. **135**, 1 (2005).

[5] K. V. Kavokin, I. A. Shelykh, A. V. Kavokin, G. Malpuech, and P. Bigenwald, Phys. Rev. Lett. **92**, 017401 (2004).

[6] P. Renucci, T. Amand, X. Marie, P. Senellart, J. Bloch, B. Sermage, and K. V. Kavokin, Phys. Rev. B **72**, 075317 (2005).

[7] M. Combescot and O. Betbeder-Matibet, Phys. Rev. B **74**, 125316 (2006).

[8] D. N. Krizhanovskii, D. Sanvitto, I. A. Shelykh, M. M. Glazov, G. Malpuech, D. D. Solnyshkov, A. Kavokin, S. Ceccarelli, M. S. Skolnick, and J. S. Roberts, Phys. Rev. B **73**, 073303 (2006).

[9] I. A. Shelykh, A. V. Kavokin, and G. Malpuech, Phys. Status Solidi B **242**, 2271 (2005).

[10] J. Kasprzak, R. Andre, L. S. Dang, I. A. Shelykh, A. V. Kavokin, Yu. G. Rubo, K. V. Kavokin, and G. Malpuech, Phys. Rev. B **75**, 045326 (2007).

[11] I. A. Shelykh, K. V. Kavokin, A. V. Kavokin, G. Malpuech, P. Bigenwald, H. Deng, G. Weihs, and Y. Yamamoto, Phys. Rev. B **70**, 035320 (2004).

[12] W. Langbein, I. A. Shelykh, D. Solnyshkov, G. Malpuech, Yu. Rubo, and A. Kavokin, Phys. Rev. B **75**, 075323 (2007).

[13] I. A. Shelykh, G. Pavlovic, D. D. Solnyshkov, and G. Malpuech, Phys. Rev. Lett. **102**, 046407 (2009).

[14] T. C. H. Liew, A. V. Kavokin, and I. A. Shelykh, Phys. Rev. Lett. **101**, 016402 (2008).

[15] R. Johne, N. A. Gippius, G. Pavlovic, D. D. Solnyshkov, I. A. Shelykh, and G. Malpuech, Phys. Rev. Lett. **100**, 240404 (2008).

[16] C. Leyder, T. C. H. Liew, A. V. Kavokin, I. A. Shelykh, M. Romanelli, J. Ph. Karr, E. Giacobino, and A. Bramati, Phys. Rev. Lett. **99**, 196402 (2007).

[17] M. Romanelli, C. Leyder, J. Ph. Karr, E. Giacobino, and A. Bramati, Phys. Rev. Lett. **98**, 106401 (2007).

[18] T. Ostatnický, D. Read, and A. V. Kavokin, Phys. Rev. B **80**, 115328 (2009).

[19] P. G. Savvidis, C. Ciuti, J. J. Baumberg, D. M. Whittaker, M. S. Skolnick, and J. S. Roberts, Phys. Rev. B **64**, 075311 (2001).

[20] The first-order approach in EC scattering is valid if the populations of the initial states exceed the remaining populations what is always fulfilled below the stimulation threshold. Second-order diffraction processes either restore the initial populations or populate states far away from the EC so that neglect of the states populated by the second-order diffraction processes is safe as well. The first-order approximation may fail, however, in the close vicinity to the excitation beams due to energy renormalizations and parametric interactions involving polaritons from one beam only. The criterion of validity of our approximation is $1-\cos\vartheta > Vm^*\sqrt{n_1 n_2}/2\hbar^2 k_0^2$ and results beyond this value may be significantly affected by the approximation. The estimates of the limiting angles in our calculations are $\vartheta > 6°$ in Figs. 2(a)–2(c) and $\vartheta > 12°$ in Figs. 2(d) and 3(c). The experiment shows a pronounced anisotropy of scattering for larger angles, with the maxima of scattering intensity around $\vartheta = 90°$. These states are perfectly within the limits of validity our model.

[21] D. D. Solnyshkov, I. A. Shelykh, N. A. Gippius, A. V. Kavokin, and G. Malpuech, Phys. Rev. B **77**, 045314 (2008).

[22] M. M. Glazov, H. Ouerdane, L. Pilozzi, G. Malpuech, A. V. Kavokin, and A. D'Andrea, Phys. Rev. B **80**, 155306 (2009).

[23] S. Schumacher, N. H. Kwong, and R. Binder, Phys. Rev. B **76**, 245324 (2007).

[24] M. Combescot, O. Betbeder-Matibet, and R. Combescot, Phys. Rev. B **75**, 174305 (2007).

[P16]

PHYSICAL REVIEW B **82**, 033302 (2010)

Exciton-polariton integrated circuits

T. C. H. Liew,[1] A. V. Kavokin,[2] T. Ostatnický,[2] M. Kaliteevski,[3] I. A. Shelykh,[4,5] and R. A. Abram[3]
[1]*Institute of Theoretical Physics, Ecole Polytechnique Fédérale de Lausanne (EPFL), CH-1015 Lausanne, Switzerland*
[2]*Physics and Astronomy School, University of Southampton, Highfield, Southampton SO17 1BJ, United Kingdom*
[3]*Department of Physics, Durham University, Durham DH1 3LE, United Kingdom*
[4]*Science Institute, University of Iceland, Dunhagi 3, IS-107 Reykjavik, Iceland*
[5]*International Institute of Physics, Av. Odilon Gomes de Lima 1722, 59078-400, Natal, Brazil*
(Received 31 May 2010; published 20 July 2010)

We show that logical signals encoded in bistable states in semiconductor microcavities can be generated and controlled electronically by exploiting the electrical sensitivity of Tamm-plasmon–exciton-polariton modes. The signals can be transported along polariton neurons, created with a patterned metal surface. Using the Gross-Pitaevskii equations, we simulate an electrically controlled transistor and find that high repetition rates (10 GHz) are possible.

DOI: 10.1103/PhysRevB.82.033302 PACS number(s): 71.36.+c, 42.55.Sa, 42.65.Pc

Exciton-polaritons are part-light part-matter quasiparticles which govern the optical properties of semiconductor crystals at low temperature.[1] Recently, a number of fascinating effects related to exciton-polaritons have been discovered in semiconductor microcavity structures where a confined optical mode is brought into resonance with an excitonic transition. The fundamental discoveries of the Bose-Einstein condensation[2–4] of exciton-polaritons and their superfluidity[5] at elevated temperatures have paved the way toward the realization of a new generation of optoelectronic devices.[6] From the technological point of view the nonlinear optical effects linked with exciton-polaritons are of particular interest. The recently demonstrated optical bistability in a biased microcavity with an extraordinarily low switching power[7] demonstrates the feasibility of optical integrated circuits based on "polariton neurons" in planar microcavities.[8] In order to produce such devices, exciton-polaritons in microcavities must be confined in lateral channels, where the propagation of domains of high-density exciton-polariton liquid may be controlled by external light or electrical bias. Recently it was shown that such channeling of polaritons is possible using hybrid Tamm-plasmon–exciton-polariton modes (TPEPMs) which are formed under thin metallic stripes deposited on the top of a planar semiconductor microcavity.[9–11] TPEPM states are redshifted from the bare cavity polariton modes by several meV, which provides efficient one-dimensional confinement. Exciton-polariton transistors, switches, and logic gates based on TPEPMs would operate at gigahertz frequencies, have extremely low switching power, and be easily integrated on a chip.

The development of practical optical integrated circuits would represent a revolutionary breakthrough in modern optoelectronics, making possible ultrafast information processing with extremely low losses. However, the realization of optical integrated circuits is a complex task which cannot be achieved without exploiting new physical effects, device concepts, and technological approaches. We propose exploiting the newly discovered effects of polariton-mediated optical bistability, plasmon-polariton coupling, and propagation of polariton domain walls in microcavities in a concept of an optical integrated circuit. It is based on several ideas, namely: (i) bistable switching of the optically driven polariton state due to nonlinear polariton-polariton interactions,[12] which has been experimentally observed recently;[13,14] (ii) channeling of polaritons below metallic stripes due to the hybridization of the Tamm-plasmon states and cavity exciton-polaritons; (iii) electrical control of the detuning between the exciton-polariton mode and the pumping laser due to the quantum confined Stark effect; and (iv) propagation of domain walls between different bistable states.

Polariton transistor scheme. Figure 1(a) shows schematically our proposed building block of future polariton integrated circuits: a polariton spin transistor. The figure illustrates a conventional planar microcavity in which Bragg mirrors confine light so that it interacts strongly with excitons in a quantum well. However, in addition our structure has a patterned metal structure on the top surface, comprising a chain of four segments. The band structure of exciton-polariton modes in a microcavity can be strongly affected by the presence of a metallic layer on the top of the structure [as apparent in Fig. 1(c)], and this can be used to provide the lateral confinement necessary for integrated circuits. The thicknesses of the metallic layer and of the semiconductor layer next to it determine the energy of the Tamm-plasmon mode localized at the metal-Bragg mirror interface.[9–11] If the Tamm plasmon is strongly detuned from the cavity polariton modes, the effect of the metal is to blueshift the cavity modes by ~ 0.4 eV.[4] On the other hand, if the Tamm plasmon is put in resonance with the cavity polaritons, a new hybrid TPEPM can appear, which has components of the exciton state, cavity photon, and Tamm plasmon. The lowest TPEPM is redshifted with respect to the lowest bare cavity polariton mode, with the size of the shift dependent on the exciton oscillator strength and the parameters of the Bragg mirror between the cavity and metal.[11] For applications in polariton integrated circuits at low temperatures, a shift of about 5 meV would provide sufficient lateral confinement, and this can be easily achieved in GaAs-based structures. For room-temperature operation, the larger lateral confinement potential necessary can be achieved in GaN-based systems. Selective optical excitation of the TPEPM is achieved by tuning the photon energy of a continuous-wave (cw) laser to lie between the lowest TPEPM and the lowest cavity polariton mode outside the channel. In this case, there is no absorption of light in the regions of the sample not covered by metal. TPEPMs are confined in the channels and the lowest TPEPM

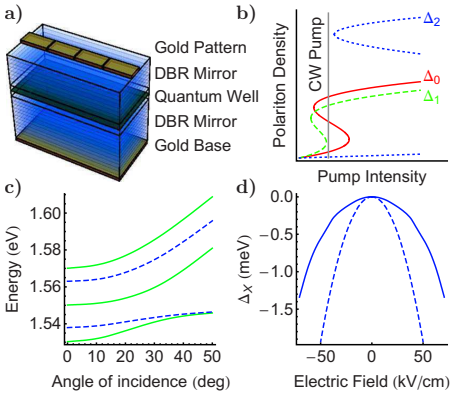

FIG. 1. (Color online) (a) Schematic diagram of a semiconductor microcavity with metallic electrodes used to realize an electrically controlled polariton neuron. A strip of metal on the surface is divided into four segments, which are individually connected to an electrical supply (not shown) allowing the polariton potential to be changed in each segment. Note that the diagram is not to scale; in reality the lateral size of the metal strip is larger than the height of the structure. (b) Dependence of the polariton density on the optical pump intensity for different values of the detuning ($\Delta_1 < \Delta_0 < \Delta_2$) between the optical pump photon energy and the lower polariton energy. The detuning can be changed in the different segments by varying the applied electric potential. For a pump intensity close to the vertical gray line, switching between the different curves can have a major effect on the polariton density. (c) Dispersion relation for cavity polaritons (blue dashed curve) and hybrid TPEPM (green solid curve). The lowest-energy hybrid state is redshifted by several meV with respect to the lowest polariton mode in the vicinity of metal overlay, providing localization of exciton-polaritons in the channels below the metallic segments. (d) Redshift of the ground TPEP modes (solid curve) and exciton modes (dashed curve).

absorbs laser light only if its energy is tuned to the laser energy. This tuning can be achieved and controlled by the application of an electric field across the cavity (in the direction normal to the cavity plane). An electric field affects the exciton energy and oscillator strength due to the quantum confined Stark effect, which leads to the shift of the TPEPMs as well. Electric fields to control the local TPEPM energy selectively can be produced by applying a potential difference relative to the structure's back contact to one or more of the four metallic segments.

Figure 1(b) shows the response of the polariton density to the intensity of a circularly polarized cw optical pump. The different curves represent the cases of different detunings between the optical pump photon energy and the lowest TPEPM energy (we define the detuning as that measured in the low-density regime rather than defining a renormalized detuning). By varying the electrical potential applied to a segment the detuning in its locality can be varied and a particular response as represented by the curves in Fig. 1(b) can be selected [an increase in the applied electric field causes an increased redshift of the TPEPM energy as shown in Fig. 1(d); see also discussion below]. We consider a device with the initial condition that all segments have the same applied potential and hence the same detuning Δ_0. Illuminating the whole system by a broad area optical pump, each segment is initially in a low polariton density state of the TPEPM [given by the intersection between the vertical gray line and the lower branch of the (red) solid curve in Fig. 1(b)].

A signal in the structure can be triggered by lowering the potential applied to the first segment so that the local detuning is reduced to the value Δ_1, corresponding to the (green) dashed S-shaped curve in Fig. 1(b). We expect the change in the potential to cause a major increase in the polariton density [given by the point where the vertical gray line intersects the (green) dashed curve]. Furthermore, polaritons have a particularly light effective mass, which allows them to propagate over micron-scale distances during their short lifetime. The high population of polaritons in the first segment thus begins to spread, tunneling across the narrow gap into the second segment. As a result the increasing polariton population in the area just inside the second segment switches to the upper branch of the (red) solid S-shaped curve in Fig. 1(b). This switching effect continues across the whole segment and indeed across segments later in the chain. In analogy with biological neurons, the signal is carried as a propagating change in the state of the system along the channel. While the signal of a biological neuron is encoded as a switch in the relative concentrations of charged ions across the axon membrane, a polariton neuron encodes the signal as a switch in the local polariton density. Note that just as biological neurons do not rely on charged ions traveling down the whole length of the neuron, the same is the case with polaritons in polariton neurons. Therefore, the signal can propagate substantially further than the distance a single polariton can be expected to travel—in fact the signal is able to propagate to the edge of the cw optical field.

Exciton redshift due to an applied electric field. Before presenting theoretical modeling of our proposed device, we give details on how the exciton redshift can be related to an applied electric field. Although excitons localized in the quantum well are electrically neutral, their components (electrons and holes) have opposite electric charges and therefore interact with the electric field. As a result, an applied electric field leads to distortion of the exciton wave function and to the change in the exciton energy and the exciton oscillator strength.[15–17] To determine the exciton energy, we use the model of Ref. 16 with a separable exciton trial wave function of the form

$$\Psi(\vec{r}_e,\vec{r}_h,z_e,z_h) = \Psi_{\parallel}(\vec{r}_e,\vec{r}_h)\Psi_e(z_e)\Psi_h(z_h), \tag{1}$$

where the unperturbed exciton in-plane wave function is

$$\Psi_{\parallel}(\vec{r}_e,\vec{r}_h) = \sqrt{\frac{2}{\pi a_B^2}}\exp\left\{-\frac{|\vec{r}_e-\vec{r}_h|}{a_B}\right\}, \tag{2}$$

in which a_B is the two-dimensional exciton Bohr radius and $\vec{r}_{e,h}$ are the in-plane components of the electron and hole spatial coordinates. The wave functions Ψ_e and Ψ_h describe the electron and hole wave function behaviors in the direction normal to the quantum well plane (the spatial coordinates are denoted as z_e and z_h for electrons and holes, respectively). The appropriate Hamiltonian for the problem is

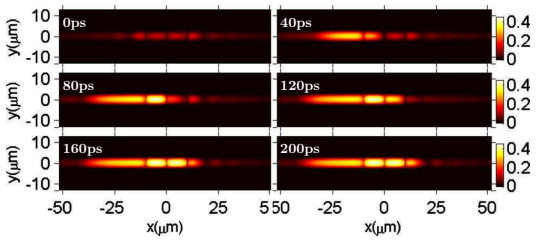

FIG. 2. (Color online) Response of the polariton intensity in the microcavity plane when the potential in the first segment is altered such that the pump-polariton detuning is changed from $\Delta_0 = 0.5$ meV to $\Delta_1 = 0.4$ meV. Initially the intensity in the first segment increases. Polaritons then propagate into the second region where there is a switching to the higher intensity state allowed by bistability. The polariton signal continues to a distance limited by the extent of the optical pump (which has a 40 μm half-width at half-maximum in the x direction in the calculation).

$$\mathcal{H} = \frac{p_e^2}{2m_e(z_e)} + \frac{p_h^2}{2m_h(z_h)} + V_e(z_e) + V_h(z_h) - eFz_e + eFz_h - \frac{e^2}{\epsilon(|z_e - z_h|^2 + |\vec{r}_e - \vec{r}_h|^2)}, \quad (3)$$

where the particle momenta are denoted by operators $p_{e,h}$, their masses (depending on the particle position either in the well or in the barrier) are $m_{e,h}$, and the quantum well confining potentials are $V_{e,h}$. The electron charge is e, the intensity of the applied external electric field perpendicular to the quantum well plane is F, and the dielectric constant of the structure is ϵ. Using the trial wave function of Eq. (2) and Hamiltonian [Eq. (3)], we solved the static Schrödinger equation iteratively, obtaining the electron and hole wave functions from which the exciton energy $E_{\rm ex}$ and relative oscillator strength $f_{\rm rel}$ are calculated according to the following equations:

$$E_{\rm ex} = \langle \Psi | \mathcal{H} | \Psi \rangle, \quad (4)$$

$$f_{\rm rel} = \frac{\int \Psi_e(z)\Psi_h(z)dz}{\int \Psi_e(z)^{F=0}\Psi_h(z)^{F=0}dz}. \quad (5)$$

Here, the wave functions unperturbed by an external electric field are denoted by the subscript "$F=0$."

Device modeling. Returning to the device proposed in Fig. 1, Fig. 2 shows the results of modeling the triggering of a propagating signal, following a change in the electric potential applied to the first segment. The spatial effects present in the system have been fully accounted for by using the Gross-Pitaevskii equation[18,19] for the polariton field $\psi(\vec{r},t)$,

$$i\hbar\frac{\partial\psi(\vec{r},t)}{\partial t} = \left(\hat{E}_{LP} - \frac{i\hbar}{2\tau} + W(\vec{r},t)\right)\psi(\vec{r},t) + \alpha|\psi(\vec{r},t)|^2\psi(\vec{r},t) + f(\vec{r},t). \quad (6)$$

Here, we neglect the polarization degree of freedom, assuming that the optical excitation $f(\vec{r},t)$ is circularly polarized. The energy of the pump can be accounted for by the inclusion of an oscillatory factor $e^{-i\omega t}$ in the time dependence. $\hat{E}_{LP}$ is the kinetic-energy operator, which should account for the nonparabolic dispersion of polaritons. The eigenvalues of $\hat{E}_{LP}$ can be written in reciprocal space as

$$E_{LP}(\vec{k}) = \frac{E_C(\vec{k}) + E_X(\vec{k})}{2} - \frac{1}{2}\sqrt{[E_C(\vec{k}) - E_X(\vec{k})]^2 + \Omega^2}, \quad (7)$$

where Ω is the Rabi splitting and E_C and E_X are the bare cavity photon and exciton energies, respectively, for which we take parabolic dispersion relations characterized by effective masses m_C and m_X. Returning to Eq. (6), τ represents the polariton lifetime and α represents the strength of polariton-polariton interactions. $W(\vec{r},t)$ is the potential experienced by polaritons, which is spatially dependent due to the metallic structure built into the microcavity design, and is time dependent because of the changes in potential applied to the metallic segments.

Equation (6) can be solved numerically with the initial condition $\psi(\vec{r},t=0)=0$. In our calculations we used the following parameters, typical for state-of-the-art GaAs-based microcavities:[7] $\Omega = 10$ meV, $m_C = 3\times10^{-5}m$ (m is the free-electron mass), $m_X = 0.22m$, $\tau = 3$ ps, $\Delta_0 = 0.5$ meV, $\Delta_1 = 0.4$ meV, and $\Delta_2 = 0.8$ meV. It was assumed that the metal strip causes a 5 meV redshift of the TPEPM beneath it with respect to the lowest-energy exciton-polariton mode elsewhere.

In Fig. 2 it is apparent that the signal propagates across all four segments. The signal propagation observed in Fig. 2 is dependent on maintaining the potential bias in the second, third, and fourth segments so that the detuning remains as Δ_0. If we were to switch the potential in the third segment so that the local detuning had the substantially larger value of Δ_2, corresponding to the (blue) dotted curve in Fig. 1(b), the signal would not be able to propagate between the second and fourth segments. The results of modeling this case are shown in Fig. 3 and demonstrate that the device can behave as an electro-optic transistor in which the optical signal is electrically controlled. The whole device can be reset by temporarily applying a potential corresponding to a detuning of Δ_2 to all segments.

Other functionalities are also straightforward to produce using polariton neurons. Signals can be duplicated by splitting channels or combined in OR logic gates simply by combining channels.[8] Polariton neurons are also able to link multiple elements in a circuit together, a facility not afforded by many other optical logic element concepts. Without requiring external optics (other than a single broad excitation field) a polariton neuron-based optical circuit fits comfortably into a single compact microcavity. Typically each element in the optical circuit functions on a time scale of 100–200 ps cor-

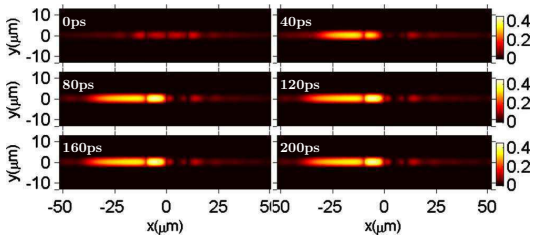

FIG. 3. (Color online) The same situation as in Fig. 2 but a potential is also applied to the third segment, such that the pump-polariton detuning there is Δ_2=0.8 meV, and blocks the signal propagation along the polariton neuron.

responding to a repetition rate of 5–10 GHz. The power requirements are also favorable; the high strength of exciton-exciton interactions makes it possible to achieve the nonlinear regime needed for bistability with relatively low optical power. For example, a power of 2.8 mW has been used to achieve bistability in GaAs-based microcavities.[13] Future samples, perhaps based on GaN, are expected to operate at even lower powers, partly due to the increased exciton-exciton interaction strength and partly due to higher cavity Q factors.

We have shown how the electrical sensitivity of optical bistability in semiconductor microcavities could be used to construct a new generation of electro-optical devices with compact size and low power consumption. Although we have focused on fully integrated electro-optical logic circuits, it is also possible to imagine using the electrical control of polariton intensity as the basis of bistable memory devices, which could switch on time scales on the order of the polariton lifetime (~3 ps) and have long memory lifetimes, at least as long as the laser coherence time. In another application, a suitably patterned metallic structure could provide the spatial control to produce an array of bistable elements acting as a spatial light modulator. It is also worth noting that spatial phase coherence can be naturally attained from the spatial coherence of the laser, suggesting that microcavities could also find application in phase array optics.

An important new functionality of polariton integrated circuits may be achieved by taking advantage of the polarization degree of freedom of exciton-polaritons.[20] The polarization multistability (i.e., coexistence of right-circularly, left-circularly, and linearly polarized stable states[12]) makes possible the realization of schemes with encoding above binary logic. A theoretical proposal for all-optical polariton polarization switches[8] has been recently demonstrated experimentally.[14]

In conclusion, until recently, semiconductor microcavities have been considered almost exclusively for applications in solid-state optical sources.[6,21] However, now it is apparent that they are extremely promising as the basis of devices with applications in ultrafast information processing. Indeed, it is clear that we have only just begun to appreciate the potential of cavity plasmon–exciton-polariton systems.

T.L. was supported by NCCR-QP; A.V.K., M.K., R.A.A. acknowledge support from the EU "POLALAS" project; I.A.S. acknowledges support from Rannis.

[1] A. V. Kavokin, J. J. Baumberg, G. Malpuech, and F. P. Laussy, *Microcavities* (Oxford University Press, Oxford, 2007).
[2] J. Kasprzak, M. Richard, S. Kundermann, A. Baas, P. Jeambrun, J. M. J. Keeling, F. M. Marchetti, M. H. Szymańska, R. André, J. L. Staehli, V. Savona, P. B. Littlewood, B. Deveaud, and Le Si Dang, Nature (London) **443**, 409 (2006).
[3] R. Balili, V. Hartwell, D. Snoke, L. Pfeiffer, and K. West, Science **316**, 1007 (2007).
[4] C. W. Lai, N. Y. Kim, S. Utsunomiya, G. Roumpos, H. Deng, M. D. Fraser, T. Byrnes, P. Recher, N. Kumada, T. Fujisawa, and Y. Yamamoto, Nature (London) **450**, 529 (2007).
[5] A. Amo, J. Lefrère, S. Pigeon, C. Adrados, C. Ciuti, I. Carusotto, R. Houdré, E. Giacobino, and A. Bramati, Nat. Phys. **5**, 805 (2009).
[6] S. I. Tsintzos, N. T. Pelekanos, G. Konstantinidis, Z. Hatzopoulos, and P. G. Savvidis, Nature (London) **453**, 372 (2008).
[7] D. Bajoni, E. Semenova, A. Lemaître, S. Bouchoule, E. Wertz, P. Senellart, S. Barbay, R. Kuszelewicz, and J. Bloch, Phys. Rev. Lett. **101**, 266402 (2008).
[8] T. C. H. Liew, A. V. Kavokin, and I. A. Shelykh, Phys. Rev. Lett. **101**, 016402 (2008).
[9] C. Symonds, A. Lemaître, E. Homeyer, J. C. Plenet, and J. Bellessa, Appl. Phys. Lett. **95**, 151114 (2009).
[10] M. E. Sasin, R. P. Seisyan, M. A. Kalitteevski, S. Brand, R. A. Abram, J. M. Chamberlain, A. Yu. Egorov, A. P. Vasil'ev, V. S. Mikhrin, and A. V. Kavokin, Appl. Phys. Lett. **92**, 251112 (2008).
[11] M. Kaliteevski, S. Brand, R. A. Abram, I. Iorsh, A. V. Kavokin, and I. A. Shelykh, Appl. Phys. Lett. **95**, 251108 (2009).
[12] N. A. Gippius, I. A. Shelykh, D. D. Solnyshkov, S. S. Gavrilov, Yuri G. Rubo, A. V. Kavokin, S. G. Tikhodeev, and G. Malpuech, Phys. Rev. Lett. **98**, 236401 (2007).
[13] A. Baas, J. Ph. Karr, H. Eleuch, and E. Giacobino, Phys. Rev. A **69**, 023809 (2004).
[14] A. Amo, T. C. H. Liew, C. Adrados, R. Houdré, E. Giacobino, A. V. Kavokin, and A. Bramati, Nature Photon. **4**, 361 (2010).
[15] G. Bastard, E. E. Mendez, L. L. Chang, and L. Esaki, Phys. Rev. B **28**, 3241 (1983).
[16] D. A. B. Miller, D. S. Chemla, T. C. Damen, A. C. Gossard, W. Wiegmann, T. H. Wood, and C. A. Burrus, Phys. Rev. B **32**, 1043 (1985).
[17] H.-J. Polland, L. Schultheis, J. Kuhl, E. O. Göbel, and C. W. Tu, Phys. Rev. Lett. **55**, 2610 (1985).
[18] I. Carusotto and C. Ciuti, Phys. Rev. Lett. **93**, 166401 (2004).
[19] M. Wouters, I. Carusotto, and C. Ciuti, Phys. Rev. B **77**, 115340 (2008).
[20] I. A. Shelykh, A. V. Kavokin, Yu. G. Rubo, T. C. H. Liew, and G. Malpuech, Semicond. Sci. Technol. **25**, 013001 (2010).
[21] S. Christopoulos, G. Baldassarri Höger von Högersthal, A. J. D. Grundy, P. G. Lagoudakis, A. V. Kavokin, J. J. Baumberg, G. Christmann, R. Butté, E. Feltin, J.-F. Carlin, and N. Grandjean, Phys. Rev. Lett. **98**, 126405 (2007).

APPLIED PHYSICS LETTERS **97**, 111110 (2010)

Longitudinal optical phonon assisted polariton laser

M. Maragkou,[1] A. J. D. Grundy,[1] T. Ostatnický,[1,2] and P. G. Lagoudakis[1,a)]
[1]*School of Physics and Astronomy, University of Southampton, Southampton SO17 1BJ, United Kingdom*
[2]*Faculty of Mathematics and Physics, Charles University in Prague, Ke Karlovu 3, 121 16 Praha 2, Czech Republic*

(Received 7 June 2010; accepted 18 August 2010; published online 16 September 2010)

We demonstrate the role of longitudinal optical (LO)-phonon assisted polariton relaxation in reducing the stimulation threshold in strongly coupled microcavities. When the energy of the relaxation bottleneck is one LO-phonon above the ground polariton state, we observe a tenfold improvement of the polariton relaxation rate in the linear regime, and a twofold reduction in the threshold to the nonlinear polariton lasing regime. © *2010 American Institute of Physics*. [doi:10.1063/1.3488012]

Microcavity polaritons are quasibosons that result from the strong-coupling of cavity photons and excitons confined in a single nanostructure.[1] Their bosonic nature gives rise to a plethora of nonlinear phenomena[2,3] epitomized by the quantum phase transition to nonequilibrium Bose–Einstein condensation.[4–6] The lifetime of polariton condensates is limited to the cavity-photon lifetime leading to the radiation of directional, coherent light, termed polariton laser.[7] Unlike conventional lasers, polariton lasers do not require population inversion and have the potential to operate with reduced thresholds. To date, polariton lasers have only been realized under optical excitation in microcavities with GaAs,[8] CdTe,[9] and GaN (Ref. 10) active material. Although electrical pumping in polariton light emitting diodes was achieved both in inorganic and organic microcavities,[11–13] polariton lasing remains elusive under electrical carrier injection. As with nonresonant optical excitation schemes, so with electrical injection relaxation bottleneck leads to substantial homogeneous broadening and loss of strong coupling in the linear regime.

In this paper we demonstrate the role of LO-phonon assisted polariton relaxation in reducing the stimulation threshold in strongly coupled microcavities. The concept of utilizing LO-phonon emission to accelerate polariton relaxation was introduced by Imamoglu and co-workers[7] and experimental evidence of the process was shown in the linear regime by Pau *et al.*[14] Here we tune the energy of the relaxation bottleneck one LO-phonon above the ground polariton state and observe a tenfold improvement of the polariton relaxation rate in the linear regime, and a twofold reduction in the threshold for polariton lasing. The introduced configuration exemplifies the potential of LO-phonon emission in appropriately designed polariton diode lasers.

The sample under study is a $\lambda/2$ AlAs cavity consisting of two $Al_{0.2}Ga_{0.8}As/AlAs$ distributed Bragg reflectors with 16 (top) and 20 (bottom) pairs, respectively.[15] Three sets of four quantum wells are located at the center of the cavity and the first antinodes of the electromagnetic field to increase the Rabi splitting.[16] A wedge in the structure makes accessible a wide range of exciton-photon energy detuning. All experiments are performed at 10 K using a cold-finger cryostat. The sample is excited at the light-hole (LH) exciton energy (E_{LH}) with 180 fs p-polarized optical pulses focused to a 40 μm spot.

Following optical excitation free electron-hole pairs rapidly form exciton-polaritons in the middle (MP) and upper polariton branches, which are subject to further energy relaxation by polariton-phonon and pair polariton scattering. Energy relaxation by longitudinal acoustic (LA) phonon emission predominantly allows for carrier thermalization within the two upper polariton branches, while LO-phonon emission and pair polariton scattering leads to population of the lower polariton (LP) branch below the bottleneck region.[17] The steep dispersion of the middle and LP branches around $k=0$ inhibits LA-phonon emission and results to relaxation bottleneck along the middle branch about 1–3 meV below E_{LH} (Fig. 1). MP states are mostly LH-like at high wave vectors, and therefore, cannot effectively relax to the heavy

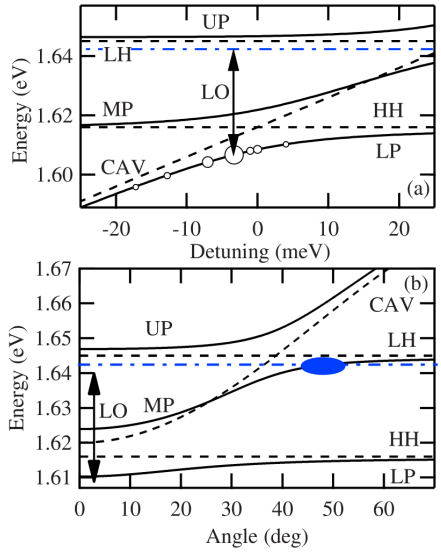

FIG. 1. (Color online) Energy dispersion of the cavity and exciton modes (dashed lines) and lower, middle, and upper polariton (solid lines) as a function of (a) detuning and (b) angle for a −4 meV detuning. The open markers in (a) correspond to experimental data and their size is proportional to the LO phonons scattering strength. The dotted-dashed line (a) and solid ellipse (b) indicate the energy of the middle polariton bottleneck.

a)Electronic mail: pavlos.lagoudakis@soton.ac.uk.

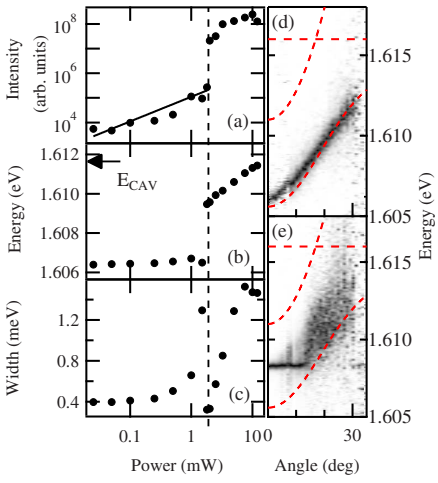

FIG. 2. (Color online) Power dependence of (a) the emission intensity, (b) the energy blueshift, and (c) the linewidth of the LP ground state as a function of the excitation power for −4 meV detuning. The below threshold power dependence data can be fitted with a straight line (a), whose slope can give information on the carrier relaxation efficiency. Strong coupling is confirmed by the below (d) and above (e) threshold snapshots of the dispersion relation.

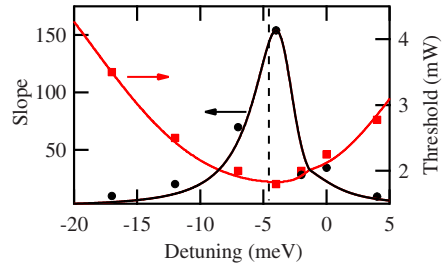

FIG. 3. (Color online) Experimental data (markers) and theoretical fits (lines) for the below threshold slope $S(D)$ (dots) and the stimulation threshold $T(D)$ (squares) for a range of detunings.

hole (HH)-like LP by LO-phonon emission (the relaxation rate is limited by the weak electron-hole exchange interaction). At the MP bottleneck region strong exciton-photon coupling mixes both LH and HH excitons rendering LO-phonon emission the strongest energy relaxation mechanism. The presence of the MP bottleneck provides a polariton reservoir from which LP states can be effectively populated by LO-phonon emission.

We excite resonantly to the E_{LH}, record photoluminescence from the ground state of the LP branch and tune the energy difference between the three polariton branches by scanning the excitation spot across the wedged cavity LP [Fig. 1(a)]. At each detuning the excitation intensity is scaled for the reflectivity of the stop-band to accurately control carrier excitation density. The detuning dependence of the ground polariton state is shown in Fig. 1(a). The open markers correspond to the LP emission energy in the linear regime. Their size is scaled with the LO phonon transition rate, discussed later. The MP bottleneck energy is indicated by the dot-dash line. The calculated angular dispersion for the optimum detuning (−4 meV) is shown in Fig. 1(b), where the MP relaxation bottleneck region is one LO-phonon energy, E_{LO}, above the LP ground state.

Time-integrated photoluminescence from the LP ground state is recorded with ±3° collection angle and is spectrally resolved using a 1200 grooves/mm grating in a 55 cm spectrometer coupled to a cooled charge coupled device. A nonlinear increase in the photoluminescence intensity by 10^2 at threshold is observed with increasing excitation density [Fig. 2(a)]. Polariton lasing occurs at threshold as the polaritons collapse to a single state. Self interaction results in a blueshift in the photoluminescence by ~3 meV [Fig. 2(b)] and an increase in coherence causes a collapse of the linewidth [Fig. 2(c)].[18] Under pulsed excitation the blueshift in the LP evolves with time. This information is lost in time-integrated measurements and the dominance of polariton lasing results in an artificially large jump in mode energy upon reaching threshold [Fig. 2(b)]. These observations are in accordance with previous reports on polariton lasing.[19] Figures 2(d) and 2(e) show snapshots of the LP dispersion in the linear regime and at threshold, respectively.

As discussed above, by changing the cavity-exciton detuning (D), the energy gap between the MP bottleneck and the LP ground state can be tuned through the E_{LO} resonance. This leads to a detuning dependence of the LO phonon transition rate $W(D)$, which is maximum at resonance. The transition rate $W(D)$ can be found from the slope S of the power dependence in the linear regime [left of the dashed line in Fig. 2(a)]. A greater slope indicates an increased transition rate: $S(D) \propto P_{LP}^2(D)W(D)$, where $P_{LP}(D)$ is the photon Hopfield coefficient of the $k=0$ LP ground state. Figure 3 shows experimental (black dots) data for the detuning dependence of $S(D)$. It can be seen that the slope is almost two orders of magnitude greater when the LO phonon resonance condition is met, at a detuning of −4 meV, compared to the off-resonance condition of +4 or −13 meV. The black line in Fig. 3 is a theoretical fit calculated using Fermi's golden rule for the relaxation rate $W(D)$, assuming that the MP bottleneck occurs 2 meV below the LH exciton and that the polariton line broadening is 1.3 meV [taken from Fig. 2(c)].

The stimulation threshold T is also dependent on $W(D)$. An increased transition rate means that the ground state is populated more efficiently, allowing the macroscopic population required for stimulation and lasing to occur at reduced pump powers. Experimental data for the detuning dependence of the threshold to polariton lasing is shown in Fig. 3 [(red) squares]. The stimulation threshold is assumed to have the form $T(D)=\alpha+\beta/W(D)$, where α and β are constants chosen to best fit the experimental data. It shows that the threshold is a minimum at the detuning where the LO phonon transition is on resonance (−4 meV), 50% lower than the off resonance case. The (red) line is a fit to the data based on the simple model and assumptions described earlier.

Further studies are performed with the pump laser tuned to be nonresonant. In this case we find similar trends to those under resonant excitation. The optimum detuning remains at −4 meV, where the lowest threshold and highest slope are achieved. Interestingly the threshold (scaled with the absorption coefficient) is similar for both excitation configurations, suggesting that LO phonons mediated relaxation mechanisms are present in both pumping schemes. However, the slope of the power dependence in the linear regime is about three times lower compared to resonant excitation. We sug-

gest that under nonresonant excitation, a smaller proportion of the injected carriers collect at the MP bottleneck and undergo LO phonon relaxation. In this case, it is likely that more carriers undergo LA phonon relaxation to the LP, which would not be desirable for electrical injection.

Using an LO phonon transition to reduce the polariton stimulation threshold may prove significant in the development of electrically pumped polariton lasers. Two parameters have been hindering the realization of such devices: the efficient population of ground polariton states and the persistence of strong coupling under high carrier injection conditions. We propose a design for an electrically injected polariton laser where carriers are injected at or above the E_{LO} resonance. LO-phonon mediated relaxation will dominate over LA-phonon, bypassing the bottleneck effects that have prevented the operation of electrically pumped polariton lasers to date. Key to the implementation of the above scheme is to design structures at the appropriate detuning so that the MP bottleneck is one E_{LO} above the ground polariton state. Carriers should be injected at, or above the MP branch energy, e.g. via resonant tunneling from a nearby QW, allowing the MP bottleneck to provide a reservoir from which LO-phonon scattering to the ground polariton state can occur. Whereas in a GaAs QW microcavity the MP branch offers a resonant state at one E_{LO} above the ground state, in InGaAs QW microcavities such state is only accessible at very negative detuning, rendering GaAs the material of choice for electrical injection in III-V microcavities. Finally our observation of a reduced lasing threshold both under resonant and nonresonant excitation suggests that the density of states of the MP branch is sufficiently large to act as a reservoir of carriers that efficiently feed the ground state during polariton lasing.

In conclusion, we have achieved a 50% reduction in the polariton stimulation threshold in a two-dimensional GaAs microcavity by using LO phonons to efficiently relax polaritons from the MP bottleneck to the LP ground state. We have studied the LO phonon transition rate using power dependences in the linear regime and found that relaxation is more efficient when carriers are injected resonantly with the LH compared to nonresonant injection. We suggest that this mechanism could be used to overcome the relaxation bottleneck which hinders electrically injected polariton lasers. Finally we propose a design that uses LO-phonon relaxation to bypass the relaxation bottleneck in an electrically injected polariton laser.

P.G.L. would like to acknowledge EPSRC grant EP/F026455/1 and FP7 grants ITN-Clermont 4 and ITN-Spinoptronics for funding. This work was also part of the research plan MSM0021620834 that is financed by the Ministry of Education of the Czech Republic. The authors thank Jacqueline Bloch and Aristide Lemaître for provision of the sample and Elena Kammann for useful discussions.

[1] C. Weisbuch, M. Nishioka, A. Ishikawa, and Y. Arakawa, Phys. Rev. Lett. **69**, 3314 (1992).
[2] P. G. Savvidis and P. G. Lagoudakis, Semicond. Sci. Technol. **18**, S311 (2003).
[3] P. G. Savvidis, J. J. Baumberg, R. M. Stevenson, M. S. Skolnick, D. M. Whittaker, and J. S. Roberts, Phys. Rev. Lett. **84**, 1547 (2000).
[4] D. Bajoni, P. Senellart, E. Wertz, I. Sagnes, A. Miard, A. Lemaître, and J. Bloch, Phys. Rev. Lett. **100**, 047401 (2008).
[5] J. Kasprzak, M. Richard, S. Kundermann, A. Baas, P. Jeambrun, J. M. J. Keeling, F. M. Marchetti, M. H. Szymańska, R. André, J. L. Staehli, V. Savona, P. B. Littlewood, B. Deveaud, and L. S. Dang, Nature (London) **443**, 409 (2006).
[6] J. J. Baumberg, A. V. Kavokin, S. Christopoulos, A. J. D. Grundy, R. Butté, G. Christmann, D. D. Solnyshkov, G. Malpuech, G. Baldassarri Höger von Högersthal, E. Feltin, J.-F. Carlin, and N. Grandjean, Phys. Rev. Lett. **101**, 136409 (2008).
[7] A. Imamoglu, R. J. Ram, S. Pau, and Y. Yamamoto, Phys. Rev. A **53**, 4250 (1996).
[8] C. W. Lai, N. Y. Kim, S. Utsunomiya, G. Roumpos, H. Deng, M. D. Fraser, T. Byrnes, P. Recher, N. Kumada, T. Fujisawa, and Y. Yamamoto, Nature (London) **450**, 529 (2007).
[9] M. Richard, J. Kasprzak, R. André, R. Romestain, L. S. Dang, G. Malpuech, and A. Kavokin, Phys. Rev. B **72**, 201301(R) (2005).
[10] S. Christopoulos, G. Baldassarri Höger von Högersthal, A. J. D. Grundy, P. G. Lagoudakis, A. V. Kavokin, J. J. Baumberg, G. Christmann, R. Butté, F. Feltin, J.-F. Carlin, and N. Grandjean, Phys. Rev. Lett. **98**, 126405 (2007).
[11] S. I. Tsintzos, N. T. Pelekanos, G. Konstantinidis, Z. Hatzopoulos, and P. G. Savvidis, Nature (London) **453**, 372 (2008).
[12] D. Bajoni, E. Semenova, A. Lemaître, S. Bouchoule, E. Wertz, P. Senellart, and J. Bloch, Phys. Rev. B **77**, 113303 (2008).
[13] A. A. Khalifa, A. P. D. Love, D. N. Krizhanovskii, M. S. Skolnick, and J. S. Roberts, Appl. Phys. Lett. **92**, 061107 (2008).
[14] S. Pau, G. Björk, H. Cao, F. Tassone, R. Huang, Y. Yamamoto, and R. P Stanley, Phys. Rev. B **55**, R1942 (1997).
[15] D. Bajoni, P. Senellart, A. Lemaître, and J. Bloch, Phys. Rev. B **76**, 201305(R) (2007).
[16] J. Bloch, T. Freixanet, J. Y. Marzin, V. Thierry-Mieg, and R. Planel, Appl. Phys. Lett. **73**, 1694 (1998).
[17] F. Tassone, C. Piermarocchi, V. Savona, A. Quattropani, and P. Schwendimann, Phys. Rev. B **56**, 7554 (1997).
[18] D. Porras and C. Tejedor, Phys. Rev. B **67**, 161310 (2003).
[19] L. S. Dang, D. Heger, R. André, F. Bœuf, and R. Romestain, Phys. Rev. Lett. **81**, 3920 (1998).

Observation of Half-Quantum Vortices in an Exciton-Polariton Condensate

K. G. Lagoudakis,[1]* T. Ostatnický,[2] A. V. Kavokin,[2,3] Y. G. Rubo,[4] R. André,[5] B. Deveaud-Plédran[1]

Singly quantized vortices have already been observed in many systems, including the superfluid helium, Bose-Einstein condensates of dilute atomic gases, and condensates of exciton-polaritons in the solid state. Two-dimensional superfluids carrying spin are expected to demonstrate a different type of elementary excitations referred to as half-quantum vortices, characterized by a π rotation of the phase and a π rotation of the polarization vector when circumventing the vortex core. We detect half-quantum vortices in an exciton-polariton condensate by means of polarization-resolved interferometry, real-space spectroscopy, and phase imaging. Half-quantum vortices coexist with single-quantum vortices in our sample.

Quantized vorticity is a property of quantum fluids that has been widely studied in various types of superfluids, either with or without spin (*1*–*4*). Superfluids with a two-component (spinor) order parameter are characterized by a different type of vortices than those found in conventional scalar superfluids (*5*–*8*). This new type of vortices is the so-called half-quantum vortices (HQV). They have lower energy with respect to full vortices and constitute the elementary excitations of spinor superfluids. When circumventing their core, the phase and the polarization vector experience a $\pm\pi$ rotation. In this sense, HQV can be understood as a half-phase vortex combined with a half-polarization vortex (*5*). In ^{4}He superfluids, the HQV cannot be formed because the spin degree of freedom is absent. However, in ^{3}He (*5*, *6*) or in triplet superconductors (*7*, *8*), the order parameter has two or more components, so the formation of HQV is possible. So far, experiments have not presented unambiguous evidence for HQV in ^{3}He (*9*), although more reliable indications of the existence of HQV have been reported in cuprate superconductors (*10*, *11*). Recently, HQV have been proposed as a smoking gun for the superfluid of exciton-polaritons in semiconductor microcavities (*12*). We report on a direct observation of HQVs in a high-temperature quantum fluid: microcavity exciton-polaritons. Exciton-polaritons are composite bosons carrying spin. They can occur in semiconductor microcavities in the strong coupling regime and are partly excitons and partly photons. The energy, wave vector, polarization, and statistics of cavity polaritons are directly transferred to light emitted by the microcavity due to photon tunneling through the mirrors of the cavity (*13*). Because of their photonic component, the cavity polaritons have an extremely low effective mass on the order of 10^{-4} of the free electron mass. This allows for their Bose-Einstein condensation (BEC) at temperatures achievable by cryogenic means. BEC of exciton-polaritons has been demonstrated in various types of microcavities composed either of II-VI (*14*) or III-V compounds (*15*). The most prominent effects found in these systems are the bosonic stimulation, the appearance of long-range spatial coherence, and the buildup of the vector polarization (*13*). Several indications of the polariton superfluidity have been reported, including the Bogoliubov-like dispersion (*16*), the appearance of phase vortices (*4*), and diffusionless motion of coherent polariton fluids in the presence of obstacles (*17*). In this work, HQVs are reported in a II-VI microcavity where BEC of the exciton-polaritons and formation of the integer phase vortices have been reported recently (*4*, *14*). Coexistence of HQV and integer vortices in the same sample is possible because of the spatially inhomogeneous

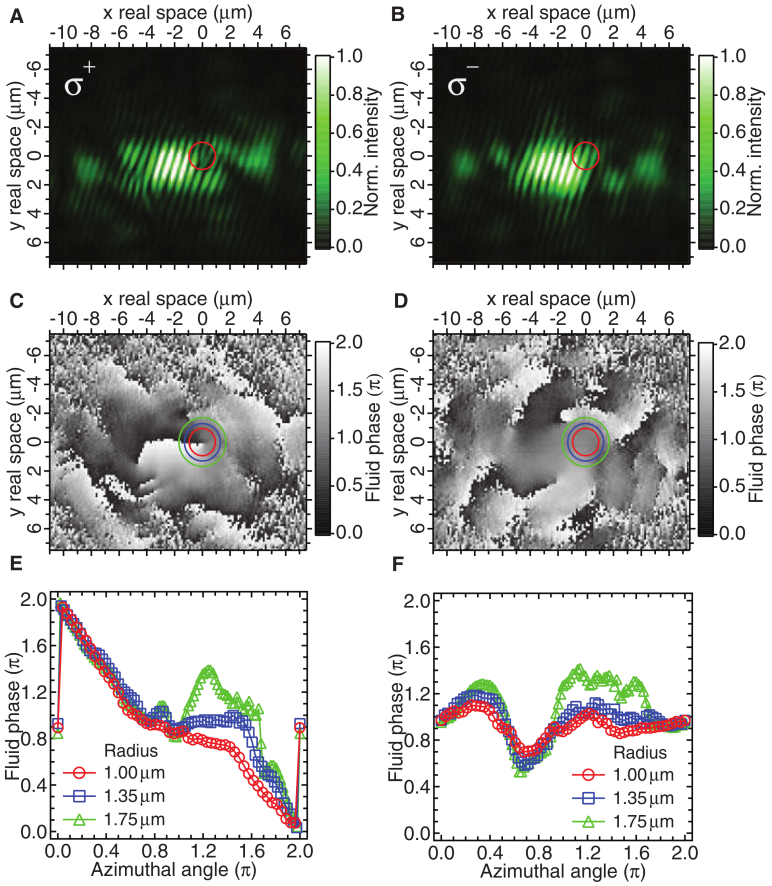

Fig. 1. (**A** and **B**) Reconstructed interferograms for σ^+ and σ^- polarizations at the energy of the condensate. (**C** and **D**) Real space phase map extracted from the interferograms (A) and (B) for polarizations σ^+ and σ^-, respectively. The three circles with different colors denote the real space paths over which we have plotted the phase as a function of the azimuthal angle in panels (**E** and **F**). The phase profiles in σ^+ polarization (E) show that the phase changes by -2π when circumventing the vortex core, which is the signature of the singularity. In contrast, for the σ^- polarization (F), we see a quasi-flat phase profile with zero overall phase shift as one goes around the core. The farther we probe the phase away from the vortex core, the more the phase diverges from the linear behavior versus angle.

[1]Institut de Photique et d'Electronique Quantique (IPEQ), École Polytechnique Fédérale de Lausanne (EPFL), 1015 Lausanne, Switzerland. [2]School of Physics and Astronomy, University of Southampton, Highfield, Southampton SO17 1BJ, UK. [3]Marie-Curie Chair of Excellence, University of Rome II, Via della Ricerca Scientifica 1, 00133 Rome, Italy. [4]Centro de Investigación en Energía, Universidad Nacional Autónoma de México, Temixco, 62580 Morelos, Mexico. [5]Institut Néel, Centre National de la Recherche Scientifique (CNRS), 38042 Grenoble, France.

*To whom correspondence should be addressed. E-mail: konstantinos.lagoudakis@epfl.ch

polarization splitting in microcavities, which is responsible for the suppression of HQV in certain areas of the sample. Thus, in different parts of the sample the polariton fluid has a different topology.

To fully characterize a vortex in a polariton condensate, one needs two winding numbers, (k,m), one for the polarization angle and one for the phase. One can express the order parameter of the condensate in the linear xy basis as

$$\psi_{lin}(\mathbf{r}) = \sqrt{n}e^{i\theta(r)}\begin{pmatrix}\cos\eta(\mathbf{r})\\ \sin\eta(\mathbf{r})\end{pmatrix} \quad (1)$$

where $\theta(\mathbf{r})$ is the phase of the coherent polariton fluid and $\eta(\mathbf{r})$ is the polar angle that characterizes the orientation of the electric field of polaritons, i.e., the polarization angle. Vortices are described in this notation by rotation of the phase and the polarization as $\eta(\mathbf{r}) \rightarrow \eta(\mathbf{r}) + 2\pi k$ and $\theta(r) \rightarrow \theta(r) + 2\pi m$ where k,m can take integer or half-integer values with $(k+m) \in \mathbb{Z}$. Four types of half vortices are described by winding numbers $(k,m) = \left(\pm\frac{1}{2},\pm\frac{1}{2}\right)$. To reveal the specific phenomenology of HQVs with respect to the integer vortices, it is convenient to analyze the circularly polarized components of the order parameter, which can be expressed as

$$\psi_{lin}(\mathbf{r}) = \frac{\sqrt{n}}{2}\left[e^{i(\theta(\mathbf{r})-\eta(\mathbf{r}))}\begin{pmatrix}1\\ i\end{pmatrix} + e^{i(\theta(\mathbf{r})+\eta(\mathbf{r}))}\begin{pmatrix}1\\ -i\end{pmatrix}\right] \quad (2)$$

One can see that for $\eta(\mathbf{r}) \rightarrow \eta(\mathbf{r}) + \pi$ and $\theta(\mathbf{r}) \rightarrow \theta(\mathbf{r}) + \pi$ a zero rotation takes place for one circular polarization and a full 2π rotation is achieved for the other circular polarization. This means that if one were to detect a half vortex, it would be easiest when looking in σ^+ and σ^- polarizations simultaneously. Then HQV would be observed as a full vortex in one polarization and no vortex in the other one. A signature for the phase vortex is a forklike dislocation in the interference pattern (*4*, *18*). In the case of full phase vortices, the forklike dislocations are expected to be seen in the same place in both circular polarizations, whereas in the case of HQV the fork appears only in one of the circular polarizations. In the circular basis, one can write the order parameter of HQV in cylindrical coordinates as

$$\psi_{k,m}(\rho,\phi) = \sqrt{\frac{n}{2}}e^{im\phi}\begin{Bmatrix}[f(\rho) + \mathrm{sgn}(km)\ g(\rho)]\cdot e^{-ik\phi}\\ [f(\rho) - \mathrm{sgn}(km)\ g(\rho)]\cdot e^{ik\phi}\end{Bmatrix} \quad (3)$$

with $\rho = \frac{r}{a}$ being the relative distance from the vortex core in vortex radii and ϕ being the angular coordinate. The form of the two radial density functions f and g is known (*12*) and will give zero density for one circular polarization $(f-g)$ and a finite density for the other polarization $(f+g)$, as it is expected for the simplistic image of a full vortex in one circular polarization and no singularities for the other circular polarization.

An important feature of polariton condensates is the presence of polarization splitting induced by the structural anisotropy and stationary disorder. This splitting pins the polarization vector of the condensate to a given crystal axis. It is theoretically predicted that HQVs still exist in this case but the spatial distribution of the polariton vector field is modified. Similarly to the vortices in multicomponent quantum Hall systems (*19*), the polariton half vortices acquire "strings" [or solitons; figure 16.1 in (*6*)], whereby the polarization angle rotates by π (*20*). The width of the string is given by $\hbar/\sqrt{2m^*\varepsilon}$, where m^* is the effective mass of polaritons and ε is the energy of the polarization splitting. HQVs remain the lowest-energy topological defects if this width is greater than or comparable to the excitation spot radius. However, when this length becomes comparable to the vortex core size ($a \approx \hbar/\sqrt{2m^*\mu}$, where μ is the chemical potential), the excitation of HQVs would require too much energy, and the integer phase vortices $(0, \pm1)$ become elementary topological excitations. For a realistic vortex core size on the order of ~2 μm and the polariton mass $m^* \approx 10^{-4}\, m_e$, pairs of HQVs will be replaced by integer phase vortices for polarization splittings $\varepsilon \geq 100$ μeV. [Two close pairs of HQVs are shown in (*21*), figs. S2 and S3].

The situation in real microcavity samples is additionally complicated by the fact that the polarization splitting ε fluctuates as a function of the coordinate in the plane of the cavity. This is why the HQV and integer phase vortices may coexist within the same condensate. The underlying mechanisms for the polarization splitting are thought to be the different penetration depths in the distributed Bragg reflectors (microcavity mirrors) for transverse electric and transverse magnetic polarizations (*22*) and the intrinsic anisotropy of the microcavity (*23*, *24*). The anisotropy is expected to be the product of a number of parameters, including the alloy concentrations, the wedge, quantum well width fluctuations, and the built-in strain. Splittings vary from zero to several tenths of μeVs. All HQVs that we observed in this sample were at regions where the splitting was less than our experimental resolution (≈ 20 μeV).

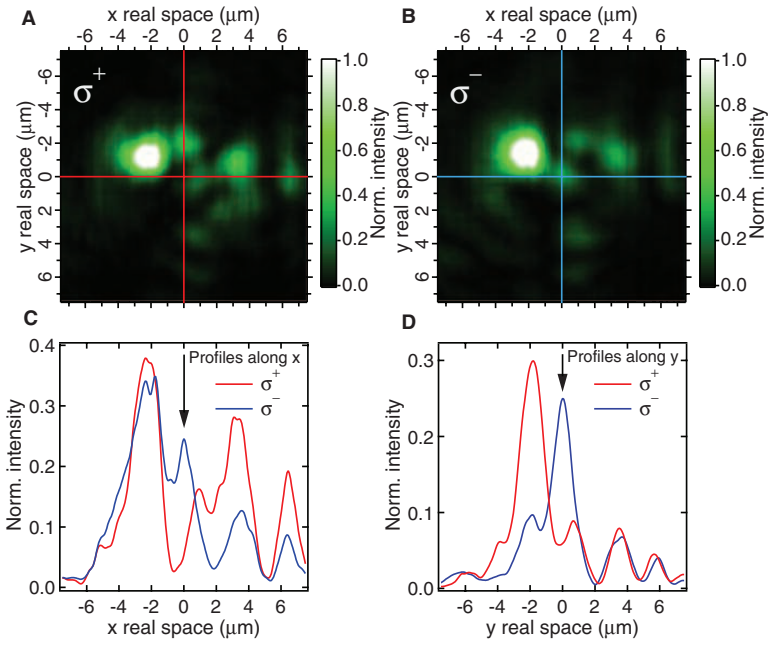

Fig. 2. (**A** and **B**) Polariton densities in real space at the frequency of the condensate for σ^+ and σ^- polarizations, respectively. It is easily seen that at the position of the vortex core (0,0), which is indicated by the red cross for σ^+ polarization and the blue cross for the σ^- polarization, there is a local minimum for σ^+ polariton density and a local maximum for the σ^- density. (**C**) Density profiles along the x direction for the two polarizations and (**D**) the corresponding density profiles along the y direction. Experimentally measured polariton density behaves in excellent agreement with the theoretical prediction [Eq. 3 and (*21*)]. This behavior is also evident from the fact that half vortices must be fully circularly polarized at the centers of their cores.

The sample we studied is the same CdTe/CdMgTe microcavity that was used in our previous experiments cooled down to ~10 K by a liquid helium flow cryostat (*4*). We used continuous-wave monomode nonresonant optical excitation. Detection was performed by means of the modified Michelson interferometer in the mirror-retroflector configuration with active stabilization (*4*) completed by a lambda quarter and a Wollaston prism. This allowed for polarization-resolved interferometry in σ^+ and σ^- polarizations simultaneously, which facilitated the identification of half vortices (*21*). All spectral studies were performed using a monochromator with $\approx$ 20 μeV resolution. The output of the interferometer could be sent to the entrance slits of the spectrometer through a polarizer, allowing for spectrally and polarization-resolved interferometry images to be acquired. The HQV were observed only at the excitation powers exceeding the condensation threshold. Once a good candidate was found, we performed a number of preliminary "test experiments" to verify unambiguously the persistence of the vortex for all possible detection configurations. The two most reliable tests were to change the overlap conditions at the output of the interferometer by shifting the mirror arm image with respect to one reflected from the retroreflector and to rotate by π the orientation of the fringes, making sure that for all orientations the singularity of the vortex is always clearly observable (*4*). We took care to verify the mutual coherence of the two cross-circular polarization components by means of polarization mixing interferometry in order to eliminate the possibility of having two independent condensates in the two polarizations. In all cases, we observed excellent mutual coherence properties with good contrast in the interference fringes between the two circular polarization components (*21*). The appearance of half vortices was quite rare; that is, one out of six regions with no polarization splitting was exhibiting a HQV.

Once the HQV was identified, the interferometric image was being sent on the entrance slits of the spectrometer. Then we performed an optical tomography experiment (*25*) for σ^+ and σ^- polarized images, which provided us with the full set of polarization-resolved interferograms in real space for all frequencies within the observable spectral window. Figure 1, A and B, shows the reconstructed interferogram coming from the frequency of the polariton condensate for the polarizations σ^+ and σ^-, on which we have added a red circle centered at the vortex core to help the reader locate the singularity. The singularity (forklike dislocation) is clearly visible for the σ^+ polarization, whereas on the same position in real space for the σ^- polarization we observe straight fringes. The interference patterns gave us access to the phase of the coherent polariton fluid. To extract the phase, we assumed that the reference field coming from a region of the condensate without a vortex has a flat phase profile. Figure 1, C and D, shows the phase of the polariton fluid in real space calculated from the interferograms. The phase has distinguishable characteristics only where there is enough signal intensity, whereas at the regions with no signal we get a noisy phase with no distinguishable features. The position of the HQV in the phase map is highlighted by circles. In σ^+ polarization, the phase rotates by 2π as one goes around the core. This behavior of the phase is clearly seen within an area of a few micrometers' size. In the same region for the σ^- polarization, there are no observable singularities and the phase is homogeneous. Figure 1, E and F, shows the phase as a function of the azimuthal angle as one goes around the core along the circles of different radii (shown by color). For the radius of 1μm, the phase changes monotonously in σ^+ polarization, decreasing by 2π as one makes a full round. Contrary to this, for the same radius in σ^- polarization, we observe a quasi-flat phase profile indicating the lack of any singularity. For larger radii, the phase dependence on the azimuthal angle becomes strongly nonlinear, whereas the total phase shift as one goes around the core remains –2π for one and 0 for the other polarization. Distortion of the phase profile at the large radii may be indicative of the existence of nearby regions with substantial vorticity but can also be indicative of formation of a string.

We note that the specific HQV shown in Fig. 1 is characterized by the winding numbers $(k,m) = \left(+\frac{1}{2},-\frac{1}{2}\right)$, while we have observed also the three remaining types of HQVs in different locations on the sample (*21*). On the basis of measurements we have done, we believe that four possible types of HQV are realized with approximately the same probability in our sample.

Using the same tomographic technique of spectrally resolved real space imaging as before, we then probed only the density of polaritons in the condensate state (Fig. 2, A and B). Locating the vortex in real space and looking at the density close to its core, we observed that a local minimum for one polarization coincides with a maximum for the other one, as Fig. 2, C and D shows. The widths of these minima/maxima coincide with the theoretical vortex core size *a*. This behavior is another signature of HQVs, as one can see from Eq. 3. The theory (*12*) predicted that at the center of the HQV the condensate should be fully circularly polarized, and this is exactly what we observe in Fig. 2, C and D).

The HQV we observed here are pinned by the disorder to specific locations on the sample. This is confirmed by the behavior of the interferometric images as a function of the pumping power. Increasing the excitation intensity, we modify the effective disorder potential acting upon the polariton condensate by changing the polariton-polariton repulsion strength. When the pumping is strong, we screen the disorder potential so that HQV get unpinned and disappear from the interferometry image of a specific spot on the sample. This is what we observed at the excitation power exceeding the threshold pumping by a factor of 4.5. Above this power, the forklike dislocation in σ^+ polarization disappears (*21*).

The stationary disorder fixes the winding numbers of the pinned vortices, so that repeating the experiment we find HQVs with the same winding numbers in the same locations. This is also true for the integer vortices. Handedness of each pinned vortex is dependent on the direction of polariton fluxes propagating in the disorder landscape during formation of the condensate, as the modeling based on the Gross-Pitaevskii equation showed (*4*, *26*).

This experimental work provides direct evidence of half-quantum vortices in a spinor condensate, by means of polarization-resolved interferometry, phase imaging, and spectrally resolved real space density imaging.

References and Notes

1. L. P. Pitaevskii, S. Stringari, *Bose-Einstein Condensation* (Clarendon Press, Oxford, 2003).
2. R. J. Donnelly, *Quantized Vortices in Helium II* (Cambridge Univ. Press, Cambridge, England, 1991).
3. M. R. Matthews *et al*., *Phys. Rev. Lett.* **83**, 2498 (1999).
4. K. G. Lagoudakis *et al*., *Nat. Physics* **4**, 706 (2008).
5. M. M. Salomaa, G. E. Volovik, *Rev. Mod. Phys.* **59**, 533 (1987).
6. G. E. Volovik, *The Universe in a Helium Droplet* (Clarendon Press, Oxford, 2003).
7. I. A. Luk'yanchuk, M. E. Zhitomirsky, *Supercond. Rev* **1**, 207 (1995).
8. M. Kato, Y. Niwa, K. Maki, *J. Phys. Conf. Ser.* **150**, 052103 (2009).
9. M. Yamashita *et al*., *Phys. Rev. Lett.* **101**, 025302 (2008).
10. J. R. Kirtley *et al*., *Phys. Rev. Lett.* **76**, 1336 (1996).
11. C. C. Tsuei, J. R. Kirtley, *Physica C* **367**, 1 (2002).
12. Y. G. Rubo, *Phys. Rev. Lett.* **99**, 106401 (2007).
13. A. V. Kavokin, J. J. Baumberg, G. Malpuech, F. P. Laussy, *Microcavities* (Oxford Univ. Press, Oxford 2007).
14. J. Kasprzak *et al*., *Nature* **443**, 409 (2006).
15. R. Balili *et al*., *Science* **316**, 1007 (2007).
16. S. Utsunomiya *et al*., *Nat. Physics* **4**, 700 (2008).
17. A. Amo *et al*., *Nature* **457**, 291 (2009).
18. M. R. Matthews *et al*., *Phys. Rev. Lett.* **83**, 2498 (1999).
19. S. M. Girvin, A. H. MacDonald, in *Perspectives in Quantum Hall Effects*, S. Das Sarma, A. Pinczuk, Eds. (Wiley, New York, 1997), chap. 5.
20. H. A. Fertig, *Phys. Rev. Lett.* **89**, 035703 (2002).
21. Materials and methods are available as supporting material on *Science* Online.
22. G. Panzarini *et al*., *Phys. Rev. B* **59**, 5082 (1999).
23. J. Kasprzak *et al*., *Phys. Rev. B* **75**, 045326 (2007).
24. Ł. Kłopotowski *et al*., *Sol. St. Com.* **139**, 511 (2006).
25. G. Nardin *et al*., *Appl. Phys. Lett.* **94**, 181103 (2009).
26. T. C. H. Liew, Y. G. Rubo, A. V. Kavokin, *Phys. Rev. Lett.* **101**, 187401 (2008).

27. We thank Le Si Dang for crucial remarks and detailed proofreading of this manuscript. We also thank T. C. H. Liew, M. Toledo Solano, M. Wouters, B. Pietka, Y. Leger, M. Richard, A. Baas, G. Nardin, D. N. Krizhanovskii, D. Sanvitto, P. G. Lagoudakis, and V. Savona for enlightening discussions. K.G.L. and B.D.-P. thank the Quantum Photonics–National Centre of Competence in Research for financial support through the Swiss National Science Foundation. A.V.K. and Y.G.R. thank the Engineering and Physical Sciences Research Council and the Dirección General de Asuntos del Personal Académico de la Universidad Nacional Autónoma de México for support.

Supporting Online Material

www.sciencemag.org/cgi/content/full/326/5955/974/DC1
Materials and Methods
Figs. S1 to S9
References

19 June 2009; accepted 8 September 2009
10.1126/science.1177980

[P18] supplement

Supplementary on-line material for

Observation of Half Quantum Vortices in an Exciton-Polariton Condensate

K. G. Lagoudakis[1], T. Ostatnický[2], A.V. Kavokin[2,3], Y. G. Rubo[4], R. André[5], B. Deveaud-Plédran[1]

[1]*IPEQ, École Polytechnique Fédérale de Lausanne (EPFL),1015 Lausanne, Switzerland.*

[2]*School of Physics and Astronomy, University of Southampton, Highfield, Southampton SO17 1BJ, United Kingdom.*

[3]*Marie-Curie Chair of Excellence, University of Rome II, 1, via della Ricerca Scientifica, Rome, 00133, Italy.*

[4]*Centro de Investigación en Energía, Universidad Nacional Autónoma de México, Temixco, Morelos, 62580, Mexico.*

[5]*Institut Néel, CNRS, Grenoble, France.*

Experimental setup

The sample was excited in a quasi-CW non-resonant way with the wavelength of the laser being tuned to the first minimum of the reflectivity spectrum below the stopband to avoid heating. We used an electronically locked, single longitudinal mode Ti:Sapphire laser which excited the sample with an excitation spot of quasi top hat intensity profile and about 10μm diameter. The linewidth of the condensate emission we observed here was of the order of 30 μeV, close to the spectral resolution of our spectrometer and narrower than the average polarization splitting (*S1*). In addition, using a monomode laser, we observed an enhanced mode-synchronization effect (*S2*) which allowed formation of a single condensate in the regions of the sample characterized by low disorder. The collection of the luminescence was done by a high numerical aperture microscope objective (N.A=0.5) allowing collection of light within a cone of ±30º and providing a submicron real space resolution. All spectral studies were performed using a

double 1m long monochromator with ~20μeV resolution. The setup is depicted in Fig. S1. We have added a λ/4 before the interferometer at 45° with respect to the polarization analyzer which in this case was a Wollaston prism with 20° polarization splitting angle, to allow for simultaneous polarization resolved interferometry in σ^+ and σ^- polarizations. The polarization resolved interferograms were sent simultaneously on two different regions of the same CCD camera and thus the images of the two polarizations were recorded at once. The four different kinds of HQVs are shown in Figs. S2 and S3. On the upper panels one has the raw data and on the lower panels we provide only the fringes, having removed numerically the CW part of the interferograms. In Fig. S2 (A,B) one can see a close pair of $(k,m)=\left(-\frac{1}{2},+\frac{1}{2}\right)$ and $(k,m)=\left(+\frac{1}{2},+\frac{1}{2}\right)$ HQVs being in the red circle and blue box respectively. In Fig. S3 (A,B) there is another pair of $(k,m)=\left(-\frac{1}{2},-\frac{1}{2}\right)$ and $(k,m)=\left(+\frac{1}{2},-\frac{1}{2}\right)$ HQVs in the orange circle and pink box, respectively.

For the spectrally resolved studies, we have replaced the CCD of Fig. S1 with the double monochromator and the Wollaston prism has been replaced with a normal polarizer. The optical tomography is then performed by shifting the lens L and acquiring one spectrally resolved image for each lens displacement. For the figures shown in the paper, we acquired ~100 slices.

Mutual coherence of the two circular polarization components

In order to rule out the possibility of having two independent condensates, one in one circular polarization carrying a full vortex and another one in the other polarization with no vortex, we have performed an additional interferometric experiment to probe the mutual coherence between the two polarizations. In this way we probe that the two polarization components are coming from the same two component spinor condensate. For this purpose we have built a modified polarization-mixing Mach-Zehnder

interferometer as depicted in Fig. S4. The two polarization components are sent through the two independent arms of the interferometer and in order to achieve interference at the output, one of the two components is rotated by means of a half wave plate in order to become co-polarized with the other component. The interference then reveals whether the two components are mutually coherent. In this experiment we provide two figures where a half vortex is imaged by two independent methods, the polarization resolved interferometry as in Fig. S5 (A), and the polarization mixing interferometry as in Fig. S5 (B). As seen in this figure, when making the two polarizations interfere, we clearly see an interference pattern which proves that the two polarizations are mutually coherent. The half vortex is easily distinguishable as a fork like dislocation at the top left corner and no forklike dislocation (straight interference fringes) at the symmetric position with respect to the autocorrelation point, the coordinates of which are extracted from Fig. S6.

Simulation of the interference patterns

All the observed interference patterns of HQVs are reproduced by the present theory for both experimental setups. We have considered a single vortex or a pair of vortices in a polariton fluid generated by a Gaussian laser beam with a half-width of 10μm. The winding numbers are denoted in the corresponding figure captions. We used Eq. (3) and the definitions of the radial functions *f* and *g* from (*S3*) in order to calculate the complex electric field amplitudes E_+ and E_- of a single vortex, emerging in each of the respective circularly polarized components. The resulting intensity of light in the experimental configuration of Fig. S1 is then expressed as:

$$I_{\pm}(x,y)=\left|E_{\pm}(x,y)\exp\left[-\mathrm{i}\left(K_x x+K_y y\right)\right]+E_{\pm}\left(x_0-x,y_0-y\right)\right|^2, \qquad \text{(S1)}$$

where we use the coordinate system relevant to the real image on the sample, (x_0, y_0) is the effective position of the inversion centre of the retro-reflector in terms of the sample coordinates and (K_x, K_y) is the wave vector which determines the inclination of the

beams from the respective interferometer arms. In order to simulate the interference pattern of a sample with two vortices, we approximated the electric field in plane of the sample by a weighted superposition of the fields of two spatially separated single HQVs:

$$E_{\pm} = \frac{\ell_2}{\ell_1 + \ell_2} E_{1\pm} + \frac{\ell_1}{\ell_1 + \ell_2} E_{2\pm}, \tag{S2}$$

where $E_{j\pm}$ is the particular circular component of the electric field emerging from the vortex $j = 1,2$ and the symbols $\ell_{1,2}$ in the weighting functions denote distances from the cores of the vortices 1 or 2, respectively. Weighting of the electric field components in Eq. (S2) ensures continuity of the overall electric field and its derivatives.

The calculated interference patterns produced by the interferometer in both Figs. S2 and S3 for the two circular polarizations are shown in Fig. S7 (A,B). The simulated interference fringes in the geometry shown in Fig. S5 (B) are plotted in Fig. S8 (A). One can see that the experimental images of Fig. S5 (B) are reproduced and the vortex is clearly identified. The calculated plot in Fig. S8 (B) shows the profile of the intensities of two circularly polarized components of the polariton field at the HQV core, which appears to be in excellent agreement with the experimental data as well.

Pumping power dependence

The observed half vortices show a strong dependence on the excitation intensity. Below the condensation threshold they do not exist and they usually appear when the condensation threshold is crossed. Then they tend to disappear at high power above threshold. The HQV shown in the main part of the paper gets unpinned when the excitation intensity crosses a value of roughly 4.5 times the condensation threshold ($P \approx 4.5 \cdot P_{th}$). In Fig. S9 (A,B) we show the interferograms for excitation powers 2.5 times above the condensation threshold ($P = 2.5 \cdot P_{th}$) and 5 times above the threshold ($P = 5.0 \cdot P_{th}$). The forklike dislocation in σ^+ polarization is clearly distinguishable for $P = 2.5 \cdot P_{th}$ (Fig.

S9 A), but it totally disappears at $P=5.0 \cdot P_{th}$ (Fig. S9 B), demonstrating unpinning of the half vortex due to the screening of the static disorder potential.

Vortex formation

It has been shown (*S4*) that the vortices are formed spontaneously above the condensation threshold as a result of the mutual action of the non-uniform pumping and decay of polaritons. In a disorder free sample one would expect formation of vortex-antivortex pairs in each of the circular polarizations. These pairs are nothing but the HQV bound pairs [(-1/2,+1/2),(+1/2,-1/2)] and [(-1/2,-1/2),(+1/2,+1/2)] (*S3*). Simulations performed using the spin-dependent Gross-Pitaevskii equations showed that vortices in the opposite circular polarizations are separated and pinned to specific locations due to the combined effect of the disorder and spin-dependent polariton-polariton interactions *(S5).* Propagation of the polariton fluxes at the early stage of formation of the condensate determines the winding numbers of the pinned vortices. Pinned vortices whose winding numbers do not vary in a large number of experimental realizations indicates that their formation dynamics is nearly identical in different experiments, and stochastic fluctuations of the order parameter are negligible for the determination of the steady state in the presence of vortices in our structure.

References

S1. D. N. Krizhanovskii *et al.*, *Phys. Rev. B* **80**, 045317 (2009).

S2. A. Baas *et al.*, *Phys. Rev. Lett.* **100**, 170401 (2008).

S3. Y. G. Rubo, *Phys. Rev. Lett.* **99**, 106401 (2007).

S4. J. Keeling, N. G. Berloff, *Phys. Rev. Lett.* **100**, 250401 (2008).

S5. T.C.H. Liew, Y.G. Rubo, and A.V. Kavokin, *Phys. Rev. Lett.,* **101**, 187401 (2008).

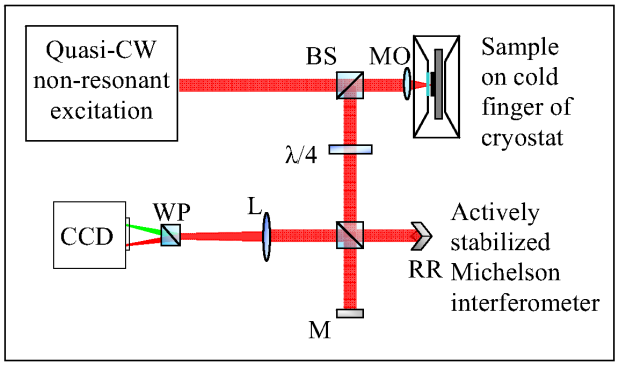

Fig. S1: Experimental setup of the polarization resolved interferometry. Two polarization components σ^+ and σ^- get separated by means of the Wollaston prism and they are sent on the two opposite sides of the same CCD. In this manner we are facilitating the simultaneous imaging of both circular polarization components. BS: beam splitter, M: mirror, MO: microscope objective, λ/4: quarter wave plate, RR: retroreflector, L: lens, WP: Wollaston prism, CCD: charge-coupled device. In this setup both circular polarizations are propagating through both arms of the interferometer and only get separated by the time they traverse the Wollaston prism.

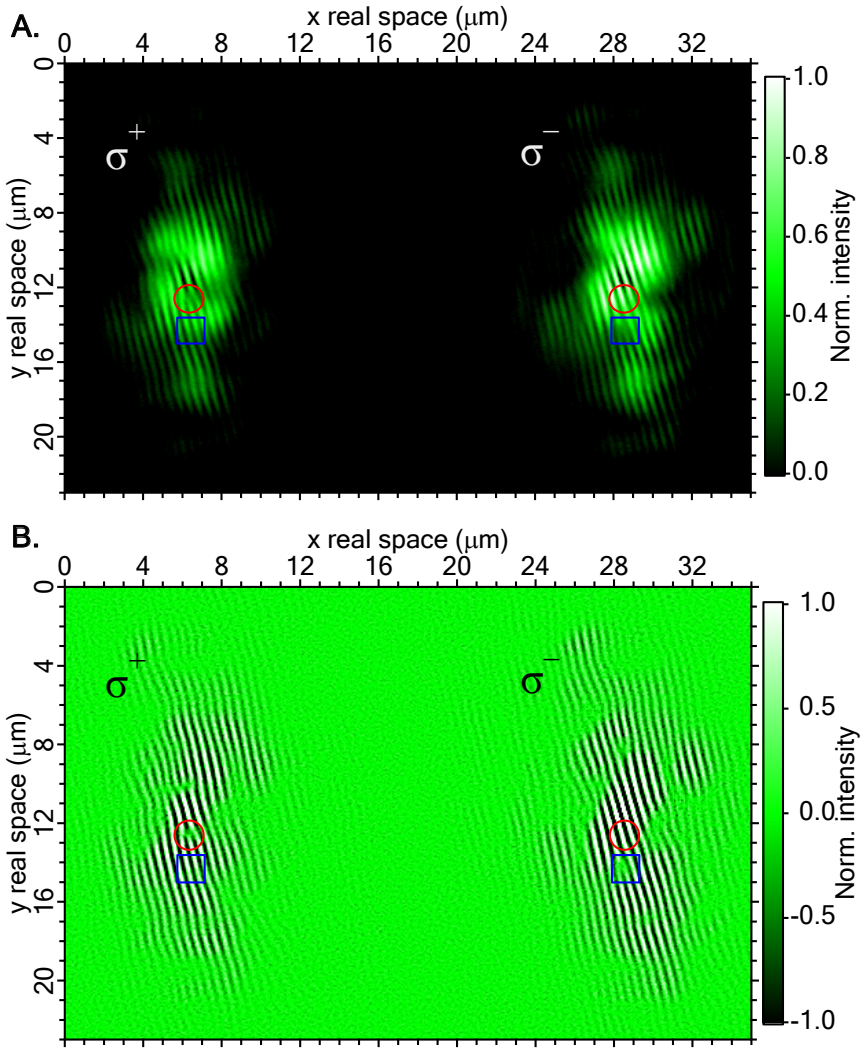

Fig. S2: Simultaneous imaging of both polarization components for the identification of half vortices. (**A**): Raw interferometric data and (**B**): interference fringes after removing numerically the CW part of the raw data interferogram. In this figure two independent HQVs are clearly distinguishable, one with winding numbers $(k,m)=\left(-\frac{1}{2},+\frac{1}{2}\right)$ in the red circle and one with winding numbers $(k,m)=\left(+\frac{1}{2},+\frac{1}{2}\right)$ in the blue box.

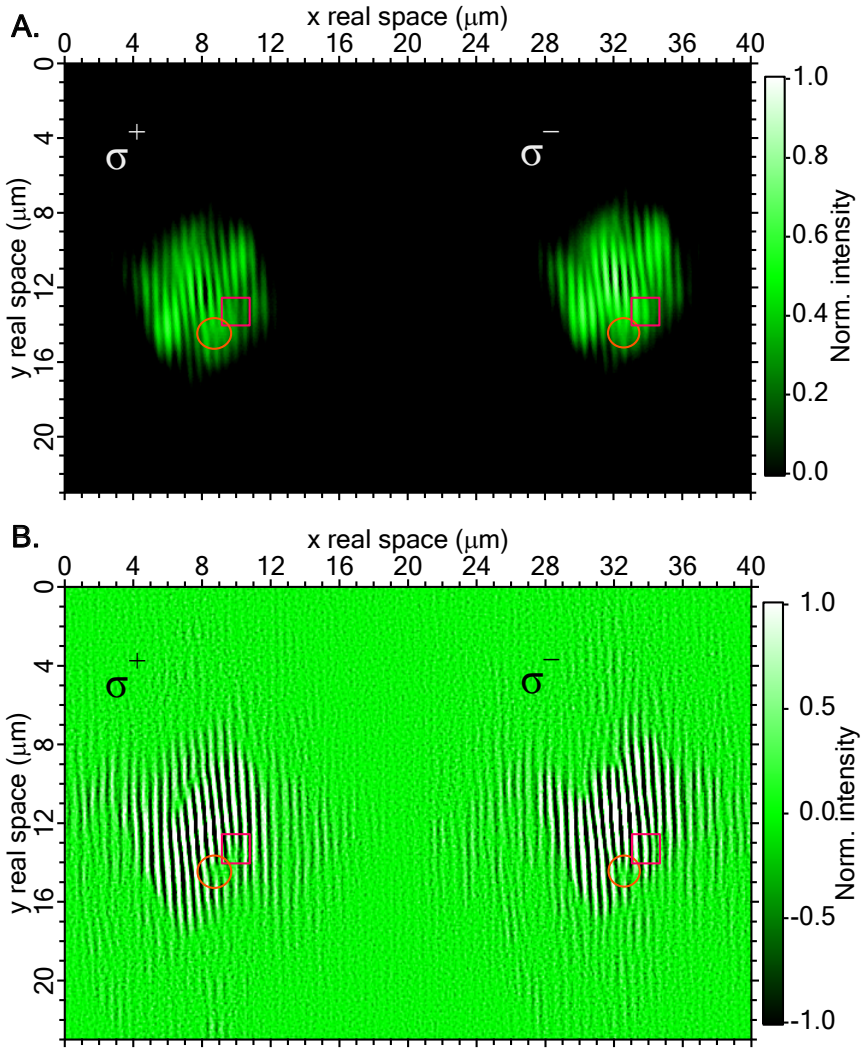

Fig. S3: Simultaneous imaging of both polarization components for the identification of half vortices at a different position on the sample showing another close pair of HQVs. (**A**): Raw interferometric data and (**B**): interference fringes after removing numerically the CW part of the raw data interferogram. In this figure two independent HQVs are also clearly distinguishable only here with winding numbers $(k,m)=\left(-\frac{1}{2},-\frac{1}{2}\right)$ and $(k,m)=\left(+\frac{1}{2},-\frac{1}{2}\right)$ in the orange circle and in the pink box respectively.

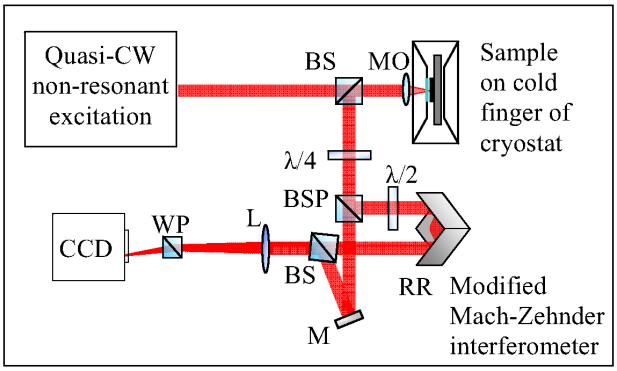

Fig. S4: Experimental setup of polarization mixing interferometry for the verification of the mutual coherence between the two circular polarization components. It consists of a polarization mixing Mach-Zehnder interferometer where the two polarizations get separated and sent on the two interferometer arms independently. The half wave plate is set at 45° and rotates one of the two polarizations by $\pi/2$ in order to coincide with the polarization in the other arm. The interference is then formed by mixing the two independent polarizations. BSP: beam splitter polarizer, $\lambda/2$: half wave plate.

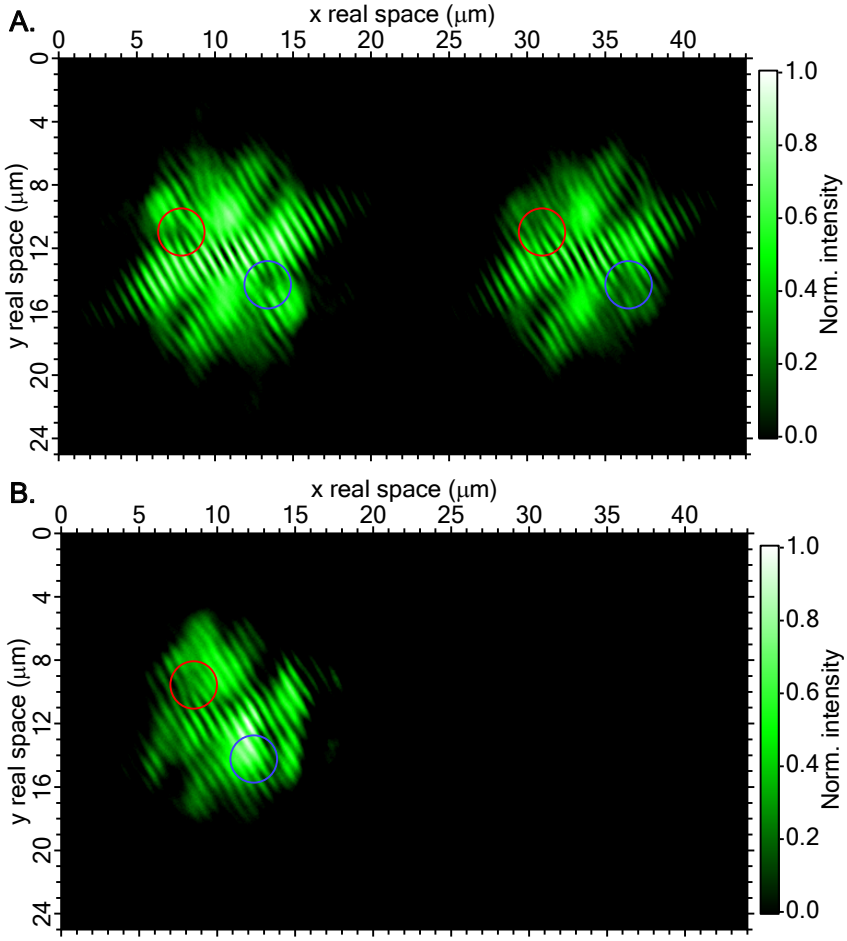

Fig. S5: (**A**): A half vortex observed with the standard method of simultaneous imaging of the interference patterns of the two polarization components. (**B**): The same HQV observed by means of polarization mixing interferometry. The half vortex shown in (**B**) is clearly observed as a forklike dislocation in the red circle and no forklike dislocation in the blue circle. The centers of the blue and red circles in both (**A**) and (**B**) are placed symmetrically with respect to the autocorrelation point. This experiment clearly demonstrates that the two polarization components are mutually coherent and that we can use whichever method facilitates our observations.

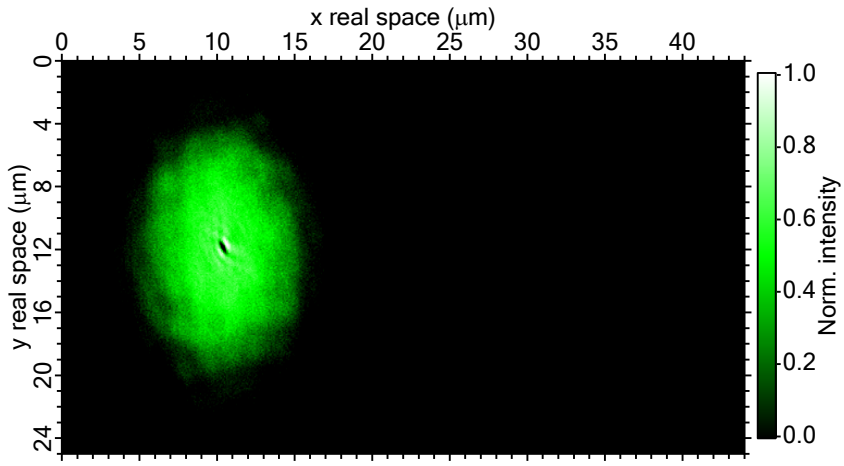

Fig. S6: Interference pattern below the condensation threshold as seen at the output of the Mach Zehnder polarization mixing interferometer. The autocorrelation point can be easily determined since it is the only place where the modulation of intensity caused by interference can be seen. Its size is defined by the response function of the microscope objective and the thermal de Broglie wavelength of polaritons. Here it is on a submicron scale. Note that the luminescence below threshold is not polarized thus we had to add a plate polarizer before the λ/4 to be able to see the interference at the autocorrelation point.

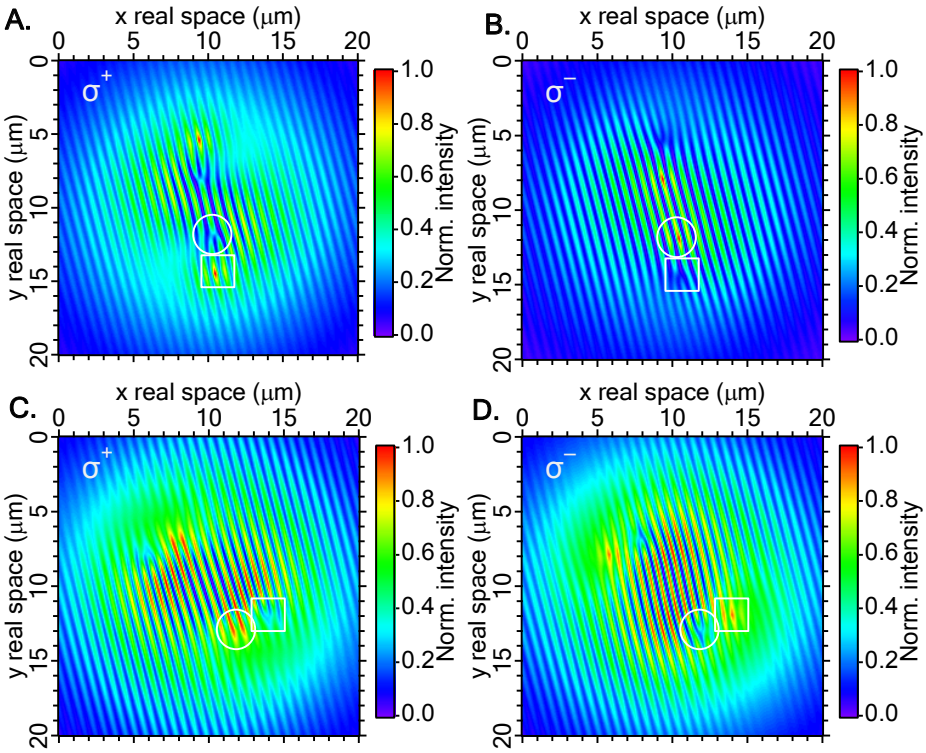

Fig. S7: Numerical simulation of the interference pattern in each of the circular polarizations for pairs of HQVs. (**A**): Simulated interferogram of a pair of HQVs with the same relative core coordinates as in figure S2. The quantum numbers are $(k,m)=\left(-\frac{1}{2},+\frac{1}{2}\right)$ and $(k,m)=\left(+\frac{1}{2},+\frac{1}{2}\right)$ in the circle and box respectively. The singularities behave identically to the experimental data. (**B**): Simulated interferogram of a pair of HQVs with the same relative core coordinates as in figure S3. The quantum numbers are here $(k,m)=\left(-\frac{1}{2},-\frac{1}{2}\right)$ and $(k,m)=\left(+\frac{1}{2},-\frac{1}{2}\right)$ in the circle and box respectively.

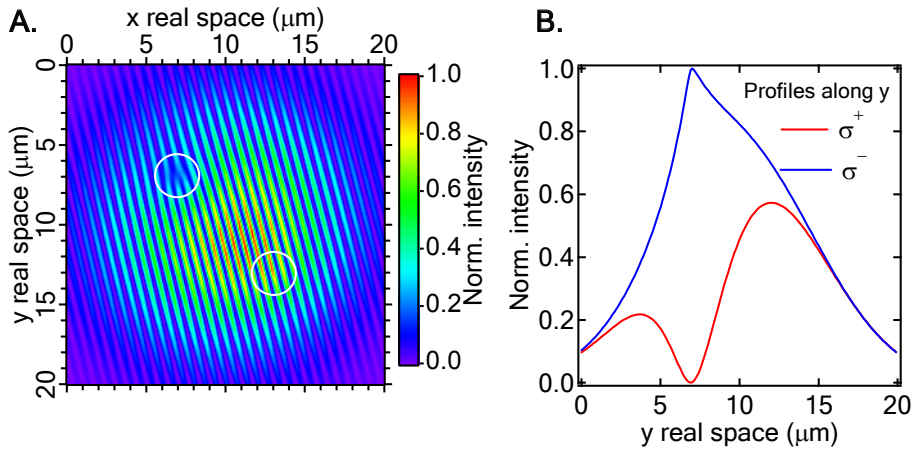

Fig. S8: (**A**) Simulated fringes emerging from interference of the two opposite circular components of the luminescence. The HQV with $(k,m)=\left(-\frac{1}{2},+\frac{1}{2}\right)$ is situated at the coordinates (7,7) where a forklike dislocation is seen. (**B**) The calculated polariton field intensity across the vortex core in the direction of the *y* axis in two circular polarisations. At the center of the vortex the minimum in σ^{+} polarisation coincides with the maximum in σ^{-} polarisation.

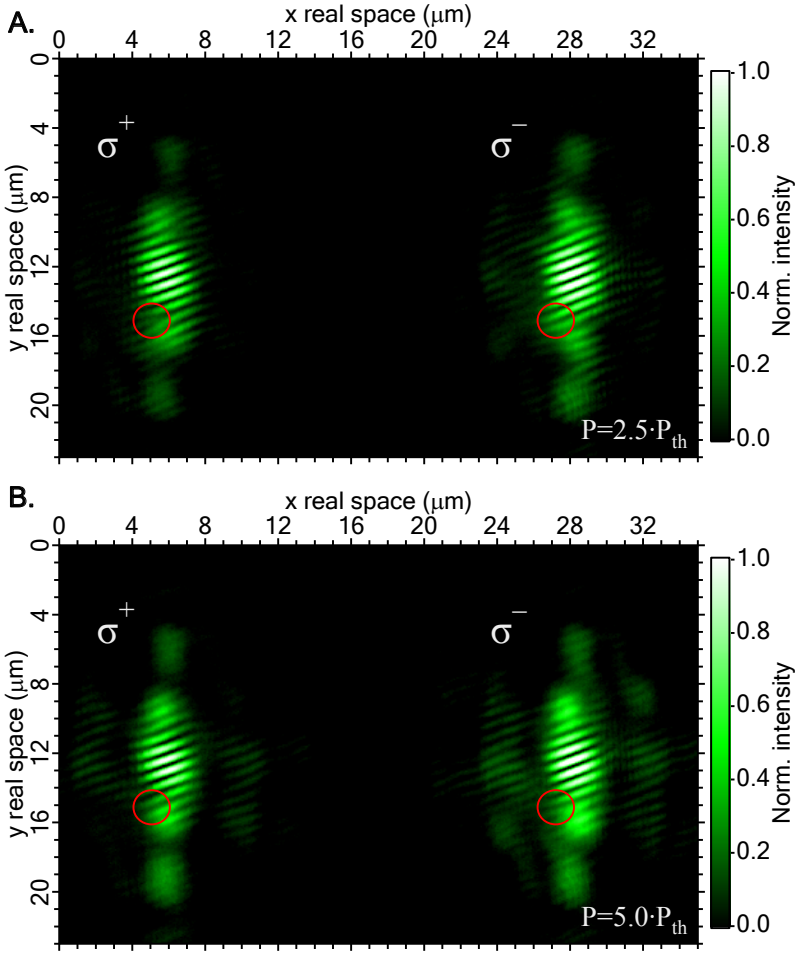

Fig. S9: Interference patterns for two excitation powers. In (**A**) the excitation was at a power 2.5 times higher that the condensation threshold whereas in (**B**) the excitation power was 5 times above the threshold. In panel (**A**) the half vortex is clearly shown by the red circles (forklike dislocation for sigma plus and straight fringes for sigma minus), whereas in panel (**B**) where the excitation power is high, in the same circles the interference pattern has changed with the most striking feature being the vanishing of the forklike dislocation. This clearly indicates the vortex unpinning from that specific location.

Optical analogue of the spin Hall effect in a photonic cavity

Maria Maragkou,[1,5] Caryl E. Richards,[1] Tomas Ostatnický,[1,2] Alastair J. D. Grundy,[1] Joanna Zajac,[3] Maxime Hugues,[4] Wolfgang Langbein,[3] and Pavlos G. Lagoudakis[1,*]

[1]*School of Physics and Astronomy, University of Southampton, Southampton SO17 1BJ, UK*

[2]*Faculty of Mathematics and Physics, Charles University in Prague, Ke Karlovu 3, 121 16 Prague, Czech Republic*

[3]*School of Physics and Astronomy, Cardiff University, The Parade, CF24 3AA Cardiff, UK*

[4]*Engineering and Physical Sciences Research Council National Centre for III-V Technologies, Sheffield S1 3JD, UK*

[5]*Present address: Departamento de Física de Materiales, Universidad Autónoma de Madrid, E-28049, Madrid, Spain*

**Corresponding author: pavlos.lagoudakis@soton.ac.uk*

Received January 12, 2011; accepted February 4, 2011;
posted February 24, 2011 (Doc. ID 141005); published March 18, 2011

We observe anisotropy in the polarization flux generated in a GaAs/AlAs photonic cavity by optical illumination, equivalent to spin currents in strongly coupled microcavities. Polarization rotation of the scattered photons around the Rayleigh ring is due to the TE–TM splitting of the cavity mode. Resolving the circular polarization components of the transmission reveals a separation of the polarization flux in momentum space. These observations constitute the optical analogue of the spin Hall effect.

OCIS codes: 240.3695, 350.5500, 290.5870, 080.0080.

The generation and manipulation of spin currents has been perceived as one of the most remarkable and desired effects in the field of spintronics. Dyakonov and Perel [1] were the first to predict the possibility of generating a spin current perpendicular to the charge current flow, in which the spin orbit interaction leads to an accumulation of opposite spin directions on the opposite boundaries. Experimentally, this has been demonstrated with electrons acting as spin carriers in GaAs systems [2–4].

The optical analogue has been easier to observe in semiconductor microcavities [5–7] because polaritons, the particles that arise from the strong coupling of excitons and photons [8], are relatively long-lived neutral quasi-particles and do not undergo the same rapid dephasing that suppresses the spin Hall effect in pure electronic systems. Initially predicted by Kavokin *et al.* [9], the optical spin Hall effect (OSHE) can be described in terms of the pseudospin formalism [10,11] that depicts the polarization state of the polariton that precesses around an effective magnetic field, induced by the longitudinal-transverse (LT) splitting of polaritons. The LT splitting originates from the polarization splitting of TE and TM optical modes [12] (TE–TM splitting) of the cavity that operates alongside the long-range part of the exciton exchange interaction [13]. The resulting spin separation arises from the combined effect of the effective magnetic field, whose orientation and magnitude depends on the polariton wavevector, and the Rayleigh scattering of the polaritons with disorder in the system.

Here, we demonstrate the generation of anisotropic polarization flux in a bare cavity and introduce a classical interpretation of the observed dynamics. By measuring the degree of circular polarization of transmitted cavity photons, we observe the same anisotropy in polarization in momentum space from the TE–TM splitting of the cavity modes. Arising from the polarization dependence of the reflection at the internal interfaces described by the Fresnel coefficients, it follows that the presence of a TE–TM splitting between the cavity optical modes is sufficient to generate the effect in the absence of any excitonic contribution. The observed effect is therefore an optical analogue of the spin Hall effect, namely the *all-optical* spin Hall effect, with practical applications in all-optical information technology.

In contrast to the spin Hall effect, where initially unpolarized carriers gain some degree of polarization through polarization-dependent scattering (extrinsic spin Hall effect [14]), the injected photons in our system are initially polarized.

Both the optical analogue of the spin Hall effect in a bare photonic cavity and OSHE in a strongly coupled microcavity can be interpreted as wave retardation within the cavity. The TE–TM splitting results in an effective birefringence whose magnitude and direction depend on the in-plane momentum. As linearly polarized photons propagate in different directions with wave vectors of equal modulus, they populate an elastic ring in momentum space. Photons in different quadrants of the k-ring experience different phase shifts under the directional birefringence that is manifest as an anisotropy in polarization rotation.

For an incidence angle $\varphi_0 > 0$ to the surface normal, TE–TM splitting arises from the difference in the phase shift and penetration of the optical modes into the Bragg mirrors for the two orthogonal polarizations. Its magnitude is determined by the energy difference Δ between the cavity mode frequency ω_c and the center of the stop band ω_s (i.e., the detuning $\Delta = \omega_c - \omega_s$). For a cavity with refractive index n_c and width L_c, the angle-dependent TE–TM splitting of the cavity mode can be approximated by [15]

$$\omega^{\mathrm{TE}}(\varphi_0) - \omega^{\mathrm{TM}}(\varphi_0) \approx \frac{L_c L_{\mathrm{DBR}}}{(L_c + L_{\mathrm{DBR}})^2} \frac{2\cos\varphi_{\mathrm{eff}} \sin^2\varphi_{\mathrm{eff}}}{1 - 2\sin^2\varphi_{\mathrm{eff}}} \Delta, \tag{1}$$

where L_{DBR} is the penetration length into the distributed Bragg reflectors and $\varphi_{\mathrm{eff}} \approx \arcsin(n_0/n_c)\sin\varphi_0$ is the

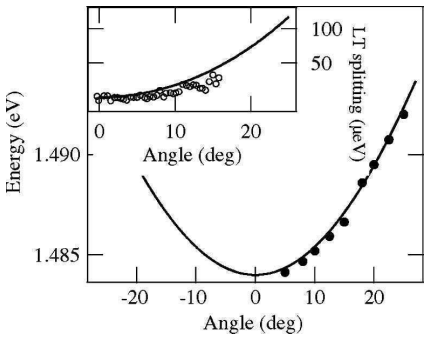

Fig. 1. Calculated bare cavity mode dispersion versus angle. Filled circles correspond to experimental points. Inset: LT splitting, derived from Eq. (1), versus angle for $\Delta = -2$ meV, plotted with experimentally measured points (empty circles).

effective refractive index of the cavity [16] determined from the cavity dispersion by averaging over the cavity mode and Bragg mirror. The resulting TE–TM splitting of the GaAs cavity increases with the incidence angle (equivalent to the in-plane k-vector), as shown in the inset of Fig. 1. Experimental points plotted (empty circles) verify the theoretical calculation of the TE–TM splitting.

The sample is a λ GaAs microcavity with 27 (top) and 24 (bottom) distributed GaAs/AlAs reflector pairs. The measured cavity mode dispersion (Fig. 1) has a linewidth of 10 μeV (at normal incidence) and a corresponding cavity photon lifetime of 30 ps. Measurements are taken with the sample held in a cold-finger cryostat at 10 K to tune the cavity resonance into the transparent region of GaAs, approximately 30 meV below the 1 s excitonic resonance. Further to previous studies with strongly coupled microcavities, we excite a large cone of angles around normal incidence to the sample with a lens of large numerical aperture (NA = 0.4) [Fig. 2]. This alternative approach, used earlier to investigate polariton propagation [17], allows direct population of all states resonant to the excitation, which due to the nearly isotropic in-plane polariton dispersion correspond to a given k-vector magnitude, forming a ring in momentum space. The sample is illuminated using a cw Ti:sapphire laser (<1.5 nm linewidth). The linear polarization of the excitation is adjusted to either the x or y direction using a half-wave plate. The excitation photon energy determines the resonant in-plane wave vector k on the ring. The photons across the elastic ring acquire different phase shifts as they propagate in various directions. The degree of circular polarization

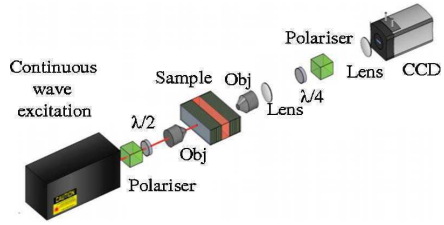

Fig. 2. (Color online) Setup collects transmission in momentum space. The incident beam is always linearly polarized and at normal incidence.

$$\rho_c = \frac{I_{\sigma^+} - I_{\sigma^-}}{I_{\sigma^+} + I_{\sigma^-}}, \tag{2}$$

where I_{σ^+} and I_{σ^-} are the measured intensities of the circularly polarized components of the transmission, reveals a separation of spin-polarized photons in the empty GaAs cavity in momentum space. Figure 3 shows ρ_c, obtained upon illumination of the sample, with energies resonant to the cavity mode with a large numerical aperture at four different x-polarized incident photon energies. A fourfold symmetry is apparent in each case. Rotation of the polarization plane of the incident beam results in inversion of the polarization of the observed anisotropic polarization flux (not shown).

As previously discussed, the TE–TM splitting defines the effective birefringence for the cavity. The photon lifetime dictates how long the light experiences the birefringence and defines the total retardation. The total retardation in our system is measured to be close to $\pi/2$, as in a quarter-wave that, using the cavity lifetime of 30 ps, yields a TE–TM splitting around 70 μeV, close to the theoretical upper limit of about 100 μeV (inset in Fig. 1).

Simulations of the anisotropic polarization flux are undertaken with wave optics, the results of which are shown in Fig. 4(b). The incident laser beam is decomposed into a superposition of TE- and TM-polarized plane waves whose transmission through the sample is calculated using transfer matrix formalism. Applying Eq. (2) gives k-space images of the circular polarization degree. For the simulations, the incident light is considered to be a Gaussian beam in k-space of the form:

$$E_{0x}(k) = \exp[-k^2/\sigma^2], \tag{3}$$

where the Gaussian width is $\sigma = 1.9\,\mu\text{m}^{-1}$. In the cylindrical coordinate system, we decompose the initial electric field intensity to its TE and TM components:

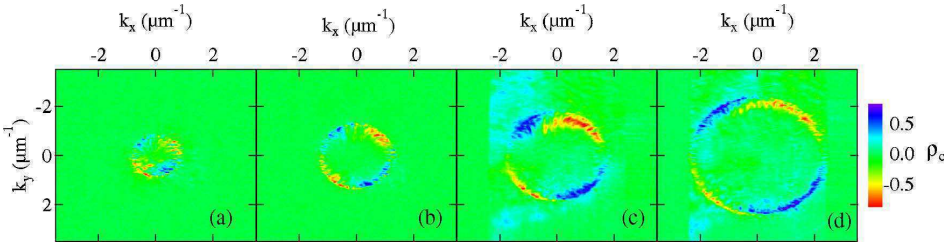

Fig. 3. (Color online) (a)–(d) Measured circular polarization degree ρ_c in momentum space. The color scale is linear in intensity. The incident beam is x-polarized at energies corresponding to (a) 5°, (b) 10°, (c) 15°, and (d) 20°.

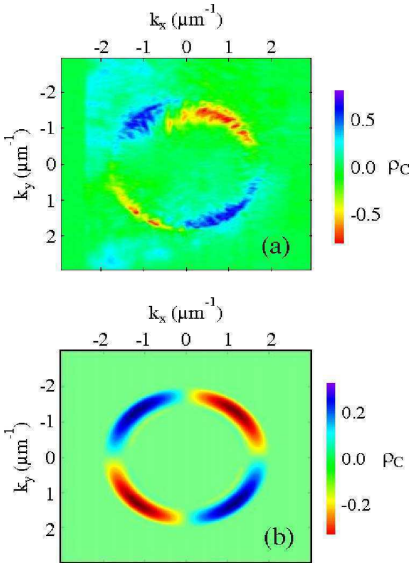

Fig. 4. (Color online) (a) Far-field circular polarization degree measured for x-polarized incident beam tuned at 1.48663 meV equivalent to 15 deg, (b) theoretical calculations for the same conditions.

$$E_{\mathrm{TE}}(k,\phi) = E_{0x}(k)\sin(\phi),$$
$$E_{\mathrm{TM}}(k,\phi) = E_{0x}(k)\cos(\phi). \tag{4}$$

Then we use the standard transfer matrix method to determine the TE and TM transmission coefficients $t_{\mathrm{TE,TM}}(k)$ and perform a backward transformation to the x–y coordinate system:

$$E_x(k,\phi) = E_{\mathrm{TM}}(k,\phi)t_{\mathrm{TM}}(k)\cos(\phi) + E_{\mathrm{TE}}(k,\phi)t_{\mathrm{TE}}(k)\sin(\phi),$$
$$E_y(k,\phi) = -E_{\mathrm{TM}}(k,\phi)t_{\mathrm{TM}}(k)\sin(\phi) + E_{\mathrm{TE}}(k,\phi)t_{\mathrm{TE}}(k)\cos(\phi). \tag{5}$$

We calculate the intensities of the circular components as $I_{\sigma^+,\sigma^-} = |E_x \pm iE_y|^2$, and the corresponding circular degree of polarization is given by Eq. (2).

Exchanging the half- and quarter-wave plates to illuminate with circularly polarized light and resolve the linearly polarized transmission yields polarization anisotropy in two orthogonal linear polarizations, and a fourfold symmetry in the carriers' spin is again achieved (not shown).

In conclusion, we have observed the optical spin Hall effect in a pure photonic cavity. Photons are distributed uniformly around the elastic circle and develop an anisotropic polarization flux due to the TE–TM splitting of the cavity mode. Their behavior can be described by a theoretical model based on classical wave optics. These results show that the optical spin Hall effect can be observed in planar microcavities in the absence of an excitonic resonance. However, there are spin effects in microcavities in which the excitonic part of polaritons is essential, such as the Zeeman splitting used in the proposed optical Berry-phase interferometer [18].

The authors would like to acknowledge Engineering and Physical Sciences Research Council (EPSRC) grant EP/F026455/1 and Seventh Framework Programme grants ITN-Clermont 4 and ITN-Spinoptronics for funding. This work is also a part of the research plan MSM0021620834 financed by the Ministry of Education of the Czech Republic and project P204/10/P326 financed by the Grant Agency of the Czech Republic.

References and Notes

1. M. I. Dyakonov and V. I. Perel, Phys. Lett. A **35**, 459 (1971).
2. Y. Y. K. Kato, R. C. Myers, A. C. Gossard, and D. D. Awschalom, Science **306**, 1910 (2004).
3. J. J. Wunderlich, B. Kaestner, J. Sinova, and T. Jungwirth, Phys. Rev. Lett. **94**, 047204 (2005).
4. H. Zhao, E. J. Loren, H. M. van Driel, and A. L. Smirl, Phys. Rev. Lett. **96**, 246601 (2006).
5. C. Leyder, M. Romanelli, J. Ph. Karr, E. Giacobino, T. C. H. Liew, M. M. Glazov, A. V. Kavokin, G. Malpuech, and A. Bramati, Nat. Phys. **3**, 628 (2007).
6. A. Amo, T. C. H. Liew, C. Adrados, E. Giacobino, A. V. Kavokin, and A. Bramati, Phys. Rev. B **80**, 165325 (2009).
7. T. C. H. Liew, C. Leyder, A. V. Kavokin, A. Amo, J. Lefrère, E. Giacobino, and A. Bramati, Phys. Rev. B **79**, 125314 (2009).
8. C. Weisbuch, M. Nishioka, A. Ishikawa, and Y. Arakawa, Phys. Rev. Lett. **69**, 3314 (1992).
9. A. Kavokin, G. Malpuech, and M. Glazov, Phys. Rev. Lett. **95**, 136601 (2005).
10. A. Kavokin, P. G. Lagoudakis, G. Malpuech, and J. J. Baumberg, Phys. Rev. B **67**, 195321 (2003).
11. K. V. Kavokin, I. A. Shelykh, A. V. Kavokin, G. Malpuech, and P. Bigenwald, Phys. Rev. Lett. **92**, 017401 (2004).
12. G. Panzarini, L. C. Andreani, A. Armitage, D. Baxter, M. S. Skolnick, V. N. Astratov, J. S. Roberts, A. V. Kavokin, M. R. Vladimirova, and M. A. Kaliteevski, Phys. Rev. B **59**, 5082 (1999).
13. M. Z. Maialle, E. A. de Andrada e Silva, and L. J. Sham, Phys. Rev. B **47**, 15776 (1993).
14. J. E. Hirsch, Phys. Rev. Lett. **83**, 1834 (1999).
15. A. Kavokin, J. J. Baumberg, G. Malpuech, and F. P. Laussy, *Microcavities* (Oxford University Press, 2007).
16. The values used in the formula are $L_{\mathrm{DBR}} = 764.66$ nm, $L_C = 235$ nm, $n_0 = 2.88$, and $|\Delta| = 2$ meV (experimentally measured).
17. W. Langbein, I. Shelykh, D. Solnyshkov, G. Malpuech, Yu. Rubo, and A. Kavokin, Phys. Rev. B **75**, 075323 (2007).
18. I. Shelykh, G. Pavlovic, D. D. Solnyshkov, and G. Malpuech, Phys. Rev. Lett. **102**, 046407 (2009).

[P20]

Linear wave dynamics explains observations attributed to dark-solitons in a polariton quantum fluid

P. Cilibrizzi,[1] H. Ohadi,[1] T. Ostatnicky,[2] A. Askitopoulos,[1] W. Langbein,[3] and P. Lagoudakis[1,*]

[1] *School of Physics and Astronomy, University of Southampton, Southampton, SO17 1BJ, United Kingdom*
[2] *Faculty of Mathematics and Physics, Charles University in Prague, Ke Karlovu 3, 121 15 Prague, Czech Republic*
[3] *School of Physics and Astronomy, Cardiff University, The Parade, CF24 3AA Cardiff, UK*

(Dated: June 25, 2014)

We investigate the propagation and scattering of polaritons in a planar GaAs microcavity in the linear regime under resonant excitation. The propagation of the coherent polariton wave across an extended defect creates phase and intensity patterns with identical qualitative features previously attributed to dark and half-dark solitons of polaritons. We demonstrate that these features are observed for negligible nonlinearity (i.e. polariton-polariton interaction) and are therefore not sufficient to identify dark- and half-dark solitons. A linear model based on the Maxwell equations is shown to reproduce the experimental observations.

Solitons are solitary waves that preserve their shape while propagating through a dispersive medium [1, 2] due to the compensation of the dispersion-induced broadening by the nonlinearity of the medium [3]. Over the years, spatial solitons have been observed by employing a variety of nonlinearities ranging from Kerr nonlinear media [4] to photorefractive [5] and quadratic [6] materials. Apart from their potential application in optical communications [7, 8], solitons are important features of interacting Bose-Einstein condensates (BECs) and superfluids. The nonlinear properties of BEC can give rise to the formation of quantized interacting vortices and solitons, the latter resulting from the cancellation of the dispersion by interactions, for example in atomic condensates. A special class of solitons are the so-called dark solitons, which feature a density node accompanied by a π phase jump. Since the first theoretical prediction in the context of Bose-Einstein condensates (BECs) [9], dark solitons were studied and observed first in the field of nonlinear optics [10] and then in cold-atom BECs [11]. The experimental observation of BEC [12] and superfluidity [13, 14] of exciton-polaritons, has sparked interest in the quantum-hydrodynamic properties of polariton fluids. In particular, the nucleation of solitary waves in the wake of an obstacle (i.e. defect) has been claimed recently [15–19]. Here, the source of nonlinearity, essential for the formation of such a solitary wave, has been identified in the repulsive polariton-polariton interactions [15–19]. In these previous works, the observation of dark notches in the intensity profiles together with a π shift in the phase have been used as sufficient signatures for dark solitons in microcavities. In addition, half-dark solitons have been found to carry a non-zero degree of circular polarization in presence of the TE–TM splitting of the cavity mode [19].

In this Letter we demonstrate that these features previously used as dark-soliton fingerprints [15–19] can also be observed without the presence of nonlinearity, which is the fundamental ingredient differentiating solitons from linear wave propagation. Specifically we investigate the propagation of polaritons with a small exciton fraction and at low polariton densities, excluding a relevant influence of nonlinearities. We show that polariton propagation in this linear regime across an extended defect can create deep notches in the intensity profile accompanied by a π phase shift. We model the observation using linear wave propagation, clarifying that these features are not indicative for a nonlinear interaction be-

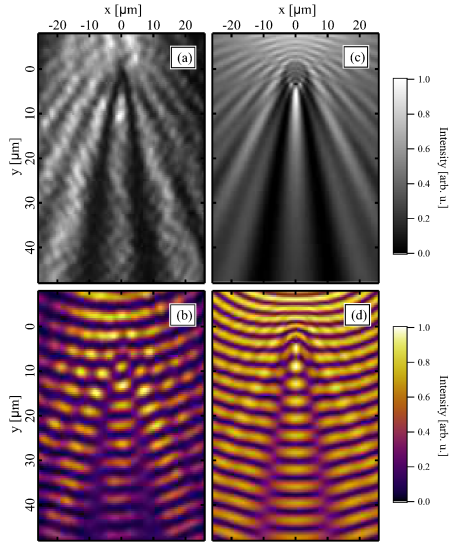

Figure 1. Experimental (a),(b) and simulated (c),(d) real space intensity and interference patterns showing the two "soliton fingerprints" generated by the scattering of a beam with a point-like defect: a dark notch in the intensity pattern together with π phase dislocations. In the images the polaritons propagating downwards, along the y-axis, are injected with a wavevector of 1.5 μm^{-1} and are scattered by a defect positioned 25 μm away from the excitation spots.

tween polaritons, but are interference patterns created by scattering from the defect. Moreover, we show that the appearance/disappearance of these features for different in-plane kinetic energies is reproduced in the linear regime and thus does not provide evidence of an interacting quantum fluid. Therefore, the previous reports of the observation of dark-solitons [15–18] and half-dark-solitons [19] which were based on these features have to be reconsidered.

The investigated sample is a bulk λ GaAs microcavity surrounded by 27 (top) and 24 (bottom) distributed GaAs/AlAs Bragg reflector pairs. The sample is held in a cold-finger cryostat at a temperature of 15 K and is illuminated by a narrow linewidth single-mode continuous wave laser, tuned to the resonance of the cavity at about 1.485 eV. The measurements were performed in transmission configuration. The phase was measured using a shearing Mach-Zehnder interferometer (see [20], S1 [21–24]). Our experiments were performed in the linear regime, facilitated by the large negative detuning of -29 meV of the cavity photon mode from the exciton resonance at 1.514 eV, resulting in a small exciton fraction of the polariton of about 1%. To verify the linear regime, we studied the excitation density dependence of our results with both a Gaussian and half-Gaussian excitation beam (see [20], S2). We find that they are independent of both the shape of the beam and the excitation density over a range of four orders of magnitude and they persist at polariton density as low as 2.3×10^2 cm^{-2}, seven orders of magnitude lower than the lasing threshold observed in standard microcavities [25].

The real space intensity and interference of a polariton wave propagating across a defect are shown in Fig. 1. The experimental results show the presence of two dark notches in the intensity pattern along with a π phase shift visible in Fig. 1(b) as paths of vortices merging in succession with alternating topological charge ±1. Simulations of the measurements using the realistic experimental parameters are shown in Fig. 1(c) and Fig. 1(d).

Solitons are predicted to appear in polariton microcavities as the result of the nonlinearity due to the polariton-polariton interactions [26]. Since our experiments are in the linear regime, it is important to understand how the nature and the size of the defect affects the formation process of these soliton-like features. In a recent study [27] of the structural and optical properties of GaAs/AlAs microcavities grown by molecular beam epitaxy it was shown that the most common point-like defects (PD) were characterized by a circular or elliptical shape [28], due to Gallium droplets emitted occasionally during the growth [29, 30]. The presence of the defect has the effect of modifying the effective thickness of the cavity layer, which typically results in an attractive potential for the cavity mode inside the defect [28]. Consequently, the wavevector of the photonic mode in the region of the defect is higher than in the rest of the cavity.

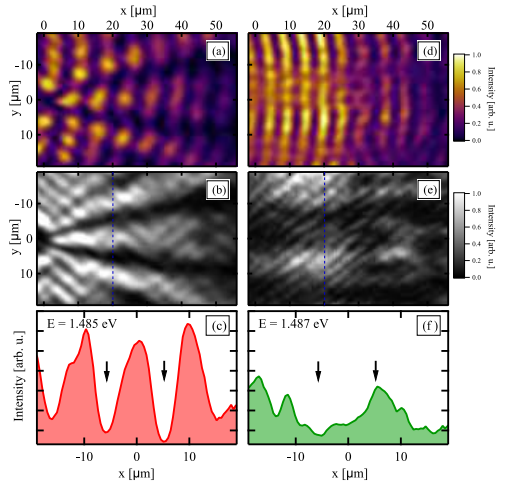

Figure 2. Experimental interference (a),(c) and intensity (b),(d) showing the transition between the regime where the soliton features are well defined (1.485 eV) to a regime where they vanish (1.487 eV). The intensity profiles (e),(f) calculated along the blue dashed line, 20μm away from the defect, confirm that the dark notches disappear when the energy of the excitation beam is increased. The two arrows indicate the positions of soliton-like fingerprints.

The polariton scattering by the defect depends on the wavevector mismatch between the polaritons outside and inside the defect at the energy of excitation. When the energy shift of the defect photon mode with respect to the unperturbed cavity mode is large enough to make the coupling between them inefficient, the defect behaves like a hard scatterer and the spatial intensity distribution is similar to the complementary case of a single-slit diffraction [31]. In our case, however, there is a finite transmission through the defect, producing dark and bright traces with a more complicated phase pattern. As it has been shown by Berry *et al.* [32, 33], wavefronts resulting from interference can contain dislocation lines. In the case of a scattered beam, dislocations are composed of phase shifts at positions where the amplitude of the electromagnetic wave and thus the intensity vanishes, representing nodes of the wave. It is worth mentioning that nonlinearities are negligible close to nodes also in the nonlinear regime, and phase dislocations at zero intensity (i.e. at the dark notches) are features of both linear [34, 35] and nonlinear waves. In our case, the analogy between linear and nonlinear waves goes beyond the mere observation of the same features and is effectively more profound. Indeed, as shown in [20] S4, the intensity, the phase jumps as well as the relative depth of the dark-notches in the linear regime satisfy the same mathematical expression as in the quantum fluid case [15–18]. In particular, also in our linear system the relative depth of the dark-notches

remains constant up to 42 μm (see [20], S4).
Beyond the qualitative discussion above, we performed simulations of the experiments, based on a numerical solution of the linear scattering problem using the classical theory of electromagnetism. The choice of such a model is justified by the fact that we operate in the linear regime and with a small exciton fraction of about 1%, such that the polariton dispersion is dominated by the cavity mode. In the model, we consider the propagation of quasi two-dimensional photons with a parabolic dispersion in a cavity with a fixed width. The incident wave has been treated as coming from a linearly polarized point-like source with polarization in the plane of the cavity. Defects have been modeled as disk-shaped perturbations of the cavity thickness resulting in an energy shift of the photon dispersion (see [20], S5). To model the defect parameters, which are not experimentally known, we use a disk shape with a radius of 3 μm and a polariton potential of -2.3 meV (in agreement to Ref. [28]). Maxwell's equations are then solved using expansion of the fields into the planar cavity eigenmodes in cylindrical coordinates fulfilling the boundary conditions for tangent component of electric and magnetic field on the interface between the cavity and the defect (see [20], S5). This linear wave dynamics model reproduces the intensity notch and the phase dislocation previously used as dark-soliton fingerprints. The results show a marked dependence on the geometry of the scattering problem, as shown in S6 [20]. In particular, the phase jump visible in the interference pattern depends on the direction of the incoming polariton wave relative to the defect (see Fig. S7). On the other hand, the size of the defect relative to the polariton wavelength affects the formation of high-order phase dislocations (see Fig. S8).
In a nonlinear cavity-polariton system, a polariton fluid has been predicted to flow almost unperturbed around the defect (i.e. disappearance of the features) or experience the nucleation of vortices and/or solitons at the position of the defect (i.e. appearance of the features), depending on the excitation density or on the energy of the pump [26]. We evaluated the possibility of observing these features, ascribed in the literature to dark-solitons resulting from the interaction within the polariton fluid, in the absence of non-nonlinearities. Fig. 2 (a) and (b) show the phase and the intensity of soliton-like fingerprints in real space. Instead of increasing the excitation power, which has no effect in the linear regime, we tune the energy of the excitation beam, and observe the appearance and disappearance of soliton-like features. As discussed above, the appearance of the intensity minima and phase dislocations is a result of interference which is sensitive to the intensity and relative phase of contributing waves. The increase of the energy of the excitation beam by 2 meV causes an increase of the in-plane wavevector of the propagating polariton mode that, in turn, changes the interference condition so that the

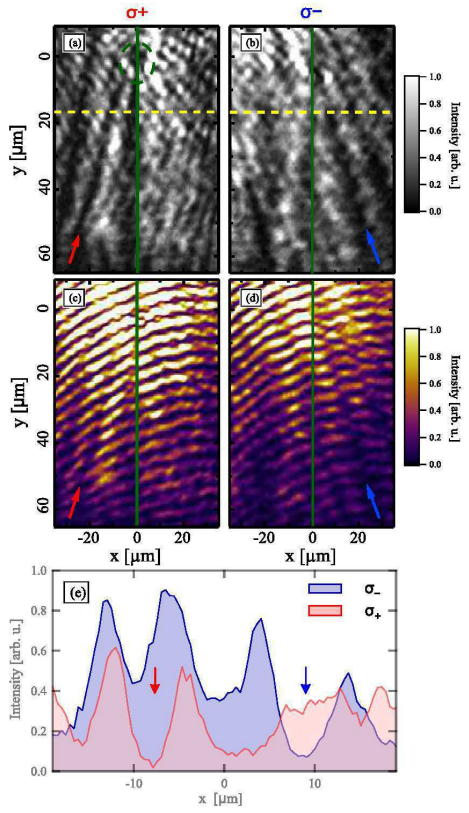

Figure 3. Experimental intensity pattern (a-b) and real space interference (c-d) showing two half-soliton features as indicated by the arrows. The red and blue arrows indicate respectively the position of the σ_+ and σ_- soliton-features: a dark-notch with an associated phase jump present in only one circular component. The green vertical line is a guide for eyes to distinguish the two different regions while the dashed circle in (a) indicates the defect. (e) The intensity profile extracts from the yellow dotted line displaying the two dark notches present respectively in only one of the opposite polarization basis, as indicated by the arrows.

straight dark notches [Fig. 2 (c)] and the phase dislocations [Fig. 2 (d)] disappear. The wavevector dependence of such transitions will depend on the defect structure and the related bound polariton states [28], so that they could be observed also with decreasing wavevector for other defects. Intensity profiles measured at a fixed distance from the defect [Fig. 2 (e) and (f)] confirm the observed transition. Thus it becomes apparent that the appearance/disappearance of soliton-like features, although independent of the excitation density, strongly depends on the wavevector of the propagating mode (see [20], S3). It is worth noting that an increase of the polariton density corresponds to an energy blueshift of the polari-

ton dispersion. For polaritons excited resonantly with a given energy, this results in an increase of the polariton wavevector with decreasing density along the polariton propagation. Specifically in non-resonantly excited experiments [36], this blueshift is dominated by the exciton density in the reservoir at high wavevectors. The interaction with the exciton reservoir is not a polariton-polariton interaction within the condensate which could provide the non-linearity needed for the formation of solitons, but instead represents an external potential sculpting the polariton energy and gain landscape.

In a different experiment, we address the observation of half-soliton fingerprints, which requires polarization-resolved measurements. The intensity images [Fig. 3(a) and (b)] are measured using an excitation linearly polarized parallel to the y-direction. The interferograms [Fig. 3(c) and (d)], are obtained by selecting the same polarization for the excitation and reference beam (see [20], S1 for details). The signature of an oblique dark half-soliton (ODHS) is a notch in only one circular polarization component [19, 37]. We excite the sample with a linearly polarized beam and detect the two circular polarization components (σ_-, σ_+) separately. The measurements are performed with the same excitation energy (1.485 eV) and negative detuning (-29 meV) as in the previous case. The measured intensity and the interferogram for the σ_- component are given in Fig. 3(a) and Fig. 3(c) respectively. The images show the presence of a σ_- soliton fingerprint, indicated by the blue arrows, that is absent in the σ_+ component [Fig. 3 (b), (d)]. The same applies to the σ_+ counterpart, where a half-soliton fingerprint is observed only on the right side of the image. By calculating the degree of circular polarization, given by $S_c = (I_{\sigma_+} - I_{\sigma_-})/(I_{\sigma_+} + I_{\sigma_-})$, with I_{σ_+} and I_{σ_-} being the measured intensities of the two components, we measure the pseudospin state inside the cavity [Fig. 4]. Here, if we look at the same position where the soliton features have been observed [Fig. 3], indicated by the black dotted lines in Fig. 4 (a), we note the presence of a pair of oblique traces with opposite circular polarization, resembling the predictions and observations attributed to a polariton superfluid [19, 37]. The high degree of circular polarization that we observe is due to the polarization splitting of transverse electric and transverse magnetic optical modes (TE-TM splitting) [38] (see [20], S7). The latter gives rise to the optical spin Hall effect [39] that has been observed in both polariton [40] and purely photonic microcavities [41]. In our simulations [Fig. 4 (b)] a linearly polarized incoming beam propagates along the y-direction and is scattered by a defect positioned at 25 μm away from the excitation spot, inducing the formation of two traces propagating in oblique directions. The detected field is a superposition of the incoming linearly polarized wave and the scattered wave. The TE-TM splitting of the optical mode in a photonic cavity is responsible for an anisotropy in the polarization flux, as previously shown on the same sample in Ref. [41]. Here the same values of the TE-TM splitting have been used to perform the simulations. The polaritons scatter from the defect with wavevectors of equal modulus but in different directions both in the real and momentum space. Because of the birefringence induced by the TE-TM splitting, polaritons propagating in different directions experience different polarization rotation and shift. Polaritons traveling to the right gain a σ_+ component while polaritons traveling to the left gain a σ_- component. The anisotropy of the effect manifests itself in the intensity pattern, where it is possible to observe the features of an oblique soliton in one circular component and not in the other.

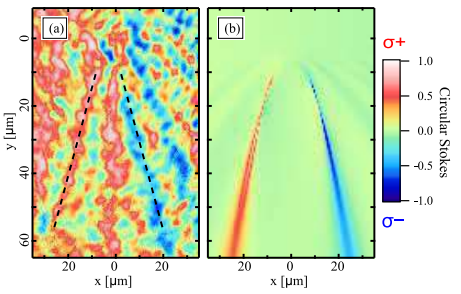

Figure 4. Experimental (a) and simulated (b) circular Stokes parameter showing half-soliton features. The two black dotted lines correspond to the position of the dark notches present in Fig. 3(a) and (b).

In conclusion, we have shown that the previously reported experimental signatures of oblique dark-solitons and half-solitons in polariton condensates can be observed in the case of polaritons propagating in the linear regime. We find that these features are the result of the interference of the incoming wave with the waves scattered by the defect. Moreover, the intensity, the phase jumps and the relative depth of the dark-notches satisfy the same analytical expression as in the polariton quantum fluid. In the case of the polarized counterpart (i.e. half-soliton-like features) the intrinsic TE-TM splitting of the cavity dispersion gives rise to oblique straight traces with opposite polarization.

Our results clarify that phase vortex lines in polariton propagation together with dark notches of constant relative depth in the intensity patterns, used as fingerprints of oblique-dark solitons and half-solitons in the literature, are present in the linear propagation regime. Consequently, these features are necessary but not sufficient evidence to identify solitons. We believe a more reliable criterion for identifying dark-solitons, based on the definition of solitons (i.e. solitary non-spreading wave), would be the size of the observed features which is determined by the healing length of the condensate (see [20], S4 for details).

The authors P.C. and P.L. acknowledge the Marie Curie ITNs Spinoptronics for funding. A.A. and P.L. acknowledge funding from Marie Curie ITN Clermont IV 235114. T.O. acknowledges financial support from the Grant Agency of Czech Republic, project number P204/10/P326. W.L. and P.L. acknowledge support by the EPSRC under Grant No. EP/F027958/1. P.C. acknowledges stimulating discussions with S. Portolan.

* correspondence address: pavlos.lagoudakis@soton.ac.uk

[1] G. I. Stegeman and M. Segev, Science **286**, 1518 (1999).
[2] M. Segev and G. Stegeman, Physics Today **51**, 42 (1998).
[3] Z. Chen, M. Segev, and D. N. Christodoulides, New J. Phys. **75**, 086401 (2012).
[4] M. Hercher, J. Opt. Soc. Am. **54**, 563 (1964).
[5] M. Segev, B. Crosignani, A. Yariv, and B. Fischer, Phys. Rev. Lett. **68**, 923 (1992).
[6] K. Hayata and M. Koshiba, Phys. Rev. Lett. **71**, 3275 (1993).
[7] M. Nakazawa and K. Suzuki, Electronics Letters **31**, 1076 (1995).
[8] P. D. Miller, Phys. Rev. E **53**, 4137 (1996).
[9] T. Tsuzuki, J. Low Temp. Phys. **4**, 441 (1971).
[10] Y. Kivshar, J. Quantum. Electron. **29**, 250 (1993).
[11] J. Denschlag, J. E. Simsarian, D. L. Feder, C. W. Clark, L. A. Collins, J. Cubizolles, L. Deng, E. W. Hagley, K. Helmerson, W. P. Reinhardt, S. L. Rolston, B. I. Schneider, and W. D. Phillips, Science **287**, 97 (2000).
[12] J. Kasprzak, M. Richard, S. Kundermann, A. Baas, P. Jeambrun, J. M. J. Keeling, F. M. Marchetti, M. H. Szymańska, R. André, J. L. Staehli, V. Savona, P. B. Littlewood, B. Deveaud, and L. S. Dang, Nature **443**, 409 (2006).
[13] A. Amo, J. Lefrère, S. Pigeon, C. Adrados, C. Ciuti, I. Carusotto, R. Houdré, E. Giacobino, and A. Bramati, Nature Physics **5**, 805 (2009).
[14] A. Amo, D. Sanvitto, F. P. Laussy, D. Ballarini, E. d. Valle, M. D. Martin, A. Lemaître, J. Bloch, D. N. Krizhanovskii, M. S. Skolnick, C. Tejedor, and L. Viña, Nature **457**, 291 (2009).
[15] A. Amo, S. Pigeon, D. Sanvitto, V. G. Sala, R. Hivet, I. Carusotto, F. Pisanello, G. Leménager, R. Houdré, E. Giacobino, C. Ciuti, and A. Bramati, Science **332**, 1167 (2011).
[16] G. Grosso, G. Nardin, F. Morier-Genoud, Y. Léger, and B. Deveaud-Plédran, Phys. Rev. Lett. **107**, 245301 (2011).
[17] G. Grosso, G. Nardin, F. Morier-Genoud, Y. Léger, and B. Deveaud-Plédran, Phys. Rev. B **86**, 020509 (2012).
[18] B. Deveaud, G. Nardin, G. Grosso, and Y. Léger, in *Physics of Quantum Fluids*, Springer Series in Solid-State Sciences, Vol. 177, edited by A. Bramati and M. Modugno (Springer Berlin Heidelberg, 2013) pp. 99–126.
[19] R. Hivet, H. Flayac, D. D. Solnyshkov, D. Tanese, T. Boulier, D. Andreoli, E. Giacobino, J. Bloch, A. Bramati, G. Malpuech, and A. Amo, Nature Physics **8**, 724 (2012).
[20] *See Supplemental Material [url], which includes Refs. [21-24].*
[21] [First reference in Supplemental Material not already in Letter] G. A. El, A. Gammal, and A. M. Kamchatnov, Phys. Rev. Lett. **97**, 180405 (2006).
[22] M. Segev, Opt. Photon. News **13**, 27 (2002).
[23] A. D. Jackson, G. M. Kavoulakis, and C. J. Pethick, Phys. Rev. A **58**, 2417 (1998).
[24] W. Langbein, Phys. Rev. B **70**, 205301 (2004) [Last reference in Supplemental Material not already in Letter].
[25] H. Deng, G. Weihs, D. Snoke, J. Bloch, and Y. Yamamoto, Proceedings of the National Academy of Sciences **100**, 15318 (2003), http://www.pnas.org/content/100/26/15318.full.pdf+html.
[26] S. Pigeon, I. Carusotto, and C. Ciuti, Phys. Rev. B **83**, 144513 (2011).
[27] J. Zajac, W. Langbein, M. Hugues, and M. Hopkinson, Phys. Rev. B **85** (2012), 10.1103/PhysRevB.85.165309.
[28] J. Zajac and W. Langbein, Phys. Rev. B **86** (2012), 10.1103/PhysRevB.86.195401.
[29] K. Fujiwara, K. Kanamoto, Y. Ohta, Y. Tokuda, and T. Nakayama, Journal of Crystal Growth **80**, 104 (1987).
[30] N. Chand and S. Chu, Journal of Crystal Growth **104**, 485 (1990).
[31] E. Hecht and A. Zajac, *Optics* (Addison-Wesley, 1982).
[32] M. V. Berry, *Huygens' Principle 1690-1990: Theory and Applications*, 1992nd ed. (Elsevier Science Publishers B.V., Amsterdam, 1992) pp. 97–111.
[33] M. V. Berry, J. F. Nye, and F. J. Wright, Philosophical Transactions of the Royal Society of London. Series A, Mathematical and Physical Sciences **291**, 453 (1979), ArticleType: research-article / Full publication date: Apr. 12, 1979 / Copyright © 1979 The Royal Society.
[34] S. V. P. Senthilkumaran, Opt Commun **283**, 2767 (2010).
[35] G. Ruben and D. M. Paganin, Phys. Rev. E **75**, 066613 (2007).
[36] G. Tosi, G. Christmann, N. G. Berloff, P. Tsotsis, T. Gao, Z. Hatzopoulos, P. G. Savvidis, and J. J. Baumberg, Nat Phys **8**, 190 (2012).
[37] H. Flayac, D. Solnyshkov, and G. Malpuech, Phys. Rev. B (2011), 10.1103/PhysRevB.83.193305, h. Flayac, D. D. Solnyshkov, and G. Malpuech, Phys. Rev. B 83, 193305 (2011).
[38] G. Panzarini, L. C. Andreani, A. Armitage, D. Baxter, M. S. Skolnick, V. N. Astratov, J. S. Roberts, A. V. Kavokin, M. R. Vladimirova, and M. A. Kaliteevski, Phys. Rev. B **59**, 5082 (1999).
[39] A. Kavokin, G. Malpuech, and M. Glazov, Phys. Rev. Lett. **95**, 136601 (2005).
[40] C. Leyder, M. Romanelli, J. P. Karr, E. Giacobino, T. C. H. Liew, M. M. Glazov, A. V. Kavokin, G. Malpuech, and A. Bramati, Nature Physics **3**, 628 (2007).
[41] M. Maragkou, C. E. Richards, T. Ostatnický, A. J. D. Grundy, J. Zajac, M. Hugues, W. Langbein, and P. G. Lagoudakis, Opt. Lett. **36**, 1095 (2011).

[P20] supplement

Supplementary Information

S1. EXPERIMENTAL SETUP

The investigated sample is a λ bulk GaAs microcavity surrounded by 27 (top) and 24 (bottom) distributed GaAs/AlAs Bragg reflector pairs (DBRs). The sample is held in a cold-finger cryostat at a temperature of 15 K and is illuminated by a narrow linewidth ($\approx$ 30 kHz) single-mode continuous wave Ti:Sapphire laser, tuned to cavity resonance at (1.485 eV).

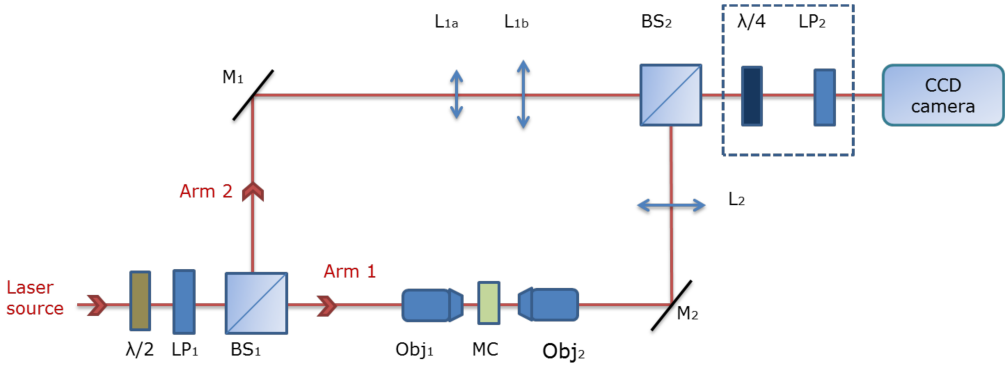

Figure **S1**. Sketch of the Mach-Zehnder interferometer used in the experiments. List of the optical components: BS_1 and BS_2 are non-polarizing beam splitters; M_1 and M_2 are mirrors; Obj_1 is the excitation objective with a 20x magnification and 0.4 numerical aperture; Obj_2 is the objective used for collection of the transmitted beam, with 10x magnification and 0.25 numerical aperture; L_{1a}, L_{1b} and L_2 are convex lenses; $\lambda/4$ and LP_2 are respectively the quarter-wave plate and the linear polarizer used to measure the circular Stokes parameters while $\lambda/2$ and LP_1 are respectively a half-wave plate and a linear polarizer used to control the excitation power. The optical elements enclosed in dashed box ($\lambda/4$ and LP_2) are introduced in the setup only in the case of polarization measurements (i.e. half-soliton like features) corresponding to Fig. 3 (a-d) of the manuscript.

The data reported in the manuscript have been acquired by using the experimental setup represented in Fig. S1. The optical elements enclosed in the dashed box ($\lambda/4$ and LP_2) are introduced in the setup only in the case of polarization measurements (i.e. half-soliton like features) corresponding to Fig. 3 (a-d) of the manuscript. The intensity measurements have been performed in transmission configuration, by blocking Arm 2 of the interferometer. The phase, on the other hand, is acquired using both Arm 1 and Arm 2. In this arrangement the setup correspond to a Mach-Zehnder interferometer, in which a laser is split into two arms: one is used to excite the sample (Arm 1), while the other with a flat phase is used as the reference (Arm 2). The excitation beam (Arm 1) is focused by a 0.4 NA microscope objective to a spot on the sample with a full width at half maximum (FWHM) $2\sqrt{ln\ 2}\sigma$ of 3 μm, resulting in a circular distribution in momentum space (i.e. k-space) with a diameter of 3 μm^{-1}. The light transmitted through the sample is then collected using a 0.25 NA microscope objective and focused on a charge-coupled device (CCD) camera by a convex lens (L_2). In this way, the transmitted beam is imaged in real space. The reference beam (Arm 2) is expanded by a telescope (formed by L_1a and L_1b in Fig. S1) so that a bigger area of the sample could be investigated and then interfered with the transmitted beam on the CCD camera. The incidence angle of the reference beam was adjusted in order to obtain interference fringes along y. The power of the excitation beam is adjusted by means of a half-wave plate ($\lambda/2$) and a linear polarizer (LP_1).

Polarization measurements. The investigation of half-soliton features, shown in Fig. 3 (a-d) of the manuscript, requires a polarization-resolved measurement. To this end we use a linear polarizer (LP_1) to prepare the excitation beam in the linearly polarized basis (parallel to the y-axis in Fig. 3 of the manuscript) and we introduce in the setup a polarimeter composed by a quarter-wave plate ($\lambda/4$) and a linear-polarizer (LP_2), oriented at 45° with respect to one another, to measure the circular Stokes parameter of the transmitted signal. In this way, by rotating the wave-plate it is possible to select the component of the Stokes parameter of which one wants to measure the relative intensity.

Then, using

$$S_c = \frac{I_{\sigma_+} - I_{\sigma_-}}{I_{\sigma_+} + I_{\sigma_-}}$$

with the measured intensities I_{σ_+} and I_{σ_-} of the two circularly polarized components, we calculate the circular component of the Stokes vector (Fig. 4 (a) of the manuscript).

Fig. **S2** shows a sketch of the linear wave dynamics in the x-y-plane of the microcavity. The polaritons propagate along the positive direction of the y-axis and are scattered by a circular defect giving rise phase singularities at points where the amplitude vanishes, i.e. at the dark notches of the intensity profile. The total detected polariton field is given by the interference of the incoming wave and the scattered wave.

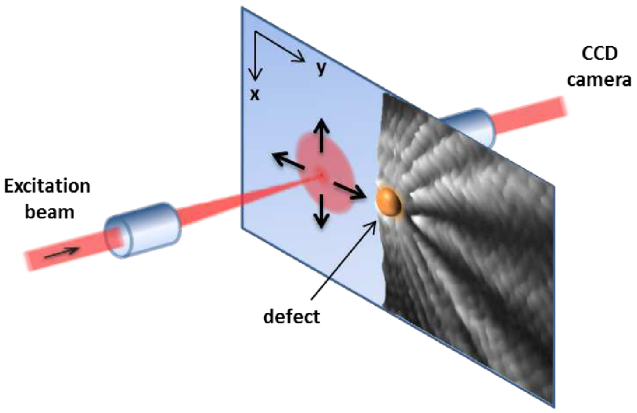

Figure **S2**. Sketch of the linear wave dynamics in the x-y-plane of the microcavity.

S2. POWER DEPENDENCE MEASUREMENTS AND CALCULATION OF THE POLARITON DENSITY AND RENORMALIZATION

In this section we demonstrate that the two "dark-soliton fingerprints" do not depend on the excitation power or on the shape of the excitation beam.

Power dependence with half-Gaussian excitation beam. To verify the linear regime, we studied the excitation density dependence of our results by performing power dependent measurements with both Gaussian and half-Gaussian excitation beams. In both cases we do not observe any significant dependence on the excitation power.

In Fig. **S3** we show the data acquired with a half-Gaussian excitation beam, focused to a spot with FWHM of 3.5 μm (see Fig. **S3** e), 90 μm away from the defect. Here we vary the excitation power by 5 orders of magnitude, from 20 mW (Fig. **S3** a,b) to 400 nW (Fig. **S3** c,d) and do not observe significant changes in the spatial structure. Two notches in intensity together with phase vortex lines in the interferograms appear in the linear regime as the result of the scattering and interference. This is confirmed by the intensity profile and by the FWHM calculated for the left dark-notches in Fig. **S3** a) and Fig. **S3** c), which is respectively 4.2 $\pm$ 0.5 at 20 mW and 3.7 $\pm$ 1 at 400 nW (see Fig. **S3** f).

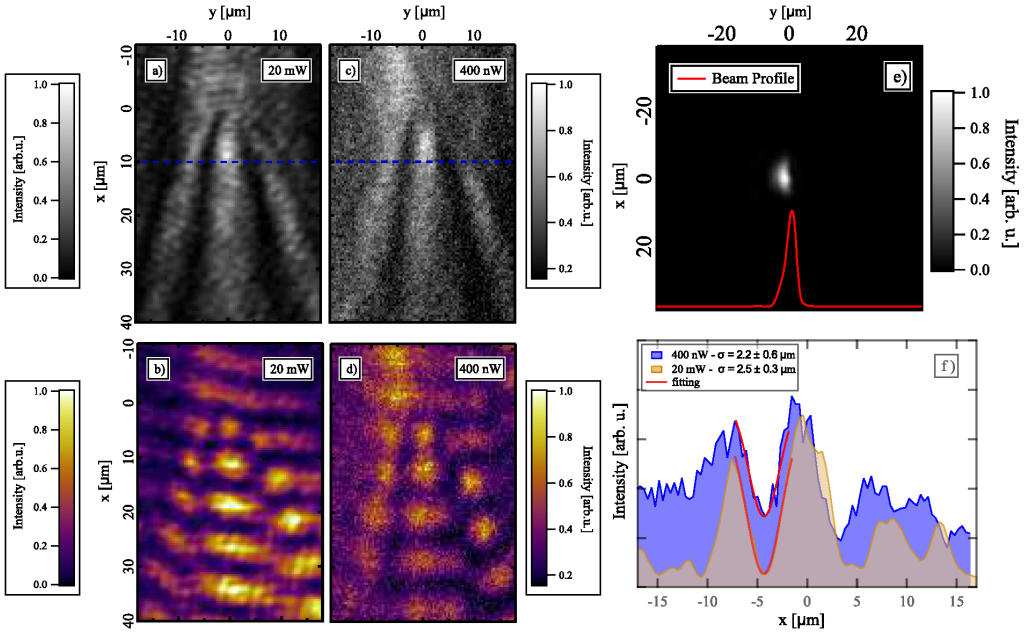

Figure **S3**. Experimental real space intensity (a), (c) and interference patterns (b), (d) acquired at 20 mW and 400 nW excitation power. Fig. (c) and (d) have been plotted with an offset of 0.16 (i.e. saturated at low intensities) for the purpose of the illustration. (e) Half-Gaussian excitation spot. (f) Intensity profiles calculated along the dashed blue lines in a) and c), 10 μm away from the defect. The red line represents the inverse Gaussian fitting used to calculate the FWHM of the left dark-notches in Fig. a) and c). The σ of the two fitting used for the calculation of the FWHM $2\sqrt{ln\ 2}\sigma$ are also reported in the legend. The 400 nW profile (blue) reported in Fig. e) has been shifted on the left by about 1 μm respect to his original position for clarity purposes.

The half-Gaussian beam was created by a confocal excitation scheme as described in the supplementary information of Ref. [1]. In this scheme, a razor blade is placed between two lenses (at a distance equal to the focal lengths of the lenses) before the excitation objective (Obj_1 in Fig. **S1**). The first lens focuses the laser on a razor blade while the second collimates the image of the razor blade on the sample. In this way, by adjusting the position of the razor blade it is possible to shape the excitation beam with a half-Gaussian profile (Fig. **S3** e). Fig. **S3** shows the data acquired with this scheme. Also in this case, as in the case of a Gaussian excitation beam (Fig. 1, 2, 3, 4 of the main manuscript and Fig. **S4**, **S8**, **S9** of the supplementary information), we observe the formation of the two "dark-soliton fingerprints".

In the microcavity polariton literature, the observation of dark-solitons has been claimed using both a Gaussian excitation beam [1, 2] and half-Gaussian excitation beam [1, 3]. We have used both excitation shapes and find that they do not affect the observed structure significantly.

Polariton density. The polariton density inside the cavity has been estimated from the number of photons transmitted through the sample and detected on the CCD camera. For a microcavity, in fact, the polariton population is proportional to the detected intensity. At the lowest excitation density of $3.8\,\mathrm{W/cm^2}$, the polariton density inside the microcavity is estimated to be $D_{pol} = 2.3 \times 10^2\,\mathrm{cm^{-2}}$, seven orders of magnitude lower than the lasing threshold observed in standard microcavities [4]. The density of polaritons have been estimated by using the following formula:

$$D_{pol} = \Phi_{hv} \times \tau, \tag{1}$$

where $\Phi_{hv} = 2.3 \times 10^{13}\,\mathrm{cm^{-2}\ s^{-1}}$ is the flux of photons transmitted through the sample and $\tau = 10\ ps$ is the polariton lifetime. The flux of photons Φ_{hv} has been calculated as:

$$\Phi_{hv} = \frac{C_{px} \times \alpha_{phe}}{t \times QE \times\ A_{px} \times \eta_{obj} \times \eta_{lens}}, \tag{2}$$

where $C_{px} = 7186$ is the maximum pixel counts corrected for the background, $\alpha_{phe} = 7.3$ is the number of photoelectrons per count (determined from the shot-noise), $t = 10\,\mathrm{s}$ is the integration time, $QE = 0.3$ is the quantum efficiency of the CCD camera at the wavelength used in the experiment and $A_{px} = 0.1225\ \mu\mathrm{m^2}$ is the real-space area of a single CCD pixel on the sample, $\eta_{obj} = 0.7$ and $\eta_{lens} = 0.9$ are the assumed intensity transmission factors due respectively to the objective (Obj_2) and the lens (L_2) used in the experiment (see Fig. **S1**).

The investigated sample has a large negative detuning of -29 meV of the cavity photon mode from the exciton resonance (1.514 eV), resulting in an exciton fraction of the polariton mode of less than 1%. The interaction energy scales with the excitonic content, and can be estimated using Eq. (9) in [5]. For the highest density used ($1.1 \times 10^8\,\mathrm{cm^{-2}}$), we find a renormalization energy of 33 neV, using the bulk exciton binding energy of 4.2 meV, a Rabi splitting of 5 meV, the bulk GaAs exciton Bohr radius of 14 nm, and an excitonic fraction of 1%. The parameters used here are approximate values, and the resulting renormalization is an order of magnitude estimate. However, since it is three orders of magnitude lower than the polariton linewidth, it is sufficiently accurate to predict that it has a negligible effect on the polariton dynamics, consistent with the experimental observation.

S3. ENERGY DEPENDENT MEASUREMENTS FOR A DIFFERENT DEFECT

In this section we demonstrate that the disappearance of the two "dark-soliton fingerprints" with detuning can be observed for different defects, and can be considered a typical behaviour.

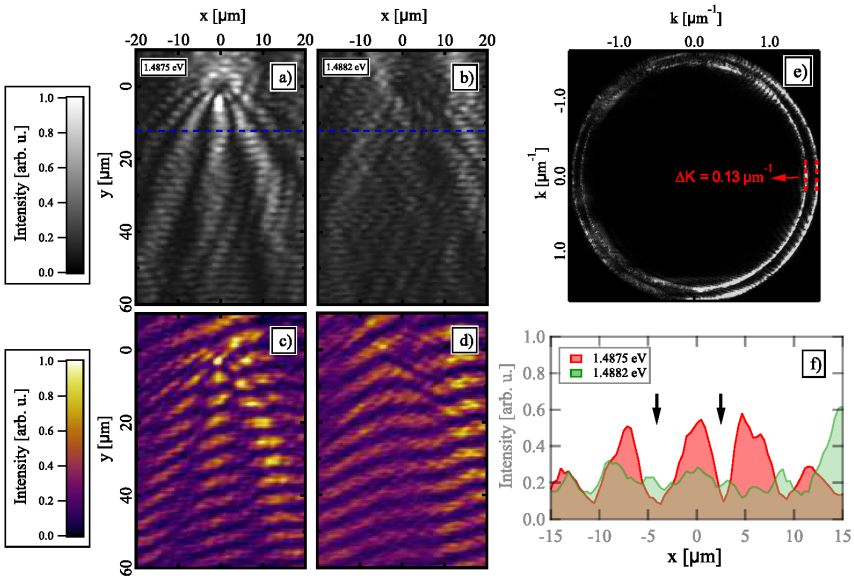

Figure **S4**. Experimental real space intensity (a), (b) and interference patterns (c), (d) showing the appearance (at 1.4875 eV) and disappearance (at 1.4882 eV) of both dark notches and phase shifts when the energy of the excitation beam is increased. In this case the excitation spot is focused 50 μm away from the defect. (e) Experimental K-space images showing the increase of polariton wavevector with the increase of the energy. The ΔK measured is 0.13 μm^{-1}. (f) Intensity profiles calculated along the blue dashed line, 12 μm away from the defect confirm the disappearance of the features (green profile). The two arrows indicate the positions of the soliton-like features.

By using the same experimental setup described in section S1, we study the scattering of polaritons from various defects and observe the appearance/disappearance of the soliton-like features when the energy of the excitation beam and consequently the wavevector of polaritons is varied. Depending on the defect, different variation of the polariton wavevector is needed in order to observe the transition. The increase/decrease of the polariton wavevector changes the interference condition of the polaritons scattered by the defect so that both the dark-notches and the phase dislocations disappear. In the case of Fig. **S4**, the dark-soliton-like features disappear when the energy of the the excitation beam is increased by 0.7 meV, which corresponds to an increase of the wavevector of 0.13 μm^{-1}, as shown in Fig. **S4** e). The disappearance of the dark-notches is confirmed by the intensity profiles extracted 12 μm away from the defect (Fig. **S4** f). We have investigated several defects and found that the same transition could be observed by decreasing the wave vector of the propagating polariton mode since also in this case the interference condition changes.

S4. EVALUATION OF THE DARK-SOLITON CONDITIONS FOR MEASUREMENTS IN THE LINEAR REGIME

Since the first observation of dark-solitons in atomic Bose-Einstein condensates (BECs) [6], the soliton speed (v_s) has been expressed in terms of either the phase shift ($0 < \delta < \pi$) or the soliton depth (n_s), the latter being the difference between the density of the condensate (n) and the density at the bottom of the notches (n_d):

$$\frac{v_s}{c_s} = \cos\ \frac{\delta}{2} = \sqrt{1-\frac{n_s}{n}} \tag{3}$$

In the above formula, c_s represents the speed of sound in the BEC, which is directly proportional to the density of the condensate [6]. Equation 3 dictates the conditions that have to be satisfied in order to identify dark-solitons in BECs. In particular, when δ tends to π:

1. $\frac{n_s}{n} \to 1$, i.e. the dark-soliton becomes deeper ($n_s = n_d$)
2. $\frac{v_s}{c_s} \to 0$, i.e. the velocity of the dark-solitons tends to zero.

Furthermore, due to the repulsive interactions within the BEC, the width of the dark-soliton tends to the healing length ξ of the condensate [6, 7]:

$$\xi \to \left(\frac{2nMg}{\hbar^2}\right)^{-1/2}.$$

Here M is the atomic mass, g is the atom-atom interaction and $\hbar$ is the Planck constant divided by 2π.

As in the atomic BECs, also in the case of polariton condensates equation 3 has been used to identify dark-solitons [1, 2, 8, 9]. However, in all the previous works the healing length condition which is related to the width of the soliton has been neglected. This aspect will be discussed in the last part of this section.

Here we evaluate the conditions 1 and 2 in the linear regime.

Depth and velocity of the dark-notch. In our case, as for the polariton quantum fluid, dark-notches are characterized by a minimum of the intensity (n_d) at their center compared to the surrounding polaritons (n). Consequently, we can evaluate the depth (n_s) of a dark-notch in the same way as in the quantum fluid case:

$$n_s = n - n_d \tag{4}$$

and calculate the relative depth of the dark-notch ($\frac{n_s}{n}$) at different distances from the defect, where the phase shift δ is close to π.

Fig. **S5** (c) shows the relative depth ($\frac{n_s}{n}$) of the dark-notch for the left notch of Fig. **S5** (a). The depth of the dark-notch has been determined by fitting the line profile of the notch with an inverse Gaussian distribution at different distances from the defect. The intensity of the surrounding polaritons (n) has been estimated from the maximum intensity along the red dotted line in Fig. **S5** (a). The fitting (red line) and the quantities n, n_s and n_d are shown in Fig. **S5** (c).

Similar to the case of a quantum fluid, in our linear system the relative depth of the dark-notch remains approximately constant up to 42 μm as shown in Fig. **S5** (d), which corresponds to a close to π phase shift in the interferogram (Fig. **S5**b). It is worth noticing that the ratio n_s/n oscillates around the mean value of 0.87 and it reaches the max value of 0.91 at 24 μm away from the defect, similar to the critical value of 0.9 reported in the literature [8, 9] for the formation of "vortex streets".

Moreover, at longer distances, at about 50 μm away from the defect we observe a decrease of the relative depth of the dark-notch together with a decrease of the phase shift. In agreement with equation 3, when the dark-notch is deeper (n_s/n tends to one in the equation 3) the ratio v_s/c_s decreases.

These observations show that a similar trend as in the polariton quantum fluid can be observed also in the linear regime.

Equivalent of the Mach number. In the case of a polariton quantum fluid it has been shown that different hydrodynamic regimes are connected to the Mach number (M), which is the ratio between the local flow velocity v_{flow} and the local speed of sound c_s [1, 2, 8, 9]:

$$M = \frac{v_{flow}}{c_s}. \tag{5}$$

Dark-solitons in polariton microcavities have been claimed to appear for $M > 1$, with values depending on the nature of the obstacle [1, 2, 8, 9]. In our linear system there is no sound, i.e. no linear dispersion range. However, we can evaluate the equivalent of the Mach number in our system, namely taking ($\frac{v_{flow}}{c_s}$) from the measured values of n_s/n (Fig. **S5** d) and using the geometrical relation [1, 2, 8, 9]:

$$v_s = v_{flow} \ \sin(\alpha) \tag{6}$$

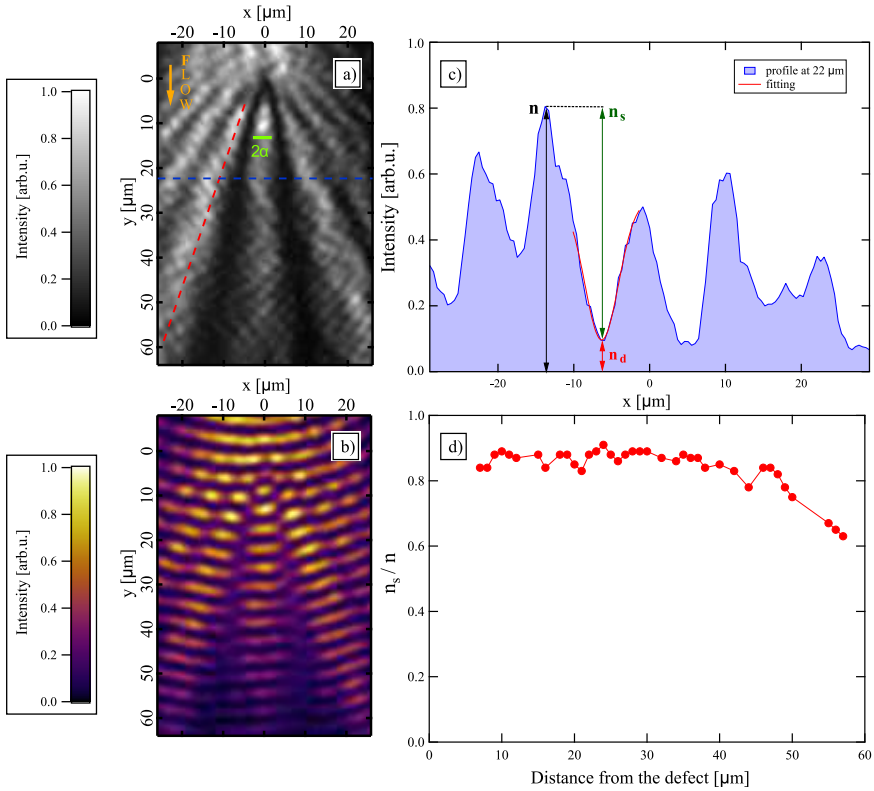

Figure **S5**. Experimental real space intensity (a) and interference (b) patterns showing the two "dark-soliton fingerprints". These images are the same as Fig. 1 (a) and (b) of the main manuscript but plotted over a larger y-axis range. (c) Horizontal intensity profile calculated along the blue dashed line in (a), 22 μm away from the defect. The inverse Gaussian fit is also shown (red line) together with the quantities n (black arrow), n_s (green arrow) and n_d (red arrow). (d) Dark-notch depth ($\frac{n_s}{n}$) calculated from (a) at different distances from the defect. As in the polariton quantum fluid case, the depth of the dark-notch is stable up to 42 μm.

where v_{flow} is the velocity of the polariton flow along the y-direction and α is the aperture angle of the oblique-dark notch with respect to the flow direction. In our case α is measured to be 16.3°.

By combining equations 3, 5 and 6 we can estimate the equivalent M of the quantum fluid case:

$$M = \sqrt{1 - \frac{n_s}{n}}\ \frac{1}{sin(\alpha)} \tag{7}$$

In our case the ratio $\frac{n_s}{n}$ varies between 0.91 and 0.63 (measured respectively at 24 μm and 57 μm from the defect (see Fig. **S5** d), which corresponds to a variation of M from a minimum value of 1.07 to a maximum value of 2.17. Dark-solitons have been predicted to appear in polariton microcavities when $M \geq 1.02$ [10]. This analysis shows show that the condition on the Mach number to observe dark-solitons can be satisfied along the whole path of the dark-notch in the linear regime.

Therefore, $M > 1$ together with the constant relative depth of the dark-notch ($\frac{n_s}{n}$) and related phase shifts in the interferograms are conditions necessary but not sufficient to identify dark-solitons, since these conditions can be observed also in the linear regime.

Healing length condition. Equation 3, initially proposed for atomic BECs [6], has been used also in polariton microcavities to identify dark-solitons [1, 2, 8, 9]. However, in all the previous works, the healing length condition

which is related to the width of the soliton has been neglected even though it represents a direct application of the definition of a soliton.
A soliton, in fact, is a solitary wave that preserves its shape while propagating through a dispersive medium [11, 12]. This feature can be considered as universal fingerprints since has been observed in all the physical systems where solitons have been studied [13]. To the best of our knowledge the formation of "oblique" dark-solitons, although predicted for both the atomic [14] and polariton condensates [10], has been experimentally reported only for polariton condensates [1, 2, 8, 9]. On the other hand, in atomic BECs, only single "straight" dark-solitons have been experimentally observed [6].

The above healing length condition specifies that solitons propagating in a condensate of homogeneous density are characterized by a constant width (i.e. non-spreading wave) which is given by the healing length ξ of the condensate [6]. When the excitation density is increased, the FWHM of the dark-notch should scale as $n^{-1/2}$, proportional to the healing length of the condensate.

We compare in Fig. **S6** the measured width of the dark notch in our linear system with the expected scaling $C/n^{1/2}$ using the measured intensity as function of distance. We find that the healing length condition is not respected by this data in the linear regime, indicating that it is suited to discriminate dark solitons from linear propagation. We therefore propose to use the healing length condition to verify dark soliton formation, which should be fulfilled over a range of polariton excitation densities to exclude coincidental matches with specific scattering patterns in linear propagation.

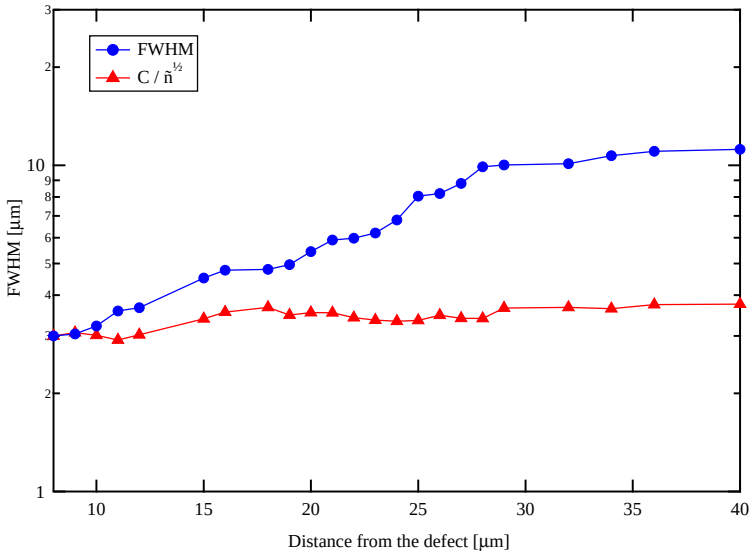

Figure **S6**. The blue circles show the measured FWHM of the left notch in Fig. **S5** a) at different distances from the defect. The red triangles show $C/n^{1/2}$ proportional to the healing length using a suitable chosen constant C. The density n has been calculated by averaging the intensity of the left and right sides of the left dark-notch in Fig. **S5** a).

S5. THEORY FOR THE CAVITY MODE SCATTERING BY A POINT DEFECT

The classical theory of electromagnetism is used in order to calculate the distribution of electric and magnetic fields inside the cavity in the presence of a disk-shaped defect and illumination of the cavity by a monochromatic laser beam. As already mentioned in the manuscript, the choice of such a model is justified by the fact that we operate in the linear regime with a polariton dispersion dominated by the cavity mode. In the model, we consider the propagation of two-dimensional photons with a quadratic dispersion in the microcavity plane, as shown in Fig. **S7**. A quadratic dispersion is found for all planar microcavity polaritons for small in-plane momenta plane. In our case, the large negative detuning provides a large range over which the dispersion is to a good approximation quadratic, covering all the relevant excitation wavevectors used.

The field distribution in a bare cavity obeys Maxwell's equations for the electric field $\boldsymbol{E}(x,y,z,t)$ and magnetic field $\boldsymbol{H}(x,y,z,t)$. Symmetry of the planar cavity allows one to separate the solutions as follows:

$$\boldsymbol{E}(x,y,z,t) = \boldsymbol{E}_\omega(x,y)\chi(z)\exp[-i\omega t]$$
$$\boldsymbol{H}(x,y,z,t) = \boldsymbol{H}_\omega(x,y)\xi(z)\exp[-i\omega t]$$

The subscript ω denotes that the in-plane components of the fields depend on the energy of radiation while the normal components $\chi(z)$ and $\xi(z)$ are independent of energy under consideration of small in-plane wave vector $k_\parallel$:

$$k_\parallel \ll \frac{n_{\mathrm{cav}}\omega}{c}$$

where n_{cav} is the refractive index of material of the cavity and c is the vacuum speed of light. The normal components $\chi(z)$ and $\xi(z)$ of the fields can be estimated inside the cavity where the most of light energy is concentrated: $\chi(z) \propto \xi(z) \propto \cos(n_{\mathrm{cav}}\omega_0 z/c)$ where ω_0 is the cavity resonance frequency at normal incidence. The in-plane wave vector then can be deduced as

$$k_\parallel(\omega) = \frac{n_{\mathrm{cav}}}{c}\sqrt{\omega^2-\omega_0^2}.$$

The cavity defect is given by a change of the Bragg mirror composition by the presence of additional GaAs due to the Ga droplet formation during the growth process [15, 16]. The presence of the defect has the effect to modify the effective thickness of the cavity layer, resulting in a red-shift of the photonic dispersion inside the defect [17]. As a result, the resonance frequency inside the defect shifts from ω_0 to ω_0' with respect to the bare cavity and accordingly the in-plane wave vector $k_\parallel$ to $k_\parallel'$, with $k_\parallel' > k_\parallel$ (Fig. **S6**). The energy shift of the cavity mode represents an attractive potential in the two-dimensional polariton propagation.

Besides the change of the resonance condition, also the normal components of the fields vary the spatial distribution and become $\chi(z) \to \chi'(z)$ and $\xi(z) \to \xi'(z)$. In our model, however, we assume that these changes are small (the relative change of the cavity energy considered in our case is only about 0.1%) and therefore we neglect them. Within this approximation, the solution of the problem of light propagation through a cavity with arbitrarily shaped defect is reduced to the solution solely in the xy plane because boundary conditions are independent of the position on the axis z. First we find two basis sets of solutions of Maxwell's equations for the bare cavity and the perturbed cavity. We denote these sets as $\boldsymbol{E}^{\mathrm{cav}}_{\omega,j,m}$, $\boldsymbol{H}^{\mathrm{cav}}_{\omega,j,m}$ and $\boldsymbol{E}^{\mathrm{def}}_{\omega,j,m}$, $\boldsymbol{H}^{\mathrm{def}}_{\omega,j,m}$ respectively. Here the index j stands for polarization (TE or TM) and m is the discrete index of the mode in the expansion.

The two respective sets of fields defined above are local solutions of Maxwell's equations outside and inside the defect area. In order to solve the whole problem of scattering, we have to find a solution on the boundary between the bare cavity and the defect where the in-plane wave vector is not continuous. Here we assume that the boundary behaves like an ordinary boundary between two dielectrics, i.e. we require continuous tangent components of all fields. Let us write the fields in the bare cavity and in the defect area in the following form:

$$\boldsymbol{E}^{\mathrm{cav}}_\omega = \boldsymbol{E}_{\mathrm{incident}} + \sum_{j,m} c^{\mathrm{cav}}_{j,m}\boldsymbol{E}^{\mathrm{cav}}_{\omega,j,m} \tag{8}$$

$$\boldsymbol{H}^{\mathrm{cav}}_\omega = \boldsymbol{H}_{\mathrm{incident}} + \sum_{j,m} c^{\mathrm{cav}}_{j,m}\boldsymbol{H}^{\mathrm{cav}}_{\omega,j,m} \tag{9}$$

$$\boldsymbol{E}^{\mathrm{def}}_\omega = \sum_{j,m} c^{\mathrm{def}}_{j,m}\boldsymbol{E}^{\mathrm{def}}_{\omega,j,m} \tag{10}$$

$$\boldsymbol{H}^{\mathrm{def}}_\omega = \sum_{j,m} c^{\mathrm{def}}_{j,m}\boldsymbol{H}^{\mathrm{def}}_{\omega,j,m} \tag{11}$$

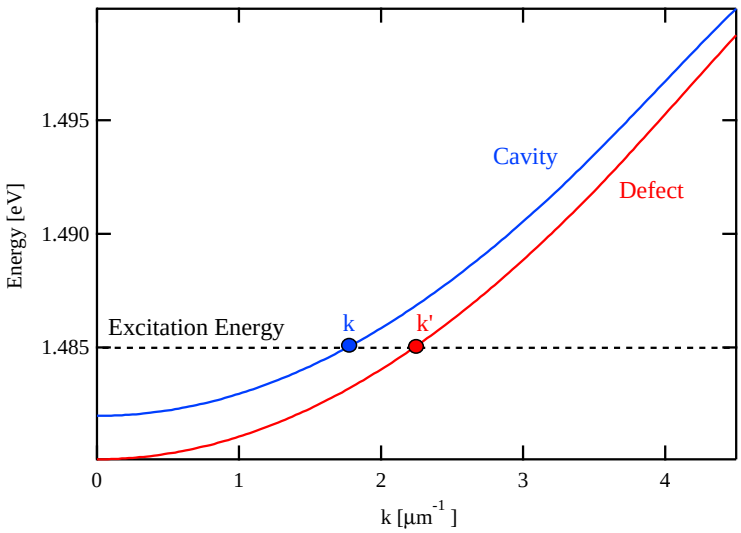

Figure **S7**. Theoretical dispersion inside (red) and outside (blue) the defect. The presence of the defect has the effect to modify the effective thickness of the cavity layer, resulting in a red-shift of the photonic dispersion inside the defect. Consequently, for a fixed energy, the wavevector of the photonic mode in the region of the defect is higher than in the rest of the cavity ($k' > k$). The black dashed line indicate the excitation energy used in the experiment.

The coefficients c^{cav} and c^{def} are finally set so that the boundary conditions are fulfilled. If the basis sets are chosen properly, the solution is unambiguous. For the case of a circular defect, it is convenient to use the basis of fields in cylindrical coordinates [18] whose boundary conditions reduce to simple algebraic equations for the unknown coefficients. Once the coefficients are known, the spatial field distribution is evaluated using the definitions above, performing the summation on right hand side. To include the TE–TM splitting in cylindrical coordinates, it suffices to discriminate between the in-plane wave vectors $k_{\parallel,\mathrm{TE}}$ and $k_{\parallel,\mathrm{TM}}$ and the same inside the defect.

S6. DEPENDENCE OF THE SOLITON-LIKE FEATURES ON THE SCATTERING GEOMETRY

The observed features depend on the shape and size of the defect and the direction and polarization of the incoming polariton wave relative to the defect. For an elliptical defect, the phase and amplitude of the scattering depend on the direction of the incoming wave. Also the polarization contributes to the anisotropy of the effect because for a given absolute polarization direction a different angle of incidence corresponds to a different polarization relative to the defect.

Fig. **S8** shows an example of the beam incident on the defect at an angle in the experiment. We use the same parameters of Fig. 1(c) and Fig. 1(d) of the manuscript to perform the simulations, but we change the direction of the incoming beam. In the previous case (Fig. 1 of the manuscript), the excitation beam is polarized orthogonal to the incidence direction, while in Fig. **S8** the beam direction has a 28 degree angle to its polarization (y), and generates a phase dislocation only in the upper dark line but not in the lower one, as indicated by the arrow in Fig. **S8**(c).

Moreover, we have investigated the case of a larger defect. The number of dark lines increases with increasing defect size, allowing the formation of quadruplet solitons-like features. This is confirmed by the simulations shown in Fig. **S9**(b) and Fig. **S9**(d). Once again we refer to the simulations shown in Fig. 1 of the manuscript to simulate high-order dislocations. In particular, Fig. **S9**(b) and Fig. **S9**(d) have been calculated by using the same parameters as Fig. 1(c) and Fig. 1(d) of the manuscript except for increasing the radius of the defect from $3\,\mu$m to $5\,\mu$m.

In Fig. **S9**(a) and Fig. **S9**(c) the experimental observation of a high order soliton-like features is shown in both intensity and phase. In the case of a bigger defect, it is possible to note how the wave appears to bend around the edges of the defect.

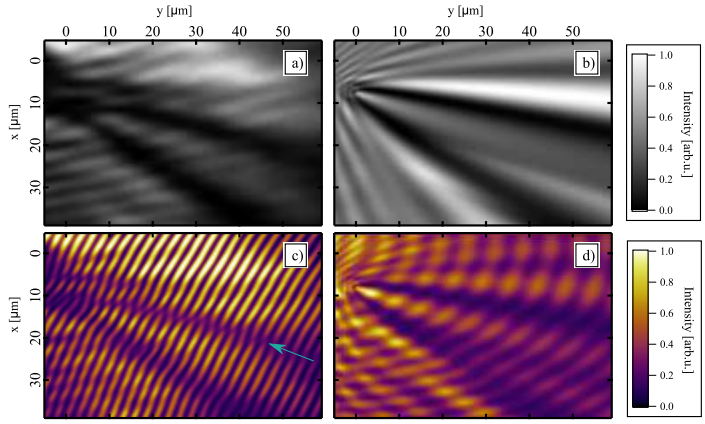

Figure **S8**. Experimental (a),(c) and simulated (b),(d) real-space intensity and interference pattern showing soliton-like fingerprints generated by the interaction of the beam with a defect. Unlike Fig. 1 of the manuscript, the phase shift is only present in correspondence of the upper soliton-like feature as indicated by the light blue arrow in (c).

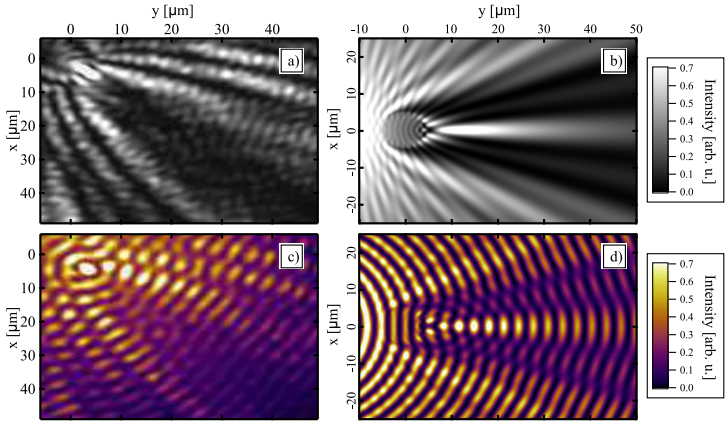

Figure **S9**. Experimental (a),(c) and simulated (b),(d) real-space intensity and interference pattern showing higher-order soliton features generated by the interaction of the beam with a defect bigger than the one present in Fig. 1 of the manuscript.

S7. HALF-SOLITON-LIKE FEATURES CAUSED BY TE-TM SPLITTING

In our simulations a linear y-polarized incoming beam, propagates along the y-direction and is scattered by a defect positioned at 25 μm away from the excitation spot, inducing the formation of two traces propagating in oblique directions. In the case of half-soliton features in the circular polarisation basis, we found that the birefringence in the scattering by the defect is due to the intrinsic TE-TM splitting of the polariton dispersion. This is confirmed by the simulations shown in Fig. **S10** where the scattered field, produced by the wave hitting the defect, is calculated in absence, Fig. **S10**(a), or in presence, Fig. **S10**(b) of the TE-TM splitting. In the latter case we use $\vec{k}_{\parallel L}/\vec{k}_{\parallel T} = 1.004$ which is the same value that has been used in reference [19] for the same sample. In order to simplify the theoretical discussion, we consider the TE-TM splitting constant across the whole cavity including the defect and no additional splitting in the defect is considered.

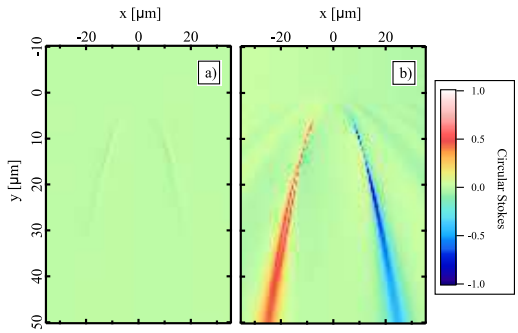

Figure **S10**. Simulated circular Stokes parameters showing half-soliton features. The images have been calculated by considering a beam hitting a circular defect in absence (a) and in presence (b) of the TE-TM splitting.

[1] A. Amo, S. Pigeon, D. Sanvitto, V. G. Sala, R. Hivet, I. Carusotto, F. Pisanello, G. Leménager, R. Houdré, E. Giacobino, C. Ciuti, and A. Bramati, Science **332**, 1167 (2011).
[2] G. Grosso, G. Nardin, F. Morier-Genoud, Y. Léger, and B. Deveaud-Plédran, Physical Review B **86**, 020509 (2012).
[3] R. Hivet, H. Flayac, D. D. Solnyshkov, D. Tanese, T. Boulier, D. Andreoli, E. Giacobino, J. Bloch, A. Bramati, G. Malpuech, and A. Amo, Nature Physics **8**, 724 (2012).
[4] H. Deng, G. Weihs, D. Snoke, J. Bloch, and Y. Yamamoto, Proceedings of the National Academy of Sciences **100**, 15318 (2003), http://www.pnas.org/content/100/26/15318.full.pdf+html.
[5] W. Langbein, Phys. Rev. B **70**, 205301 (2004).
[6] J. Denschlag, J. E. Simsarian, D. L. Feder, C. W. Clark, L. A. Collins, J. Cubizolles, L. Deng, E. W. Hagley, K. Helmerson, W. P. Reinhardt, S. L. Rolston, B. I. Schneider, and W. D. Phillips, Science **287**, 97 (2000).
[7] A. D. Jackson, G. M. Kavoulakis, and C. J. Pethick, Phys. Rev. A **58**, 2417 (1998).
[8] G. Grosso, G. Nardin, F. Morier-Genoud, Y. Léger, and B. Deveaud-Plédran, Physical Review Letters **107**, 245301 (2011).
[9] B. Deveaud, G. Nardin, G. Grosso, and Y. Léger, in *Physics of Quantum Fluids*, Springer Series in Solid-State Sciences, Vol. 177, edited by A. Bramati and M. Modugno (Springer Berlin Heidelberg, 2013) pp. 99–126.
[10] S. Pigeon, I. Carusotto, and C. Ciuti, Physical Review B **83**, 144513 (2011).
[11] G. I. Stegeman and M. Segev, Science **286**, 1518 (1999).
[12] M. Segev and G. Stegeman, Physics Today **51**, 42 (1998).
[13] M. Segev, Opt. Photon. News **13**, 27 (2002).
[14] G. A. El, A. Gammal, and A. M. Kamchatnov, Phys. Rev. Lett. **97**, 180405 (2006).
[15] K. Fujiwara, K. Kanamoto, Y. Ohta, Y. Tokuda, and T. Nakayama, Journal of Crystal Growth **80**, 104 (1987).
[16] N. Chand and S. Chu, Journal of Crystal Growth **104**, 485 (1990).
[17] J. Zajac, Physical Review B **86** (2012), 10.1103/PhysRevB.86.195401.
[18] A. W. Snyder and L. J. D., *Optical Waveguide Theory* (Chapman and Hall, 1983).
[19] M. Maragkou, C. E. Richards, T. Ostatnický, A. J. D. Grundy, J. Zajac, M. Hugues, W. Langbein, and P. G. Lagoudakis, Optics Letters **36**, 1095 (2011).